

GALVANIC CORROSION

Harvey P. Hack, *editor*

STP 978



STP 978

Galvanic Corrosion

Harvey P. Hack, editor



ASTM
1916 Race Street
Philadelphia, PA 11103

Library of Congress Cataloging-in-Publication Data

Galvanic corrosion/Harvey P. Hack, editor.
(STP; 978)

"The symposium on galvanic corrosion was presented at Phoenix, AZ, on 3-4 Nov. 1986. ASTM Committee G-1 on Corrosion of Metals sponsored the symposium"—Foreword.

"ASTM publication code number (PCN) 04-978000-27."

Includes bibliographies and index.

ISBN 0-8031-0981-4

I. Electrolytic corrosion—Congresses. I. Hack, Harvey P.
II. American Society for Testing and Materials. Committee G-1 on Corrosion of Metals. III. Series: ASTM special technical publication; 978.

TA462.G35 1988

620.1'623—dc19

88-19029
CIP

Copyright © by AMERICAN SOCIETY FOR TESTING AND MATERIALS 1988

NOTE

The Society is not responsible, as a body,
for the statements and opinions
advanced in this publication.

Peer Review Policy

Each paper published in this volume was evaluated by three peer reviewers. The authors addressed all of the reviewers' comments to the satisfaction of both the technical editor(s) and the ASTM Committee on Publications.

The quality of the papers in this publication reflects not only the obvious efforts of the authors and the technical editor(s), but also the work of these peer reviewers. The ASTM Committee on Publications acknowledges with appreciation their dedication and contribution of time and effort on behalf of ASTM.

Foreword

The symposium on Galvanic Corrosion was presented at Phoenix, AZ, on 3-4 Nov. 1986. ASTM Committee G-1 on Corrosion of Metals sponsored the symposium. Harvey P. Hack, David Taylor Naval Ship R&D Center, served as chairman of the symposium and editor of the resulting publication.

Contents

Overview	1
-----------------	---

THEORY

Electrochemical Theory of Galvanic Corrosion—JOHN W. OLDFIELD	5
Galvanic Corrosion Caused by Corrosion Products—S. MARK WILHELM	23
Hydrogen Embrittlement of Plated High-Strength 4340 Steel by Galvanic Corrosion—WILLIAM J. POLLOCK AND BRUCE R. W. HINTON	35

COMPUTER PREDICTION

Use of the Microcomputer for Calculation of the Distribution of Galvanic Corrosion and Cathodic Protection in Seawater Systems—DAVID J. ASTLEY	53
Galvanic Corrosion Prediction and Experiments Assisted by Numerical Analysis—JOHN W. FU	79
Computer Modelling of Galvanic Corrosion—ROBERT A. ADEY AND SEYYED M. NIKU	96
Comparisons of Localized Ionic Currents as Measured from 1-D and 3-D Vibrating Probes with Finite-Element Predictions for an Iron-Copper Galvanic Couple—ROLF G. KASPER AND C. ROBERT CROWE	118
Prediction of Tube-Tubesheet Galvanic Corrosion Using Finite Element and Wagner Number Analyses—JOHN R. SCULLY AND HARVEY P. HACK	136

TESTING AND CONTROL

Quantitative Assessment of Atmospheric Galvanic Corrosion—DESMOND P. DOYLE AND T. EDMUND WRIGHT	161
Integration of Galvanic Corrosion Control Technology into Design—JAMES F. JENKINS	174
Controlling Galvanic Corrosion in Soils with Cathodic Protection—JANE M. TURNER	178

ENVIRONMENTS

The Effect of Soil Resistivity and Soil Temperature on the Corrosion of Galvanically Coupled Metals in Soils—EDWARD ESCALANTE	193
--	-----

Evaluation and Prediction of Galvanic Corrosion in Oxidizing Solutions— NARASI SRIDHAR AND JURI KOLTS	203
Galvanic Corrosion of Duplex Fe-Cr-10%Ni Alloys in Reducing Acids— YUNG-HERNG YAU AND MICHAEL A. STREICHER	220
Galvanic Corrosion Resistance of Welded Dissimilar Nickel-Base Alloys— RICHARD A. CORBETT, WILLIAM S. MORRISON, AND ROBERT J. SNYDER	235

INDUSTRIES

Galvanic Corrosion on Automobiles— ROBERT BABOAIN, GARDNER HAYNES, AND ROGER TURCOTTE	249
Galvanic Corrosion in Oil and Gas Production— K. D. EFIRD	260
Avoiding Galvanic Corrosion Problems in the Telephone Cable Plant— GEORGE SCHICK	283
Galvanic Corrosion in Navy Ships— ALASTAIR G. S. MORTON	291
Galvanic Corrosion in Power Plant Condensers— GEORGE A. GEHRING, JR.	301
Experience with Cathodic Protection of Power Plant Condensers Operating with High Performance Ferritic Stainless Steel Tubing— LAWRENCE S. REDMERSKI, JOHN J. ECKENROD, KENNETH E. PINNOW, AND CURTIS W. KOVACH	310
Bimetallic Joints in Multistage Flash Desalination Plants— SALEH G. AL ZAHARANI, B. TODD, AND J. W. OLDFIELD	323

SUPPLEMENTARY ARTICLE ON ENVIRONMENTS

Galvanic Corrosion of Piping and Fitting Alloys in Sulfide-Modified Seawater— HARVEY P. HACK	339
Index	353

Overview

The increasing demands being placed on structures and equipment have led to the requirement to use a mix of materials to obtain the desired performance. Galvanic corrosion is the unfortunate result in many cases. The first Special Technical Publication (STP) containing much galvanic corrosion information was published by ASTM in 1976. Since then, significant progress has been made in the field, particularly in computer prediction and testing for galvanic corrosion, but also in describing the latest computer and testing techniques and summarizing how galvanic corrosion affects various industries. This symposium was held on 3–4 Nov. 1986 in Phoenix, AZ. Most of the papers presented there are included in this volume.

The papers are organized into a format typical of a manual on the subject. Many of the papers are tutorial in nature, starting with the basics and proceeding to the level of detail necessary for full understanding of the subject. The first paper on the electrochemical theory of galvanic corrosion, by Oldfield, is designed to start at an introductory level and build to the most recent developments in electrochemical theory. This is a good introduction for any reader, regardless of background. More specialized theory relating to corrosion products and hydrogen embrittlement follow in the papers by Wilhelm et al. and by Pollock and Hinton. The use of semiconductor theory from solid-state physics to describe the interaction of corrosion products with the base alloy is a new and exciting development in the field. Hydrogen embrittlement is often overlooked as a form of galvanic corrosion, since it occurs on the cathode, but increases in importance as the quest for higher strength materials leads to the use of more hydrogen-sensitive alloys in structures.

Typically, galvanic prediction has been based on the use of galvanic series, galvanic compatibility tables, or on short-term polarization curves. The next set of papers describes newer and better techniques for galvanic corrosion prediction based on the use of computers and long-term data. Computational techniques are discussed first by Astley. These techniques solve the equations of electrical continuity throughout the electrolyte by making assumptions about the geometry and boundary conditions to reduce the problem to a form that is sufficiently simple to be solved directly, or by the use of relatively fast computer routines. This is an extremely valuable technique for specific types of galvanic corrosion problems. For more general analyses, discretization techniques, including finite element analysis, are extremely valuable for making galvanic corrosion predictions. The theory and application of finite element analysis and boundary element analysis are discussed in the papers by Fu and by Adey and Niku. Finally the paper by Scully and Hack ties together the use of finite element analysis and the use of long-term data to show how these techniques work in a real application, that of a heat exchanger configuration.

Testing and preventative techniques make up the next set of papers. Wright and Doyle discuss a standard test technique called the CLIMAT or wire-on-bolt test for galvanic corrosion in the atmosphere. The importance of the interface between designers and corrosion engineers is next detailed by Jenkins, who believes that improved communications at the outset of the design process will prevent a large number of galvanic corrosion problems. Turner discusses a powerful method for prevention of galvanic corrosion called cathodic protection. This technique is widely and successfully utilized, and the paper describes the design process for a cathodic protection installation.

The next group of papers discusses how galvanic corrosion manifests itself in a number of environments of concern. Soil is discussed by Escalante. Here the major concerns are the limited conductivity and variability of the electrolyte. It is interesting to note the effect of minor

2 GALVANIC CORROSION

pollutants can dramatically change galvanic corrosion behavior, as pointed out for seawater in the paper by Hack, which appeared in the *Journal of Testing and Evaluation* (Vol. 8, No. 2, March 1980, pp. 74-79). The strong influence of minor constituents in the electrolyte on galvanic corrosion has received too little consideration in the literature. More sophisticated interpretation of polarization curves is necessary in some environments, as shown for highly corrosive fluids in the paper by Sridhar and Kolts. Galvanic corrosion in reducing acids is next discussed by Streicher and Yau. The last paper by Corbett et al. is an example of a well-designed test in a less typical environment. Although galvanic corrosion was found to not be a concern, the systematic approach to exploring the possibility is a good example for all to follow.

The last papers are summaries of the galvanic corrosion problems experienced in a variety of industries. They include for each industry problem areas where galvanic corrosion had been found to occur, including examples, and typical preventative measures. The paper by Baboian et al. describes galvanic corrosion in automobiles, where interaction with trim can lead to problems and cladding can lead to solutions to problems. The next paper by Efird is a comprehensive treatment of the subject of galvanic corrosion in the oil and gas production industry. Useful data to aid in making predictions are included in this paper. Galvanic corrosion in the telephone communications industry is discussed by Schick. Shipbuilding is next addressed by Morton, who discusses the areas of ships where problems can occur, and what is typically done to prevent them. Galvanic corrosion on components in power plants is discussed in the papers by Gehring, and also by Redmerski et al. Finally, galvanic corrosion is a significant problem in desalination plants, as noted by Zaharani et al.

The variety and depth of these papers should make this book a valuable reference tool for anyone in any industry who may have concerns about galvanic corrosion. Supplemental material may be found in *Galvanic and Pitting Corrosion—Field and Laboratory Studies (STP 576)* and in several standard guides and test methods concerning galvanic corrosion published in Volume 03.02 of the *Annual Book of ASTM Standards*.

Harvey P. Hack

David Taylor Naval Research Center, Bethesda, MD; symposium chairman and editor.

Theory

Electrochemical Theory of Galvanic Corrosion

REFERENCE: Oldfield, J. W., "Electrochemical Theory of Galvanic Corrosion," *Galvanic Corrosion, ASTM STP 978*, H. P. Hack, Ed., American Society for Testing and Materials, Philadelphia, 1988, pp. 5-22.

ABSTRACT: Galvanic corrosion can be defined simply as that corrosion that occurs as a result of one metal being in electrical contact with another in a conducting corrosive environment. The corrosion is stimulated by the potential difference that exists between the two metals, the more noble material acting as a cathode where some oxidizing species is reduced, the more active metal, which corrodes, acting as the anode. To fully understand this process it is first necessary to understand the basic thermodynamics and kinetics of electrochemical reactions. These are considered with particular reference to exchange current densities and the factors that control them, linear and Tafel kinetics, concentration and mass transfer effects, and mixed potential theory. The practical side of galvanic corrosion and its relationship to electrochemical parameters is considered with particular reference to the most important cathodic processes, that is, oxygen reduction and hydrogen evolution, as they occur on engineering materials, for example, steel, stainless steel, copper base alloys, and so forth and to the general form of the anodic processes that occur. Finally the use of galvanic series as a predictive tool is discussed. In addition methods used to model galvanic situations with the aim of predicting corrosion are briefly mentioned and their advantages and limitations outlined.

KEY WORDS: galvanic corrosion, mixed potentials, galvanic series, mathematical modelling, oxygen reduction, hydrogen evolution, electrochemical theory

Galvanic corrosion can simply be defined as the corrosion that occurs as a result of one metal being in contact with another in a conducting, corrosive environment. The corrosion is stimulated by the potential difference that exists between the two metals, the more noble material acting as a cathode where some oxidizing species is reduced, the more active metal, which corrodes, acting as the anode.

The anodic reaction is, by definition, some form of metal dissolution; the cathodic reaction is, in the majority of practical situations, either oxygen reduction or hydrogen evolution, or a combination of both. There are situations however where other oxidizing species can play a part, for example, chlorine in chlorinated systems, the presence of ferric ions in solution, and so on.

In this paper these reactions are considered from an electrochemical viewpoint, and the major parameters determining their rates are highlighted. Their interaction on a single metal is examined, and how this relates to the bimetallic situation is reviewed.

The practical aspects of galvanic corrosion and how they relate to electrochemical parameters are considered with particular reference to the most important cathodic processes occurring on the more important engineering materials. The general form of the anodic reactions are also noted.

Finally, the use of the galvanic series as a predictive tool is discussed and methods used to model galvanic situations with the aim of predicting corrosion are briefly mentioned and their advantages and limitations outlined.

¹Manager of corrosion, Cortest Laboratories Ltd., Shepherd St., Sheffield S3 7BA, United Kingdom.

6 GALVANIC CORROSION

Electrochemical Theory

Thermodynamics of Electrode Reactions

Consider the simple electrode reaction under equilibrium conditions



where O is the oxidized species, R the reduced species, and n the number of electrons associated with the reaction.

If all the components of the reaction are in the standard state, that is, the electrolyte solution has unit activities of all ions that determine the electrochemical potentials and the gases have a pressure of one atmosphere, then the standard electrode potential for the reaction is defined by [1]

$$E^\circ = -\Delta G^\circ/nF \quad (2)$$

where ΔG° is the Gibbs free energy for the reaction.

The electrode potential under nonstandard conditions is given by

$$E = E^\circ - \frac{RT}{nF} \ln \frac{C(R)}{C(O)} \quad (3)$$

where $C(R)$ and $C(O)$ represent the activities of R and O , respectively.

Equation 3 is the Nernst equation, used to describe the potential variation of electrode reactions at equilibrium.

Kinetics of Electrode Reactions

Again consider Reaction 1, but this time under nonequilibrium conditions.

When a reaction current i flows at an electrode, there are in fact two opposing currents, one anodic $i(a)$ and one cathodic $i(c)$ of which i is the resultant. Thus

$$i = i(c) - i(a) \quad (4)$$

At equilibrium, when no resultant current flows

$$i_o = i(c) = i(a) \quad (5)$$

where i_o is called the exchange current.

The relationship between current and potential for Reaction 1 in the absence of mass transfer effects is given by

$$i = i_o \left[\exp\left(-\frac{\alpha nF\eta}{RT}\right) - \exp\left(\frac{(1-\alpha)nF\eta}{RT}\right) \right] \quad (6)$$

where α is the transfer coefficient, η is the overvoltage, and F , R , and T have their usual meaning.

The exchange current density is given by

$$i_o = nFk_o C(O)_o^\alpha C(R)_o^{1-\alpha} \quad (7)$$

where $C(O)_s$ and $C(R)_s$ represent the activities of O and R at the electrode surface at equilibrium and where k_o is the reaction rate constant in metres per second (m/s).

The current-overvoltage variation described by Eq 6 is illustrated graphically in Fig. 1 by plotting the parameter i/i_o against $\alpha nF\eta/RT$.

Equation 6 is usually simplified at high overvoltages, where the reverse reaction current can be neglected, to the well known Tafel equation, namely

$$\log i = \log i_o + \frac{\alpha nF\eta}{2.3RT} \tag{8}$$

At low overvoltages a linear expansion of the exponential terms can be carried out to give

$$i = i_o \frac{nF\eta}{RT} \tag{9}$$

where it has been assumed that $2\alpha = 1$.

The range of validity of these expressions is also illustrated in Fig. 1 where Eqs 8 (Tafel equation) and 9 (linear approximation) are plotted and compared with Eq 6 (Butler, Volmer equation). The linear approximation underestimates the current by 4 and 15% for $\alpha nF\eta/RT$ values of 0.5 and 1, respectively. The Tafel approximation overestimates the current by 5 and 16% for $\alpha nF\eta/RT$ values of 1.5 and 1, respectively.

The influence of mass transfer can be introduced into Eq 6, which then takes the form [2]

$$i = i_o \left[\frac{i_1(a)}{i_1(a) - 1} \exp\left(\frac{-\alpha nF\eta}{RT}\right) - \frac{i_1(c)}{i_1(c) - 1} \exp\left(\frac{(1 - \alpha)nF\eta}{RT}\right) \right] \tag{10}$$

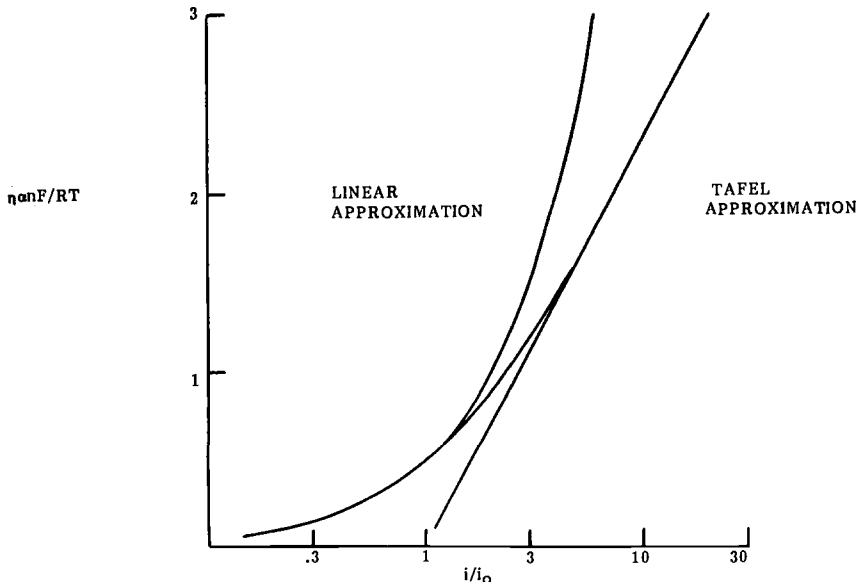


FIG. 1—Graphic representation of the Butler-Volmer equation together with Tafel and linear expansion approximations.

8 GALVANIC CORROSION

where the concentration terms in i_o now refer to the bulk concentrations rather than those at the electrode surface and where $i_1(a)$ and $i_1(c)$ are the anodic and cathodic diffusion limited currents given by

$$i_1(a) = \frac{nFD(R)}{\delta} (C(R)_B - C(R)_S) \quad (11)$$

and

$$i_1(c) = \frac{nFD(O)}{\delta} (C(O)_B - C(O)_S) \quad (12)$$

where the subscript B refers to bulk concentrations, $D(R)$ and $D(O)$ are the diffusion coefficients of R and O , respectively, and δ is the thickness of the diffusion layer.

At high overvoltages Eq 10 is usually simplified by ignoring the back reaction, thus the cathodic reaction for example becomes

$$i = \frac{i_o \exp \frac{-\alpha n F \eta}{RT}}{1 + \frac{i_o}{i_1(a)} \exp \frac{-\alpha n F \eta}{RT}} \quad (13)$$

The influence of mass transfer is shown graphically in Fig. 2 where Eq 13 is compared with the Tafel Eq 8.

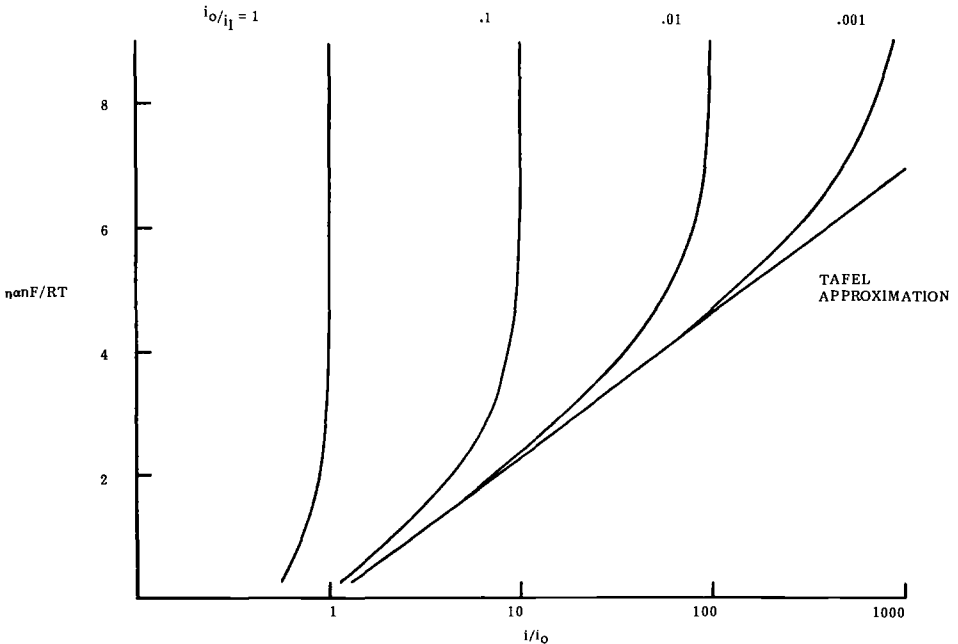


FIG. 2—Influence of mass transfer on the Butler-Volmer equation.

Equations 6 and 10, and simplified versions of them, serve as general expressions for the rate of an electrode reaction in terms of the reaction rate constant, concentration of reacting species, and the electrode overvoltage.

Mixed Potential Theory on a Single Metal

In corrosion of course, even in the simplest situation, we are dealing with at least two different reactions, one anodic and one cathodic normally occurring at the same rate.

In many cases Eq 6 can be used to represent both reactions and thereby allow a relatively simple analysis of the situation, which results in a mixed potential. As an example consider the situation described in Fig. 3, namely, the dissolution of a metal in a reducing acid. If the Tafel approximation can be made to the cathodic arm of the hydrogen evolution process and the anodic arm of the metal dissolution process then the following equations apply

$$i(c, H^+/H_2) = i_{corr} \exp \frac{-\eta_{corr}}{\beta_c} \tag{14}$$

where

$$i_{corr} = i_o \exp \frac{E^\circ - E_{corr}}{\beta_c},$$

$$\eta_{corr} = E - E_{corr}, \text{ and}$$

$$\beta_c = \frac{RT}{\alpha n F}.$$

similarly for the metal dissolution process

$$i(aM/M^{2+}) = i_{corr} \exp \frac{\eta_{corr}}{\beta_a} \tag{15}$$

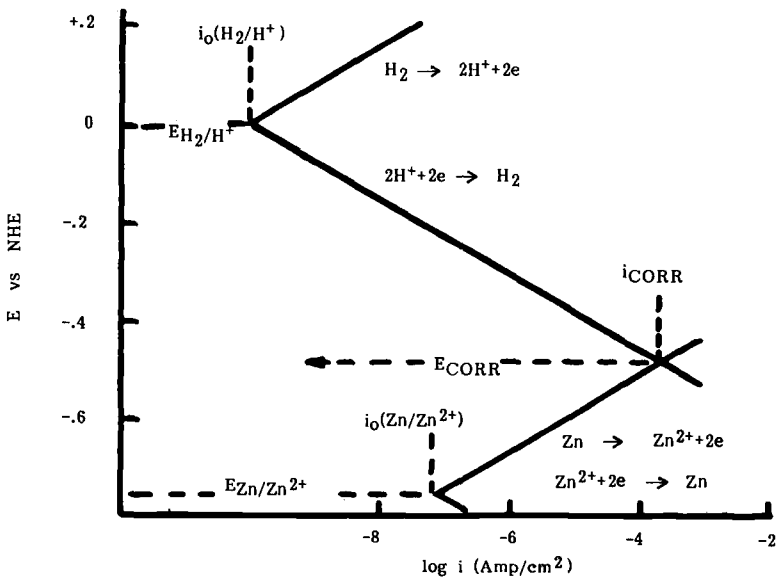


FIG. 3—Kinetic behavior of a metal in a reducing acid, for example, zinc in hydrochloric acid.

10 GALVANIC CORROSION

The current resulting from any excursion from E_{corr} is simply given by

$$i = i_{\text{corr}} \left[\exp - \frac{\eta_{\text{corr}}}{\beta_c} - \exp \frac{\eta_{\text{corr}}}{\beta_a} \right] \quad (16)$$

Under small excursions from E_{corr} the exponential terms can be expanded to give

$$i = i_{\text{corr}} \eta_{\text{corr}} \left(\frac{1}{\beta_c} + \frac{1}{\beta_a} \right) \quad (17)$$

which is of course the basis of linear polarization methods for determining the corrosion rate.

This illustrates in simple terms the electrochemical aspects of mixed potential theory used to handle reaction rates and corrosion potentials on a single metal when only two reactions are involved.

More complicated situations involving additional reactions can be handled in a similar way. For example, Fig. 4 illustrates the situation of a metal corroding in a reducing acid when ferric ions are present in the system.

General Theory of Galvanic Corrosion

Mixed Potential Theory on Two Metals

When two metals are connected together as in a galvanic couple, the principles involved are again based on simple mixed potential theory [3]. The situation illustrated in Fig. 3 now only represents half the picture, the second metal or alloy in the couple has, associated with it, anodic and cathodic reactions, and these must be considered. This gives a minimum of four reactions as illustrated in Fig. 5.

The position of these curves for a given situation depends on area ratios, area distribution, solution conductivity, mass transport, and so on. To obtain quantitative predictions of galvanic currents requires all these factors to be considered. However in some instances qualitative infor-

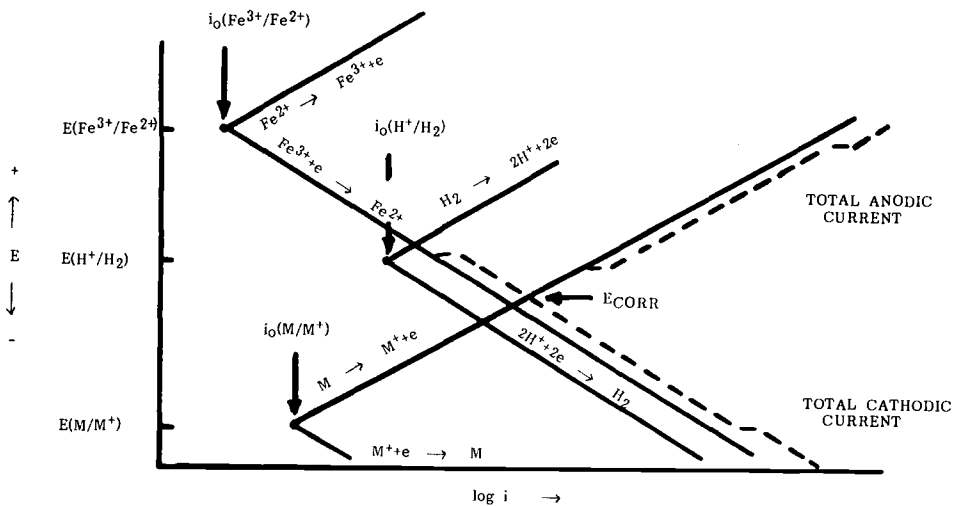


FIG. 4—Kinetic behavior of a metal in a reducing acid containing ferric salts.

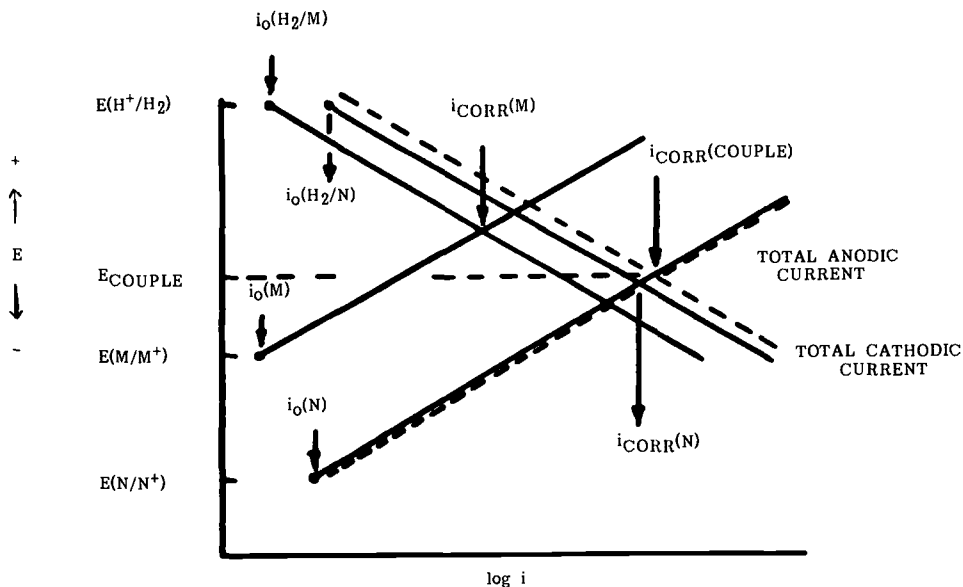


FIG. 5—Galvanic couple between two corroding metals.

mation serves a useful purpose, and simple curves of the type shown in Figs. 6a, b, and c are often used based on the mixed potential approach described above [4].

The Wagner Parameter

It is worthwhile mentioning at this point the Wagner parameter, or polarization parameter as it is sometimes known. This was defined by Wagner [5] as

$$\left[\rho \frac{di}{dE} \right]^{-1} = \sigma R_p \quad (18)$$

and has units of length, where ρ is the solution resistivity, and dE/di is the slope of the steady state polarization curve, namely, the polarization resistance R_p , and σ is the solution conductivity.

This parameter has great significance in galvanic corrosion studies. In any scaling operation, for example, either practical or modelling, the ratio of the Wagner parameter to the characteristic length of the system, that is, the Wagner number, must be kept constant.

The value of the Wagner number determines the behavior of the galvanic cell, a small value, for example, results in what Waber [6] termed "macroscopic" behavior. By this he means that current density varies significantly over the electrode surface. Alternatively, large values of the Wagner parameter result in "microscopic" behavior where current density is fairly uniform over each electrode.

Laplace's and Poisson's Equations

The corrosion rate at any point on a metal surface submerged in an electrolyte can be predicted exactly if the electrochemical potential in the electrolyte adjacent to that point is known.

The equation governing the potential distribution in a galvanic system can be derived from

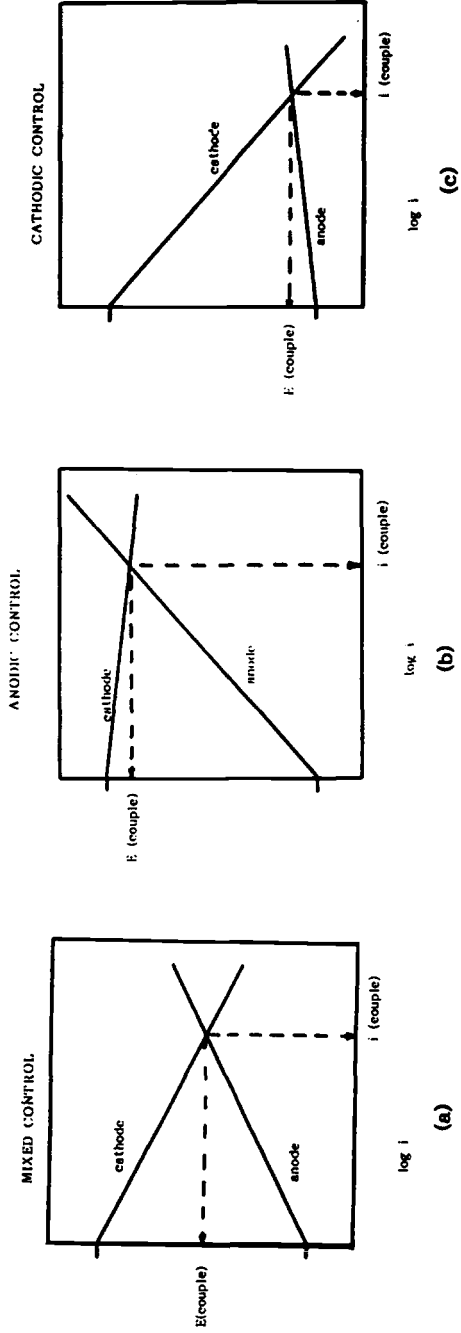


FIG. 6—The use of mixed potential theory to give qualitative information on galvanic corrosion.

first principles [7]. The continuity equation (charge conservation) requires that the current per unit volume i relates to the charge density q by

$$-\nabla \cdot i = \frac{\partial q}{\partial t} \quad (19)$$

where $\nabla = (\partial/\partial x) + (\partial/\partial y) + (\partial/\partial z)$. For a steady state system $\partial q/\partial t = 0$.

Taking account of the relationship for electric field intensity

$$E = -\nabla\phi \quad (20)$$

and Ohms law

$$i = \sigma E \quad (21)$$

the continuity equation transforms to

$$\nabla\sigma\nabla\phi = 0 \quad (22)$$

For uniform, isotropic conductivity

$$\nabla^2\phi = 0 \quad (23)$$

which is the Laplace equation.

At points in the electrolyte where polarization currents i_p enter or exit, this continuity equation becomes the Poisson equation

$$\nabla\sigma\nabla\phi + i_p = 0 \quad (24)$$

Solution of this equation with the appropriate anodic and cathodic polarization expressions and the relevant boundary conditions will give the potential distribution throughout the electrolyte and thus the corrosion rates on the constituent metals in the system.

Factors Affecting Galvanic Corrosion

Many factors including the electrochemical ones already discussed go to determining whether or not galvanic corrosion will occur in a particular instance and if so at what rate. It is important when considering the theory of galvanic corrosion to be aware of these factors, illustrated in Fig. 7, and a brief summary of their significance is given below.

Electrode Potentials

The standard electrode potential of a metal in a solution of its ions gives a rough guide to the position of that metal in a galvanic series. In practice however we are usually concerned with alloys rather than pure metals, and in environments that do not contain the metal ions. To date, the best method of obtaining a "galvanic series" of potentials is to actually measure these potentials in the environment under consideration.

Reaction Kinetics

Electrode potential data will indicate whether or not galvanic corrosion can occur. The reaction kinetic data indicate how quickly corrosion can take place. The metal dissolution kinetics

14 GALVANIC CORROSION

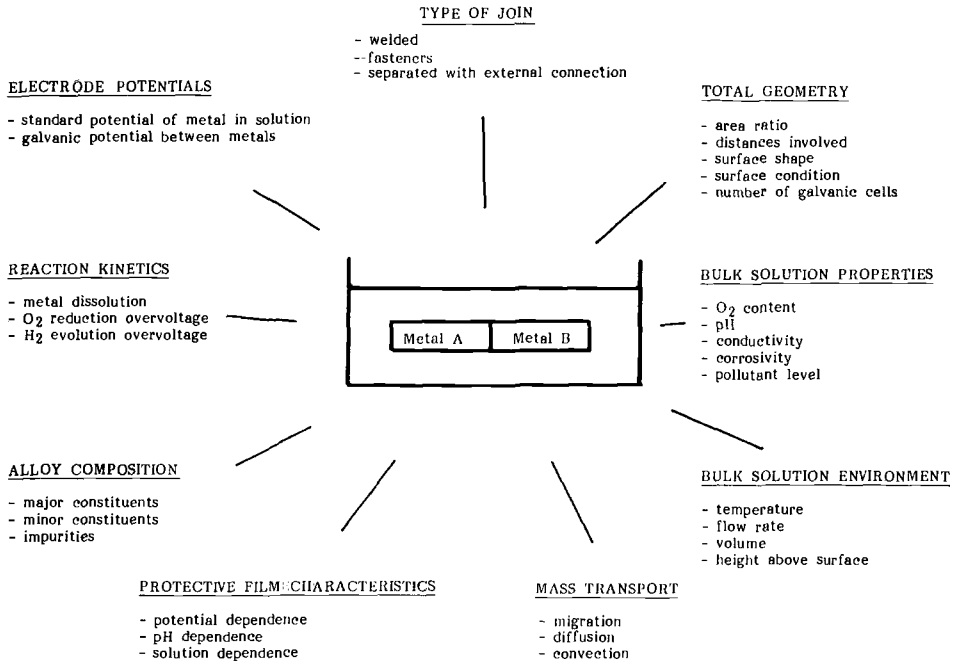


FIG. 7—Factors affecting galvanic corrosion.

give information on the rate of the anodic reaction in the corrosion cell; the oxygen reduction or hydrogen evolution overvoltages on the metals or alloys involved, or both, give information on the rate of the cathodic reactions and whether they will occur on one or both materials.

Alloy Composition

The composition of an alloy affects galvanic corrosion by directly affecting the alloy's corrosion resistance. In addition the constituents affect the corrosion potential and the kinetics of the cathodic processes involved; minor constituents and impurities can play an important role in this respect.

Protective Film Characteristics

The characteristics of the protective film, which exists on most metals and alloys, are important in determining whether or not galvanic corrosion will occur and what form it will take, for example, general or localized, in a particular environment. In particular the potential dependence, pH dependence, and resistance to various solution constituents are important.

Mass Transport

Depending on the particular system being considered, one, two, or all of the three forms of mass transport, migration, diffusion, and convection can play an important role in galvanic corrosion.

Bulk Solution Environment

Included in this group of factors are the solution temperature, volume, height above the couple, and the flow rate across the surface. All these can affect whether or not galvanic corrosion will occur to any great extent.

Bulk Solution Properties

This group of factors is one of the most important; the oxygen level and pH, for example, determine whether a cathodic reaction is possible for a specific system. The corrosivity of the solution determines whether corrosion can occur, and the conductivity determines the geometric extent to which it can occur. The pollutant level can affect all these other factors.

Total Geometry

One of the most important parameters in galvanic corrosion is the "area ratio," a high cathode to anode ratio usually resulting in rapid corrosion or a high anode to cathode ratio giving slow or no corrosion. Distribution of the area is obviously important as is surface shape and condition. The number of galvanic cells in a given system is also important.

Type of Join

The way in which the two alloys comprising a galvanic couple are joined together is important. Welding, where a gradual transition from one material to another may occur, could well give different corrosion properties to a system where the two materials are insulated by a gasket but electrically connected somewhere else in the system. Yet another type of join is via fasteners.

It is clear from the above list that galvanic corrosion is an extremely complex form of corrosion involving the interplay of many factors. These factors can conveniently split into groups under the following headings:

- (1) electrode potentials and reaction kinetics,
- (2) alloy composition and protective film characteristics,
- (3) bulk solution properties and environment, and
- (4) galvanic couple geometry and join.

Whether one is concerned with interpreting natural exposure data or making predictions relating to galvanic corrosion it is necessary to know, where possible, the inter-relationship between the many factors associated with each group. Such inter-relationships can be determined empirically or by mathematical modelling. As will be noted later, the majority of attempts at predicting galvanic corrosion rates are hybrid systems comprising mathematical modelling using empirical data as part of the input.

Anodic and Cathodic Reaction in Galvanic Corrosion*Anodic Reaction*

The anodic reaction in a galvanic couple is some form of metal dissolution, either localized or general. One indication of the tendency of a metal to corrode in a galvanic couple is its standard reduction potential. Table 1 lists a number of standard reduction potentials of metals [8]. From a practical point of view these are of little use since most engineering materials are alloys. A more accurate prediction of galvanic relationships can be obtained by measuring the corrosion potential of a material in the environment of interest. Table 2 gives a typical galvanic series for some materials in ambient temperature seawater [4].

Tables 1 and 2 relate to equilibrium conditions as opposed to corroding conditions. They give information on potential differences that are available to drive a galvanic couple, but they say nothing about the rate at which the corrosion will occur. This is embedded in the kinetics of the reactions involved. The kinetics of specific anodic reactions are difficult to consider in a paper such as this since each metal and alloy has its own dissolution characteristics.

However the active corrosion of most metals can be represented by some form of Tafel or linear kinetics, and such assumptions are usually made when modelling galvanic systems. The localized corrosion of some materials, which occurs in various practical cases, is more difficult to quantify electrochemically, and the modelling of such situations has not to my knowledge been attempted.

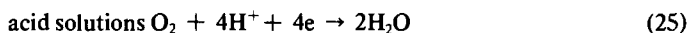
Because the corrosion tendency of most metals in a given environment as a function of potential is known, for example, the active potential region of a stainless steel in sulfuric acid, it is the cathodic reaction in a galvanic couple that is less well defined. The major cathodic reactions, which determine the maximum extent of galvanic corrosion, are discussed in the next section.

Cathodic Reactions

In the vast majority of practical situations the cathodic reaction occurring in galvanic corrosion is oxygen reduction or hydrogen evolution or both. The electrochemical aspects of these two reactions are described in some detail in this section.

Oxygen Reduction Reaction—Because of the many complexities associated with the overall oxygen reduction reaction the modelling of galvanic corrosion systems where it is the cathodic process usually adopt an empirical approach by obtaining the reaction polarization curve under the required conditions. This experimental data are then fed into the appropriate mathematical model or used directly to interpret practical data. Notwithstanding this, it is considered appropriate to have a sound knowledge of the electrochemical theory of the reaction, since in many situations this determines the extent of galvanic attack. The reaction is discussed in detail below.

The reduction of oxygen occurs as follows



At 25°C and under a pressure of 1 atm of oxygen E° in acid solutions (pH 0) is +1.229 V versus normal hydrogen electrode (NHE) and in alkaline solutions (pH 14) is +.401 V versus NHE.

A characteristic feature of the oxygen electrode is that the equilibrium potential calculated by a thermodynamic procedure is never established in practice [9]. When an inert electrode, such as platinum or carbon, is immersed in an electrolyte in contact with oxygen gas, a potential of between 0.8 and 1.1 V is established, that is, 0.1 to 0.4 V less positive than the thermodynamic value. This difficulty in attaining the equilibrium potential of the oxygen electrode is based on its sensitivity to the surface condition of the electrode. This effects the extent to which the various reaction mechanisms, discussed below, are catalyzed with respect to one another.

Hydrogen peroxide can form as an intermediate in the overall four electron reactions (25) and (26)

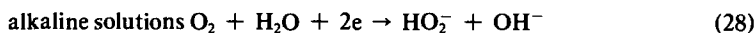
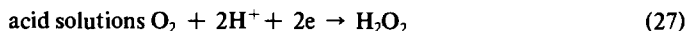


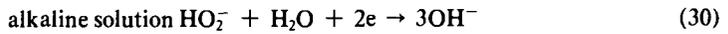
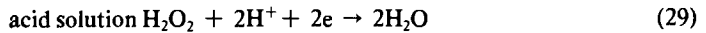
TABLE 1—Standard potentials of some metals [8].

Range	Metal-Metal Ion Equilibrium (Unit Activity)	Electrode Reduction Potential Versus Normal Hydrogen Electrode at 25°C, V
Noble to	Au-Au ⁺³	+1.498
	Pt-Pt ⁺²	+1.2
	Pd-Pd ⁺²	+0.987
	Ag-Ag ⁺	+0.799
	Hg-Hg ₂ ⁺²	+0.788
	Cu-Cu ⁺²	+0.337
	H ₂ -H ⁺	0.000
	Pb-Pb ⁺²	-0.126
	Sn-Sn ⁺²	-0.136
	Ni-Ni ⁺²	-0.250
	Co-Co ⁺²	-0.277
	Cd-Cd ⁺²	-0.403
	Fe-Fe ⁺²	-0.440
	Cr-Cr ⁺³	-0.744
	Zn-Zn ⁺²	-0.763
	Al-Al ⁺²	-1.662
	Mg-Mg ⁺²	-2.363
	Na-Na ⁺	-2.714
Active	K-K ⁺	-2.925

TABLE 2—Galvanic series of some commercial metals and alloys in seawater.

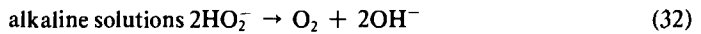
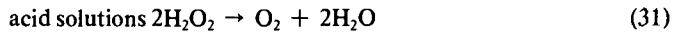
Range	Metals
Noble to	graphite
	platinum
	Ni-Cr-Mo alloy C
	titanium
	Alloy 20 stainless steels
	Type 316, 317 stainless steels
	nickel-copper alloys 400, k-500
	silver
	nickel
	Ni aluminum bronze
	70-30 copper nickel
	Lead
	Type 430 stainless steel
	90-10 copper-nickel
	Type 410 stainless steel
	manganese bronze
	admiralty brass, aluminum brass
	copper
	naval brass
	aluminum bronze
	austenitic nickel cast iron
	low alloy steel
	mild steel
cadmium	
aluminum alloys	
zinc	
Active	magnesium

Further electrochemical reduction of hydrogen peroxide proceeds according to the equations



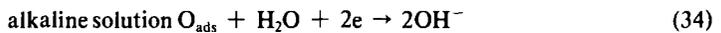
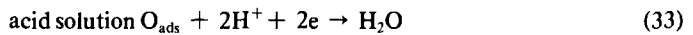
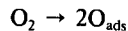
The normal equilibrium potential of Reactions 27 and 29 calculated from thermodynamic data are +0.723 and +1.744 V versus NHE, respectively. Thus the formation of hydrogen peroxide is unstable thermodynamically and can only appear and accumulate as an intermediate caused by kinetic factors. As a result hydrogen peroxide appears under certain conditions whereas in others it can not be detected.

Any hydrogen peroxide formed can disappear not only as the result of further electrochemical reduction but also as a result of its decomposition catalyzed by the electrode material itself



This catalytic decomposition is often the reason for the low electrochemical efficiency of the oxygen reduction reaction, that is, the current expected from a four electron change is very rarely observed.

Reactions 25 and 26 can proceed via a mechanism that does not involve hydrogen peroxide but involves the dissociation of oxygen molecules into atoms that are adsorbed onto the surface



The determination of the actual reaction pathway is difficult unless hydrogen peroxide is observed. The individual Reactions 27, 28, 29, 32, 33, and 34 are themselves complex and can involve a number of intermediate stages in each of which one species, either proton or electron, is added.

In practice the situation is aggravated by the fact that the reduction of oxygen occurs at potentials at which oxide layers are present on many metals. The variation of the nature and properties of these layers with potential and with the specific set of conditions, including the previous history of the surface, has different effects on the possible individual stages and reactions.

Much has been written on the oxygen reduction reaction. On the majority of materials the rate determining step is the addition of the first electron to form the peroxy radical union



This gives a theoretical Tafel slope of 120 mV assuming a transfer coefficient value of $\frac{1}{2}$. For example the Tafel slope for the reaction on mercury, platinum, silver, and gold is reported as 110 mV [10].

Bianchi et al. [11] have studied the process on platinum, palladium, iridium, gold, silver, copper, nickel, cobalt, chromium, stainless steel, graphite, magnetite, aluminum, zirconium, titanium, and tantalum in acid, slightly acid, neutral, and alkaline solutions. He concludes that the reaction occurs at different rates depending on the nature of the cathode material. Rates are high in alkaline solutions but vary markedly in acid solution.

Of the noble metals platinum is the most efficient but can easily be poisoned by oxidizing substances or ions that can easily be adsorbed for example, Cl^- , BI^- . Chromium and chromium containing alloys show low reaction rates in both acid and neutral solutions.

In many practical situations of galvanic corrosion, the potential of the system is such that the oxygen reduction reaction occurs under some form of mass transport control. This can be simple diffusion through the solution or it can be diffusion through some surface layer as occurs in natural seawater. Under these conditions, it is the environment and not the reaction kinetics that determine the reaction rates.

Hydrogen Evolution Reaction—The hydrogen evolution reaction is represented by



The standard potential of this reaction at 25°C under 1 atm pressure of hydrogen is 0 V on the NHE scale.

The principal mechanism of the evolution and ionization of hydrogen is based on three reactions. The first is Volmers reaction



The adsorbed hydrogen atom can participate in two other reactions whereby a hydrogen molecule is formed, one of these, Tafels reaction, is the recombination of two hydrogen atoms



The other, Heyrovsky's reaction is the electrochemical desorption of $\text{H}_{(\text{ads})}$ as follows



The relative rates of these processes depend on the Gibbs free energy of adsorption of the hydrogen atom, which is a function of the electrode material and its structure.

In acid solutions the discharge reaction is the slow step, and on iron this is followed by the Tafel reaction at low overpotentials and electrochemical desorption at higher overpotentials [12].

The exchange current density gives a general idea of the reaction rate in the standard state at equilibrium and allows the classification of the substrate in terms of being a good or bad electrocatalyst for the reaction. Some values of the exchange current density, together with values of the Tafel slope on different metals, are shown in Table 3 [13].

The hydrogen evolution reaction has been studied much more extensively than the oxygen reduction reaction. There are data available on alloys, Table 4 shows for example the range of values of exchange current and Tafel slope obtained by Wilde [14] on some stainless steels in acid solutions. Similar data in alkaline solutions are also shown in Table 4 [15].

The cathodic reduction of hydrogen on metals and alloys can give rise to hydrogen entering the material and causing hydrogen embrittlement. The extent to which this occurs is effected by other species present. For example, on steel, the amount of hydrogen that enters the steel compared with that which is evolved is effected by various elements. The effectiveness of a number of elements in "promoting" hydrogen entering steel is as follows [16]



The subject of hydrogen entry into metals and alloys is a complex one and not the subject of this paper. Nevertheless, because it plays a part in galvanic corrosion the reader should be aware of the possibility of this occurring in practice.

TABLE 3—Exchange currents and Tafel slopes for hydrogen evolution on various metals.

Metal	$\log i_0, \text{ A/m}^2$	Tafel Slope, V	Solution
Platinum	3.2	0.130	1 N HCl
Cobalt	-0.4	0.140	1 N HCl
Iron	-1.6	0.125	1 N HCl
Nickel	-2.4	0.100	0.1 N NaOH
Copper	-3.0	0.115	1 N H ₂ SO ₄
Silver	-4.2	0.116	1 N HCl
Tin	-6.7	0.116	1 N HCl
Zinc	-6.5	0.118	1 N H ₂ SO ₄
Cadmium	-7.7	0.120	1.3 N H ₂ SO ₄
Mercury	-8.7	0.113	1 N H ₂ SO ₄
Lead	-10.2	0.110	1 N H ₂ SO ₄

TABLE 4—Exchange currents and Tafel slopes for hydrogen evolution on various alloys.

Alloy	$\log i_0, \text{ A/m}^2$	Tafel Slope, V	Solution
Type 304 stainless steel	-1.1 to 1.7	0.91 to 0.125	1 N H ₂ SO ₄
Type 303 stainless steel	-1.4 to 1.6	0.115 to 0.142	1 N H ₂ SO ₄
Type 316 stainless steel	-1.2 to 1.7	0.110 to 0.127	1 N H ₂ SO ₄
Type 304 stainless steel	-1.4	0.134	0.1 N NaOH
Type 304 stainless steel	-1.1	0.133	1 N NaOH
Type 304 stainless steel	-1.4	0.105	10 N NaOH

Modelling Galvanic Corrosion

Galvanic Series

Galvanic series, as illustrated in Table 2, have been used for many years as a guide to whether or not galvanic corrosion will occur. Quite often qualitative statements about the possible degree of attack are associated with the series [4].

Such tables and guides are clearly useful, however they do not give any quantitative assessment of the extent of corrosion or over what area it can be expected. This can only be done either by elaborate and time consuming testing in the environment of interest or by some form of mathematical modelling. The latter approach is discussed below.

Mathematical Modelling of Galvanic Corrosion

We have discussed earlier the ways of expressing the electrochemical reactions involved in galvanic corrosion in mathematical terms and have pointed out that Laplace's and Poisson's equation must be solved with the relevant boundary conditions to give the current and potential distribution of the system.

As noted by Astley [17] and others the solution to these equations is not trivial, even for relatively simple geometries, and analytical solutions are usually not possible; various numerical approaches have therefore been adopted.

For the simplest geometries (for example, semi-infinite linear coplanar, cylindrical, and circular) and for the simplest boundary conditions (for example, identical linear polarization kinetics for anode and cathode) a number of series solutions have been derived [6,18-26]. More complex geometries or boundary conditions, or both (for example, Butler-Volmer polar-

ization kinetics) have been studied using finite difference [27,28] or finite element procedures [29-33] or a discrete "source sink" method [32]. These approaches can involve complex programming and can require access to mainframe computers.

An alternative approach is to make the assumption of unidirectional current flow in the electrolyte; this enables analytical solutions to be obtained in many cases [17].

The value of the Wagner number helps to define the conditions under which the unidirectional current flow assumption is a good approximation to the solution of Laplace's equation. In general the larger the Wagner parameter compared to the characteristic length of a system, for example, tube radius, the better the assumption of unidirectional current flow.

Summarizing, the following approaches have been taken to solving Laplace's equation

- (1) analytical techniques—series solutions for simple geometries and boundary conditions and exact solutions under unidirectional current flow assumption (large Wagner parameter),
- (2) finite difference techniques, and
- (3) finite element techniques.

The advantages of the analytical techniques are that they provide an exact solution based on the assumptions made. Whereas the series solutions based on simple geometries and boundaries are instructive, they are not of real practical use. The unidirectional current flow solutions give practical data for situations where the unidirectional current flow assumption is justified, that is, a large Wagner parameter.

The finite difference technique can be used for situations somewhat more complicated than those assumed to give analytical solutions, nevertheless the geometries involved are still relatively simple.

The finite element approach on the other hand can handle boundary conditions involving complex geometry and polarization relationships.

The accuracy of the results obtained using the finite difference and finite element techniques is determined to a great extent by the computer capacity that is available. This determines the number of "differences" and "elements," respectively, which can be handled.

Summary and Conclusions

This paper reviews the thermodynamics and kinetics of electrochemical reactions and mixed potential theory. The application of this to galvanic corrosion theory is outlined, and the major factors that must be considered in any study of galvanic corrosion are noted.

Anodic and cathodic reactions are discussed from a practical point of view, and the two most important cathodic processes in galvanic corrosion, namely, oxygen reduction and hydrogen evolution, are reviewed in some detail.

Finally methods of predicting galvanic corrosion are considered, including use of the galvanic series and the various types of mathematical modelling.

References

- [1] Brenet, J. P. and Traore, K., *Transfer Coefficients in Electrochemical Kinetics*. Academic Press, London, 1971, p. 36.
- [2] Pickett, D. J., *Electrochemical Reactor Design*, Elsevier, Amsterdam, The Netherlands, 1977, p. 53.
- [3] Mansfeld, F., *Corrosion*, Vol. 27, 1971, p. 436.
- [4] Lee, T. S., *Chemical Engineering*, 1 April 1985, p. 89.
- [5] Wagner, C., *Journal of the Electrochemical Society*, Vol. 98, 1951, p. 116.
- [6] Waber, J. T., *Journal of the Electrochemical Society*, Vol. 101, 1954, p. 271.
- [7] Munn, R. S., *Materials Performance*, Vol. 21, August 1982, p. 29.
- [8] Bethune, A. J. de and Loud, N. A. S., *Standard Aqueous Electrode Potentials and Temperature Coefficients at 25°C*, Clifford A. Hampel, Skokie, IL, 1964.
- [9] Frumkin, A. N., *Russian Chemical Reviews*, Vol. 34, No. 10, 1965, p. 717.

22 GALVANIC CORROSION

- [10] Bockris, J. O'M., *Modern Aspects of Electrochemistry*, Butterworth Press, London, 1954, p. 220.
- [11] Bianchi, G., Mezza, F., and Mussini, T., *2nd International Congress on Metallic Corrosion*, New York, 1963, p. 893.
- [12] Devanathan, M. A. V. and Stachurski, Z., *Journal of the Electrochemical Society*, Vol. 111, 1964, p. 619.
- [13] Frumkin, A. N., Bagotsky, V. S., Iofa, Z. A., and Kabonov, B. N., *Kinetics of Electrode Processes* (in Russian) MGU, Moscow, U.S.S.R., 1952, p. 126.
- [14] Wilde, B. E., *Corrosion Science*, Vol. 7, 1967, p. 315.
- [15] O'Brien, R. N. and Seto, P., *Journal of the Electrochemical Society*, Vol. 117, 1970, p. 32.
- [16] Newman, J. F. and Shreir, L. L., *Corrosion Science*, Vol. 9, 1969, p. 631.
- [17] Astley, D. J., *Corrosion Science*, Vol. 23, 1983, p. 801.
- [18] Waber, J. T. and Rosenbluth, M., *Journal of the Electrochemical Society*, Vol. 102, 1955, p. 344.
- [19] Waber, J. T., *Journal of the Electrochemical Society*, Vol. 102, 1955, p. 420.
- [20] Kennard, E. and Waber, J. T., *Journal of the Electrochemical Society*, Vol. 117, 1970, p. 880.
- [21] Simmons, J. A., Coriel, S. R., and Ogburn, F., *Journal of the Electrochemical Society*, Vol. 114, 1967, p. 782.
- [22] Gal-Or, L., Raz, Y., and Yahalon, J., *Journal of the Electrochemical Society*, Vol. 120, 1973, p. 598.
- [23] McCafferty, E., *Corrosion Science*, Vol. 16, 1976, p. 183.
- [24] McCafferty, E., *Journal of the Electrochemical Society*, Vol. 124, 1977, p. 1869.
- [25] Melville, P. H., *Journal of the Electrochemical Society*, Vol. 126, 1979, p. 2081.
- [26] Melville, P. H., *Journal of the Electrochemical Society*, Vol. 127, 1980, p. 864.
- [27] Klingert, J. A., Lynne, S., and Tobias, C. W., *Electrochimica Acta*, Vol. 9, 1964, p. 297.
- [28] Doig, P. and Flewitt, P. E. J., *Journal of the Electrochemical Society*, Vol. 126, 1979, p. 2057.
- [29] Fu, J. W., *Corrosion*, Vol. 38, 1982, p. 295.
- [30] Sautebin, R., Froidevaux, H., and Landolt, D., *Journal of the Electrochemical Society*, Vol. 127, 1980, p. 1096.
- [31] Forrest, A. W., Fu, J. W., and Bicicchi, R. T., Paper 150, NACE National Conference, Chicago, March 1980.
- [32] Helle, H. P. E., Beck, G. H. M., and Ligtelijn, *Corrosion*, Vol. 37, 1981, p. 522.
- [33] Kasper, R. G. and April, M. G., *Corrosion*, Vol. 39, 1983, p. 181.

Galvanic Corrosion Caused by Corrosion Products

REFERENCE: Wilhelm, S. M., "Galvanic Corrosion Caused by Corrosion Products," *Galvanic Corrosion, ASTM STP 978*, H. P. Hack, Ed., American Society for Testing and Materials, Philadelphia, 1988, pp. 23-34.

ABSTRACT: Experiments were conducted to quantify the magnitude of galvanic currents and potentials that exist between metals (iron, copper, titanium, aluminum, chromium, and nickel) and their corrosion products in oxygen-containing environments. Current measurements using a zero resistance ammeter and potential measurements of metal electrodes and oxide electrodes are reported. The effects of solution and electrode compositions on galvanic currents and potentials were determined. A galvanic series of corrosion products was constructed.

Galvanic interactions between metals and surface compounds are dependent on electronic conduction type (insulator, *n*-type, *p*-type, metallic) and thickness of corrosion product layers. It may be possible to modify semiconductor film conductivity by doping with impurity elements present as alloy constituents or via environmental addition and thereby mitigate galvanic corrosion.

KEY WORDS: galvanic corrosion, semiconductor oxides, metal oxides, metal sulfides, pitting, crevice corrosion

The relationship between corrosion and the solid reaction products that accompany a corrosion process is, in many cases, sympathetic. Rather than merely surface occluders or diffusion barriers, many oxides and sulfides that originate from metallic corrosion have a direct influence on the corrosion process, sometimes in a negative fashion. A principal way in which surface films or deposits influence corrosion is by providing a galvanic couple that increases the corrosion rate of active areas.

Quantification of galvanic corrosion caused by corrosion products is difficult *in situ* and, as yet, has not been accomplished. Qualitatively, scale-enhanced galvanic effects are exemplified by crevice corrosion, pitting, and sometimes stress corrosion cracking. This paper describes occluded cell experiments that provide data on galvanic influences to pitting caused by surface oxides and sulfides. Data consist of measurements of galvanic currents and potentials between metal electrodes and metal oxide electrodes. From these data, a galvanic series for corrosion products has been constructed.

Background

In Fig. 1, a conceptual illustration is provided that depicts the situation of pitting on an oxide covered metal surface. As shown in the figure, iron undergoes pitting while the majority of the metal surface is covered with oxide upon which is supported the cathodic reaction. The film can be small in thickness, that is, a passive film, or larger in thickness such as where pits form on steel covered by mill scale (ferric oxide [Fe_2O_3]).

The point illustrated in the figure is that there is a galvanic influence to corrosion in the pit caused by the (dissimilar) oxide on the surface. In the situation illustrated, the galvanic cor-

¹Senior engineer, Cortest Laboratories, Inc., 11115 Mills Rd., Suite 102, Cypress, TX 77429.

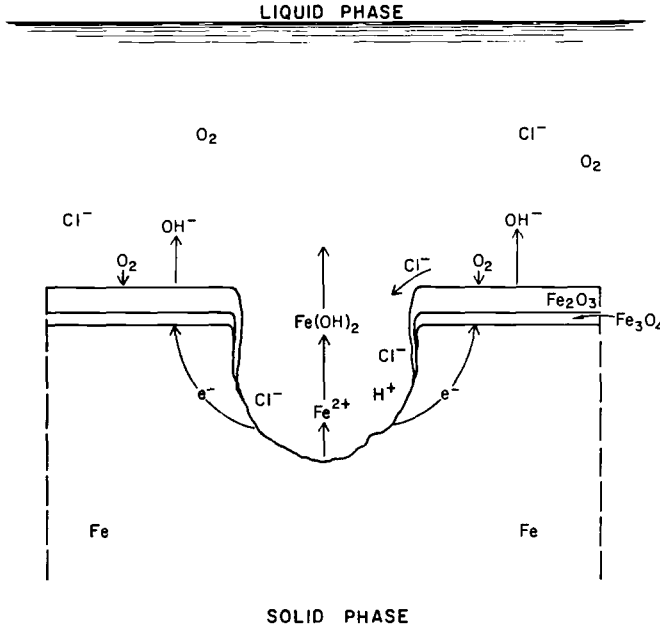
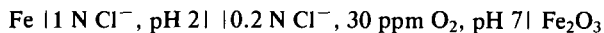


FIG. 1—Pitting of oxide covered steel.

rosion is exacerbated by a pH difference caused by iron hydrolysis in the pit and reduction of O_2 on the surface outside the pit. Conventionally this situation is referred to as a concentration cell, however, the two half cells are not equivalent from the standpoint of the solid phase. One is iron oxide; one is "bare" metal.

Thus, the corrosion rate in the pit can be larger in magnitude than iron would experience were it exposed to the pit environment alone or, in addition, subjected to a galvanic acceleration produced by concentration differences. The actual rate is that of iron at low pH coupled to a large area of iron oxide at higher (5-8) pH. Electrochemically this situation can be described as (approximately)



Theoretical confirmation of the ability of surface films to function as cathodes may be obtained from semiconductor electrochemistry [1-3]. Research in this field has been intensive and directed toward elucidation of mechanisms of electrocatalysis and photoelectrochemical catalysis. To summarize the entirety of developed theory is beyond the scope of this paper, but certain relevant points should aid discussion.

Corrosion products, as with solids in general, fall into three categories as far as their abilities to serve as electrodes are concerned: these being insulators, semiconductors, and conductors. The dividing line between categories is quite hazy, and a particular oxide or sulfide may exhibit a range of conductivities depending on its degree of stoichiometry.

Electronic conduction in compound materials is theoretically described by consideration of the distribution of energy levels. The overlap of energy states from individual atoms (ions) gives rise to bands of states; some occupied, and some unoccupied. The uppermost (in energy) filled band is referred to as the valence band; the lowermost unoccupied band is the conduction band. The relative position or energy separation of the valence band and conduction band determines

intrinsic conductivity. The separation in energy of the valence band and conduction band is referred to as the band gap. Thermal excitation of electrons gives rise to holes (unoccupied energy states) in the valence band and free electrons in the conduction band. Holes and electrons move under the influence of an applied potential field to provide conductivity.

Impurities (metal ions) or nonstoichiometry (for example, Fe^{+1} or Fe^{+2} in Fe_2O_3) in a compound material have energy levels that provide charge carriers. Energy states that accept electrons from the valence band to provide holes are termed acceptors. Those that donate electrons to the conduction band are termed donors.

Insulators (Table 1) are distinguished by large band gaps E_g with little contribution to conductivity by donors or acceptors. In this category are oxides of most refractory metals (zirconium, hafnium, and tantalum) plus alumina (aluminum oxide) among others.

In the category of semiconductors (Table 1) are classified the majority of oxides of engineering metals. Band gaps usually range between 1 and 4 eV, and conductivity derives from donor or acceptor levels in proximity to either the valence band (acceptors) or conduction band (donors).

Compound conductors have either small (in energy) band gaps that provide intrinsic conductivity or have a high density of acceptors or donors in the band gap (degeneracy). In this category are many metal sulfides.

Oxide and sulfide corrosion products classified as semiconductors derive conductivity from nonstoichiometry. One can show that p-type semiconductors are metal ion deficient and n-type semiconductors are oxygen or sulfur deficient. Conducting compounds can have small band gaps and can derive conductivity from nonstoichiometry or from impurities (mixed oxides or sulfides).

Both semiconductor and conductor corrosion products furnish a galvanic couple to their substrate when both contact a liquid medium. The way in which semiconductors function as electrodes is very much different, however, than the way "bare" metals function. The main

TABLE 1—Dielectric properties of corrosion products.

Type	Metal	Product	E_g , eV ^a	V_f , Volts Versus SCE ^a
Insulator	Al	Al_2O_3	8.7	...
Insulator	Zn	ZnS	3.7	...
Insulator	Zn	ZnO_2	5.0	-1.60
Insulator	Ta	Ta_2O_5	4.6	+0.90
Insulator	Hf	HfO_2	5.6	...
n-type	Ti	TiO_2	3.5	-0.30
n-type	Fe	Fe_2O_3	2.2	+0.10
n-type	Sn	SnO_2	3.6	-0.14
n-type	Zn	ZnO	3.3	-0.22
n-type	Cd	CdS	2.5	-0.65
n-type	Pb	PbO	2.7	+0.10
p-type	Ni	NiO	3.7	+0.93
p-type	Cu	Cu_2O	1.6	+0.26
p-type	Cu	CuO	2.0	+0.50
Conductor ^b	Cr	Cr_2O_3	1.7	...
Conductor	Co	CoO	0.7	...
Conductor	Pt	PtO	0.2	...
Conductor	Fe	FeS_2	1.2	...
Conductor	Ni	NiS	0.1	...

^a E_g = band (mobility) gap. V_f = flat band potential.

^bDegenerate, or n-type.

difference is that charge transfer across the semiconductor/liquid interface is often limited by the electronic distribution in the solid phase as opposed to metals where this is seldom the case.

Oxide or sulfide films on the surface of a metal exposed to a conductive liquid function as electron transfer agents by a number of mechanisms [4] (electron tunnelling, resonance tunnelling, surface states, and so forth). Thus their ability to serve as galvanic couples (cathodes) to active areas is not strictly a function of the indigenous conduction mechanism of the oxide. The electronic properties of metal oxides and sulfides do, however, bear an important relationship to their ability to serve as surface electrodes when present as corrosion products. These properties have a dominant influence when product layers are thick (greater than 5 nm).

In Fig. 2, an interfacial energy level diagram is depicted for an n-type semiconductor (Fe_2O_3) in equilibrium with an aqueous electrolyte. It has been demonstrated [4] that n-type semiconductors are rectifiers from the standpoint of interfacial charge transfer in that they donate electrons to solution species more readily than they accept electrons from solution. As illustrated in Fig. 2, reductive capability derives from overlap of the conduction band with the energy levels associated with the solution species and from the availability of conduction band electrons for charge transfer. Note that adiabatic transfer of electrons between reactants and products applies to metal oxide and electrolyte energy levels, at least to a first approximation.

Similarly, p-type semiconductors function more readily as anodes because if overlap of their valence band with the reduced form of solution redox couples. An interfacial energy level diagram for a p-type material is depicted in Fig. 3. Of key importance is the position of the Fermi

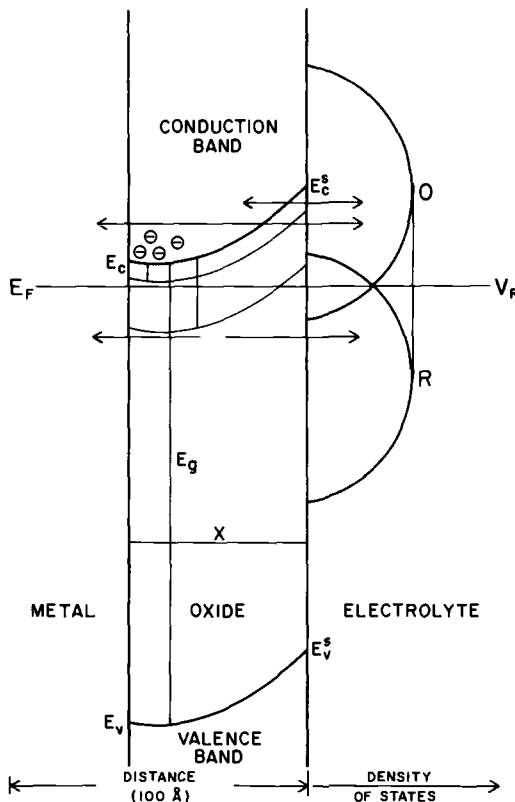


FIG. 2—Interfacial energy level diagram for an n-type passive film.

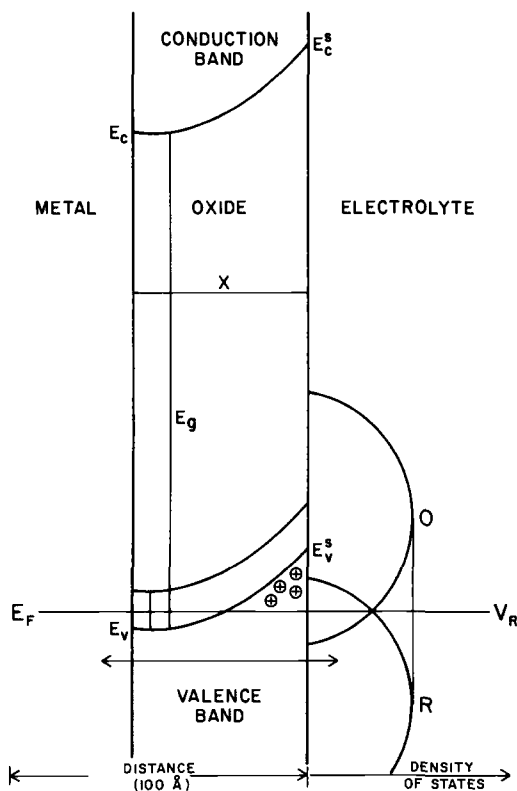


FIG. 3—Interfacial energy level diagram for a p-type passive film.

energy E_f , which locates not only the band edge of the semiconductor but also, on an electrochemical scale, the solution redox potential V_R . Conductors and insulators can also be treated in the fashion described to provide a phenomenological picture of interfacial charge transfer.

The position of the conduction band (n-type) or valence band (p-type) relative to solution redox potentials is located by determination of the flat band potential V_f . The determination is accomplished by means of electrochemical capacitance measurements [5]. The position of a band and the energy states it contains relative to solution energy states plays a key role in charge transfer. Suffice it to say that if the conduction band edge (E_c , n-type materials) is not approximately adjacent to the solution redox potential (V_R , see Figs. 2 and 3) then charge transfer between oxide and solution is not favored.

From a more practical standpoint, these principles have direct consequence when applied to galvanic corrosion. Those metals that have conducting or n-type semiconducting products (passive films, scales, and so forth) are at risk from the standpoint of localized attack caused by the ability of the surface film to support cathodic reactions and hence to provide a galvanic influence to the corrosion process. That is not to say that materials with nonconducting or p-type semiconducting films are not at risk. Aluminum is an obvious exception, as are metals with very thin films (nickel and copper) that support electron transfer by tunnelling or surface states. It can be said, however, that the galvanic influence to localized corrosion, when it occurs in aqueous systems, requires a cathode material capable of supporting reduction of O_2 or H^+ . This is most likely to be the case for n-type semiconductors, intrinsic or degenerate conductors, or for very thin films.

Experimental Procedure

Equipment

Occluded cell experiments were conducted using apparatus depicted in Fig. 4. Three test electrodes were employed in each experiment along with a calomel (standard calomel electrode [SCE]) reference. One electrode consisted of a metal rod (600 grit surface finish) that was allowed to equilibrate with the environment. Before placing the electrode in the cell, it was reduced galvanostatically (5 mA/cm^2 , 2 min) to remove any air formed oxide. This electrode is referred to as the passive film electrode (PFE).

The second electrode was identical to the first with the exception that it was oxidized in an oxygen rich propane flame (1800 F [982°C]) for 2 min to provide a thermal oxide coating on the electrode. This treatment, in general, caused the electrode to take on a grey or bluish-grey tint. No attempt was made to characterize the oxide layer. This electrode is referred to as the thermal oxide electrode (TOE). Alternatively, some materials (aluminum) that do not readily form thermal oxides were anodized in 1 N Na_2SO_4 to provide a thick anodic oxide on the electrode surface. Details of the methods to form oxide films on electrodes have been discussed previously [5,6].

The third electrode was also identical to the first (600 grit finish, cathodically treated) but was contained in a compartment designed to simulate an occluded cell. This electrode is referred to as the active anode electrode (AAE). Details of the materials examined and methods of oxidation are provided in Table 2.

The main cell compartment contained 650 mL of 1 N Na_2SO_4 , unbuffered, in equilibrium with air. The cell was stirred to prevent current limitation by convection. PFE and TOE were exposed to the solution in the main cell compartment. The reference electrode compartment and the occluded cell compartment contracted the main cell compartment via porous Vicor thus allowing electrical contact and ion migration without substantive mass transport. The solution volume of the occluded cell compartment was 2.0 mL and contained (generally) 0.9 N KCl +

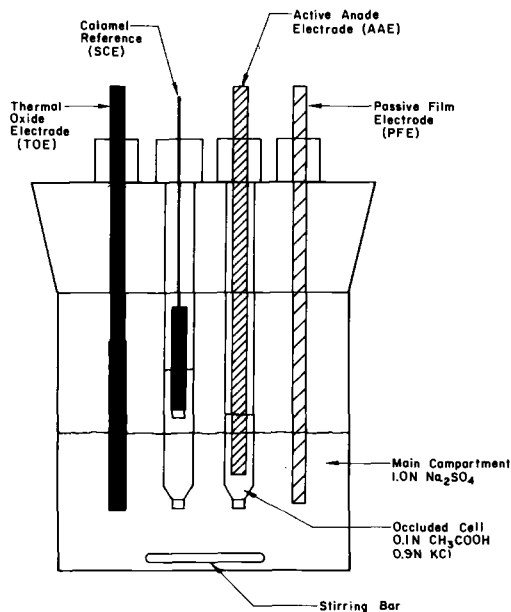


FIG. 4—Experimental apparatus for galvanic measurements.

TABLE 2—*Electrode materials.*

Electrode Material	Chemistry	Oxidation Procedure
Al	99.9 Al	anodized at +1.0 V in 1.0 N Na ₂ SO ₄ (3 min)
Ti	3 Al, 8 V, 6 Cr, 4 Mo, 4 Zr	flame oxidation, ^a blue oxide
Fe	99.9 Fe	flame oxidation, grey oxide
Ni	0.4 Fe, 0.2 Cu	flame oxidation, blue-grey oxide
Cu	99.9 Cu	flame oxidation, red-brown oxide
304SS	18.6 Cr, 9.2 Ni	flame oxidation blue-grey oxide

^aMetal heated in flame until opaque oxide forms, 2 to 3 min.

0.1 N CH₃COOH. The exposed areas of AAE, TOE, and PFE were 1.0, 4.0, and 4.0 cm², respectively.

Procedure

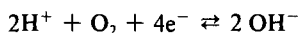
Measurements consisted of determining open circuit potentials of each electrode in a set of three (PFE, TOE, and AAE) of several metals (iron, nickel, copper, aluminum, titanium, and 304 stainless) and, similarly, galvanic current measurements between pairs (PFE/TOE, PFE/AAE, and TOE/AAE). Measurements were made with and without solution agitation (stirring). The solution in the main compartment (1.0 N Na₂SO₄) was equilibrated with air. The occluded cell compartment was deaerated.

The experimental arrangement was designed to simulate a situation of pitting or crevice corrosion in which a small volume of low pH, deaerated electrolyte contacts an active area. Coupled to the active electrode (AAE) is a large area of passive oxide film or a corrosion scale, which is simulated by a thermal oxide electrode.

In addition to occluded cell measurements, cathodic polarization curves were obtained using standard techniques. The reference electrode was saturated calomel (SCE). A carbon counter electrode was employed that was separated from the main compartment by a porous glass frit. The solution was 1 N Na₂SO₄ saturated with air.

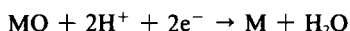
Results

Potential measurements of oxide electrodes (TOE and PFE) in air saturated electrolyte (1 N Na₂SO₄) are reported in Table 3. In general, potentials of thermal oxide electrodes are more noble than passive film electrodes. Potentials in both cases are mixed reflecting the competing redox of metal/metal ion and oxide/oxygen



One would expect the oxygen couple to have the dominant influence on the TOE potential because of the limitation of metal dissolution by the oxide layer.

For p-type oxides, reduction of the oxide is a viable cathodic reaction [7]. The potential of a p-type TOE is therefore influenced by (for divalent metals)



as well as by metal dissolution and oxide reduction. Thus for a heavily oxidized metal, oxide reduction may depolarize the electrode in the same manner as oxygen or other reducible spe-

TABLE 3—*Electrode potentials.*

Metal	Oxide	Oxide Conduction Type ^a	Potential, Volts Versus SCE		
			PFE ^b	TOE ^b	AAE ^c
Al	Al ₂ O ₃ ^d	I	-0.627	-0.606	-0.767
Ti	TiO ₂	N	-0.268	-0.156	-0.468
Fe	Fe ₂ O ₃	N	-0.642	-0.601	-0.682
Ni	NiO	P	-0.151	-0.372	-0.420
Cu	Cu ₂ O/CuO	P	-0.082	-0.075	-0.269
304SS	Cr ₂ O ₃	C	-0.116	-0.369	-0.262
Pt	PtO	C	+0.365		

^aConduction type: I = insulator, N = n-type semiconductor, P = p-type semiconductor, and C = conductor.

^bAir saturated 1 N Na₂SO₄.

^c0.9 N KCl, 0.1 N CH₃COOH.

^dAnodized + 1.0 V.

cies. The magnitude of potential measured in oxygen containing electrolyte reflects the activity of the metal, counter-balanced by the stability of the oxide film.

Galvanic current measurements (Table 4) provide a direct measure of the cathodic ability of surface oxides, which, in turn, is a function of factors previously discussed (conductivity type, thickness, position of band edges, and so forth). From a purely empirical standpoint, the data in Table 3 indicate three cases of facile O₂ reducing cathodes, those being Fe₂O₃, Cr₂O₃, and (possibly) CuO/Cu₂O.

In the modeling of occluded cell corrosion, currents as high as 135 μ A were measured for Cr₂O₃ TOE coupled to iron. Iron was chosen as the AAE in this case to simulate pitting of 300 series stainless steels in which the pit is active. Similar results could be obtained by using a more aggressive (pH = 1) electrolyte in the occluded cell compartment. High currents were also obtained for Fe TOE/Fe, NiO PFE/Ni and with copper electrodes.

In the case of iron, some 50 μ A of galvanic current are produced for a potential difference of only 80 mV (Table 3). This contrasts with aluminum in which only 4 μ A are recorded with a 180-mV potential difference. No attempt was made to accurately model the geometry of pitting, therefore actual galvanic corrosion currents between an active pit and a large oxide cathode could be much different. In the case cited, the cathode/anode area ratio was 4. Realistic ratios are likely between 10 and 100.

TABLE 4—*Galvanic current.*

Metal	Oxide	Oxide Conduction Type ^b	Current, μ A/cm ^{2a}		
			TOE AAE	PFE AAE	TOE PFE
Al	Al ₂ O ₃	I	4	5	0
Ti	TiO ₂	N	2	1	3
Fe	Fe ₂ O ₃	N	49	-1	205
Ni	NiO	P	1	16	-11
Cu	CuO/Cu ₂ O	P	30	36	1
304SS	Cr ₂ O ₃	C	135+	120 ^c	0

^aPFE/TOE (oxide) area 4 cm²; AAE area 1 cm²; positive current indicates electrode in top row (TOE, PFE, and TOE) is the cathode.

^bSee Table 3.

^cAAE is iron.

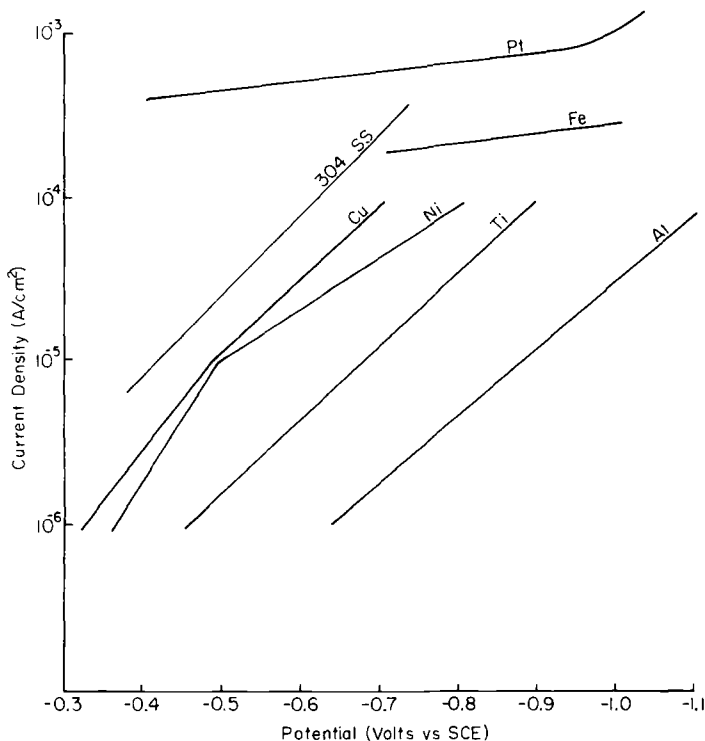


FIG. 5—Current density/potential for O_2 reduction on passive film electrodes: thickness less than 100 Å.

Tafel plots for O_2 reduction on PFE and TOE are provided in Figs. 5 and 6, respectively. The ability of the various electrode types to support reduction of O_2 varies widely. At -0.6 V, for example, the current densities range between 10^{-6} and 10^{-3} A/cm². Tafel slopes vary considerably because of the fact that several mechanistic pathways are available on oxide materials [8].

Discussion

The phenomenon of pitting of engineering materials in aqueous environments has been roughly modeled in these experiments. The objective was to determine the galvanic influence to localized corrosion caused by surface films or scales. The situation investigated was limited to aerated systems containing chloride.

Several questions are relevant to the analysis of galvanic corrosion in this context:

1. Which metal oxides are effective cathodes for O_2 reduction?
2. Are galvanic influences sufficient to account for penetration (pitting) rates observed on metals?
3. Can oxide semiconductor properties be correlated with galvanic corrosion?

It is certainly true that metal oxides support O_2 reduction and that some oxides perform in this capacity more adeptly than others. Referring to Fig. 6, one observes current densities for O_2 reduction that vary by some three orders of magnitude. The general trend is that predicted by semiconductor electrochemical theory.

For example, the lowest current densities are observed for insulator oxides (Al_2O_3) or p-type

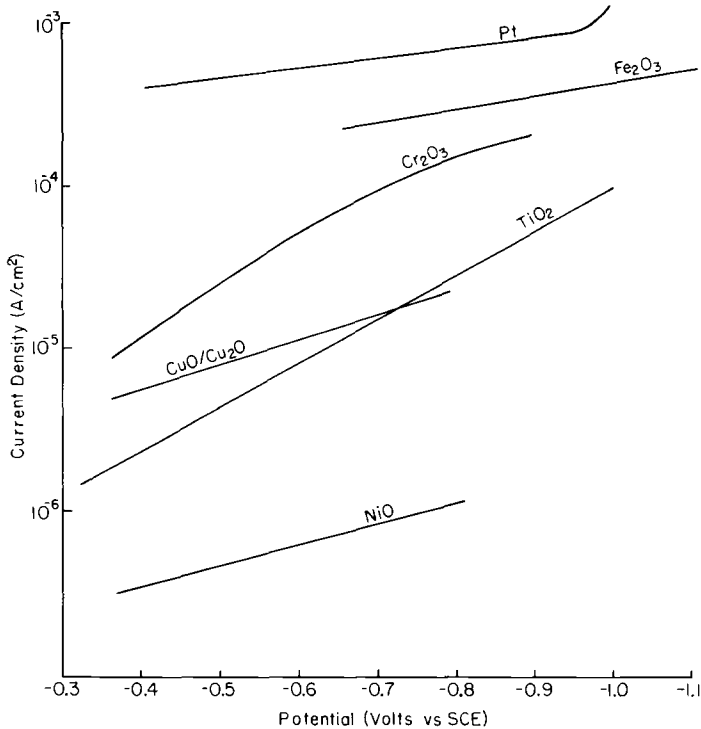


FIG. 6—Current density/potential for O_2 reduction on thermal oxides: thickness greater than 1000 Å.

semiconductors (NiO). The data for Cu_2O/CuO are somewhat misleading in that the oxide itself is reducible and contributes to the current observed. p-type materials, specifically in this case NiO and Cu_2O/CuO , have conduction band energies that exceed the redox potential for O_2 reduction (approximately 0.0 V versus SCE). Therefore, the overlap of conduction band with O_2 redox electrolyte energy levels is insufficient to allow charge transfer. More importantly, however, the conduction band for p-type materials is empty (likewise for insulators) and, even with sufficient overlap, reduction of O_2 could not proceed readily.

For thin films, such as the nickel passive film, other charge transfer mechanisms supplant direct electron transfer from the oxide. These include tunnelling from the conduction band and resonance tunnelling (see Ref 4 for details). Transfer rates then depend on film thickness primarily. In Fig. 5, the current density (at -0.6 V) for O_2 reduction on nickel PFE is some 100 times greater than for nickel TOE (Fig. 6). The difference is attributable to oxide thickness. This trend is seen for the majority of materials examined.

The highest current densities for O_2 reduction (Figs. 5 and 6) and the greatest galvanic currents in occluded cell experiments (Tables 3 and 4) are observed for n-type semiconductor oxides (Fe_2O_3 , TiO_2) or conducting oxides (Cr_2O_3). For n-type materials, the position of the conduction band edge (E_c^f , see Fig. 2) relative to O_2 energy levels determines the O_2 reduction rate. For this reason, Fe_2O_3 reduces O_2 more readily than does TiO_2 . The position of the conduction band edge is obtained from the flat band potential ($E_c^f = V_f$). See Ref 1 for details. The more positive the value of E_c^f the higher the O_2 reduction rate.

This generality does not apply if surface oxide films are quite thin (0.5 to 2.0 nm, one to four monolayers of oxide). Here electron tunnelling mechanisms dominate.

Figure 7 illustrates a set of galvanic series for the oxides studied. Galvanic series are constructed in three ways:

1. Potentials of PFE and TOE are ranked.
2. The galvanic currents between TOE and AAE and between PFE and AAE are ranked. The currents are those reported in Table 4.
3. The O_2 reduction currents at -0.6 V are ranked for TOE and PFE. The current densities are obtained from Tafel plots recorded in Figs. 5 and 6.

As mentioned previously, the potentials measured for oxidized electrodes are actually mixed potentials, reflecting both O_2 reduction and metal oxidation. Therefore, measured electrode potentials do not provide information to assess the cathodic ability of oxides. In modeling galvanic corrosion between metal oxide and metal, it would be advantageous to know the potential of the oxide alone and of the metal alone. Experimentally, as an alternative to the approach adopted here, this could be accomplished using oxide electrodes in which the oxide is synthesized by sintering.

The efficiency of oxide cathodes, however, are clearly delineated by both galvanic current rankings and O_2 reduction rankings (Fig. 5) and provide strong evidence to support the postulates set forth previously concerning conduction properties of oxides. Here again, insulators (Al_2O_3) and p-type oxides are inefficient and n-type (Fe_2O_3) or conducting oxides (Cr_2O_3) are highly efficient. The only exception to this ranking is Ti/TiO_2 , which, as mentioned, has a conduction band edge above (more negative than) the O_2 reduction potentials.

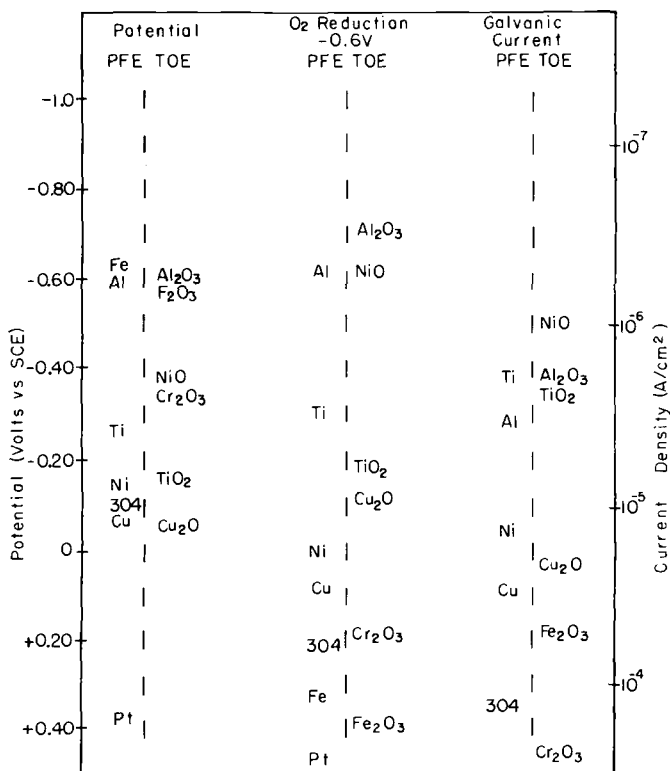


FIG. 7—Galvanic series for metal oxides.

The utility of this data is twofold. First, conceptual modeling of corrosion processes is aided by quantification of semiconductor influences to galvanic corrosion. Second, it may be possible to modify the cathodic ability of oxide films using principles of semiconductor electrochemistry and thereby mitigate galvanic corrosion. As an example of the later, nickel additions (1%) to iron are known to affect the oxide semiconductor properties by compensation of donors, which in turn reduces the concentration of conduction band electrons. Fe_2O_3 scales on iron (1% nickel), therefore, should have a lessened capacity for O_2 reduction. Less efficient oxide cathodes translate into lower corrosion rates and a lower tendency to pit. Work along these lines is in progress.

Conclusions

Oxide films on metals that arise because of passivation in aqueous environments or that develop from thermal treatment during processing provide a galvanic couple to the metal substrate. A cathode/anode areas ratio of 4 provides currents between 50 and 100 $\mu\text{A}/\text{cm}^2$ (anode) for facile O_2 reducing oxides (Fe_2O_3 , Cr_2O_3). The magnitude of the galvanic interaction may be deduced by consideration of the electronic properties and thickness of the films. This conclusion is attributable to the fact that the rate of charge transfer to reduce solution species (O_2 , H^+) is a direct consequence of the density of electronic states in the solid oxide phase and their positive relation to solution energy levels.

References

- [1] Morrison, S. R., *Electrochemistry at Semiconductor and Oxidized Metal Electrodes*, Plenum, New York, 1980.
- [2] Myamlin, V. A. and Pleskov, Y. V., *Electrochemistry of Semiconductors*, Plenum, New York, 1967.
- [3] Heller, A., *The Semiconductor Liquid-junction Solar Cell*, Electrochemical Society, Princeton, NJ, 1977.
- [4] Schultze, J. W. and Elfenthal, L., *Journal of Electroanalytical Chemistry*, Vol. 204, 1986, p. 153.
- [5] Wilhelm, S. M., Yun, K. S., Bullenger, L. W., and Hackerman, N., *Journal of the Electrochemical Society*, Vol. 126, March 1979, p. 419.
- [6] Wilhelm, S. M., Tanizawa, Y., Liu, C. Y., and Hackerman, N., *Corrosion Science*, Vol. 22, Aug. 1982, p. 791.
- [7] Diggle, J. W., in *Oxides and Oxide Films*, Vol. 2, J. W. Diggle, Ed., M. Dekker, New York, 1973, pp. 281-386.
- [8] Tarasevich, M. R. and Efremov, B. N., *Electrodes of Conductive Metallic Oxides*, S. Trasatti, Ed., Elsevier, New York, 1980, p. 211.

Hydrogen Embrittlement of Plated High-Strength 4340 Steel by Galvanic Corrosion

REFERENCE: Pollock, W. J. and Hinton, B. R. W., "Hydrogen Embrittlement of Plated High-Strength 4340 Steel by Galvanic Corrosion," *Galvanic Corrosion, ASTM STP 978*, H. P. Hack, Ed., American Society for Testing and Materials, Philadelphia, 1988, pp. 35-50.

ABSTRACT: Slow strain rate methods are used to quantify the degree of embrittlement in high-strength 4340 steel after coating with porous electroplated cadmium or ion-vapor-deposited aluminum and subsequently exposing to aqueous sodium chloride environments for various times. Porosity in the coatings is primarily responsible for the establishment of galvanic couples at the steel/coating interface, resulting in the generation and absorption of hydrogen in the steel. Data from hydrogen permeation and galvanic corrosion experiments are used to establish a model for hydrogen generation in coated tensile specimens. Estimates of the total hydrogen absorbed in cadmium-plated tensile specimens are consistent with the results of slow strain rate tests whereas similar calculations grossly underestimate the total hydrogen absorbed in aluminum-coated specimens where localized corrosion processes are believed to enhance the rate of hydrogen generation.

KEY WORDS: aluminum coatings, cadmium coatings, low-alloy steel, high-strength steel, hydrogen embrittlement, galvanic corrosion

Most engineering alloys are susceptible to some form of corrosion damage when exposed to aqueous environments. The severity and type of corrosion are often specific to particular combinations of environment and alloy-microstructure, and small changes in either of these parameters can substantially affect susceptibility to corrosion. In particular, care must be taken in situations where residual or applied stresses are present since most forms of localized corrosion can facilitate initiation of fatigue or stress-corrosion cracks. When cost factors or design considerations preclude the use of the most corrosion-resistant alloys, supplementary methods of corrosion protection must be adopted. Metallic, inorganic, and organic coatings have all been used extensively to protect metals from the deleterious effects of corrosion, and all three types are sometimes applied sequentially.

When an environment can penetrate a damaged or porous metallic coating to expose the underlying substrate, prevention of substrate corrosion relies on the galvanic nature of the metallic couple. The coating must always be anodic to the substrate to prevent corrosion of the latter. Care must be taken in choosing the most appropriate coating since the polarity of the galvanic couple is not only dependent on the chosen environment but can also change with time during prolonged exposure [1-3]. The electrochemical nature of galvanic corrosion requires an equivalent cathodic reaction to balance the anodic reaction on the metallic coating. This cathodic reaction can occur on both the substrate metal and the coating, and the proportion is dependent on both the galvanic potential and the efficiency of the cathodic reduction process on each metal. This aspect is extremely important when the substrate metal is susceptible to hydrogen embrittlement. Thus, cathodic reduction of water to produce adsorbed hydrogen on the

¹Principal research scientist and senior research scientist, respectively, Aeronautical Research Laboratories, Defence Science and Technology Organization, Department of Defence, Melbourne, Victoria 3001, Australia.

substrate surface can lead to absorption of hydrogen and subsequent embrittlement of the metal. This situation is particularly hazardous since localized cathodic generation of hydrogen can take place on the substrate without any signs of external attack. Since most coatings are practically impermeable to hydrogen at room temperature, hydrogen absorbed in the substrate metal cannot escape readily, and delayed failure could result at some later stage even after removal of the deleterious environment. Many high-strength steels are susceptible to hydrogen embrittlement, and particular care should be exercised when using metallic coatings on these substrates.

Porous electroplated cadmium (Cd) and ion-vapor-deposited (IVD) aluminum (Al) are frequently used to protect high-strength low-alloy steels from corrosion in aqueous environments. Few systematic attempts have been made to study the effects of environment in causing hydrogen embrittlement in plated high-strength steel components, largely because there has not been a precise method for quantifying the degree of hydrogen embrittlement in steel. In the past, time to failure of statically loaded specimens has been used to estimate the degree of hydrogen embrittlement, but this method takes long times (~ 30 days), and scatter is large [4]. Recent work [5] has demonstrated that slow strain rate testing of notched tension specimens can provide a rapid quantitative method for determining the degree of hydrogen embrittlement in plated high-strength 4340 steels. This method has been used in the present work to assess the degree of hydrogen embrittlement in IVD aluminum-coated and cadmium-plated 4340 steel specimens after exposure to aqueous sodium chloride (NaCl) environments for various times. Galvanic and hydrogen-permeation experiments have also been conducted to provide a better understanding of the processes leading to embrittlement of the steel.

Experimental Procedure

Slow Strain Rate Specimen Preparation

Notched tension specimens were manufactured from 9.5-mm round 4340 steel bar that complied with the Military Standard specification for Steel, Chrome-Nickel-Molybdenum (E4340) Bars and Reforging Stock (MIL-S-5000E). Specimen geometry complied with the reduced load requirements for the Type 1a specimen as detailed in ASTM Method for Mechanical Hydrogen Embrittlement Testing of Plating and Aircraft Chemicals (F 519) (Fig. 1). Specimens were austenitized at $815^{\circ}\text{C}/\text{h}$ in salt, oil-quenched to 40 to 60°C and double tempered at $260^{\circ}\text{C}/1 + 1$ h, with air-cooling between tempers. The notch was prepared by low-stress grinding after heat treatment.

Specimens were porous cadmium-electroplated in accordance with either Qantas Processing Specification P65 (Batch A) or Hawker de Havilland Process Specification HPS 1.03.00 (Batch B). Both specifications include baking at 190°C for 23 h within 4 h of the plating treatment. In the Al-IVD procedure, specimens were degreased, suspended vertically in a vacuum chamber,

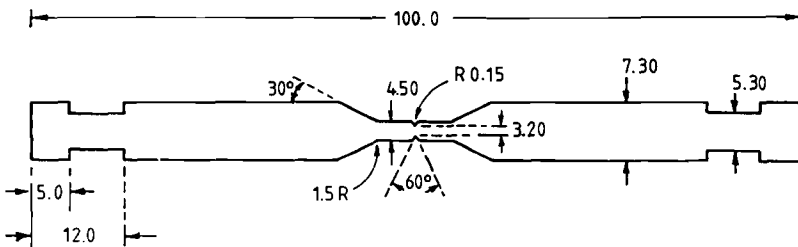


FIG. 1—4340 steel notched tension specimen dimensions in mm.

coated with four passes of IVD aluminum in an argon plasma (~ 1 Pa pressure) and then glass-beaded to consolidate the coating and minimize porosity. Some cadmium-plated and aluminum-coated specimens were subsequently immersed in a pH 1 to 2 chromate bath, washed in warm water, and dried to leave a chromate-conversion coating on the plated surface.

Pre-exposure and Slow Strain Rate Tests

The cadmium-plated and aluminum-coated tension specimens were immersed in 0.6 M NaCl (pH 7) and 0.1 M NaCl (pH 7), respectively, for periods up to 1000 h during which time the specimen potential was monitored with reference to a saturated calomel electrode (SCE). Specimens were then washed in distilled water and dried before loading to failure in air at a crosshead displacement rate of 2×10^{-4} mm/s using a 20-kN motor-driven hard-beam tensile testing machine. Fracture stress was calculated from the failure load and used to estimate the degree of embrittlement in the steel by comparison with the unembrittled fracture stress obtained by testing unexposed bare steel specimens in air. All tests with cadmium-plated specimens were conducted in triplicate, and mean fracture stress values calculated.

The structure of all coatings was studied using both optical and scanning electron microscopy.

Hydrogen-Permeation Tests

A Devanathan and Stachurski two-compartment Teflon[®] cell [6] was used to study hydrogen-permeation kinetics in high-strength 4340 steel in which hydrogen was generated by galvanic coupling of the steel to either 99.99% aluminum in 0.1 M NaCl (pH 7) or electrolytic cadmium in 0.6 M NaCl (pH 7) (Fig. 2). Steel specimens (35 by 24 by 4 mm) were cut from 12-mm-thick bar and given the same heat-treatment schedule as the notched tensile specimens. After low-stress grinding to a thickness of 0.2 mm and mechanically polishing with 600-mesh silicon-carbide paper, one face of the specimen was electropolished and then plated with palladium

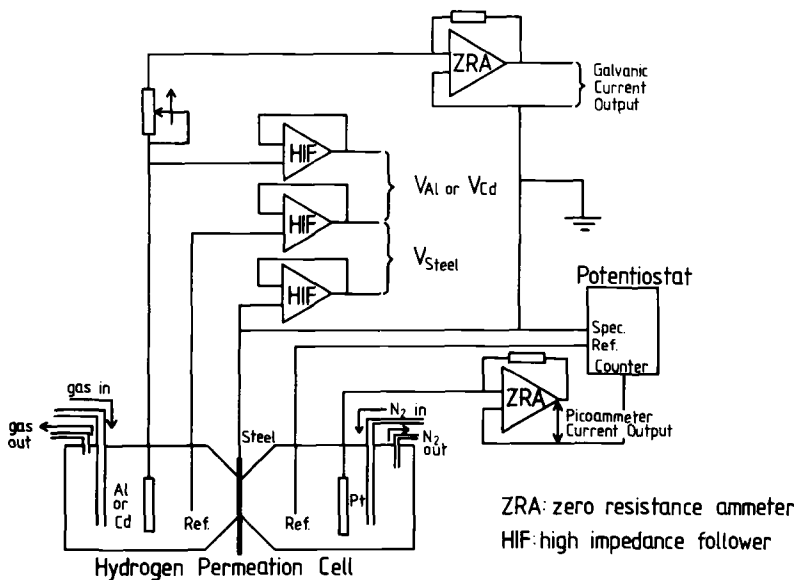


FIG. 2—Hydrogen permeation cell and associated electronic circuitry.

(Pd) in an aqueous solution containing dinitrito-diammonium palladium salt and ammonium sulfamate [7]. A stoved alkyd varnish was applied to regions of the steel membrane that came in contact with the Teflon® cell to prevent development of crevices during permeation experiments [8]. Cadmium and aluminum specimens were mounted in a quick-setting epoxy resin, mechanically polished to a 600-mesh finish and positioned approximately 50 mm from the steel specimen in the input side of the hydrogen-permeation cell. A variable resistor (0 to $10^7 \Omega$) was placed in the galvanic circuit to allow permeation/galvanic current measurements to be made at values of potential intermediate between open circuit and the coupled galvanic potential. High-impedance follower and zero-resistance ammeter circuits were used to measure galvanic potential and current, respectively.

A potentiostat maintained the potential of the palladium-coated face of the steel membrane at 0.04 V (SCE) in pre-electrolyzed deaerated 0.1 M sodium hydroxide. A commercial picoammeter was installed in the platinum counter electrode section of this circuit to measure the permeation current produced by oxidation of hydrogen at the palladium-coated face of the steel specimen. Nitrogen (99.995% purity) was used to deaerate solutions, and all experiments were conducted at $21 \pm 2^\circ\text{C}$.

NaCl solution was admitted to the input side of the cell after the background permeation current density became constant at a value $< 0.1 \mu\text{A}/\text{cm}^2$. Steady-state galvanic and hydrogen permeation currents were recorded at various potentials determined by appropriate choice of resistance in the galvanic circuit.

Galvanic Corrosion Tests

A separate series of tests was undertaken to measure the galvanic current and coupled potential values of aluminum/steel and cadmium/steel in NaCl solutions at values of area ratio (A_C/A_A) ranging from 0.01 to 1, where A_C and A_A are the cathode and anode areas, respectively. Galvanic corrosion tests at low values of area ratio were intended to reproduce the conditions found in porous coatings. All experiments were conducted with a constant value for A_A (1.28 cm^2), while values for A_C were varied to give the appropriate area ratio. Since galvanic potentials fluctuated immediately after immersion in the solution, measurements were made after 18 h.

Results

Slow Strain Rate Tests

The mean fracture stress of unembrittled bare steel specimens tested in air was $2456 \text{ MN}/\text{m}^2$. Tests conducted with bare steel specimens after immersion in aerated 0.1 M NaCl for times ranging from 20 to 120 h showed that the steel remained unembrittled.

Cadmium-Plated Specimens

The degree of embrittlement increased with time of exposure in NaCl at a rate that depended on (1) whether the coating was passivated, (2) the degree of porosity in the coating, and (3) the presence of oxygen in the solution (Fig. 3).

Effect of Porosity—Fracture stresses of passivated specimens after immersion in deaerated NaCl were lower in Batch B specimens than in Batch A specimens (Fig. 3). The porosity of the coating in Batch B specimens was approximately an order of magnitude greater than in Batch A specimens, whereas the coating thickness in both batches was not uniform and varied between 10 and $40 \mu\text{m}$ (Figs. 4 and 5).

Effect of Passivation—Tests conducted with Batch A specimens in aerated NaCl and with

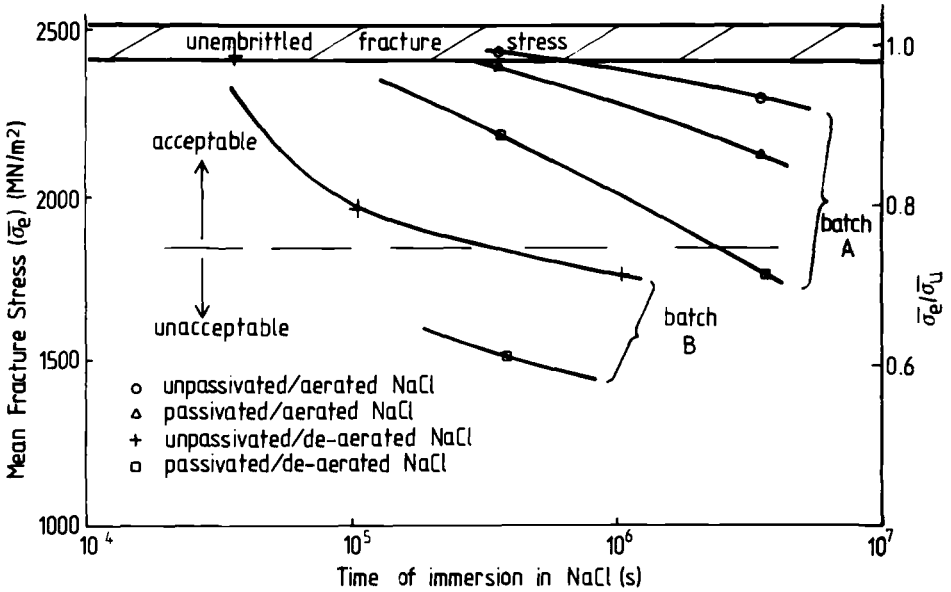


FIG. 3—Variation in mean fracture stress $\bar{\sigma}_c$ and mean fracture stress ratio ($\bar{\sigma}_c/\bar{\sigma}_u$) with time of immersion in 0.6 M NaCl (pH 7) for cadmium plated-and-baked steel specimens tested in air at a crosshead displacement rate of 2×10^{-4} mm/s, where $\bar{\sigma}_u$ is the mean unembrittled fracture stress.

Batch B specimens in deaerated NaCl both showed that passivated specimens became embrittled more rapidly than unpassivated specimens (Fig. 3).

Effect of Oxygen—Fracture stresses of passivated Batch A specimens exposed to deaerated NaCl were lower than for similar specimens exposed to aerated NaCl for equivalent times (Fig. 3). The potentials of all cadmium-plated specimens exposed to aerated and deaerated 0.6 M NaCl were -0.78 and -0.83 V (SCE) ± 0.01 V (SCE), respectively, and remained constant during immersion.

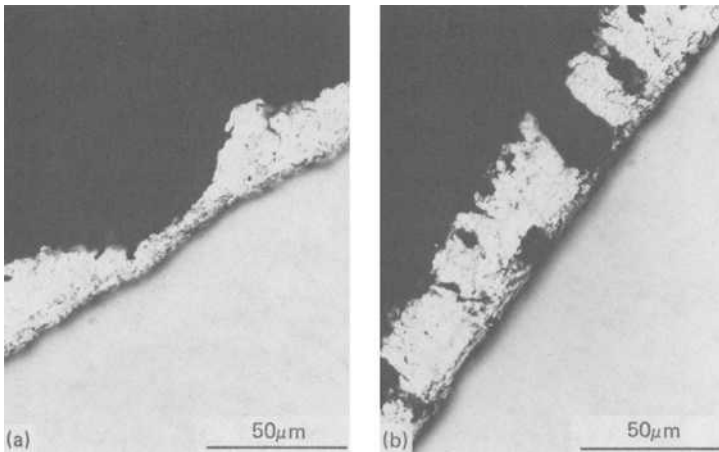


FIG. 4—Metallographic section of porous cadmium plate deposited on 4340 steel: (a) Batch A and (b) Batch B.

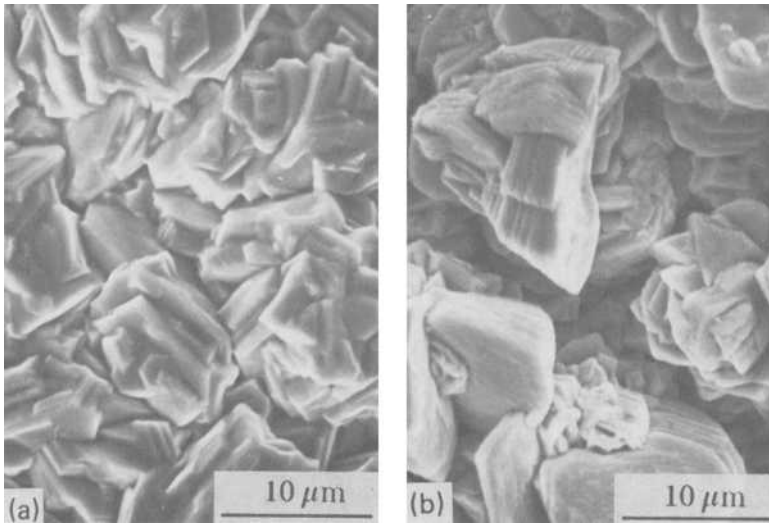


FIG. 5—Scanning electron micrographs of porous cadmium plate deposited on 4340 steel: (a) Batch A and (b) Batch B.

Aluminum-Coated Specimens

A metallographic section of a coated specimen showed that the thickness was approximately $40\ \mu\text{m}$ on the specimen shank and $20\ \mu\text{m}$ at the base of the notch. The coating had a columnar grain structure and appeared compact with little evidence of large-scale porosity (Fig. 6). Examination of fractured slow strain rate specimens by scanning electron microscopy revealed many fine pores of diameter 0.1 to $0.5\ \mu\text{m}$ (Fig. 7).

The fracture stress of the steel was unaffected by the IVD process but was markedly reduced

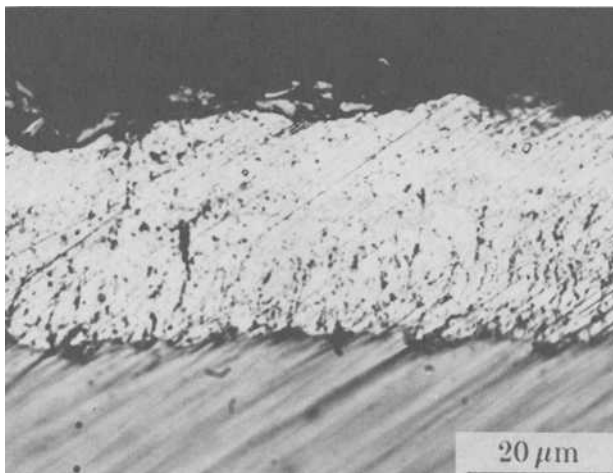


FIG. 6—Metallographic section of IVD aluminum coating deposited in notch of 4340 steel tension specimen.

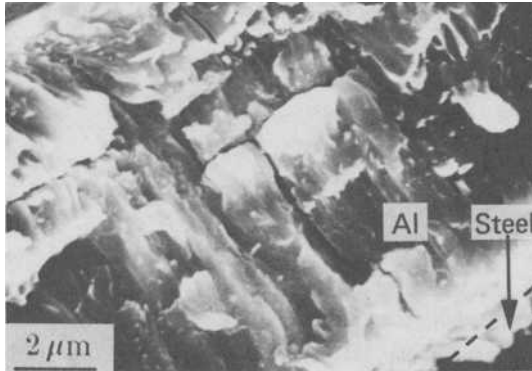


FIG. 7—Scanning electron micrograph of fractured IVD aluminum coating located at base of notch on 4340 steel tension specimen. Arrows indicate regions of porosity.

after exposure of coated specimens to either aerated or deaerated 0.1 M NaCl (Fig. 8). The rate and degree of embrittlement in aluminum-coated specimens was greater than for cadmium-plated specimens. The rate of embrittlement was the same for passivated and unpassivated specimens. Coated specimens, where only the notch was exposed to the solution, also became embrittled at the same rate as similar specimens that were totally immersed.

In experiments where only the specimen notch was exposed to the NaCl, the specimen potential decreased from -0.68 to -1.03 V (SCE) ± 0.05 V (SCE) after exposure for 3 to 4 h. In deaerated environments the potential remained at values < -1.0 V (SCE), whereas in aerated environments, the potential subsequently rose to -0.85 V (SCE) (Fig. 9). Exposure of only the

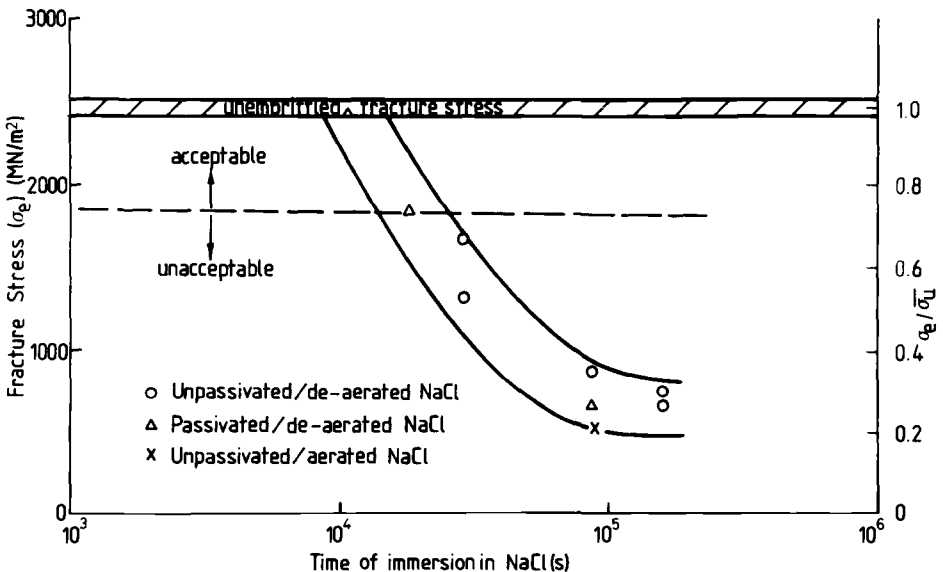


FIG. 8—Variation in fracture stress σ_c and fracture stress ratio ($\sigma_c/\bar{\sigma}_u$) with time of immersion in 0.1 M NaCl (pH 7) for IVD aluminum-coated steel specimens tested in air at a crosshead displacement rate of 2×10^{-4} mm/s.

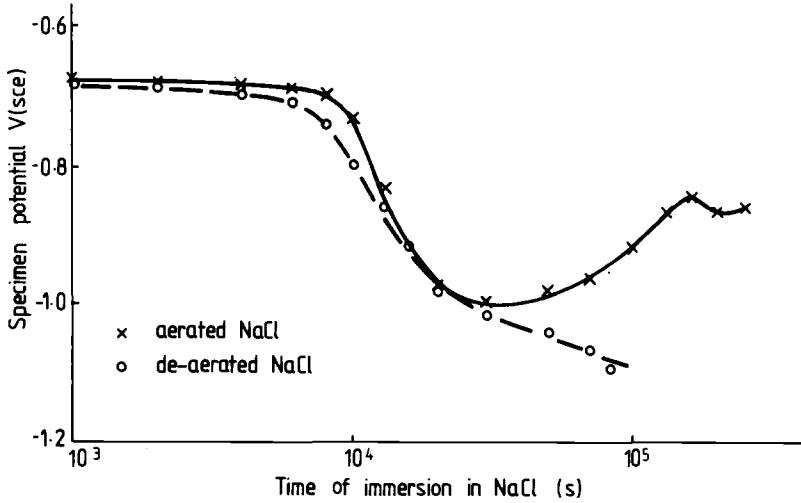


FIG. 9—Variation in corrosion potential with time during exposure of notched region of IVD aluminum coated 4340 steel tension specimen to 0.1 M NaCl (pH 7).

thicker coating on the specimen shank to aerated NaCl resulted in a delay period (~ 30 h) before the potential dropped below -0.7 V (SCE).

Galvanic Corrosion Tests

Steady-state galvanic potentials for both aluminum/steel and cadmium/steel couples in aerated NaCl were within the range -0.7 to -0.8 V (SCE) for all values of area ratio (A_C/A_A). In deaerated environments, reducing the area ratio by a factor of 10 decreased the galvanic potential by 10 mV for the cadmium/steel couple in 0.6 M NaCl and by 100 mV for the aluminum/steel couple in 0.1 M NaCl (Fig. 10). The cathodic current density on the steel remained constant with decreasing area ratio for the cadmium/steel couple whereas a rapid increase was observed for corresponding area ratios with the aluminum/steel couple (Fig. 11). For an area ratio of 0.01, the rate of hydrogen production at the steel cathode for the aluminum/steel couple was 100 times higher than for the equivalent cadmium/steel couple.

Hydrogen-Permeation Tests

Values of hydrogen permeation current density were calculated after subtraction of residual background currents (Fig. 12). In deaerated environments, coupling of the steel membrane (area ~ 0.6 cm²) to aluminum in 0.1 M NaCl, and to cadmium in 0.6 M NaCl, produced identical values for hydrogen-permeation current density for potentials > -0.83 V (SCE). Results at more negative potentials were obtained only with the aluminum/steel couple where the permeation current density ($J(V)$ in $\mu\text{A}/\text{cm}^2$) could be related to potential V over the range -0.82 to -1.03 V (SCE) by the expression

$$\log J(V) = -3.8V - 3.6 \quad (1)$$

Values of hydrogen-permeation current density at constant applied potential on the steel were independent of area ratio (0.1 to 1).

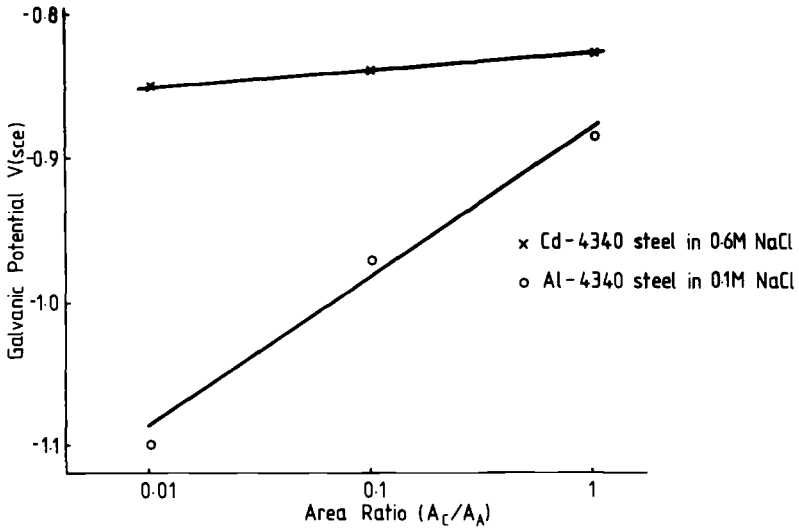


FIG. 10—Variation in potential with area ratio of 4340 steel coupled to either cadmium or aluminum in deaerated 0.6 M or 0.1 M NaCl (pH 7), respectively.

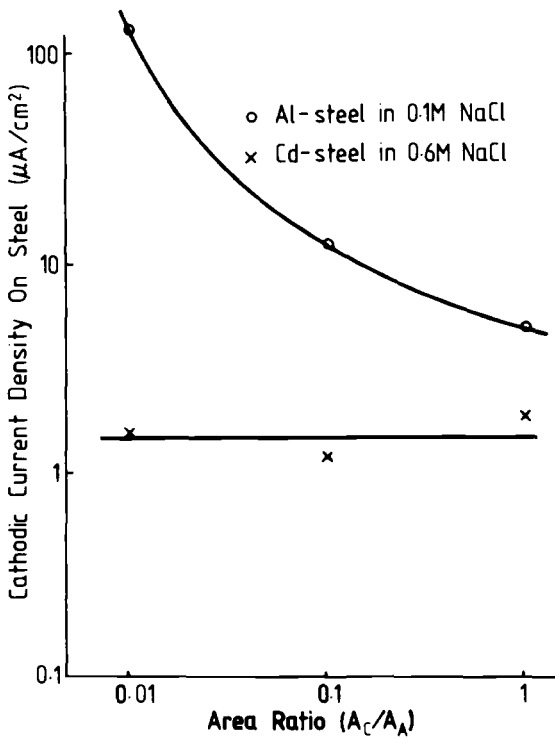


FIG. 11—Cathodic current density on steel at different values of area ratio for Cd/4340 steel and Al/4340 steel galvanic couples immersed in deaerated 0.6 M and 0.1 M NaCl (pH 7), respectively.

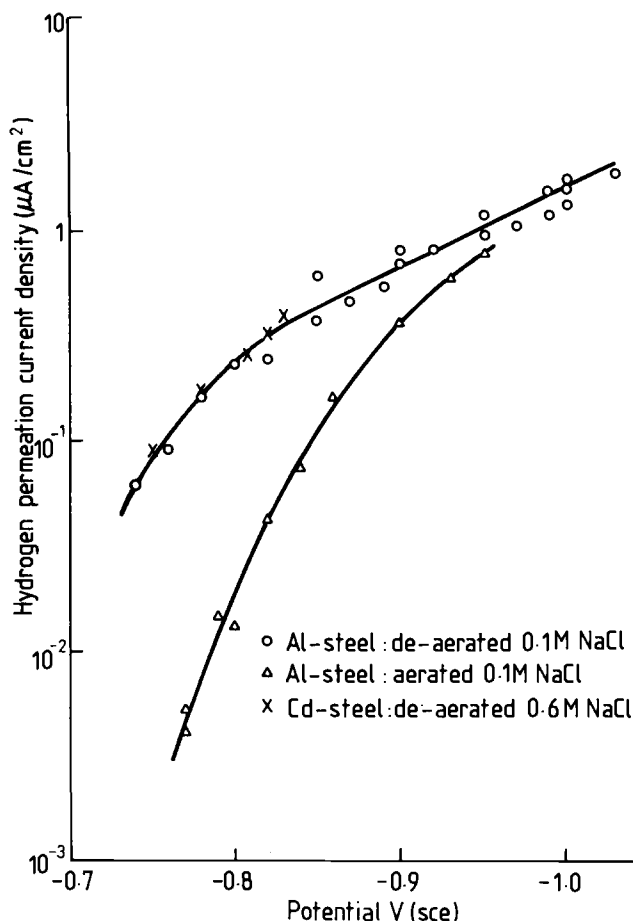


FIG. 12—Variation of hydrogen permeation current density with potential for 4340 steel in aerated and deaerated NaCl (pH 7).

Hydrogen-permeation current densities at potentials > -0.8 V (SCE) were also obtained in aerated 0.1 M NaCl by coupling the steel membrane to a freshly polished aluminum specimen mounted in epoxy resin. When the aluminum specimen was left in the solution for 1 to 2 weeks, deep crevices developed at the interface between the aluminum and the epoxy resin. Subsequent coupling to the steel membrane resulted in galvanic potentials that were sensitive to the degree of aeration of the solution in the vicinity of the cathode. If air was bubbled near the steel electrode, the galvanic potential remained in the range -0.7 to -0.8 V (SCE), whereas if bubbling was stopped or performed in regions of the cell remote from the steel, hydrogen permeation experiments could be conducted at potentials as low as -0.95 V (SCE) (Fig. 12). At this potential, the hydrogen-permeation current density was only marginally lower than the corresponding value in deaerated solutions, but this difference increased significantly at more positive potentials. The corresponding galvanic cathodic current densities on the steel electrode for both aerated and deaerated NaCl are displayed in Fig. 13.

- Al-steel:de-aerated 0.1M NaCl
- Al-steel:aerated 0.1M NaCl
- × Cd-steel:de-aerated 0.6M NaCl

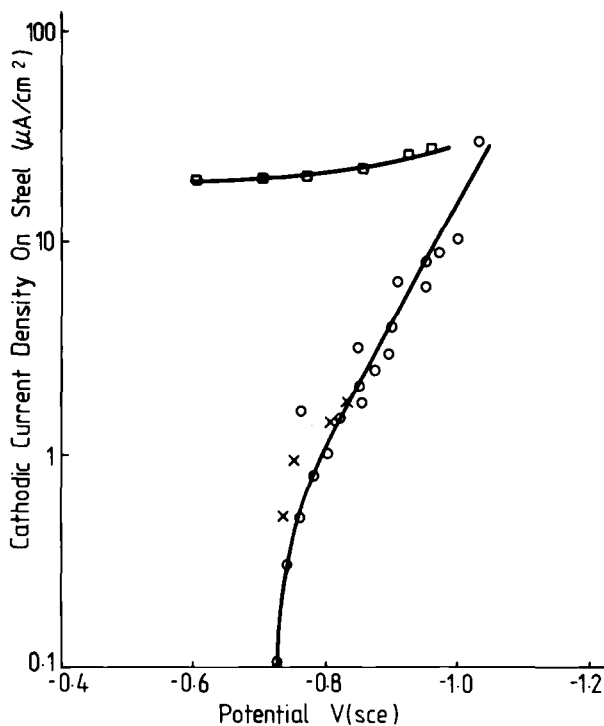


FIG. 13—Variation in steady state galvanic current density on steel for Al/4340 steel and Cd/4340 steel couples immersed in aerated and deaerated NaCl (pH 7).

Discussion

Cadmium-Plated Steel

Comparison of fracture stresses determined with and without immersion of cadmium-plated specimens in 0.6 M NaCl confirms that the steel is embrittled during exposure. The effects of (1) porosity of the coating, (2) chromate passivation, and (3) aeration of the solution, on the degree of embrittlement in cadmium-plated steel can be explained as follows.

Specimen Porosity—Since the rate at which plated specimens become embrittled in deaerated NaCl increases with increasing porosity in the coating (Fig. 3), an understanding of the parameters affecting hydrogen entry into the steel can be obtained by studying the effect of area ratio in galvanic corrosion and hydrogen-permeation experiments. These tests confirm that both the cathodic current density at the steel surface and the hydrogen permeation current density are independent of area ratio (Figs. 11 and 12). Since the area of exposed steel in coated specimens decreases as the porosity of the coating is reduced, the amount of hydrogen entering the steel will also decrease proportionately.

Oxygen in Solution—The results of galvanic corrosion experiments in the potential range -0.75 to 0.85 V (SCE) show that the cathodic current density at the steel surface in aerated NaCl is 20 to 50 times greater than in deaerated NaCl (Fig. 13). Oxygen reduction in aerated solutions will cause considerable alkalinity to develop at the steel cathode by the reaction



Since the reversible hydrogen potential decreases by 59 mV for unit decrease in pH, the overvoltage for hydrogen production becomes smaller with increased alkalinity at the steel surface in specimens maintained at a constant coupled potential. This effect is responsible for lower hydrogen-permeation current densities in aerated NaCl than in deaerated NaCl when comparisons are made at the same potential. This interpretation explains why plated specimens are embrittled more rapidly in deaerated NaCl than in aerated NaCl (Fig. 3).

Chromate-Conversion Coating—Cadmium-plated steel components are generally given a chromate-conversion coating to provide additional corrosion protection from the effects of deleterious aqueous environments. Part of this hydrated chromate film is soluble in water and available for protecting the underlying cadmium and steel [9]. Since the chromate is deposited within the porous cadmium network, any residual acidity retained by the conversion coating could be released upon subsequent exposure to an aqueous environment. A small decrease in pH within the pores would increase the overvoltage for hydrogen production at the steel surface and explain why passivated specimens embrittle at a greater rate than unpassivated specimens when exposed to both aerated and deaerated 0.6 M NaCl (Fig. 3).

Model for Hydrogen Generation in Plated Specimens—Previous work with cadmium-plated steel has established that the coating provides a barrier to the escape of hydrogen from the steel at room temperature [10, 11]. When applied to the present work, these results indicate that any hydrogen absorbed by the plated steel specimen during exposure to NaCl cannot readily escape after removal of the environment. If the rate of hydrogen absorption into the steel during exposure to the chloride environment could be evaluated, it should be possible to determine a relationship between the total mass of absorbed hydrogen and the fracture parameters determined in subsequent slow strain rate tests. Such a model can be developed by using experimentally determined hydrogen-permeation current densities in conjunction with estimated values for the degree of porosity in the coating. The total mass in grams of hydrogen m absorbed in the notched region of a plated tension specimen during exposure to a chloride environment is postulated to be

$$m = \frac{A \times f}{F} \times \int_0^t J(V) dt \quad (3)$$

where $J(V)$ is the hydrogen permeation current density in A/cm^2 and is a function of the galvanic potential V , f is the porosity factor of the coating, and defined to be the steel/cadmium area ratio, and F is Faraday's constant, and t is the total time (s) of exposure in the NaCl solution. Since most of the absorbed hydrogen contributing to premature failure in slow strain rate tests originates from hydrogen generated at the notch, the parameter A is taken to be the area of the notch.

Values of $J(V)$ were determined from Fig. 12 for potentials of -0.78 and -0.83 V (SCE) for tests conducted in aerated and deaerated solutions respectively; A was calculated to be 0.184 cm^2 , and values of f were estimated to be 0.01 and 0.1 for cadmium-plate Batches A and B, respectively. Calculations show that the total hydrogen content of the steel in the vicinity of the notch varies by over three orders of magnitude, and the greatest reduction in fracture stress is produced in specimens containing the most hydrogen (Fig. 14). The full line drawn through points linking tests conducted with unpassivated plated specimens is estimated to provide the

The results displayed in Fig. 14 show that failure of unpassivated cadmium-plated specimens occurs at the minimum acceptable fracture stress (1850 MN/m^2) when the total concentration of hydrogen entering the notched region is estimated to reach ~ 1 ppm. This hydrogen concentration value, calculated by assuming the mass of steel in the notch to be 0.069 g , is considered realistic since high-strength steel is known to be severely embrittled when the hydrogen content is only a few parts per million (ppm). The present calculations also suggest that amounts of hydrogen equivalent to only a few ppb may cause a measurable reduction in fracture stress, thereby highlighting the extreme sensitivity of the slow strain rate method for detection of hydrogen embrittlement in high-strength 4340 steel.

Since the cadmium plate must fulfill the dual roles of (1) allowing hydrogen to escape during baking and (2) preventing ingress of hydrogen during immersion in NaCl, a compromise in the degree of porosity must be achieved to ensure optimum performance by the coating. The cadmium coating in Batch A specimens fulfills both requirements and is therefore considered to be the most suitable coating for application on high-strength steel.

Aluminum-Coated Steel

Application of Model for Hydrogen Generation in Aluminum-Coated Specimens—Significant embrittlement of aluminum-coated specimens occurs after exposure to both aerated and deaerated 0.1 M NaCl for only a few hours. Since the degree of embrittlement is equally severe when only the specimen notch is exposed to the environment for the same period of time, application of Eq 3 requires detailed knowledge of the degree of porosity in the aluminum coating located in the notched region of the tensile specimen. A value for f of 0.01 is assumed since the steady-state potential of aluminum-coated tension specimens in deaerated NaCl is the same as the galvanic potential of the aluminum/steel couple at an area ratio of 0.01 . Values of $f > 0.01$ are unlikely because of the limited distribution and size of pores in the aluminum coating (Fig. 7).

Galvanic corrosion experiments show that the rate of hydrogen generation at the steel cathode in deaerated chloride environments is approximately 100 times higher for aluminum/steel couples compared with cadmium/steel couples at an area ratio of 0.01 (Fig. 11). Since the galvanic potential of the aluminum/steel couple at this value of area ratio is -1.10 V (SCE) , reproduction of these conditions in low porosity aluminum-coated specimens would result in much greater rates of hydrogen absorption in the steel than in cadmium-plated specimens of similar porosity. Since the potential of aluminum-coated specimens decreases from -0.68 to -1.05 V (SCE) during the first few hours of exposure to deaerated 0.1 M NaCl (Fig. 9), calculation of the total hydrogen entering the steel requires integration of the equivalent hydrogen permeation current density curve during this period. Values for $J(V)$ were taken from the curve shown in Fig. 12 and extrapolated to -1.08 V (SCE) using Eq 1. Insertion of calculated $J(V)$ values in Eq 3 for aluminum-coated tension specimens in deaerated NaCl environments for various periods of time produce values for the total mass of hydrogen that are grossly inadequate to explain the severe degree of embrittlement experienced by these specimens (Fig. 14). Agreement with the results of unpassivated cadmium plated-and-baked specimens requires an amount of hydrogen approximately 100 times greater than values calculated using Eq 3. An increase in cathode/anode area ratio to values approaching unity are difficult to envisage bearing in mind the sub-micron scale of the pores in the aluminum plate and the absence of undercutting along the aluminum-steel interface after exposure. Further analysis of probable electrochemical conditions existing within the pores of the aluminum coating provides some explanation why calculations based on galvanic studies alone do not correctly predict observed behavior in aluminum-coated steels.

The rapid decrease in potential displayed by coated specimens after immersion in aerated NaCl provides strong support for initiation of localized corrosion within the pores in the alumi-

num coating. A similar drop in potential has been observed during initiation of pitting in pure aluminum [13] and crevice corrosion in stainless steels in NaCl solutions [14]. Simultaneous deaeration of the solution and dissolution of aluminum in the pores will establish a localized acidic environment which can ultimately penetrate to the steel substrate. This acidity would substantially increase the rate of hydrogen production at the steel substrate compared to values obtained in galvanic studies in neutral NaCl solutions.

The feasibility of hydrogen generation at pore walls followed by diffusion of hydrogen through the aluminum to the steel substrate must also be considered. The hydrogen diffusion coefficient D in pure aluminum has recently been determined to be approximately 10^{-10} cm²/s at 22°C [15]. Values of $(Dt)^{1/2}$ are commonly used to estimate an approximate distance that a diffusing species can travel in time t [16]. For immersion of aluminum-coated specimens for 12 h in deaerated NaCl, values of $(Dt)^{1/2}$ are 20 μm, and hence it is theoretically possible for hydrogen generated at pore walls to diffuse through the aluminum coating to the steel substrate during the period of immersion. Before realistic estimates of the total hydrogen diffusing through the aluminum coating can be made, the following quantitative information is required:

- (1) realistic hydrogen permeation data in aluminum exposed to simulated pit environments and
- (2) determination of diffusivity of hydrogen in partially oxidized aluminum coatings displaying a columnar grain structure.

Since coatings are built up in layers during the IVD process in an argon plasma maintained at a pressure of ~1 Pa, some oxidation within the coating is anticipated.

Practical Considerations—The present results show that the structure of the aluminum coating in the notch facilitates rapid embrittlement of the steel when exposed to NaCl environments. The inferior quality of the coating is attributed to (1) poor throwing power of the aluminum IVD process in the notch and (2) restricted penetration of glass beads in this area. The improved corrosion resistance of the aluminum coating deposited on the shank of the tension specimens supports this argument. Other work [17] with 40-μm thick-coatings has also shown that beading of the aluminum layer after the first and final passes followed by chromate passivation successfully prevents detectable rust formation for periods of 100 h in aerated 0.1 M NaCl. The beading process appears to break up and close off porosity in the coating while chromate passivation prevents localized attack developing at the external aluminum surface. Unfortunately, these processes have little beneficial effect on thin coatings that display evidence of fine porosity.

Conclusions

The present work demonstrates that anodic protection of high-strength steels by the use of aluminum and cadmium coatings can lead to severe embrittlement of the steel during exposure to aqueous NaCl environments. Since plated high-strength steel components are frequently exposed to a large variety of environments during their service lifetime, it is important to identify potentially dangerous situations before catastrophic failure occurs or expensive repairs are required. Quantitative information concerning the rate of hydrogen produced during exposure of plated steels to deleterious environments and a knowledge of the mechanism are essential to provide a scientific base for improving the performance of coatings exposed to such environments during service.

Acknowledgments

The authors wish to thank Mr. P. G. Bushell and Mr. P. N. Trathen for assistance with the experimental program, Dr. S. P. Lynch for critical discussion, and to Hawker de Havilland Australia P/L and Qantas Airlines for permission to use their plating facilities.

References

- [1] Shalaby, L. A., *Corrosion Science*, Vol. 11, 1971, pp. 767-778.
- [2] Mansfield, F. and Kenkel, J. V., *Corrosion Science*, Vol. 15, 1975, pp. 183-198.
- [3] Jones, D. A., *Corrosion*, Vol. 40, 1984, pp. 181-185.
- [4] *Hydrogen Embrittlement Testing, ASTM Special Technical Publication STP 543*, American Society for Testing and Materials, Philadelphia, 1974.
- [5] Pollock, W. J., *Hydrogen Embrittlement Testing: Prevention and Control, STP 962*, American Society for Testing and Materials, Philadelphia, 1988.
- [6] Devanathan, M. A. V. and Stachurski, Z., *Proceedings of the Royal Society*, Vol. A270, 1962, pp. 90-102.
- [7] Driver, R., *Journal of the Electrochemical Society*, Vol. 128, 1981, pp. 2367-2369.
- [8] Bombaci, S. A. and Taylor, R. J., *Corrosion*, Vol. 42, 1986, pp. 118-119.
- [9] Shreir, L. L., *Corrosion*, Newnes-Butterworths, London, 1976, Chapter 16, p. 36.
- [10] Lawrence, S. C., *Hydrogen Embrittlement Testing, STP 543*, American Society for Testing and Materials, Philadelphia, 1974, pp. 83-105.
- [11] Berman, D. A., *Materials Performance*, Vol. 24, Nov. 1985, pp. 36-41.
- [12] Pollock, W. J. and Grey, C., *Hydrogen Embrittlement Testing: Prevention and Control, STP 962*, American Society for Testing and Materials, Philadelphia, 1988.
- [13] Wood, G. C., Sutton, W. H., Richardson, J. A., et al., *Localized Corrosion, NACE-3*, Houston, TX, 1974, pp. 526-546.
- [14] Oldfield, J. W. and Sutton, W. H., *British Corrosion Journal*, Vol. 13, 1978, pp. 104-111.
- [15] Ishikawa, T. and McLellan, R. B., *Acta Metallurgica*, Vol. 34, 1986, pp. 1091-1095.
- [16] Crank, J., *Mathematics of Diffusion*, Clarendon Press, Oxford, 1956, p. 12.
- [17] Hinton, B. R. W., Pollock, W. J., Trathan, P. N., and Crosky, A., 26th Annual Conference of Australasian Corrosion Association, Adelaide, Nov. 1986.

Computer Prediction

Use of the Microcomputer for Calculation of the Distribution of Galvanic Corrosion and Cathodic Protection in Seawater Systems

REFERENCE: Astley, D. J., "Use of the Microcomputer for Calculation of the Distribution of Galvanic Corrosion and Cathodic Protection in Seawater Systems," *Galvanic Corrosion, ASTM STP 978*, H. P. Hack, Ed., American Society for Testing and Materials, Philadelphia, 1988, pp. 53-78.

ABSTRACT: Use of an assumption that electric current flows only in one direction in seawater-carrying equipment constructed of more than one metal enables rapid calculation of the corrosion rate distribution employing small-memory microcomputers. There is negligible error associated with this assumption for typical seawater systems of essentially cylindrical geometry. Analytical expressions can usually be obtained, depending upon the experimentally determined electrode kinetics. The scope of the modelling procedure is indicated by examples of various practical seawater systems that have been examined at the design stage.

The distribution of cathodic protection has been analyzed within copper-alloy pipework attached to a steel hull, or to a small sacrificial anode, and also in a mixed-metal marine propulsion unit protected by zinc anodes. The cathodic electrode kinetics involved various combinations of potential-independent current density and linearly potential-dependent current density.

The distribution of galvanic corrosion has been calculated within a heat-exchanger system consisting of a cathodic tube-bundle and tubeplate connected via a copper-alloy header to a 7-m long copper-alloy pipe. Assessment was made for linear cathodic electrode kinetics and anodic electrode kinetics of the Butler-Volmer type. Calculations were also made for when the header was electrically insulated at both of its flanges. Assessment of the heat-exchanger system has been extended to cater for the copper-alloy pipe being electrically connected to a steel hull, although physically separated by an intervening plastic pipe, and to cover the case where the header is made from a cathodic material.

KEY WORDS: galvanic corrosion, impressed current protection, cathodic protection, seawater corrosion, mathematical models, computers, BASIC (programming language), mathematical prediction, one-dimensional flow, electrode potential, cathodic polarization, anodic polarization, electric fields, differential equations, heat exchangers, condensers, steam condensers, cooling systems, tubes, metal pipes, plastic pipes, piping systems, marine propulsion, marine engineering, ship hulls, sacrificial anodes, copper alloys, nickel alloys, titanium alloys

Nomenclature

- A Net area of tubeplate, cm^2
- α Transfer coefficient
- E Electrode potential, V
- $E_{\text{beg(end)}}$ Potentials at beginning (or end) of a tube (beginning = location of maximum polarization)
- E_c Corrosion potential
- $E_{c(\text{app})}$ Apparent corrosion potential (back extrapolation of hydrogen evolution curve)

¹Senior technical officer, Research and Development Department, IMI, Birmingham B6 7BA, United Kingdom.

ΔE_c^{c-a}	Positive difference in corrosion potential of cathodic and anodic sections
ΔE_c	Positive difference in corrosion potential of header and pipe
$E_{tr1, tr2}$	Potentials of transition on cathodic polarization curve
η	Polarization ($E - E_c$)
F	Faraday (96,540 C/g equivalent)
i	Current density, A/cm ²
i_c	Corrosion current density
i_d	Totally diffusion-controlled current density
I	Current, A
k	Coefficient for linear electrode kinetics in $i = k\eta$, A/cm ² /V
K	$r/(2\rho k)$, cm ²
L	Total length of tube, cm
n	Number of tubes in a tube-bundle
N	Number of electrons transferred/molecule
P	Electrostatic potential
r	Tube radius (or radial coordinate), cm
r_o, r_i	Outer, inner radii
R	Gas constant (8.3144 J/degree/mole)
R	Resistance of seawater in a section, Ω
ρ	Resistivity of electrolyte, Ω cm
T	Absolute temperature, K
x	Distance, cm
$x_{end lin}$	Length of tube subject to hydrogen-evolution electrode kinetics
$x_{end diff}$	Length of tube subject to totally diffusion-controlled electrode kinetics

Introduction

It is rarely possible to build seawater-carrying equipment, such as heat-exchangers, pumps, pipework or ducting, without resorting to mixed metal systems [1,2]. It is therefore necessary to take account of the effects of intermetallic contact upon the corrosion resistance of the constructional materials in such systems, ideally at the design stage. Intermetallic contact will give rise to increased corrosion of the less noble materials and to decreased corrosion of the more noble materials, that is, some measure of cathodic protection. In some cases cathodic protection may be deliberately applied by the use of sacrificial anodes or of impressed current. Clearly identification of the extent of risk and of the need for protective measures is greatly facilitated if the magnitude of corrosion rate at various locations in equipment can be calculated.

It is the purpose of this paper to describe a simple modelling procedure that facilitates corrosion rate calculation for equipment of essentially cylindrical geometry using small-memory microcomputers. The scope of the modelling procedure will be illustrated by examples of various seawater-carrying systems that have been examined at the design stage.

Modelling Procedure

Corrosion rate is related to electrode potential by means of the Tafel equation and Faraday's second law of electrolysis. A necessary precursor to corrosion rate calculation for equipment is therefore an assessment of the electrode potential distribution on each metal in the system.

The exact prediction of electrode potential distribution within a cylindrical system at a given time involves the solution of the Laplace equation for the electrostatic potential P in the seawater at any position given by the longitudinal coordinate x and the radial coordinate r ,

$$\frac{\partial^2 P}{\partial x^2} + \frac{\partial^2 P}{\partial r^2} + \frac{1}{r} \frac{\partial P}{\partial r} = 0 \quad (1)$$

This assumes that there are no significant concentration variations in the seawater [3] and thus that mass transfer occurs only as a result of ionic migration, a condition usually satisfied by corroding systems in the presence of moving seawater. The solution of the Laplace partial differential equation is not trivial even for relatively simple geometries and the analytical solution is usually not possible. Various numerical approaches to the solution of the Laplace equation have been used. For a very simple bimetal tube system, with each metal being subject to identical linear polarization kinetics (that is, the same linear dependence of surface current density upon polarization from the corrosion potential), Waber has produced a Fourier series solution [4]. More complex systems have been dealt with by finite difference, finite element, or boundary element methods [5-8], but the numerical procedures require access to minicomputers.

An alternative and simpler modelling approach is to assume that potential only changes in the axial direction in a cylindrical system, that is, there is no radial change of potential. This is, in effect, an assumption of unidirectional current flow in the seawater and enables analytical solutions to be obtained which are amenable to calculation using small-memory microcomputers. The concept of unidirectional current flow was first seriously considered by Frumkin [9] who showed that the assumption becomes progressively less viable as the system diameter is increased. Upon substituting in Eq 1 the value obtained for $(\partial^2 P/\partial x^2)$ by assuming unidirectional current flow, it is possible to derive the radial potential drop and hence ascertain the limit to be put on diameter (or radius) to ensure that the radial potential drop is negligible with respect to the axial potential drop. By this means Frumkin derived the following expression to define when unidirectional current flow conditions could be assumed for the specific case where the rate of the metal dissolution and oxygen reduction reactions at the metal surface have a linear polarization dependence

$$r < \frac{2}{\rho} \left(\frac{dE}{di} \right) \quad (2)$$

where r is the radius, ρ is the electrolyte resistivity, and (dE/di) is the gradient of the linear electrode polarization curve ($V \cdot \text{cm}^2/I$). In a subsequent study for linear electrode kinetics, de Levie [10] set an upper limit on radius as $(1/8\rho)(dE/di)$, although inspection of his figures reveal that $(1/2\rho)(dE/di)$ is a more reasonable limit. The latter limit indicates an upper diameter of about 500 mm in freshly exposed copper-alloy pipework carrying rapidly flowing seawater, but filming of the metal very often brings about conditions where the upper diameter will be much higher.

The very good agreement between calculated electrode potential values obtained by solution of the Laplace equation with linear electrode kinetics [4] and by assuming unidirectional current flow with linear electrode kinetics is clearly shown in Figs. 1 and 2. Figure 1 relates to small diameter tube with corresponding experimental results (obtained upon insertion of a 2-mm-diameter Luggin probe), and Fig. 2 relates to a more typical system diameter of 400 mm. In Fig. 2 there are three independent curves relating to (a) cathodically filmed pipe, (b) corroding pipe with a low corrosion current density i_c of $1 \mu\text{A}/\text{cm}^2$, and (c) corroding pipe with a high corrosion density of $10 \mu\text{A}/\text{cm}^2$. Case c corresponds to parameters that set an upper diameter of 500 mm according to the less stringent de Levie condition quoted previously, indicating that even this condition can be too severe. Calculations for Case c conditions for larger system diameters indicate that unidirectional current flow analysis is acceptable for diameters of up to about 800 mm.

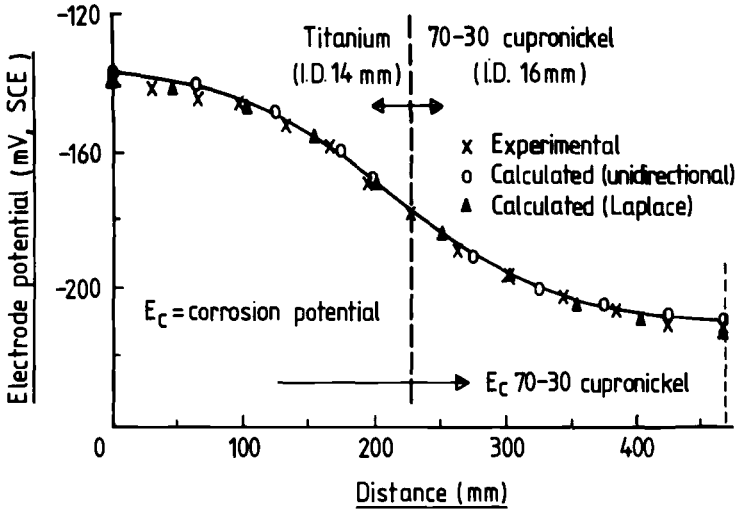


FIG. 1—Potential distribution along electrically connected titanium and 70-30 cupronickel tubes containing static seawater.

Considerations similar to those of Frumkin [9] indicate that Expression 2 should be replaced by the following relationship when Tafel electrode kinetics apply

$$r < (2/\rho i_c) \left\{ \frac{E_{beg} - E_{end}}{\exp\left(\frac{\alpha NF(E_{beg} - E_c)}{RT}\right)} \right\} \tag{3}$$

where E_{beg} and E_{end} are the potentials at the beginning (position of maximum polarization) and

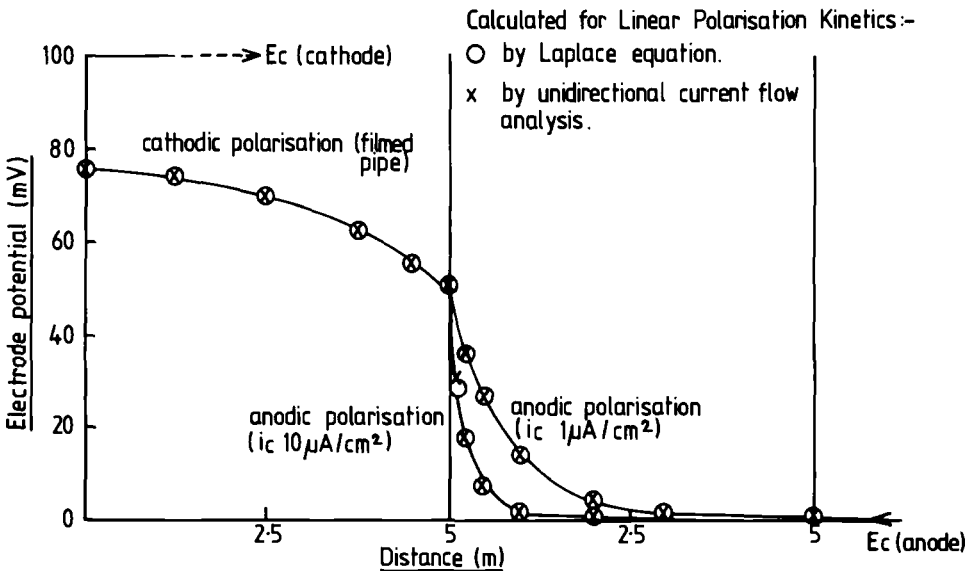


FIG. 2—Comparison of potential distributions calculated for 400-mm-diameter 5-m-long pipes.

end of a tube, respectively, E_c is the corrosion potential, α is the transfer coefficient, N is the number of electrons transferred/molecule, F is the Faraday, R the gas constant, and T the absolute temperature. A typical value for $(E_{\text{beg}} - E_{\text{end}})$ is 50 mV, and this limits the ability to use unidirectional analysis for Tafel electrode kinetics to diameters about 70% of those indicated for linear electrode kinetics. In the case of totally diffusion-controlled electrode kinetics, the limiting tube radius is related to the total tube length and decreases linearly with distance from the beginning of the tube. Thus, at the beginning of the tube, the radius must be less than $\sqrt{2}$ times the tube length, whereas at 98% along the tube it must be less than $\sqrt{2}/50$ times the tube length. Beyond this distance the size of the denominator increases rapidly, but the error involved in assuming unidirectional current flow very close to the far end of the tube can be safely ignored.

Unidirectional current flow analysis for cylindrical systems has been made by a number of workers [9-16] but has been restricted to simple tubes of one metal, although Frumkin considered a simple, infinitely long bimetallic combination [9]. The present work describes its use for practical marine systems that can be constructed from a number of different metals and have some parts that are not truly cylindrical. In addition, calculations have been made for cathodic electrode kinetics pertinent to cathodic protection in seawater, a particular dependence of current density upon polarization not hitherto examined by unidirectional analysis.

The fundamental equation for derivation of electrode potential E distribution in a cylindrical system assuming unidirectional current flow is

$$\frac{d^2E}{dx^2} = \frac{2\rho i}{r} \quad (4)$$

where i is the surface current density at distance x [17]. This equation is obtained by combining Ohm's law, applied to the current flowing parallel to the tube-walls in the seawater, and Kirchoff's law, applied to the surface (electrochemical) reaction. In the case of concentric cylindrical systems, where seawater is confined to the annular gap, the relevant differential equation to be solved is

$$\frac{d^2E}{dx^2} = \frac{2\rho i(r_o + r_i)}{r_o^2 - r_i^2} = \frac{2\rho i}{r_o - r_i} \quad (5)$$

where r_o and r_i are the outer and inner radii, respectively.

The ordinary second-order differential equations, (4) and (5), can be solved according to the dependence of i upon electrode potential, that is, the electrode kinetics involved for the corrosion or cathodic protection process. It is important that the electrode kinetics used accurately reflect changes of surface behavior with time if long-term projections are to be made, that is, the dependence of current density upon polarization used should be that relating to corrosion-product filmed or calcareously filmed metal. The relevant electrode kinetics, corresponding equation solution, and programming sequence will be described for a number of practical examples.

Calculations for Practical Systems

Cathodic Protection of Copper-Alloy Pipework Attached to a Steel Hull

Copper-alloy pipework is often attached to the steel hull of a vessel and therefore enjoys some adventitious cathodic protection, even though the hull is painted. The hull itself may also be cathodically protected by an impressed current system. The extent and efficacy of the cathodic protection afforded to the pipework improves as calcareous films are deposited from the sea-

water as a result of the generation of local alkalinity. Modelling enables the interplay between these factors to be determined so that an indication may be gained of where corrosion suppression effectively ceases.

The electrode kinetics applicable to cathodically polarized metal in aerated seawater are shown in Fig. 3. The magnitude of the diffusion-limited current density for oxygen reduction i_d decreases as calcareous deposits and corrosion products are formed, and is a critical parameter in determining the extent of protection at a given time. The potential dependence of the current density at more electropositive (that is, more negative) potentials (Zone iii of Fig. 3) may be associated with hydrogen evolution, although laboratory tests indicate that such a zone can also be ascribed to the formation of porous calcareous deposits adjacent to the inlet-end of a tube.

Modelling based on electrode kinetics corresponding to Fig. 3 must allow for the six different combinations of the three zones that can arise in practice, according to the values of the inlet-end and outlet-end potentials of the pipe, that is, (i) alone, (ii) alone, (iii) alone, (iii) + (ii), (ii) + (i), and (iii) + (ii) + (i). The solution of Eq 4 for each of these combinations, obtained by integration with respect to distance, is given in Ref 17; the results for the ((iii) + (ii) + (i)) zone combination are given in Appendix A of this paper. Equations requiring numerical solution are involved for the double and triple zone combinations, and these are easily effected using Newton's method. The programming sequence for the case where all three zones of Fig. 3 are involved is shown in Fig. 4. Primes in lines 1030, 1040, and 2020 indicate first derivatives. Lines 1010 to 1500 solve Eqs B and C simultaneously for the distance X corresponding to Zone (iii), and the distance Y corresponding to Zone (ii). Lines beginning at 1060 are "escape" lines designed to avoid looping conditions arising. Lines 2000 to 2040 determine the potential at the beginning of the metal pipe E_{beg} for the case where there is a plastic pipe between the hull and the metal pipe, with electrical contact being maintained by supporting structures. In these calculations, the potential of the hull E_{hull} is regarded as constant in view of its relatively large area.

Total program length in BASIC, covering all six possible combinations from Fig. 3 and including "user-friendly" graphics, is 16 kbytes, and computation takes only a few seconds (Hewlett-Packard HP85 microcomputer).

Verification of computed results for a cathodically polarized tube has been obtained in a number of laboratory tests. Experimental details for these tests are given in Ref 17; electrochemical measurements were made on tubes made up from electrically connected 20-mm-long,

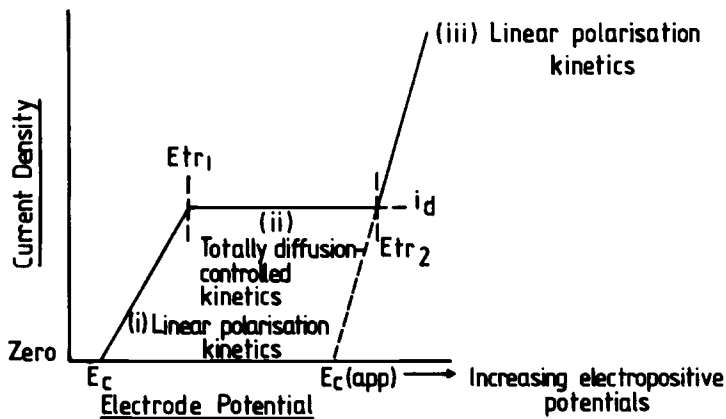


FIG. 3—Schematic cathodic polarization curve for metal in aerated seawater.

```

1000   X = x_end lin   =   0.1 * L  @ Y = x_end diff   =   0.3 * L

1005   E1 = E_c(app) - E_beg

-----
1010   B = x_end lin - K_(iii)^(1/2)   (etc.)   (Equation A(1))

1020   C = E_tr1 - E_tr2 - (e^i_d / r)   (etc.)   (Equation A(2))

1030   N1 = (B - (B'(Y) / C'(Y)) * C) / (B'(Y) / C'(Y) - B'(X))

1040   N2 = (C - (C'(X) / B'(X)) * B) / (C'(X) / B'(X) - C'(Y))

1050   IF ABS(N2) < 0.0001 * Y AND
       ABS(N1) < 0.0001 * X THEN 2000

1060   IF X > L (etc. etc)

1500   Y = Y + N2 @ X = X + N1 @ GO TO 1010

-----
2000   I = (pi * r^2 / l) (etc.)   (Equation A(3))

2010   F = E_hull + IR - E_beg   (R = resistance of seawater in plastic
                                pipe)

2020   F1 = F'(Ei_beg)

2030   F2 = -(F/F1) @ IF ABS(F2) < 0.00001 * ABS(Ei_beg) THEN 2050

2040   E_beg = E_beg + F2 @ GO TO 1005

-----
2050   output line
    
```

FIG. 4—Programming sequence for cathodic protection of pipework calculations (all three zones on Fig. 3, hull connection via plastic pipe).

70-30 cupronickel sections joined by silicone rubber tubing with a 1-mm gap between each section, each tube being potentiostatically polarized at the seawater inlet-end to a potential of -600 mV with respect to a saturated calomel electrode (SCE). Use of the experimentally derived polarization curves given in Fig. 5 gave rise to the calculated potential values shown in Fig. 6 for an 11-mm-diameter 70-30 cupronickel tube. After 2 h of testing, all three zones of Fig. 3 were involved, but only Zones (ii) and (iii) had to be considered after 13 days as increasing calcareous film formation improved the throw of potential. The divergence of calculated and experimental results in Fig. 6 near the seawater-outlet end of the tube resulted from the use of recirculated seawater, which allowed some extra potentiostatic polarization at the outlet-end. Potentials fell to the calculated values for a "once-through" system on breaking the circulation.

Computation indicates how cathodic protection of seawater-carrying copper-alloy pipework

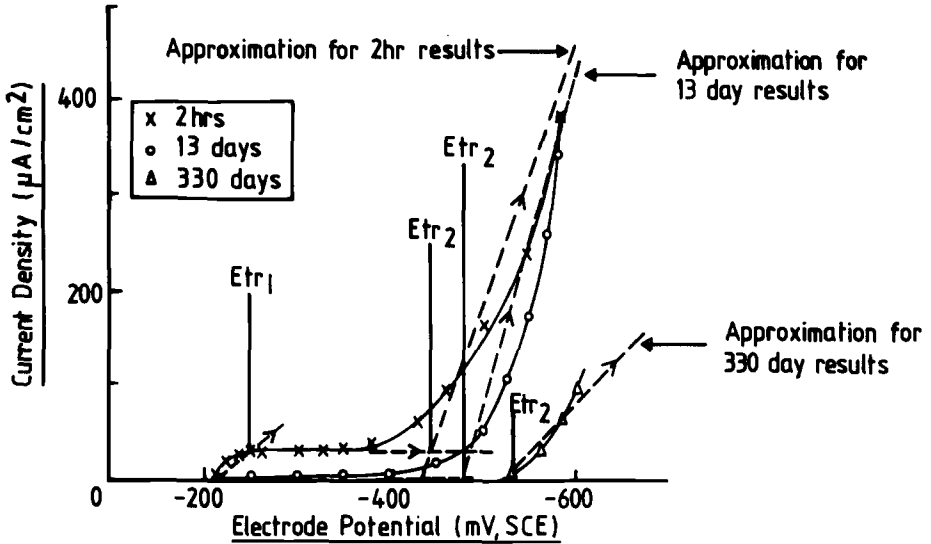


FIG. 5—Cathodic polarization curves for 11-mm-diameter 510-mm-long 70-30 cupronickel tube at a seawater flow rate of 1.5 m/s; inlet-end potential -600 mV, SCE.

attached to a steel hull varies with such parameters as pipe diameter, length, and calcareous film formation. Figure 7 has been derived using electrochemical polarization data obtained in laboratory tests and indicates the extent of protection in metres within a 10-m-long pipe, as defined by the distance at which cathodic polarization falls to 100 mV (when the corrosion rate of [divalent] copper is 2% of its normal rate). The significant improvement in protection with film deposition is clearly shown in this figure. Shorter pipes enjoy cathodic protection over

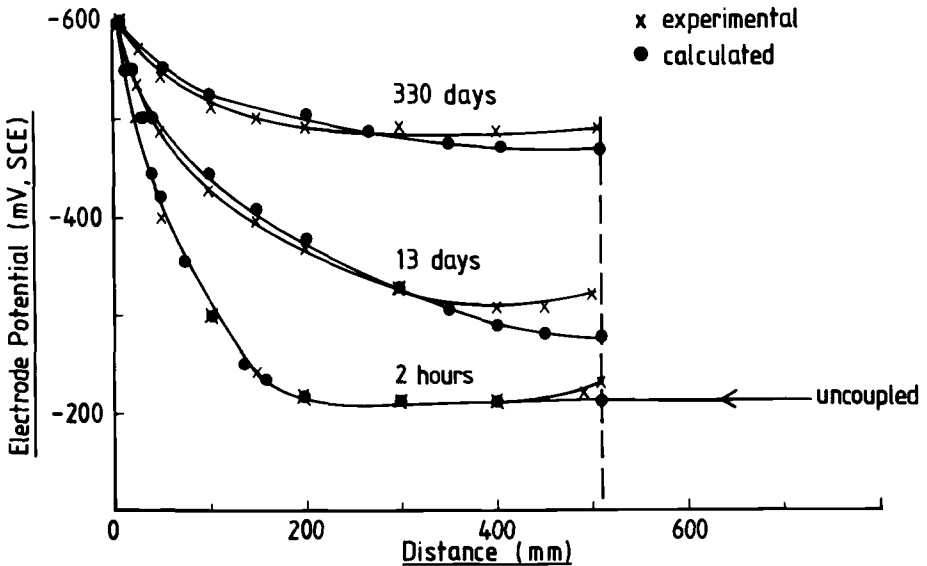


FIG. 6—Potential distribution along 11-mm-diameter 70-30 cupronickel tube at a seawater flow rate of 1.5 m/s.

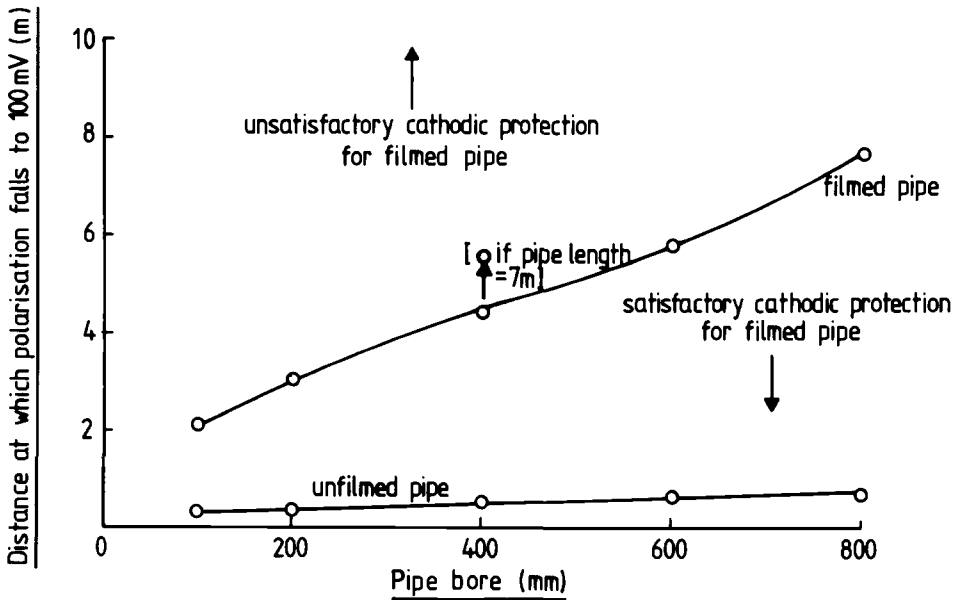


FIG. 7—Cathodic protection of 10-m-long copper-alloy pipe by steel hull; maximum pipe polarization, 400 mV.

longer lengths, as indicated by the result for a pipe 7 m long and 400 mm in diameter, because potential decay with distance within shorter pipes is more shallow as less current is flowing. This is one reason why it is dangerous to make blanket statements with regard to (protected length-/diameter) ratios for pipe.

In some pipework systems, cathodic protection may be obtained by the use of small sacrificial anodes located at the seawater inlets. A suitable programming sequence for calculations for these systems is indicated in Appendix B.

Cathodic Protection of a Mixed-Metal Marine Propulsion Unit

Because of concern about possible crevice corrosion of the nickel-alloy shaft of a marine propulsion unit during limited inactive periods, calculations were made to ascertain the viability of using sacrificial zinc anodes to cathodically protect the shaft.

A diagram of the propulsion unit is given in Fig. 8, which shows the proposed position of the ring of sacrificial zinc anodes. In essence, the unit is cylindrically symmetrical with a concentric geometry and can be made amenable to unidirectional analysis by (1) making an allowance for the seawater resistance from the anodes to the adjacent entrance to the unit based on integration of the resistances of elemental shells of seawater and (2) letting the total wetted surface areas of the titanium-alloy spiral impeller and of the copper-alloy vaned housing be represented by surface roughness factors (3.32 and 5.68, respectively) for the inner cylinder of a simple concentric model of the unit (that is, roughness factors calculated as total wetted surface area divided by surface area of inner cylinder of simple model). Modelling was required in order to calculate the potential at the gap between the copper-alloy and titanium-alloy components (Position A on Fig. 8). It was assumed that during inactive periods seawater would become quickly deaerated within the cavity region (Position B), so that no further potential drop would occur to the actual potential at the mouth of the nickel-alloy shaft crevice (Position C).

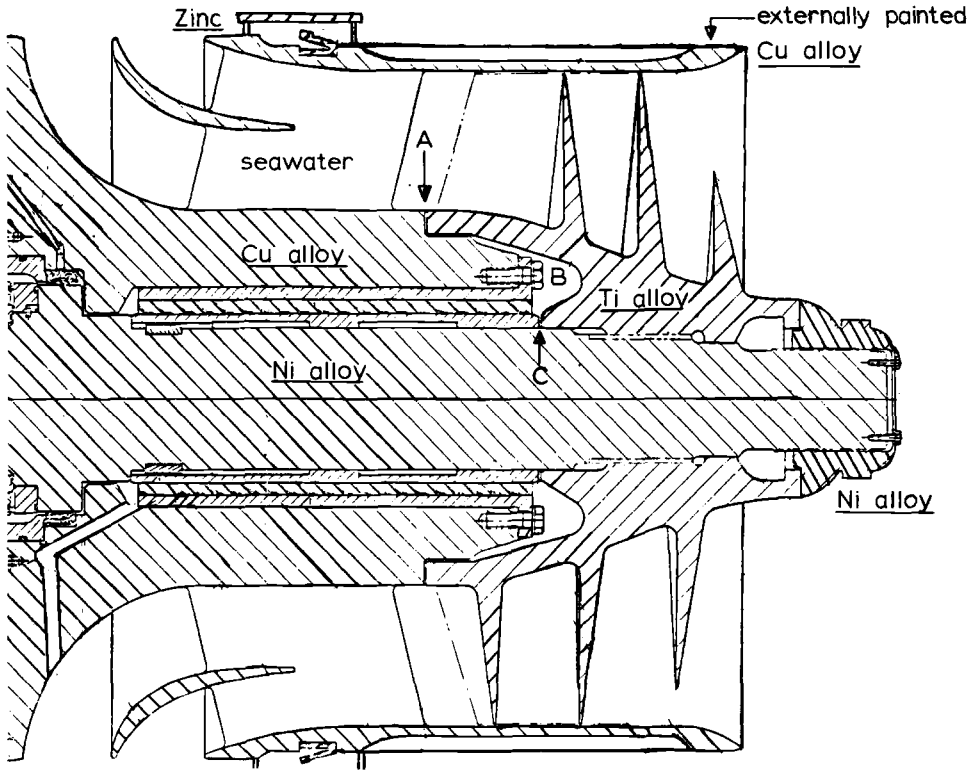


FIG. 8—Mixed-metal marine propulsion unit.

Figure 9 shows the simple concentric model used in calculations for the unit; small corrections were made to final calculated potential values to allow for features that were ignored in the simple concentric model, such as the extended seawater path through the spiral impeller. It was assumed that during inactive periods there was adequate natural convection through the propulsion unit, so that it was right that only ionic migration need be considered (an assumption supported by small-scale laboratory tests). The error involved in using a unidirectional current flow analysis for a system of this size was estimated as less than 2 mV [4].

Electrochemical measurements on separate specimens of the metals of interest gave polarization curves of the types shown in Fig. 10 for aerated and polluted (2 mg/dm^3 of sulfide) static seawater conditions. The measurements were made at regular intervals over several months on continuously potentiostatically polarized metal specimens to determine the effects of film formation. The potential at which these specimens was polarized was the value calculated to be at Position A (Fig. 8) as obtained by computation based on unidirectional analysis. The potential of the specimens was adjusted according to the computed potential at Position A after each set of polarization measurements. Analysis had to be made for four different combinations of electrode kinetics over six months, although after about one month linear (hydrogen evolution) electrode kinetics were found to apply to all parts of the propulsion unit.

The solution of the appropriate form of Eq 5 for the concentric model shown in Fig. 9, assuming linear cathodic electrode kinetics, is given in Appendix C, which also includes a suitable programming sequence for propulsion unit calculations. Computer calculations took a matter of seconds (Hewlett-Packard HP85), and the program length in BASIC to deal with all four possible combinations of electrode kinetics was 12 kbytes.

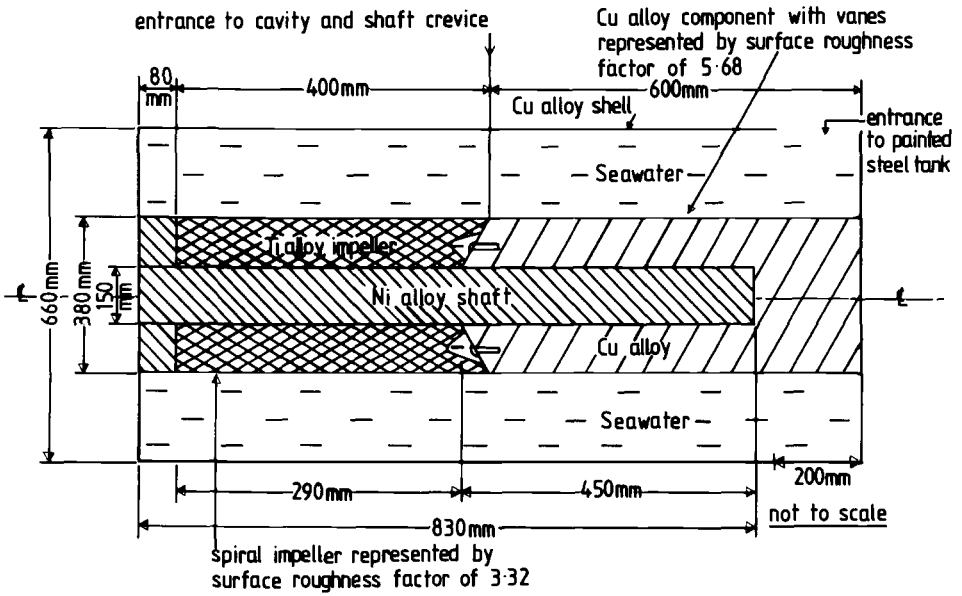


FIG. 9—Simplified model of propulsion unit for cathodic protection calculation purposes.

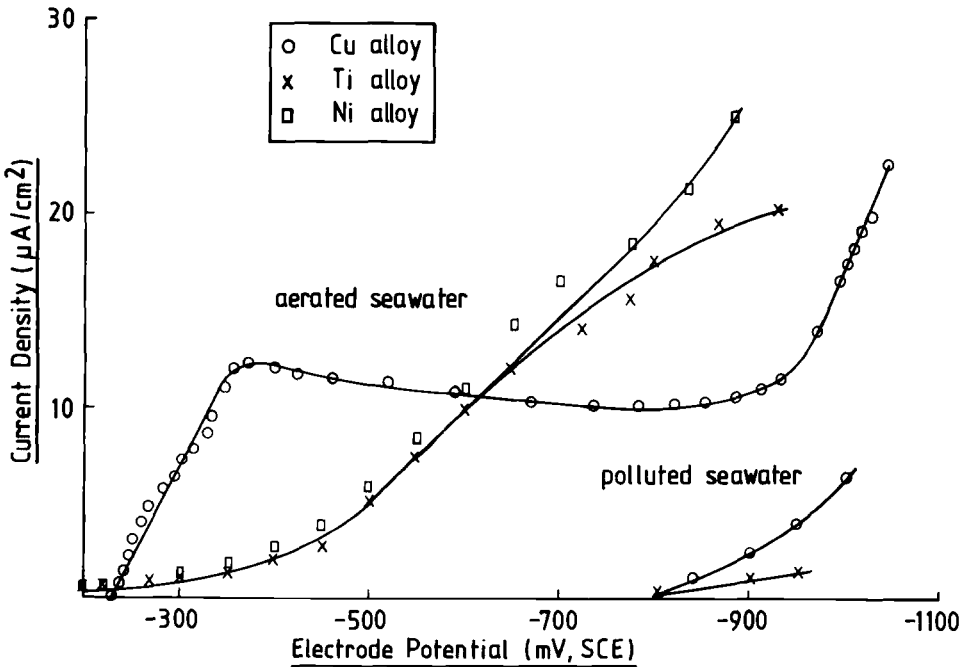


FIG. 10—Initial cathodic polarization curves for metals in propulsion unit.

The computed variation of the potential at Position A in Fig. 8 (equivalent to the crevice-mouth potential) with time, based on the data from the six-month polarization tests, is shown in Fig. 12. From this figure it is clear that very good protection would be afforded to the nickel-alloy shaft in the propulsion unit, even in periodically polluted seawater. It was calculated that in the unlikely event of the estimated seawater resistance from the unit entrance to the zinc anodes being double that assumed, an error of only 10 mV would have arisen in the calculated Position A potential at 20°C for filmed-metal conditions. It was considered that the scale of the geometric and electrochemical assumptions made in calculations for the propulsion unit was justified in view of the degree of cathodic protection predicted.

Galvanic Corrosion within a Mixed-Metal Marine Heat-Exchanger System

The need arose to assess the corrosion rate of copper-alloy components (particularly the header) in the proposed symmetrical heat-exchanger system illustrated in Fig. 12 in which both the tubes and the tubeplate were to be constructed of a relatively cathodic material in order to avoid corrosion at the tube inlets. The header and pipe were to be made of two different copper alloys. The problem was therefore to estimate the corrosion allowance to be made for the copper-alloy header and the 7-m-long, 350-mm-diameter pipe, and in the event of header corrosion being indicated as excessive, to assess the corrosion rate of the pipe if the header were electrically insulated at both flanges. The pipe would remain in electrical contact with the tubeplate and tube-bundle by means of supporting structures when the header was insulated.

Analytical solution assuming unidirectional current flow is not possible for a conical header geometry in the case where the header is electrically connected. Analysis for this case was therefore made on the basis that the header had a cylindrical cross-section with a diameter taken as

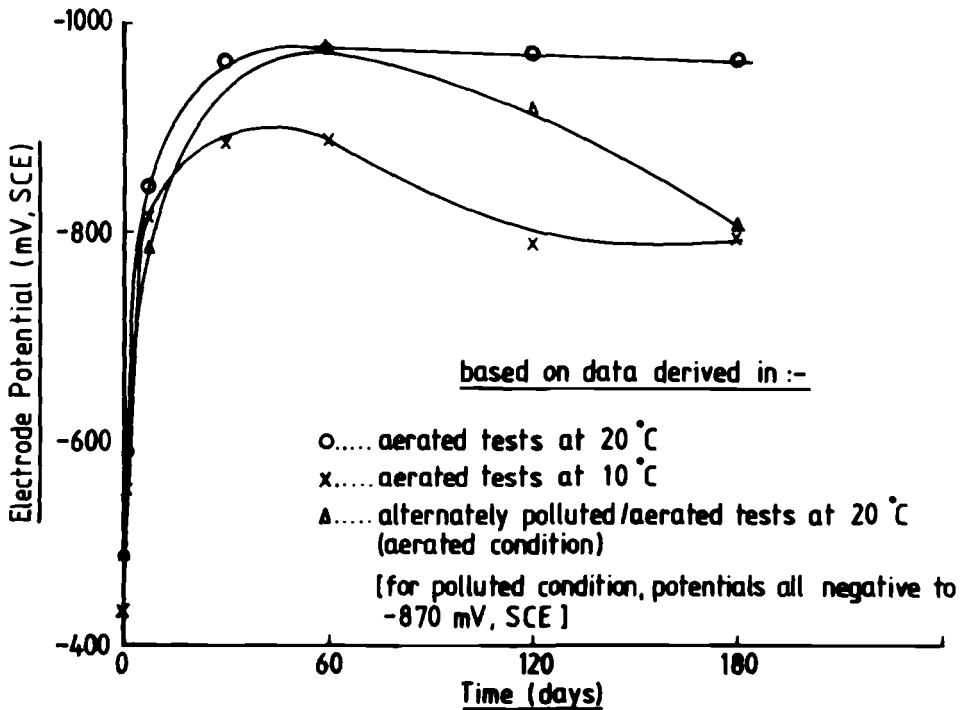


FIG. 11—Change of shaft crevice mouth potential with time in propulsion unit.

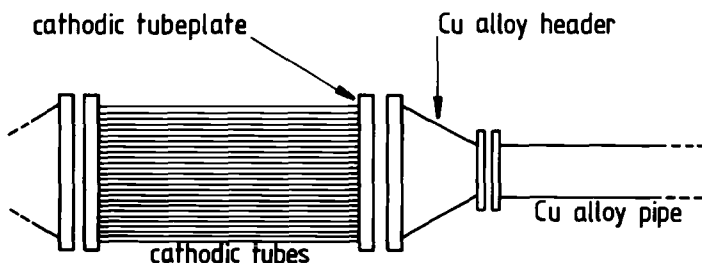


FIG. 12—Mixed-metal heat-exchanger system.

the mean diameter of the two cylinders, which give rise to the same current from and potential drop over the conical header, respectively, assuming that current density is independent of potential. It was estimated that the error involved in assuming a potential-independent current density in the "equivalent" cylinder diameter derivation was less than 2 mV. The calculated equivalent cylinder diameter obtained (by approximate methods) when an exponential dependence of current density upon potential was assumed, was actually within half a percent of the mean physical diameter of the header.

Laboratory and pilot-scale potentiostatic polarization measurements indicated that linear polarization kinetics applied to the cathodic material to be used for the tubeplate and tube-bundle, and that Butler-Volmer anodic (divalent) electrode kinetics applied to the two copper alloys to be used. Butler-Volmer electrode kinetics are described by the following equation relating anodic current density (i) to anodic polarization η for a divalent metal

$$i = i_c \left\{ \exp\left(\frac{\alpha 2F\eta}{RT}\right) - \exp\left(-\frac{\alpha 2F\eta}{RT}\right) \right\} \quad (6)$$

Equation 6 assumes that the oxygen reduction process involves a rate-determining two-electron transfer and that the surface concentration of dissolved oxygen is equal to the bulk concentration. Unidirectional current flow analysis for the heat-exchanger system was therefore made for a combination of linear cathodic electrode kinetics and Butler-Volmer anodic electrode kinetics, although a preliminary assessment was made assuming linear electrode kinetics throughout to provide initial "ranging" data. Because of symmetry about a point mid-way along the tube-bundle, analysis was carried out using half the total length of the tube-bundle. Use of Waber's results [4] indicated a maximum error of about 2 mV for a unidirectional current flow assumption for a system of the size being considered.

Equations and a programming sequence are given in Appendix D. The length of a "user-friendly" program in BASIC enabling calculations for both linear electrode kinetics and (linear plus Butler-Volmer) electrode kinetics was 19 kbytes. Computing time is a matter of seconds for linear electrode kinetics but can be several minutes when Butler-Volmer electrode kinetics are introduced because of the slow numerical integration step (Hewlett-Packard HP85).

Computed results for the proposed heat-exchanger system, based on electrochemical polarization data obtained from a pilot-scale test after about one year, are shown in Fig. 13 in terms of the corrosion rate distribution within the header and pipe. It is apparent that the corrosion rate of the electrically connected header adjacent to the tubeplate would be increased by about ten times because of contact with cathodic components and that electrical insulation of the header would lead to the pipe having a corrosion rate adjacent to the header seven times its normal value. Quantitative confirmation of these factors was obtained in a one-third size pilot-scale test carried out over a period of two years using both connected and insulated headers. The decision as to whether to insulate the header was influenced by the tendency of the copper alloy

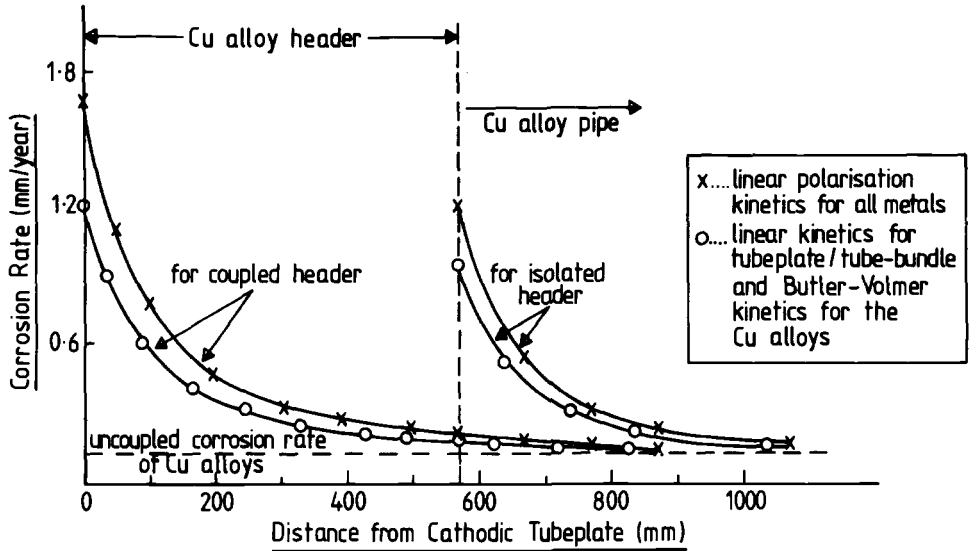


FIG. 13—Corrosion rate distribution along copper-alloy header and pipe.

chosen for the header to be prone to deep pitting. It is clear from Fig. 13 that extra corrosion allowance for the pipe (if the header were insulated) need only be made for about 100 mm from the header.

Analysis can be effected for mixed-metal heat-exchanger systems having other combinations of component polarity than the Fig. 12 system. For example, where the header is of a relatively cathodic metal or even undergoes a polarity change along its length, that is, it may be galvanically corroding adjacent to the (cathodic) tubeplate but be cathodically protected adjacent to the (anodic) pipe. Calculations can also easily be made for cases where the tubeplate metal differs from the tube-bundle metal.

Mixed-Metal Heat-Exchanger Electrically Connected to Steel Hull

In practice the proposed heat-exchanger system illustrated in Fig. 12 would be joined to a steel hull by means of a 15-m-long plastic pipe as indicated in Fig. 14. Electrical connection between the hull and the heat-exchanger would be maintained by supporting structures so that the plastic-pipe end of the copper-alloy pipe would enjoy some cathodic protection. The analysis described in the previous section was therefore extended to ascertain how far cathodic protection would occur along the copper-alloy pipe and whether galvanic corrosion of the header and pipe would be significantly affected by connection to the hull.

Unidirectional analysis was carried out assuming the same combination of linear and Butler-Volmer electrode kinetics as before for the tube-bundle, tubeplate, header, and the "anodic" part of the pipe, with linear electrode kinetics for the cathodically polarized, calcareously filmed part of the pipe. This latter assumption proved to be valid because the cathodic polarization of the copper-alloy pipe was calculated to be less than 100 mV, that is, Zone (i) of Fig. 3 was appropriate; cathodic polarization would be insufficient to reach Zone (ii). The analysis and programming sequence are described in Appendix E. The length of a "user-friendly" program in BASIC embracing all possible system variations was 30 kbytes, viz for with and without connection to the hull, for with and without insulation of the header, for all linear electrode kinetics, and for (linear plus Butler-Volmer) electrode kinetics. The computing time for a "+"

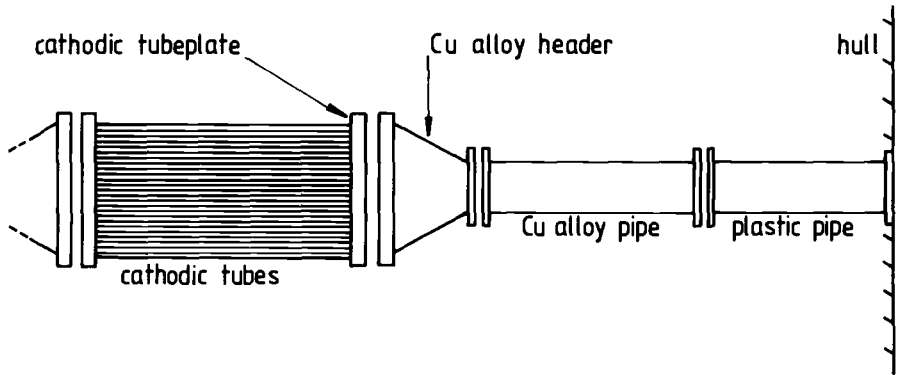


FIG. 14—Mixed-metal heat-exchanger connected to hull.

hull" calculation for a connected header was about 20 s for linear electrode kinetics, and several minutes for Butler-Volmer electrode kinetics (Hewlett-Packard HP85).

Results of calculations using electrochemical polarization data derived for filmed 70-30 cupronickel from one-year old ambient-temperature laboratory tests for the cathodically polarized part of the pipe and from pilot-scale tests for the other parts of the system are shown in Fig. 15. The circles represent results of "independent" calculations made ignoring the hull (as on Fig. 13), or the cathodic tube-bundle and tubeplate, and the crosses relate to results of "interacted" calculations for the entire connected system shown in Fig. 14. It is evident from Fig. 15 that electrical connection to the hull will have very little influence on the galvanic corrosion likely to occur on the header and on the pipe close to the header (circles and crosses overlap in this region), whereas connection to the cathodic tube-bundle and tubeplate will decrease the cathodic polarization of the metal pipe at the plastic-pipe end by about 5 mV. The extent of significant cathodic protection (defined as a 70% corrosion rate reduction) likely to be

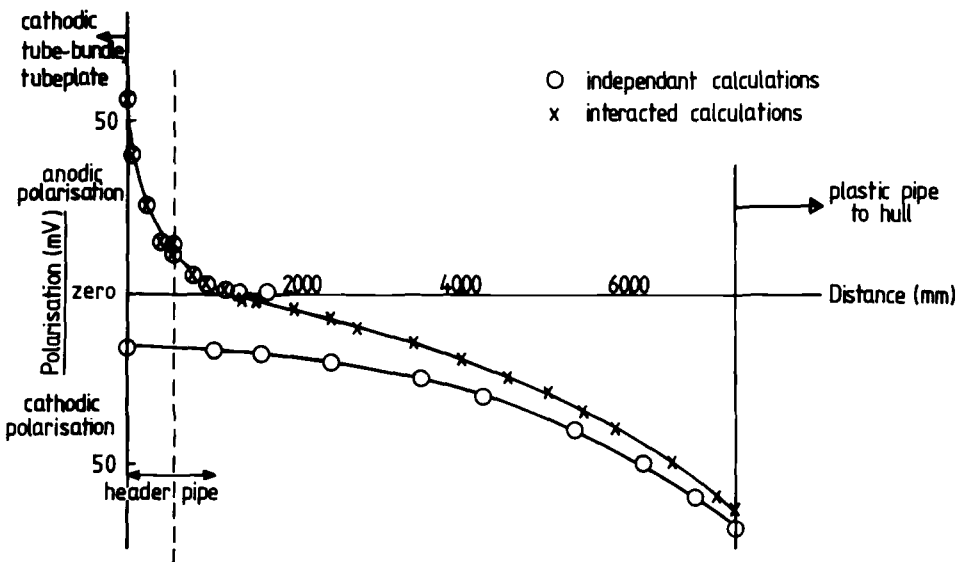


FIG. 15—Polarization distribution along copper-alloy header and pipe.

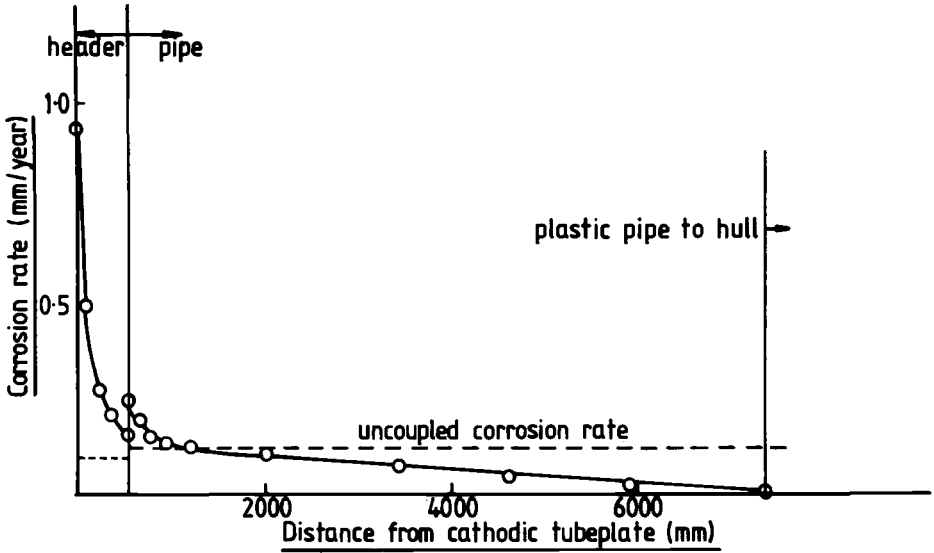


FIG. 16—Corrosion rate distribution along copper-alloy header and pipe.

enjoyed by the metal pipe can be assessed as about 2 m from Fig. 16 (which relates directly to Fig. 15 and is based on the uncoupled corrosion rate relating to the anodically polarized part of the pipe). It is interesting to note that laboratory tests have shown that calcareous deposit formed at about 10°C (predominantly calcite) is much less coherent than that formed at about 20°C (predominantly aragonite). In consequence, the final extent of protection along the metal pipe in this system would be much less if the ambient temperature of the seawater were consistently “low” during film formation.

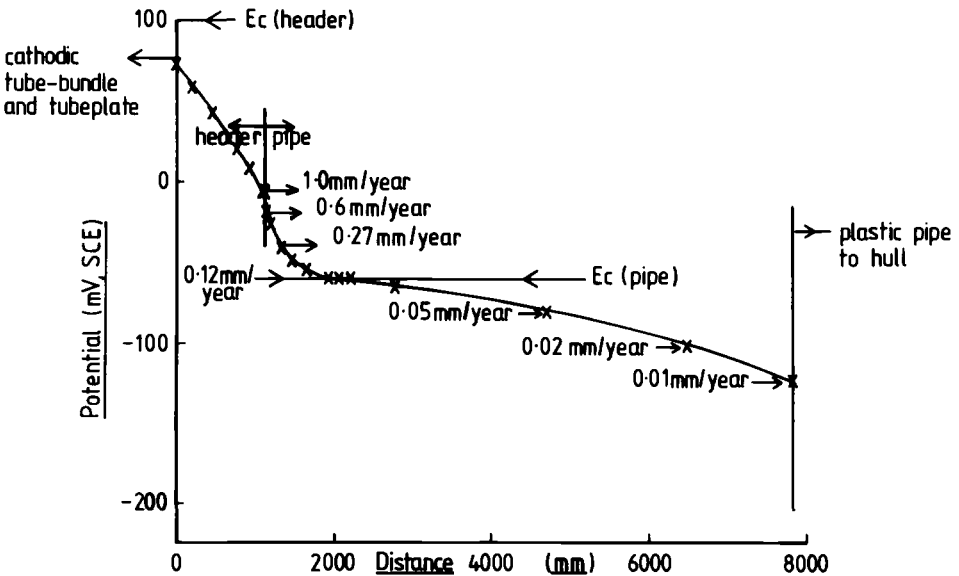


FIG. 17—Potential distribution along nickel-alloy header and copper-alloy pipe.

In view of the risk of deep pitting associated with the use of cast-metal headers made from relatively anodic metal, and uncertainty as to the feasibility of ensuring complete header insulation, unidirectional analysis has been made for the case of a cathodic header. This analysis is less involved than for the anodic header case because linear electrode kinetics apply to the header, and Butler-Volmer electrode kinetics only pertain to the anodic part of the metal pipe. Solutions can be deduced by analogy with those given in Appendix E. Results of computation for a cathodic nickel-alloy header (obtained using a potentiostatically determined cathodic polarization curve for the nickel alloy measured after one year's polarization) are given in Fig. 17, which shows both the electrode potential distribution and the corrosion rate distribution over the copper-alloy pipe. Although a significant corrosion rate enhancement of about eight times would clearly occur on the pipe adjacent to the cathodic header, this would be quickly dissipated. It should be noted that the header for Fig. 17 is twice as long as for Figs. 13, 15, and 16. It has been shown that the use of a connected cathodic header will double the corrosion rate of the copper-alloy pipe that would occur if the header could be electrically insulated.

Conclusion

It is possible to use small-memory microcomputers to rapidly calculate how corrosion will be distributed within practical mixed-metal equipment, such as heat-exchangers, pumps, and pipework that carry seawater. The assumption of unidirectional current flow results in negligible error for equipment of diameter up to at least 500 mm.

Acknowledgment

This work has been supported by Procurement Executive, United Kingdom Ministry of Defence.

APPENDIX A

Solution of Eq 4 for Cathodic Electrode Kinetics of Fig. 3

For all three zones of Fig. 3 to be involved, the tube inlet-end potential must be in Zone (iii) and the outlet-end potential in Zone (i). Two unknown lengths of tube (total length L) must be found, that is, the lengths corresponding to Zones (iii) and (ii), designated $x_{end\ lin}$ and $x_{end\ diff}$, respectively.

For Zone (iii), where $i = k_{(iii)}(E_{c(app)} - E)$, integrating Eq 4 with respect to x , and substituting for the potential gradient at E_{tr2} by the expression obtained upon integrating Eq 4 for Zones (ii) + (i) kinetics

$$\begin{aligned} \left(\frac{dE}{dx}\right)^2 - \left\{ \left(\frac{2\rho i_d x_{end\ diff}}{r}\right) + \left(\frac{1}{K_{(i)}^{1/2}}\right)(E_c - E_{tr1}) \tanh\left(\frac{L - x_{end\ diff} - x_{end\ lin}}{K_{(i)}^{1/2}}\right) \right\}^2 \\ = \left(\frac{1}{K_{(iii)}}\right) [(E_{c(app)} - E)^2 - (E_{c(app)} - E_{tr2})^2] \end{aligned}$$

where

$$K_{(i)} = \frac{r}{2\rho k_{(i)}} \text{ and}$$

$$K_{(iii)} = \frac{r}{2\rho k_{(iii)}}$$

- (iii) calculate cathodic current I_c for the pipe (using equations, such as A3);
- (iv) calculate anodic current I_A from the anode of known area using the Butler-Volmer equation (see Eq 6), taking the anode potential as E_{beg} over all its surface;
- (v) obtain the correct value for E_{beg} by Newton's method

- (a) $F = I_c - I_A$
- (b) $F_1 = F'(E_{beg})$
- (c) $F_2 = -(F/F_1)$ and IF ABS(F_2) < 0.00001 * ABS(E_{beg})
THEN (vi)
- (d) $E_{beg} = E_{beg} + F_2$ and GOTO (ii);

(vi) output line, or pass onto the next computation stage if the cathodic electrode kinetics assumed for the last stage are obviously inappropriate (for example, pipe-end potential was calculated to be positive to E_{iri} in Fig. 3 when only Zones (iii) and (ii) had been considered in the analysis for the last stage).

Analysis for cathodically protected pipework can also be made for the case where the small sacrificial anode at the inlet-end is in the form of a short in-line pipe constructed from, or coated with, anodic material subject to Tafel-law electrode kinetics. Details are given in Appendix F of Ref 17.

APPENDIX C

Equations for the Mixed-Metal Marine Propulsion Unit

Assuming linear cathodic electrode kinetics throughout the unit, the forms of the differential Eq 5, which were to be solved were as follows:

- (a) for the portion of the unit having the titanium-alloy (and nickel-alloy end-piece) at radial position r_i

$$\frac{d^2E}{dx^2} = \frac{2\rho\{k_{Ti}(E - E_{c(Ti)})3.32r_i + k_{Cu}(E - E_{c(Cu)})r_o\}}{r_o^2 - r_i^2} \tag{C1}$$

- (b) for the portion of the unit having the copper-alloy vaned housing at radial position r_i

$$\frac{d^2E}{dx^2} = \frac{2\rho k_{Cu}(E - E_{c(Cu)})\{^2/3r_o + 5.68r_i\}}{r_o^2 - r_i^2} \tag{C2}$$

The factor of $2/3$ preceding the r_o term in the numerator of Eq C2 is to take into account the 200-mm shorter length of the copper-alloy shell.

Consecutive integration of Eq C1 with respect to x leads to a linear equation for the potential at the end of the nickel-alloy end-piece E_E in terms of the potential at Position A in Fig. 8 E_A . This latter equation is used in the equation for the potential gradient at Position A, $(dE/dx)_A$, in order to relate $(dE/dx)_A$ to E_A , that is

$$\left(\frac{dE}{dx}\right)_A = \left(\frac{4\rho}{r_o^2 - r_i^2}\right)^{1/2} \left\{ \left(\frac{3.32}{2} r_i k_{Ti} + \frac{r_o k_{Cu}}{2}\right) \times (E_A^2 - E_E^2) - (3.32r_i k_{Ti} E_{c(Ti)} + r_o k_{Cu} E_{c(Cu)})(E_A - E_E) \right\}^{1/2} \tag{C3}$$

Consecutive integration of Eq C2 with respect to x leads to the following equation for the distance between the unit's seawater entrance and Position A (600 mm), in terms of the potential at

the unit entrance E_{beg} , and the potential E_A

$$60 = K_1^{1/2} \ln \left[\left\{ (E_{c(\text{Cu})} - E_{\text{beg}}) + \left[(E_{c(\text{Cu})} - E_{\text{beg}})^2 + K_1 \left(\frac{dE}{dx} \right)_A^2 - (E_{c(\text{Cu})} - E_A)^2 \right]^{1/2} \right\} / \left\{ (E_{c(\text{Cu})} - E_A) + K_1^{1/2} \left(\frac{dE}{dx} \right)_A \right\} \right] \quad (\text{C4})$$

where

$$K_1 = \frac{r_o^2 - r_i^2}{2\rho k_{\text{Cu}}(5.68r_i + \frac{2}{3}r_o)}$$

Equation C4 has to be solved numerically for E_A for given values of E_{beg} , using Eq C3 to obtain $(dE/dx)_A$ for each E_A value.

A suitable overall programming sequence for propulsion unit calculations was found to be

- (i) adopt initial values for E_{beg} and E_A ;
- (ii) numerically solve Eq C4 using Newton's method to obtain new E_A value;
- (iii) calculate the current from the Unit I as $[\pi(r_o^2 - r_i^2)/\rho](dE/dx)_{\text{beg}}$;
- (iv) calculate the polarization of the zinc anodes η from I, assuming divalent Butler-Volmer electrode kinetics for zinc, that is

$$\eta = \frac{RT}{F} \ln(\theta + (\theta^2 + 1)^{1/2})$$

where

$$\theta = I/(2i_c A_t),$$

i_c = corrosion current density of zinc, and

A_t = total anode area;

- (v) revise E_{beg} from

$$E_{\text{beg}} = E_{c(\text{zinc})} + \eta + IR$$

where R = estimated average seawater resistance from the unit entrance to the anodes (0.2Ω at 20°C);

- (vi) repeat sequence with mean of old and new E_{beg} values until new and old values differ by less than 0.1 mV.

APPENDIX D

Solution of Eq 4 for Cathodic (Tube-bundle/Tubeplate) Connected to Anodic (Header/Pipe)

The tube-bundle and tubeplate are assumed to be of the same metal.

(a) For Linear Polarization Kinetics on All Components

Solutions for the simple "cathodic tube-anodic (tube-tube)" case were derived in Ref 17. These solutions are easily modified for the case of a cathodic tube-bundle and tubeplate, as indicated below for the expressions for maximum anodic polarization.

(i) When the Header Is Electrically Insulated at Both Flanges

Maximum anodic polarization of the pipe is

$$\Delta E_c^{c-a2} \left\{ \frac{r_2^2}{K_2^{1/2}} \frac{\pi R}{\rho} \tanh\left(\frac{L_2}{K_2^{1/2}}\right) + \frac{\left[\frac{\left(\frac{\pi r_2^2}{\rho K_2^{1/2}}\right) \tanh\left(\frac{L_2}{K_2^{1/2}}\right)}{\left(\frac{n \pi r_c^2}{\rho K_c^{1/2}}\right) \tanh\left(\frac{L_c}{K_c^{1/2}}\right) + k_c A \right]}{\right\} + 1 \quad (D1)$$

where

ΔE_c^{c-a2} = the (positive) difference between the corrosion potentials of the tubeplate and the pipe,

r_2, L_2 = radius and length of the pipe, respectively,

r_c, L_c = radius and length of each tube in the tube-bundle, respectively,

R = resistance of the seawater within the header,

n = number of tubes in the tube-bundle, and

A = net area of the tubeplate.

K and k type factors are as defined in Appendix A.

(ii) When the Header Is Electrically Connected to the Tubeplate and Pipe

Maximum anodic polarization of the header

$$n \Delta E_c^{c-a1} \left(\frac{r_c}{r_1} \right)^2 \left(\frac{K_1}{K_c} \right)^{1/2} \tanh\left(\frac{L_c}{K_c^{1/2}}\right) + \left(\frac{K_1^{1/2} \rho}{r_1^2 \pi} \right) A \Delta E_c^{c-a1} k_c$$

$$\pm \left\{ \frac{\left(\frac{r_2}{r_1} \right)^2 \left(\frac{K_1}{K_2} \right)^{1/2} \tanh\left(\frac{L_2}{K_2^{1/2}}\right) \Delta E_c}{\cosh\left(\frac{L_1}{K_1^{1/2}}\right) + \left(\frac{r_2}{r_1} \right)^2 \left(\frac{K_1}{K_2} \right)^{1/2} \tanh\left(\frac{L_2}{K_2^{1/2}}\right) \sinh\left(\frac{L_1}{K_1^{1/2}}\right)} \right\} \quad (D2)$$

$$\left\{ \frac{\sinh\left(\frac{L_1}{K_1^{1/2}}\right) + \left(\frac{r_2}{r_1} \right)^2 \left(\frac{K_1}{K_2} \right)^{1/2} \tanh\left(\frac{L_2}{K_2^{1/2}}\right) \cosh\left(\frac{L_1}{K_1^{1/2}}\right)}{\cosh\left(\frac{L_1}{K_1^{1/2}}\right) + \left(\frac{r_2}{r_1} \right)^2 \left(\frac{K_1}{K_2} \right)^{1/2} \tanh\left(\frac{L_2}{K_2^{1/2}}\right) \sinh\left(\frac{L_1}{K_1^{1/2}}\right)} \right\}$$

$$+ n \left(\frac{r_c}{r_1} \right)^2 \left(\frac{K_1}{K_c} \right)^{1/2} \tanh\left(\frac{L_c}{K_c^{1/2}}\right) + \left(\frac{K_1^{1/2} \rho}{r_1^2 \pi} \right) A k_c$$

where ΔE_c^{c-a1} = the (positive) difference between the corrosion potentials of the tubeplate and the header; ΔE_c = the (positive) difference between the corrosion potentials of the header and pipe; and r_1, L_1 = "mean" radius and length of the header, respectively.

In Eq D2, a positive sign preceding the term in ΔE_c in the numerator indicates that the pipe is noble to the header (and vice versa).

The equation for the minimum anodic polarization of the header (that is, at its junction with the pipe) is given in Ref 17 (Eq D7).

(b) For Linear Cathodic Electrode Kinetics and Butler-Volmer Anodic Electrode Kinetics

Numerical methods of solution are necessary when Butler-Volmer electrode kinetics are considered. Newton's method can be used to solve the equations for maximum anodic polarization and Simpson's method to carry out numerical integrations to evaluate minimum header polar-

ization. The values for these polarizations calculated assuming only linear polarization kinetics are used as initial values in these numerical calculations.

The equations to be solved are indicated below.

(i) *When the Header Is Electrically Insulated at Both Flanges*

The equation to be numerically solved by Newton's method to obtain the maximum anodic polarization of the pipe η is greatly simplified if the pipe is assumed to be effectively infinite, an assumption involving negligible error for the heat-exchanger system under consideration. Under these conditions, using divalent Butler-Volmer kinetics for the pipe as in Eq 6 with $\alpha = 0.5$, and equating the anodic and cathodic currents (derived after a single integration of Eq 4)

$$\frac{\left[\exp\left(\frac{F\eta}{2RT}\right) - \exp\left(-\frac{F\eta}{2RT}\right) \right] 2\pi r_2^{3/2} \left(\frac{i_c RT}{\rho F}\right)^{1/2}}{\Delta E_c^{-\alpha_2} - \eta - 2r \pi r_2^{3/2} \left(\frac{i_c RT}{\rho F}\right)^{1/2} \left[\exp\left(\frac{F\eta}{2RT}\right) - \exp\left(-\frac{F\eta}{2RT}\right) \right]} = \left(\frac{n\pi r_c^2}{\rho K_c^{1/2}}\right) \tanh\left(\frac{L_c}{K_c}\right) + k_c A \quad (D3)$$

(ii) *When the Header Is Electrically Connected to the Tubeplate and Pipe*

Assuming an effectively infinitely long pipe and divalent Butler-Volmer kinetics for both header and pipe ($\alpha = 0.5$), the equation to be numerically solved to obtain the maximum header polarization (η_{\max}), is as follows, where η_{\min} is the minimum header polarization and $(\eta_{\max})_2$ is the maximum pipe polarization

$$\begin{aligned} & \frac{\pi r_1^2}{\rho} \left\{ \left(\frac{4\rho i_{c1} RT}{Fr_1}\right) \left[\exp\left(\frac{F(\eta_{\max})_1}{RT}\right) + \exp\left(-\frac{F(\eta_{\max})_1}{RT}\right) \right. \right. \\ & \quad \left. \left. - \exp\left(\frac{F\eta_{\min}}{RT}\right) - \exp\left(-\frac{F\eta_{\min}}{RT}\right) \right] + \left(\frac{r_2}{r_1}\right)^4 \left(\frac{4\rho i_{c2} RT}{Fr_2}\right) \right. \\ & \quad \left. \times \left[\exp\left(\frac{F(\eta_{\max})_2}{RT}\right) + \exp\left(-\frac{F(\eta_{\max})_2}{RT}\right) - 2 \right] \right\}^{1/2} = [\Delta E_c^{-\alpha_1} - (\eta_{\max})_1] \\ & \quad \times \left\{ \left(\frac{n\pi r_c^2}{\rho K_c^{1/2}}\right) \tanh\left(\frac{L_c}{K_c}\right) + k_c A \right\} \quad (D4) \end{aligned}$$

The value of η_{\min} (potential, E_{end}), and hence $(\eta_{\max})_2$, for a given value of $(\eta_{\max})_1$ (potential, E_{beg}) is defined by the following numerical integration over the length of the header

$$\begin{aligned} L_1 = & \int_{E_{\text{end}}}^{E_{\text{beg}}} dE \left\{ \left(\frac{4\rho i_{c1} RT}{Fr_1}\right) \left[\exp\left(\frac{F\eta}{RT}\right) + \exp\left(-\frac{F\eta}{RT}\right) \right. \right. \\ & \quad \left. \left. - \exp\left(\frac{F\eta_{\min}}{RT}\right) - \exp\left(-\frac{F\eta_{\min}}{RT}\right) \right] + \left(\frac{r_2}{r_1}\right)^4 \left(\frac{4\rho i_{c2} RT}{Fr_2}\right) \left[\exp\left(\frac{F(\eta_{\max})_2}{RT}\right) \right. \right. \\ & \quad \left. \left. + \exp\left(-\frac{F(\eta_{\max})_2}{RT}\right) - 2 \right] \right\}^{1/2} \quad (D5) \end{aligned}$$

where $\eta = (E - E_c)_1$.

Equation D4 is solved by Newton's method, and Eq D5 by Simpson's method. The following programming sequence was adopted:

- (i) adopt initial values for E_{beg} (header) and E_{end} (header) from the previous "all linear kinetics" calculation;
- (ii) carry out a subroutine calculation for E_{end} (header) using Eq D5; modify η min by step until the integral is within 1% of L_1 ;
- (iii) numerically solve Eq D4 to obtain a new value for E_{beg} (header); and
- (iv) proceed to (ii), unless the new E_{beg} (header) value differs from the previous value by less than 0.1 mV.

APPENDIX E

Solution of Eq 4 for Mixed-Metal Heat-Exchanger Connected to Steel Hull

The solutions described in Appendix D for the connected-header case are extended to allow for electrical connection of the heat-exchanger to a steel hull (the solutions for the insulated-header case can be easily deduced from the results given in this Appendix). In addition to calculating the potentials at each end of the header (E_{beg} at the tubeplate-end and E_{end} at the metal-pipe end), it is necessary to derive the potential at the plastic-pipe end of the metal pipe, $E_{\text{pipe(hull)}}$, and the potential gradient at the point of zero polarization on the metal pipe (dE/dx).

(a) For Linear Polarization Kinetics on All Components

Calculations are first made assuming linear electrode kinetics throughout to provide ranging data for subsequent, more complex calculations involving Butler-Volmer electrode kinetics. It is assumed that the corrosion potentials of the anodic and cathodic parts of the metal pipe are the same, and that a sharp transition of effective corrosion current density occurs at the point of zero polarization on the metal pipe. The effect of these assumptions will be to slightly overestimate the influence of the hull.

The potential at the metal-pipe end of the header is given by numerical solution of the following equation derived by a double integration of Eq 4 over the length of the header

$$L_1 = K_1^{1/2} \ln \left\{ \left(\eta \max + K_1^{1/2} \left[n \left(\frac{r_c}{r_1} \right)^2 \frac{\tanh \left(\frac{L_c}{K_c^{1/2}} \right)}{K_c^{1/2}} + \frac{k_c A \rho}{\pi r_1^2} \right] \eta c^{\max} \right) \right. \\ \left. \div \left(\eta \min + \left\{ \eta \min^2 - \eta \max^2 + K_1 \left[n \left(\frac{r_c}{r_1} \right)^2 \frac{\tanh \left(\frac{L_c}{K_c^{1/2}} \right)}{K_c^{1/2}} + \frac{k_c A \rho}{\pi r_1^2} \right] \eta c^{\max^2} \right\}^{1/2} \right) \right\} \quad (\text{E1})$$

where

$$\begin{aligned} \eta \max &= (E_{\text{beg}} - E_c)_1, \\ \eta \min &= (E_{\text{end}} - E_c)_1, \text{ and} \\ \eta_c^{\max} &= (E_c - E_{\text{beg}})_c. \end{aligned}$$

The potential at the tubeplate-end of the header is given by numerical solution of the following equation obtained by a summation of equations for (dE/dx)² from the tubeplate-end of the

header to the plastic-pipe end of the metal pipe

$$\left[n \left(\frac{r_c}{r_1} \right)^2 \frac{\tanh \left(\frac{L_c}{K_c^{1/2}} \right)}{K_c^{1/2}} + \frac{k_c A \rho}{\pi r_1^2} \right]^2 \eta_c^{\max^2} - \frac{\eta \max^2}{K_1} - \left(\frac{r_2}{r_1} \right)^4 \times [(E_{\text{pipe(hull)}} - E_{\text{hull}})\rho / (R \pi r_2^2)]^2 - \left(\frac{r_2}{r_1} \right)^4 \frac{(\eta \max)_2^2}{K_2} + \left(\frac{r_2}{r_1} \right)^4 \frac{(\eta_c^{\max})_2^2}{K_{2c}} + \frac{\eta \min^2}{K_1} = 0 \quad (\text{E2})$$

where

- E_{hull} = the potential of the steel hull,
- R = resistance of the seawater within the plastic pipe,
- $(\eta \max)_2$ = maximum anodic polarization of the metal pipe,
- $(\eta_c^{\max})_2$ = maximum cathodic polarization of the metal pipe, and
- K_{2c} = K term for the cathodic portion of the metal pipe.

The potential gradient at the point of zero polarization on the metal pipe is given by numerical solution of the equation for pipe length as a sum of its "anodic" and "cathodic" parts (each part given by a double integration of Eq 4)

$$L_2 = K_2^{1/2} \ln \left\{ \left((\eta \max)_2 + \left\{ (\eta \max)_2^2 + \left(\frac{dE}{dx} \right)_z K_2 \right\}^{1/2} \right) / \left(\left(\frac{dE}{dx} \right)_z K_2^{1/2} \right) \right\} + K_{2c}^{1/2} \ln \left\{ \left((\eta_c^{\max})_2 + \left\{ (\eta_c^{\max})_2^2 + \left(\frac{dE}{dx} \right)_z K_{2c} \right\}^{1/2} \right) / \left(\left(\frac{dE}{dx} \right)_z K_{2c}^{1/2} \right) \right\} \quad (\text{E3})$$

The potential at the plastic-pipe end of the metal pipe is given by numerical solution of the following equation obtained by a single integration of Eq 4 for the cathodically polarized part of the pipe

$$\left(\frac{dE}{dx} \right)_z^2 - \left(\frac{(E_{\text{pipe(hull)}} - E_{\text{hull}})\rho}{R \pi r_2^2} \right)^2 = \frac{-(\eta_c^{\max})_2^2}{K_{2c}} \quad (\text{E4})$$

Taking initial values for E_{beg} and E_{end} as calculated by the equations in Appendix D(a), consecutive solution of Equations E1 to E4 employing Newton's method enables the determination of the potential distribution in the heat-exchanger/hull system to an accuracy of ± 0.1 mV in about 20 s using a Hewlett-Packard HP85 microcomputer.

(b) For Linear Cathodic Electrode Kinetics and Butler-Volmer Anodic Electrode Kinetics

The introduction of Butler-Volmer electrode kinetics leads to the requirement for numerical integrations for the corresponding equations to Eqs E1 and E3. The equations corresponding to Eqs E1 to E3 when divalent Butler-Volmer anodic electrode kinetics are considered are as follows.

For the potential at the metal-pipe end of the header (equation corresponding to Eq E1)

$$L_1 = \int_{E_{\text{end}}}^{E_{\text{beg}}} dE \left/ \left\{ \left(\frac{4\rho_{i_{c1}} RT}{Fr_1} \right) \left[\exp\left(\frac{F\eta}{RT}\right) + \exp\left(-\frac{F\eta}{RT}\right) - \exp\left(\frac{F\eta \text{ max}}{RT}\right) - \exp\left(-\frac{F\eta \text{ max}}{RT}\right) \right] + \left[n\left(\frac{r_c}{r_1}\right)^2 \frac{\tanh\left(\frac{L_c}{K_c^{1/2}}\right)}{K_c^{1/2}} + \frac{k_c A \rho}{\pi r_1^2} \right]^2 \eta_c^{\text{max}^2} \right\}^{1/2} \quad (\text{E5})$$

where $\eta = (E - E_c)_1$.

For the potential at the tubeplate end of the header (equation corresponding to Eq E2)

$$\begin{aligned} & \left[n\left(\frac{r_c}{r_1}\right)^2 \frac{\tanh\left(\frac{L_c}{K_c^{1/2}}\right)}{K_c^{1/2}} + \frac{k_c A \rho}{\pi r_1^2} \right]^2 \eta_c^{\text{max}^2} - \left(\frac{4\rho_{i_{c1}} RT}{Fr_1} \right) \left[\exp\left(\frac{F\eta \text{ max}}{RT}\right) \right. \\ & + \exp\left(-\frac{F\eta \text{ max}}{RT}\right) - \exp\left(\frac{F\eta \text{ min}}{RT}\right) - \exp\left(-\frac{F\eta \text{ min}}{RT}\right) \left. \right] - \left(\frac{r_2}{r_1}\right)^4 \left[\frac{(E_{\text{pipe(hull)}} - E_{\text{hull}})\rho}{R \pi r_2^2} \right]^2 \\ & - \left(\frac{r_2}{r_1}\right)^4 \left(\frac{4\rho_{i_{c2}} RT}{Fr_2} \right) \left[\exp\left(\frac{F(\eta \text{ max})_2}{RT}\right) + \exp\left(-\frac{F(\eta \text{ max})_2}{RT}\right) - 2 \right] + \left(\frac{r_2}{r_1}\right)^4 \frac{(\eta_c^{\text{max}})_2^2}{K_{2c}} = 0 \end{aligned} \quad (\text{E6})$$

For the potential gradient at the point of zero polarization on the metal pipe (equation corresponding to Eq E3)

$$\begin{aligned} L_2 = & \int_{E_{c2}}^{E_{\text{end}}} dE \left/ \left\{ \left(\frac{4\rho_{i_{c2}} RT}{Fr_2} \right) \left[\exp\left(\frac{F\eta}{RT}\right) + \exp\left(-\frac{F\eta}{RT}\right) - 2 \right] \right. \right. \\ & + \left. \left(\frac{dE}{dx} \right)_z^2 \right\}^{1/2} + K_{2c}^{1/2} \ln \left\{ \left((\eta_c^{\text{max}})_2 + \left\{ (\eta_c^{\text{max}})_2^2 + \left(\frac{dE}{dx} \right)_z^2 K_{2c} \right\}^{1/2} \right) \right. \\ & \left. \div \left(\left(\frac{dE}{dx} \right)_z K_{2c}^{1/2} \right) \right\} \end{aligned} \quad (\text{E7})$$

where $\eta = (E - E_c)_2$. For the potential at the plastic-pipe end of the metal pipe, Eq E4 still applies as this equation only involves linear electrode kinetics.

A suitable programming sequence was found to be as follows:

(i) Take initial values for E_{beg} and E_{end} from the previous calculation involving Butler-Volmer electrode kinetics, but ignoring the hull connection (Appendix Db); initial values for $E_{\text{pipe(hull)}}$ and $(dE/dx)_z$ are taken from the previous calculation for linear electrode kinetics throughout, with involvement of the hull connection (Appendix Ea).

(ii) Revise E_{end} by a subroutine calculation (Simpson's method) using Eq E5; modify E_{end} by step until the integral is within 1% of L_1 .

(iii) Revise E_{beg} by numerical solution (Newton's method) of Eq E6 using a subroutine; return to (ii) until an accuracy of ± 0.1 mV is achieved.

(iv) Revise $(dE/dx)_z$ by numerical solution (Newton's method) of Eq E7; this necessitates subroutine numerical integrations (Simpson's method) both for the definite integral in Eq E7 and for the first derivative of this definite integral with respect to $(dE/dx)_z$.

(v) Revise $E_{\text{pipe(hull)}}$ by numerical solution (Newton's method) of Eq E4.

(vi) Proceed to output if the new value of $E_{\text{pipe(hull)}}$ differs from the previous value by less than 0.1 mV; otherwise recalculate E_{beg} using Eq E6 and return to (iv) if the new value of E_{beg} differs from the previous value by less than 0.1 mV; otherwise return to (ii).

References

- [1] Astley, D. J. and Rowlands, J. C., *British Corrosion Journal*, Vol. 20, No. 2, 1985, pp. 90-94.
- [2] Gehring, G. A., Kuester, C. K., and Maurer, J. R., "Effective Tube Length—a Consideration on the Galvanic Corrosion of Marine Heat-Exchanger Materials," *Corrosion 80*, Paper 32, National Association of Corrosion Engineers (NACE), Houston, TX, 1980.
- [3] Newman, J., *Electrochemical Systems*, Prentice-Hall Inc., Englewood Cliffs, NJ, 1973, p. 232.
- [4] Waber, J. T. and Ruth, J. M., "Mathematical Analysis of Galvanic Corrosion Part VI: Electrode Systems with Cylindrical Geometry," Los Alamos Scientific Laboratory Report LA-1993 (Physics), University of California, Berkeley, CA, July 1956, pp. 15-31.
- [5] Doig, P. and Flewitt, P. E., *Journal of the Electrochemical Society*, Vol. 126, No. 12, 1979, pp. 2057-2063.
- [6] Forrest, A. W., Fu, J. W., and Bicchici, R. T., "Validation of Finite Element Technique for Modeling Cathodic Protection Systems," *Corrosion 80*, Paper 150, NACE, Houston, TX, 1980.
- [7] Helle, H. P., Beek, G. H., and Ligtelijn, J. Th., *Corrosion*, Vol. 37, No. 9, 1981, pp. 522-530.
- [8] Danson, D. J. and Warne, M. A., "Current Density/Voltage Calculations using Boundary Element Techniques," *Corrosion 83*, Paper 211, NACE, Houston, TX, 1983.
- [9] Frumkin, A. N., *Zh. fiz. Khim.*, Vol. 23, No. 12, 1949, pp. 1477-1482.
- [10] de Levie, R., *Advances in Electrochemistry and Electrochemical Engineering*, Vol. 6, Paul Delahay, Ed., Interscience Publishers, New York, 1967, pp. 337-340.
- [11] Sato, S. and Yamauchi, S., Sumitomo Light Metal Technical Report, Vol. 17, No. 3, 1976, pp. 24-30.
- [12] Chizmadzhev, Yu. A., Markin, V. S., Tarasevich, M. R., and Chirkov, Yu. G., *The Macrokinetics of Processes in Porous Media*, Nauka, Moscow, USSR, 1971, p. 254.
- [13] Mueller, W. A., *Journal of the Electrochemical Society*, Vol. 110, No. 6, 1963, pp. 698-703.
- [14] Reingeverts, M. D., Parputs, I. V., and Sukhotin, A. M., *Soviet Electrochemistry*, Vol. 16, No. 1, July 1980, pp. 35-38.
- [15] Alkire, R. and Mirarefi, A. A., *Journal of the Electrochemical Society*, Vol. 120, No. 11, 1973, pp. 1507-1515.
- [16] Posey, F. A., *Journal of the Electrochemical Society*, Vol. 111, No. 10, 1964, pp. 1173-1181.
- [17] Astley, D. J., *Corrosion Science*, Vol. 23, No. 8, 1983, pp. 801-832.

Galvanic Corrosion Prediction and Experiments Assisted by Numerical Analysis

REFERENCE: Fu, J. W., "Galvanic Corrosion Prediction and Experiments Assisted by Numerical Analysis," *Galvanic Corrosion. ASTM STP 978*, H. P. Hack, Ed., American Society for Testing and Materials, Philadelphia, 1988, pp. 79-85.

ABSTRACT: Principles used in the finite element modeling and boundary element modeling methods are explained in this paper. These methods are useful to corrosion engineers in analyzing corrosion cell current distributions. The paper begins with a description of how the current distribution phenomenon is represented by mathematical equations and how these equations can be solved using numerical calculations. A one-dimensional corrosion cell is used to demonstrate the methods. Later, the procedures used in the numerical modeling methods are described. Suggestions are given to corrosion engineers who are interested in using numerical modeling to analyze their corrosion problems. An example of the numerical analysis of galvanic corrosion is given. Factors affecting the accuracy of these methods are discussed.

KEY WORDS: galvanic corrosion, computers, simulation, numerical analysis, finite element, boundary element, cathodic protection

One of the key elements in the galvanic corrosion mechanism is current conduction in electrolytes. Calculation of current distribution as a function of geometry is important in both corrosion rate prediction and corrosion test design because of the geometric dependence of galvanic corrosion. For example, in galvanic corrosion rate prediction, the galvanic current distribution is nonuniform on the metal surface. Consequently, the corrosion rate cannot be expressed by a single value. The proper way of expressing the galvanic corrosion rate is to show the rate as a function of geometry. Furthermore, in galvanic corrosion tests, the simulation of geometry effect should be guided by a calculation of current distribution.

In recent years, several computer-aided engineering tools have been developed in the corrosion engineering field. These methods are the finite element method (FEM) by Kasper [1], Munn [2], DeCarlo [3], and Fu [4] and the boundary element method by Gartland and Johansen [5], Fu and Chow [6], and Danson and Warne [7]. These methods are useful in analyzing galvanic cell current distribution. There is an increasing use of these methods. However, they have not been applied to their fullest potential because these methods are somewhat difficult to understand because of the multi-discipline needed in the formulation of the methods. In this paper, the author demonstrates these methods using a simple one-dimensional corrosion cell. The purpose is to explain the principles involved in these methods. The full details of these methods cannot be described in a single paper. The reader should consult books written on these subjects for further information [8-9].

An example of the finite element analysis of a galvanic corrosion problem is given. The example illustrates how the analysis was used to predict galvanic corrosion rate and to design a simulation test. Finally, a discussion on the accuracy of numerical calculation is presented.

¹Manager of corrosion, Pennzoil Technology Center, 1520 Lake Front Circle, The Woodlands, TX 77387.

Numerical Analyses

In this section, the formulation of the numerical methods for modeling galvanic cells is explained. The phenomenon of the galvanic cell is described first and followed by mathematical equations that represent the phenomenon. The numerical procedures for solving these equations are also provided. A one-dimensional galvanic cell is used as an example because the derivation of the numerical procedures is clearer in one-dimensional space. A graphic analysis of the cell using polarization curves is also given to show that the principles involved in the numerical analyses are the same as those in the graphic analysis.

Galvanic Phenomenon

The one-dimensional galvanic cell may be a glass tube of uniform cross-sectional area filled with an electrolyte of a known concentration. The ends of the tube are capped with two metals. One metal is more anodic than the other. The electrochemical behavior metals is uniform over the surface of each metal. When the two metals are electrically connected with a low resistance wire, a galvanic cell is established. The electrolytic current originates at the anode surface, flows through the electrolyte, and ends at the cathode surface. To complete the circuit, the electrolytic current at the metal surface is converted into electrical current, which flows from the cathode to the anode through the low resistance wire. There are electrical resistance voltage (IR) drops in both the electrolytic and electric paths.

Before the two metals are connected, each metal surface is at its free corrosion potential. After the two are connected, a current starts between the two and their potentials come closer to each other. In fact, for each metal surface, the potential change, or polarization, can be measured as a function of current density. Of course, this relation of current density versus potential is the polarization curve of the metal in the electrolyte. The potential on the surface, because it is generated by an electric double layer, is a voltage step across the metal/electrolyte interface similar to that observed in electric capacitors. In Fig. 1, the potential change in the galvanic cell is shown. In this drawing, the IR voltage across the electrical wire has been ignored, so the potentials on the metal side of both the anodic and cathodic surfaces are identical. In corrosion cells, the resistance through the electric path is usually very small compared to that in the corrosive environment.

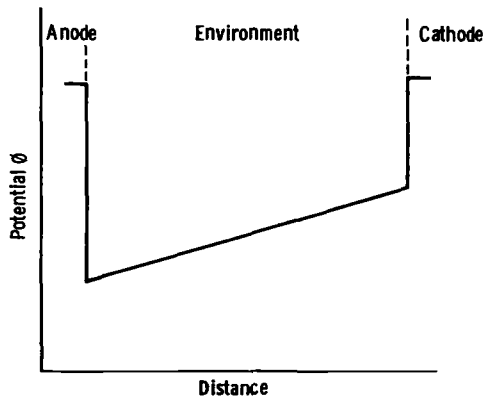


FIG. 1—IR voltage in the one-dimensional corrosion cell.

Equations for Galvanic Cells

The IR voltage in the electrolyte is the result of current passing through a resistive electrolytic path, which in the present case, is the electrolyte in the glass tube. The IR voltage is described by Ohm's law

$$i = k \nabla \phi \quad (1)$$

where i is the current density, k is the conductivity of the electrolyte, $\nabla \phi$ is the potential gradient, and ϕ is the potential. In one-dimensional space, the Ohm's law is reduced to

$$i = k(\partial \phi / \partial x) \quad (2)$$

The current in the galvanic cell must also obey the electroneutrality law, which states that at any point in the electrolyte, the net current must be zero. The equation representing this condition is

$$\nabla \cdot i = 0 \quad (3)$$

For a homogeneous environment where the conductivity is independent of coordinates, one can substitute Eq 1 into Eq 3, and then eliminate k from the equation and obtain

$$\nabla^2 \phi = 0 \quad (4)$$

Equation 4 is the Laplace equation, which is the equation governing the potential distribution in galvanic cells.

Graphic Analysis

In one-dimensional space, the galvanic cell can be graphically modeled using polarization curves (Fig. 2), provided that the polarization curves of the two metals and the conductivity of the electrolyte are known. From the conductivity, the resistance of the cell R can be calculated using the equation

$$R = L/(Ak) \quad (5)$$

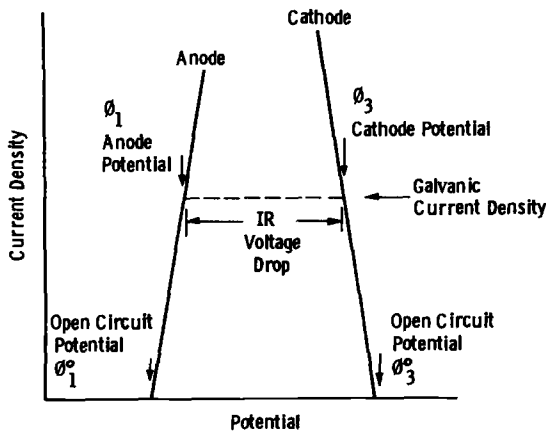


FIG. 2—Graphic analysis of a one-dimensional galvanic cell on a polarization diagram.

where L is the cell length and A is the cell cross-sectional area. The galvanic current in the cell I is equal to A times i . The IR voltage in the galvanic cell is the galvanic current I multiplied by the resistance R . Moreover, the currents on the two metal surfaces must be the same because of the electroneutrality consideration. Therefore, one can search a current density on the polarization curves, where the galvanic potential difference is equal to the IR voltage. After this current density is found, one can obtain the metal potentials from the graph. The potential distribution in the cell can then be calculated since it is a linear distribution between the two metal surfaces.

The above analysis shows that the graphic method can be used to model one-dimensional galvanic cells in homogeneous environment. Unfortunately, few practical corrosion problems can be characterized in one-dimensional homogeneous cells. For complex corrosion problems, two- or three-dimensional analyses are necessary. In these cases, the IR voltage calculation cannot be performed using the one-dimensional formula because both I and R have spatial distributions, which can only be calculated by numerical methods.

The basic principles used in numerical analyses are the same as those used in the graphic analysis, namely, polarization curves, Ohm's law, and electroneutrality law. In fact, the numerical methods described in the following sections are merely geometric scaling tools extending the principles in graphic analysis to complex galvanic cells.

Finite Element Modeling (FEM)

In the finite element modeling of corrosion cells, the first step is to represent the corrosion cell by an element mesh. For the one-dimensional galvanic cell, the mesh is just a series of straight line segments. Each segment is an element that is bound by nodes at two ends. Adjoining elements share the node between the two elements. One can use as many elements as necessary to model the corrosion cell. For simplicity, two elements are used for the present case. The node coordinates are shown in Fig. 3. Node 1 is the anode surface, which has an open circuit potential of ϕ_1^0 and a polarization curve (Fig. 2). Node 2 is a node in the solution. The solution is modeled by two elements, a and b . Element a has a conductivity of k_a and is bound by Nodes 1 and 2; Element b has a conductivity of k_b and is bound by Nodes 2 and 3. Node 3 is the cathode surface, which has an open circuit potential and a polarization curve as shown in Fig. 2.

Corrosion engineers are interested in knowing what the current and potential on the metal surfaces after the two metals are electrically connected. At the moment, both current and potential are unknowns. However, one can establish a series of linear equations, one equation for each node, to solve for the potentials. The derivation of the linear equations here is not a formal derivation, which is more complex and difficult to understand. For Node 1, the electro-neutrality law requires that the net current is zero. Thus, the anodic current generated at the metal surface must be equal to the current from Node 1 to Node 2. The same charge balance

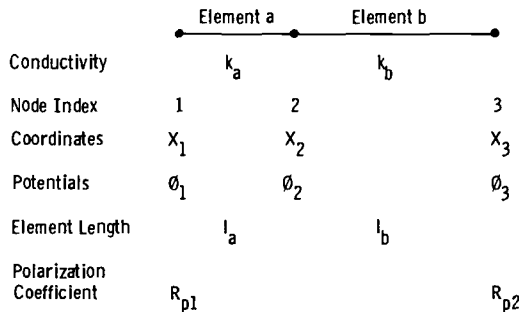


FIG. 3—The one-dimensional finite element mesh.

consideration requires that the current from Node 2 to Node 3 is equal to the cathodic current at Node 3. At Node 2, the current influx from Node 1 must be equal to the outflux to Node 3. Using Ohm's law and the charge balance gives the following three equations

$$i_1 - k_a \left(\frac{\phi_2 - \phi_1}{x_2 - x_1} \right) = 0$$

$$k_a \left(\frac{\phi_2 - \phi_1}{x_2 - x_1} \right) - k_b \left(\frac{\phi_3 - \phi_2}{x_3 - x_2} \right) = 0$$

$$i_3 + k_b \left(\frac{\phi_3 - \phi_2}{x_3 - x_2} \right) = 0$$

To calculate the three potentials, one has to express the currents on the metal surfaces as a function of potential on the surfaces. This expression, called the boundary condition in numerical analyses, can be the conventional Tafel equation or other equations as long as the polarization behavior of the metal surface is accurately represented. In this paper, an empirical equation is used to express experimentally determined polarization curves

$$i = (1/R_p)(\phi - \phi^\circ) \quad (6)$$

where R_p is the polarization coefficient of a metal/electrolyte interface, and i is positive for anodic current density. For a polarization curve shown in Fig. 4, the R_p is a function of potential. On a polarization curve, the polarization coefficient is the inverse slope of a straight line connecting the open circuit point to any point on the curve. For polarization curves where R_p is a

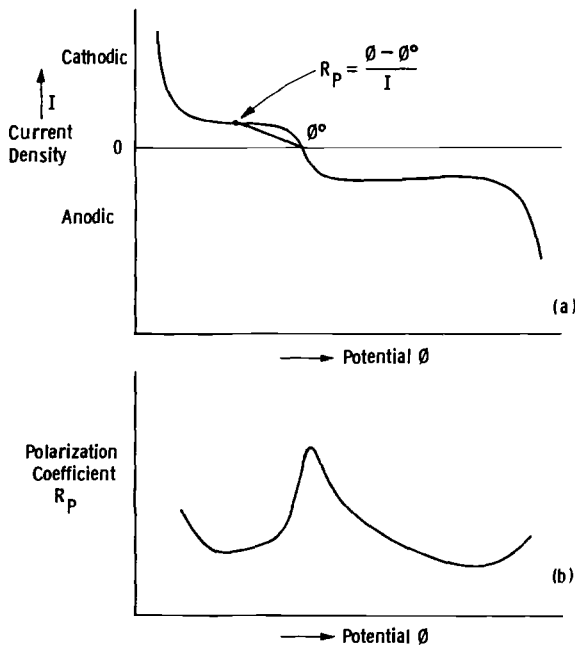


FIG. 4—(a) R is the inverse slope of a straight line connecting any point on the polarization curve to the open circuit point and (b) R_p is a function of the potential.

constant at any potential, the boundary condition is called linear. If R_p is a function of potential, the boundary condition is nonlinear.

Substituting Eq 6 into the three linear equations, one obtains

$$\frac{1}{R_{p1}} (\phi_1 - \phi_1^\circ) - k_a \left(\frac{\phi_2 - \phi_1}{x_2 - x_1} \right) = 0$$

$$k_a \left(\frac{\phi_2 - \phi_1}{x_2 - x_1} \right) - k_b \left(\frac{\phi_3 - \phi_2}{x_3 - x_2} \right) = 0$$

$$\frac{1}{R_{p3}} (\phi_3 - \phi_3^\circ) + k_b \left(\frac{\phi_3 - \phi_2}{x_3 - x_2} \right) = 0$$

Now, if the polarization coefficients at the anode and cathode are known constants we can obtain the three unknown potentials, ϕ_1 , ϕ_2 , and ϕ_3 by solving the three linear equations. Once the potentials on the anode and cathode are calculated, the current density on the anode and cathode can be determined by Eq 6.

As mentioned earlier, the R_p is, in general, a function of potential. To obtain solutions of nonlinear boundary conditions, one can use an iterative procedure. In this procedure, the polarization curves of anode and cathode are stored in the computer as tables of polarization coefficients versus potentials. One table is used for each material involved in the galvanic couple. Initially, a potential distribution on the metal surfaces is assumed. The R_p values corresponding to the potential distribution are used to calculate the potential using the linear equations. The calculated potentials are then used to determine new R_p for the second iteration. The calculated potentials for successive iterations should converge toward a solution. The selection of the initial R_p value has effects on the convergent speed but has no effect on the accuracy of the final result. The procedure is completed when the calculated potentials for successive iterations are within a specified tolerance.

Boundary Element Modeling (BEM)

For a homogeneous environment, there is a second method of calculating current and potential distributions, the boundary element method or the integral equation method. In the boundary element method, one models the surface of the corrosion cell only. Mathematically, this is accomplished by using Green's theorem. The theorem states that if the electroneutrality condition exists in a homogeneous environment the potential distribution on a surface surrounding the environment must satisfy Green's formula. This requirement of surface potential distribution is a property of homogeneous body, which is somewhat more difficult to accept than the FEM, since it does not relate to the current conduction in the environment. However, Green's theorem has been verified in many applications.

Green's formula for three-dimensional surfaces is

$$\phi_p = \frac{1}{2\pi} \int_S \left(\phi_q \frac{\partial}{\partial n_q} \frac{1}{r_{pq}} - \frac{1}{r_{pq}} \frac{\partial \phi_q}{\partial n_q} \right) dS \quad (7)$$

where p and q are two points on the surface, r_{pq} is the distance between the two points, and \mathbf{n}_q is a unit vector normal to the surface at q pointing toward the electrolyte. The integration in Eq 7 is performed over a closed surface surrounding the environment. This closed surface need not be a surface containing the entire environment.

In two-dimensional space, an environment is bound by a closed line, and the formula is

$$\phi_p = \frac{1}{\pi} \int_L \left(\phi_q \frac{\partial \ln r_{pq}}{\partial n_q} - \ln r_{pq} \frac{\partial \phi_q}{\partial n_q} \right) dL \quad (8)$$

where L is the line surrounding the homogeneous environment.

For one-dimensional space, there is no established formula for Green's theorem. The author derived a formula for one-dimensional space by the same procedures used in multi-dimensional space [9]. For one-dimensional space, an environment is bound by two points, and Green's formula may be taken as

$$\phi_p = \phi_q + r_{pq}(\partial \phi_q / \partial n_q) \quad (9)$$

In these equations, one can see that in a homogeneous environment, the potential at any point is dependent on the potential distribution over the entire surface. This is the case whether p point is on the surface or inside the environment. If p is inside the environment, the equations above are changed by dividing the surface integration by 2. For example, if p is inside the environment the equation for the three-dimensional space is

$$\phi_p = \frac{1}{4\pi} \int_S \left(\phi_q \frac{\partial \frac{1}{r_{pq}}}{\partial n_q} - \frac{1}{r_{pq}} \frac{\partial \phi_q}{\partial n_q} \right) dS \quad (10)$$

For corrosion analyses, the primary interest is the potential and current distributions on the metal surfaces. One can establish a boundary element mesh over a closed surface surrounding the corrosive environment including the metal/environment interface. One can select the center point of each element as the representative point for the element. The selection of one representative point for each element is called zero-order. An element can also be represented by multiple points, which is a higher-order element. For each p point, the potential can be expressed by the integration over all the other representative points on the surface by Eq 7. So the surface integration can be performed as a summation of individual elements. Each element has its dS , r_{pq} , \mathbf{n}_q , and ϕ_q , which are used on the surface integration. If the surface is divided into N elements, one can take every representative point as point p and establish N simultaneous linear equations. Thus, the N linear equations can be used to obtain solutions for the N potentials at the representative points. The calculated potentials are used to obtain the current distribution using the polarization curves. After the surface potential distribution is obtained, the potential distribution in the environment can be calculated using Eq 10 for a point or a series of points.

The one-dimensional corrosion cell is again used here to demonstrate the solution of the Green's formula. The solution conductivity is taken as k in the entire environment to satisfy the uniformity requirement. The term in Eq 9 multiplied by the solution conductivity k is equal to the current density i_q at q point according to Ohm's law. Therefore, by Eq 6 and Eq 2, Eq 9 is reduced to

$$\phi_p = \phi_q + \frac{r_{pq}}{R_p k} (\phi_q - \phi_q^\circ) \quad (11)$$

Since in one-dimensional space a region is closed by just two points, two boundary elements, at Points 1 and 3 of Fig. 3, are used to model the one-dimensional cell. Point 1 is taken as the p

point first, and one obtains

$$\phi_1 = \phi_3 + \frac{(x_1 - x_3)}{R_p k} (\phi_3 - \phi_3^o)$$

For Point 3 as the p point, one gets

$$\phi_3 = \phi_1 + \frac{(x_3 - x_1)}{R_p k} (\phi_1 - \phi_1^o)$$

These two linear equations can then be used to obtain the solution for the two unknowns, ϕ_1 and ϕ_3 . A closer examination of the two equations shows that these are electroneutrality conditions at Point 1 and 3 identical to those used in the FEM. In fact, one can derive the same equations by the FEM example if the conductivity of the two elements, k_a and k_b , is the same, and only one element is used in the environment. By two different mathematical approaches, the final equations are identical. Therefore, it is not surprising that the two methods are equally accurate in modeling corrosion cells as demonstrated in Ref 6.

The boundary element method can also be used to analyze cells with variations in conductivity. This is accomplished by dividing the environment into several subregions in such a way that a nonuniform environment is approximated by a series of step changes where within each step is a uniform environment contained in a subregion. One can see that the BEM is very similar to the FEM in this approach. However, in the BEM, this procedure can be tedious when used to model a gradual change in the corrosive environment because of the large number of subregions needed to approximate the environment.

Numerical Procedures

In both the FEM and BEM, there are three steps in the execution of the methods. These steps are generating models, solving equations, and displaying results. Because of the difference in mathematical formulation, the two methods are not equal in their procedures. A comparison of the procedure in the two methods is described in the following sections.

Generating Models

Before the potential distribution in a corrosion cell can be calculated, the geometry of corrosive environment must be represented mathematically, so that it can be processed by a computer. This is performed by a model generator program that graphically displays the geometry by an element mesh and calculates the positions of elements for later calculations of potential distribution.

In the FEM, the method calculates the potential distribution in the corrosive environment, which requires an element mesh representing the volume of the corrosive environment. An example of a two-dimensional finite element mesh is given in Fig. 5.

In the BEM, the method calculates the potential distribution on the surface of the corrosive environment; therefore, only an element mesh representing the surface is required. An example of a three-dimensional boundary element mesh is given in Fig. 6. Therefore, the BEM has an advantage over the FEM in that it requires a simpler mesh for its calculations, which is easier to generate in some analyses. The advantage is more significant in preparing three-dimensional mesh, for example, an offshore drilling platform. In two-dimensional analyses, the task of generating an element mesh has been simplified by the development of an intelligent mesh generator code [10], such that the advantage of BEM is unimportant.

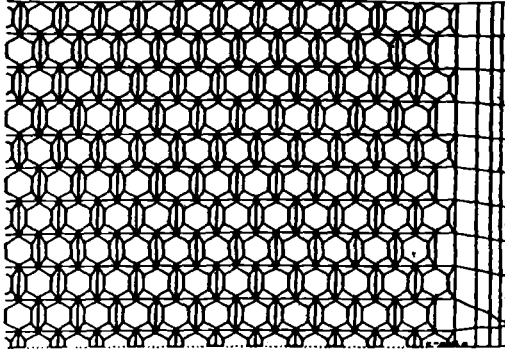


FIG. 5—A two-dimensional finite element mesh representing a horizontal plane in a steam generator.

Equation Solver

In both FEM and BEM, the calculation of potentials is carried out by the solution of simultaneous linear equations. Many equation solvers, which obtain solutions by matrix algebra, can be used to perform this task. At first glance, one might think that the BEM equation solver would be faster than the FEM for a corrosion problem, since the BEM calculation involves only the surface potentials. In the author's experience, this is true only for some geometries that have high volume to surface ratios. The BEM does not offer a clear advantage in equation solving

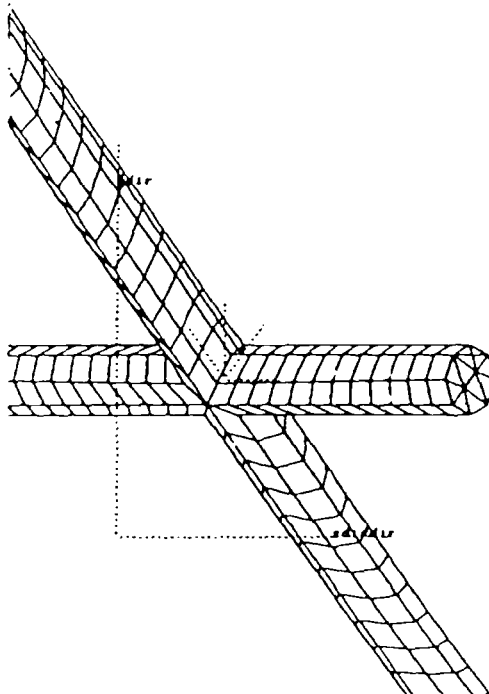


FIG. 6—A three-dimensional boundary element mesh for a junction of two beams of an offshore platform.

because of the nature of matrices in the two methods. In the FEM, the matrix is symmetrical on the diagonal line and has nonzero terms only in the vicinity of the diagonal. Such a matrix can be solved by utilizing properties of the symmetry. In the BEM, the matrix is nonsymmetrical and has a nonzero value for every element in the matrix. There is no special property to use for such a matrix; therefore, the advantage of a smaller matrix is offset by the complexity of the matrix.

Post Processor

After the potential distribution is obtained, the examination of thousands of potentials, one for each node, requires graphic displays. This task is performed by a post processor, which plots iso-potential or iso-current density lines against the background of the element mesh [11]. In this step, the two methods have no difference in their procedures. Examples of iso-potential plots are given in Figs. 7 and 8.

Example of Numerical Modeling

Corrosion engineers interested in using numerical analyses should begin with two-dimensional analyses. There are techniques by which a three-dimensional problem can be modeled by a two-dimensional finite element mesh. One of the techniques is to use axial symmetry; so, a potential distribution that has a cylindrical shape can be calculated on a plane. The second technique is by manipulating the conductivity and surface area to produce a two-dimensional mesh that has an equivalent current distribution as that in the three-dimensional problem. An example is described in Ref 12 where a steam generator galvanic corrosion problem was analyzed by a two-dimensional finite element method, which is described below.

In order to remove sludge and deposits from steam generators, the Electric Power Research Institute (EPRI) has developed a chemical cleaning process using an ethylenediaminetetraacetic acid (EDTA) solution. In steam generators, the EDTA solution serves as an electrolyte for the galvanic action between carbon steel structures and the I-600 tube bundle, which may result in metal loss on the carbon steel structures during the chemical cleaning period.

This potential corrosion issue was analyzed using a finite element modeling (FEM) method for a geometrical configuration representative of a steam generator. The galvanic corrosion rates between the carbon steel structures and the I-600 tube bundle were calculated using two-dimensional (2D) FEM with the following objectives:

1. Provide preliminary assessments of galvanic corrosion rates in the steam generator during chemical cleaning.

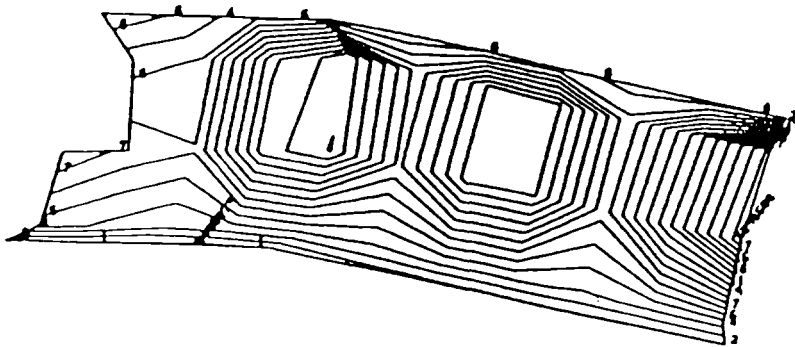


FIG. 7—Iso-potential lines at the junction on Fig. 6.

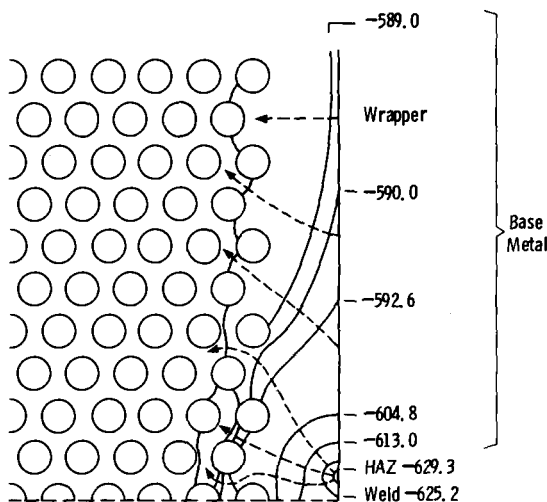


FIG. 8—Iso-potential lines and current flow pattern for the mesh in Fig. 5. Numbers linked with the iso-potential lines are the electrochemical potentials in millivolts versus standard calomel electrode (SCE).

2. Assist in the design of experimental simulations for evaluating the galvanic action in the steam generator during chemical cleaning.

FEM Model

The plane used in the analyses is shown in Fig. 9, which is a radial plane in the tube sheet region of the steam generator. The width of the circumferential weld is 5.08 cm (2 in.). Twelve rows of tubes were included in the FEM, which is the number of rows determined in an earlier analysis to be the extent of the galvanic action between the tube bundle and the wrapper (Appendix A). Thus, there is no need to include more than 12 rows of tubes in the FEM. Assumptions used in this model include the following:

- The galvanic action in the region between the tube sheet and the first support plate is symmetrical across plane midway between the tube sheet and the first support plate. Therefore, the FEM only needs to include the region from the tube sheet surface to the midway plane.
- The width of the heat affected zone (HAZ) is 0.635 cm ($\frac{1}{4}$ in.).
- Appendage structures, for example, blow down pipes, wedge blocks, and associated small welds, are negligible in their effects on the galvanic action between the shell weld and the tube bundle. Therefore, there is no need to include these structures in the model. This assumption should be valid since the surface areas of these appendage structures are small compared with the shell, wrapper, and tube sheet surfaces.
- The galvanic action in this model has an axial symmetry along the vertical center of the steam generator. This assumption should be valid since the geometries of these structures in the galvanic cell have this symmetry. Consequently, one can use a 2D axially symmetrical analysis to calculate the 3D (three-dimensional) galvanic action using axisymmetrical elements.

One difficulty in reducing the 3D geometry to a 2D analysis is that individual tubes in the tube bundle do not have an axial symmetry along the vertical center of the steam generator. Therefore, the tube bundle geometry must be modified in order to use the 2D axisymmetrical model. The modification is fully explained in Appendix A. Briefly, the tube bundle is treated as a structure that is constructed with layers of concentric 1-600 sheets. Each layer represents one

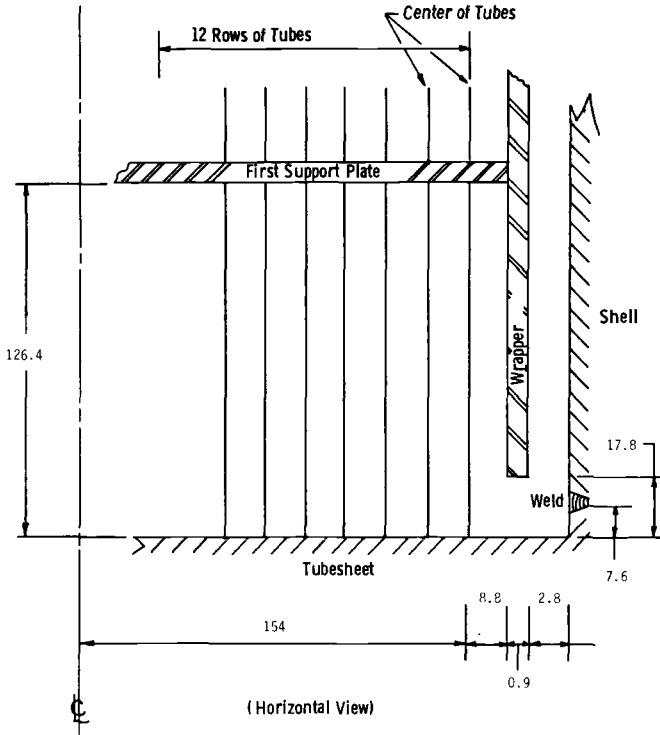


FIG. 9—The geometry used in the FEM for the radial plane analysis of a steam generator. The dimensions are in centimetres.

row of tubes. This modified tube bundle geometry generates the same galvanic action as the true tube bundle geometry, which is demonstrated in Appendix A.

In this analysis, the boundary conditions for the carbon steel, weld metal, HAZ, and I-600 tubes were selected from an earlier study [13] (Fig. 10). The polarization curve of SA-S33A was assigned as the boundary condition for the carbon steel structures.

Results

The results of FEM were electrochemical potentials on every element in the finite element models. Based on the potentials on every element, potential distributions on the models were produced using iso-potential lines. Galvanic current flow patterns, which are perpendicular to the iso-potential lines, were generated. Galvanic current densities on metal surfaces were computed according to the appropriate polarization curves and the potentials on metal surfaces. The galvanic corrosion rates were calculated by adding the self-corrosion rates to the rates caused by galvanic current. Faraday's law was used in converting galvanic current densities to material loss rates: a current density of $2.2 \mu\text{A}/\text{cm}^2$ was calculated to give $25.4\text{-}\mu\text{m}/\text{year}$ (1-mpy) corrosion rate for carbon steels.

The FEM results are shown in Fig. 11. On the base metal tube sheet surface, the galvanic corrosion rate varies with location. On surface, it is the highest at a position 12 rows of tubes from the shell and decreases toward the shell. On the shell surface, the rates are low due to the shielding effect of the wrapper. On the wrapper surface, the shell side has similar low galvanic corrosion rates as the shell surface, whereas the tube side has higher galvanic corrosion rates.

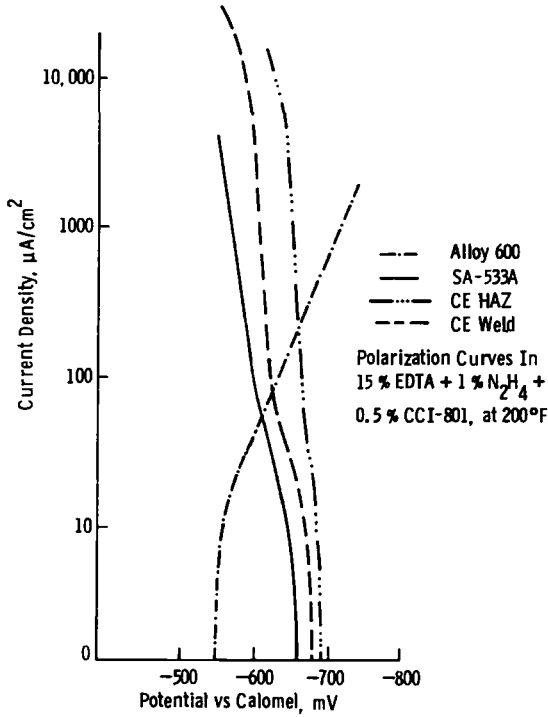


FIG. 10—Polarization curves used in the study as the boundary conditions for the FEM.

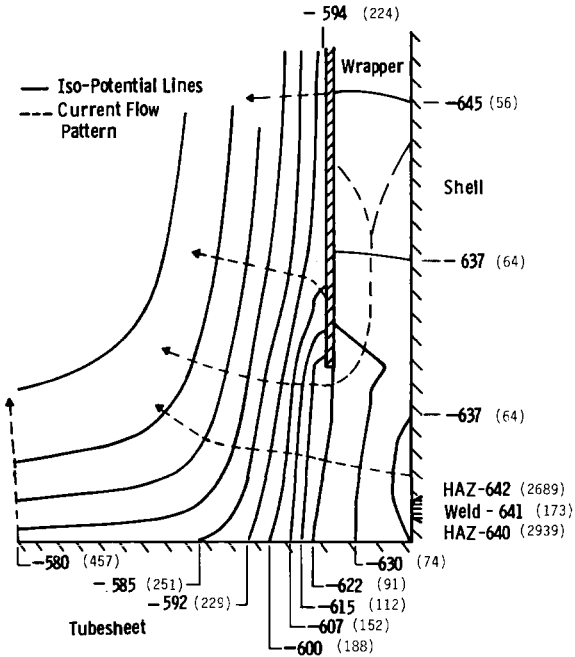


FIG. 11—Iso-potential lines and current flow pattern. Numbers linked with the iso-potential lines are the electrochemical potentials in millivolts versus SCE. The numbers in parentheses are the galvanic corrosion rates in mils per year.

For a two-day chemical cleaning period, these galvanic corrosion rates appear to be acceptable. The same statement cannot be made for the HAZ of the circumferential weld where galvanic corrosion rates are over 2.54 cm/year (1000 mpy). In contrast with the HAZ, the weld metal has a low galvanic corrosion rate similar to that of the base metal.

Assessments of Galvanic Corrosion

Before the present analyses there were concerns that the galvanic corrosion rates might be excessively high on all of the carbon steel structures in the steam generator. The present calculated results using assumed polarization curves show that the galvanic corrosion rates are low except for the HAZ of welds. For a 48-h chemical cleaning period, the uniform metal loss is less than 1 mil for the base and weld metals.

Unlike the galvanic corrosion rate on the base metal surfaces, the rate on the HAZ is high. The high galvanic corrosion rates of the HAZ on the wrapper and shell are due to the fact that the HAZ is acting as a sacrificial anode partially protecting the carbon steel structures in the steam generator. The more active behavior of the HAZ is clearly demonstrated in Fig. 10 where the anodic polarization curves of SA-533A, weld metal, and HAZ are shown. The HAZ has a more active corrosion potential and a steeper polarization curve than those of the SA-533A and weld metal. As the results of this protecting effect, weld metals investigated in the present analyses have low galvanic corrosion rates.

Design of Simulation Tests

The results are useful in assisting the design of simulation tests. In the past, galvanic corrosion studies used surface area ratios as the only parameter in simulating galvanic action. This is a valid approach when the galvanic current distributions on anodes and cathodes are uniform so that the effective surface area ratio can be easily estimated. Furthermore, the IR voltage in the galvanic cell must be negligible for this approach to give useful results. For geometrically complex structures, for example, steam generators, this approach has serious difficulty in estimating the effective surface area ratio and the IR voltage. Frequently, researchers are forced to use the worst possible anode versus cathode surface area ratio to simulate the galvanic action, which always gives unrealistically high galvanic corrosion rates. These difficulties are, of course, the results of the fact that galvanic current distribution is dependent on geometry of a galvanic cell. For steam generators the effect of geometry on galvanic current distribution is clearly demonstrated in the analyses. Conventional galvanic corrosion tests will not yield accurate corrosion information. Laboratory tests simulating steam generator geometries will have to be performed. Simulating a full size steam generator in great detail is not feasible because of financial constraints. A scaled down model is also discarded because of the need to scale down the conductivity of the cleaning solvent, which would lead to a modification of the galvanic action in the cell. The recommended alternative is to use a true size model of a portion of the steam generator in the simulation tests.

The dimensions of the test configuration can be derived according to the present calculations. A rectangular tank can be used as the test configuration in which a carbon steel tank wall simulates the shell and the carbon steel tank bottom simulates the tube sheet. Other walls are made of insulating materials such as glass or plastic. In the tank are the carbon steel wrapper and the I-600 tube bundle. The tube bundle should be sufficiently large to simulate the galvanic action in the steam generator. For the galvanic corrosion of the wrapper and shell, the number of rows of I-600 tubes is important. Based on the present results, only the first 12 rows of tubes are involved in the galvanic action with the shell and wrapper. Beyond the 12 rows of tubes, the galvanic action is restricted to between the tube sheet and the tube.

Accuracy of Numerical Analyses

The accuracy of numerical modeling methods, both FEM and BEM, has been verified by several researchers [1-7]. Calculated results have been found to agree with closed form solutions, laboratory tests, and cathodic protection systems in the North Sea. However, corrosion engineers should be aware that a number of factors can affect the accuracy. These factors are discussed in this section.

Boundary Condition

The boundary conditions in the numerical analyses are polarization curves of metals in the corrosive environment. Polarization curves can be generated by several different methods, for example, potentiodynamic, galvanostatic, and so forth. The proper method to produce the boundary conditions depends on applications. For impressed current cathodic protection systems with potential controlling mechanism, the potentiostatic method should be used. For galvanic corrosion and sacrificial anode cathodic protection, the galvanostatic method should be used. The general rule in determining the method is that the polarization curves should be generated in a condition as closely simulating the service conditions as possible.

The fact that polarization curves are a function of time further complicates the modeling effort. It is unlikely that numerical analyses can simulate all conditions experienced by a structure during its service. One must define several conditions as the limits and use these limits to determine a range of service performance by the numerical analyses.

Mesh Size

The accuracy of numerical analyses is affected by the element size selected in the mesh. Finer mesh produces more accurate results but requires longer computer time to obtain the result. The optimum approach is to supply fine elements in a region where a sharp potential gradient is expected, for example, in the vicinity of a cathodic protection anode. One method in determining the size requirement is by trial and error. One normally begins with coarser mesh and slowly reduces the element size until the calculated potential distribution reaches a steady value.

Diffusion Potential

In the development thus far, the question of diffusion potential has not been discussed. Diffusion potential is a phenomenon that produces a potential difference between two points in the environment when there is a difference in ionic concentrations. A detailed description on diffusion potential can be found in Ref 14. In a nonuniform environment, the diffusion potential is superimposed on the IR voltage potential distribution. In both the FEM and BEM derivations, the diffusion potentials are not considered. Consequently, both methods are inexact in modeling nonuniform environments. Fortunately, in many aqueous environments, the diffusion potential is in the range of several millivolts, which is much smaller than IR voltage produced by the galvanic current. In any case, corrosion engineers should verify that the diffusion potential is negligible in the environment before using either method.

Summary

Galvanic corrosion is dependent on the current distribution in the electrolyte. Calculation of the current distribution can be performed by either the finite element or the boundary element method. The methods are explained using a one-dimensional galvanic cell as an example. The application of the finite element method to a galvanic corrosion situation of a nuclear steam generator is given.

APPENDIX A

Modification of Tube Bundle

In the finite element modeling (FEM) of the galvanic action between the tube bundle and the carbon steel structures, the cylindrical shape of the carbon steel structures, for example, the shell, tube sheet, and wrapper, can be modeled using 2D axisymmetrical elements. The procedure of using axisymmetrical elements cannot be applied to model the tube bundle, since individual tubes in the tube bundle do not have an axial symmetry along the vertical center of the steam generator. Thus, a modification of the tube bundle geometry must be made in order to use 2D axisymmetrical analyses to calculate the galvanic action in the steam generator.

In the FEM, a modified tube bundle that produces the same galvanic action as the true tube bundle can be formulated. The effects of two important parameters, the tube surface area and the cross section of the current conducting path, must be preserved in the modification. The modification in the present work is performed by taking the tube bundle as a structure consisting of layers of concentric sheets. Each layer of concentric sheets represents one row of tubes in the tube bundle. The center of concentration for these sheets is the vertical center of the steam generator. The sheets have no thickness and are made to allow galvanic current penetration. These assumptions are, of course, physically impossible. However, mathematically these assumptions produce the same galvanic effect as that of the true tube bundle geometry.

To preserve the effects of the I-600 tube surface area, the cathodic polarization curve of I-600, which is used as the boundary condition in the FEM, was multiplied by a correction factor. This factor is the surface area ratio of one layer of the concentric sheet versus one row of tubes in the tube bundle.

To verify the accuracy of this approach, FEM analyses, using the true geometry, was performed on the galvanic couple of one column of tubes versus the wrapper segment facing the column (Fig. 12). It was assumed that

1. The galvanic effect of one column of tubes acts only on the wrapper segment facing that column such that other carbon steel surfaces, for example, adjacent wrapper segments and support plates, do not drain away the galvanic current produced by this column of tubes. This model will slightly overestimate the galvanic corrosion rate, since in the steam generator, the galvanic effect of one column of tubes does not act only on the wrapper segment facing that column. Because of the cylindrical shape of the steam generator, a small portion of the galvanic current produced by one column of tubes is drained by the wrapper segments facing adjacent columns of tubes.

2. There is a mirror symmetry across the vertical plane midpoint in the column. Therefore, modeling one half of the column is sufficient.

Twenty rows of tubes were included in the column. In the analysis for the true geometry, the

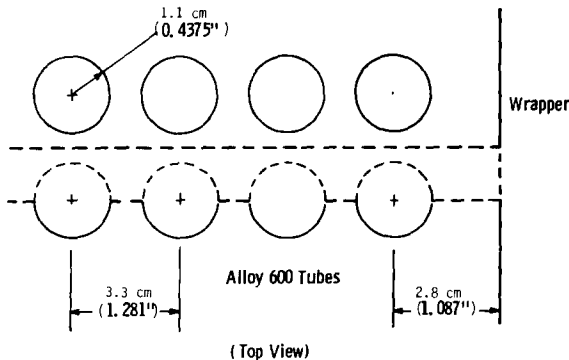


FIG. 12—Model for the wrapper analysis. Dotted line section contains the finite element mesh, which includes 20 tubes in the model.

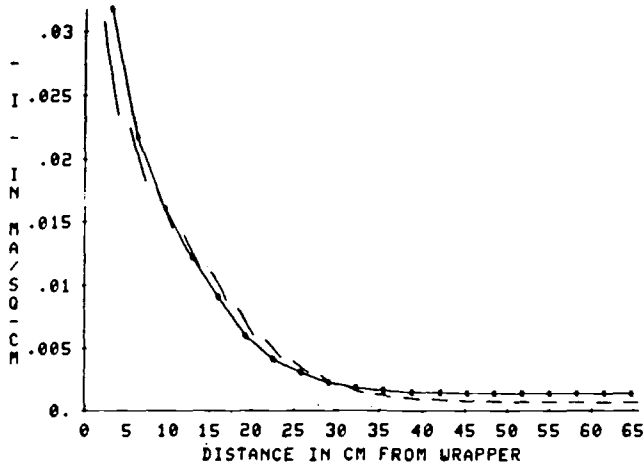


FIG. 13—A comparison of the cathodic current distributions on the I-600 tubes as calculated using the true and modified tube bundle geometry. The broken line is the distribution for the true geometry, and the solid line is the distribution for the modified geometry.

shape of every tube was modeled; in the analysis for the modified geometry, the tubes were represented as sheets located at the center of the tubes. The wrapper material was taken as SA-533A.

The results of the analyses are shown in Fig. 13 where the cathodic current densities on the I-600 tubes are plotted versus the distance from the wrapper surface. The galvanic corrosion rate calculated for the wrapper segment facing the column is $2946.4 \mu\text{m}/\text{year}$ (116 mpy) using the true geometry and $2895.6 \mu\text{m}/\text{year}$ (114 mpy) using the modified geometry. Clearly, the two analyses agree very well in the cathodic current density distribution and in the galvanic corrosion rate on the wrapper. The agreements suggest that the approach of using the modified tube bundle to simulate the galvanic effect of the true bundle is valid.

The results yield the important observation that the galvanic action between the wrapper and tube bundle is limited to the first 12 rows of tubes from the wrapper. Beyond 12 rows of tubes from the wrapper surface, the current density approaches a low steady value of $0.001 \text{ mA}/\text{cm}^2$. Based on the area under the curve in Fig. 13, the first 12 rows of tubes generate 94% of the total galvanic current. This observation suggests that in FEM of the galvanic action between the tube bundle with the wrapper or shell, there is no need to extend the model beyond 12 rows of tubes from the wrapper surface.

References

- [1] Kasper, R. G. and April, M. G., *Corrosion*, Vol. 39, No. 5, May 1983.
- [2] Munn, R. S., *Corrosion/82*, Paper 171.
- [3] DeCarlo, E. A., *Materials Performance*, Vol. 22, July 1983, p. 38.
- [4] Fu, J. W., *Corrosion*, Vol. 38, No. 5, May 1982, p. 295.
- [5] Gartland, P. O. and Johansen, R., *Corrosion/85*, Paper 319.
- [6] Fu, J. W. and Chow, S. K., *Materials Performance*, Vol. 21, No. 10, Oct. 1982.
- [7] Danson, D. J. and Warne, M. A., *Corrosion/83*, Paper 211.
- [8] Segerlind, L. J., *Applied Finite Element Analysis*, 2nd ed., Wiley, New York, 1984.
- [9] Brebbia, *Boundary Element Techniques in Engineering*, 1983.
- [10] Morris, J. W., Newman, B., and Snyder, J. R., *Figures 11 User Guide*, Westinghouse Report 81-7E7-FIGTO-R1, June 1981.
- [11] Van Buren, W., *WAPPP User's Manual*, July 1982.
- [12] Fu, J. W. and Chan, S., *Corrosion/85*, Paper 190.
- [13] Hausler, R. H., EPRI Report NP-3030, Project S148-1, Final Report, June 1983.
- [14] Bockris and Reddy, *Modern Electrochemistry*, Plenum Press, New York, 1977.

Computer Modelling of Galvanic Corrosion

REFERENCE: Adey, R. A. and Niku, S. M., "Computer Modelling of Galvanic Corrosion," *Galvanic Corrosion, ASTM STP 978*, H. P. Hack, Ed., American Society for Testing and Materials, Philadelphia, 1988, pp. 96-117.

ABSTRACT: The computer simulation of galvanic corrosion systems has been shown to provide accurate information that can be used to improve design and avoid costly failure. The systems capability to model any general geometry coupled with the ability to accept a wide variety of forms of polarization data enables its effective use in a wide variety of marine and industrial applications. A number of cathodic protection applications are presented as a special case of galvanic corrosion.

KEY WORDS: galvanic corrosion, computers, computer modelling, marine applications

The designs of many industrial projects are directly or indirectly affected by considering corrosion or corrosion related problems. Although apparently simple in principle, the prediction and control of a corrosion process requires careful examination, as the cost of corrosion induced failure can be often high, both in material terms and human lives.

In the past, the prediction of corrosion behavior and the design of corrosion has been mainly based upon the experience and the judgment of a data base of corrosion information with a human expert's knowledge in the form of rules [1,2]. These systems can then be used for consultation interactively. Thus, human and computer system experts can initiate a design and provide valuable clues about important issues such as material selection or how the system can be best protected. However, for most problems with complex geometry and environmental conditions such recommendations have to be accurately verified in the final stage of design for the sake of both safety and the economy. As an example, consider the standard rules used in the analysis and the design of cathodic protection systems for offshore structures. In general, the purpose of these systems is to supply electrons to the surface of the metal so that the potential on the structural surface is changed to a level where the anodic reaction (or corrosion rate) is reduced and lies within an acceptable limit.

The design, therefore, should provide sufficient current capacity to achieve these objectives for a desired structure's design life. In practice, this is accomplished by considering the total surface area to be protected and the current density requirement that is recommended by codes of practice and is, in general, dependent upon the structural material, location, as well as environmental variables such as temperature, salinity, oxygen content, and the waterflow. The type of anode and configuration are then chosen by considering the total current demand, structural design life time, and the geometry.

In reality, during the short period after the installation the current demand is high, and the bulk of current is taken by the surface close to anodes. At this stage unless the anodes are very carefully distributed some areas on the structure may be left unprotected long enough to cause

¹Director, Computational Mechanics, 25 Bridge St., Billerica, MA 01821.

²Software engineer, Computational Mechanics, Ashurst Lodge, Ashurst, Southampton SO4 2AA, England.

severe damage. In fact, there have been a number of cases of unsatisfactory cathodic protection performance [3], which have appeared shortly after installation of offshore platforms as a direct result of underestimating the geometric effect and relying purely on the experience of the designers and sufficiently high current capacities.

In the long term, however, the design based on common rules leads to systems having excessive spare current capacity. This is because the current density allowance recommended by the codes of practice ensures the achievement of the initial polarization and has been increased over the years as protection systems were required to operate in deeper and more hazardous environments. In practice, however, although the initial current requirement is high, it reduces with time dramatically as a result of deposition of calcareous scale. This is verified by evidence from a number of surveys that observed the subsequent current outputs following the initial polarization were seen to be significantly below the design basis. In one example (B.P. West Sole platform in the North Sea), after the removal of the platform at the end of its designed operating life 50% of the capacity of the sacrificial anodes were found remaining.

In short, the use of current design rules for complex problems can result in an unsafe, as well as uneconomic design. The economy of the design not only concerns the number of anodes, but the significant extra weight added to the structure. This can play an important part in the structural design of floating and deep water structures where dynamic effects are important. In addition, the size of the cathodic protection (CP) system can seriously effect the cost of the maintenance of the structure. Mathematical modelling can provide a means of verifying and accurately evaluating the safety and economy of any design based on human judgments or recommendations made by a knowledge based system.

Mathematical Modelling

Although computerized numerical methods have been employed in many areas of engineering for some time, it is only recently that such techniques have attracted interest in the field of electrochemistry and, in particular, the analysis of galvanic corrosion.

The application of analytical methods [4-6] in the past were all limited to simple geometries and cathodes with linear polarization kinetics.

These techniques and the classical design schemes are therefore no longer adequate for complex structures subjected to exceedingly severe environmental conditions, such as water resistivity, oxygen content, temperature, seasons, past history of cathodic polarization behavior, and so on.

Similar arguments can be made for other galvanic corrosion applications where the desire for an increased competitive edge, reliability, and performance make engineers demand more accurate and powerful analytical tools.

Modern numerical methods are used to solve a wide range of partial differential equations based on discretization techniques by which the domain of the problem is divided into a number of imaginary finite regions called elements, interconnected at joints or nodes. The solution is then approximated within each element and expressed in terms of nodal values. The problem is then solved by an appropriate procedure for minimizing the overall error caused by the approximation. The degree of accuracy of the result is directly dependent on the refinement of the mesh and the order of approximation used. However, the more refined the mesh or the higher the order of approximation, the larger the number of nodes and hence the higher the cost of the analysis.

The early attempts at modelling cathodic protection problems were made using the finite difference method [7-9]. This method's main advantage is the simplicity of the mathematics involved and its efficiency for problems with simple geometries, but it has severe limitations when dealing with complex shape boundaries. In recent years, the application of the finite element method [10-13] has become increasingly popular mainly because of its accuracy and

flexibility when dealing with problems with complex geometries. With the variety of element shapes available, it is possible to create a finite element model of almost any conceivable geometry.

Although the finite element method offered a significant improvement to the finite difference method, both have major disadvantages when applied to the problems of galvanic corrosion. These methods are based on the evaluation of domain integrals, which are required to describe the problem's domain by elements. This is a very inefficient process both in modelling and computation, as most nodes are introduced in the electrolyte and not on the structural surface. The application of these methods to problems like the analysis of marine structures becomes impractical since the problem's domain (seawater) tends to be infinite, leading to a very complex model and a large number of equations for which a time dependent nonlinear analysis has to be carried out.

The boundary element method has overcome these problems and become increasingly popular for the solution of corrosion problems [14-17]. Using this technique requires the evaluation of boundary integrals, and therefore only the surface of the structure has to be considered, not the electrolyte. Yet, the solution can be obtained for selected regions inside the electrolyte, as well as on the boundary. A comparison of a finite difference, finite element, and boundary element model is shown in Fig. 1.

The boundary element method is based on a mixed formulation by which the voltage and current density are approximated independently. Therefore, the current density can be calculated with the same degree of accuracy as the voltage, and also the polarization boundary condition can be modelled more accurately. Readers are advised to refer to a paper by Adey and Niku

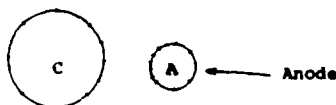
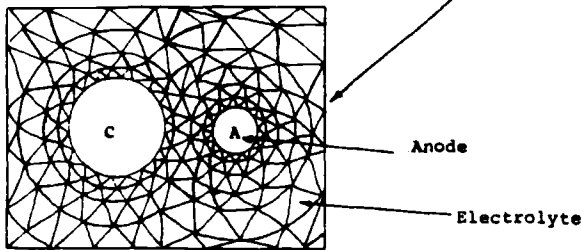
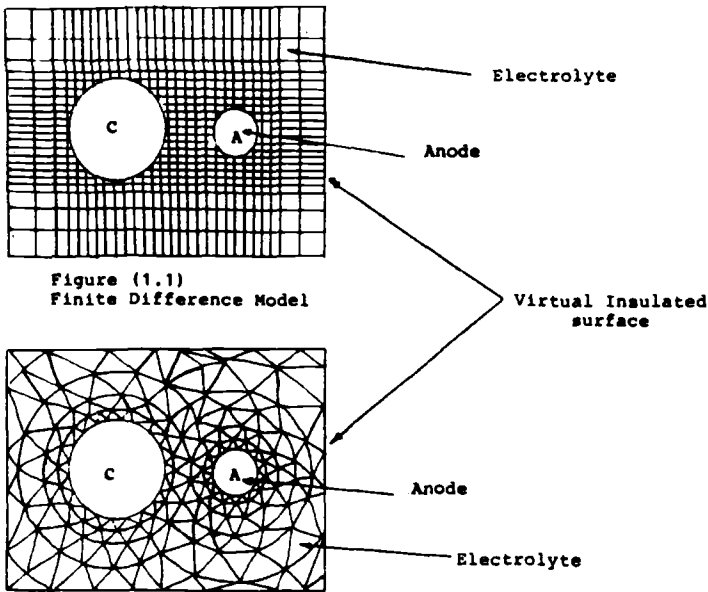


FIG. 1—Boundary element model.

[16] where a comparison between finite element and boundary element methods when applied to corrosion problems is studied in more detail.

Formulation of the Boundary Element Method

The governing equation for the potential distributions in the corrosive medium is derived on the electro-neutrality law and known to be a Laplace equation (Fig. 2)

$$\nabla U = 0 \quad \text{in } \Omega \tag{1}$$

The Laplace equation can be used providing the electrolyte can be assumed to be free of significant variations in solute concentrations. It can be also assumed that there is equilibrium in the exchange of current between the anode and cathode providing there are no sources or sinks of charge in the electrolyte.

The boundary conditions at electrolyte-metal interface can be in the form of

$$U = u \quad \text{in } \Gamma_1$$

$$K(du/dn) = K(n_i, U_i) = q \quad \text{in } \Gamma_2 \tag{2}$$

where

- U = potential in the electrolyte,
- q = current density in the electrolyte (normal flux),
- K = conductivity of the electrolyte,
- u = prescribed value of potential,
- q = prescribed value of current density,
- n = direction of the unit normal,
- Γ_1 = prescribed potential boundary,
- Γ_2 = prescribed current density boundary,
- Ω = volume of the problem,
- $\Gamma = \Gamma_1 = \Gamma_2$ boundary of the problem, and
- i = directions of reference cartesian coordinates.

The weighted residual formulation for the approximate solution of Eq 1 can be written as

$$\int_{\Omega} (\nabla^2 U)W^*d\Omega + \int_{\Gamma_1} (U - Uq^*)d\Delta + \int_{\Gamma_2} (q - q)W^*d\Gamma = 0 \tag{3}$$

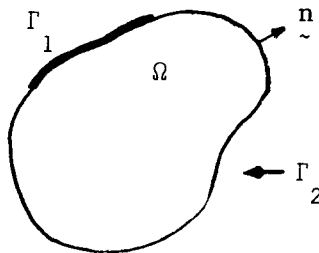


FIG. 2—Representation of Laplace equation.

where

- U = the approximate solution,
- W^* = the weight function, and
- $q^* = K(dW^*/dn)$.

By integrating the first integral twice by parts

$$\int (\nabla^2 W^*) U d\Omega = - \int_{\Gamma_2} q W^* d\Gamma - \int_{\Gamma_1} q W^* d\Gamma + \int_{\Gamma_2} U q^* d\Gamma + \int_{\Gamma_1} U q^* d\Gamma \quad (4)$$

By choosing the weighting function W^* such that in infinite medium, $\nabla^2 W^* = \Delta_j$, then one can write

$$C_j U_j = \int_{\Gamma} U q^* d\Gamma = \int_{\Gamma} q U^* d\Gamma \quad (5)$$

where

- j = reference point
- C_j = the constant dependent on the position of the reference point
- $C_i = 1/2$ if i is chosen on a smooth boundary.

The function W^* satisfying $\nabla^2 W^* = \Delta_j$ is called the fundamental solution, which for two- and three-dimensional isotropic medium are known to be

$$W^* = (1/2)\ln(1/r) \quad \text{and} \quad W^* = (1/4r), \quad \text{respectively}$$

where r is the distance from the reference point to the point under consideration.

Finally by subdividing the boundary of the problems into the number of elements and evaluating the integrals (Eq 5) over each element and adding them up together

$$k = \begin{matrix} \text{total number of} \\ \text{elements} \end{matrix} \quad k = \begin{matrix} \text{total number of} \\ \text{elements} \end{matrix}$$

$$C_j U_j + \sum_{k=1}^k \int_{\Gamma_k} u q^* d\Gamma_k = \sum_{k=1}^k \int_{\Gamma_k} q U^* d\Gamma_k \quad (6)$$

By choosing the suitable interpolation function to approximate U and q over each element, Eq 6 can be written in the following matrix form

$$\mathbf{H}\mathbf{U} = \mathbf{G}\mathbf{q}$$

where

- \mathbf{U} = nodal potential vector,
- \mathbf{q} = nodal flux density vector,
- \mathbf{H} and \mathbf{G} = global influence matrices obtained from combining $\int_{\Gamma_k} q^* \Phi_k d\Gamma$ and $\int_{\Delta_k} U^* \Phi_k d\Gamma_k$ for all elements, and
- Φ = interpolation function used over element k .

Building a Model

The boundary element technique requires the user to describe the boundaries or surfaces of the problem he wishes to model using elements. An advanced boundary element analysis system should provide the user with a range of elements that can be used to describe the most complex problems.

Table 1 describes the element types that are available, for example, in the BEASY™ system (a commercially available system from Computational Mechanics). For two-dimensional and axisymmetric problems a family of constant, linear, and quadratic isoparametric elements is

TABLE 1—Element types.

Element Type	Geometry Type			Shape
	Two Dimensional	Axisymmetric	Three Dimensional	
<u>Boundary Line Elements</u>				
Constant Line	*	*		
Linear Line	*	*		
Quadratic Line	*	*		
<u>Surface Elements</u>				
Constant Quadrilateral			*	
Linear Quadrilateral			*	
Quadratic Quadrilateral			*	
Mixed Constant Quadratic Quadrilateral			*	
<u>Tubes Elements</u>				
Constant Tube			*	
Linear Tube			*	
Quadratic Tube			*	

indicates node

x indicates mesh points

TABLE 2—Point and line sources.

Source Type	Two Dimensional	Axisymmetric	Three Dimensional	Shape
Point Source	*		*	•
Constant Line Source	*		*	
Linear Line Source	*		*	
Quadratic Line Source	*		*	

available (Table 2). For three-dimensional problems a family of rod or tube elements is also available to represent frame (jacket) type structures and anodes, in addition to plate type elements that can be used to conveniently model surfaces.

To perform analysis the user has to first cover the surface of his problem with elements. The number and type of elements are dictated by the geometry and the expected variation in the potential or current density. For example, if the potential is varying sharply near an anode the user should imagine each element representing the potential solution. Therefore, the user can represent the curve by using one or two quadratic elements or a larger number of linear elements. It has been found that users quickly become adept at choosing a mesh of elements, and in general the boundary element method is not as sensitive to mesh selection as other techniques. Figure 3 shows half of a structural member (note symmetry about $x = 0$), which has been described using quadratic elements and the anodes represented by line elements. Figure 4 shows the predicted potential distribution on the surface member.

Models can be built using general modelling systems like PATRAN, SUPERTAB, FEMGEN, FEMVIEW, or the special boundary element; pre- and post-processors supplied with systems like BEASYTM.

Polarization

The discussion so far has concerned the mathematical description of the electrolyte and how for any geometry a model may be developed to predict the potential and current densities simply by covering the surface with elements. The boundary elements describe the electrolyte and not the metal, and the surface is the surface of the electrolyte. However, for an object submerged in

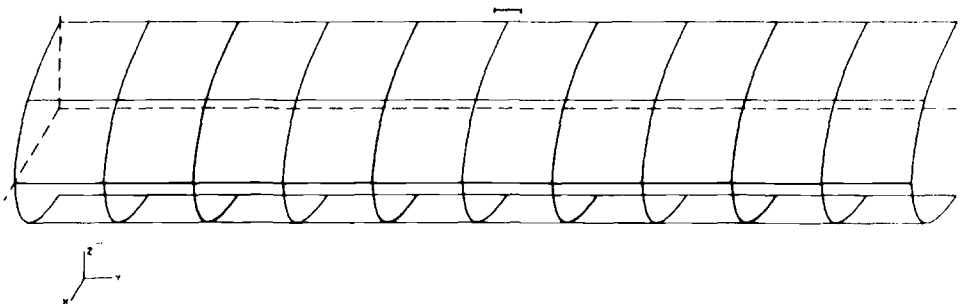


FIG. 3—Pipeline with stand-off anode system.

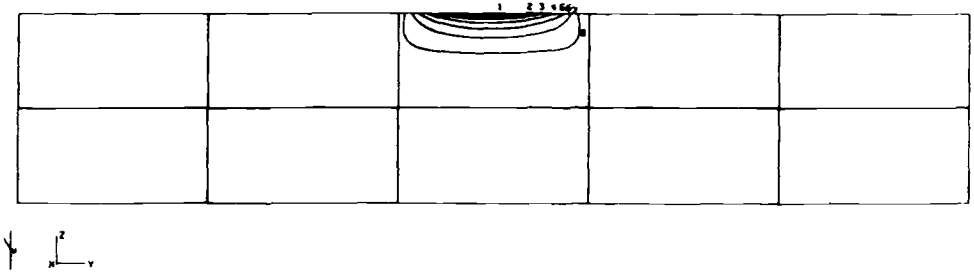


FIG. 4—Pipeline with stand-off anode, voltage distribution mV.

the electrolyte the position of the surface of the object and that of the electrolyte are obviously the same. The potential that is computed is the potential of the electrolyte in contact with the surface, which is not the same as the metal potential.

This discussion is necessary because of the complex electrochemical reaction that takes place on the surface of the metal in contact with the electrolyte. The reaction kinetics strongly influence the potential and current density distribution and must be modelled to provide realistic solutions to corrosion problems.

Figure 5 shows typical polarization curves for zinc, steel, and copper. Polarization can be influenced by a number of factors: type of metal, temperature, salinity, oxygen content, and flow velocity of electrolyte are just a few. Polarization also exhibits time dependent behavior as might be, for example, caused by calcareous scale deposition on the metal surface.

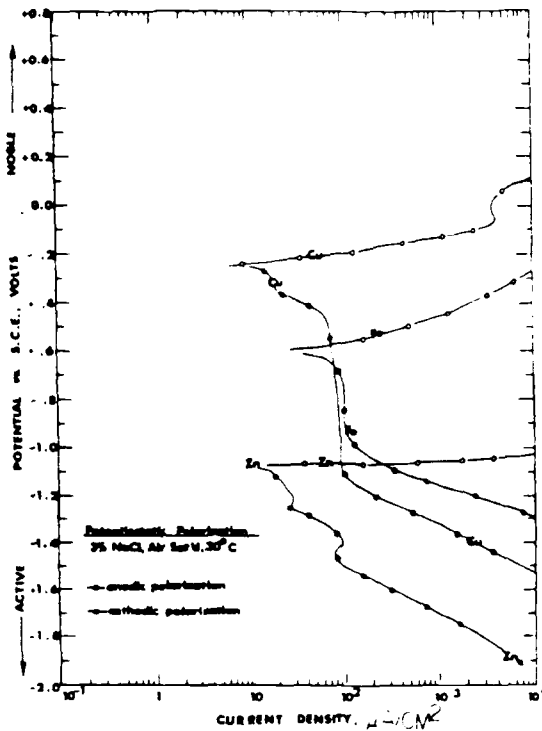


FIG. 5—Polarization curves for zinc, steel, and copper [20].

To include polarization in a computer model the relationships between the various parameters must be defined. The simplest approach is to use the Butler Volmer equation and neglect time dependent effects. For a time dependent prediction the system will need to know how the polarization ($E-i$) relationship changes with time.

An advanced system should be able to simulate corrosion problems using linear polarization, nonlinear polarization, or time dependent linear or nonlinear polarization.

Note a further advantage of the boundary element method (BEM) where the nodes are only on the surfaces is that the resulting nonlinear equations only involve the surfaces. Domain type solutions have much larger numbers of equations of which only a small number represent the surface nodes. However, a nonlinear solution scheme has to be used to solve the whole system. Computationally this makes the BEM approach much more efficient.

During the development of BEASY-CP, it became clear that there is not one unique description of polarization and, in particular, not one set of equations describing its changes with time calcareous scale, and so forth. A number of clients have described their own recipe for polarization based on their experience and data. Although each of these schemes are valid for the type of problem they solved they do not cover all the cases that we require from a general purpose program, like BEASY-CP.

The system, therefore, provides the user with a general data structure for specifying a polarization data and how it varies with the key environmental and electrochemical parameters. The user can supply tabular data relating the key factors that the system uses to drive the polarization algorithm. The user has also the option of defining his own set of equations to describe the time dependent polarization behavior.

Using the System

The previous discussion has identified the key factors in simulating a corrosion problem and how they are solved using the BE technique. At this point before specific examples are considered the steps required from the user of the systems point of view are identified.

When the engineer has determined the need for a computer prediction, he must assemble the following data:

- (1) details of the geometry of the problem,
- (2) details of the properties of the electrolyte (that is, resistivity),
- (3) a polarization curve for the metals that are to be studied, and
- (4) if a time dependent prediction is required, data on the change of polarization with time, current density, age, potential, and so forth must be assembled (note the user has the option to use a very simple age rule, for example, $\text{age} = i \times \text{time}$ and relate this to polarization or use a more complex system involving the other parameters).

Having assembled the data, the next steps are as follows:

Create the Model

The user covers all the surfaces with elements. Elements must be placed on the anodic and cathodic surfaces and any other significant boundaries, for example, insulated. The free surface if present can normally be represented by a symmetry plane. Creation of the model is normally carried out using a graphics based pre-processing system.

Establish Material Types

Each of the elements used to describe the problem can be related to a type of material. In principle, polarization data could be specified for each individual element. However, in prac-

tice, the polarization data are related to specific groups of elements using the material name. In this way the user can simply define a surface as STEEL and the system will automatically attach the polarization data to that surface.

Once the simulation commences and nodes on the STEEL surface undergo different histories of current, potential, and so forth the polarization will be different for all parts of that surface dependent upon the age rule specified.

Supply the Polarization Data

Polarization data must be specified for each material type. This can range from the specification of a single number (that is, the slope of the polarization curve) if linear polarization is adopted to a detailed tabular description of the relationship between current density, potential, age, and so forth. The amount of detail is left to the user to decide based on the information he has available and the accuracy of the results he requires.

Run the Analysis

Examine the Predictions

The analysis provides detailed numerical values of the predicted current density and potential on all the surfaces and in the electrolyte if required. This can be displayed on graphic displays as contour plots, graphs, or color fringes.

Galvanic Corrosion

In many industries galvanic corrosion is an important problem. For example, in heat exchangers and in process industries many different metals may be located near each other in a corrosive environment. In addition, complex geometry makes the prediction of corrosion rates extremely difficult.

The system can be used to model general galvanic corrosion problems with any number of different metals. The system will determine which metals act cathodically or anodically depending upon the potential distributions. The corrosion rate can also be determined using the predicted values of density.

Figure 6 shows a three metal galvanic corrosion problem with zinc, steel, and copper. Symmetry is used to reduce the size of the problem, which involved a zinc block positioned centrally on top of a steel rod with a copper alloy shield located at the end of the rod. Although this particular example is not part of a real structure, it is interesting because a finite-element model of this problem was developed by Kasper [18]. A comparison can therefore be made of the resources required to build the model and solve the problem in the computer. The BEM model of this problem required 65 boundary elements compared with 3700 three-dimensional finite elements in the Kasper model.

This model has been developed using an analysis package, BEASY-CP, by covering the metal surfaces with quadratic quadrilateral elements. The polarization data were specified as in Fig. 5 by entering into the system a table of points from the EI curve. Figure 7 shows the predicted values of potential on the surface of the steel. Similar diagrams can be plotted for the current density or potential on any of the metal surfaces.

Example Applications

Modern underground and marine pipelines are protected against corrosion by the combined use of insulating coatings and cathodic protection. In practice, the current density requirements

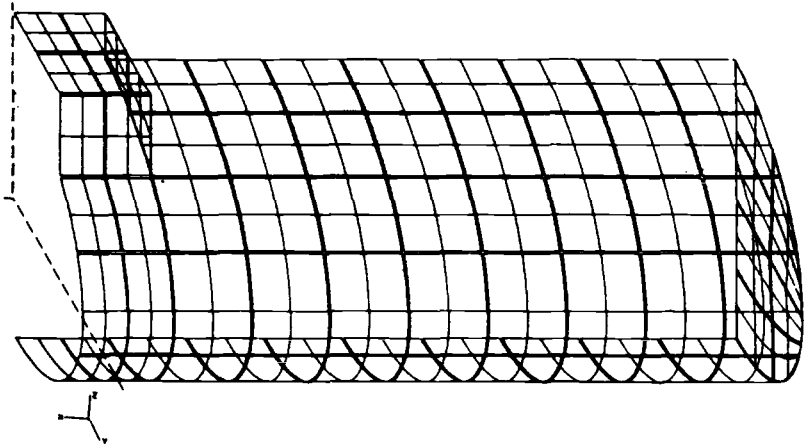


FIG. 6—Boundary element model of steel bar and anode. The anode is supported on top of the bar on the left side of the diagram.

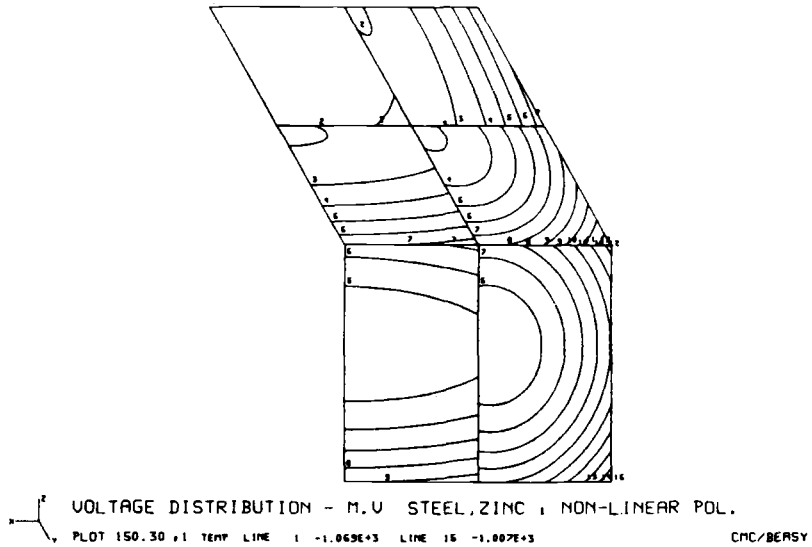
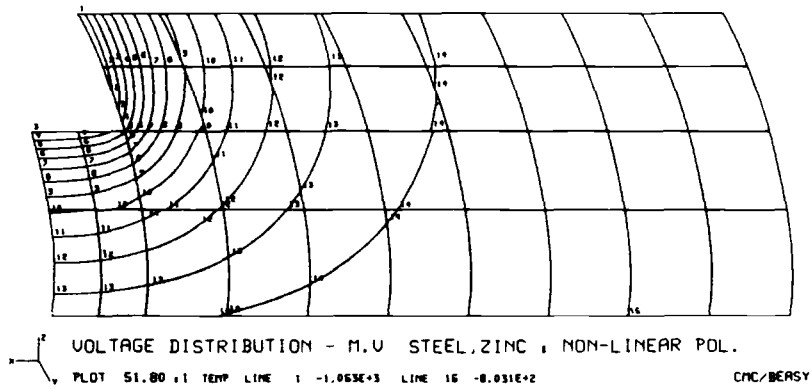


FIG. 7—Predicted potential on steel-zinc metal surfaces with nonlinear polarization.

used in the design of a cathodic protection system of a pipeline, are based on the coating resistance of the pipe. However, the local current requirement can drastically change in the presence of coating defects. Accurate modelling of the pipelines is therefore essential to ensure a sufficient design current capacity and also to evaluate the problems caused by defects.

The pipelines can be modelled using line or plate elements depending upon the type of anodes used.

A pipeline with bracelet sacrificial anode systems is considered an axisymmetric problem, and therefore it is adequate to use tubular or axisymmetric line elements. This condition is no longer applied when stand-off anode systems are in use, where the whole geometry must be modelled by plate elements.

In the first application, an underground pipeline of 0.8 m diameter, which is buried to a depth of 5 m in mud of $0.9 \Omega\text{-m}$ resistivity is analyzed. The surface of the pipeline is assumed to be coated and cathodically protected by impressed current bracelet anodes of 1.26 m^2 surface area and 170 m-spacing, which supply a current of 628 mA.

There are some coating defects considered on the surface of the pipe (Fig. 8) at which the cathodic current density is assumed to be uniform at 54 mA/m^2 . The problem was modelled using axisymmetric line element shown in Fig. 9. The predicted distribution of current density and voltage along the surface of the pipe with and without defects are given in Fig. 10 through 12. As predicted, sharp local decreases in the negative potential were observed because of defects. The area of the largest defect is unprotected if the required protective potential is specified at -900 mV .

Analysis of a Jacket Type Offshore Structure

A typical jacket type offshore structure consists of hundreds of tubular members for which the normal practice of modelling and analysis is very costly.

Therefore, in order to improve efficiency, it is convenient to deal with these problems in two stages, global and local analysis. In global analysis, tubular elements are used for modelling and analyzing the whole structure. In this way the complex task of modelling is reduced to the

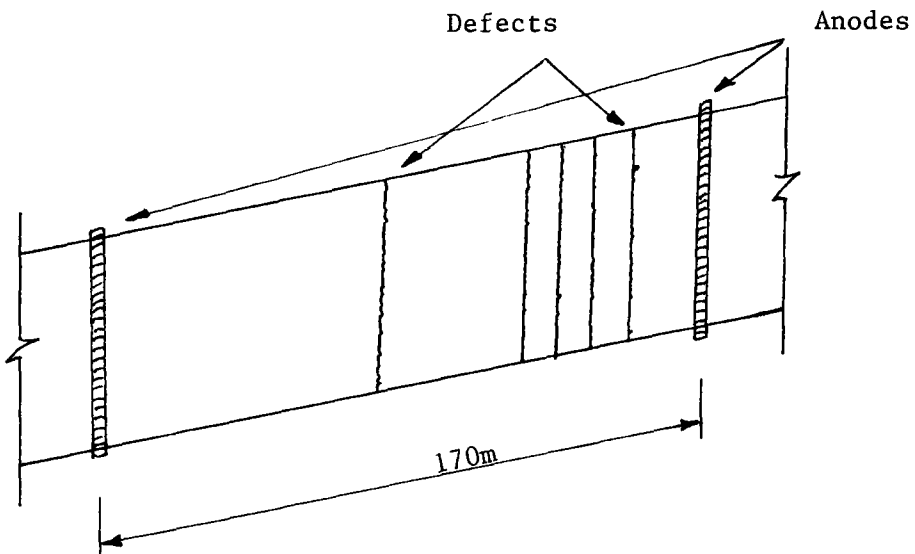


FIG. 8—Underground pipeline with defects.

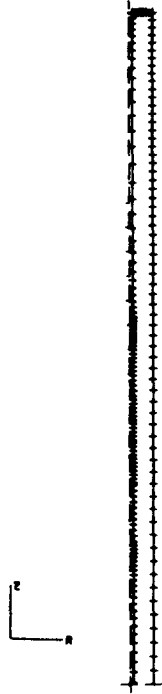


FIG. 9—Axisymmetric pipe buried in mud.

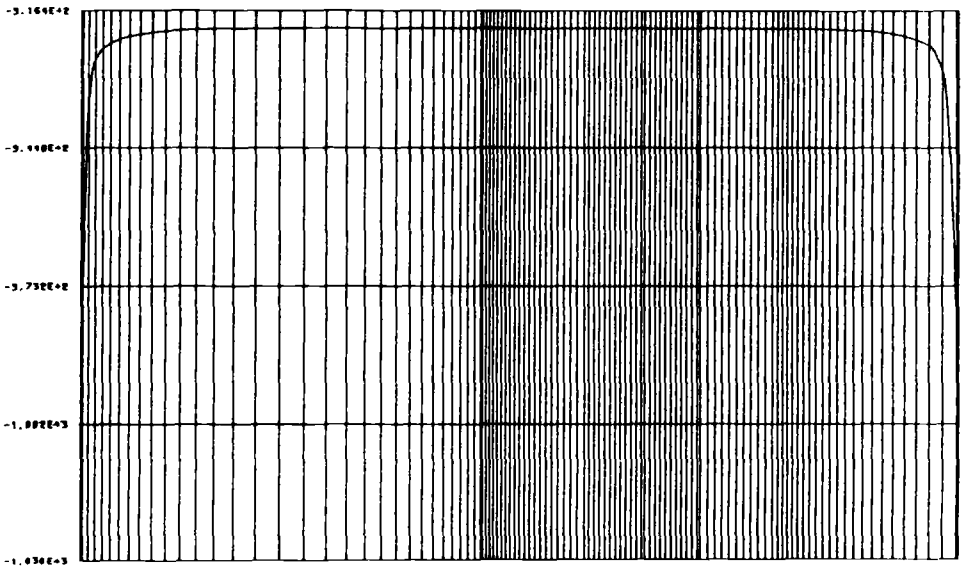


FIG. 10—Pipe with no defect buried in mud, voltage mV.



FIG. 11—Pipe with defect buried in mud, voltage mV.

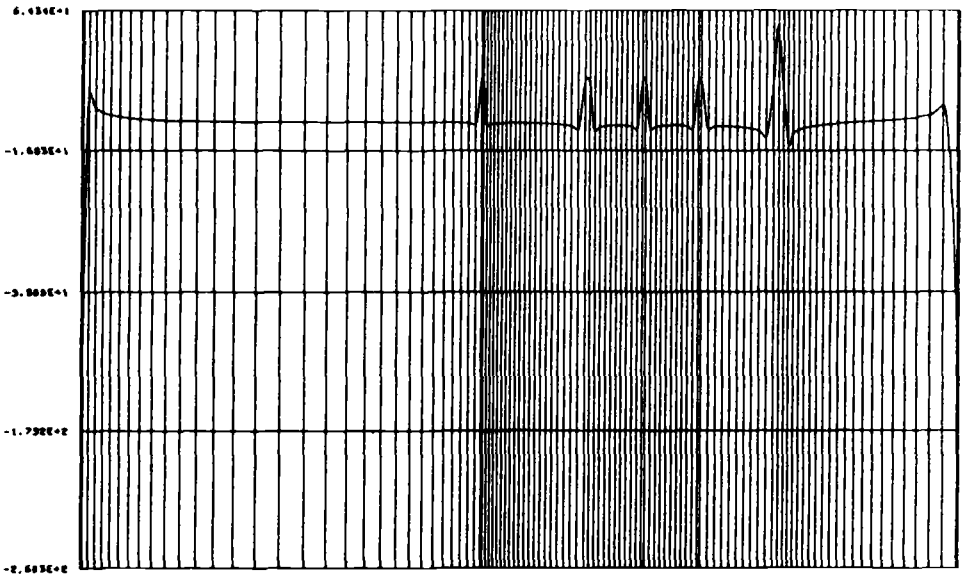


FIG. 12—Pipe with defect buried in mud—current density mA/m².

definition of axes and the radius of the tubes. Although the tube elements can adequately describe the geometry of such structures, they allow only the axial variation of voltage and current density and cannot accurately predict the solution at critical regions such as joints. For this reason, in the second step, a local analysis is carried out where the geometry of the particular area of interest is isolated and modelled independently using quadrilateral or triangular elements, or both. The isolation of the local model is completed by the introduction of an imaginary external boundary surface normally used in a shape of a BOX as shown in Figs. 13 and 14. The boundary condition on the "local box" is defined using the results from the global analysis.

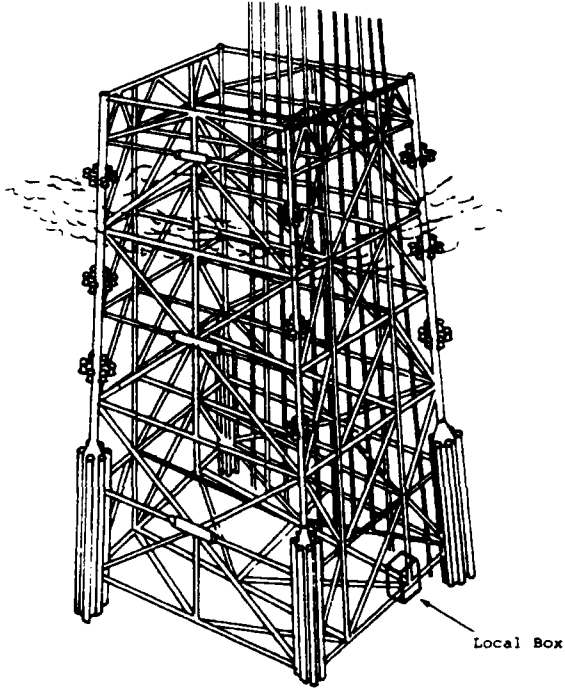


FIG. 13—Deep-water offshore platform.

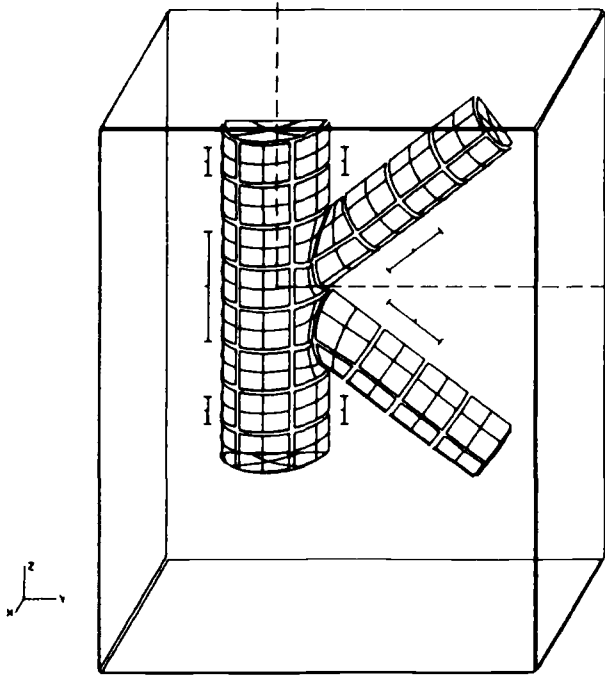


FIG. 14—K joint.

In this application a local analysis of a joint is investigated.

The structure is assumed to be made of mild steel, which is protected by sacrificial anodes system. The zinc anodes are used and designed using Dwights's formula to meet the design specification, which requires an overall average current density of 120 A/m^2 at a structural potential of -800 mV versus silver/silver chloride (Ag/AgCl). The family of polarization curves shown in Fig. 15 are chosen to consider the effects of time on cathodic polarization behavior. The data were obtained in seawater at a controlled temperature of 18°C and resistivity of $0.23 \text{ }\Omega\text{-m}$ on the same mild steel specimen [11].

The potential and current density distribution on the joint, at the start, and after 2 h, one day, one week, and one month of the installation, are shown by Figs. 16 through 22, respectively.

It can be seen that initially, the potential over the structure stands at values between -712 and -765 mV (with the exception of small regions close to the anodes), which is above the protective potential. The average current supplied at this stage was found to be 196 mA/m^2 .

The potential profile after one day (Fig. 18) shows that the required protective potential has almost been achieved. After one week the potentials have shifted well below the protective potential and are more evenly distributed.

The results do not show a significant change in potential distribution after one week when it is compared with potential profile at one month. It is however, interesting to see the fall in the current supply, as average current has dropped from the initial value of 196 to 81 mA/m^2 after one month (see Fig. 23).

This design based on common procedure is therefore extremely uneconomic, leading to an estimation of an excessive required current capacity.

Final Remarks

The objective of this paper has been to describe the methodology and requirements of computer modelling of galvanic corrosion. The full mathematical background on the numerical techniques described has not been included as it is well covered in the published literature described in the references.

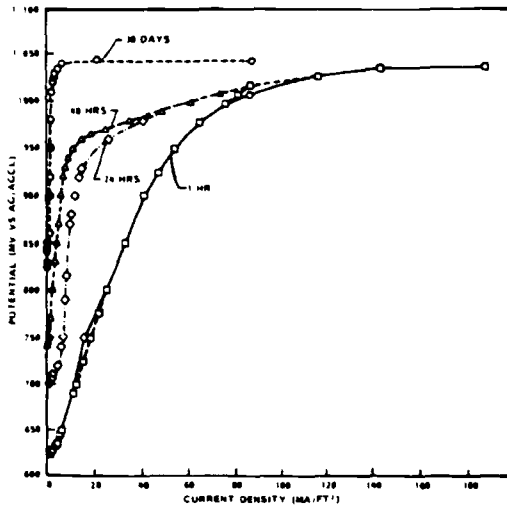


FIG. 15—Polarization curves for mild steel held at 215 mA/m^2 for various periods given by Ref 11.

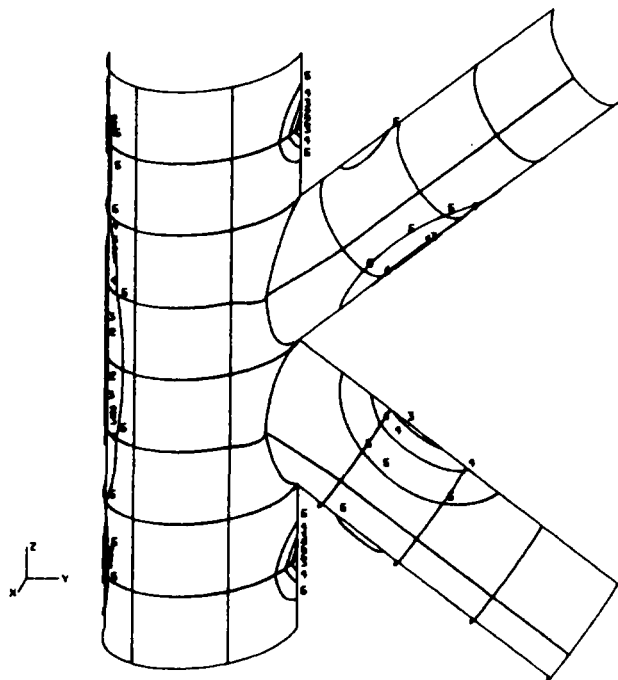


FIG. 16—Initial potential distribution, mV.

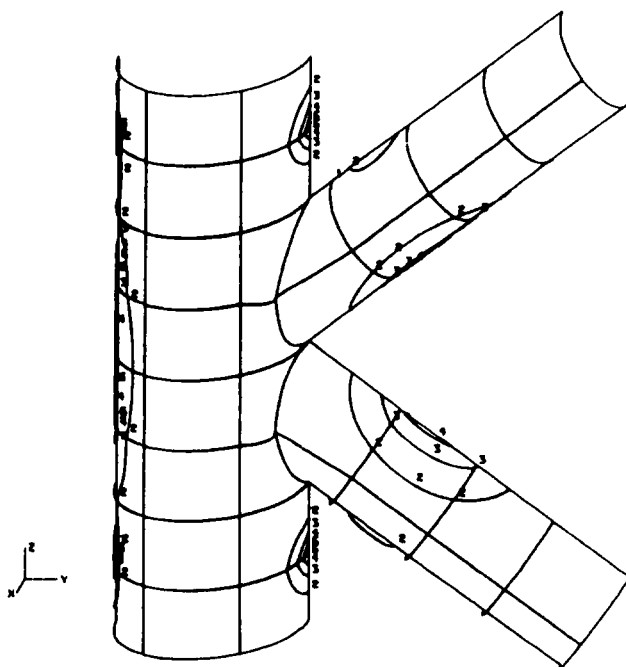


FIG. 17—Initial current density distribution, mA/m².

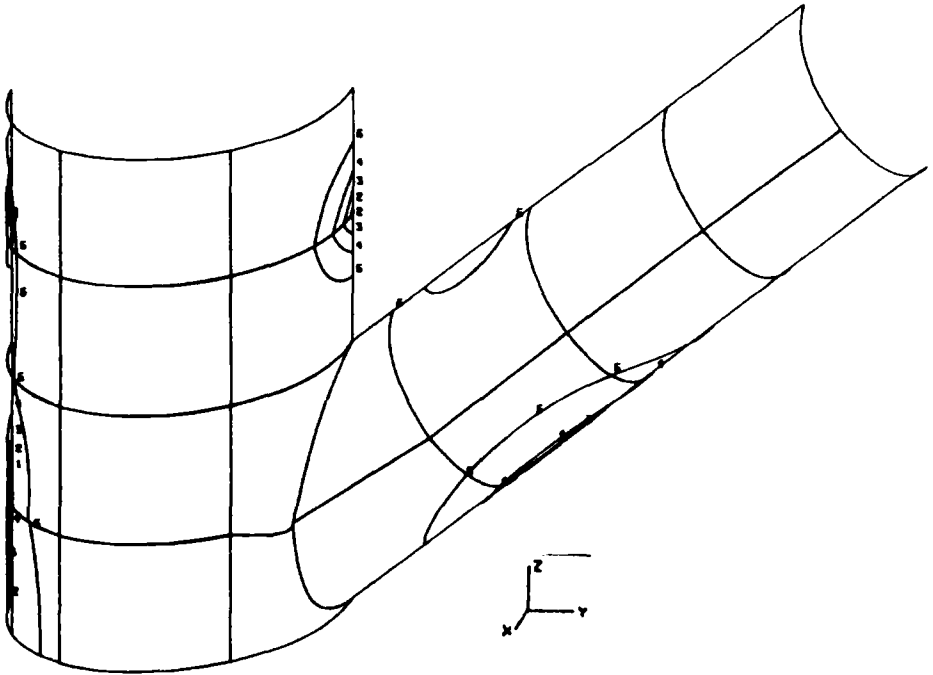


FIG. 18—Potential distribution after 2 h, mV.

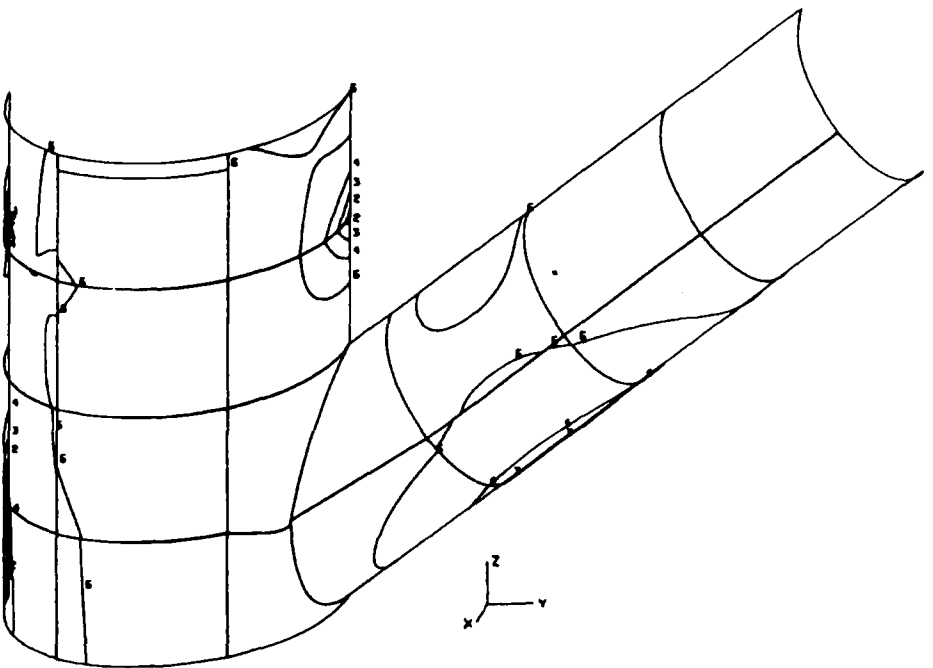


FIG. 19—Voltage distribution after one day, mV.

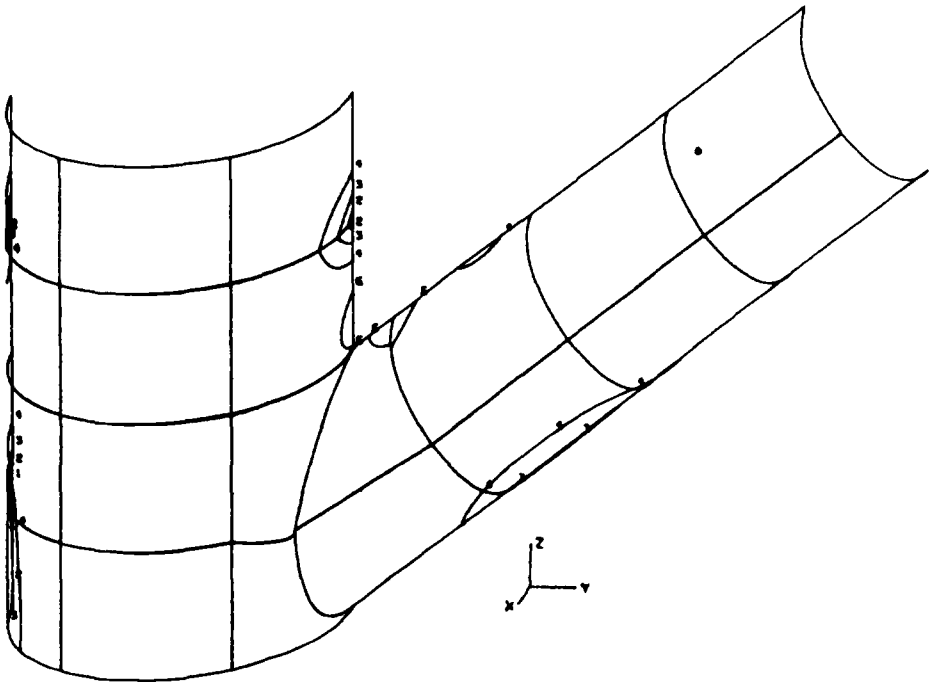


FIG. 20—Voltage distribution after one week, mV.

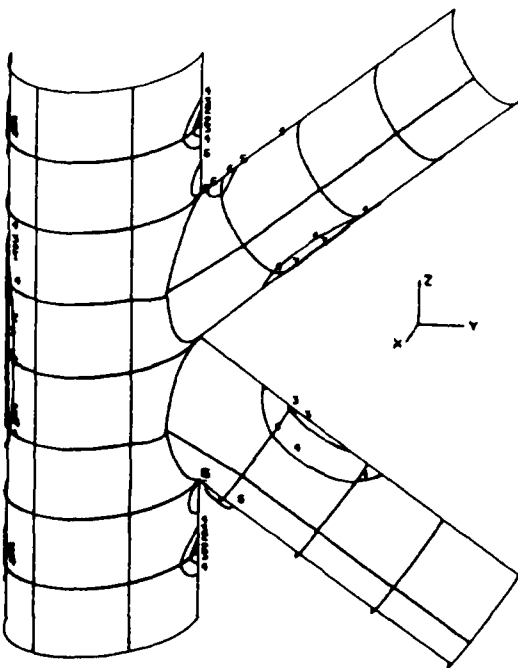


FIG. 21—Potential distribution after one month, mV.

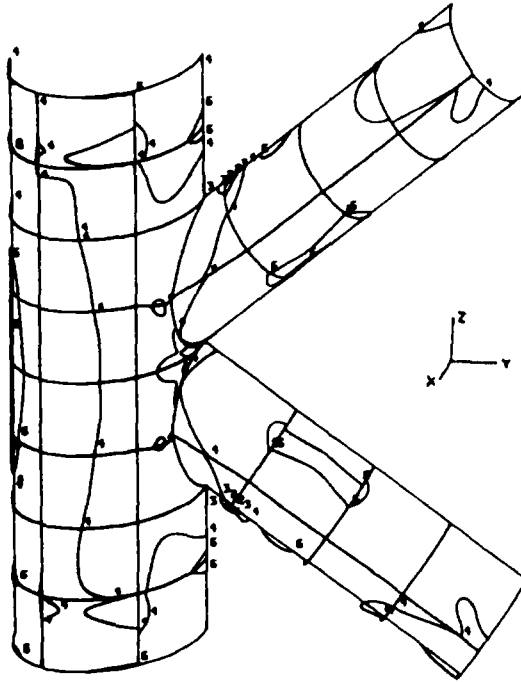


FIG. 22—Current distribution after one, mA/m².

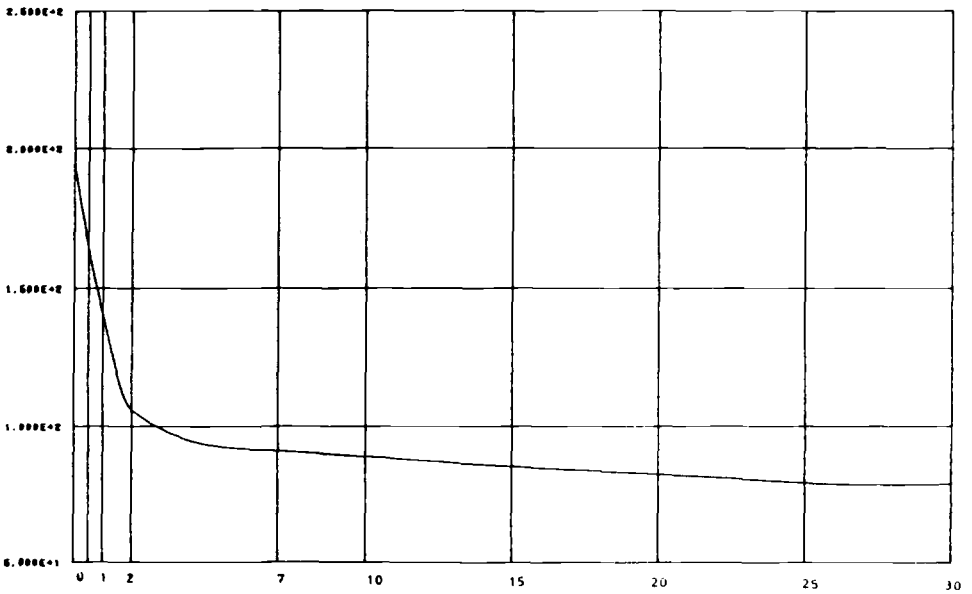


FIG. 23—Variation of average current with time, mA/m².

The BEASY-CP system has been developed for computer modelling of galvanic corrosion and the analysis and design of cathodic protection problems. The boundary element method is believed to be the most appropriate technique for the modelling of galvanic corrosion problems for the following reasons:

1. It is conceptually very easy to describe the problem as only the surfaces have to be defined. Therefore, models can be created quickly, and modified easily by engineers who are not necessarily specialists in analysis.
2. The BEM approach has nodes only on the metal surfaces, which results in improved accuracy and solution time.

The complex electrochemical processes that have to be modelled require a flexible data representation. The authors believe the approach described where the user can specify complex or simple polarization dependent upon the data he has available is the most appropriate for galvanic corrosion.

The computer model has a valuable role to play in galvanic corrosion and is expected to provide

- (1) an increased understanding of the basic processes of corrosion and their interaction,
- (2) increased confidence in design,
- (3) optimized designs,
- (4) accurate lifetime predictions, and
- (5) interpretation of results from monitoring systems.

Acknowledgments

PATRAN—A software product of PDA Engineering Inc., Santa Ana, CA, USA.

FEMGEN—A software product of FEGS Ltd, Cambridge, England.

FEMVIEW—A software product of FEMVIEW Ltd, England.

SUPERTAB—A software product of SDRC Inc., Cincinnati, OH, USA.

BEASY—A software product of Computational Mechanics Inc., Billerica, MA, USA.

References

- [1] Williams, D. E. et al., "The Applications of Expert Systems to Corrosion Problems," *UK Corrosion '85*, Harrogate, Nov. 1985.
- [2] Stead, J. P. and Strutt, J. E., "Progress Towards a Computer Aided Risk Evaluation System," *International Conference on the Prediction of Materials' Performance in Plants Operating with Corrosive Environments*, Cranfield Institute of Technology, Feb. 1986.
- [3] Strommen, R. D., "Computer Modelling of Offshore Cathodic Protection Systems Utilized in C.P. Modelling," *Offshore Technology Conference*, Houston, Texas, May 1982.
- [4] Waber, J. T. and Fagen, B., "Mathematical Studies on Galvanic Corrosion," *Journal of the Electrochemical Society*, Vol. 103, No. 1, 1956, pp. 64-72.
- [5] Kenard, E. and Waber, J. T., *Journal of the Electrochemical Society*, Vol. 117, No. 7, 1970, p. 880.
- [6] McCafferty, E., "Naval Research Laboratory Report 8107," Aug. 1977.
- [7] Fleck, R. N., "Numerical Evaluation of Current Distribution in Electrical Systems," MSc thesis, University of California, Berkeley, CA, Sept. 1964.
- [8] Diog, P. and Flewitt, P. E., "A Finite Difference Numerical Analysis of Galvanic Corrosion," *Journal of the Electrochemical Society*, Vol. 126, No. 12, 1979, pp. 2057-2063.
- [9] Strommen, R., "Computerized Techniques Applied in Design of Offshore Cathodic Protection Systems," Paper 241, *Conference of Corrosion/80*, March 1980.
- [10] Braver, J. R., "Finite Element Analysis of Electric Fields Using MSC/NASTRAN," *Conference of Computer Techniques Applicable to 3-D Field Analysis*, Santa Barbara, CA, July 1978.
- [11] Decarlo, E. A., "Computer Aided Cathodic Protection Design Technique for Complex Offshore Structures," Paper 165, *Corrosion/82 Conference*, March 1982.
- [12] Munn, R. S., "A Mathematical Model for Galvanic Anode Cathodic Protection Systems," *Material Performance*, Aug. 1982, pp. 29-32.

- [13] Fu, J. W., "A Finite Element Analysis of Corrosion Cells," *Corrosion/NACE*, Vol. 28, No. 5, 1982, pp. 9-12.
- [14] Brebbia, C. A., *The Boundary Element Method for Engineers*, Pentech Press, London, 1978.
- [15] Adey, R. A., Niku, S. M., Brebbia, C. A., and Finnegan, J., "Computer Aided Design of Cathodic Protection Systems," *Boundary Element VII Conference*, Villa Olmo, Lake Como, Italy, 24-27th Sept. 1985.
- [16] Adey, R. A. and Niku, S. M., "Comparison Between Boundary Elements and Finite Elements for CAD of Cathodic Protection Systems," *BETECH Conference*, South Australian Institute of Technology, Adelaide, Australia, Nov. 1985.
- [17] Fu, J. W. and Chow, J. S., "Cathodic Protection Design Using an Integral Numerical Method," *Corrosion/82 Conference*, Houston, TX, Paper 163.
- [18] Kaper, R. G. and April, M. G., "ElectroGalvanic Finite Element Analysis of Partially Protected Marine Structures," Vol. 39, No. 5, May 1983, pp. 181-188.
- [19] Danson, D. J. and Warne, M. A., "Current Density/Voltage Calculation using Boundary Element Techniques," *NACE 1983 Conference*, Los Angeles, CA.
- [20] *Corrosion*, Vol. 39, No. 5, May 1983.

Comparisons of Localized Ionic Currents as Measured from 1-D and 3-D Vibrating Probes with Finite-Element Predictions for an Iron-Copper Galvanic Couple

REFERENCE: Kasper, R. G. and Crowe, C. R., "Comparisons of Localized Ionic Currents as Measured from 1-D and 3-D Vibrating Probes with Finite-Element Predictions for an Iron-Copper Galvanic Couple," *Galvanic Corrosion. ASTM STP 978*, H. P. Hack, Ed., American Society for Testing and Materials, Philadelphia, 1988, pp. 118-135.

ABSTRACT: The ionic current density in the near-field of a corroding iron-copper galvanic couple was measured, and the results were compared with the predictions of a finite-element model, which calculates near-field potential and current density distributions. All three components of the ionic current density vector were measured using a three-dimensional vibrating microprobe. The calculated current densities were based on the measured polarization curves of the individual constituent materials forming the couple. Agreement between the predicted and measured results was excellent. Agreement between one-dimensional ionic current density distributions from previous work was also excellent.

KEY WORDS: scanning vibrating electrodes, numerical methods, nonlinear polarization, three-dimensional electric fields, current density mappings

Recent advances in the techniques of measuring localized currents in electrolytes have made possible methods to measure ionic currents associated with corrosion microcells. The new techniques use vibrating probes to measure ionic currents with high spatial and current resolutions so that local cell activity on a scale closely related to many of the microstructural features of the material can be delineated. This capability is particularly useful for studying phenomena such as galvanic, pitting, and crevice corrosion. In these situations, the highly interactive coupling that exists between the multiple anodes and cathodes on the metal surface results in electrogalvanic interactions between anodic and cathodic regions, which are very complex. On characterizing these interactions, geometric and polarization effects and inhomogeneous electrolytic media are major variables.

Historically, the vibrating probe techniques were developed for biological studies [1,2] but have recently been used to study corrosion phenomena [3-6]. Jaffee and Nuccitelli [2] developed a one-dimensional vibrating microprobe technique that illustrates the method. The 1-D microprobe operates by oscillating a single electrode along a line. The mechanical vibration induces a time varying potential in the vibrating electrode, which is measured relative to a fixed, distant reference electrode. The vibrating metal electrode is a small metal sphere 10 to 30 μm in diameter, which is vibrated between two points typically 10 to 30 μm apart. The voltage at the two extremes of vibration is measured and used to calculate the current density component in the electrolyte at the center of the vibration stroke and along the axis of vibration using the relation

¹Staff scientists, Naval Underwater Systems Center, New London, CT.

²Supervisory materials engineer, Naval Research Laboratory, Washington, DC 20375-5000.

$$J_1 = \sigma \Delta V / \Delta r$$

where J is the current density vector component parallel to the probe vibration, V is the voltage difference between the points at the extremes of vibration, r is the length of the vibration stroke, and σ is the conductivity of the solution.

Ishikawa and Isaacs [3] have adapted the 1-D vibrating probe method to study pitting corrosion of aluminum alloys. Their method uses a scanning technique whereby the vibrating probe is held fixed in a mechanical stage driven by two stepping motors arranged to translate the probe parallel to the surface of the specimen. The probe vibrates normal to the plane of the specimen so that the current density normal to the specimen is measured. This technique was used by Crowe [5,6] and Crowe and Kasper [4] to measure near-field, normal ionic current densities of corroding composite materials and of a corroding Fe-Cu galvanic couple to compare these measurements with the predictions of a finite-element model. One of the important conclusions derived from this latter work was that all three components of the current density vector are needed to completely characterize the potential and current density fields of corroding systems.

The present work used a 3-D vibrating probe to measure the total ionic current density vector in the near-field of a corroding Fe-Cu galvanic couple. The method is an extension of the 2-D technique developed by Freeman et al. [7,8] to three dimensions. In this method, a single electrode is moved rapidly (300 Hz) in a small circle (15 μm diameter), and the potential relative to a remote, nonvibrating reference electrode is measured at each of 256 points around the circumference of the circle. From this data, two orthogonal components of the current density in the plane of the circle can be obtained. By vibrating the probe tip in orthogonal planes, the 2-D method has been extended to 3-D, thus extracting measurements of all three ionic current density components.

Experimental Procedures

Materials

A galvanic couple was constructed of 6.35-mm-diameter Marz grade iron and 50.8-mm-diameter Marz grade copper obtained from MRC Inc., Orange, NJ. The iron anode was press fit into a centrally located hole in the copper cathode to produce a cylindrically symmetrical planar galvanic couple as depicted in Fig. 1. The couple was metallographically polished using standard techniques. The final finish of the galvanic couple was obtained with 1.0- μm diamond paste. Individual specimens for polarization measurements were produced from the same materials. All specimens were thoroughly cleaned in ethanol before testing.

Electrochemical Measurements

Electrochemical tests were conducted in open cells in laboratory air. All electrochemical measurements were made using 0.6 M sodium chloride (NaCl) electrolytes prepared with reagent grade chemicals and distilled water. The pH was adjusted to 1.75 with hydrochloric acid (HCl). The measured solution conductivity σ was 63 mS/cm at pH = 1.75.

Potentiostatic Polarization Measurements

Standard potentiostatic polarization response of the constituent materials was measured. The specimens for these tests were machined from the same copper and iron rods used to construct the galvanic couple. Polarizations were performed using a PAR Model 173 potentiostat in combination with a PAR Model 175 universal programmer at a stepping rate of 0.1 mV/s.

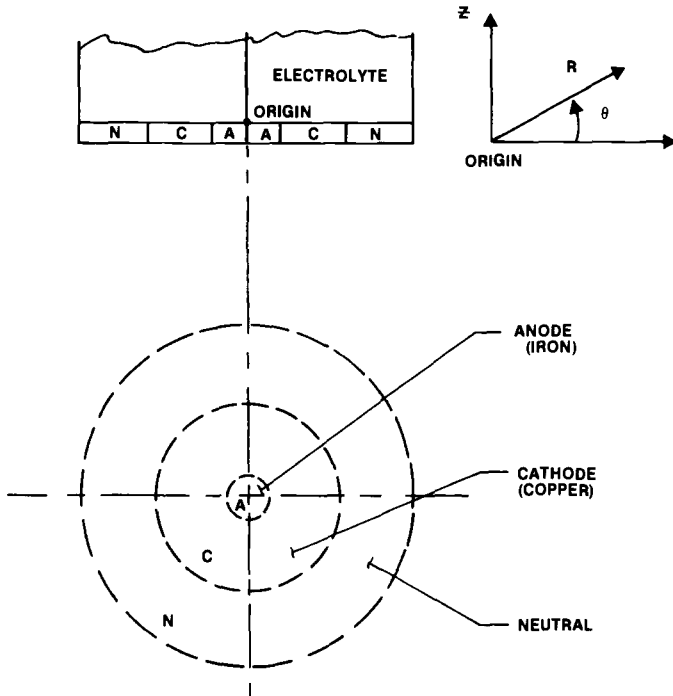


FIG. 1—A schematic of the Fe-Cu galvanic couple.

ASTM Practice for Standard Reference Method for Making Potentiostatic and Potentiodynamic Anodic Polarization Measurements (G 5) procedures were used.

Vibrating Probe Measurements

Ionic current density measurements were performed using the three-dimensional vibrating probe instrument shown schematically in Fig. 2. This instrument was designed and built by E and B Systems, Nashville, TN. It has six major components. These are the microcomputer, the drive heads, and amplifiers, the microelectrodes, the microelectrode preamplifier, and two constant current sources.

The IBM PC microcomputer provides instrument control, data acquisition, signal processing, and display and storage functions. Instrument control and data acquisition are accomplished by computer interface to a Tekmar Lab Master AD/DA converter. In addition to controlling the motion of the vibrating probe and the measurement currents, the computer and interactive software provide for calibration of the system, measurement of the electrode impedance, and data analysis and output.

The drive heads consist of three electromagnetic drivers, which are connected to the measuring microelectrode by 3-mm mylar tubes arranged in such a fashion that the three orthogonal drive axes form a cube (Fig. 3). The diagonal of the cube is positioned vertically. Each driver consists of a modified permanent-magnet loudspeaker, which vibrates the measuring microelectrode through the mylar tubes using a push-pull motion. The drivers respond to sinusoidal signals generated in the microcomputer. These signals are applied to the drive heads through the driver amplifiers. This results in a circular motion of the probe tip in a plane angled at 54.7° to the axis of the probe. The relationship between the X-Y-Z specimen coordinate system and

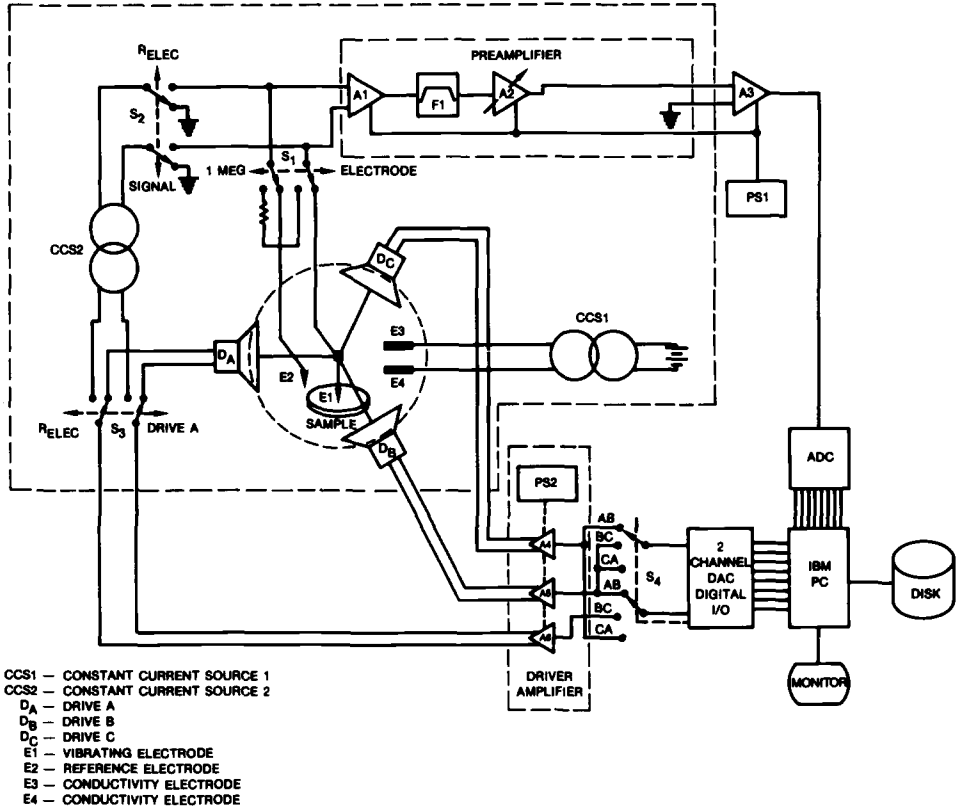


FIG. 2—A schematic of the three-dimensional vibrating probe.

the A-B-C probe drive coordinate system is shown in Fig. 4. The frequency response of the drivers is shown in Fig. 5. As can be seen, the drivers provide adequate displacements for measurement of the current density at off-resonance frequencies. This is in contrast to the piezoelectric drivers used in one-dimensional probes, which lose their stroke rapidly when operated off-resonance.

The microelectrode system consists of two electrodes: the measuring electrode and the reference electrode. The measuring electrode is a platinized, gold plated, tungsten wire electrode, which is insulated with paralene mounted in the junction of the mylar drive tubes. The tip of the probe is exposed as shown in Fig. 6. The reference electrode is a silver/silver chloride electrode rigidly attached to the preamplifier. The preamplifier contains a two-stage differential preamplifier, which provides a gain of 104 in the voltage difference between the vibrating measuring electrode and the reference electrode.

Sensitivity

The theoretical limit of sensitivity of the electrode is determined by the electrode impedance and the Johnson or thermal noise of the electrode. The exposed area of the tip determines both the spatial resolution and the impedance of the electrode. Thus tip preparation is important.

When the electrode area is small, as is required for fine spatial resolution, the resistive component of the electrode impedance is high causing an appreciable noise level. This electrode impedance depends upon both the area of the electrode and the frequency of vibration. The

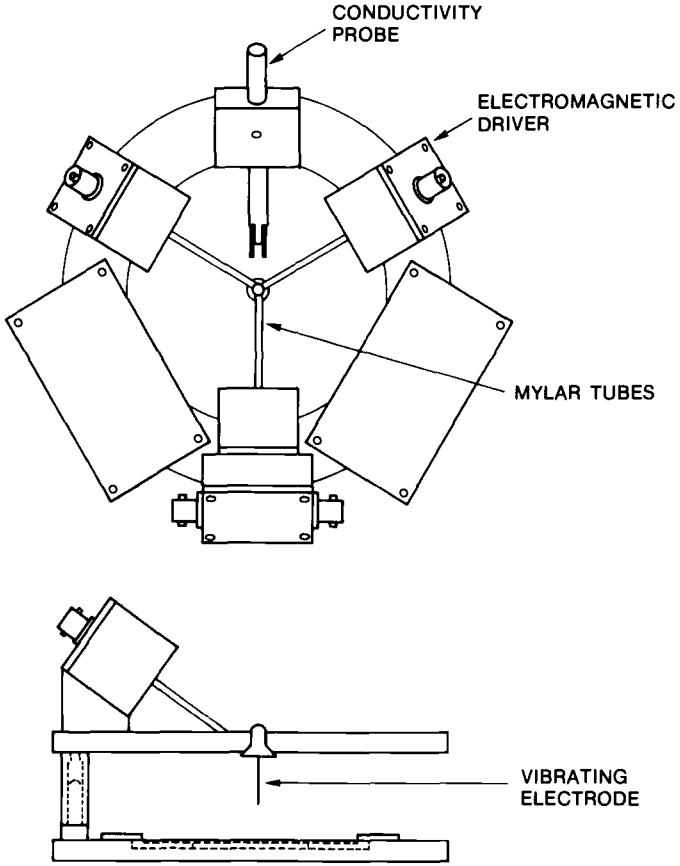


FIG. 3—Arrangement of the probe components.

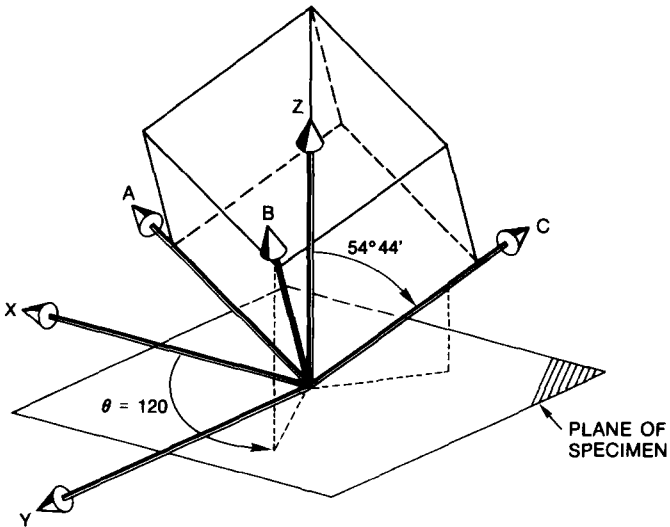


FIG. 4—The relationship between the X-Y-Z specimen coordinate system and the A-B-C probe drive coordinate system.

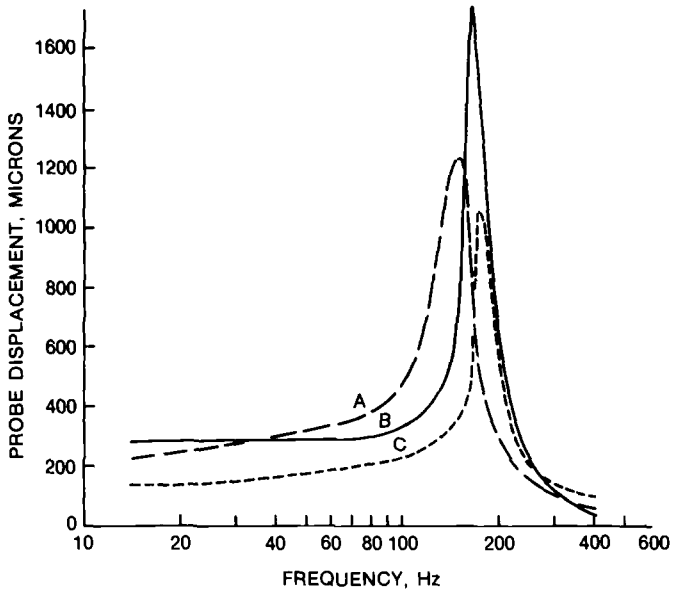


FIG. 5—The frequency response of the probe drivers.

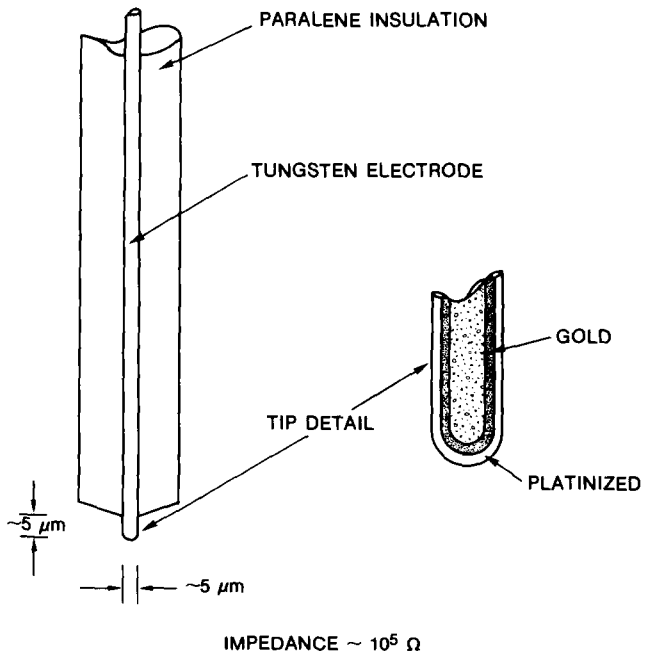


FIG. 6—Schematic of the probe tip.

relationship between these parameters is given by Geddes as approximately [9]

$$z = \frac{0.225 \times 10^{14}}{kaf^{(1-\alpha)}}$$

where z is the electrode impedance, k is a constant that depends on the type and condition of the electrode, a is the electrode area (in μm^2), f is the frequency of vibration, and α is a constant that relates the rate at which the electrode capacitance c decreases with frequency, that is, $c = kf^{-\alpha}$. The electrode impedance was measured before each run. The electrode impedance was typically 1 to $1.5 \times 10^5 \Omega$ at 1.5 kHz and 5 to 6×10^5 at 300 Hz. For the data presented herein, a frequency of 400 Hz was used for the measurements.

The ability of the electrode to efficiently detect the electric field depends upon the noise level of the electrode and the amplification of the signal. Electrode noise arises from random movement of charge carriers at the electrode/electrolyte interface as the electrode establishes and maintains equilibrium with the electrolyte or as the electrode responds to the passage of current. This random movement of charge carriers creates a resistive component to the electrode impedance, which becomes the noise generator. The noise voltage is generated at all frequencies and is given by the relation

$$E = [4kTR(f_h - f_l)]^{0.5}$$

presented by Johnson [10]. In this relation, E is the root-mean-square noise voltage, k is Boltzmann's constant, T is the absolute temperature, R is the universal gas constant, and f_h and f_l are the upper and lower cutoff frequencies of the measuring system. The quantity $(f_h - f_l)$ is therefore the bandwidth.

In order to minimize the noise, it is therefore necessary to have as narrow a bandwidth as possible. An ultra-narrow bandwidth is obtained during data reduction using the ultra-narrow-band phase coherent filtering algorithm derived by Freeman et al. [7]. This algorithm allows the gradients as well as the current density components to be extracted from the data measured during rotation of the electrode in a circle in a plane. The measured voltages from the rotating electrode are represented by a Taylor's series expansion about the central point (A_0 , B_0) of the circle of radius r swept out during rotation through angle θ of the probe tip. Thus

$$\begin{aligned} \phi(A, B) &= \phi(A_0, B_0) + \frac{\partial\phi}{\partial A}(A - A_0) = \frac{\partial\phi}{\partial B}(B - B_0) \\ &= \phi(A_0, B_0) + r \cos \theta \left. \frac{\partial\phi}{\partial A} \right|_{(A_0, B_0)} + r \sin \theta \left. \frac{\partial\phi}{\partial B} \right|_{(A_0, B_0)} \end{aligned}$$

where $(A - A_0) = r \cos \theta$, $(B - B_0) = r \sin \theta$ and the partial derivatives are evaluated at (A_0, B_0) . The current density at the central point (A_0, B_0) has components J_A and J_B given by the convolution integrals

$$J_A = -\frac{\sigma}{r} \int_0^{2\pi} V(\theta) \cos \theta d\theta$$

and

$$J_B = -\frac{\sigma}{r} \int_0^{2\pi} V(\theta) \sin \theta d\theta$$

where $V(\theta)$ is the measured voltage at rotation angle θ , and σ is the conductivity of the electrolyte at (A_0, B_0) . Using this procedure, currents densities of $5 \mu\text{A}/\text{cm}^2$ can be detected.

Operation of the Probe

In operation, the computer feeds sinusoidal driving signals to the drive heads, in sequence, two at a time so that the probe tip is forced to rotate in circles in the three orthogonal planes angled at 54.7° to the probe axis. The diameter of the circle is adjusted as an experimental variable. The differential voltage is then sampled at 256 points around the circumference of each circle. These data are averaged over a 1000 cycles or more and then stored in the computer for analysis.

During analysis, the microcomputer evaluates the convolution integrals for the 1000 or more cycles of the probe rotation, adjusts for orientation relative to the specimen, averages the current densities, and calculates the gradients.

As each of the combinations of drives are energized in sequence, a 3-dimensional volume of electrolyte is sampled and a redundant set of the components of the current density vector and gradients are obtained (Fig. 7). Transformation of coordinate systems from the A-B-C coordinate system to the X-Y-Z coordinate system are performed in the computer, displayed on the computer monitor, and stored in ASCII files on the disks for future additional analysis.

Calibration

Calibration of the probe is accomplished by measuring a known, uniform current density field in an electrolyte contained in a separate calibration dish, which is mounted on a turntable. The field is rotated through 12 standard positions 30° apart. At each standard position, the output voltage is measured when a single drive is energized. This allows the average line of motion of the electrode in the horizontal plane to be determined for that drive, as well as the

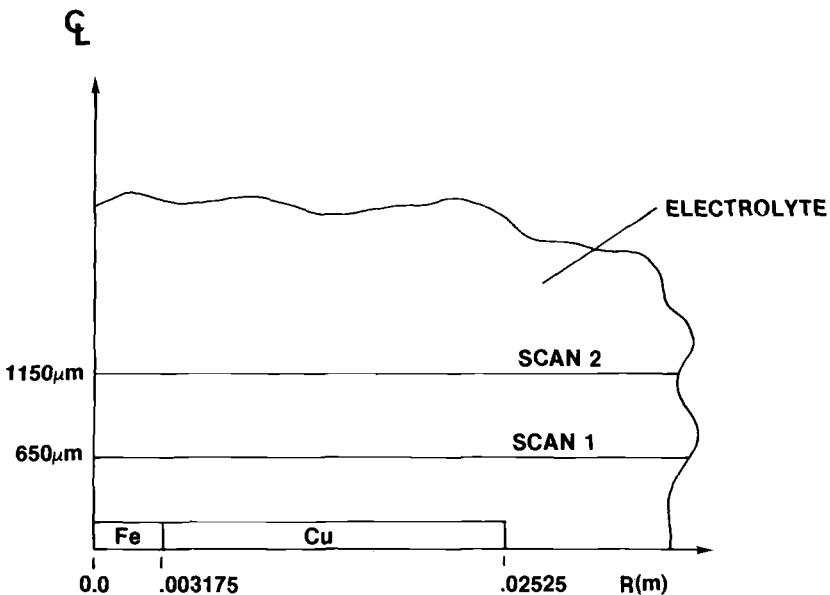


FIG. 7—The geometric arrangement of the 3-D scans.

mechanical lag between the drive voltage and the mechanical response of the probe. Appropriate mathematical calculations of these data provide an exact description of the probe motion and the measured values of the known field from which calibration factors are extracted and stored for data reduction.

Mechanical positioning of the probe in the X - Y plane parallel to the specimen surface is achieved using two Klinger Model MT 160 stepping motor driven translation stages mounted at right angles. These translation stages allowed indexing of the specimen relative to the probe in $1\text{-}\mu\text{m}$ increments to an average accuracy of $2\text{ }\mu\text{m}$. Control of the stages is achieved either manually or by computer using a Klinger Model CC-1 universal programmable indexer.

For the experiments reported here, the vibration probe tip was positioned above the surface of the Fe-Cu galvanic couple at either 650- or $1150\text{-}\mu\text{m}$ elevation and current density measurements were made. The arrangement is shown schematically in Fig. 6 so that the 3-D probe measurements were directly comparable to the 1-D measurements reported earlier [4]. At each elevation, a single line scan was performed so that the probe tip traveled parallel to a line that passed through the center of the galvanic couple.

Experimental Results

The anodic and cathodic potentiostatic polarization curves for the uncoupled iron and copper in 0.6 M NaCl at a pH level of 1.75 and at a temperature of 25°C are shown in Fig. 8. These polarization characteristics were reflected in the experimental setup as well as the impedance controlled boundary conditions of the finite-element model.

The components of the measured ionic current density vectors, in polar coordinates, as a function of position, are listed in Table 1.

Numerical calculations were performed using the finite-element model developed in Ref 4 and summarized in Fig. 9. This finite-element model contains a geometric description (Fig. 9a) of the galvanic couple and the electrolyte, the fundamental electrical laws in partial differential equation form that govern the behavior of the galvanic couple (Fig. 9b), and the associated Dirichlet and Neumann boundary conditions (Fig. 9c). The numerically predicted values for J_r and J_z are listed in Tables 2 and 3 for assumed electrolyte conductivities of 42 and 62.5 mS/cm ,

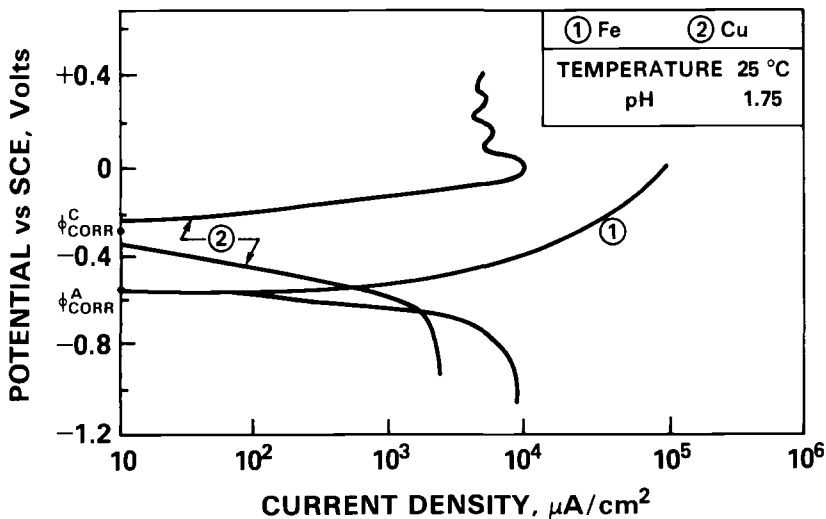


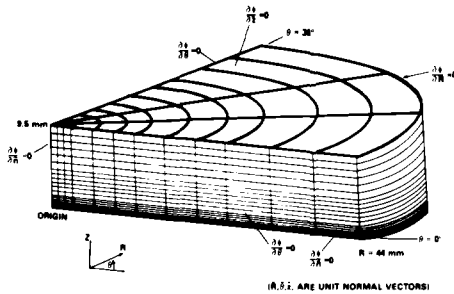
FIG. 8—Potentiostatic polarization curves for the iron and copper constituents of the galvanic couple.

TABLE 1—Measured ionic current density ($pH = 1.75$ and $\sigma = 42 \text{ mS/cm}$).

Radius, mm	Height, μm	J_z , A/m	J_r , A/m	J , A/m
0	650	14.300	5.430	15.296
1	650	8.420	12.250	14.865
2	650	4.400	11.210	12.043
3	650	2.350	9.320	9.612
5	650	0.225	5.350	5.355
7	650	-0.100	2.790	2.792
9	650	-0.044	2.030	2.030
11	650	-0.139	1.670	1.676
13	650	0.007	1.500	1.500
15	650	-0.068	1.370	1.372
17	650	-0.162	1.310	1.320
19	650	0.005	1.180	1.180
21	650	-0.009	1.090	1.090
23	650	-0.142	0.990	1.000
25	650	-0.007	0.710	0.710
0	1150	6.910	2.960	7.517
1	1150	3.520	4.320	5.573
2	1150	2.310	4.480	5.040
3	1150	1.660	4.250	4.563
4	1150	0.858	3.980	4.071
6	1150	0.407	3.070	3.097
8	1150	0.111	1.650	1.654
10	1150	0.608	1.050	1.213
12	1150	0.061	1.120	1.122
14	1150	0.049	0.940	0.941
16	1150	-0.008	0.940	0.940
18	1150	-0.050	0.950	0.951
20	1150	0.071	0.840	0.843
22	1150	-0.004	0.800	0.800
24	1150	0.051	0.770	0.772
0	650	14.300	5.430	15.296
0	1150	6.910	2.960	7.517
0	1650	5.290	7.080	8.830
0	2150	4.360	1.850	4.730

respectively. Figure 10 shows the calculated and measured J_z ionic current density component as a function of radial position at $650 \mu\text{m}$ above the electrode surface. Figure 11 shows the comparison of the measurements at $z = 1150 \mu\text{m}$ with the calculated results at $z = 1125 \mu\text{m}$. The agreement between the measurements using the 1-D probe (small insert in Fig. 11) is excellent, and both sets of measurements are in excellent agreement with the finite-element model calculations. As can be seen in these figures, the anodic current density normal to the couple is highest near the center of the iron. The normal current density falls rapidly to a low value just past the Fe-Cu interface, and there is a dispersion in J as the elevation above the surface increases.

Figure 12 shows the measurements of J_R obtained using the 3-D probe compared with the finite-element calculations at $z = 650 \mu\text{m}$. It should be pointed out that the measured components of $J(J_x, J_y, J_z)$ were changed to a set of J_r and J_z components to compare with the finite-element results. The x and y components of J were squared, and the square root of the sum of the squares resulted in J_r . This resulted in a clearer point-to-point comparison between theory and measurement. Tables 1 through 3 already include this information. The measured results at $1150 \mu\text{m}$ are shown compared with the finite-element calculations at $1125 \mu\text{m}$ in Fig. 13. Since the 1-D probe can not measure these components of the current density vector, there are



BOUNDARY CONDITIONS OF THE THREE-DIMENSIONAL FINITE ELEMENT MESH (36°)

(a)

NON-LINEAR SOLUTIONS TO:

$$\nabla \cdot \sigma \nabla \Phi = - \frac{\partial \rho}{\partial t} \quad (1)$$

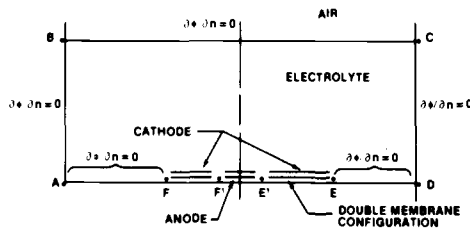
$$\bar{J} = -\sigma \nabla \Phi \quad (2)$$

WHERE

- σ = CONDUCTIVITY (S/m)
- \bar{J} = CURRENT DENSITY (A/m²)
- Φ = POTENTIAL (VOLTS)
- ρ = CHARGE DENSITY (C/m³)
- t = TIME (sec)
- ∇ = DEL OPERATOR

USING MEASURED CONSTITUENT POLARIZATION CURVES

(b)



BOUNDARY CONDITIONS OF MODELED ELECTROCHEMICAL SPACE

(c)

FIG. 9—(a) Schematic of the finite-element model with boundary conditions; (b) the fundamental electrical laws governing the galvanic couple behavior; (c) the boundary conditions of the electrochemical space.

TABLE 2—Numerical modeling results.

R, m	$J_R, A/m^2$	$J_Z, A/m^2$	$J \text{ Total}, A/m^2$
$Z = 650 \mu\text{M AND } \sigma = \text{mS/CM}$			
0.7	+2.414	10.57	10.842
1.786	3.7582	7.4759	8.367
2.778	3.6514	4.8028	6.033
4.375	3.3654	2.5709	4.235
5.897	2.6823	0.93195	2.839
7.713	1.5649	0.0633	1.566
9.73	0.98767	0.1707	1.002
11.29	0.689	0.1820	0.7126
13.875	0.44	0.1975	0.4822
17.125	0.2558	0.2232	0.33948
20.375	0.1185	0.2239	0.2533
23.65	0.03638	0.15278	0.15705
$Z = 1125 \mu\text{M AND } \sigma = 42 \text{ mS/CM}$			
0.7	1.497	7.596	7.742
1.786	2.967	5.989	6.684
2.778	2.9182	4.1926	4.726
4.375	2.894	2.293	3.692
5.897	2.3986	0.9784	2.591
7.713	1.486	0.10215	1.4895
9.73	0.96688	0.10625	1.002
11.29	0.6828	1.71371	0.7039
13.875	0.436	0.19835	0.479
17.125	0.25559	0.20559	0.328
20.375	0.1195	0.202514	0.235
23.65	0.1641	0.13939	0.215

TABLE 3—Numerical modeling results.

R, mm	$J_R, A/m^2$	$J_Z, A/m^2$	$J \text{ Total}, A/m^2$
$Z = 650 \mu\text{M AND } \sigma = 62.5 \text{ mS/CM}$			
0.7	5.039	15.99	16.765
1.786	6.833	8.2107	10.682
2.778	4.8525	2.46	5.44
4.375	2.593	0.6134	2.664
5.897	1.33	0.0568	1.33
7.713	0.8353	0.07133	0.83836
9.73	0.55485	0.010757	0.56518
11.29	0.3961	0.10948	0.406
13.875	0.2557	0.11634	0.2809
17.125	0.1507	0.1316	0.19959
20.375	0.070059	0.1308	0.14835
23.65	0.020349	0.0885	0.0908
$Z = 1125 \mu\text{M AND } \sigma = 62.5 \text{ mS/CM}$			
0.7	3.0225	10.1026	10.545
1.786	5.1936	6.406	6.246
2.778	3.8138	2.722	4.685
4.375	2.3307	0.813686	2.468
5.897	1.323	0.1998	1.338
7.713	0.8142	0.1831	0.8345
9.73	0.5468	0.081539	0.5528
11.29	0.3931	0.1088	0.4078
13.875	0.2544	0.12016	0.2813
17.125	0.15058	0.1226	0.194
20.375	0.07069	0.12016	0.139
23.65	0.009918	0.08258	0.083

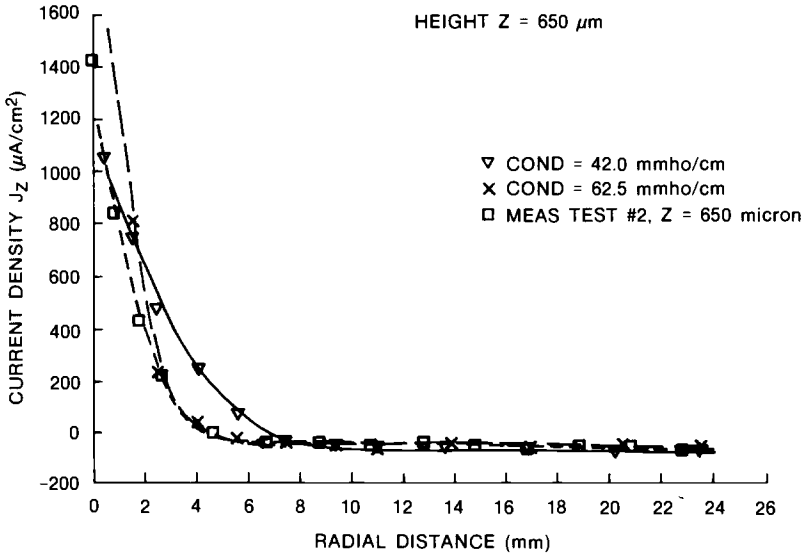


FIG. 10—Calculated and measured J_z components of the ionic current density at 650 μm elevation.

no comparable 1-D measurements. Again, the agreement between the measurements and the calculations is excellent.

Figures 14 and 15 show the measured and calculated total current density versus radial distance at $z = 650 \mu\text{m}$, respectively. The ionic currents flowing from the iron are readily discernible. The finite-element values and the measured values from the 3-D probe are plotted in Figs. 11 through 15. The iron-copper interface is located at a radial distance of 3.175 mm from the center. The measured values from the second scan at 1150 μm above the electrode surface as

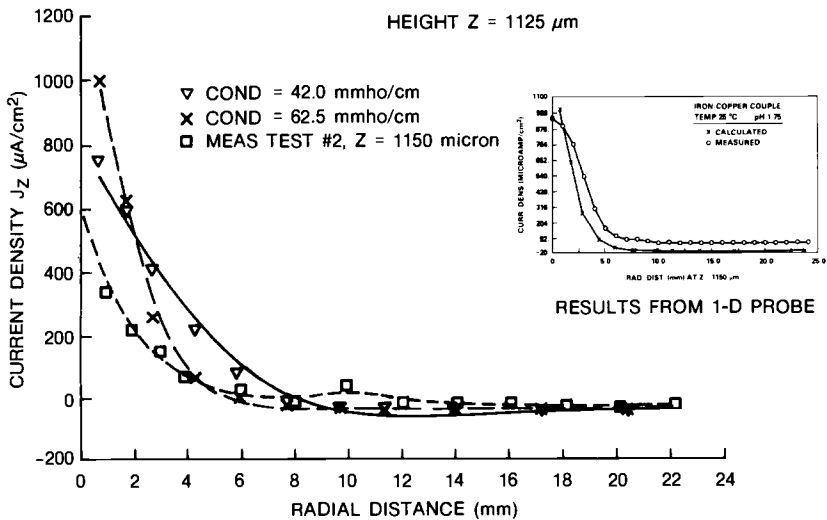


FIG. 11—Calculated and measured J_z components of the ionic current density at 1125- μm elevation (measurement at 1150 μm).

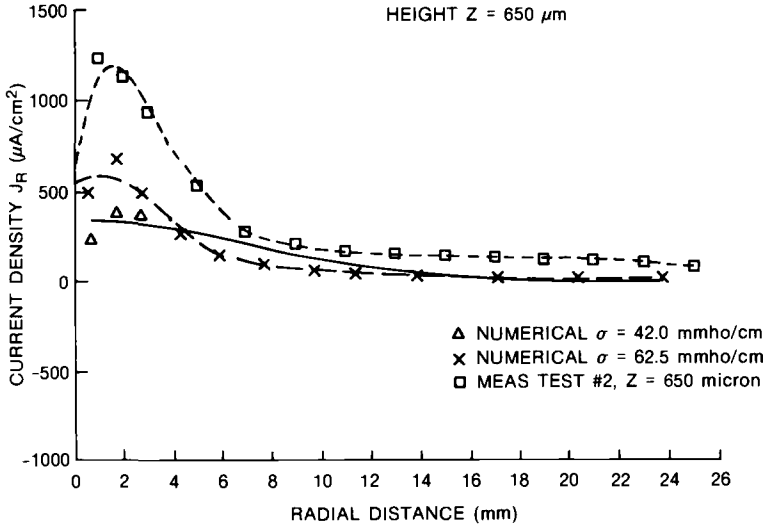


FIG. 12—Calculated and measured J_R components of the ionic current density at 650- μm elevation.

well as the finite-element results at 1125 μm above the electrode surface show excellent correlation. At both elevations, it appears that the current density emanating from the anode surface is quite high with a fairly evenly distributed current density response on the copper surface. The total calculated current leaving the anodic surface was $+2.857612 \times 10^{-5}$ A, and the total current arriving over the copper surface was -2.857670×10^{-5} A. This highly accurate match in magnitude between the anodic and cathodic currents illustrates the accuracy of the current accounting system in the model.

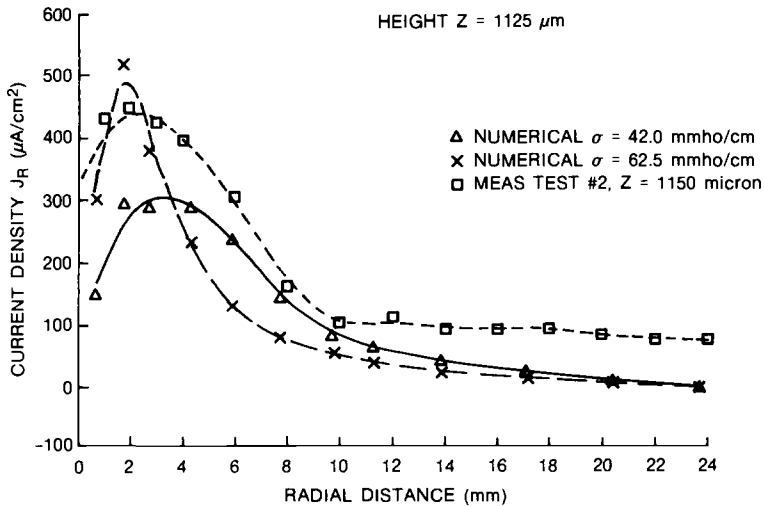


FIG. 13—Calculated and measured J_R components of the ionic current density at 1125- μm elevation (measurements at 1150 μm).

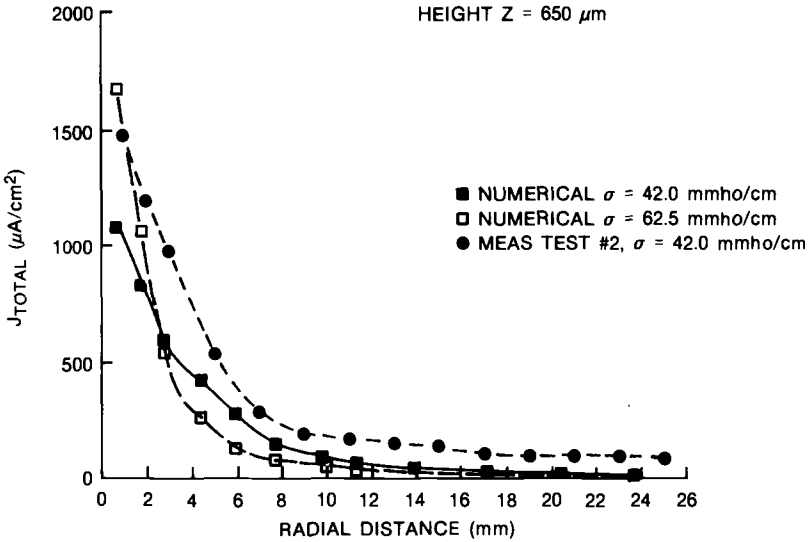


FIG. 14—Calculated and measured total ionic current density at 650- μm elevation.

Discussion

In a previous paper, an extensive discussion of the numerical procedures was developed for the three-dimensional finite-element model illustrated in Fig. 9. Further discussions and amplification on the theoretical aspects will not be necessary for purposes of this work because of the detailed development in Ref 4. With the emphasis in this communication on the spatial comparison of current density vectors in cylindrical coordinates very near the electrode surfaces, it is important that several aspects of the mathematical procedures be discussed at some length because of the significant sensitivity of the current density vector field response to nonlinear

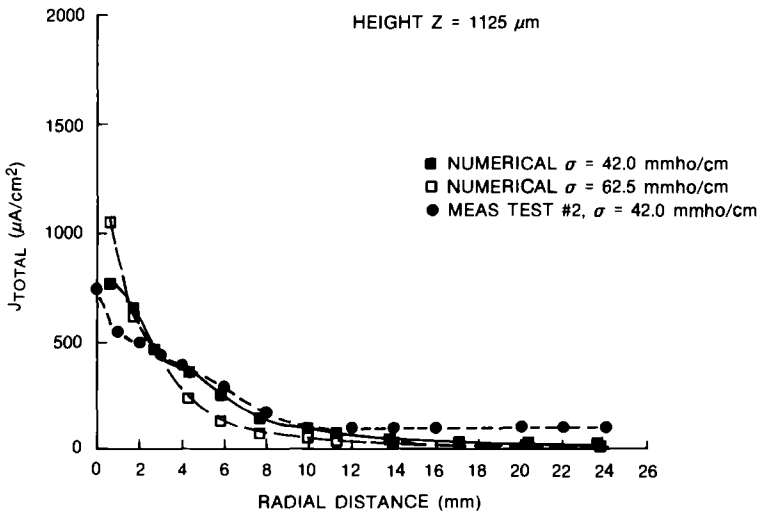


FIG. 15—Calculated and measured total ionic current density at 1125- μm elevation (measurements at 1150 μm).

polarization effects, choices of interpolation functions, manner of discretization, geometry, and so forth. The introduction of the double nonlinear convective film membrane to represent the nonlinear polarization of iron and copper is fully discussed elsewhere [4,11]. However, some discussion on the finite-element modeling subtleties is essential. The finite-element model developed for this investigation was constructed from three dimensional elements using the COSMIC/NASTRAN³ program. Because three-dimensional finite elements are more difficult to implement, careful numerical tracking for accuracy and consistency is required to develop numerical confidence. The results reported herein provide a first step in exercising the model for 3-D. Before presenting the results, it is worthwhile to discuss several aspects of the model and the resulting computations.

First, the electrolyte was represented with CHEXA2 and CWEDGE elements. The CHEXA2 element is a three-dimensional solid with eight vertices and six quadrilateral faces that is represented by two overlapping tetrahedra. The CWEDGE element is a three-dimensional solid with three quadrilateral faces and two opposing triangular faces. Complete descriptions of the CHEXAZ and CWEDGE elements can be found in Ref 12. These elements use linear interpolation functions for the potential between adjacent grid points. The general geometric configurations of the electrolyte and the anodic/cathodic surfaces have been illustrated in Fig. 9.

The model was bounded by the following cylindrical coordinates: $0.0 < R < 0.044$ m, $0^\circ < \theta < 36^\circ$, $0.0 < Z < 0.0095$ m. The selection of the 36° wedge angle was governed mainly by the choice of the CWEDGE and CHEXA2 elements and the anodic area such that the total number of 3-D elements would be reasonable for computational purposes (Fig. 9a). The aspect ratios for the elements appeared reasonable, although somewhat greater discretization in the radial direction, especially in the anodic area, would have been more desirable. On all the surfaces of the model, the normal derivative of the potential function was assumed to be zero (insulated). This includes the surfaces $\theta = 0^\circ$ and $\theta = 36^\circ$ where the normal derivative is the θ direction.

The idea of dealing with a geometric singularity, such as a pit or a crevice, appeared to rule out the possibility of using any axisymmetric finite elements. Even though similar techniques, when applied to axisymmetric problems, appeared to provide reasonable results, axisymmetric finite elements are not adequate in addressing the geometric changes of pits or crevices evolving with time. Therefore, it was necessary to introduce three-dimensional elements that would ultimately be required to address general pitting and crevice corrosion.

Furthermore, if three-dimensional elements, such as CWEDGE and CHEXA2, were used in a model development, the question of whether these elements are mathematically accurate enough to capture the various potential gradient changes, especially near the iron electrode, required attention. The CWEDGE and CHEXA2 elements use linear interpolation functions such that the potential is expressed as a linear algebraic equation in R , θ , and z . They have an additional advantage in that these three-dimensional elements do not suffer from singularity problems because of the local formulation of the interpolation function. As constructed, the model provides the continuous variation of ϕ as a function of z at $R = 0$.

Finally, it was desirable to attempt to control the current flow through the polarization layers by introducing surface-dependent nonlinear current-potential relationships (polarization curves), as shown in Fig. 9c. It is also anticipated that these polarization curves may vary with time. The current flow problem across the electrode-electrolytic interface appears to be conveniently modeled using convection elements instead of conduction elements [9,13]. Like the convection boundary problem in thermal science the determining factors for electrode performance are surface area, film resistance location, and local potential difference. The boundary conditions on the electrode surfaces are constructed by assigning the anodic and cathodic

³NASTRAN is an acronym for the National Aeronautics and Space Administration Structural Analysis Computer Program. COSMIC/NASTRAN indicates that it is a Government Proprietary NASTRAN code.

potential in the interfaces to by assigning the uncoupled open-circuit corrosion potentials of the constituents. As depicted in Fig. 9c, two nonlinear film elements (CHBDY) are connected to the electrolyte. The bottom film elements are bounded by the measured open-circuit potentials for the anodic and cathodic surfaces physically described in Fig. 8 [4,11].

The additional requirement imposed in the model is that the divergence of the current density vector \mathbf{J} must be equal to zero. In this investigation, special adjustments were made to the COSMIC/NASTRAN finite-element program to fulfill this condition. The COSMIC/NASTRAN program and related postprocessing program are resident on a VAX-11/780 computer at the Naval Underwater Systems Center.

A number of planes were identified in order to retrieve more easily current densities and voltage information from the elements and grid points, respectively. Since the measurements for the current density were performed at 650 and 1150 μm above the electrode surfaces, it was desirable to obtain calculated current density information at the centroids of the associated elements. The lowest plane was assumed to exist at $z = 0$. The centroid for the elements coincides with the elevation of the measured values ($z = 650 \mu\text{m}$). Similarly, the other elements from the finite-element model have a centroidal vertical distance of $z = 1125 \mu\text{m}$, while the experimental elevation value was 1150 μm . The topmost plan (electrolyte/air interface) is located at $z = 9500 \mu\text{m}$.

It was determined in the course of the analysis that the current density of the 0 direction was indeed zero normal to the R - z planes for $\theta = 0^\circ$ and $\theta = 36^\circ$. Thus the boundary conditions were satisfied. Over the entire $\Delta\theta$ slice, the current density was identically zero, since the electrical potentials at $\theta = 0^\circ$ and at $\theta = 36^\circ$ were identical. However, within the finite-element model very small current densities (approximately less than 5% of the J_z and J_r) in the 0 direction were evident. This amount of error is expected for the relatively simple interpolation functions chosen. Increased numerical resolution can be achieved by finer discretization in areas of high gradient variation and the possible introduction of higher order interpolation functions for the finite elements.

Conclusions

The three-dimensional current density structure in the nearfield of an iron-copper galvanic structure was characterized by finely measured scanning vibrating electrode techniques at incremental positions in an electrolyte in space at $z = 650 \mu\text{m}$ and $z = 1125 \mu\text{m}$ above the electrode surface. A corresponding finite-element current density field was calculated for similar positions in space as those measured. Three-dimensional current density vectors $J(J_x, J_y, J_z)$ were calculated, measured, and subsequently plotted (Figs. 11 through 15) to create a point-by-point comparison of vector variables in electrolytic space. The comparison, component-versus-component was in excellent agreement for this relatively simple galvanic configuration.

Based on the completed experimental electric field scans and the corresponding finite-element field predictions, it appears that the finite-element technique presents a strong analytical tool for calculating the near-field electric field distributions around active electrode surfaces in homogeneous media. The finite-element model described in this paper made reference to an a priori measured set of uncoupled nonlinear polarization curves for pure iron and pure copper (Fig. 8). Using a local tangent slope definition of the potential difference at a given position of the electrode surface, the current densities were calculated everywhere within the electrolyte and on the boundaries.

The measurement technique described herein provides an exciting method to provide careful comparison with theory in the very near field of active galvanic cells. With further advances in understanding overall progress could lead to a method to predict the onset of crevice corrosion and pitting in field situations.

Acknowledgment

The authors would like to express their appreciation to Dr. E. McCafferty of the Naval Research Laboratory and Dr. J. Wikswo, Jr. from Vanderbilt University for their assistance during the course of this work. Funding for this work was provided by the Office of Naval Research, Dr. John Sedriks.

References

- [1] Freeman, J. S. and Nicholson, C., *Journal of Neurophysiology*, Vol. 38, No. 2, 1975, p. 369.
- [2] Jaffee, L. F. and Nuccitelli, R., *Journal of Cell Biology*, Vol. 63, 1974, p. 14.
- [3] Ishikawa, Y. and Isaacs, H. S., Brookhaven National Laboratory Report BNL 33095, 1983.
- [4] Crowe, R. C. and Kasper, R. G., *Journal of Electrochemistry*, Vol. 133, No. 5, 1986, p. 879.
- [5] Crowe, C. R., Naval Research Laboratory Memorandum Report 5416, 1984.
- [6] Crowe, C. R., Naval Research Laboratory Memorandum Report 5415, 1984.
- [7] Freeman, J. A., Mayes, B., Snipes, G. J., Wikswo, J. P., *Neuroscience Research*, Vol. 13, 1985, p. 251.
- [8] Freeman, J. A. and Wikswo, J. P., *Biophysics Journal*, Vol. 37, 1982, p. 79a.
- [9] Geddes, L. A., *Electrodes and the Measurement of Bioelectric Events*, Wiley-Interscience, New York, 1972, p. 147.
- [10] Johnson, J. B., *Physics Review*, Vol. 32, 1928, p. 97.
- [11] Kasper, R. G. and April, M. G., *Corrosion*, Vol. 39, 1983, p. 181.
- [12] Kasper, R. G. and Duffy, M. O., Naval Underwater Systems Center Technical Report 6921, New London, CT, 1983.
- [13] *NASTRAN User's Manual*, National Aeronautics and Space Administration Report NASA SP-222 (06), Washington, DC, 1983, pp. 1.3-31 to 1.3-48.

Prediction of Tube-Tubesheet Galvanic Corrosion Using Finite Element and Wagner Number Analyses

REFERENCE: Scully, J. R. and Hack, H. P., "Prediction of Tube-Tubesheet Galvanic Corrosion Using Finite Element and Wagner Number Analyses," *Galvanic Corrosion, ASTM STP 978*, H. P. Hack, Ed., American Society for Testing and Materials, Philadelphia, 1988, pp. 136-157.

ABSTRACT: Galvanic corrosion predictions for heat exchanger tube/tubesheet galvanic couples are presented and discussed. The predictions were performed using finite element analysis using two programs, WECAN and MARC, and by Wagner number analysis under conditions of secondary and tertiary current distribution. Long-term electrochemical potentiostatic polarization data generated over 120 days in natural seawater were used to account for time effects. Results of the predictions are presented in the form of potential and galvanic current density as a function of distance from the tubesheet along the tube axis.

Seawater exposures of some tube/tubesheet material combinations were performed to compare with the predictions. These exposures used segmented tubes connected in series through the use of zero resistance ammeters. Material combinations exposed included a Monel Alloy 400 tubesheet coupled to a 90-10 copper-nickel tube, a 90-10 copper-nickel tube coupled to a zinc anode at the position of the tubesheet, and a nickel-aluminum-bronze tubesheet coupled to an Alloy 625 tube. Tube/tubesheet data obtained from the literature were also compared to predictions.

This study is directed towards determining not only the degree of accuracy of the predictions from the finite element and Wagner number analysis techniques, but also the sensitivity of the analyses to small changes in the electrochemical data used to obtain the predictions. The feasibility of these two analysis techniques for accurate qualitative as well as quantitative galvanic corrosion prediction for the tube/tubesheet configuration is discussed.

KEY WORDS: galvanic corrosion, solution resistivity, potential distribution, finite element analysis, Wagner number analysis, primary current, secondary current, tertiary current, current distribution, heat exchangers, tubing

Prediction of the rate of galvanic corrosion by the use of galvanic corrosion rate tables or by techniques based on electrochemical polarization and mixed potential theory are useful but do not take into account current distribution effects. Thus, these methods are only directly applicable when the system of interest has a high conductivity electrolyte and a simple geometry with exactly known electrochemically active surface areas. These conditions are necessary to insure that the current is uniformly distributed over both the anode and cathode. For most actual components in service these conditions are not satisfied, resulting in the nonuniform distribution of galvanic current, which makes the use of simple prediction methods such as those above impossible.

A common geometric configuration that exists where dissimilar metals are used and where galvanic current distribution is not expected to be uniform is the tube and tubesheet configuration in a condenser or heat exchanger. Higher galvanic current densities are expected on the tube surface close to the tubesheet, with the current falling to insignificant levels at some dis-

¹Materials engineers, David Taylor Naval Ship Research and Development Center, Code 2813, Annapolis, Md 21402.

tance away from the tubesheet. Prediction of the distance of galvanic interaction is most important since it changes the effective anode to cathode ratio, which has a significant bearing on the overall corrosion rate of the anode material.

Two techniques are available to predict the extent and distribution of galvanic current in the tube-tubesheet configuration in seawater: finite element analysis and Wagner number analysis. The advantages and limitations of these techniques will be explored in this paper by a combination of prediction, experimental verification, and literature review. Polarization characteristics of the tube and tubesheet materials used in the analyses described below were obtained from long-term potentiostatic polarization curves [1,2] in seawater to predict corrosion over an extended period of time with the greatest accuracy.

The results of finite element analysis using two different programs, WECAN (Westinghouse Electric Computer Analysis) and MARC, are compared with current distributions reported in the literature and with an experimental verification that was performed using segmented tubes electrically coupled to tubesheets. Several tube/tubesheet material combinations were studied under quiescent and flowing (2.4 m/s) conditions: 90-10 copper-nickel tubing coupled to a Monel Alloy 400 tubesheet, Alloy 625 tubing coupled to a nickel-aluminum-bronze tubesheet, and 90-10 copper-nickel tubing coupled to anode zinc at the tubesheet position. In addition, several material combinations were studied under quiescent conditions only: a titanium (Ti-50) tube coupled to a nickel-aluminum-bronze tubesheet, and a 90-10 copper-nickel tube coupled to a simulated Muntz metal tubesheet represented by a fixed potential of -250 mV (versus Ag/AgCl). All material combinations investigated by finite element analysis are summarized in Table 1. Wagner number analysis was also performed on the above material combinations and compared with data from the experimental verifications or the literature.

Previous Work

The data from previous investigations used in the analyses are discussed briefly below. The findings of these studies are interpreted in terms of galvanic interaction distance in Table 2. This distance was estimated as the number of tube diameters where current density had decreased to within roughly $0.1 \mu\text{A}/\text{cm}^2$ of the uniform value far from the tubesheet or where the potential was within 20 mV of the value far from the tubesheet.

Gehring et al. [3-5] studied "simulated" Muntz alloy tubesheets by potentiostatic polarization of tubes to -250 mV versus standard calomel electrode (SCE) at the tube inlet, actual Muntz alloy tubesheets as well as aluminum-bronze tubesheets coupled to more noble tube materials in flowing seawater at 7 ft/s (2.1 m/s). Noble tube materials included AL-6X austenitic stainless steel, AL-29-4 ferritic stainless steel, titanium 50A, 90-10 copper-nickel, and

TABLE 1—Tube/tubesheet finite element predictions.

Tube Material	Tubesheet Material	Polarization Data		Tube Diameter, cm
		Velocity	Time, Days	
Alloy 625	Ni-Al-bronze	2.4 m/s	120	2.66
90-10 Cu-Ni	Monel alloy 400	2.4 m/s	120	1.34
Alloy 625	Ni-Al-bronze	2.4 m/s	1	2.66
90-10 Cu-Ni	Monel alloy 400	2.4 m/s	1	1.34
Alloy 625	Ni-Al-bronze	quiescent	120	2.66
90-10 Cu-Ni	Monel alloy 400	quiescent	120	1.34
90-10 Cu-Ni	Anode zinc	quiescent	30	1.34
Ti-50	Ni-Al-bronze	quiescent	1	1.34
90-10 Cu-Ni	-250 mV	2.4 m/s	1	2.66

TABLE 2—Summary of tube/tubesheet galvanic corrosion literature.

Investigators	Material Combination		Galvanic Interaction Distance, diameters	Velocity, m/s	Time
	Anode Tubesheet	Cathode Tube			
Gehring, Kuester, and Maurer	-250 mV SCE	AL-6X	120-480	2.1	...
		AL-29-4	120-480
	Muntz	Ti-50A	120-480
		90-10 Cu-Ni	12-24
		Al-brass	12-24
Gehring	Muntz	Ti-50A	120-240	2.1	...
Gehring and Kyle	Muntz	AL-6X	120-240	2.1	...
Astley	Al-bronze	Ti-50A
	Ni-Al-bronze	Titanium	60	1	...
	-600 mV SCE	70-30 Cu-Ni	50	0	1 day
			18	1.5	2 h
			35	1.5	13 h

aluminum-brass. For both simulated and actual tube/tubesheet studies, cathodic polarization of more noble tube materials along the length of the tube to a distance of 120 to 480 tube diameters was observed for the AL-6X, AL-29-4, and Ti-50A tubes. For couples involving both 90-10 copper-nickel and aluminum-brass coupled to a Muntz metal tubesheet, cathodic polarization down the length of the tube was only observed for a distance of 12 to 24 tube diameters.

Astley studied a titanium tube coupled to a nickel-aluminum-bronze plate in seawater flowing at 1 m/s [6]. The length of titanium tube that was cathodically polarized was 60 tube diameters. In a separate study, a 70-30 copper-nickel tube was potentiostatically polarized to -600 mV at the tube inlet, simulating cathodic protection. Under quiescent conditions the length of tube receiving cathodic polarization after 1 h was 50 tube diameters. At a 1.5-m/s flow rate, 2 h, the length of tube receiving cathodic polarization was 18 tube diameters but increased to 35 diameters after 13 days.

In summary, the galvanic interaction distance from all studies was found to vary from several tube diameters to several hundred depending upon the materials polarization behavior, the geometry, and the electrolyte.

Experimental Procedure

The details of the experimental verification used to generate some of the data used in the later analyses are discussed below.

Tube/Tubesheet Exposure Apparatus and Procedure

Two tube/tubesheet combinations were tested, both at quiescent and under flowing (2.4 m/s) conditions. The tubesheet was simulated by a ring of material mounted around, but insulated from, the tube end. This ring was coated on all surfaces except that surface that would face the waterbox in a real condenser. The tube was cut into insulated segments, which were shorter closer to the tubesheet. The inside of the tube segments were ground using 600 grit sandpaper. The tube segments were electrically connected to each other and to the tubesheet ring by means of zero-resistance ammeters. Holes were drilled through the tube wall periodically to facilitate installation of micro-reference electrodes for potential measurements. Natural seawater, filtered and maintained at 25°C, was placed in contact with the inside of the tube and the uncoated face of the tubesheet. Current and potential profiles were recorded regularly over a 120-day period. At the conclusion of the quiescent exposure of the copper-nickel tube, this tube

was connected to a sacrificial zinc anode and the new current and potential profiles monitored over an additional 30 days under quiescent conditions. The experimental setup is illustrated in Figs. 1 and 2. The two material combinations used were Alloy 625 tube with Ni-Al-bronze tubesheet and 90-10 Cu-Ni tube with Monel Alloy 400 tubesheet. Dimensions of the tubes and tubesheet rings are listed in Table 3, and the dimensions of the tube segments are listed in Table 4.

Polarization Data Generation Procedures

Polarization data indicative of the long-term behavior of condenser materials in natural seawater were generated as described elsewhere [1,2] by holding individual samples at a constant potential for 120 days. Applied currents were monitored for the duration of the exposure. Surface finish on the samples was the same as that on the inside of the tubes, ground with 600 grit sandpaper. In the case of the 2.4-m/s flowing seawater polarization data, a Reynolds number of 30 500 was obtained, identical to that in a 1.34-cm diameter tube with 2.4-m/s flow, and indicative of turbulent conditions similar to those in a 2.66-cm-diameter tube with the same flow.

Finite Element Analyses

Use of finite element and boundary element techniques has shown great promise for predicting potential and current distributions for galvanic corrosion, crevice corrosion, and cathodic protection [7-14]. These techniques are computationally intense, and require powerful computing capabilities for all but the most simple geometries. They require as input the geometry of the configuration of interest and the conductivity of the electrolyte through which current flows. Boundary conditions on free or insulated surfaces are that current cannot flow through the surface, creating a "reflection" effect. At metal surfaces, the polarization characteristics of the metal involved at the appropriate flow and exposure duration are used as the boundary conditions. Output from these analyses are potential and current density as a function of position along the structure.

For this study, finite element analyses were conducted by John Fu, formerly of Westinghouse Research, using a program called WECAN on both material combinations in the experimental verification, but for quiescent conditions only. An element mesh shown in Fig. 3 was designed using axi-symmetrical (cylindrical) elements to reduce the three-dimensional situation to a two-

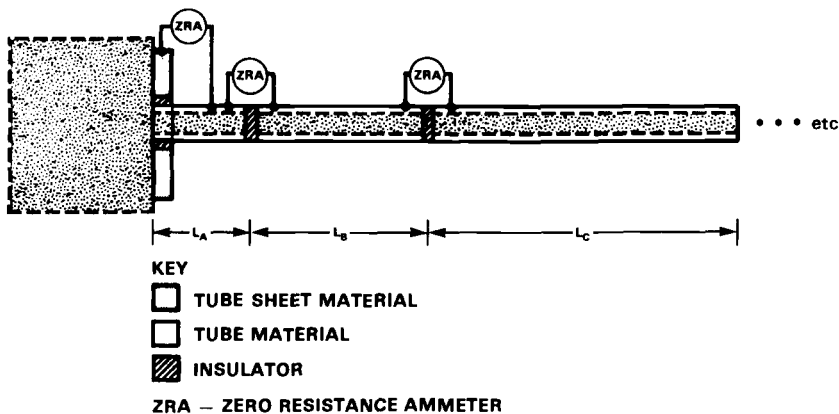


FIG. 1—Schematic of segmented Tube galvanic corrosion experiment.

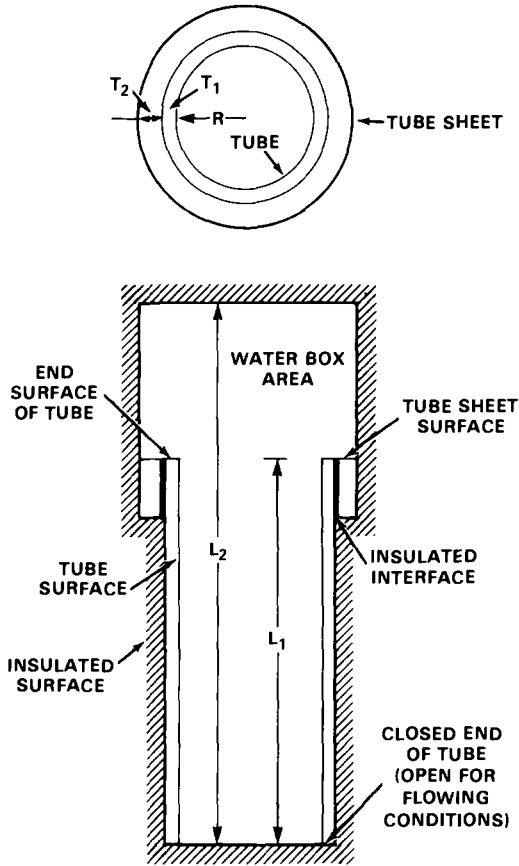


FIG. 2—Experimental tube/tubesheet arrangement.

dimensional analysis. WECAN models electrochemical polarization data by a series of straight lines connecting points on a polarization resistance curve derived from the polarization curve for the material involved at the appropriate flow rate. The polarization resistance is the overpotential divided by the current density at that overpotential and thus looks like a secant line on the polarization curve connecting the current at the freely corroding potential to the current at the potential of interest.

TABLE 3—Dimensions of tube/tubesheet simulated condensers.

Condenser	Tube: Alloy 625 Tubesheet: Ni-Al-Bronze		Tube: 90-10 Cu-Ni Tubesheet: Monel 400	
	R	1.328 cm	(0.52 in.)	0.6693 cm
T ₁	0.0889 cm	(0.035 in.)	0.1245 cm	(0.049 in.)
T ₂	0.5715 cm	(0.225 in.) ^a	0.2374 cm	(0.0937 in.) ^b
L ₁	304.8 cm	(10 ft)	304.8 cm	(10 ft)
L ₂	335.28 cm	(11 ft)	335.28 cm	(11 ft)

^aCalculated based on a tube center to center distance of 3.9624 cm (1.56 in.) on a triangular pitch.

^bCalculated based on a tube center to center distance of 2.062 cm (0.812 in.) on a triangular pitch.

TABLE 4—Segmented tube sections for tube/tubesheet galvanic corrosion analysis.

Tube: Alloy 625 Tubesheet: Ni-Al-Bronze		Tube: 90-10 Cu-Ni Tubesheet: Monel 400	
Distance from Tubesheet, cm	Length, cm	Distance from Tubesheet, cm	Length, cm
0	1.0	0	3.0
1.0	2.0	3.0	3.0
3.0	3.0	6.0	3.0
6.0	5.0	9.0	3.0
11.0	5.0	12.0	4.0
16.0	25.0	16.0	4.8
41.0	50.0	20.8	5.0
91.0	63.8	25.8	5.0
154.8	75.0	30.8	5.0
229.8	75.0	35.8	8.0
...	...	43.8	8.0
...	...	51.8	8.0
...	...	59.8	9.0
...	...	68.8	10.0
...	...	78.8	10.0
...	...	88.8	10.0
...	...	98.8	10.0
...	...	108.8	26.0
...	...	134.8	30.0
...	...	164.8	30.0
...	...	194.8	40.0
...	...	234.8	70.0

Finite element analyses were also conducted for this study by Raymond Munn at the Naval Underwater Systems Command using a program called MARC. A variety of material combinations from the experimental verification and from the literature were modelled under both quiescent and flowing conditions. These analyses used a slightly different axi-symmetric mesh, but with roughly the same number of elements as the WECAN analyses. For the MARC analysis, polarization behavior is input by fitting an analytical expression to the actual polarization data. The program then uses the potential at the nearest integration point to substitute into this expression to calculate the current density at any given point on the surface. This current density is then used as the boundary condition for the next iteration in the solution of the problem.

The finite element analyses are compared to the experimental verification and literature data for each material combination below. The data for all materials are summarized in Table 5.

Alloy 625/Ni-Al-Bronze

The WECAN analysis for the 120-day quiescent case is compared to 120-day measured data in Fig. 4. There is considerable scatter in the current densities measured, probably because of crevice corrosion of the Alloy 625 observed at the conclusion of the test. Considering the scatter, agreement is good between predicted and measured current densities. There is some difference between the actual potentials observed and those predicted. This is because the polarization data utilized in the analysis does not have the same open circuit potential for the Alloy 625 as the tube material, thus shifting the whole predicted curve below the measured data. Figure 5 illustrates the open circuit potential versus time behavior for Alloy 625 in quiescent seawater. Note the fluctuations possible even for one sample in quiescent seawater. These fluctuations were considered to be due to the localized corrosion. The difference between predicted and measured

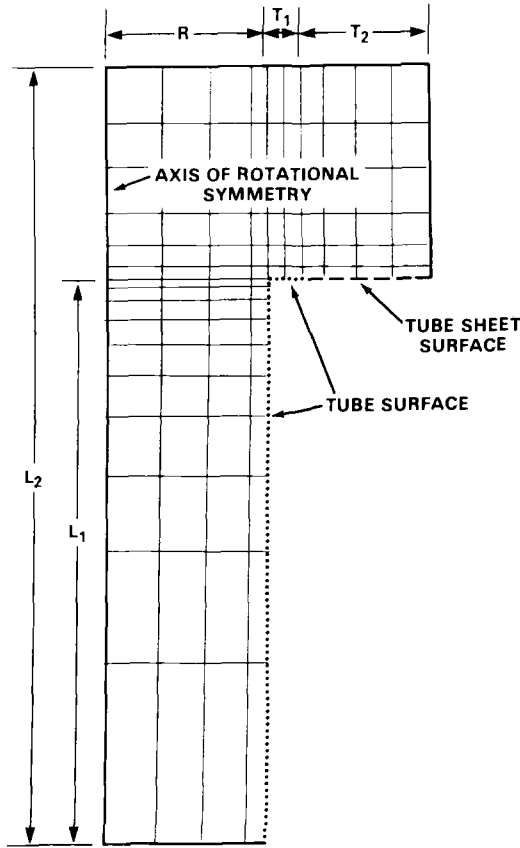


FIG. 3—Axisymmetric finite element mesh of tube/tubesheet arrangement.

TABLE 5—Distances of galvanic interaction.

Tube	Tubesheet	Technique	Interaction Quiescent	Distance, Diameter 2.4 m/s	Time, Days
Alloy 625	Ni-Al-bronze	measured	60	15	120
		25	1
		WECAN	60	...	120
		MARC	60	15	120
90-10 Cu-Ni	Monel 400	measured	100	100	120
		WECAN	8	...	120
		MARC	100	20	120
		20	1
		measured	50	...	30
90-10 Cu-Ni	zinc	measured (Astley)	40	...	1 h
		MARC	50	...	30
		measured (Astley)	60
Ti-50	Ni-Al-bronze	MARC	100	...	30
90-10 Cu-Ni	-250 mV	measured (Gehring)	...	15 (2.1 m/s)	...
		MARC	...	15	1

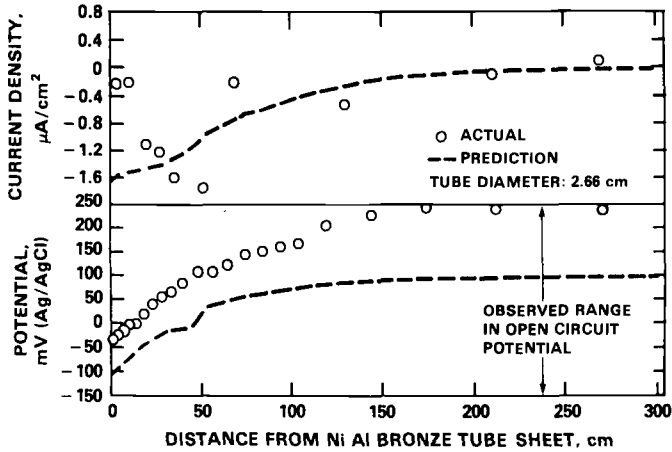


FIG. 4—Alloy 625 tube coupled to Ni-Al-bronze after 120 days, WECAN analysis.

potentials indicates the importance of using the correct open circuit potentials in the finite element analysis. Even with the discrepancy in potentials, the important parameter, interaction distance, is similar between the predicted and measured data. This distance is about 150 cm, which is about 60 tube diameters. Therefore it can be concluded that a large area of cathode is present in this case. A large corrosion rate was predicted for the Ni-Al-bronze, and this finding was actually observed once the cell was disassembled.

The MARC analysis for the 120-day quiescent case is shown in Fig. 6. Since the same polarization data were used in this analysis, the same results were found as in the WECAN analysis, good prediction of interaction distance, and less accurate prediction of potentials.

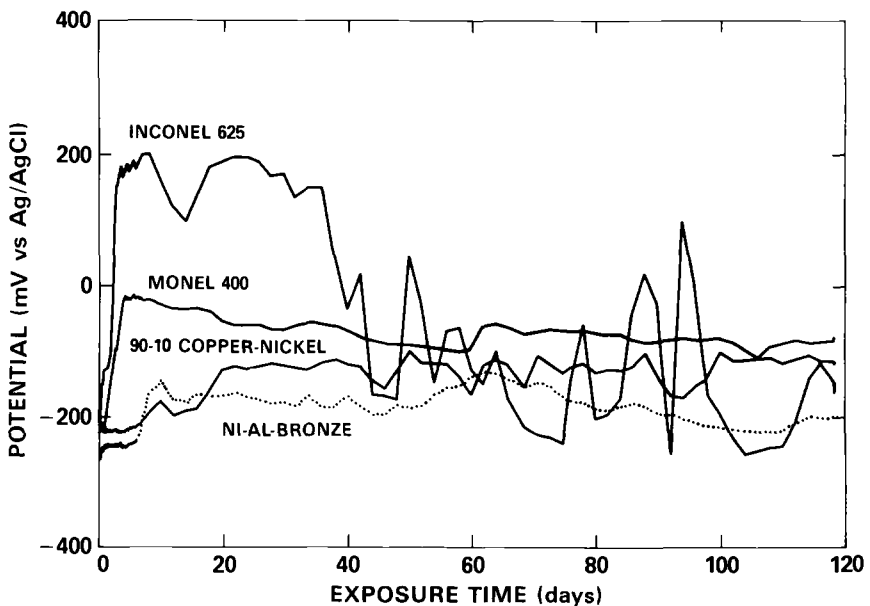


FIG. 5—Time dependence of corrosion potentials in quiescent seawater.

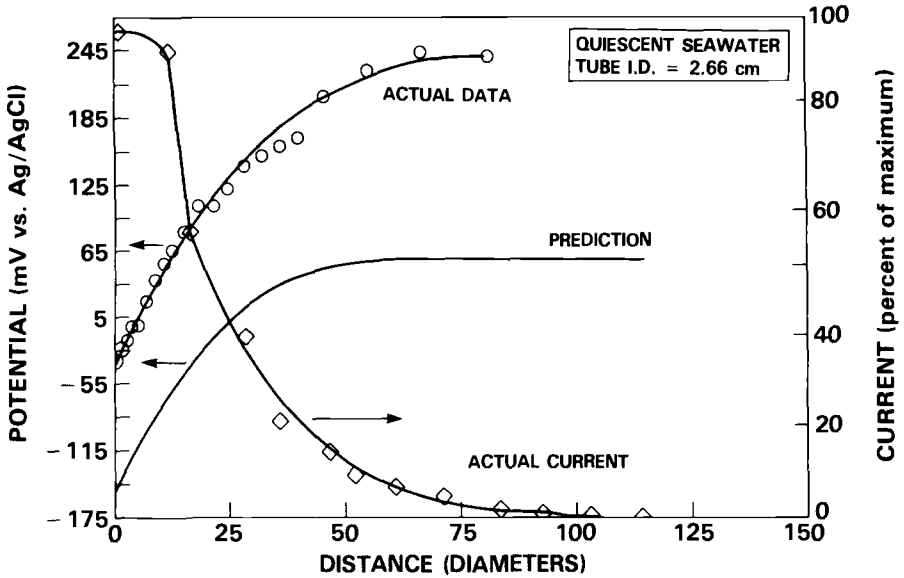


FIG. 6—Alloy 625 tube coupled to Ni-Al-bronze after 120 days. MARC analysis.

Only MARC was used to analyze this material combination under flowing (2.4 m/s) conditions. Analyses were run using polarization data after 1 day as well as 120 days. The 120-day data is shown in Fig. 7 and the 1 day data in Fig. 8. Current density predictions were not supplied with the MARC analyses, so no conclusions can be drawn about the prediction accuracy with regards to current distribution. As with the quiescent data, the freely corroding potential of Alloy 625 used in the analysis at either 120- or 1-day exposure appears not to match

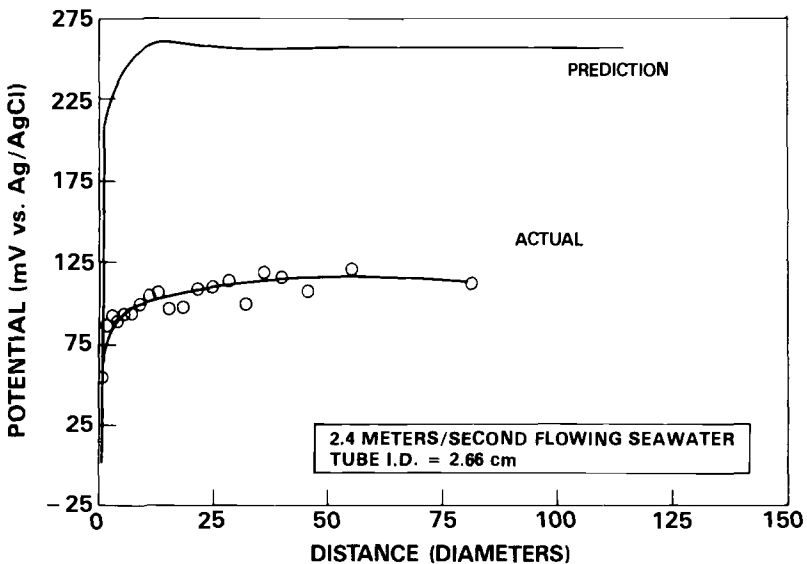


FIG. 7—Alloy 625 tube coupled to Ni-Al-bronze tubesheet after 120 days. Flowing seawater, MARC analysis.

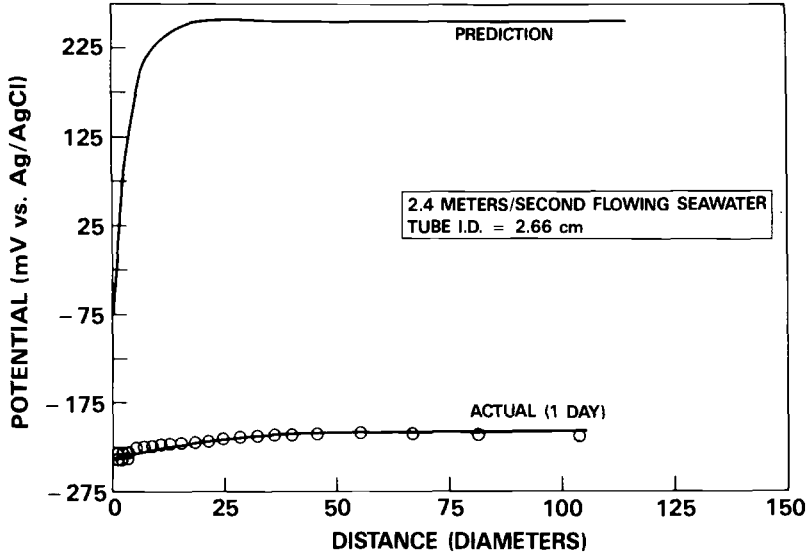


FIG. 8—Alloy 625 tube coupled to Ni-Al-bronze tubesheet after 1 day. Flowing seawater, MARC analysis.

that actually observed. Figure 7 shows that the interaction distance has decreased to about 15 diameters because of the flow, and that this distance has adequately been predicted by MARC. Figure 9 shows the observed tube/tubesheet potential profiles as they develop over time. The tube polarization is initially low (day one) when the potential difference between the Ni-Al-bronze and Alloy 625 is small (Fig. 10), and accordingly the galvanic current is low. When the

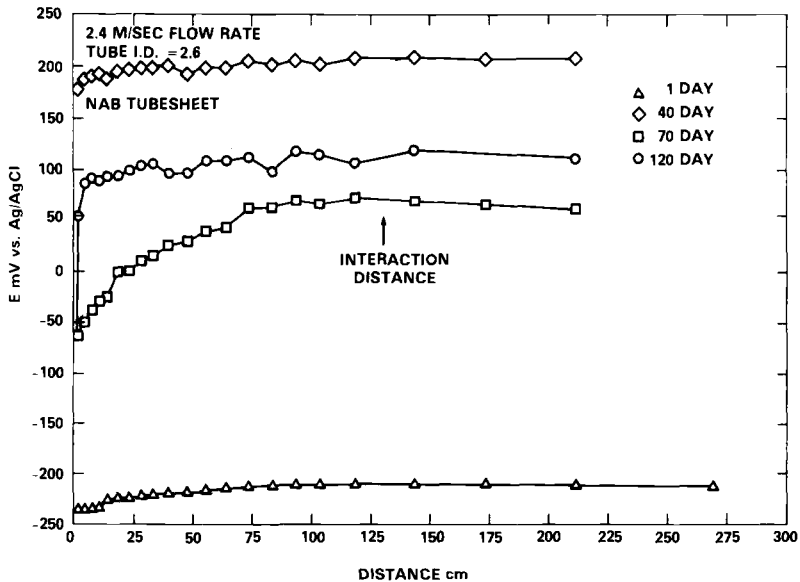


FIG. 9—time effects for Alloy 625 tube coupled to Ni-Al-bronze tubesheet. Flowing seawater, 1 to 120 days.

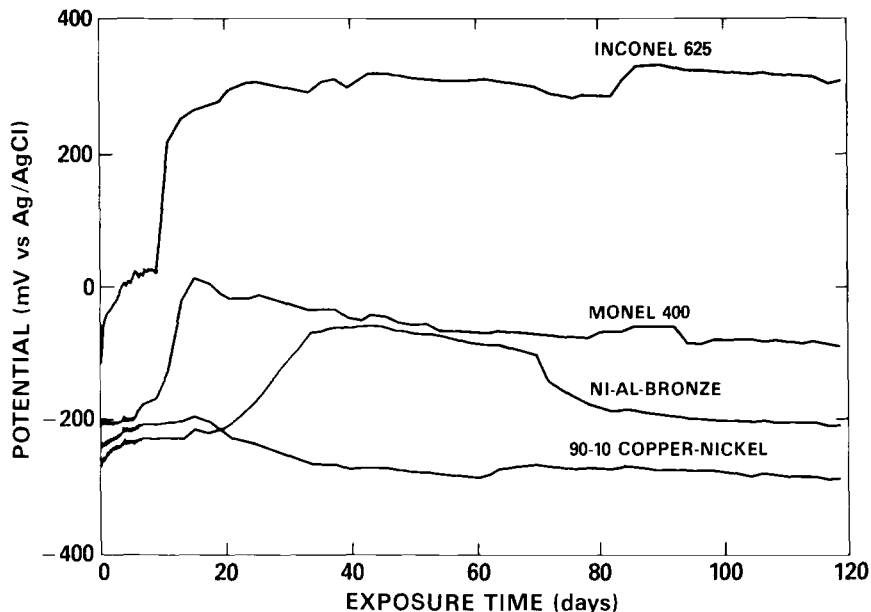


FIG. 10—Time dependence of corrosion potentials in flowing seawater.

open circuit potential of Alloy 625 increases, the interaction distance increases until it reaches a maximum after 70 days. This points out the necessity for careful consideration of time effects. Small interaction distances under flowing conditions can still lead to greater galvanic corrosion than under quiescent conditions since the cathodic limiting current density on Alloy 625 is greater under flowing conditions than in the quiescent case.

90-10 Cu-Ni/Monel Alloy 400

The WECAN analysis of this material combination under quiescent conditions at 120 days is presented in Fig. 11. The analysis of this material combination is complicated by the similarity in freely corroding potentials of the two materials. Inlet end current density are adequately predicted, but the predicted interaction distance based on current density is about 8 diameters, versus a measured interaction distance of 100 diameters. This discrepancy should be considered in light of the fact that all of the current is at least a factor of 3 below the average general corrosion current for freely corroding 90-10 Cu-Ni, and all current values in the figure are insignificant. The difference between predicted and observed potentials appears large, as with the earlier material combination. All potentials lie within the observed range of freely corroding potentials for the copper-nickel, and thus the differences are insignificant. In summary, when an insignificant galvanic corrosion problem is expected, WECAN was successful in predicting this fact but was not in predicting the details of the galvanic interaction.

The MARC analysis for quiescent 120-day conditions in Fig. 12 predicts potentials similar to the WECAN analysis, but an interaction distance more in agreement with that actually measured. The reason for the difference between the two analyses is not known, but MARC was successful in predicting the interaction distance.

Figures 13 and 14 present the MARC analyses and measured potentials under flowing conditions. Potentials were different between predictions and measurements in both cases. In addition, predicted interaction distances were around 20 diameters after both 120 and 1 days, whereas the observed distance after 1 day was negligible and at 120 days was close to 100 diame-

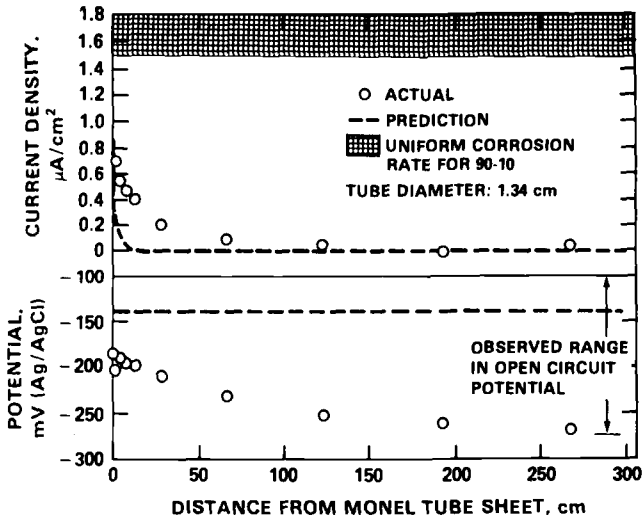


FIG. 11—90-10 Cu-Ni tube coupled to Monel 400 after 120 days, WECAN analysis. Quiescent seawater.

ters. As in the quiescent case, despite these differences, an insignificant amount of galvanic corrosion between these alloys was predicted as might be expected from the small open circuit potential differences and the area ratio favorable to the anode material.

In Fig. 15 the measured tube material potential profiles can be seen as they develop over time. The potentials start out low at one day then increase so that with the exception of the 60-day data all potentials are above the initial value. The reason for this can be seen in Fig. 10. The freely corroding potentials for both alloys increase over the first few days of the test. The small potential difference at the beginning few days of the test leads to an insignificant galvanic

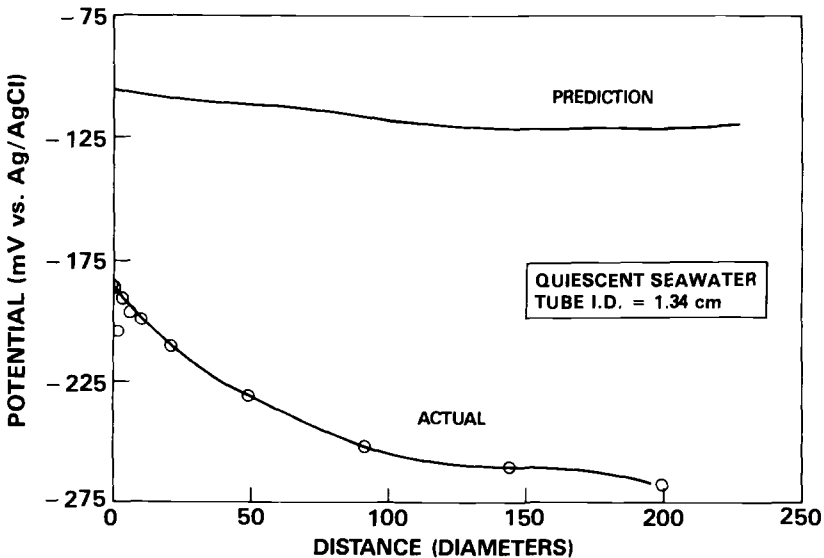


FIG. 12—90-10 Cu-Ni tube coupled to Monel 400 after 120 days, MARC analysis. Quiescent seawater.

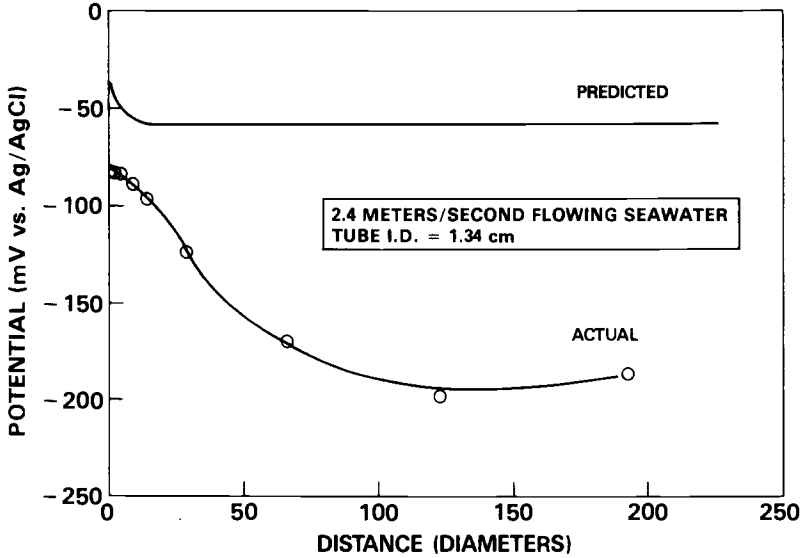


FIG. 13—90-10 Cu-Ni tube coupled to monel 400 tubesheet after 120 days. Flowing seawater, MARC analysis.

couple as observed and predicted for the 1-day case. This was reflected in the measured tube potentials after one day, where no interaction distance could be observed. Like the quiescent prediction, MARC was successful in predicting a lack of significant galvanic effect under these circumstances, although this could be predicted without the finite element analysis. Again, exposure time effects are shown to be quite substantial.

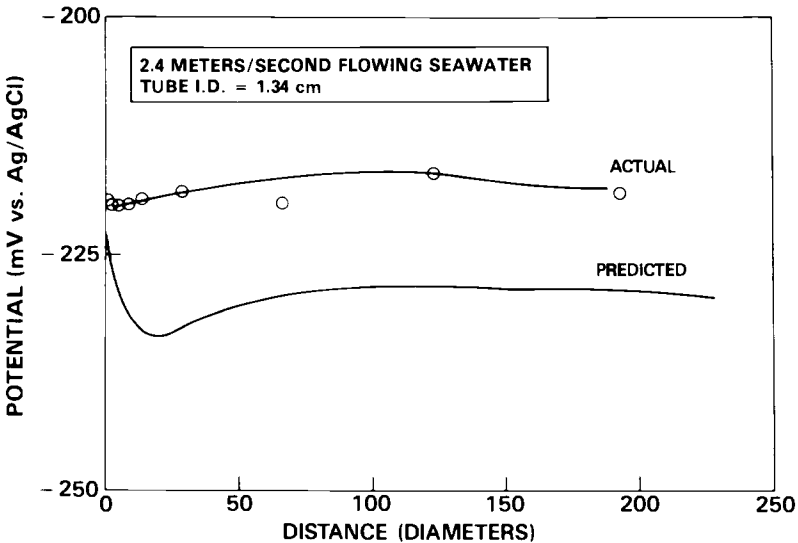


FIG. 14—90-10 Cu-Ni tube coupled to Monel 400 tubesheet after 1 day. Flowing seawater, MARC analysis.

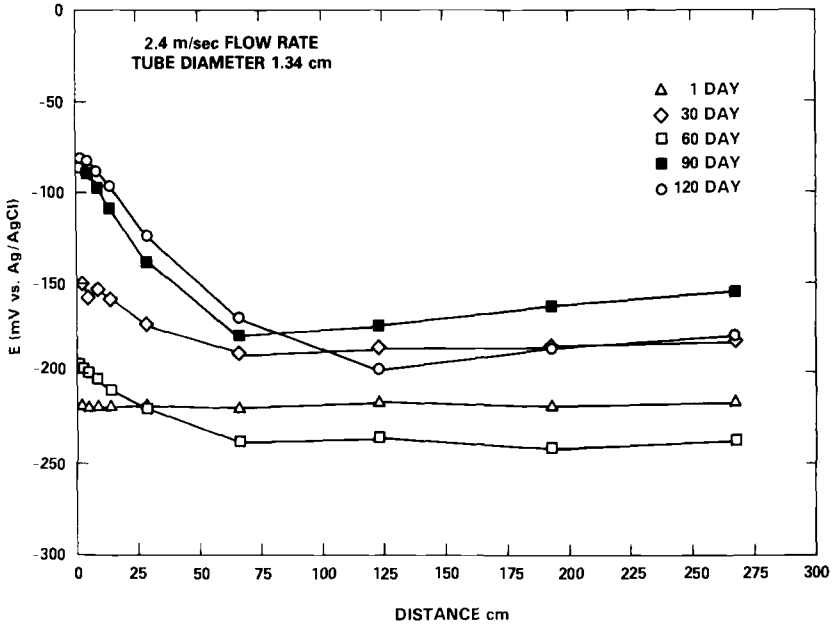


FIG. 15—Time effects for 90-10 Cu-Ni tube coupled to Monel 400 tubesheet. Flowing seawater Day 1 to 120.

90-10 Copper-Nickel/Zinc

Figure 16 illustrates the results of the MARC analysis for 90-10 copper-nickel tubing coupled to sacrificial zinc anode material after 30 days. This prediction is compared to the measured values from this study, keeping in mind that the measurements were on copper-nickel that had

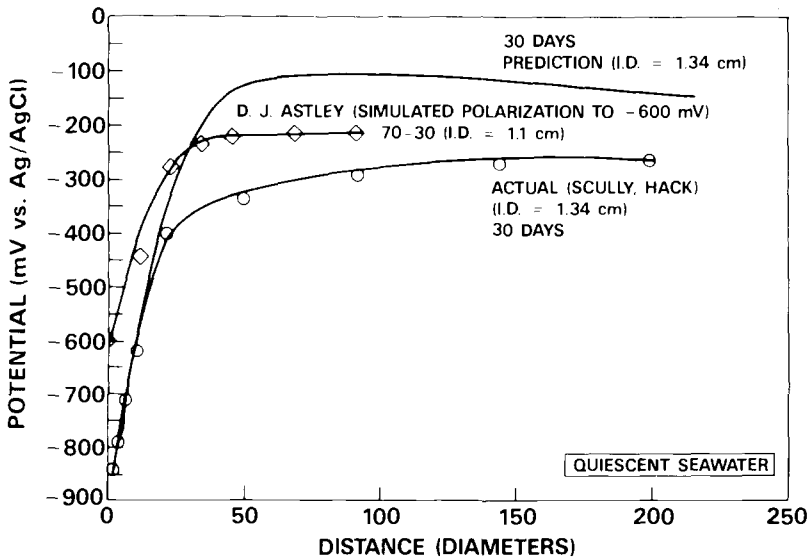


FIG. 16—90-10 and 70-30 Cu-Ni tubes coupled to anode grade zinc at the tubesheet, MARC analysis. Quiescent seawater.

already been exposed for 120 days, while the analysis was based on polarization data from only a 30-day exposure. This figure also contains measured data from Astley [6] on a 1.1-cm-diameter 70-30 copper-nickel tube cathodically protected at the end to -600 mV. Although the predicted potentials are higher than those measured in both cases, interaction distances were 50 diameters for the prediction, 50 for the measurements from this study, and 40 for Astley's work. This is excellent agreement considering the differences in the various studies.

Titanium/Ni-Al-Bronze

Figure 17 illustrates a potential profile predicted for a 1134-cm-diameter titanium tube coupled to a Ni-Al-bronze tubesheet. The MARC prediction is based on quiescent polarization behavior after 30 days, and the experimental measurements are from Astley's 1.46-cm-diameter tube with 1-m/s flow. Predicted potentials are quite different from those measured. The predicted interaction distance is over 100 diameters whereas the measured distance was 60 diameters. These discrepancies are probably caused by a large change in conditions to a flow of 1 m/s. Qualitatively, a large cathode to anode area ratio is predicted, and galvanic corrosion of the bronze was observed to be severe.

90-10 Copper-Nickel/Muntz

Figure 18 shows experimental measurements on a 1.34-cm-diameter 90-10 copper-nickel tube at 2.1 m/s coupled to a constant potential source of -250 mV, simulating a Muntz metal tubesheet [3]. The polarization data used for the MARC prediction in the figure was at 2.4-m/s flow for one day. The measured current distribution data are from work by Gehring [3-5], who did not report potential distribution. Although no direct comparisons can be made between predicted and compared. The predicted interaction distance and the measured distance are essentially identical at about 15 diameters. In this case galvanic corrosion is limited to the tube entrance despite the presence of the large cathodic tube surface.

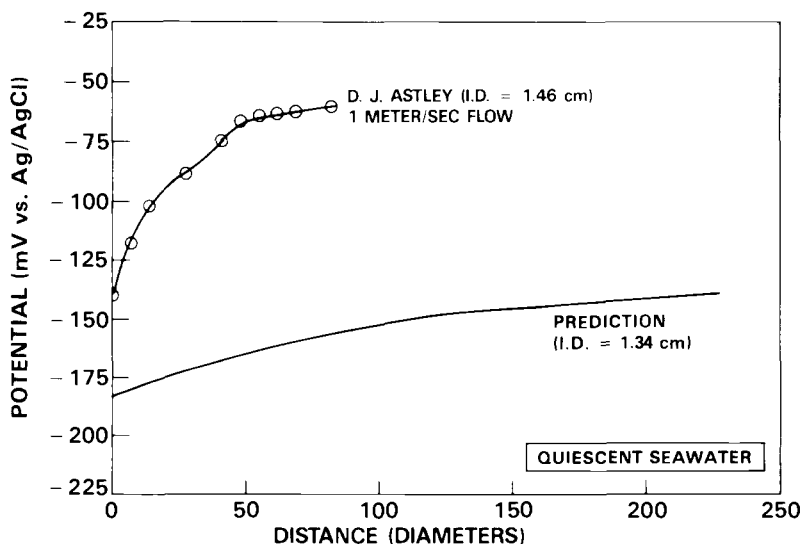


FIG. 17—Titanium tube coupled to Ni-Al-bronze tubesheet after 30 days, MARC analysis. Quiescent seawater.

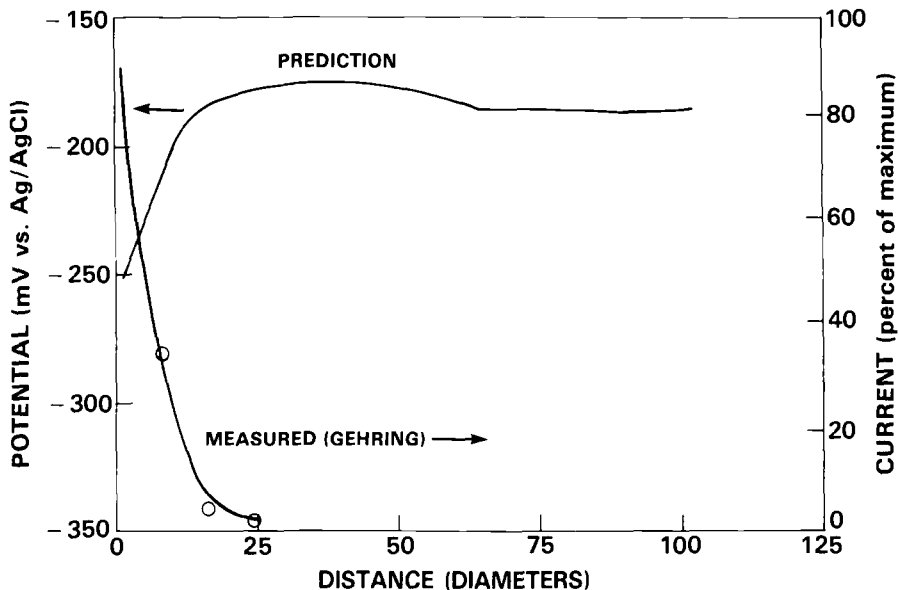


FIG. 18—90-10 Cu-Ni tube coupled to Muntz Metal alloy tubesheet after 1 day, MARC analysis.

Prediction by the Use of Finite Element Analysis

As described in the preceding section, agreement between predicted and measured potential profiles is generally not very good. This may be due to sensitivity in the computer analysis to small changes in the shape of the polarization curves used for boundary conditions. The potential-history-dependence of passivity of some materials and the high polarization resistances encountered in passive regions may also have contributed to the problems with the potential predictions. Also, the discrepancy may be due to the variable nature of the freely corroding potential of a material in seawater, which can lead to a displacement of the potential profiles, but seems to affect the shape of these profiles only slightly.

On the other hand, with only a few exceptions, measured and predicted interaction distances were very close for the wide variety of situations studied, and two of these exceptions occurred in the tube/tubesheet combination where the total amount of galvanic interaction was extremely small because of similarity in the materials' freely corroding potentials and the passive behavior of these alloys in seawater. Thus the finite element technique is a good way to predict the interaction distance down tubes, and thereby the effective area ratio of a tube/tubesheet galvanic couple. This was the case over a range of material combinations, exposure periods, flow velocities, computer programs, and data sources.

There is insufficient information in this study to make any statement about prediction accuracy for galvanic corrosion rates.

Wagner Number Analyses

The Wagner number [15,16] can be used to evaluate the relative degree of uniformity of current distribution such as galvanic current. This parameter describes the ratio of the interfacial or polarization resistance, here called kinetic, to the resistance to ionic conduction in the

electrolyte separating the anode and the cathode, here called ohmic, as follows

$$W = \frac{\text{kinetic resistance}}{\text{ohmic resistance}}$$

When the Wagner number gets very large, a uniform current distribution over the anode and cathode is promoted. When the Wagner number gets very small, a nonuniform current distribution is promoted. The Wagner number can be changed by modifying either the polarization characteristics of the anode and cathode materials involved, or the solution conductivity, or both, thus changing the uniformity of current distribution.

The Wagner number analysis can be applied to primary, secondary, or tertiary current distribution, as shown in Table 6. For the primary case, only the solution conductivity and a characteristic length between anode and cathode are considered

$$W = K/L$$

where K is the solution conductivity, and L is a characteristic length. For secondary and tertiary current distribution, linear, Tafel, or concentration type polarization conditions are considered through the following relationship

$$W = K(dE/di)_{i_{avg}}/L$$

In the secondary current distribution case a large Tafel coefficient B or B' causes a large Wagner number, permitting uniformity of current distribution. In the case of tertiary current distribution, currents near the limiting current density promote large Wagner numbers. Figures 19 and 20 show the effect of the relative size of the Wagner number on galvanic current distribution for both the case of an anode as the tube material and a cathode as the tube material. The exact magnitude of the galvanic current is not determined from this type of treatment. The quantitative solution to these types of problems requires the use of numerical methods as discussed above.

Alloy 625/Ni-Al-Bronze

Figure 21 is a schematic cathodic polarization curve for Alloy 625 in quiescent seawater. The anodic curve for nickel-aluminum-bronze intersects this curve in the diffusion limited region, which would indicate that the Wagner number of the cathodic tube should be large, approaching infinity. A large Wagner number should indicate current uniformity, which should result in a large interaction distance on Alloy 625. Observed interaction distances are in fact quite large, 60 diameters. Under flowing conditions, the diffusion limited portion of the cathodic curve for Alloy 625 should occur at more electronegative potentials, causing the Wagner number at any given potential, and thus the resultant interaction distance to shrink. This was actually

TABLE 6—Wagner polarization number determination.

Current Distribution	Overpotential-Current Relationship	Polarization Resistance Term	Wagner Number
Primary	K/L
Secondary	$E = Bi$ (linear)	B	KB/L
Secondary	$E = B' \ln(i/i_0)$ (Tafel)	B'/i	KB'/iL
Tertiary	$E = -RT/nF \ln(1 - i/i_1)$ (diffusion)	$RT/nF 1/(i_1 - i)$	$KRT/nF(i_1 - i)L$

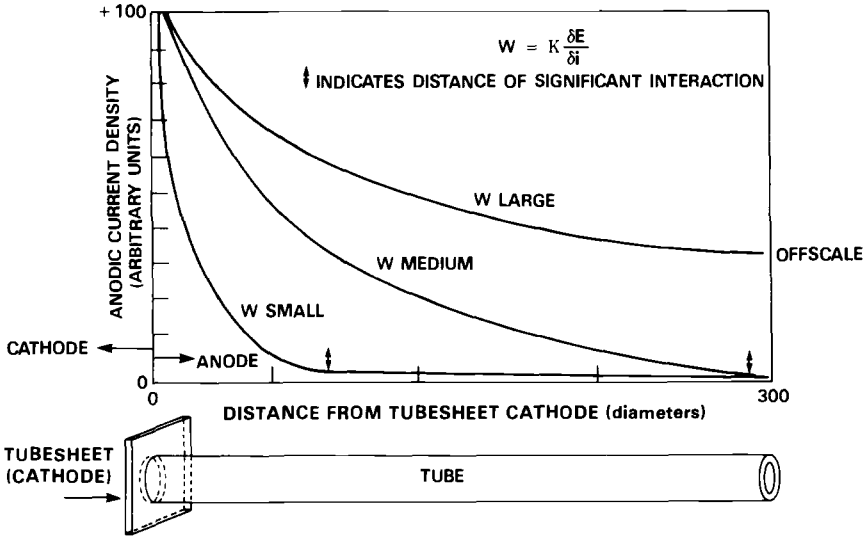


FIG. 19—Schematic galvanic current versus distance plot for an anode tube coupled to a cathode tubesheet for various magnitudes of the Wagner polarization parameter.

observed as the interaction distance was only 15 to 25 diameters at 2.4-m/s flow. The Wagner number gives a good qualitative indication in this case of the amount of tube surface that has a significant effect in the galvanic couple.

90-10 Copper-Nickel/Monel Alloy 400

The couple between a Cu-Ni tube and a Monel Alloy 400 tubesheet will result in a low Wagner number, as illustrated schematically in Fig. 22. This should result in galvanic current being

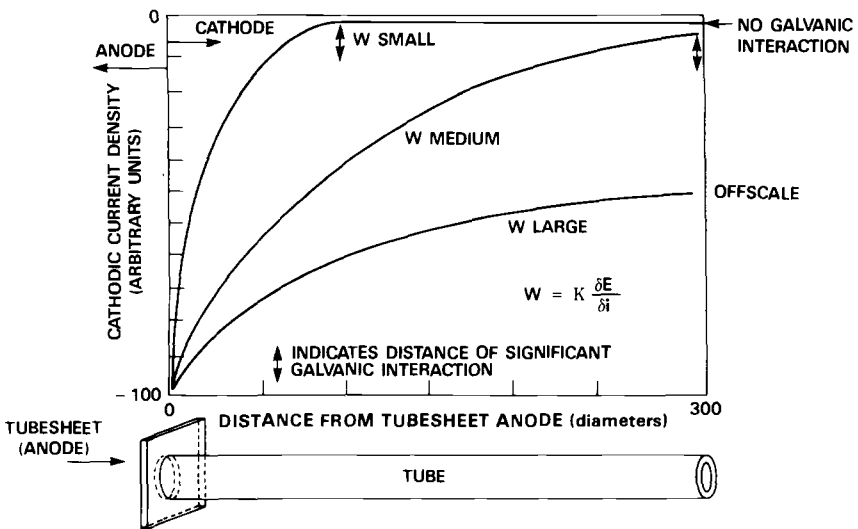


FIG. 20—Schematic galvanic current versus distance plot for a cathode tube coupled to an anode tubesheet for various magnitudes of the Wagner polarization parameter.

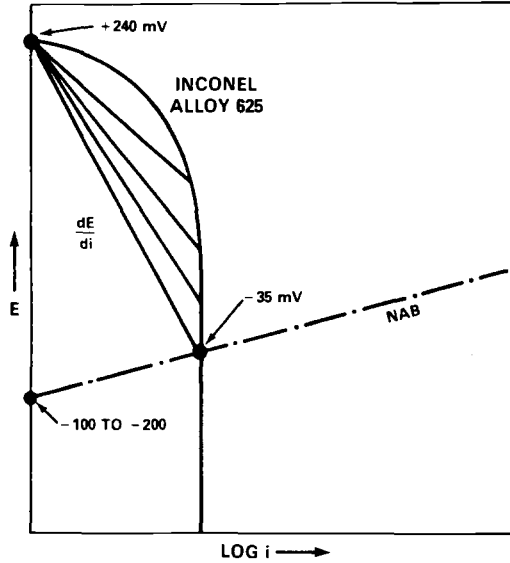


FIG. 21—Schematic polarization plot describing galvanic corrosion behavior of Alloy 625 coupled to Ni-Al-bronze.

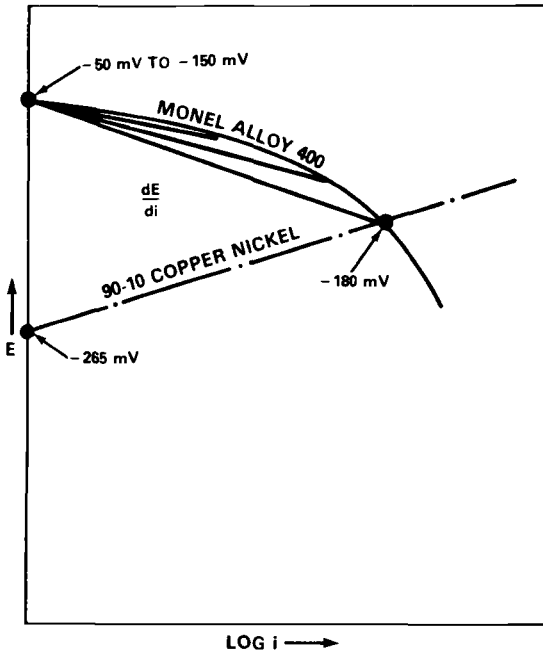


FIG. 22—Schematic polarization plot describing galvanic corrosion behavior of Monel 400 coupled to 90-10 Cu-Ni.

limited to the entrance of the anodic tube. Low interaction distances are predicted in this case, but in this study the observed interaction distances are very large, 100 diameters at 120 days. This behavior is thought to occur as a result of the passive film formation on the anodically polarized 90-10 copper-nickel near the tubesheet. Thus the Wagner number was unsuccessful in predicting this material combination, possibly because of the use of incorrect polarization curves for the situation observed.

90-10 Copper-Nickel/Zinc

Figure 23 is the cathodic polarization and Wagner analysis of copper-nickel in quiescent natural seawater. A galvanic couple between a zinc anode at the position of the tubesheet and a Cu-Ni tube would produce a large Wagner number, since cathodic currents on the tube are near the limiting current density for oxygen reduction. Large interaction distances are predicted by large Wagner numbers and were observed at 40-50 diameters both in this study and by Astley, as seen in Table 5.

Titanium/Ni-Al-Bronze

Since titanium has similar polarization characteristics to Alloy 625, similar behavior should be observed with couples using titanium tubes, resulting in large interaction distances. As Table 5 illustrates, Astley measured a large (60-diameter) interaction distance on titanium tubes coupled to nickel-aluminum-bronze tubesheet. The Wagner analysis was successful in predicting the behavior in this situation.

90-10 Copper-Nickel/Muntz

A Cu-Ni tube coupled to a Muntz metal or similar brass tubesheet would result in a low Wagner number since the cathodic current on the Cu-Ni is far below the limiting current density

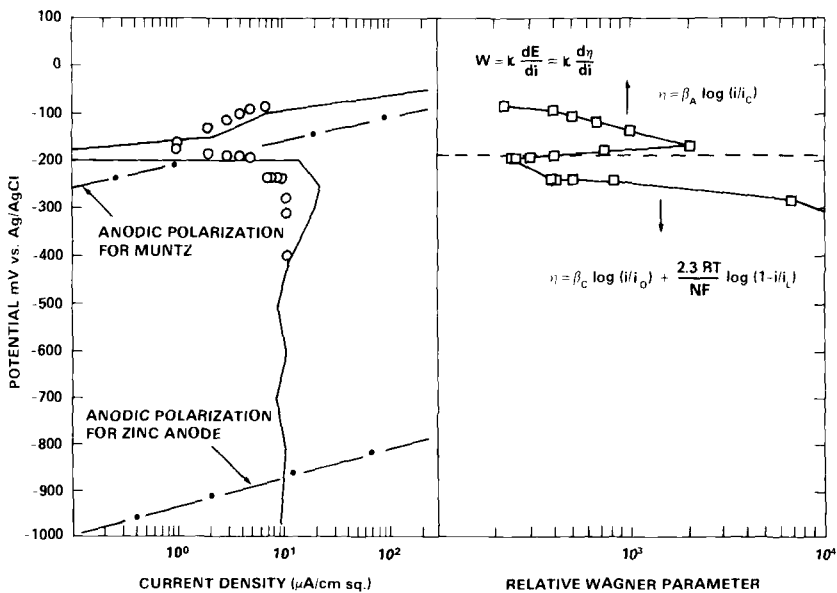


FIG. 23—Polarization plot and Wagner polarization analysis for 90-10 Cu-Ni in quiescent seawater.

and the Tafel slope is modest. This is seen in Fig. 23, where the Wagner number is relatively low at potentials of -250 mV or above. Table 5 shows that Gehring reported only a 15 diameter interaction distance under these circumstances. Again the Wagner number prediction is accurate for this situation.

Other Material Combinations from the Literature

The experimental results from the literature reported in Table 2 can also be analyzed using the Wagner number. Following the same logic used above, a large interaction distance is predicted for all studies in this table except those involving copper-nickel or brass. With no exceptions the interaction distances were all observed to be from 60–480 diameters, in agreement with the prediction. The copper-nickel and brass couples all are predicted to have short interaction distances, and all were reported in the range of 12–35 diameters, except for one short duration exposure, which had a 50-diameter interaction distance.

Prediction by the Use of Wagner Number Analysis

The above analyses indicate how good a predictor the Wagner number is for interaction distance in the tube/tubesheet galvanic couple. Although quantitative prediction is not possible using this analysis, qualitative predictions of interaction distance appear to be quite accurate.

Conclusions

Quantitative predictions of galvanic corrosion by finite element methods can be extremely accurate in predicting distances of galvanic interaction down the inside of heat exchanger tubes in seawater, provided that long-term electrochemical polarization data and open circuit potential behavior are carefully considered and incorporated into such analyses. Predictions of potentials are not very accurate because of the time dependence of open circuit corrosion potentials in seawater. Qualitative indications of galvanic corrosion interaction distances may be obtained with confidence by using Wagner number analysis. This method does not give quantitative data, however.

References

- [1] Hack, H. P. and Scully, J. R., "Galvanic Corrosion Prediction Using Long-Term Potentiostatic Polarization Curves," *Corrosion*, Vol. 42, No. 2, 1976, p. 79.
- [2] Scully, J. R., Hack, H. P., and Tipton, D. G., *Corrosion*, Vol. 42, No. 8, p. 462, 1986.
- [3] Gehring, G. A., Kuester, C. K., and Maurer, J. R., *Corrosion/80*, Chicago Paper 32, 1980.
- [4] Gehring Jr., G. A., "Galvanic Corrosion of Selected Tubesheet/Tube Couples Under Simulated Seawater Condenser Conditions," *Corrosion/81*, Toronto, Canada, April 1981.
- [5] Gehring, G. A. and Kyle, R. J., "Galvanic Corrosion in Steam Surface Condensers Tubed with Either Stainless Steel or Titanium," *Corrosion/82*, Houston, TX, March 1982.
- [6] Astley, D. J., "A Method for Calculating the Extent of Galvanic Corrosion and Cathodic Protection in Metal Tubes Assuming Unidirectional Current Flow," *Corrosion Science*, Vol. 23, No. 8, 1983, pp. 801–832.
- [7] Fu, J. W., Technical Note: "A Finite Element Analysis of Corrosion Cells," *Corrosion*, Vol. 38, No. 5, May 1982, p. 295.
- [8] Fu, J. W., "A Finite Element Analysis of Corrosion Cells with Mathematical as Well as Experimental Verifications," Scientific Paper 80-IDZ-MEEIC-P1.
- [9] Fu, J. W. and Chow, J. D. K., "Cathodic Protection Designs Using an Integral Equation Numerical Method," *Materials Performance*, Oct. 1982, p. 9.
- [10] Kasper, R. G. and April, M. G., "Electrogalvanic Finite Element Analysis of Partially Protected Marine Structures," *Corrosion*, Vol. 39, No. 5, May 1983, p. 181.
- [11] Strommen, R. and Rodland, A., "Computerized Techniques Applied in Design of Offshore Cathodic Protection System," *Materials Performance*, April 1981, p. 15.

- [12] Munn, R. S., "A Mathematical Model for Galvanic Anode Cathodic Protection System," *Materials Performance*, Aug. 1982, p. 29.
- [13] Decarlo, E. A., "Computer Aided Cathodic Protection Design Technique for Complex Offshore Structures," *Corrosion/82*, Paper 165, Houston, TX, March 1982.
- [14] Doig, P. and Flewitt, P. E. J., "A Finite Difference Numerical Analysis of Galvanic Corrosion for Semi-Infinite Linear Coplanar Electrodes," *Journal of the Electrochemical Society*, Dec. 1979, p. 2057.
- [15] Wagner, C., *Journal of the Electrochemical Society*, Vol. 98, No. 116, 1951.
- [16] Wagner, C. and Traud, W., *Zeitschrift Fuer Electrochemie Bc-Bunsenges Phys. Chem.*, 1938, p. 44.

Testing and Control

Quantitative Assessment of Atmospheric Galvanic Corrosion

REFERENCE: Doyle, D. P. and Wright, T. E., "Quantitative Assessment of Atmospheric Galvanic Corrosion," *Galvanic Corrosion, ASTM STP 978*, H. P. Hack, Ed., American Society for Testing and Materials, Philadelphia, 1988, pp. 161-173.

ABSTRACT: The test method for assessing galvanic corrosion that is described in this paper is applicable to bare metals. Its main advantages over existing techniques are that the results are quantitative and require only a short exposure period—typically 90 days—in the environment of interest. The test units are quite simple in concept, and experience has shown that the results are reliable and reproducible. Because the results are quantitative they are less subject to bias by the evaluator. The test units involve winding a wire of the anodic component of the galvanic couple onto the threads of a bolt of the cathodic member of the couple. The weight loss of the wire after a short exposure period relative to that of a similar wire wound onto a threaded plastic bolt gives a measure of the galvanic activity at any given location. The basic idea for the test unit was developed at Bell Telephone Laboratories over 30 years ago, but it has not achieved widespread acceptance as a test method. The present authors adopted the technique several years ago and have improved the laboratory procedures for assembling the test units and determining the weight losses of the wires. Many thousands of specimens have been exposed at a variety of locations around the world. The main emphasis in these tests was to measure the marine or industrial corrosivity components of the atmosphere, or both. Several technical papers have been written on the results of this application of the technique. In the present paper emphasis will be placed on the use of the technique to measure the amount of galvanic corrosion between different combinations of metals rather than its use to measure the corrosivity of the atmosphere. Because the work has been prepared by an aluminum producer, where galvanic corrosion is, naturally, a sensitive issue, there was emphasis on the behavior of aluminum in contact with several metals.

KEY WORDS: atmospheric corrosion testing, galvanic corrosion, quantitative assessment

Galvanic corrosion is the adverse influence that one metal may have on another when they are coupled together in any given environment. The extent of galvanic corrosion depends on the nature of the environment and on the metals that are involved. This study was limited to atmospheric environments and bare metals. Extensive work has been done by others in the study of the galvanic behavior of various combinations of metals particularly under conditions of immersion in saltwater. From this work a "galvanic series" indicating the order of the corrosion tendencies of the various metals has been established [1]. Although it was thought likely that the metals would behave in similar order in different industrial, rural, or other atmospheres, there was a need to develop a technique for obtaining a quantitative measure of the extent of galvanic corrosion.

The results of work by ASTM Subcommittee VIII using riveted specimens and disks bolted together have been reported [2]. An ASTM test method for assessing galvanic corrosion caused by the atmosphere based on the use of plates is currently at the approval stage.

Inspiration for the technique used in the present work was taken from work by Compton et al. [3] of Bell Laboratories. Included in their methods to obtain a quantitative assessment of the extent of galvanic corrosion between any two metals was a bolt and wire type galvanic couple,

¹Joint researchers, Alcan International Research Centre, P.O. Box 8400, Kingston, Ontario K7L 4Z4, Canada.

which permitted weight loss determination of the anodic member (wire) of the couple. Quantitative data were thus obtainable for design engineers and others who might have to cope with various combinations of metals under different service conditions.

At Alcan the Bell method has been developed to determine not only quantitative data on galvanic couples but also to characterize the corrosivity of the atmosphere at the test locations. Over 13 000 individual tests in various parts of the world have been carried out, and several technical papers have been published on this aspect of the test [4-6]. In order to avoid cumbersome descriptions of the test it has been termed the CLIMAT test and the test units CLIMAT units. The test period is only 90 days. Despite this short period the fact that the exposures are carried out in the natural environments significantly improves the credibility of the results. A correlation of CLIMAT data with service experience has been previously published [5].

Procedures

Basic Test

The bimetallic test unit consists of fine wire, 0.89 mm (0.035 in.) tightly wound onto a 10 cm length of a 1.27-cm-diameter threaded rod with approximately 5 threads/cm ($\frac{1}{2}$ -UNC). About 100 cm of wire of the anodic metal of the galvanic couple are wound onto one end of about half the length of the rod and joined electrically to the rod at binding posts set into the rod. An apparatus for winding the wire ensures uniform tension. This tension is maintained by tightly securing the ends of the wires to the two binding posts. The wires are carefully weighed before assembly, and if any wire is snipped off during assembly it is weighed and subtracted from the weight. For control purposes similar wires are wound onto plastic rods. The assembled CLIMAT units are mounted vertically in Plexiglas® holders for ease of exposure as shown in Fig. 1. It should be emphasized that great care is taken in cleaning the components before assembly and in avoiding contamination during assembly.

The units are exposed for 90 days to the weather at the location under test. Precautions are taken to ensure bold exposure and to avoid shelter, for example, from buildings or trees. Standard record forms are completed for each site. Where possible, information is obtained on experience with dissimilar metal combinations in the test area. Such background information helps in interpreting the results of the tests.

After the test period the units are returned to the laboratory where they are disassembled. The wires are cleaned free of corrosion products and dirt using methods that are appropriate for the metals involved according to ASTM Recommended Practice for Preparing, Cleaning, and Evaluating Corrosion Test Specimens (G 1). The losses in weight and the "percent weight losses" are then calculated making suitable corrections including adjustment for the exposure period of 90 days, where necessary. The "percent weight losses" in 90 days are termed CLIMAT indices in order to simplify presentation of the data. A useful feature in presenting the data as percent weight losses is that the results for different metals are directly comparable provided that the wire diameter is the same for each metal.

Experimental Work

Preliminary Program

Initially an extensive program was carried out to determine the galvanic influence on aluminum of several common metals when exposed to marine, industrial, and rural atmospheres. In all cases aluminum wire (AA1050) was employed. The rods were mild steel, copper,

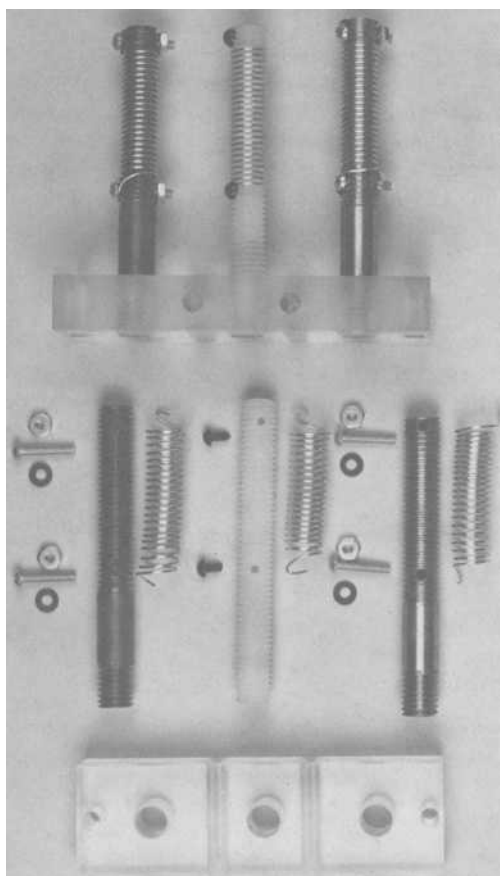


FIG. 1—CLIMAT test specimens. Above: 3-unit holder. Below: components.

lead, graphite, Monel, Type 304 stainless steel, chromium plated steel, and galvanized steel. Nylon rods were used for control purposes. Ten exposure sites were employed as follows:

- (1) Chebucto Head, Nova Scotia, Canada, severe marine,
- (2) Cape Beale, British Columbia, Canada, severe marine,
- (3) Kure Beach, NC, 25 m, severe marine,
- (4) Kure Beach, NC, 250 m, marine,
- (5) Durban, South Africa, marine industrial,
- (6) Halifax, Nova Scotia, Canada, industrial,
- (7) Montreal, Quebec, Canada, industrial,
- (8) Toronto, Ontario, Canada, industrial,
- (9) Vancouver, British Columbia, Canada, industrial-marine, and
- (10) Kingston, Ontario, Canada, semi-rural.

These sites were selected because they were being used for other atmospheric exposures and were known to vary widely in corrosivity.

Industrial Corrosivity

The sensitivity of CLIMAT units for measuring small changes in the corrosivity of atmospheres has been used as an important tool to monitor the atmospheres around industrial plants, storage areas, and so forth. As just one example of this application of the test a program was carried out at two similar industrial plants in order to determine their effect on the environment in the vicinity of the plants. Many of the buildings in the vicinity of the plants were covered with galvanized steel. The CLIMAT units selected for exposure at the plants and for distances up to 16 km in different directions were zinc wires on plastic and steel rods, and aluminum wires on plastic, steel, and copper rods.

Railway Tunnel, British Columbia, Canada

After a relatively short period of time, it was discovered that bare copper conductors in a long railway tunnel through the Rocky Mountains were suffering quite severe corrosion. It was extremely wet in the tunnel, and sulfur gases and ammonia were present. A program was developed to examine the interactions of different metals using the following CLIMAT units:

- (1) aluminum wire on plastic rod,
- (2) aluminum wire on Type 304 stainless steel rod,
- (3) aluminum wire on graphite rod,
- (4) zinc wire on plastic rod,
- (5) zinc wire on mild steel rod,
- (6) copper wire on plastic rod, and
- (7) copper wire on graphite rod.

The CLIMAT units were placed at intervals through the tunnel for 90 days.

Results*Preliminary Program*

The CLIMAT indices (percent weight losses in 90 days) for aluminum wires wound onto mild steel, Type 304 stainless steel, monel, lead, copper, galvanized steel, chrome plated steel, and graphite rods at ten locations are shown in Figs. 2 through 9. The indices were adjusted by subtracting the small amount of corrosion that occurred on aluminum wires wound onto plastic rods at each site. Thus the results reflect the increase in the amount of corrosion caused by

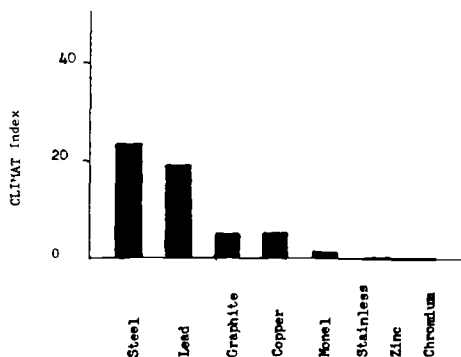


FIG. 2—CLIMAT indices at Vancouver, British Columbia, industrial marine.

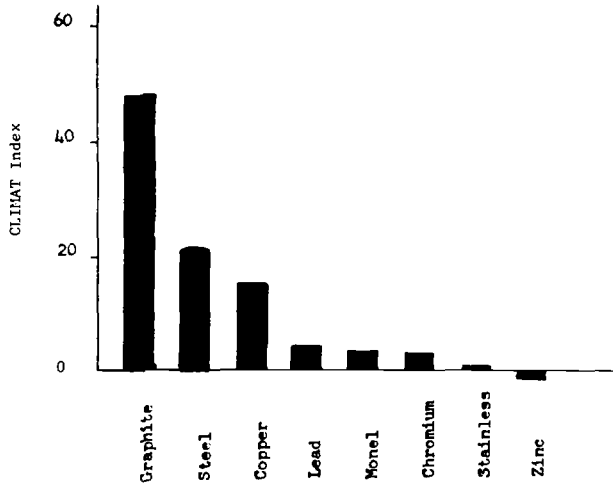


FIG. 3—CLIMAT indices at Chebucto Head, Nova Scotia, marine.

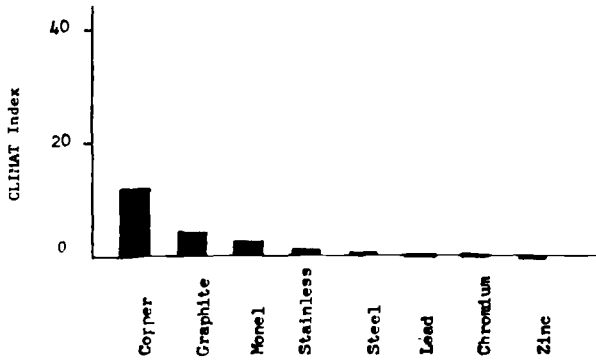


FIG. 4—CLIMAT indices at Halifax, Nova Scotia, industrial.

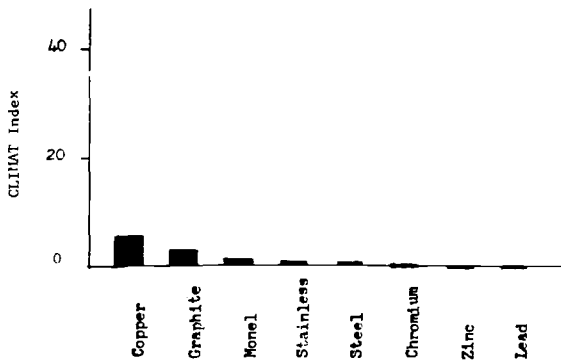


FIG. 5—CLIMAT indices at Montreal, Quebec, industrial.

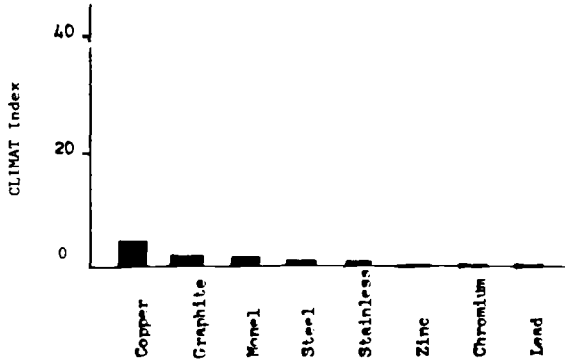


FIG. 6—CLIMAT indices at Toronto, Ontario, industrial.

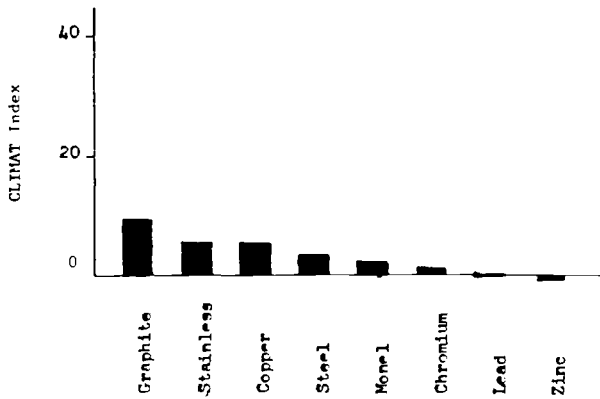


FIG. 7—CLIMAT indices at Kingston, Ontario, semi-rural.

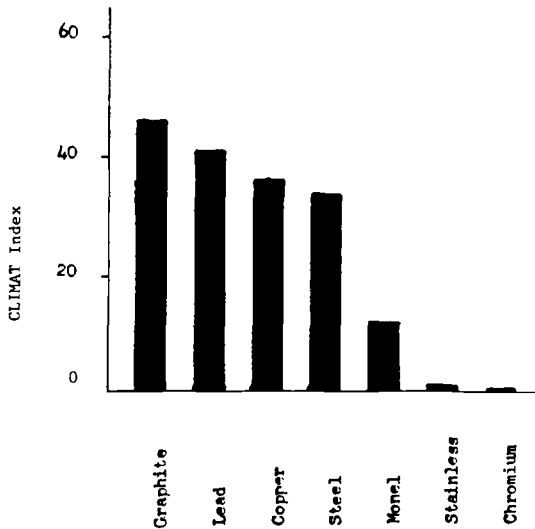


FIG. 8—CLIMAT indices at Cape Beale, British Columbia, marine.

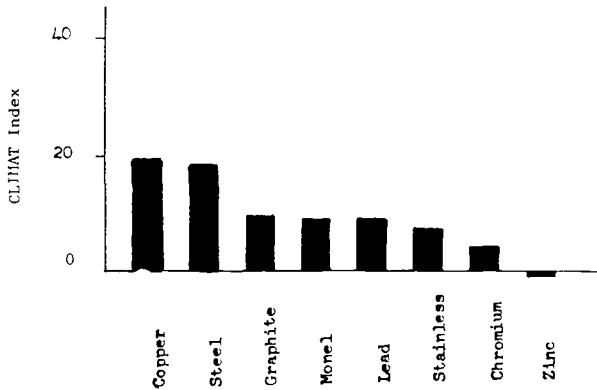


FIG. 9—CLIMAT indices at Durban, South Africa, marine and industrial.

galvanic influences. Incidentally some of the aluminum wires broke during the exposure period, and it was decided to standardize on a thicker gage (0.89 mm) for all subsequent work.

When the data on these bar graphs were studied it was obvious that marine conditions produced much more galvanic corrosion than industrial conditions. Looking at Figs. 10 and 11, for example, for Kure Beach it is interesting to note the rapid reduction in the severity of galvanic corrosion in going from 25 to 250 m from the ocean. The ranking of corrosion severity by the cathodic member is exactly the same for the 25- and 250-m environments. It is also interesting that graphite and steel cause more galvanic corrosion than copper. Monel, although composed of 67% nickel and 31.5% copper has little galvanic influence at 250 m from the ocean. The high nickel content is probably responsible for this behavior. This helps explain how monel fasteners are frequently used successfully for joining aluminum and steel structures.

From a practical point of view it can be appreciated that it is a valuable tool to measure how far inland marine influences penetrate from the ocean. Several examples of this application of

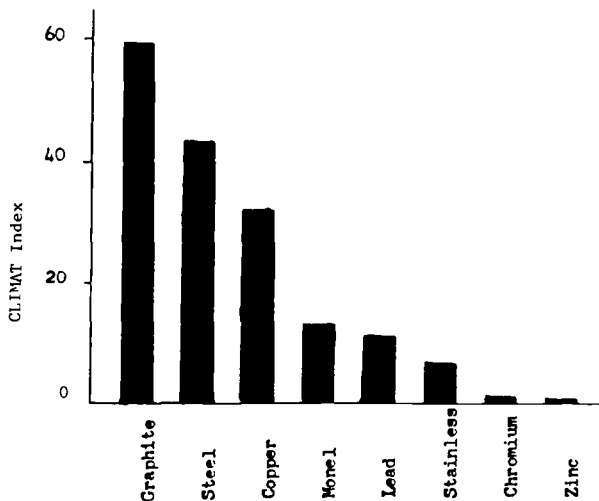


FIG. 10—CLIMAT indices at Kure Beach (25 m), marine.

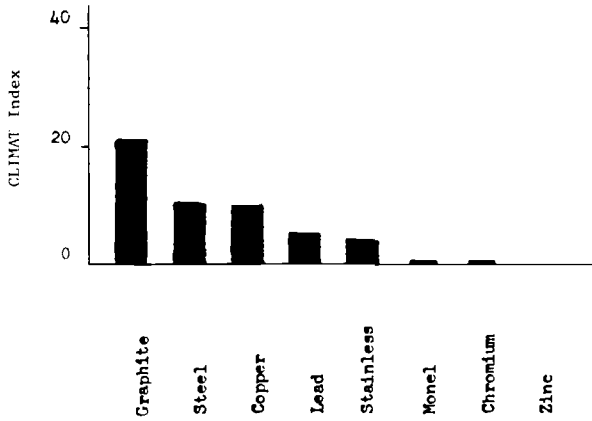


FIG. 11—CLIMAT indices at Kure Beach (250 m), marine.

the test method have been previously published [4-6]. After examining all the results it can be seen that mild steel causes quite severe galvanic corrosion of aluminum at all the marine sites, but there is negligible effect at the Toronto, Montreal, and Halifax industrial sites. Hence, CLIMAT units consisting of aluminum wires on steel rods are a sensitive tool for measuring marine influences.

The results confirm that zinc is very compatible with aluminum in all atmospheres, in several cases showing that aluminum was actually cathodically protected by zinc.

The detrimental influence of copper in all atmospheres, particularly in marine atmospheres, shows that copper and aluminum should not be used together without careful consideration of the environment.

The good behavior of aluminum in contact with chromium plated steel in all atmospheres may have practical implications for this combination of metals.

The behavior of lead is consistent with the successful application of lead washers on nails for fastening aluminum roofing and siding in all but severe marine atmospheres.

Industrial Corrosivity

The results of testing the environment around two industrial plants are shown in Fig. 12 through 16 for aluminum and zinc wires on plastic and mild steel rods and also for aluminum wire on copper rods. Note that the same scale is used for all the results using aluminum wires, but that because of the higher weight losses of the zinc wires different scales were used.

So far as the initial intent of the work was concerned the results showed that Plant A created much more pollution than Plant B and that the CLIMAT indices decreased rapidly with distance from the center of the plants. As would be expected the corrosive influence was greater to the leeward side of the plants. The zinc wires on mild steel rods were the most sensitive to these particular environments.

Railway Tunnel, British Columbia, Canada

The results of testing aluminum wires on plastic, Type 304 stainless steel and graphite rods, zinc wires on plastic and mild steel rods, and copper on plastic and graphite rods are shown in Table 1.

The CLIMAT data from the tunnel showed very clearly that copper was subject to severe corrosion caused by sulfur gases and ammonia whereas aluminum was quite resistant. The

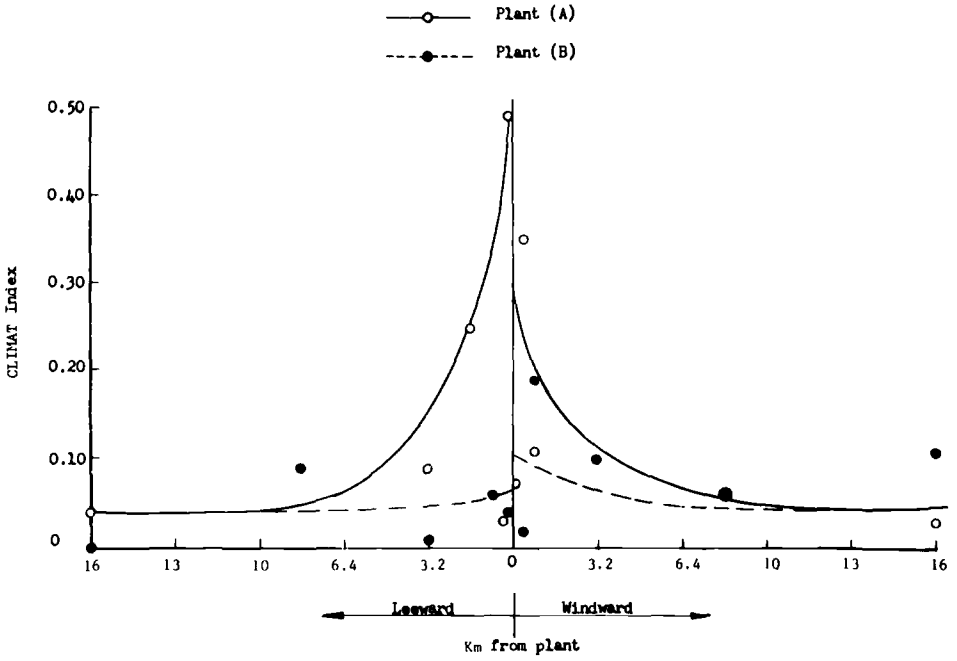


FIG. 12—Al-plastic results from Plants A and B.

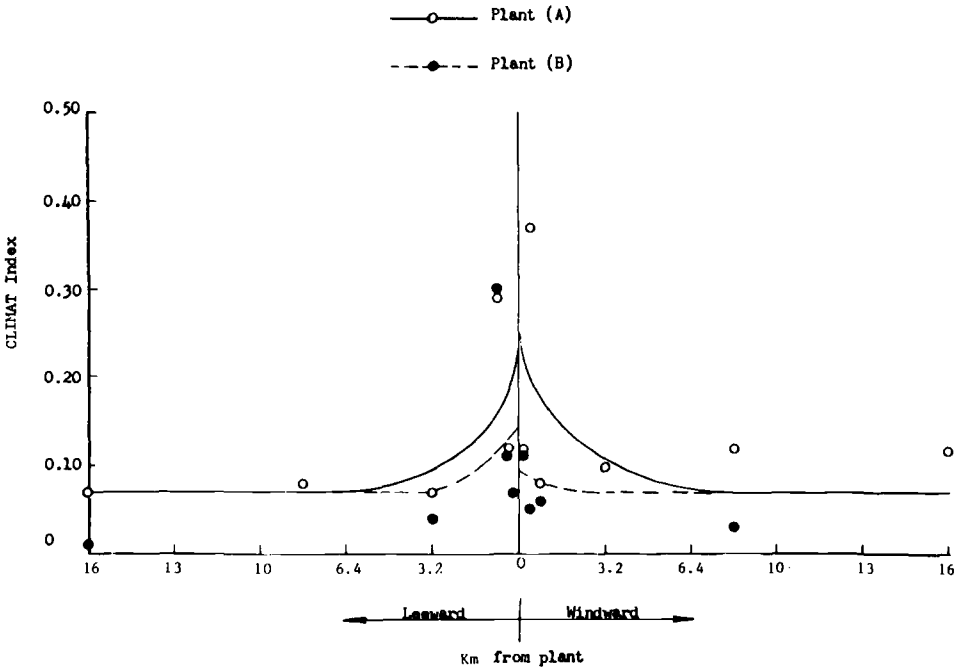


FIG. 13—Al-Fe results from Plants A and B.

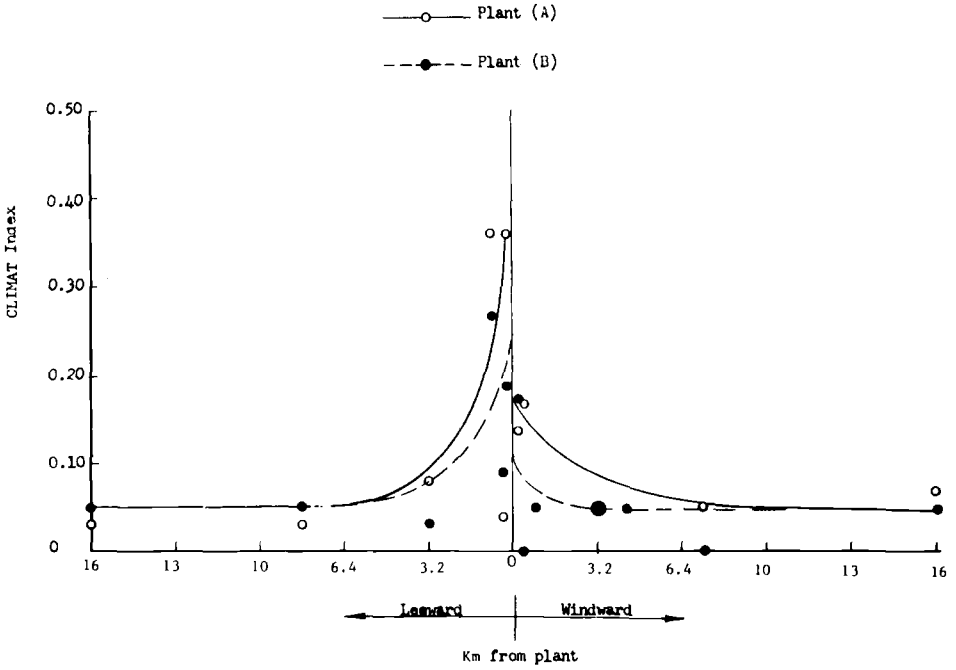


FIG. 14—Al-Cu results from Plants A and B.

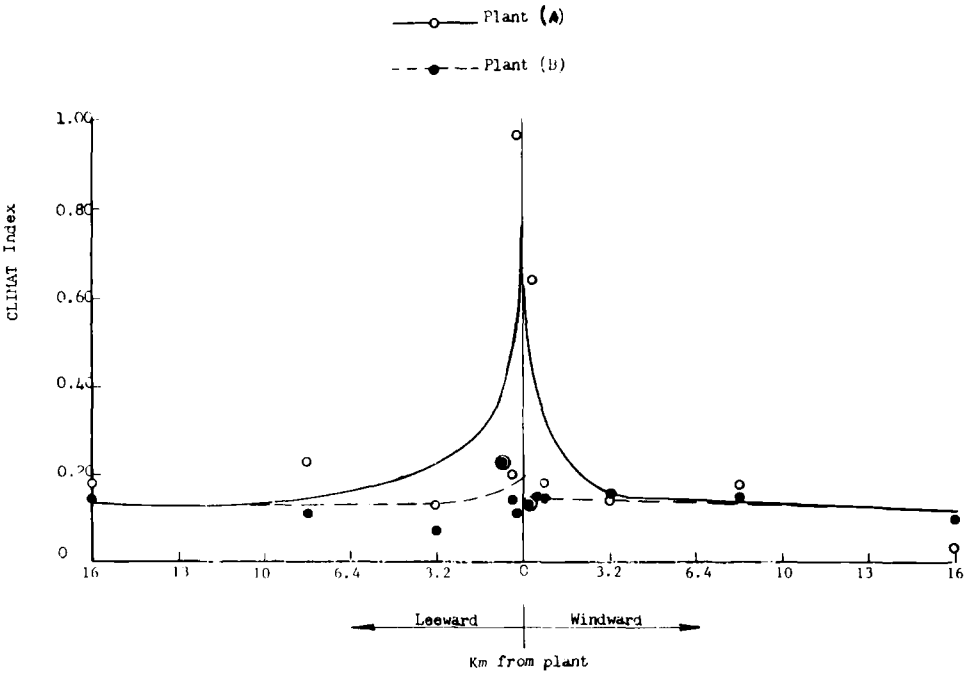


FIG. 15—Al-plastic results from Plants A and B.

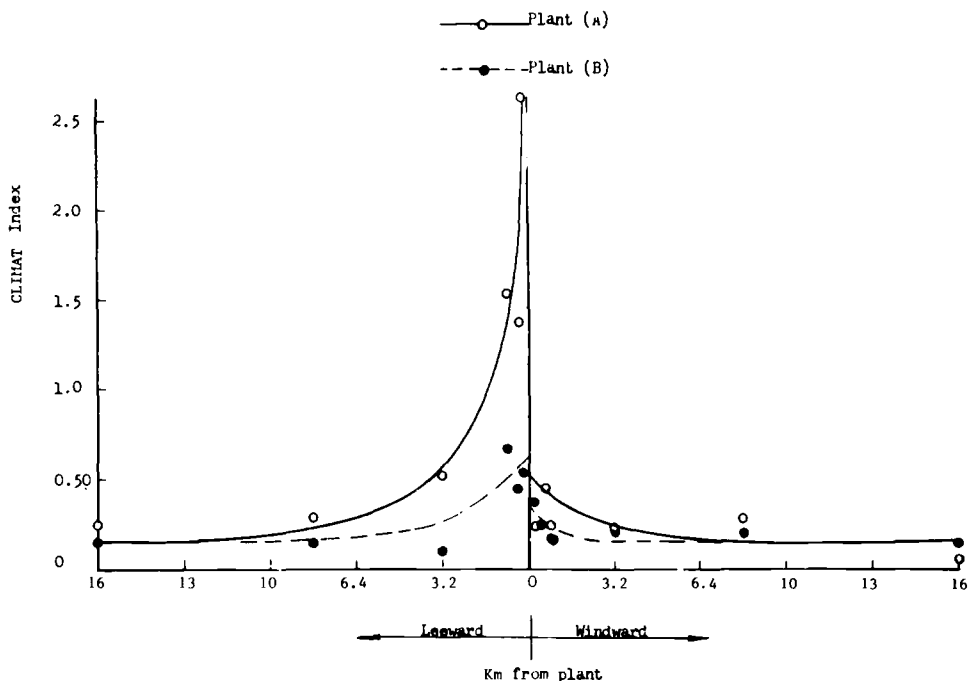


FIG. 16—Zn-Fe results from Plants A and B.

results also showed that zinc behaved relatively well. Graphite did not stimulate much galvanic corrosion, and stainless steel demonstrated good polarization characteristics in the tunnel.

Overall, it was possible to obtain an excellent idea of the galvanic performance of the combinations of metals that were of interest and also the basic behavior of zinc, copper, steel, and aluminum.

Discussion

The CLIMAT test has been shown to be an excellent method for assessing galvanic corrosion between two metals in the atmosphere. It is applicable whenever the anodic member of the couple can be produced in wire form. Sometimes a preliminary test may be necessary to establish which metal is anodic. The results of tests with aluminum wire on zinc rods (Fig. 4) showed that zinc was anodic to aluminum by the negative index shown for the aluminum. One of the features of the CLIMAT test not emphasized in this paper is its sensitivity. Early unpublished work (Table 2) showed that the results were sufficiently reproducible so that it was decided to use only single units for any given location. Also it was learned that tests could be carried out indoors in industrial plants by weighing the wires on more sensitive balances.

The CLIMAT numbers for galvanic corrosion do require a certain amount of interpretation. The data for a different 90-day period in some other season would likely consist of a different set of numbers. Sometimes it might be necessary to repeat the tests to take seasonal variations into account. However the test can always provide a clear indication of the relative galvanic behavior of different combinations of metals.

This paper is presented with hope that it might stimulate interest in having the CLIMAT test standardized for widespread use for assessing galvanic corrosion in the atmosphere. The sim-

TABLE 1—Results for CLIMAT units exposed in the Railway Tunnel, British Columbia.

CLIMAT Unit Type	Location 1 ^a		Location 2		Location 3		Location 4		Location 5	
	June/ Sept.	Sept./ Dec.	June/ Sept.	Sept./ Dec.	June/ Sept.	Sept./ Dec.	June/ Sept.	Sept./ Dec.	June/ Dec.	Dec./ March
Al on plastic	0.15	0.02	0.34	0.00	0.64	0.10	0.00	0.02	0.02	0.07
Al on stainless (304)	0.07	0.00	0.16	0.04	0.00	0.27	0.00	0.05	0.00	...
Al on graphite	0.45
Zn on plastic	0.21	0.32	0.74	0.07	1.1	0.13	0.70	0.12	0.03	...
Zn on steel	1.0	0.89	1.09	0.19	1.1	0.73	0.85	0.36	0.66	...
Cu on plastic	8.8
Cu on graphite	8.3

^aOutside tunnel.

TABLE 2—An example of ranges of CLIMAT indices obtained for ten replicates at each of two sites.

Unit	Industrial Site Halifax, Nova Scotia	Marine Site Chebucto Head, Nova Scotia
Aluminum wire on mild steel rod	1.2 to 2.0	8.9 to 11.3
Aluminum wire on copper rod	4.0 to 4.7	12.2 to 14.4

plicity of the test, the production of quantitative data, and the reliability of the test have much to recommend it.

References

- [1] Uhlig, H. H., *Corrosion Handbook*, Wiley, New York, 1948, p. 415-426, 481-496.
- [2] ASTM Subcommittee VIII on Galvanic and Electrolytic Corrosion, *ASTM B3 Proceedings*, Vol. 5, No. 167, 1935; Vol. 39, No. 247, 1939; and Vol. 48, No. 167, 1948.
- [3] Compton, K. G., Mendizza, A., and Bradley, W. W., *Corrosion*, Vol. 11, No. 9, Sept. 1955, pp. 383t-392t.
- [4] Doyle, D. P. and Godard, H. P., *Nature*, Vol. 200, No. 4912, 21 Dec. 1963, pp. 1167-1168.
- [5] Doyle, D. P. and Godard, H. P., *Proceedings of the Third International Congress on Metallic Corrosion*, MIR, Moscow, U.S.S.R., 1969, pp. 429-437.
- [6] Doyle, D. P. and Wright, T. E., *Atmospheric Corrosion*, W. H. Ailor, Ed., Wiley, New York, 1982, pp. 227-243.

Integration of Galvanic Corrosion Control Technology into Design

REFERENCE: Jenkins, J. F., "Integration of Galvanic Corrosion Control Technology into Design," *Galvanic Corrosion, ASTM STP 978*, H. P. Hack, Ed., American Society for Testing and Materials, Philadelphia, 1988, pp. 174-177.

ABSTRACT: Corrosion and design are synergistic. Design affects the type and amount of corrosion that is likely to occur, and corrosion affects the functionality of a given design. As galvanic corrosion can result in rapid localized attack, its effects are often severe.

The general relationship between open circuit potential, polarization, electrolyte resistivity, area ratio, and galvanic corrosion is well understood by corrosion engineers but is often not considered during design. Control of galvanic corrosion is most often accomplished by identifying probable sites for galvanic attack and either eliminating the possibility of galvanic corrosion through elimination of the dissimilar metals or by other means.

Where atmospheric exposure is encountered, mitigation of galvanic effects can be accomplished by eliminating design features that trap and hold moisture, the use of sealants, or the use of welded versus bolted joints. The selection of fastener materials must also consider galvanic compatibility.

In applications where the surfaces subject to galvanic attack are submerged, electrical isolation of dissimilar metals, control of the relative anodic and cathodic areas, the use of protective coatings, and the application of cathodic protection should be considered.

The technology to control galvanic corrosion is well known to corrosion engineers but is often not considered during the design process. It is the responsibility of corrosion engineers to insure that corrosion control technology is incorporated into the design process. This may be achieved either by education of design engineers regarding galvanic corrosion or by the inclusion of a corrosion engineer in the design team.

KEY WORDS: corrosion, galvanic corrosion, corrosion prevention, design, designers, design criteria, value engineering

Design and corrosion are interactive, and both affect the ability of structures or equipment to meet their intended use. Design can affect corrosion in many ways. Corrosion, both the type and extent, can affect the suitability of a given design for a specific service environment. A successful design is one where there is an optimum combination of those features, which result in reduction of corrosion with appropriate allowances for the corrosion that is likely to occur. Corrosion should be a consideration throughout the design process.

As most structures and equipment are constructed of a combination of materials, there is a potential for the electrochemical interaction of these dissimilar materials when exposed to the service environment. The term "galvanic corrosion" is used to describe this electrochemical interaction. Galvanic corrosion is an important form of corrosive attack because it can occur at high rates and is often localized. Localized corrosion caused by galvanic corrosion can have extremely detrimental effects on function as it often occurs at joints or interfaces between components where a small amount of corrosion can have a large effect on function.

¹Metallurgist, Naval Civil Engineering Laboratory, Port Hueneme, CA 93043.

Galvanic Corrosion Control Technology

Identification of potential sites for galvanic attack is fairly straightforward as is the prediction, at least qualitatively, of the amount and location of attack to be expected. Factors, such as the open circuit potential of the metals to be combined, their long-term polarization behavior, the effects of electrolyte resistivity, and the effect of area ratio on the rates of galvanic corrosion are well known at least qualitatively, and methods for their quantitative prediction appear to show promise [1,2]. Once the potential sites for galvanic corrosion have been located, the impact of the likely attack must be assessed. The most obvious method for preventing galvanic corrosion is to eliminate the possibility of galvanic attack by changing the materials selected so that the same material is used throughout the system. This is most often not practical, particularly for complex systems, and other methods for the mitigation of the galvanic corrosion must be used.

The methods selected for the mitigation of galvanic corrosion often depend upon the service environment. For atmospheric exposure, the effects of galvanic corrosion are normally limited to the interface between the dissimilar metals or to the immediate vicinity of the interface. Design features that trap and hold moisture in such areas should be avoided. The use of sealants to eliminate the possibility of moisture entering the interface between the dissimilar metals or the use of gaskets to prevent direct metal to metal contacts in such situations is often successful in mitigating galvanic corrosion in atmospheric environments. Penetration of moisture into metal to metal interfaces through seal welding or the use of metallurgically bonded bi-metallic transition joints should also be considered where appropriate. Fasteners of material dissimilar to the materials being fastened together are commonly a source of galvanic corrosion in atmospheric environments. Through judicious selection of fastener materials, galvanic corrosion can often be reduced to acceptable levels and may often be further reduced through the use of sealants or insulating gaskets.

Where the suspected galvanic couple is to be submerged, galvanic corrosion is likely to occur not only at the interface between the dissimilar metals but can be expected to occur at some distance from contact site. In this case, complete electrical isolation of the couple is often the best means of preventing galvanic attack. In many cases, particularly where there are large numbers of connections or where mechanical or electrical considerations make isolation impractical, control of relative surface areas through the application of protective coatings or the use of cathodic protection to mitigate the effects of galvanic corrosion may be applicable.

Many of the papers in this symposium as well as material presented in most texts on corrosion are directed to these and other aspects of the prediction and control of galvanic corrosion. Pludek [3] has devoted an entire text to the topic of design and corrosion control. The technology to control galvanic corrosion is well known to corrosion engineers. However, the question is not whether corrosion engineers understand galvanic corrosion and its control but whether this knowledge is used in the design process.

Integration of Galvanic Corrosion Control Technology into the Design Process

The corrosion engineer is, or should be, responsible for implementing effective corrosion control measures during the design process. There are two main avenues for integrating corrosion control technology into the design process. The first is the inclusion of a corrosion engineer in the design team. The second is the education of the engineers in the design team regarding corrosion. The optimum solution is often a combination of the two.

Inclusion of a corrosion engineer in the design process can be effective only if the corrosion engineer can communicate effectively with the other members of the design team and if the recommendations of the corrosion engineer are considered in an interactive manner throughout the entire design process. In order for the corrosion engineer to communicate effectively with other members of the design team it is necessary that the other members of the design team

know enough about corrosion to understand what the corrosion engineer is saying. This can often be accomplished through meetings between the corrosion engineer and a particular member of the design team on a case by case basis but can often be more effectively accomplished through a more structured group training program.

A training program of 10 to 20 h is often all that is required for most engineers to learn enough about corrosion technology to communicate effectively with a corrosion engineer. While such programs are available through a wide variety of technical societies and training groups, it is often more effective for the corrosion engineer to train the other members of the design team directly. This usually results in improved communication within the design team as a whole through the interaction between engineers with different fields of expertise. No matter how the training is accomplished, it is, or should be, the responsibility of the corrosion engineer to insure that all members of the design team can communicate effectively with regard to corrosion control.

Education of the engineers in the design team regarding corrosion control to the level that they can directly integrate corrosion technology into the design process is also an effective means of integrating corrosion control into the design process. In general, engineering education in the fields responsible for design does not emphasize corrosion control. In many schools, corrosion control is not even included in the program. In some schools, corrosion control is offered as an elective subject, and in a few progressive schools, corrosion is included in the required curriculum. Overall, it is safe to assume that the education of engineers regarding corrosion control is inadequate. How then can engineers learn about corrosion, and who is responsible for their education? There are many sources for the education of engineers regarding corrosion including technical societies, technical training experts, and academic institutions. A combination of "in-house" training by a staff corrosion engineer or consultant with more formal training in corrosion is often the most optimum method of developing the direct capability within the design team to integrate corrosion control into design.

A combination of training design team members and the inclusion of a corrosion engineer in the design process is often the best optimum method of integrating corrosion control technology into the design process. A well trained engineer will be able to identify most potential corrosion problems and solve many of them directly. The well trained design engineer will also be able to recognize those instances where further assistance from a corrosion engineer is required and will be able to make effective use of either a staff corrosion engineer or consultant in solving the problem as the description of both the problem and the possible solutions can be effectively communicated.

During the design process, the recommendations of the corrosion engineer should always be presented in a constructive manner. The corrosion engineer should take the approach that there are no "bad" designs, only ones that offer an opportunity for improvement. Major redesigns to incorporate corrosion control are always disruptive to the design process and can be avoided only if corrosion control is considered early on in the design process. As galvanic corrosion is often associated with interfaces between dissimilar metals, it often occurs because of inadequate consideration of metal combinations made during the assembly of an overall system from components that are themselves adequately designed. Thus, galvanic corrosion in particular must be considered in all stages of design including configuration management, which considers the final overall assembly and interfacing between major system components.

Conclusions

The technology to control galvanic corrosion is well developed but is often not effectively applied to engineering design. It is the professional responsibility of corrosion engineers to insure that corrosion control technology is effectively applied. Whatever must be accomplished in order to integrate the application of corrosion control technology into the design process,

whether it be training for the purpose of improving communications between design engineers and corrosion engineers or direct training of design engineers in corrosion control, is the responsibility of the corrosion engineer. If corrosion engineers fail to do what is necessary to insure that corrosion technology is effectively applied, who will?

References

- [1] Hack, H. P., "Galvanic Corrosion Prediction Using Long-Term Potentiostatic Polarization Curves," *Corrosion 83/73*, National Association of Corrosion Engineers, Houston, TX.
- [2] Scully, J. R. and Hack, H. P., "Galvanic Corrosion Prediction Using Long and Short Term Polarization Curves," *Corrosion 84/34*, National Association of Corrosion Engineers, Houston, TX.
- [3] Pludek, V. R., *Design and Corrosion Control*, MacMillan, London, 1977.

Controlling Galvanic Corrosion in Soils with Cathodic Protection

REFERENCE: Turner, J. M., “Controlling Galvanic Corrosion in Soils with Cathodic Protection,” *Galvanic Corrosion, ASTM STP 978*, H. P. Hack, Ed., American Society for Testing and Materials, Philadelphia, 1988, pp. 178–190.

ABSTRACT: Galvanic corrosion of buried external metallic surfaces can be controlled and mitigated by proper design, installation, and maintenance of the cathodic protection system. The design criteria typically used by corrosion engineers have been well documented and are supported by successful field applications. Design considerations discussed include selecting the appropriate type of cathodic protection system, electrolyte resistivity, coating quality, and types of anodes available.

KEY WORDS: cathodic protection, magnesium anodes, underground corrosion, underground corrosion control

Corrosion is all around us. It is a phenomenon that occurs naturally, but one that can often be controlled once understood. “Energy cannot be created or destroyed; it may be transformed from one form into another, but the total amount of energy never changes” [1]. Therefore, energy added to iron ores during processing into finished steel products is released when the finished metal product is placed back in the earth. The release of this energy is called corrosion. The relative position of some metals in terms of the energy required to convert an ore to the metallic state is listed in Table 1.

For the corrosion process to occur, four items must be present. These items are (1) an anode, (2) a cathode, (3) an electrolyte, and (4) a metallic path connecting the anode and cathode. ASTM Definitions of Terms Relating to Corrosion and Corrosion Testing (G 15) defines an anode as “the electrode of an electrolytic cell at which oxidation is the principal reaction. (Electrons flow away from the anode in the metallic path, or external circuit. It is the electrode where corrosion occurs and [usually where] metal ions enter solution).” Cathode is defined as “the electrode of an electrolytic cell at which reduction is the principal reaction. (Electrons flow toward the cathode in the [metallic path or] external circuit.)” An electrolyte is an ionic conducting substance in which the anode and cathode are immersed, and the metallic path is the external circuit that connects the anode to the cathode and permits the flow of electrons between the two. In general, if all four items are present the metal that required the most energy to produce will corrode at a faster rate than one that required less.

A galvanic series of metals has been established that lists the potential of several metals and alloys in seawater with reference to a saturated calomel half-cell reference electrode. A practical galvanic series was also established that lists metal potentials normally observed in water and neutral soils with reference to a copper/copper sulfate reference electrode. If a metallic path is installed between any two metals listed in the series and the two metals are placed in the same electrolyte, the metal with the more negative potential will be anodic and corrode more rapidly whereas the less negative metal will be cathodic and corrosion will be reduced or eliminated. For a corrosion reaction to occur, the reaction must be thermodynamically possible. The reaction

¹Project engineer, CORRPRO Companies, Inc., P.O. Box 72187, Roselle, IL 60172.

TABLE 1—Position of metal in terms of energy required to convert ore to a metallic state.

Most energy required	potassium magnesium aluminum zinc chromium iron nickel tin copper silver platinum gold
Least energy required	

will be spontaneous if the change in energy is from a higher state to lower state as stated by Gibb's free energy equation [3]

$$\Delta G = -nFE$$

where

- ΔG = the change in Gibb's free energy,
- n = number of equivalents,
- F = Faraday's constant, and
- E = cell EMF, V.

The spontaneity of the reaction can be determined as shown in Table 2 [3]. The cell EMF is determined using the Nernst equation; however, the metal ion concentration is difficult to determine, in practical situations, especially when surface oxide films are formed. The Nernst equation states [3]

$$E = E^\circ + (RT/nF)\ln Q$$

where

- E° = EMF under standard conditions,
- R = universal gas constant,
- n = number of equivalents,
- T = temperature, K,
- F = Faraday's constant, and
- Q = quotient of metal ion concentrations.

The practical galvanic series is quite useful when selecting materials for new construction and when repairing an existing structure. A typical example is the repair of an old ferrous metal pipe

TABLE 2—Chart for determination of spontaneity of reaction.

ΔG	E	Cell Reaction
-	+	spontaneous
+	-	nonspontaneous
0	0	at equilibrium

by installing a new ferrous metal pipe section. A metallic connection between the buried new and old pipes creates a galvanic corrosion cell in which the new pipe will be the corroding anode, the old pipe will be the protected cathode, the metallic path is the pipe itself, and the electrolyte is the soil. Galvanic corrosion of the new pipe will proceed. A more obvious problem is created when copper pipe or tubing is directly connected to steel. The steel will corrode to protect the copper (Table 3) [4]. In addition to bimetallic couples and the connection of old ferrous pipe to new ferrous pipe, corrosion cells can also be caused by dissimilar soil conditions. These dissimilar conditions could be created by mixtures of different soils, differences in oxygen concentration, soil pH, or partial encasement in concrete. Galvanic corrosion will also occur any time a refined metal is placed in an electrolyte. The time to corrosion failure will vary according to the metal and the environment. These facts have been established and are recognized by the engineering community.

Title 49 of the *Code of Federal Regulations*, Part 195, Subpart F requires that, "After March 31, 1973, no operator may operate a [natural gas] pipeline that has an external surface coating material, unless that pipeline is cathodically protected" [5]. Also, "Each operator shall, at intervals not exceeding 15 months, but at least once each calendar year, conduct tests on each underground facility in its pipeline systems that is under cathodic protection to determine whether the protection is adequate" [6].

Federal Law (P.L.) 98-616 Hazardous and Solid Waste Amendment of 1984 requires that, "After May 7, 1985, no person may install an underground storage tank unless: (1) it will prevent releases resulting from corrosion or structural failure for the life of the tank; (2) it is cathodically protected against corrosion, constructed of non-corrosive material, steel clad with non-corrosive materials, or its equivalent; and (3) the materials of the tank or liner are compatible with the stored substances" [7]. Galvanic corrosion of buried steel tanks will with time result in perforation of the tank wall. Once perforated, the stored product is free to leak into the surrounding environment polluting ground water and soil. Corrosion failure is costly; the public liability risks are even greater. These leaks can be virtually eliminated if a properly designed cathodic protection system is installed and maintained.

The Federal Highway Administration has taken an aggressive stance in promoting cathodic protection as an economical means for mitigating galvanic corrosion of reinforcing steel in chloride contaminated bridge decks [8]. Many states, including Pennsylvania, New York,

TABLE 3—*Practical galvanic series typical potential normally observed in neutral soils and water, measured with respect to copper/copper sulfate reference electrode.*

Metal	Volts
Commercially pure magnesium	-1.75
Magnesium alloy (6% Al, 3% Zn, 0.15% Mn)	-1.6
Zinc	-1.1
Aluminum alloy (5% zinc)	-1.05
Commercially pure aluminum	-0.8
Mild steel (clean and shiny)	-0.5 to -0.8
Mild steel (rusty)	-0.2 to -0.5
Cast iron (not graphitized)	-0.5
Lead	-0.5
Mild steel in concrete	-0.2
Copper, brass, bronze	-0.2
High silicon cast iron	-0.2
Mill scale on steel	-0.2
Carbon, graphite, coke	+0.3

Missouri, and Florida, have installed cathodic protection systems on bridge decks that were still structurally sound but were deteriorating due to galvanic corrosion of the reinforcing steel.

Chicago's O'Hare International Airport, currently undergoing a billion dollar expansion program, has made cathodic protection or corrosion monitoring, or both, of all newly installed underground metallic structures a requirement. The decision was one of economics based on past history of utility failures caused by galvanic and electrolytic corrosion.

Some Design Considerations

If corrosion will have a detrimental impact on the environment, result in increased or unacceptable maintenance/repair costs, or impact the structural stability, the question becomes, "How do we prevent corrosion from occurring or at least slow it down to an acceptable rate?" A properly designed and maintained cathodic protection system can extend indefinitely the life of a facility. When designing a cathodic protection system several questions need to be answered. Among the questions are the following:

1. What is the structure to be protected?
2. What are the soil characteristics? (resistivity, pH, chemistry, moisture content, and so forth)
3. What is the intended life of the structure and desired life of the cathodic protection system?
4. What other facilities are in the area? Are the other facilities cathodically protected? If so, what type of system is being used?
5. Is the structure coated with a high quality coating?
6. How much current is required to achieve cathodic protection?
7. What type of system should be installed? Galvanic or impressed? If an impressed current system is required, is AC power readily available?
8. What time of year will construction take place?
9. What would be the environmental impact of a corrosion failure?
10. If the structure is existing, how was it installed?
11. Is the structure electrically continuous?
12. What provisions should be made to facilitate future testing?

To provide the best suited cathodic protection system, the design engineer needs to determine the clients' expectations and needs. It can then be determined how the needs can best be met.

Designing Cathodic Protection Systems

Whether designing a cathodic protection system for new or existing structures, certain tests must be conducted. The results of these tests will determine which system, impressed or galvanic, is the best engineering choice. If the system is being designed for an existing structure, the first test will be to determine the amount of DC current required to achieve protection. This test is commonly called a current requirement test.

Conducting a current requirement test requires several pieces of equipment. These items include the following:

- temporary anode
- direct current (DC) source current interrupter
- hunts
- high impedance voltmeter
- reference electrode
- wire reel
- cable

The intent of the test is to actually install a temporary impressed current cathodic protection system, interrupt the current, and record both the structure to electrolyte potential at each test point when the current is on and off. This will provide information pertaining to electrical continuity and discontinuity and approximate current distribution. Polarization tests are run to determine how readily the structure can be polarized, and to determine how much current will be required to achieve cathodic protection. The results of the polarization tests and past experience with similar structures will provide the designer with the information necessary to design an appropriate protection system.

If the system is being designed for a new structure, several items in addition to those already stated must be known:

1. Dimensions of the structure to be protected.
2. Type of coating.
3. Location of structure with reference to other structures.

This information will assist the designer in determining the approximate current required. Table 4 [9] lists some approximate numbers.

Soil Resistivity

The next test to be conducted is determining the soil resistivity in the area where the cathodic protection anodes are to be placed. Soil resistivity is typically measured according to ASTM Method for Field Measurement of Soil Resistivity Using the Werner Four-Electrode Method (G 57). Soil resistivity is a determining factor when calculating the current output of a galvanic anode or the voltage required for an impressed current cathodic protection system. After the anode type, size, and shape is selected the resistance of the anode to earth is calculated. If the resistance is too high, another size and shape may be required.

To determine the current output of a single anode installed vertically, the anode resistance-to-earth is calculated using Dwight's equation [10]

$$R_v = \frac{(0.00521)(SR)}{L} [2.3 \log(8L/d) - 1]$$

TABLE 4—Approximate current requirements for cathodic protection of steel.

Environment	mA/ft ²	mA/m ²
Sulfuric acid pickle (hot)	35 000	380 000
Seawater		
Cook Inlet	35 to 40	380 to 430
North Sea	8 to 15	90 to 160
Persian Gulf	7 to 10	80 to 110
U.S. West Coast	7 to 8	80 to 90
Gulf of Mexico	5 to 6	50 to 60
Indonesia	5 to 6	50 to 60
Soil	1 to 3	10 to 30
Poorly coated steel in soil or water	0.1	1.0
Well coated steel in soil or water	0.003	0.03
Very well coated steel in soil or water	0.0003 or less	0.003 or less

where

- R_v = resistance of vertical anode to earth, Ω ,
- SR = resistivity of electrolyte (or earth), $\Omega\text{-cm}$,
- L = length of anode, ft, and
- d = diameter of anode, ft.

Similar calculations are used for determining the resistance of multiple anodes and anodes installed horizontally.

For galvanic anode systems the theoretical current output for each individual anode will be

$$I = \frac{\text{open circuit anode potential} - \text{expected polarized potential}}{\text{anode resistance } (\Omega)}$$

The total resistance is derived by adding together total anode-to-earth resistance, wire resistance, resistance to earth of the pipeline, and back voltage between the anodes and pipe. The current required is determined by conducting current requirement tests, polarization tests, or by calculating the total exposed surface area. The theoretical voltage required is calculated using Ohm's Law ($E = IR$).

Soil Chemistry

The design life of a cathodic protection system is dependent on the amount of current driven from the anode, and the size and composition of the anode. As a structure polarizes, less current is required from the anode to maintain the polarized potentials, and the anode life will be increased. Electrolyte chemistry will often determine the ease with which a structure can be polarized. For this reason, an analysis for substances, such as chlorides, sulfides, moisture content, pH, and soil moisture hardness, are often suggested.

Electrolyte chemistry will also dictate which anode material to use. Zinc anodes are often used in low resistivity soils and marine environments. Aluminum anodes are used in seawater, but do not operate well in soil. Magnesium anodes are used in both high and low resistivity soils. There is no anode that is suitable for all applications. The sacrificial anode must be chosen with regard to its performance characteristics in a particular environment.

Impressed Current Systems for Piping Systems in Soils

Selecting an impressed current cathodic protection system leads us to other decisions:

1. What type of anode material should be used?
2. How long should the anode material last?
3. What type of lead wire connection should be used?
4. Should the anodes be prepackaged or bare?
5. Is special insulation required for the lead wire?
6. What type of rectifier should be used?
7. What type of groundbed geometry should be used? Distributed, remote (conventional), or deep?
8. Where should the groundbed be located? Is there sufficient right-of-way?
9. Does the possibility of stray current interference exist?
10. What type of test points and monitoring devices are needed?

Each question results in its own investigation and analysis in order to provide the most economical and practical design.

Impressed Current Anodes

There are several types of impressed current anodes available to the designer. The anode selection must be based on the desired life of the system and the manner in which the anode will be installed. The most common impressed current anodes are graphite and high silicon cast iron. These anodes can be treated or untreated, and the lead wire can be connected to the longitudinal center. The anode lead wire connection is a critical factor when determining the useful anode life. More recent entries into the impressed current anode are the precious metal oxide coated rod and wire. These anodes are specified and purchased according to the desired current output and life of the anodes.

Lead Wire Insulation

All lead wire used to connect the anode to the rectifier must be installed to prevent damage to the insulation. Any nick in the cable insulation that exposes the wire core will allow current to discharge from the cable, thus causing premature failure of the cable. Once the cable is severed, one or more anodes (depending on where the insulation damage occurred) will no longer be a part of the system. This has some rather obvious ramifications.

The typical wire and cable insulation specified for cathodic protection installations is a high molecular weight polyethylene (HMWPE) made to ASTM Specification for Polyethylene Plastics Molding and Extrusion Materials (D 1248). In severe environments, insulations, such as polyvinylidene fluorides or fluoropolymers, may be necessary.

Backfill

Special backfill material is used around impressed current anodes placed in soil. This material is low resistivity, in the range of 50.0 to 0.1 Ω -cm, and consists of metallurgical or calcined petroleum coke. The particle size can range from dust to $\frac{3}{4}$ in. (10 m) and larger. The backfill material lowers the anode-to-earth resistance and provides a homogenous environment for the anode. This permits uniform current distribution from the anode surface. The ionic energy transfer between an impressed current anode and earth theoretically takes place at the anode backfill earth interface and thus extends the anode life.

Impressed current anodes can be purchased in prepackaged canisters. The canister is fabricated from steel of sufficient length and diameter to contain the anode and required amount of coke backfill. The ends of the canister are sealed with wooden or plastic plugs. The anode lead wire is extended through the plug at one end for connection to the rectifier or a header cable. If the installation procedure does not specify a prepackaged anode, the backfill material must be purchased separately and installed around the anode at the job site.

Rectifiers

Every impressed current cathodic protection system requires an external direct current power source to force current to flow from the anodes to the structure being protected. This direct current power source is provided by a rectifier.

Rectifiers are typically powered by AC (some installations require solar power sources, wind generators, thermoelectric units, and so forth, because of availability of an AC power source.) The alternating current is rectified to direct current by diodes that allow current to flow in only one direction.

Rectifiers can be purchased to meet a multitude of design parameters. They can be ordered with automatic potential control, constant voltage, constant current, solid state with no tap settings, or standard tap settings to adjust the output. These can also be supplied with a variety of optional features, such as lightning protection for the AC input or DC output, or both,

indicator lights, efficiency filters, and slide out racks. Rectifiers can be air cooled, oil cooled, oil cooled-explosion proof, fan air cooled, or forced oil cooled. Transformers, AC input, and the type of cabinet to house the rectifier must also be selected.

Because of the wide range of available components, rectifiers are normally custom built.

Groundbed Geometry

A groundbed in cathodic protection jargon refers to the anode(s) when they are placed in the earth relative to the structure being protected. Anodes can be distributed (Fig. 1), concentrated (Fig. 2), or a point source (Fig. 3). A point source is often termed a deep anode system. Each of the three systems have advantages and disadvantages, but the geometry selected is often dictated by existing conditions.

A distributed anode system is most useful when protecting large surface areas, which are either poorly coated or bare, where shielding caused by congestion may be a problem, or where sufficient right-of-way is not available to accommodate a concentrated groundbed. Also a distributed system is more difficult to maintain when installed in areas where future construction could damage the anode collector cable. The collector cable, sometimes referred to as a header cable, is used to connect the anode lead wires to a main cable, which is then terminated at the rectifier positive connection (Fig. 1).

A concentrated groundbed is most useful on well coated structures regardless of the amount of surface area requiring protection. The cost of installing this type of system would probably be less than the equivalent distributed system. Damage resulting from future construction would be minimized since the anode header cable would be remote from the structure (Fig. 2).

A point source or deep anode groundbed has many advantages over either the distributed or conventional groundbed designs. The system can be installed in areas where open trenches and excavations must be kept to a minimum and right-of-way is restricted. The location of the system can be close to the structure being protected when minimizing the probability of future damage is desirable. One disadvantage of this type system is its higher installation cost compared to that of concentrated groundbeds (Fig. 3).

Galvanic Anode Systems

A variety of galvanic anodes are available to the engineer for use in a galvanic anode cathodic protection system. Selection of the appropriate anode is important in order to provide a system that will meet the specified design life and protection levels. In addition to the questions posed under *Design Considerations*, the following questions must also be investigated:

1. What type of anode material should be used?
2. What size anode will give the desired system life?

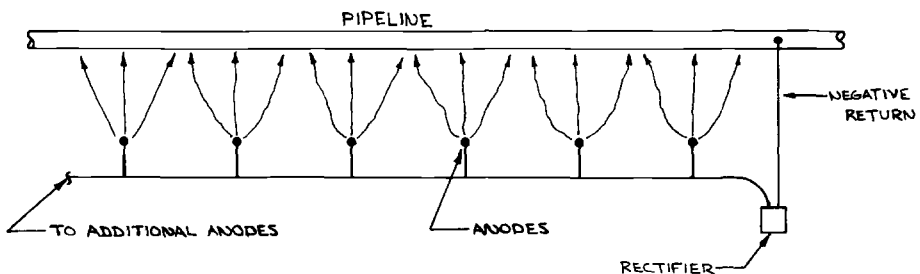


FIG. 1—Distributed groundbed.

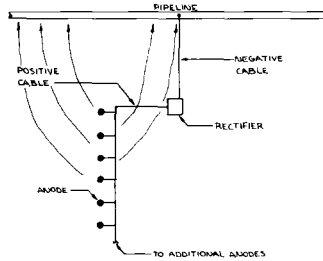


FIG. 2—Concentrated groundbed.

3. What geometry is best suited for the system?
4. What electrical isolation is required to assure a properly functioning design?
5. What type of monitoring devices and test points are necessary?

Galvanic Anode Material

For steel and iron structures, the choices for galvanic anodes are more limited than for the impressed anodes. There are three types of galvanic anodes: magnesium, zinc, and aluminum. Magnesium anodes are by far the most widely used galvanic anode in soil. Zinc is used in low resistivity soils and in seawater, whereas aluminum is used primarily in seawater or brackish water.

Magnesium anodes are available in several grades, but those typically used are the high potential and the H-1 alloy. One of the significant differences between the two anodes is their solution potential. The potentials as referenced to a copper/copper sulfate reference electrode are approximately -1.7 and -1.5 V, respectively. The difference in potential between the

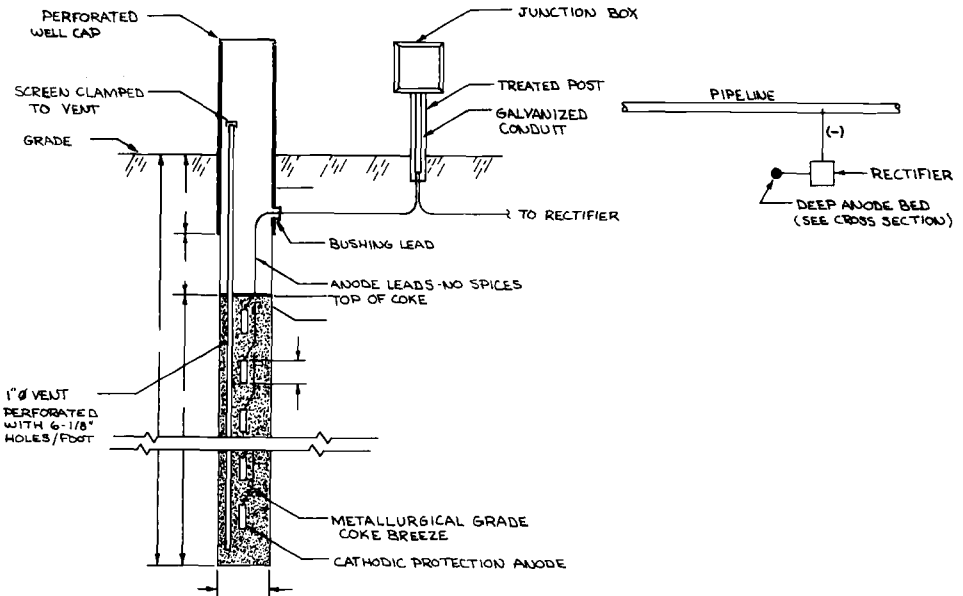


FIG. 3—Point source groundbed.

structure being protected and the anode, plus the soil resistivity adjacent to the anode, determines the amount of current available from the anode for protection.

Zinc anodes are more efficient than those made of magnesium, however zinc's driving voltage is $\frac{1}{3}$ that of the high potential magnesium. Because of this, zinc is primarily used in low resistivity soils.

Aluminum anodes will passivate if buried in soil. Therefore, they are used only in seawater and brackish environments.

Geometry

Galvanic anodes are either individually connected to the pipe being protected or placed on a collector (header) cable, which is then connected directly to the pipe or through a test station. The lead wire insulation on a galvanic anode system does not require the strength and durability of the impressed current anodes. This is because any nick in the galvanic anode lead wire insulation will normally be protected by the anode provided that the protective current reaches the exposed conductor. In practice, care should still be taken to preserve the integrity of the insulation.

Monitoring

Regardless of the type of protection system selected, it is important to provide a means for measuring performance. This is accomplished by installing test stations. A test station can be used to monitor several facets of a cathodic protection system. Some examples where test stations prove beneficial are as follows:

1. To monitor the actual current output of a galvanic anode and to provide means for interrupting their output during testing of the system effectiveness.
2. To monitor the potential of the structure in an area that is not accessible to a portable reference electrode.
3. At crossings between pipelines protected by different cathodic protection systems.
4. To provide periodic connections to a structure, so that potential measurements can be made without needing to use hundreds or thousands of feet of wire.
5. At buried insulators.

Test stations come in a variety of sizes and shapes. The type of test station specified will need to endure the environment in which it is placed.

Installation Procedures

Once the cathodic protection system design has been accepted by the client, the system needs to be installed. The need for qualified technical supervision or inspection services during construction cannot be over emphasized. Many times a cathodic protection system installed without such supervision or inspection requires extensive post installation troubleshooting. The hours and money spent investigating and then correcting a malfunctioning system will often far exceed the time that would have been spent supervising the installation. Qualified technical supervision during installation will help assure a properly functioning cathodic protection system.

Scope of Work

The inspector will require certain information to assure that the system is being installed according to the design parameters. Among the required information will be the design report.

The design report should contain information on the anticipated anode backfill material (in this context, backfill refers to the soil in which the packaged anode will be buried), the structures to be protected and structures to be isolated, the expected coating quality, and the theoretical current required per square foot or pertinent current requirement calculations. With this information, the inspector or supervisor knows precisely what to expect in terms of system performance. He will also know when field conditions are encountered that were not anticipated during the design.

Galvanic Anode Installation

During new construction, galvanic anodes are often selected to provide the cathodic protection. The earth in which the packaged anode is placed will determine the amount of current available from the anode. Galvanic anodes, installed in an electrolyte with higher resistivity than anticipated, will not be able to provide the amount of current required to meet the cathodic protection criteria. This situation is typically encountered in areas that are undercut or where footings are installed before pipe installations.

Sacrificial anodes must be placed in an electrolyte whose resistivity is within the design tolerances.

Impressed Current Anodes

Conditions surrounding the installation of impressed current anodes are similar to those of galvanic anodes. The design will be based on the impressed current anodes being placed in a certain resistivity environment, but because the current from impressed current anodes can be adjusted there is more flexibility. A significant variation in anticipated backfill will, however, affect the rectifier voltage output.

Electrical Isolation

Electrical isolation of the structure being protected is often a critical aspect of a cathodic protection installation. Cathodic protection systems are typically designed to protect a finite surface area. This surface area takes into account the quality of the coating and maintaining electrical isolation where needed. Failure to assure electrical isolation will increase the amount of surface area requiring cathodic protection. Galvanic anodes will typically not be able to provide the additional protective current required. Impressed current systems may have sufficient capacity to protect the additional surface area, but the increased current output of the system will have an impact of the system life. Examples of shorted conditions are as follows:

1. Where reinforcing steel contacts underfloor piping risers.
2. Where a cased pipe comes in metallic contact with the casing.
3. Where above grade piping is connected to an electrical ground.
4. Where pipe penetrates walls or manholes and comes in contact with the steel sleeve or reinforcing steel.
5. At crossings between buried pipelines (often referred to as foreign line crossings).

The possibilities are endless, but if the system is being monitored during installation, the existence of such conditions can be detected and corrected before they become a serious problem.

Electrical Continuity

Just as electrical isolation is a necessity between protected and unprotected structures, it is usually imperative that the facility being designed for cathodic protection be electrically contin-

uous throughout. Mechanical connections, bell and spigot joints, sections of buried pipes, or other buried metallic structures must be electrically continuous with each other if they are to be protected. Electrical continuity is accomplished by thermite brazing an insulated conductor between the structures and across each mechanical or bell and spigot joint. Failure to assure continuity will result in pipe not being cathodically protected or pipe that will suffer accelerated corrosion from electrolytic corrosion.

When designing impressed current systems, close attention must be paid to the bond resistance across joints and between structures. Insufficiently sized bond cables can have the same effect as an electrical discontinuity.

During the installation, continuity tests must be conducted as sections of pipe are laid and backfilled. Continuity tests during installation will assure that all improperly bonded joints are located before job completion.

Discontinuities can be located after the installation is complete, but the task is very time consuming and expensive, especially if the pipe is under concrete. Having heavy equipment return to a job site for excavation of open bond wires is quite frustrating, costly, and unnecessary.

Coating Inspection

During transportation and handling, pipe coating often becomes damaged. Coating quality is an important parameter of the cathodic protection design and should be specified in the contract documents. If the contractor is unfamiliar with the coating material, the manufacturer of the field coating should be required to visit the job site and instruct the workers in the proper procedure for coating joints and repairing coating damage. Valves and other irregular fittings are typically coated with a brush applied mastic or sprayed with an epoxy coating. The need for proper surface preparation must be emphasized in order to assure proper bonding of the coating to the pipe.

All coated pipe should be field tested to locate the areas where coating has been damaged during transport and handling. Coating flaws, also known as holidays, are detected using a high voltage, low amperage power source. The electrode of the instrument is passed over the pipe surface and emits an audible signal and visual spark when it passes over a coating flaw (holiday). The damaged area must be marked and properly repaired.

Monitoring Test Stations

Test stations are installed to facilitate future testing of the cathodic protection system. Some uses for test stations are as follows:

1. To measure the amount of current drain from one structure to the next.
2. To determine the effectiveness of isolating flanges or dielectric unions.
3. To determine if a cased pipeline is shorted to the casing.
4. To provide an electrical connection to the pipe for measuring pipe-to-soil potentials.

Test stations are an important part of a cathodic protection installation, and care must be taken to assure that the lead wires are not damaged during construction. This point cannot be overstressed when site construction is underway simultaneously with the cathodic protection installation. Test wires should be protected immediately after installation, otherwise they may require replacement.

Attention must also be given to the test station wiring. If permanent reference electrodes are installed, they must be terminated separately from all other wires. If a reference electrode is wired to an anode or the pipe it may be polarized to the extent that it no longer provides a useful means for testing. There are two basic types of test stations, flush mounted and post mounted. Each can be purchased with a variety of hardware.

Conclusion

Whether designing a cathodic protection system for an existing or new structure, several field tests must be conducted. The results of these tests and information obtained during conversations with the client will provide the designer with the information necessary to select the required cathodic protection system.

During installation, the system components must be protected from damage caused by construction activities. The testing agency must assure that all system components are installed where shown on the contract drawings, and as required in the specifications. Revisions to the structure layout may have a detrimental impact to the design of the cathodic protection system. A qualified testing agency will have the knowledge to modify the cathodic protection system to assure that the system meets or exceeds the specified criteria.

Summary

Corrosion is a phenomenon that occurs naturally to all metals not in their natural state. Corrosion can be mitigated by installing a properly designed cathodic protection system and maintaining the system. Tests must be conducted in order to determine which of the two cathodic protection systems, galvanic or impressed, is the best engineering choice.

With proper design, installation, and maintenance, a cathodic protection system will extend indefinitely the life of a buried or submerged metal structure.

References

- [1] Smith, A. W. and Cooper, J. N., *Elements of Physics*, McGraw-Hill, New York, 1972, p. 80.
- [2] LaQue, F. L., *NACE Basic Corrosion Course*, 11th printing, NACE, Houston, TX, 1970, pp. 1-2.
- [3] Castellan, G. W., *Physical Chemistry*, 2nd ed., Addison-Wesley Publishing Co., Reading, MA, 1971, p. 392.
- [4] Peabody, A. W., *Control of Pipeline Corrosion*, National Association of Corrosion Engineers, Houston, TX, 1967, p. 5.
- [5] *Code of Federal Regulations*, Title 49-Transportation, Part 195, Subpart F, 27 July 1981, p. 633.
- [6] *Code of Federal Regulations*, Title 49-Transportation, Part 195, Subpart F, 27 July 1981, p. 633.
- [7] Rowe, L. C., Ed., *Materials Performance*, Vol. 24, No. 6, June 1985, p. 65.
- [8] Barnhart, R. A., *FHWA Position of Cathodic Protection Systems*, HH0-31, Washington, DC, 23 April 1982.
- [9] Treseder, R. S., Ed., *NACE Corrosion Engineer's Reference Handbook*, National Association of Corrosion Engineers, Houston, TX, 1980, p. 61.
- [10] Peabody, A. W., *Control of Pipeline Corrosion*, National Association of Corrosion Engineers, Houston, TX, 1967, p. 5.

Environments

The Effect of Soil Resistivity and Soil Temperature on the Corrosion of Galvanically Coupled Metals in Soil

REFERENCE: Escalante, E., "The Effect of Soil Resistivity and Soil Temperature on the Corrosion of Galvanically Coupled Metals in Soil," *Galvanic Corrosion, ASTM STP 978*, H. P. Hack, Ed., American Society for Testing and Materials, Philadelphia, pp. 193-202.

ABSTRACT: Galvanic corrosion current measurements carried out on stressed Type 301 stainless steel coupled to zinc at six underground test sites over a period of four years indicate that the galvanic current is controlled by soil resistivity or oxygen availability in the soil. In well aerated soils, resistivity plays a dominant role, but in poorly aerated soils, oxygen controls the corrosion process. Furthermore, at a certain depth, approximately 1 m, soil resistivity is strongly influenced by soil temperature and only slightly affected by soil moisture. Finally, Type 301 stainless steel in a half-hard or full-hard condition is susceptible to hydrogen embrittlement failure in soil when exposed to potentials capable of causing hydrogen evolution.

KEY WORDS: corrosion, soils, galvanic corrosion, hydrogen embrittlement, metallic corrosion, soil resistivity, soil temperature

It is recognized that the resistivity of a soil plays a critical role in the corrosion performance of a metal in an underground environment [1]. The effects of polarization resistance at the metal surface and electrolyte media resistance on galvanic currents have been described [2]. The various factors that affect soil corrosivity have also been discussed in some detail [3]. Many of these discussions include reference to the role of oxygen; however, only recently has a field study shown the effects of oxygen diffusion on the corrosion of metals in soil [4].

This study is part of a program described previously, which reported on the corrosion behavior of a variety of stainless steels with various treatments and conditions of exposure at six underground test sites [5,6]. The results of galvanically coupling several stressed stainless steels to iron, zinc, and magnesium in these soil environments have also been reported before [7]. However, the effect of the soil environment on these galvanically coupled specimens has not been described previously. This report will be limited to a description of the results of Type 301 stainless steel coupled to zinc, but the effects described apply to all the galvanically coupled stainless steels in this study. The investigation, carried out over a period of four years at six underground test sites included examination of the behavior of two galvanically coupled and two uncoupled stainless steels for every system at each site. Every time that corrosion measurements were made, the soil environment was characterized by measurements of soil resistivity, soil temperature, and soil pH in the vicinity of the specimens.

Material and Environment

Austenitic Type 301 stainless steel was exposed in both a half-hard (HH) and a full-hard (FH) condition. Table 1 lists the materials and their chemical composition, and Table 2 is a summary

¹Metallurgist, Corrosion Group, National Bureau of Standards, Gaithersburg, MD 20899.

TABLE 1—*Chemical composition of stainless steels.*

Component	Material, wt%	
	301 HH	301 FH
Cr	17.43	16.98
Ni	7.14	7.23
C	0.10	0.13
Si	0.34	0.54
S	0.016	0.013
P	0.030	0.020
Mn	1.02	0.86
Mo	0.22	...

of the mechanical properties and applied stresses. The high strength of Type 301 is obtained through the formation of martensite during cold rolling. The stainless steel specimens were galvanically coupled to a 30-cm-long zinc bar extruded over a 0.3-cm-diameter iron core. The diagonal dimensions of the diamond cross-sectional bar were 1.5 by 2 cm.

The specimens were buried at six underground test sites in the United States, all of which are located on federally owned land. The advantages of using such grounds is that the sites are accessible and use of the land is closely controlled. This second factor is important for long-term studies of this kind. Soil properties at the six test sites are given in Table 3, and a brief description of each of the sites follows.

Site A

Sagemoor sandy loam is located in an arid (annual precipitation less than 25 cm/year) section of the state of Washington. It is an alkaline soil with a normally high resistivity of over 10 000 Ω -cm. When water saturated however, its resistivity drops to very low values.

Site B

Hagerstown loam is an acid soil typical of those found in large areas of the eastern United States. It is a permeable soil supporting an abundant growth of vegetation. Average annual precipitation is 110 cm.

Site C

This is a clay pit with very low permeability and is located within 100 m of the ocean. The area has an average precipitation of 140 cm/year and is the most acid of the six sites.

TABLE 2—*Mechanical properties and applied stresses.*^a

Material	Tensile Strength, ksi	Yield Strength, ksi	% Elongation 5.08 cm Gage	Hardness Rockwell C	Applied Stress	
					% Yield	ksi
301 HH	162	116	25	34	36	42
301 FH	203	175	9	44	22	38

^aTo convert from ksi to MPa, multiply by 6.9.

TABLE 3—*Properties of soils.*

Site	Soil	Location	Range of Resistivity, Ω -cm	Average Resistivity, Ω -cm	pH
A	Sage Moor sandy loam	Toppenish, WA	400	...	8.8
B	Hagerstown loam	Loch Raven, MD	12 600 to 37 300	32 990	5.4 + 0.27
C	clay	Cape May, NJ	400 to 1 150	660	4.3 + 0.21
D	Lakewood sand	Wildwood, NJ	13 800 to 57 500	33 550	5.6 + 0.35
E	coastal sand	Wildwood, NJ	13 200 to 49 500	23 780	7.1 + 0.32
G	tidal marsh	Patuxent, MD	400 to 15 500	4 520	5.6 + 0.77

Site D

Lakewood sand is a white loose sand located on the land-side of sand dunes about 4000 m from the ocean. The site supports a lush growth of beach grasses and brush with an average precipitation of 120 cm/year.

Site E

This coastal sand site is within 60 m of the ocean and is a typical white beach sand. It is on the ocean-side of the sand dunes and is occasionally under water.

Site G

This tidal marsh is located in an estuary along a creek that empties into the Chesapeake Bay near the southern tip of Maryland. The area supports a very lush growth of plants and a high concentration of soil bacteria. Precipitation averages 125 cm/year in this area.

Procedure*Specimen Preparation*

The stainless steel specimens were sheared from 0.162-cm-thick sheet. Each specimen was stamped with a number identifying the material, burial site, and specimen number. Those coupled to the zinc electrodes were 2.54 by 30.5 cm with the rolling direction parallel to the long axis of the specimen. An oblong hole, 0.63 by 1.3 cm, was punched near each end to allow bolting of the specimen in a U bend configuration. A 0.24-cm hole was drilled near one corner for electrical attachment of an electrical conductor providing contact to the specimen. The specimens were then preformed around a 3.2-cm-diameter mandrel to facilitate final stressing and bolting. Before final stressing, the specimens were passivated in a 30% by volume solution of nitric acid at 60°C for 25 min, rinsed, and dried. A 14 gage insulated copper wire was then soldered to the small hole by the corner of the specimen, and the solder area coated with coal tar epoxy. Finally, the specimens were stressed to the applied load identified in Table 2. Specimens that were stressed but not galvanically coupled to zinc were treated in the same manner as those that were galvanically coupled.

Electrical contact to the zinc was made by soldering 14 gage insulated copper wire to the iron wire core and coating the solder joint. All wires were carefully labeled for identification.

Exposure

At each test site, two specimens from each system were buried approximately 30 cm apart in a trench 0.8 m deep and 0.6 m wide. Each stainless steel specimen to be galvanically coupled was placed in the trench approximately 30 cm from its corresponding zinc electrode with the electrical leads, carefully labeled, extending above ground level. These wires were attached to wood posts before backfilling. After backfilling, the electrical leads were connected to terminal strips on the post, and the couples were then electrically connected together at the terminal strip.

Electrical Measurements

The galvanic current of each couple was measured every few months using a zero-impedance ammeter circuit [7]. The measurement was made by first connecting the ammeter to the two leads of the coupled specimens and then removing the shorting connection between the couple causing the current to flow through the ammeter circuit. This current measurement was useful in that it provided a measure of the galvanic corrosion current and the direction of current flow. The direction of current flow indicated which of the two electrodes was acting as a cathode or anode.

Soil Measurements

The soil was characterized each time galvanic current measurements were made at all sites except for Site A. This characterization took the form of soil resistivity measurements using the Wenner four-pin method [8], soil temperature measurements at the depth of the specimens using a thermocouple sheathed in a stainless steel tube, and pH measurements at the depth of the specimens.

Soil resistivity measurements were made using a commercial soil resistivity meter and following the ASTM Method for Field Measurement of Soil Resistivity Using the Wenner Four-Electrode Method (G 57). Four metal pins are inserted into the soil surface in line 1 m apart. The instrument is used to apply a 100-Hz alternating square wave current to the outer pins and measure the voltage drop across the inner pins. Soil resistivity was then calculated taking into consideration the pin spacing and the measured soil resistance in the manner described by Wenner.

The soil temperature was measured using a thermocouple at the end of a 0.63-cm-diameter stainless steel probe 1 m long. The probe was inserted to the depth of the specimens, and the temperature was measured.

Soil pH was measured at the sites using the ASTM Test Method for pH of Soil for Use in Corrosion Testing (G 51). Briefly, the sequence is as follows. First, an auger is used to bore a hole into the soil to the depth of the specimens. A probe, holding the electrode for measuring the pH (glass electrode) and a calomel electrode, is lowered into the boring, and the pH of the soil is measured. Temperature compensation of the equipment is set to the temperature of the soil.

Results and Discussion

The interaction of the various factors determining the extent of galvanic corrosion underground is certainly complex, and in this study an attempt is made at consolidating the observations made over a period of four years. It is known that the potential between the galvanically coupled electrodes provides the driving force to the couple and is directly related to the magnitude of the galvanic current and its direction of flow. The resistance of the soil between the coupled electrodes limits the amount of current that the driving potential can produce in accordance to Ohms law and is the reason that the average soil resistivity at a given site is an

important parameter. One might guess that changes in soil resistivity from day to day would affect the magnitude of the galvanic current. The results of this study indicate that this is generally not the case. The data reveal that soil temperature plays a very important role and affects soil resistivity and oxygen concentration in a manner that tends to inhibit the magnitude of their effect on the galvanic current. Thus, as the soil temperature increases, the resistivity of the soil decreases, which tends to favor an increase in galvanic current. However, an increasing temperature also causes the solubility of oxygen in the soil to decrease, resulting in a decrease in galvanic current. Since oxygen controls the cathodic reaction, its availability as a soluble specimen is critical to the rate of the corrosion reaction. The net effect of these competing processes, oxygen concentration versus soil resistivity, on the galvanic current is thus reduced. Indeed, the data reveal that changes in soil resistivity and soil temperature, with one exception, have practically no effect on galvanic current. Oxygen concentration was not measured, but it is assumed that temperature affects its solubility in soil in the same way that it affects its solubility in water. That is, there is an increase of approximately 25% in dissolved oxygen with each 10°C decrease in temperature from 25 to 0°C [9].

It must be emphasized that the average soil resistivity at a given site has a very important effect on the galvanic corrosion observed. In general the lower the soil resistivity, the higher the galvanic current. This is especially true immediately after burial when oxygen is available because of disturbance of the soil. During this period of oxygen availability, the galvanic current is controlled by the resistivity of the soil. Figure 1 illustrates a plot of this initial galvanic current as a function of soil resistivity between Type 301 stainless steel and zinc at five of the underground corrosion test sites. The initial galvanic current measurements were made within 48 h of burial of the specimens. An examination of this plot reveals a direct relationship between the soil resistivity and initial galvanic current over several decades of resistivity and current.

As oxygen is depleted over a period of months the galvanic currents, in general, decrease. This effect is shown in Fig. 2 where the galvanic current for the same system at five sites is shown as a function of time. Note that the galvanic current at Site E decreases the most rapidly. This is attributed to the fact that Site E is within a few metres of the ocean in saltwater saturated sand with the specimens below sea level. Oxygen concentration immediately after burial is high, but within a few months the concentration drops causing the galvanic current also to decrease. In contrast to this, the galvanic current for the couple at Site D increases with time. This is attrib-

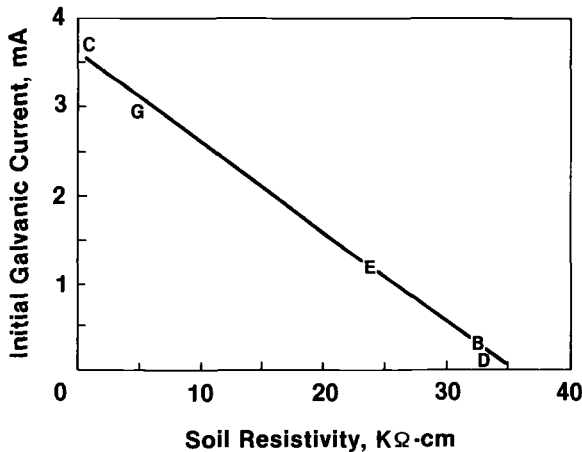


FIG. 1—A plot of initial galvanic current as a function of soil resistivity at five sites illustrating that when oxygen is available resistivity controls the galvanic current.

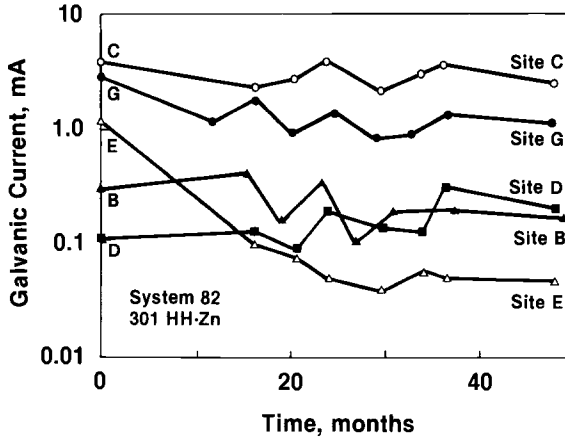


FIG. 2—A plot of galvanic current as a function of time at the five sites showing that soil resistivity at a given site determines the magnitude of the galvanic current. Oxygen depletion decreases galvanic current at all sites except Site D where exceptionally good aeration in the presence of chloride leads to increasing galvanic current.

uted to the exceptionally good aeration of this soil and the presence of chloride ions. This site is located within a few 100 m of the ocean with the specimens well above the waterline in sand where water is readily available. This figure also demonstrates the general observation that the low resistivity soils (Sites C and G) cause the highest galvanic currents, and the high resistivity soils (Sites B and D) cause low currents.

Though soil resistivity has an important effect on galvanic current from one site to another, as demonstrated, changes in soil resistivity within a site over a period of time have a minimal effect on this current. Figure 3 is a plot of soil temperature, soil resistivity, and galvanic current versus time at Site B. Note that changes in galvanic current are not related to changes in soil resistivity in any obvious way even though resistivity changes by almost an order of magnitude. Similarly, the galvanic current is independent of soil temperature. However, soil temperature has a dramatic effect on soil resistivity. Note that as the temperature increases, the resistivity decreases, and *visa versa*. These same comments can be made for the data from Site C as illustrated in Fig. 4.

The results obtained at Sites E and G, illustrated in Figs. 5 and 6, also show that changes in soil resistivity have no obvious effect on galvanic current. This is expected in these poorly aerated water saturated soils located within a few metres of water. Site E is a sandy beach bordering the Atlantic ocean, and Site G is part of an estuary where high tides bring in saltwater from the Atlantic ocean and low tides allow freshwater from an adjacent stream to flow to the ocean. In fact, both of these sites may be under water when tides are exceptionally high. The unusual feature of these two sites is that soil resistivity is not affected by soil temperature as observed at the other sites. It is not clear why this is so, but there is a strong possibility that the nature of the soil actually changes with time. That is, the chloride concentration of the soil may change as freshwater or saltwater is introduced to the sites. Sandy soil is particularly prone to leaching out of salts during a heavy rain resulting in an increased soil resistivity.

Site D is unlike the other sites in that the galvanic current for couples at this location does show a relationship to changes in soil resistivity with time, as might be expected in this well aerated sand and as illustrated in Fig. 7. Corrosion at this site is not limited by oxygen availability but by soil resistivity. Over the four years of exposure, the resistivity of this soil gradually decreased with a corresponding increase in galvanic current. Thus, of the five sites described only at this well aerated site were galvanic current controlled by soil resistivity. Galvanic cur-

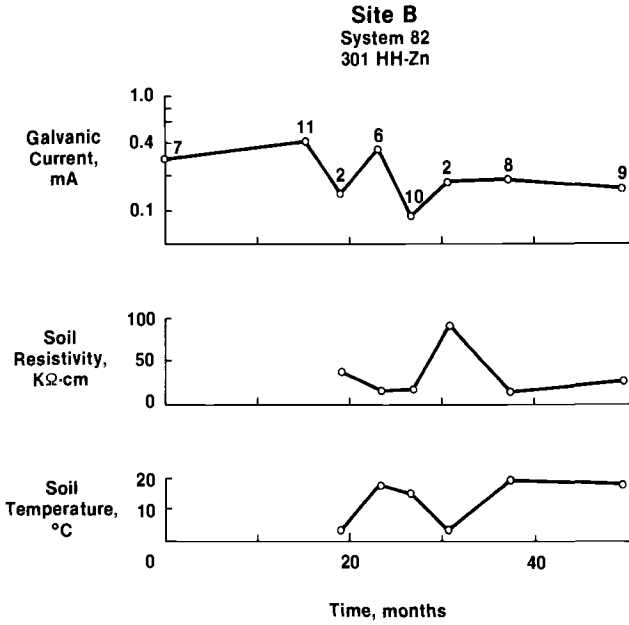


FIG. 3—Galvanic current, soil resistivity, and soil temperature as a function of time at Site B.

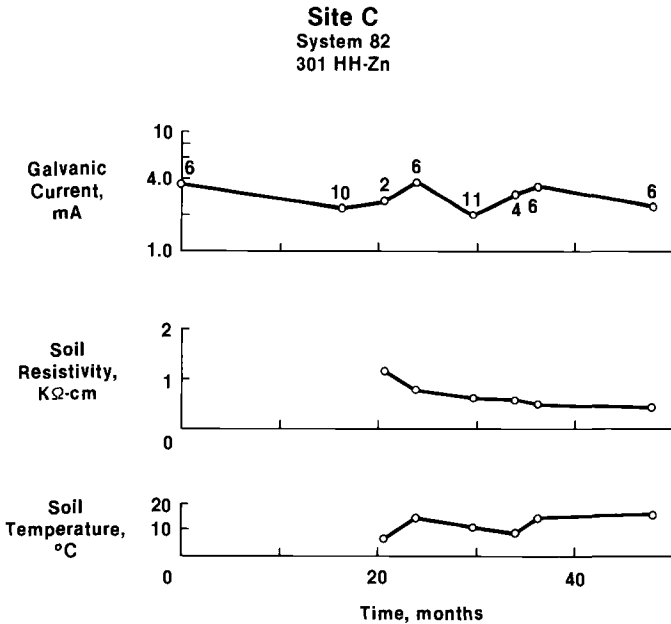


FIG. 4—Galvanic current, soil resistivity, and soil temperature as a function of time at Site C.

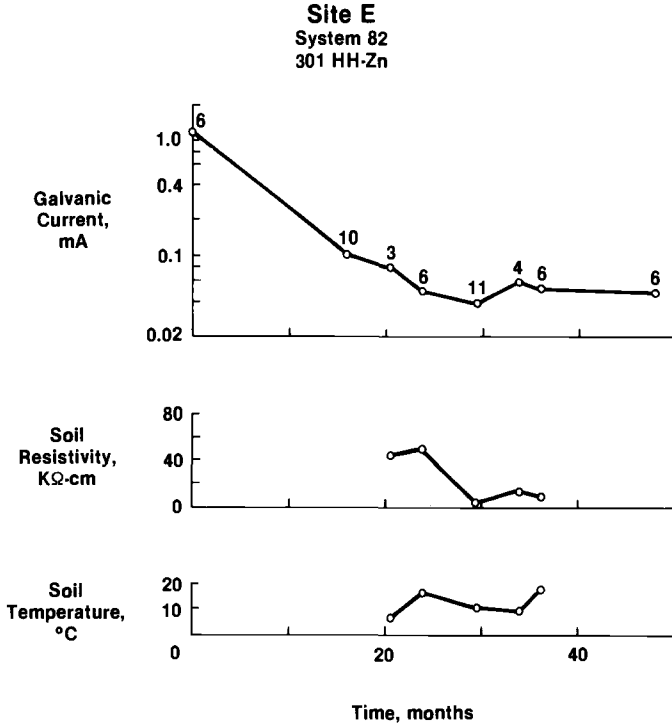


FIG. 5—Galvanic current, soil resistivity, and soil temperature as a function of time at Site E.

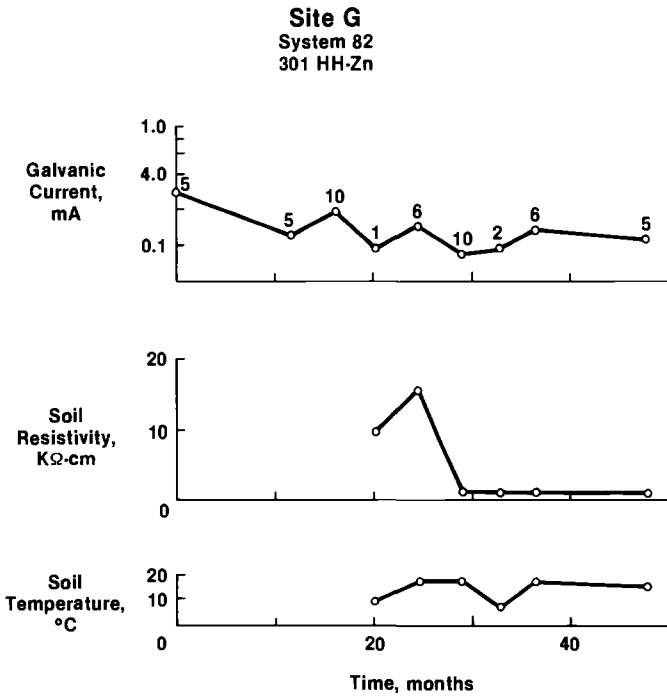


FIG. 6—Galvanic current, soil resistivity, and soil temperature as a function of time at Site G.

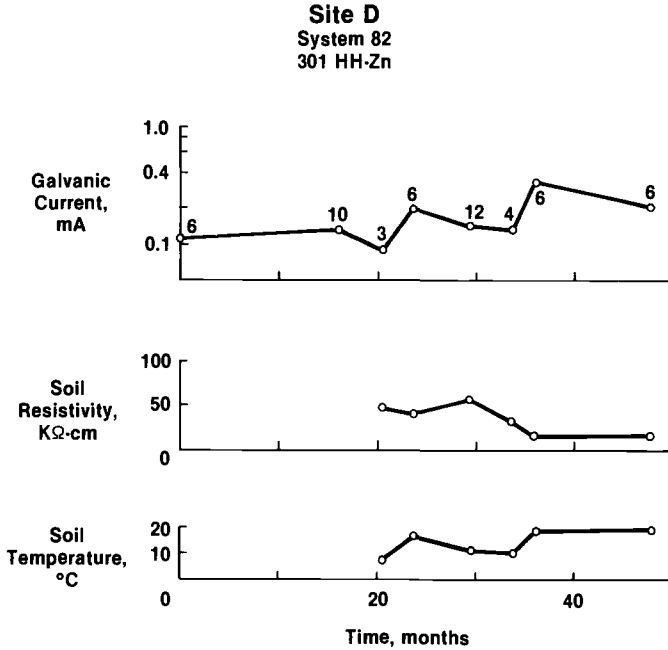


FIG. 7—Galvanic current, soil resistivity, and soil temperature as a function of time at Site D.

rents at the other four sites, with relatively poor aeration, were controlled by oxygen concentration.

Moisture content of the soil was not measured during the course of this project, and there is no doubt that moisture of the soil was changing during the four-year period of exposure. Examination of the data did not reveal any changes in galvanic current or soil resistivity that could be attributed to seasons of the year. The number above each data point on the galvanic current curves (Figs. 3 through 7) corresponds to the number of the month that the measurement was made.

All galvanic currents discussed here are cathodic to the stainless steel and effectively protected the U-bend specimens from any corrosion attack. Examination of the specimens on retrieval revealed that practically all the cathodically charged specimens had failed, and only those in an alkaline soil resisted failure. Table 4 summarizes the results of the number of failures and the current density at the six sites. Of the stressed specimens that were not cathodically charged, not one failure occurred.

TABLE 4—Average galvanic current and number of failures.

Site	301 HH - Zn		301 FH - Zn	
	$\mu\text{A}/\text{cm}^2$	Failures	$\mu\text{A}/\text{cm}^2$	Failures
A	2.58	0	4.17	0
B	1.43	2	1.51	2
C	20.0	2	20.5	2
D	0.94	2	1.23	2
E	1.14	2	0.98	2
G	10.3	2	14.7	2

These results strongly suggest that the mode of failure was by hydrogen embrittlement. The lack of any failures in the alkaline environment supports this since the potential of the stainless steel zinc couple was approximately -0.8 V versus the hydrogen electrode, which is above the hydrogen evolution potential for steel at a pH of 8.8. The results, as described in an earlier publication, show that at this higher pH, failure occurred only when the stainless steel was coupled to magnesium at a potential of approximately -1.3 V versus the hydrogen electrode, a potential well within the hydrogen evolution potential [10]. Thus, the results indicate that when the potential of the stainless steel specimens was sufficiently negative to cause hydrogen evolution, failure by hydrogen embrittlement took place.

Summary and Conclusions

1. In soils that are well aerated, soil resistivity has a strong influence on the magnitude of galvanic corrosion current.
2. In poorly aerated soils, oxygen controls the magnitude of the galvanic corrosion current.
3. At a depth of 1 m, the resistivity of a soil is strongly influenced by soil temperature, and only slightly affected by seasonal moisture changes.
4. 301 stainless steel stressed above the yield point in a half-hard or full-hard condition is susceptible to hydrogen embrittlement failure in soil when exposed at potentials capable of causing hydrogen evolution.

References

- [1] Romanoff, M., *Underground Corrosion*, NBS Circular 579, NTIS PB 168 350, Springfield, VA, April 1957.
- [2] Gallaceio, A., *Galvanic Corrosion Test Methods, Handbook on Corrosion Testing and Evaluation*, John Wiley and Sons, New York, 1971, p. 143.
- [3] Scully, J. R., "An Experimental Electrochemical Investigation of Corrosion Evaluation Methods for Selected Pipe Surfaces in Soil," Masters thesis, Johns Hopkins University, Baltimore, MD, 1982.
- [4] Khizhnyakov, V. I., "The Effect of Oxygen Penetration of Soils in the Taiga Swamp Zone of the Central Part of Western Siberia on the Operation of Galvanic Macrocouples in the Corrosion of Underground Oil Pipelines of Large Diameter," *Korroziia i Zashchita V Neftegazov Promyshlennosti*, Vol. 4, 1982, pp. 1-2.
- [5] Gerhold, W. F., Escalante, E., and Sanderson, B. T., The Corrosion Behavior of Selected Stainless Steels in Soil Environments, NBSIR 81-2228, National Bureau of Standards, Gaithersburg, MD, Feb. 1981.
- [6] Escalante, E. and Gerhold, W. F., "The Galvanic Coupling of Some Stainless Steels to Copper—Underground," *Materials Performance*, Vol. 14, No. 10, Oct. 1975, pp. 16-20.
- [7] Escalante, E. and Gerhold, W. F., "Galvanic Coupling of Some Stressed Stainless Steels to Dissimilar Metals Underground," *Galvanic and Pitting Corrosion—Field and Laboratory Studies, STP 576*, American Society for Testing and Materials, Philadelphia, 1976, pp. 88-93.
- [8] Wenner, F., *A Method For Measuring Earth Resistivity*, Bulletin 12, National Bureau of Standards, Gaithersburg, MD, 1916, p. 469.
- [9] Prutton, C. F. and Maron, S. H., *Fundamental Principles of Physical Chemistry*, The Macmillan Co., New York, 1957, p. 150.
- [10] Pourbaix, M., *Atlas of Electrochemical Equilibria in Aqueous Solutions*, Pergamon Press, New York, 1966, pp. 307-321.

Evaluation and Prediction of Galvanic Corrosion in Oxidizing Solutions

REFERENCE: Sridhar, N. and Kolts, J., "Evaluation and Prediction of Galvanic Corrosion in Oxidizing Solutions," *Galvanic Corrosion, ASTM STP 978*, H. P. Hack, Ed., American Society for Testing and Materials, Philadelphia, 1988, pp. 203-219.

ABSTRACT: Galvanic corrosion of several alloys has been examined before in simple acids or salt solutions, and good predictive capability has been achieved using numerical solution of appropriate Tafel equations. In this paper, more complex solutions, containing an acid and an oxidizing agent, are examined. Galvanic current measurements and gravimetric (weight-loss) corrosion measurements indicated that galvanic current measurement is not always a reliable method to determine the difference in corrosion rate of an alloy between the coupled and uncoupled conditions. Sometimes an alloy showing a cathodic current showed an increase in corrosion rate while another alloy showing an anodic current showed a decrease in corrosion rate. Graphical superposition of polarization curves in the oxidizing solutions did result in correct prediction of galvanic potential and current in most cases. However, in order to predict the change in corrosion rate of an alloy on coupling to another, polarization curves of the coupled alloys in both the oxidizing solution and the solution without the oxidizing agent have to be superimposed.

KEY WORDS: galvanic corrosion, oxidizing solutions, acids, zero resistance ammeter, nickel-base alloys, duplex stainless steels, titanium, graphite, austenitic stainless steels, corrosion potential, polarization, current, coupling, active-passive regions

Galvanic corrosion in corrosive media can occur in chemical and other industries because many alloys are used along a process stream, depending on temperature, pressure, acidity, and so forth. Because of a dearth of galvanic corrosion data in such environments, the corrosion potentials (open-circuit potentials, OCP) are often used to gage the compatibility of various alloys. The inadequacies of such measurements have been demonstrated amply [1-3]. In simple environments, for materials showing a Tafel behavior in the potential region of interest, it has been shown [1,4] that numerical solutions of the Tafel equations for the anode and cathode can be used to predict galvanic corrosion rate. However, this procedure is invalidated when active-passive behavior and additional redox reactions are involved. The additional redox reactions are often found in practical situations because of impurities such as iron from corrosion of steel parts. They can also be intentionally introduced in some processes.

This paper examines the galvanic corrosion of alloys exhibiting varying degrees of active-passive behavior in environments containing varying amounts of redox reagents. The objective of the paper is to determine what techniques can be used reliably to measure and predict galvanic corrosion under these circumstances.

Experimental Procedures

A potentiostat was used as a zero-resistance ammeter to determine galvanic current between two alloys in a solution. The alloys were polished to a 600-grit finish, degreased, dried, and

¹Engineer, Haynes International, Inc., 1020 W. Park Ave., Kokomo, IN 47901.

²Research associate, Conoco Inc., Ponca City, OK 74603.

mounted in a Stern-Makrides holder. The solutions were purged 30 min before and during the test with 1-atm pressure hydrogen. The open-circuit potentials (OCPs) were determined on separate samples for 48 h. Gravimetric corrosion rates were also determined on these specimens. The specimens for the galvanic corrosion tests were similarly weighed before and after exposure to determine their corrosion rates. The galvanic corrosion tests were conducted for 48 h, the potentials of the two electrodes and the galvanic current being recorded by a computer. Anodic and cathodic potentiodynamic polarization curves were run separately on alloys at a scan rate of 0.167 mV/s from the OCP. All specimens were visually inspected for crevice corrosion at the area of contact with the holder. In selected cases, specimens were polarized to various constant potentials for 48 h, and the weight-loss corrosion rates determined. All potentials were measured with respect to saturated calomel electrode (SCE). The alloys tested are shown in Table 1. All alloys were in the mill-annealed condition.

Galvanic Corrosion Measurements

It was shown in a previous paper [1] that, in simple acidic environments, the corrosion potentials (OCPs) were not good predictive tools. Similar results have been observed in the present investigation on more complex environments. This is illustrated in Fig. 1 where the difference in corrosion rate of an alloy between coupled and uncoupled condition (galvanic corrosion rate) is plotted against the difference in OCP between that alloy and the alloy it is coupled to. A variety of alloys and environments are included in this figure. There is a lack of correlation, not only with the magnitude of the galvanic effect, but, more surprisingly, with the direction of the galvanic corrosion. In some cases, the more active metal of the couple showed an increase in corrosion rate compared to its uncoupled state, but in other cases there was a decrease in corrosion rate of the active metal. Similarly, in some cases the alloy possessing a nobler OCP exhibited an increase in corrosion rate. These seemingly odd effects are examined in more detail in the following sections.

Sulfuric Acid + Ferric Sulfate Mixtures

The galvanic effects of a variety of alloys in 10% sulfuric acid without any ferric-ion addition were examined previously [1]. The weight-loss [1] corrosion rates of various alloys in this environment are shown in Table 2. In some cases, for example, Ti-2/B-2 and alloy 255/B-2 couples, the cathodic alloy showed a reduction in corrosion rate. However, in other cases, for example, 304 stainless steel (SS)/alloy 255, the cathode material showed a great increase in corrosion rate compared to its uncoupled state. These results were explained [1] on the basis of superposition of polarization curves of the alloys coupled and on the basis of the effect of polarization on dissolution rate.

If an oxidizing agent, such as, ferric sulfate, is added the OCPs of the various alloys change depending on the concentration of the oxidizing agent. Two levels of ferric-ion concentration were examined: 5.2 and 520 ppm. The galvanic effects in the boiling 10% sulfuric + 5.2 ppm ferric ion solution are shown in Table 3. The addition of 5.2 ppm ferric ion increased the OCP of graphite in the acid from +268- to +600-mV SCE. The alloy 255, which is a high chromium containing duplex stainless steel, also showed an increase in OCP from -234 to +520 mV with the addition of 5.2-ppm ferric ions. The increase in OCP of alloy B-2, which does not passivate in this environment, was slight from -147 to -80 mV. The concentration of ferric ions was too small to shift the potential of Ti-2 into the passive region. In all these cases the OCP remained quite stable after an initial change. This is shown for alloys 255 and B-2 in Fig. 2.

However, galvanic coupling of these alloys resulted in significant changes in potentials with time (Table 3). The galvanic potentials also seemed to depend on the initial conditions of immersion indicating active/passive instability in some alloys. For example, when alloys 255

TABLE 1—Nominal chemical composition, in wt%, of alloys examined in this paper.

Alloy	UNS Number ^d	C	Cb	Cr	Cu	Fe	Mo	Ni	Ti	W	Others
HASTELLOY® alloy B-2	N10665	0.01 ^b	...	1.0 ^b	...	2.0 ^b	28	bal
HASTELLOY alloy C-276	N10276	0.01 ^b	...	15.5	...	5.5	16	bal	...	4	...
HASTELLOY alloy C-22	N06022	0.015 ^b	...	22	...	3.0	13	bal	...	3	...
HASTELLOY alloy G-30	N06030	0.03 ^b	0.8	29.5	2.0	15	5.5	bal	...	2.5	...
FERRALIUM® alloy 255	S32550	0.04 ^b	...	26	1.7	bal	3.0	5.5	N = 0.17 H = 0.015 ^b N = 0.03 ^b O = 0.25 ^b
Titanium Grade 2	RS0550	0.1 ^b	0.3 ^b	bal
Type 304 Stainless	S30400	0.08 ^b	...	19	...	bal	...	10

^dUnified Number System.

^bMaximum.

® HASTELLOY is a registered trademark of Cabot Corporation.

® FERRALIUM is a registered trademark of Bonar Langley Alloys Ltd.

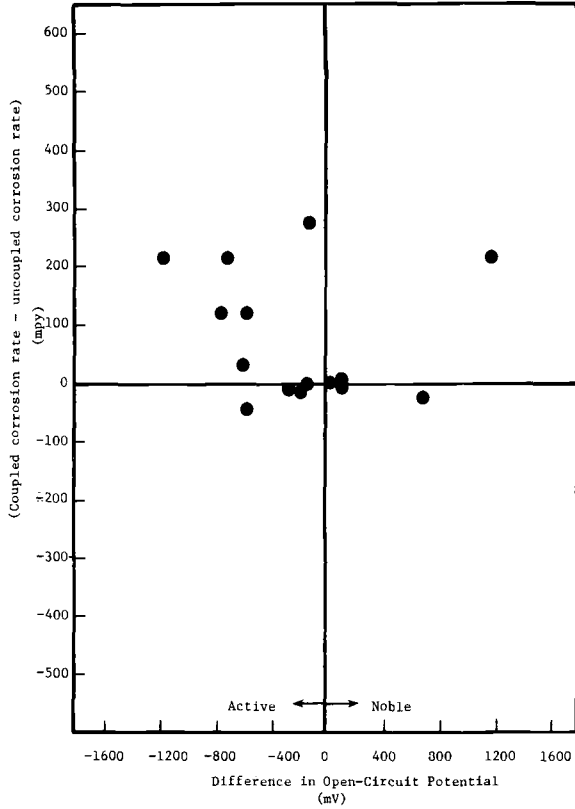


FIG. 1—Open-circuit potentials versus galvanic compatibility of various alloys.

and B-2 were coupled, in one test the galvanic potential shifted from -68 to -219 mV, whereas in another test, the potential shifted from -120 to -59 mV (Fig. 2). The galvanic corrosion rates reflected these differences (Table 3). In the first test, the corrosion rate of alloy 255 increased from zero to 1.43 mm/year (57 mpy) whereas in the second test the corrosion rate did

TABLE 2—Corrosion rates calculated from the weight loss data of various galvanic couples in boiling 10% H_2SO_4 .

Couple	Corrosion Rate, mpy	
	Anode	Cathode
Titanium-Alloy B-2	1 376	3.7
Titanium-Alloy 255	265	442
Titanium-AISI 304 SS	1 040	25 000
Alloy 255—Alloy B-2	185	4.4
AISI 304 SS—Alloy B-2	6 800	19
AISI 304 SS—Alloy 255	13 000	1 600
Uncoupled Alloy 255	230	...
Uncoupled Alloy B-2	2	...
Uncoupled 304 SS	2 300	...
Uncoupled titanium	4 600	...

TABLE 3—Galvanic effects. Environment: 10% sulfuric + 18.6 ppm ferric sulfate (5.2 ppm Fe^{3+}). Temperature: boiling. Duration: 48 h. Area ratio: 1: 1.

Alloys	Open-Circuit Potential, mV Versus SCE		Open-Circuit Corrosion, mm/year		Galvanic Potential, mV Versus SCE	Galvanic Current-Density on Electrode 2, $\mu A/cm^2$	Galvanic Corrosion, mm/year		
	1	2	1	2			1	2	
B-2	255	-80	+520	1.2	0	-68 to 219	-80 ^a to +14	0.15	1.43
B-2	255	-120 to -55	-60	1.23	0.01
Ti-2	B-2	-650	-80	>100	1.2	-200 to -720	-400 to -15,000	>100	0.15
Ti-2	255	-650	+520	>100	0	-250	-1100 to -630	7.2	5.4
304 SS	255	50	0	-280	+2500	48	10
Graphite	B-2	+600	-80	...	1.2	-90	-100 to -4	...	0.55

^aNegative indicates cathodic current.

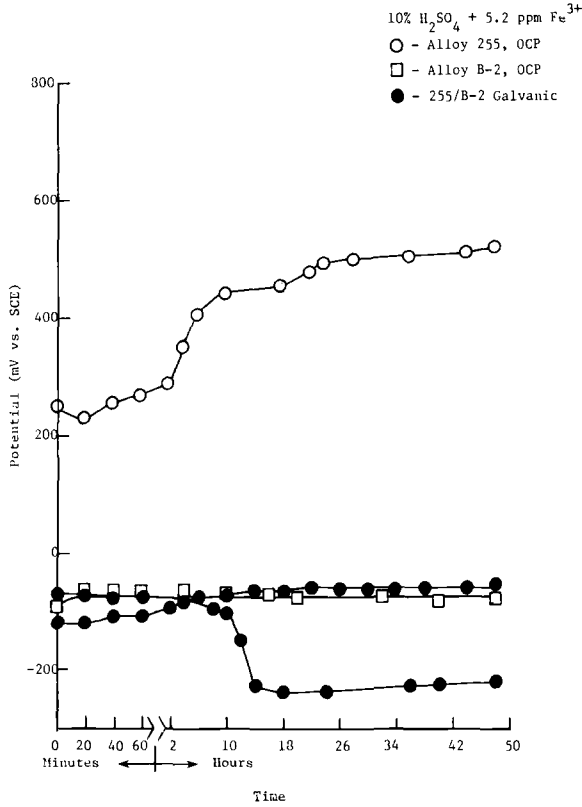


FIG. 2—Variation of potential with time in sulfuric acid + 5.2 ppm Fe³⁺ solution.

not change significantly from the OCP. The behavior of alloy B-2 was the opposite of that of alloy 255. The measured galvanic current density in the first test varied from -80 to $+14 \mu\text{A}/\text{cm}^2$. The current density shifted abruptly from a cathodic current (on alloy 255) to anodic current at the same time the galvanic potential shifted from -152 to -219 mV (Fig. 2). These changes reflect the instability of the active/passive behavior in this alloy at such a low level of oxidizing agent. It must also be noted that the weight-loss corrosion rates are averaged over a period of 48 h and thus do not accurately reflect instantaneous corrosion current. In the case of Ti-2/B-2 couple, the shift in galvanic potential from -220 to -720 mV was much more gradual. Alloy B-2 was cathodic to Ti-2 and showed a decrease in corrosion rate compared to its corrosion rate at OCP (Table 3). In the case of alloy 255/Ti-2 couple, alloy 255 was the nobler of the two in OCP. However its corrosion rate increased from zero to 5.4 mm/year (216 mpy) on galvanic coupling in spite of the galvanic current being cathodic. Similar results were noted for the alloy 255/304 SS couple. This point will be amplified later.

In the case of B-2/graphite couple, an increase in corrosion rate of alloy B-2 was anticipated because of the high potential of graphite compared to B-2. However, the galvanic corrosion rate was actually less than the OCP rate. The galvanic potential was also slightly below the OCP (-80 mV) in this solution but above the OCP in straight 10% sulfuric acid (-147 mV).

If a much higher level of ferric ion is added, the results are different as shown in Table 4. Both Ti-2 and alloy 255 quickly attained high OCP indicative of stable passivity. The potential of alloy B-2, which does not show an active-passive transition in this environment, increased only slightly to -60 mV. Both Ti-2 and alloy 255 acted cathodic to alloy B-2 and showed a decrease

TABLE 4—Galvanic effects. Environment: 10% sulfuric + 1860 ppm ferric sulfate (520 ppm Fe^{3+}). Temperature: boiling. Duration: 48 h. Area ratio: 1:1.

Alloys	Electrode 2	Open-Circuit Potential, mV Versus SCE		Open-Circuit Corrosion, mm/year		Galvanic Potential, mV Versus SCE	Galvanic Current-Density on Electrode 2, $\mu A/cm^2$	Galvanic Corrosion, mm/year	
		1	2	1	2			1	2
B-2	255	-60	+710	11.5	0.09	-60	-2 000 to -75 ^a	14.5	0
B-2	Ti-2	-60	+520	11.5	1.23	-70	-10 000 to -50	14.5	0.15
Ti-2	255	+520	+710	1.23	0.09	+520	-10	0.9	0
B-2	graphite	-60	+660	11.5	...	0 to 122	-12 000 to -50	16.9	...

^aNegative indicates cathodic current.

in corrosion rate on coupling with alloy B-2. Coupling of alloy 255 to Ti-2 resulted in a slight decrease in corrosion rate of both alloys. Alloy B-2, which already showed a high corrosion rate in this environment, suffered a slight increase in corrosion rate on being coupled to graphite.

Hydrochloric + Nitric Acid Mixtures

The corrosion behavior of several Ni-base alloys in these acid mixtures have been examined before [5]. The addition of nitric acid to hydrochloric acid increases the OCP because of the high redox potential of the nitric acid reduction reaction. The higher chromium alloys generally show higher OCP and lower corrosion rate in the high nitric acid concentrations. At low nitric acid concentrations, a suitable combination of chromium and molybdenum is needed for high corrosion resistance [5]. Thus, alloy C-22, possessing 22% Cr and 13% Mo, performs better in 4% hydrochloric acid (HCl) + 1% nitric acid (HNO₃) solution than alloy C-276 (16% Cr and 16% Mo) and G-30 (29.5% Cr and 5.5% Mo). The effects of galvanic coupling in these solutions are examined below.

At low concentrations of nitric acid, similar to the case of low-concentration ferric ions in sulfuric acid, the OCP and galvanic potentials show a considerable variation with time for some alloys (Table 5). The OCP for alloy G-30 varied from -240 to +110 mV, indicating a slow passivation caused by the small amount of nitric acid addition. This is illustrated in Fig. 3. The OCP of alloy C-276 showed an initial rapid rise to +180 mV, then decreased to -40 mV, and remained constant at that potential. This decrease in OCP may indicate an unstable passivity. When alloys G-30 and C-276 were coupled, the galvanic potential followed the trend in OCP of alloy G-30 (Fig. 3). In contrast to these two alloys, alloy C-22 showed rapid passivation, with the OCP increasing to about +225 mV and thereafter remaining stable (Fig. 3). Coupling alloy C-22 to C-276 again resulted in stable galvanic potential of +250 mV after about 30 min. However, on coupling alloy C-22 to G-30, the galvanic potential initially followed the trend of the OCP of alloy G-30, but later increased to a higher potential than the OCP of G-30.

Coupling alloy C-276 with C-22 decreased the corrosion rate of the former slightly reflecting the increase in potential from -40 to +250 mV. The corrosion rate of alloy C-22 increased slightly. Alloy C-22 would be expected to be the cathode because of its higher OCP. However, as seen in Table 5, the current density on the alloy is slightly anodic. Coupling alloy C-22 to G-30 resulted in an increase in the corrosion rate of both alloys though the former is the cathodic alloy as indicated by the galvanic current measurement. Coupling alloy C-276 to G-30 resulted in a slight decrease in corrosion rate of the former while the corrosion rate of the latter was not affected.

At high concentrations of nitric acid, the above patterns change quite drastically (Table 6). The OCPs of all three alloys were quite stable. Alloy G-30 showed the highest OCP and the lowest corrosion rate. Alloy C-276 showed a high corrosion rate, which did not change very much on galvanic coupling. Coupling alloy C-276 to C-22 resulted in a slight decrease in the corrosion rate of both alloys. Coupling alloy C-276 to G-30 resulted in a slight increase in corrosion rate of the latter even though it is cathodic. These small changes in corrosion rates may also be due to experimental scatter.

Discussion

Numerical solution of the Tafel equations cannot be attempted for the galvanic corrosion behavior observed in these environments because the potentials of interest are in the active/passive region. Graphical superposition of the total anodic and cathodic curves has been used extensively in the literature [2,6]. This technique, with some modifications, will be used to rationalize the observed galvanic effects.

TABLE 5—Galvanic effects. Environment: 4.3% hydrochloric + 0.98% nitric acid. Temperature: 90°C. Duration: 48 h. Area ratio: 1:1.

Alloys	Open-Circuit Potential, mV Versus SCE		Open-Circuit Corrosion, mm/year		Galvanic Potential, mV Versus SCE	Galvanic Current-Density on Electrode 2, $\mu\text{A}/\text{cm}^2$	Galvanic Corrosion, mm/year
	1	2	1	2			
Electrode 1							
Electrode 2							
C-22	+240	+180 to -40	0.005	0.46	+250	-2 to -3 ^a	0.09
G-30	-240 to +110	+240	3.03	0.005	-255 to +320	-1900 to -2	10
C-276	+180 to -40	-240 to +110	0.46	3.03	-235 to +170	-1700 to +5	0.19
							3.0

^aNegative indicates cathodic current.

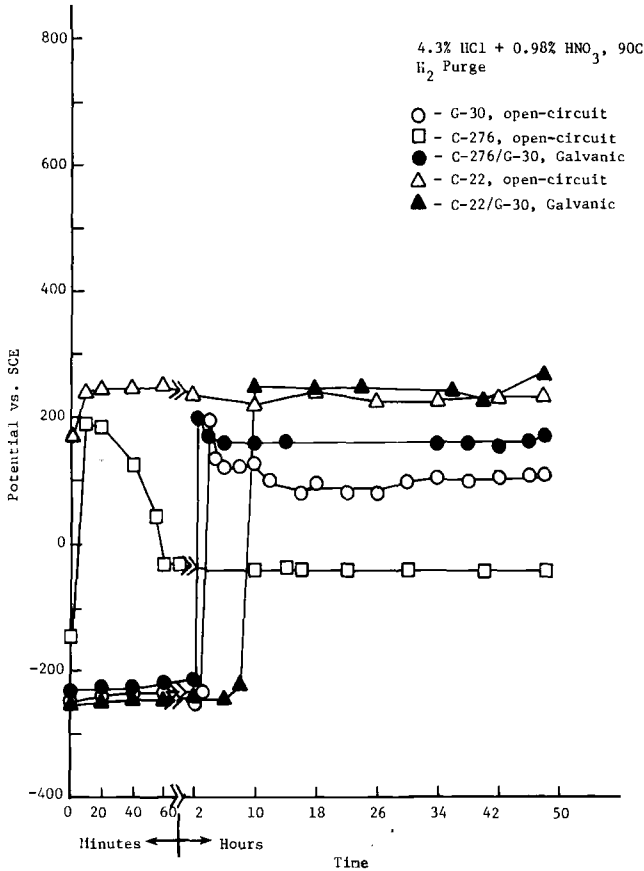


FIG. 3—Variation of potential with time in a HCl + HNO₃ mixture.

Sulfuric Acid + Ferric Sulfate Solutions

Because the presence of redox reactions can mask the underlying anodic curves, the anodic polarization curve in sulfuric acid without ferric ions has to be considered. The potentiodynamic polarization curves for alloys B-2 and 255 are shown in Fig. 4. Curve 1A is the polarization curve for alloy 255 in boiling, 10% sulfuric acid (H₂SO₄). Curve 2A is the result of the addition of 5.2-ppm ferric ions to the acid. Note that the OCP has shifted to a more positive value while the passive current density has remained relatively unaffected. Curve 3A, which is in 10% H₂SO₄ + 520 ppm Fe³⁺, is shifted further upwards. Curves 2C and 3C are the cathodic curves on alloy 255 in the 5.2 and 520 ppm Fe³⁺ solutions, respectively. They essentially reflect the ferric ion reduction reaction until a lower potential of about -200 mV is reached where the hydrogen ion reduction reaction takes over (note an inflection in curve 2C). Curves 4A and 5A are the anodic polarization curves for alloy B-2 in these solutions. In 10% H₂SO₄ solution, the anodic curve of alloy B-2 (not shown in the figure) essentially coincides with curve 4A.

The galvanic corrosion between alloy 255 and B-2 in the 5.2-ppm Fe³⁺ solution would be expected to be predicted by the intersection of curves 2C and 4A (indicated in Fig. 4). If this were the case, the galvanic potential would be expected to be about -100 mV versus SCE and galvanic current-density about 80 μA/cm² on alloy B-2 (-80 μA/cm² on alloy 255). However, Table 3 and Fig. 2 indicate that the galvanic current density can change from -80 to +14

TABLE 6—Galvanic effects. Environment: 3.7% hydrochloric + 33.3% nitric acid. Temperature: 90°C. Duration: 48 h. Area ratio: 1:1.

Alloys	Open-Circuit Potential, mV Versus SCE		Open-Circuit Corrosion, mm/year		Galvanic Potential, mV Versus SCE	Galvanic Current-Density on Electrode 2, $\mu\text{A}/\text{cm}^2$	Galvanic Corrosion, mm/year	
	Electrode 1	Electrode 2	1	2			1	2
C-276		+470	+550	2.05	+490	-65 to -35 ^a	1.42	0.11
C-22	C-22	+550	+570	0.2	+640 to +768	-6 to -1	0.13	0.08
C-276	G-30	+470	+570	2.05	+470	-110 to -15	2.25	0.08

^aNegative indicates cathodic current.

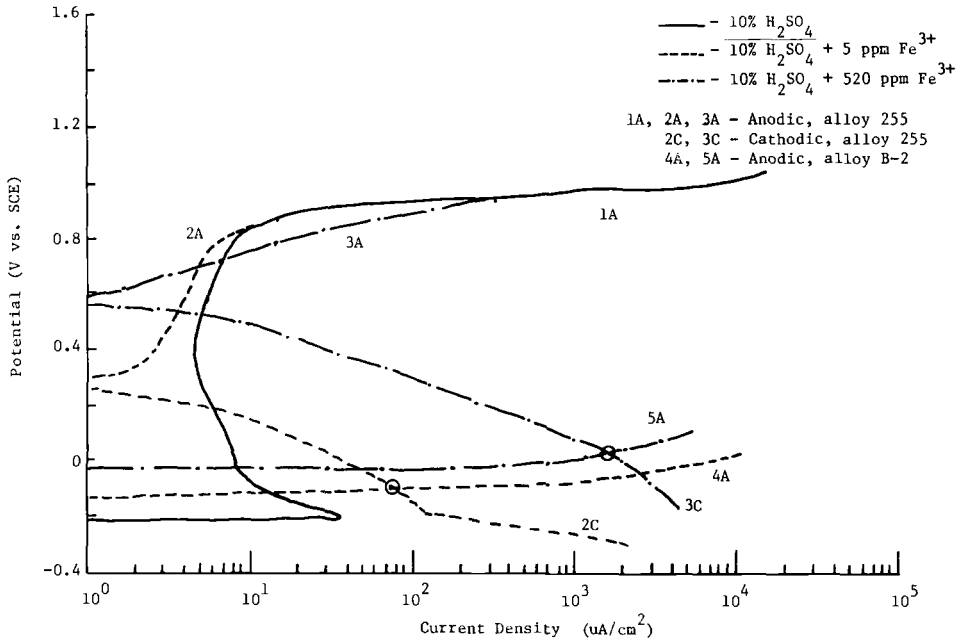


FIG. 4—Effect of ferric ions on the intersection of polarization curves of alloys 255 and B-2. Boiling, 10% H_2SO_4 , H_2 purge. 0.167 mV/s.

$\mu A/cm^2$ on alloy 255. In addition, variable corrosion of alloy 255 was observed. The explanation for these discrepancies may lie in the underlying anodic curve of alloy 255 in 10% H_2SO_4 (curve 1A). The passivation current peak in this curve depends on the scan-rate and the initial potential from which the polarization curve is started. Hence at a slower scan-rate, which simulates the galvanic tests more closely [6], the peak current density of curve 1A may well be higher and may intersect curve 2C. In such a case, the intersection of the total cathodic curve (2C) with the total anodic curve (1A + 4A) may result in multiple intersection points. This would further entail a change in galvanic potential with time and initial immersion conditions. The galvanic current density can also shift from anodic to cathodic in such a case. Finally, because the potential decreased from the passive region to the active-passive region of curve 1A, an increase in corrosion rate of alloy 255 may be expected despite being cathodic. A classic analogy to this is the experiment performed by Lillie [7] in the 1920s on passivated iron in concentrated nitric acid. He found that an iron wire, passive in 60 vol% nitric acid, when activated by touching one end with zinc, propagated a wave of active corrosion along the wire. This was due to galvanic effect between the adjoining regions of passive and active iron, the former being polarized cathodically into the active region and the latter anodically into passivity.

If the ferric ion concentration was increased to 520 ppm, the galvanic corrosion would be predicted by the intersection of cathodic curve 3C with anodic curve 5A both of which approximate closely the total anodic and cathodic curves. Note that this point of intersection is well away from the active-passive transition of curve 1A. Hence the corrosion rate of alloy 255 would be expected to be low as indicated in Table 4. The galvanic potential predicted from Fig. 4 is about 0 mV as opposed to the measured value of -60 mV. The galvanic current density predicted is $2000 \mu A/cm^2$ whereas the measured galvanic current density decreases from 2000 to $75 \mu A/cm^2$. However, this may be due to the short-term nature of the polarization curves.

The superposition of the polarization curves for alloy 255 and Ti-2 are shown in Fig. 5. Curve 1A is the anodic curve of alloy 255 in 10% H. Curve 2A is the anodic curve of Ti-2 in 10% H + 5.2 ppm Fe^{3+} . The anodic curve of Ti-2 in 10% H (not shown here) slightly below curve 2A but has the same shape). Curve 1C is the cathodic curve of alloy 255 in 10% H_2SO_4 + 5.2 ppm Fe^{3+} . The galvanic potential would be expected to be the point of intersection of curves 1C and 2A, which is about -300 mV. This compares favorably with the measured galvanic potential of -250 mV shown in Table 3. The galvanic current-density predicted from Fig. 5 would be $1000 \mu\text{A}/\text{cm}^2$ whereas the measured galvanic current-density varied from 1100 to $630 \mu\text{A}/\text{cm}^2$. The short time periods of the polarization-curve data may account for this difference. More significantly, alloy 255 showed an increase in corrosion rate from 0 to 5.4 mm/year (216 mpy) despite being a cathode. Referring to Fig. 5, the galvanic potential is at or slightly below the passivation peak of alloy 255 in 10% H_2SO_4 (curve 1A). Hence at this potential alloy 255 can be expected to corrode at higher rate than at $+520$ mV, which is in the passive region. Thus while the superposition of polarization curves in the ferric-ion containing solution will predict galvanic potential and current-density, the actual corrosion rate of the anode or cathode can be predicted only by knowing the polarization behavior in the acid without ferric ion. The corrosion rate of Ti-2 decreased on galvanic coupling because the potential was shifted upward from -650 to -250 mV into the transition region.

If the Fe^{3+} concentration is increased to 520 ppm, the cathodic reactions on alloy 255 and Ti-2 are represented by curves 2C and 3C, respectively (Fig. 5). Curve 3A is the anodic curve for Ti-2 in this solution. The anodic curve for alloy 255 is higher and is not considered here. The galvanic potential is given essentially by the intersection of curves 2C and 3A since curve 3C makes only negligible contribution to the total cathodic curve. The predicted galvanic potential in this case is about 450 mV and compares fairly well with the measured potential of 520 mV (Table 4). The predicted galvanic current density of about $11 \mu\text{A}/\text{cm}^2$ agrees well with the

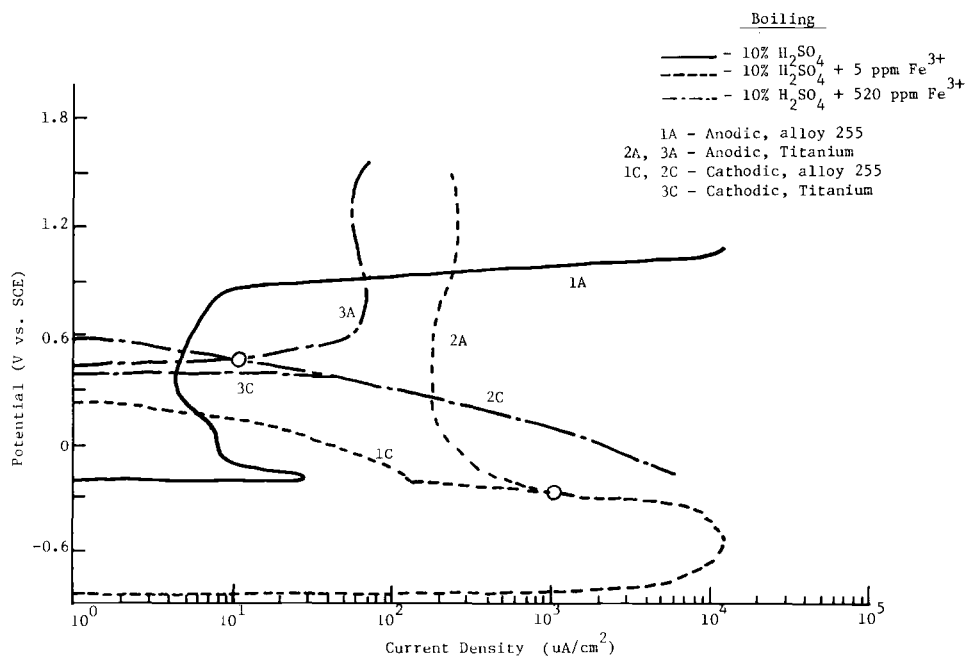


FIG. 5—Effect of ferric ions on the intersection of polarization curves of alloy 255 and titanium in boiling sulfuric acid. H_2 purge. 0.167 mV/s.

measured current density of $10 \mu\text{A}/\text{cm}^2$ (Table 4). The corrosion rate of both alloys are low because the galvanic potential is well within the passive region for both alloys in 10% sulfuric acid (curves 1A and 2A).

Hydrochloric + Nitric Acid Mixtures

In these mixtures, it is instructive to examine the high concentrations of nitric acid first, as the behavior is more simple. The polarization curves for alloys C-276 and G-30 are shown in Fig. 6. Curves 1A and 1C are the anodic and cathodic polarization curves in 3.7% HCl at 90° for alloy C-276. Addition of 33% HNO_3 shifted both the anodic and cathodic curves of this alloy to 2A and 2C, respectively. Curves 3C and 3A are the cathodic and anodic curves of alloy G-30 in the 3.7% HCl + 33.3% HNO_3 mixture. The anodic curve of alloy G-30 in 3.7% HCl is not considered here because it is below the curve 1A and hence is not expected to contribute significantly to the total anodic curve. The galvanic potential in this case is given by the intersection of curve 2A with the sum of curves 2C and 3C, curve 3A being too high to contribute to the total anodic curve. This predicted galvanic potential (Fig. 6) of about 500 mV is close to the measured value of 470 mV (Table 6). The predicted galvanic current of $100 \mu\text{A}/\text{cm}^2$ also agrees well with the measured current-density (Table 6) if the time dependency of the polarization curve is taken into account. The corrosion rate of alloy C-276 in the coupled condition is not significantly different from that in the open-circuit condition (Table 6), and this can also be understood from Fig. 6 because the galvanic potential is close to OCP and falls within the passive region of curve 1A. Indeed, corrosion rate of alloy C-276 in this environment is relatively constant at potentials ± 150 mV from the OCP as indicated by Fig. 7.

The galvanic behavior of C-22/C-276 couple can be deduced along similar lines of argument. As shown in Fig. 8, the predicted galvanic potential of about 490 mV is close to that observed

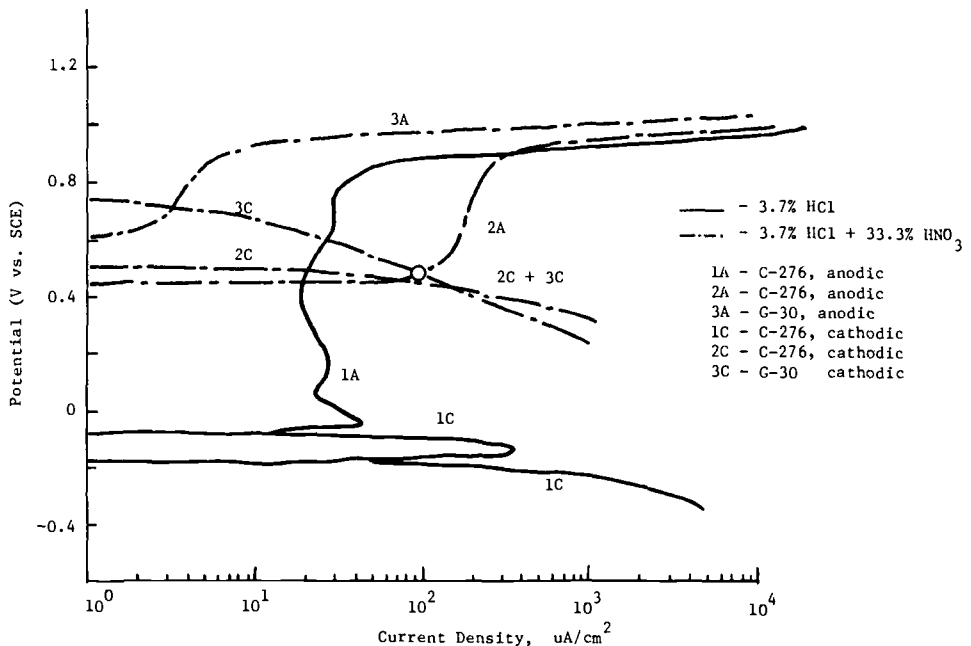


FIG. 6—Superposition of polarization curves of alloys C-276 and G-30 in acid solutions. H_2 purge. 0.167 mV/s. Temperature = 90°C .

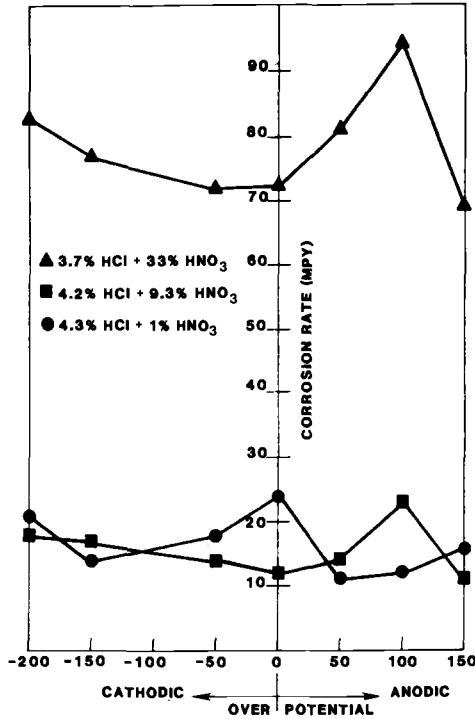


FIG. 7—Effect of polarization on actual (weight-loss) corrosion rate of alloy C-276 in HNO₃ + HCl mixture at 90°C (24-h test).

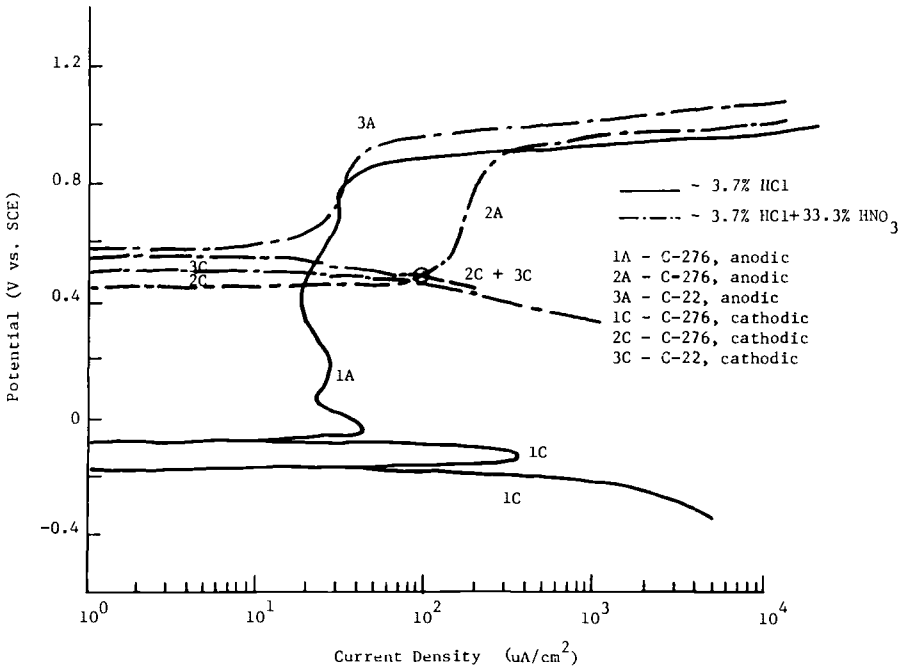


FIG. 8—Superposition of polarization curves of alloys C-276 and C-22 nitric + hydrochloric acid solutions. H₂ purge. 0.167 mV/s. Temperature = 90°C.

(Table 6). The predicted galvanic current density is $100 \mu\text{A}/\text{cm}^2$, which is somewhat higher than the observed current density of 65 to $35 \mu\text{A}/\text{cm}^2$.

When one considers the galvanic behavior in the more dilute nitric acid solution, the superposition of curves becomes more complicated as indicated in Fig. 9. Here curves 1A and 2A are the anodic polarization curves of alloys G-30 and C-276, respectively, in 3.7% HCl. Curves 3A and 4A are the anodic curves of C-276 and G-30, respectively, in the 4.3% HCl + 0.98% HNO_3 solution. Note that for alloy G-30 there is not only an upward shift in OCP but also an extension of the passive region on addition of nitric acid. On the other hand, in alloy C-276, which, owing to its high molybdenum content, shows an extensive passive region even in 3.7% HCl, the addition of nitric acid merely shifts the OCP to a more positive value. Curve 1C is the cathodic curve of alloy G-30 in 4.3% HCl + 0.98% HNO_3 . In this case, the galvanic potential can not be predicted by the intersection of the cathodic curve 1C of alloy G-30 with the anodic curve of C-276, 4A, because it is below the anodic curve. It seems that, in this system, where alloy G-30 shows a rather unstable passivity, galvanic potential is predicted by intersection of curve 1C with curve 1A + 2A. Thus, the galvanic potential is expected to change with time from 0 to -230 mV , which is similar to the observed potential changes in Table 5.

The galvanic current-density predicted from Fig. 9 would range from about 700 to $40 \mu\text{A}/\text{cm}^2$, but the direction of this galvanic current is exactly opposite of what is observed (Table 5). Superposition of alloys C-22 and G-30 also leads to the same type of results. Further work is needed in understanding the time dependency of polarization curves in this solution.

Conclusions

The galvanic corrosion of a number of alloys exhibiting varying degrees of active-passive behavior was investigated in two different acids with oxidizing agents. It was found that open-circuit potential measurements do not indicate correctly either the magnitude or the direction of galvanic corrosion. Superposition of appropriate anodic and cathodic polarization curves en-

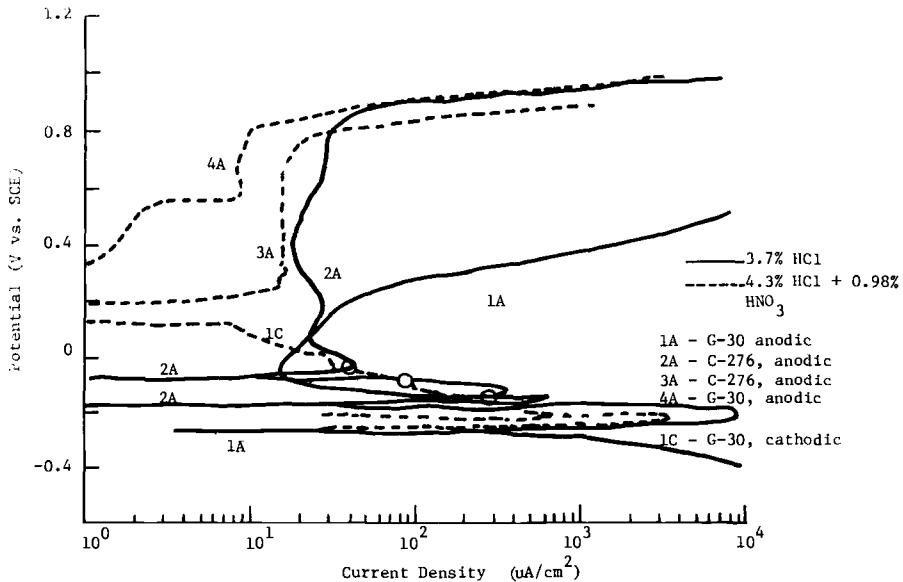


FIG. 9—Superposition of polarization curves of alloys G-30 and C-276 in a nitric + hydrochloric acid mixture. H_2 purge. 0.167 mV/s . Temperature = 90°C .

abled correct prediction of galvanic potential and current-density in most cases. More importantly however, the change in dissolution rate on galvanic coupling could not be predicted by this technique in many cases. In such cases, not only did the polarization curves in the oxidizing acids have to be considered but also the polarization behavior in the acid without oxidizing agents. Measuring galvanic current density alone did not lead to correct prediction of the change in dissolution rate of the alloys in these solutions. Weight-loss measurements were needed to supplement the galvanic current data. When low concentrations of nitric acid were present, considerable instability in polarization and galvanic corrosion behavior was observed and superposition of polarization curves did not lead to successful prediction.

Acknowledgment

The assistance of J. R. Dillman and P. M. Miller in generating the electrochemical data, R. A. Dague in typing the manuscript, and B. L. Maggart in drawing the figures is acknowledged.

References

- [1] Davis, G. O., Kolts, J., and Sridhar, N., *Corrosion*, Vol. 42, No. 6, 1986, p. 329.
- [2] Shreir, L. L., Ed., "Bimetallic Corrosion," *Corrosion*, Chapter 1.7, p. 1.192-1.221.
- [3] Mansfeld, F. and Kenkel, J. V., *Corrosion*, Vol. 31, No. 8, 1975, p. 298.
- [4] Mansfeld, F., *Corrosion*, Vol. 29, No. 10, 1973, p. 403.
- [5] Sridhar, N., Wu, J. B. C., and Corey, S. M., *Corrosion/86*, Chapter 182, National Association of Corrosion Engineers, 1986, to be published in *Materials Performance*.
- [6] Scully, J. R. and Hack, H. P., *Corrosion/84*, Paper 34, National Association of Corrosion Engineers, 1984.
- [7] Lillie, R. S., *Science*, Vol. 67, 1928, p. 593; also refer to Uhlig, H. H., *Passivity of Metals*, R. P. Frankenthal and J. Kruger, The Electrochemical Society.

Galvanic Corrosion of Duplex Fe-Cr-10%Ni Alloys in Reducing Acids

REFERENCE: Yau, Y.-H. and Streicher, M. A., "Galvanic Corrosion of Duplex Fe-Cr-10%Ni Alloys in Reducing Acids," *Galvanic Corrosion, ASTM STP 978*, H. P. Hack, Ed., American Society for Testing and Materials, Philadelphia, 1988, pp. 220-234.

ABSTRACT: The effect on corrosion of composition and microstructure in a series of Fe-Cr-10%Ni alloys with increasing chromium content has been investigated in reducing acids. In the range of 25 to 35% chromium there is a wide variation in the relative amounts of ferrite and austenite. In reducing acids (H₂SO₄ and HCl) there is preferential attack on the ferrite phases. However, the rate of attack on ferrite is considerably greater than expected on the basis of its chromium and nickel contents alone. This is because corrosion on the ferrite phase is significantly increased by galvanic action with the austenite in the microstructure. This galvanic effect is a function of the relative surface areas of the ferrite (anode) and the austenite (cathode).

Previous investigators have derived equations for the effect of relative surface areas of anodes and cathodes on galvanic corrosion of two dissimilar metals in the form of parallel sheets of constant composition. However, in the alloys of this investigation there are simultaneous changes, not only in the areas of ferrite and austenite, but also in the compositions of these two phases. In the analysis of the data on the Fe-Cr-10%Ni alloys, the mathematical treatment developed for relative areas with constant compositions has been used to separate this factor from that of the varying composition of ferrite and austenite. The results may contribute to an understanding of the action of duplex microstructures in castings, weldmetal, and duplex stainless steels when these are exposed to reducing acids during pickling and plant service.

KEY WORDS: galvanic corrosion, duplex alloys, austenite, ferrite, reducing acids

In a study of the effect of chromium content on the corrosion resistance of Fe-Cr-10% alloys in boiling 1.0 *N* sulfuric acid (H₂SO₄), it was found that corrosion rates were a function of the microstructure [1]. As the chromium content is increased in the range of 20 to 40%, the microstructure changes from pure austenite to austenite/ferrite duplex and then to pure ferrite. In the austenite/ferrite duplex structures, the ferrite phase is preferentially attacked. The difference in corrosion rates of austenite and ferrite phases suggests that there may also be galvanic action between these phases. Several investigators [2-5] have discussed the theory of galvanic corrosion in terms of the effect of cathode/anode surface-area ratios for two different metals of constant composition in the form of parallel plates of the same shape. It is the purpose of this study to investigate the applicability of macro-galvanic corrosion theory to the dissolution of microstructures consisting of austenite and ferrite whose volume fractions and compositions are changing simultaneously.

Experimental Procedures

A series of high purity laboratory heats of Fe-Cr-10%Ni alloys was made for this investigation (Table 1). The carbon and nitrogen contents were very low; therefore, their effects on both the

¹Bethlehem Steel Corp., Homer Research Laboratories, Bethlehem, PA 18016; formerly, Department of Chemical Engineering, University of Delaware, Newark, DE 19716.

²Department of Mechanical Engineering, University of Delaware, Newark, DE 19716.

TABLE 1—Chemical analyses of Fe-Cr-10%Ni alloys.

Alloy	Analysis, wt%			
	Cr	Ni	C	N
20%Cr	19.99	9.86	0.006	0.033
25%Cr	24.20	11.85	0.003	0.004
27%Cr	27.00	10.00	nd	nd
28%Cr	28.00	10.00	nd	nd
29%Cr	29.00	10.00	nd	nd
32%Cr	32.00	10.00	nd	nd
35%Cr	34.87	9.75	0.004	0.004
40%Cr	40.00	10.00	nd	nd

microstructure and corrosion resistance may be ignored. There was no intergranular attack in any of the corrosion tests of this investigation. In order to study the effect of heat treatment on microstructure and corrosion resistance, specimens were heated at 1066, 1200, and 1350°C (Table 2). The microstructures were examined on a light microscope and analyzed by scanning electron microscope (SEM) and an energy dispersive spectrometer (EDS) to determine the chemical compositions of the various phases.

Immersion Tests

Corrosion rates were determined from weight-loss measurements in boiling 1.0 N H₂SO₄. Specimens, 1 by 0.5 by 0.1 in. (25.4 by 12.7 by 2.5 mm), were cut from mill-annealed sheets of the laboratory heats. Heat treatments were carried out in a three-zone Lindberg furnace in the presence of argon gas. All heat treatments were for 2 h followed by a water quench. The specimens were polished to a 6- μ m finish, rinsed in distilled water and acetone. Their weight and dimensions were then measured. Corrosion tests were made in 1-L Erlenmeyer flasks with an Allihn drip tip condenser. The specimens were held in a glass cradle with several holes to permit circulation of the acid solution. Specimens with chromium contents higher than 25% were passive in the boiling 1.0 N H₂SO₄ solution. Contact with an iron rod was used to activate these specimens. After 4 min of immersion, which seems to be the optimum time interval for appreciable weight-loss without too much change in the austenite/ferrite surface-area ratios, the specimens were taken out, rinsed in distilled water and acetone, dried, and weighed.

TABLE 2—Analyses of α and γ in Duplex Fe-Cr-10%Ni alloys treated at 1066°C.

Alloy	Concentration, wt% ^a					
	Austenite (γ)		Ferrite (α)		$\Delta = \alpha - \gamma$	
	Cr	Ni	Cr	Ni	Cr	Ni
25% Cr	23.3	12.4	32.5	6.5	+9.2	-5.9
27% Cr	23.7	12.8	32.9	6.9	+9.2	-5.9
29% Cr	25.0	12.7	34.9	6.6	+9.9	-6.1
32% Cr	26.0	14.3	36.8	7.3	+10.8	-7.0
35% Cr	26.2	15.4	37.7	8.4	+11.5	-7.0

^aDetermined by EDS analysis.

Metallographic Examination

After the immersion tests, the specimens were examined on a metallograph for identification of preferential attack. For SEM and EDS analyses, the specimens were polished to a 6- μm surface finish and then electrolytically etched in 10% solution of oxalic acid at room temperature to delineate the grain boundaries. Both the line-scan and spot analysis techniques were used to determine the compositions (iron, chromium, and nickel) of the austenite and ferrite in the duplex structures.

Results

Figure 1 shows concentration profiles for iron, chromium, and nickel in an austenite island and in the ferrite matrix for the Fe-35%Cr-10%Ni alloy. While the austenite island has 15.4% nickel, which is 7.3% higher than that in the ferrite matrix, it has only 26.2% chromium, which is 11.5% lower than that in the ferrite. The variation in the concentration of iron between ferrite, 54.1%, and austenite, 58.4%, is relatively small.

Table 2 summarizes the results of EDS analyses and gives the concentrations of chromium and nickel in the austenite and the corresponding ferrite phases for all alloys. Note that the ferrite has about 9% higher chromium, but 6% lower nickel than the corresponding austenite. The composition data for 1066°C have been plotted (Fig. 2) on a phase diagram for the

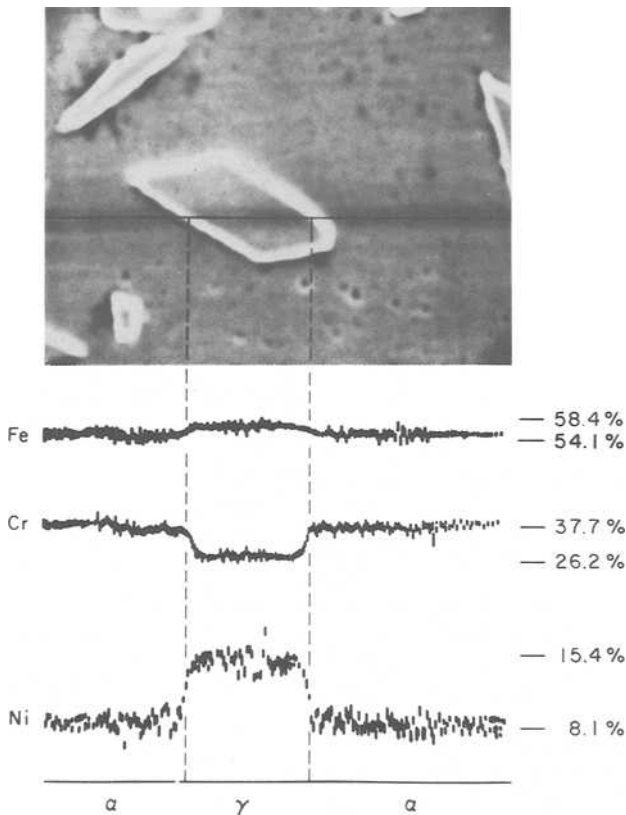


FIG. 1—Concentration profiles for iron, chromium, and nickel in duplex Fe-35%Cr-10%Ni alloys. Specimen heated 2 h at 1066°C; SEM X2500; oxalic acid etch, austenite islands in ferrite matrix.

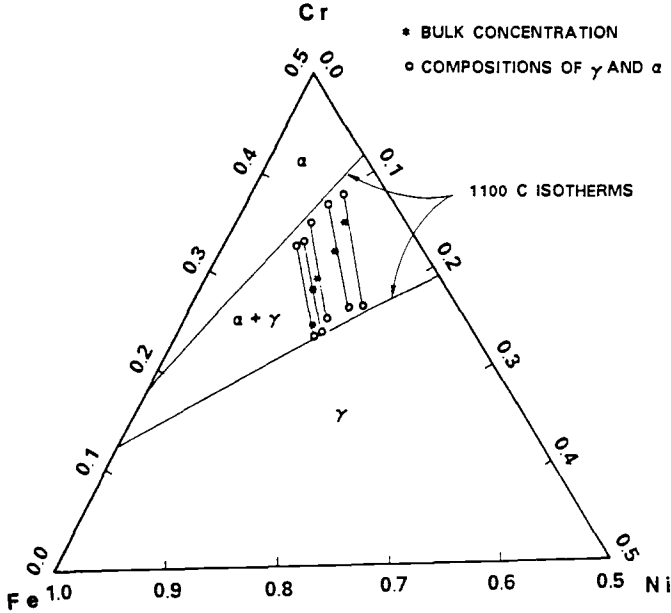


FIG. 2—Equilibrium phases in Fe-Cr-Ni alloys at 1066°C (1100°C isotherms obtained from Metals Handbook [6]).

Fe-Cr-Ni ternary system at 1100°C taken from the *Metals Handbook* [6]. Even though there is a 34°C difference between our data at 1066°C and the equilibrium diagram at 1100°C, Fig. 2 shows that there is good agreement between our data and the diagram.

The volume fraction of ferrite f , which is equal to the surface-area fraction of the ferrite on a cross section [7], can be calculated from the tie lines connecting the equilibrium concentrations of the austenite and the corresponding ferrite. Assuming that the densities of the austenite and the ferrite are equal, then, by a mass balance, the volume fraction of the ferrite can be calculated by the following equation

$$fC_i^\alpha + (1 - f)C_i^\gamma = C_i^b \tag{1}$$

where C_i^α and C_i^γ are the weight-percentages of alloying element i , iron, chromium, or nickel, in the ferrite and the austenite, respectively; and C_i^b is the bulk concentration of the i th component in weight percent. The calculated volume fractions of ferrite are listed in Table 3.

Ferrite is more stable at higher temperatures. Thus, as the temperature of heat treatment is raised from 1066 to 1200°C, more ferrite is formed. As a result, for alloys with chromium contents between 32 and 35%, the duplex structure converts to pure ferrite at this temperature. For chromium contents between 25 to 29%, the structure remains in the duplex range and the volume fraction of ferrite increases. These volume fractions of ferrite, as estimated on photomicrographs by linear analysis, are also listed in Table 3. At an even higher temperature, 1350°C, alloys with chromium contents of 27% or more are pure ferrite.

Thus, the microstructures of Fe-Cr-10%Ni alloys are a function of the chromium contents and the temperatures of heat treatments. The volume fractions of ferrite in duplex structures increase with increasing chromium content and temperature of heat treatment, as shown in Fig. 3.

The corrosion rates of the alloys depend not only on the chromium contents but also on the microstructures (Fig. 4). The corrosion rate of the Fe-20%Cr-10%Ni alloy, which has a pure

TABLE 3—Effect of chromium content and annealing temperature on the microstructures of Fe-Cr-10%Ni alloys.

Alloy	Structure: Surface Area (or volume), %					
	Annealing Temperature					
	1066°C ^a		1200°C ^b		1350°C	
	α	γ	α	γ	α	γ
20%Cr	0.0	100.0	0.0	100.0
25%Cr	9.5	90.5	23.5	76.5
27%Cr	29.0	71.0	54.0	46.0	100.0	0.0
28%Cr	47.3	52.7	76.7	23.3
29%Cr	42.1	57.9	73.2	26.8	100.0	0.0
32%Cr	58.5	41.5	100.0	0.0
35%Cr	84.3	15.7	100.0	0.0
40%Cr	100.0	0.0	100.0	0.0

^aCalculated by Eq 1 from EDS analysis.

^bCalculated by linear analysis from photomicrographs.

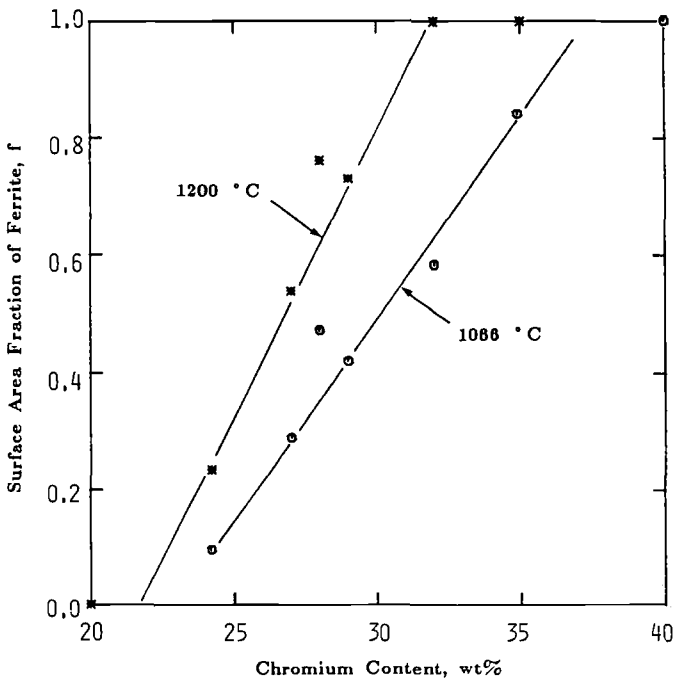


FIG. 3—Effects of chromium content and annealing temperature on the surface-area fraction of ferrite in Fe-Cr-10%Ni alloys.

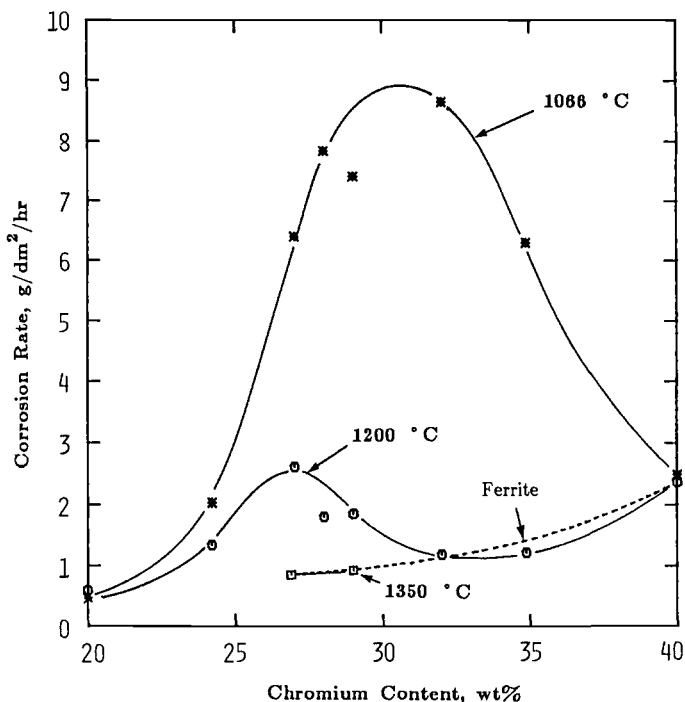


FIG. 4—Effect of chromium content and annealing temperature on corrosion of Fe-Cr-10%Ni alloys in boiling 1.0 N sulfuric acid.

austenitic structure, is very low regardless of the heat treatments. When the chromium content exceeds 20% and there is ferrite formation, the corrosion rates increase, particularly for specimens heat treated at 1066°C. They reach a maximum for the alloy with about 32% chromium, which has 58.5% ferrite. Above 32% chromium, corrosion rates decrease with further increases of chromium content up to 40%. In the austenite/ferrite duplex structures, high corrosion rates are a result of preferential attack on ferrite. The austenite is essentially free of attack (Fig. 5).

As the temperature of heat treatment is raised from 1066 to 1200°C, the microstructures of alloys with chromium contents higher than 32% are converted to pure ferrite. Heating at 1350°C produces pure ferrite in alloys with chromium content higher than 27%. The corrosion rates of the specimens that are pure ferrite are all relatively low. The maximum for specimens heated at 1200°C is only 2.5 g/dm²/h. It occurs at 27% chromium and 54% ferrite (Fig. 4).

In the completely ferritic Fe-Cr-10%Ni alloys, the corrosion rates increase with increasing chromium content (dotted line in Fig. 4). If the microstructure does not change with temperature, the corrosion rate is essentially independent of the temperature. For example, the corrosion rates of the completely ferritic Fe-40%Cr-10%Ni alloy and completely austenitic Fe-20%Cr-10%Ni alloy remain constant as the temperature of heat treatment is raised from 1066 to 1200°C. Thus, even though in duplex structures attack occurs preferentially on the ferrite phase, alloys that are 100% ferrite or which have more than 60% ferrite have relatively low corrosion rates. This suggests that the presence of austenite in the microstructure increases the rate of dissolution of the ferrite phase. However, this effect of microstructure is much greater for specimens heated at 1066°C than for those heated at 1200°C.

Discussion

Figures 5 and 6 show that the high corrosion rates of duplex structures are a result of preferential attack on ferrite in boiling 1.0 *N* sulfuric acid, that is, there is essentially no attack on austenite and the polishing lines can still be seen. Two possible reasons may account for this:

- (1) the concentration effect, that is, the high chromium and low nickel contents in ferrite increase its corrosion rate and
- (2) the galvanic effect, caused by the composition difference between the austenite and the ferrite phases, which increases the corrosion rate of the ferrite and decreases that of the austenite.

It is known [1,8] that addition of chromium to either Fe-Cr alloys or Fe-Cr-10%Ni alloys having completely ferritic structures increases corrosion rates in boiling 1.0 *N* sulfuric acid. In the case of the alloys with 10% nickel, corrosion rates are all much lower than those of the Fe-Cr alloys (Fig. 7). Thus, increases in chromium and decreases in nickel contents of ferrite phases in duplex structures increase their corrosion rates in boiling 1.0 *N* sulfuric acid. Because there is almost no corrosion of austenite in the duplex structure, the corrosion rate of the ferrite can be estimated by dividing the average corrosion rate by the surface-area fraction of the ferrite (assuming that all the weight-loss comes from dissolution of the ferrite). This has been done in Fig. 7 for the curve "ferrite in duplex Fe-Cr-10%Ni." Note that in four cases ferrite in duplex structures has corrosion rates even higher than those of the nickel-free Fe-Cr alloys. Because the

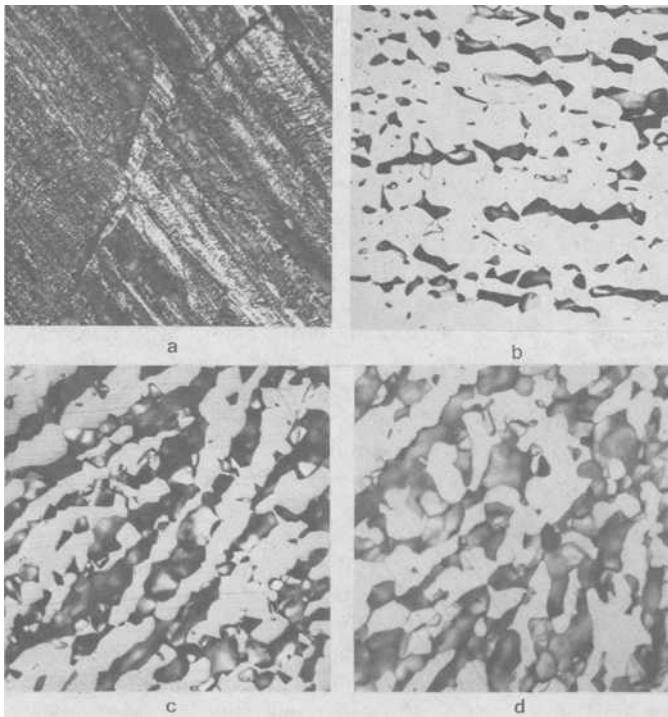


FIG. 5—Effect of microstructure of duplex Fe-Cr-10%Ni alloys on their corrosion in boiling 1.0 *N* H_2SO_4 . Specimen heated 2 h at 1066°C, 4-min exposure, X400. Surface area fractions were calculated from EDS analysis. (a) Fe-20%Cr-10%, 0% α . (b) Fe-25%Cr-10%Ni, 9.5% α . (c) Fe-27%Cr-10%Ni, 29.0% α . (d) Fe-28%Cr-10%Ni, 47.3% α .

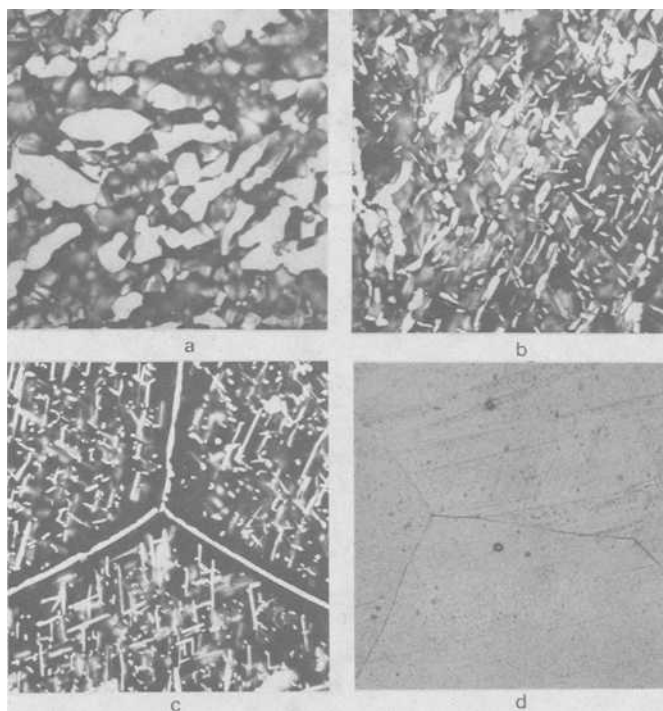


FIG. 6—Effect of microstructure of duplex Fe-Cr-10%Ni alloys on their corrosion in boiling 1.0 N H_2SO_4 . Specimens heated 2 h at 1066°C, 4-min exposure, X400. Surface area fractions were calculated from EDS analysis. (a) Fe-29%Cr-10%Ni, 42.1% α . (b) Fe-32%Cr-10%Ni, 58.5% α . (c) Fe-35%Cr-10%Ni, 84.3% α . (d) Fe-40%Cr-10%Ni, 100% α .

ferrite phases in the duplex region have about 6 to 8% nickel (Table 3), their individual corrosion rates should fall between the curves of Fe-Cr and ferritic Fe-Cr-10%Ni alloys. Alloy concentration effects alone are not likely to cause such high corrosion rates in duplex structures. Thus, there must be some other reason for the high corrosion rates of the ferrite phases.

The corrosion potentials of iron, chromium, and nickel in 1.0 N sulfuric acid are in the order: $E_{\text{corr}}^{\text{Cr}} < E_{\text{corr}}^{\text{Fe}} < E_{\text{corr}}^{\text{Ni}}$ [1]. It seems reasonable to assume that the high chromium and low nickel contents in ferrite make it anodic to the corresponding austenite with its lower chromium but higher nickel contents. The resulting galvanic effect would be expected to increase the corrosion rates of ferrite phases and, perhaps, to decrease the dissolution of austenite phases. This assumption is supported by galvanic currents measured between Type 304 (18%Cr-8%Ni) and Type 430 (16%Cr) stainless alloys exposed in boiling 1.0 N sulfuric acid [1] and between ferritic Fe-5%Ni and austenitic Fe-60%Ni alloys in 0.001 and 10.0 N sulfuric acid as reported by Economy et al. [9].

A schematic polarization diagram for galvanic corrosion of duplex Fe-Cr-10%Ni alloys in boiling 1.0 N sulfuric acid is shown in Fig. 8. Here, it is assumed that the only significant anodic reaction is the dissolution of ferrite, and the only significant cathodic reaction is the reduction of hydrogen ions on austenite. Both assumptions are not entirely correct when the surface-area fraction of ferrite is close to 1, and the reduction of hydrogen ions in local cells on ferrite has to be taken into account. Also, as shown in Figs. 5 and 6, there is some attack on the austenite phases. Nevertheless, the assumptions may be useful as a first approximation.

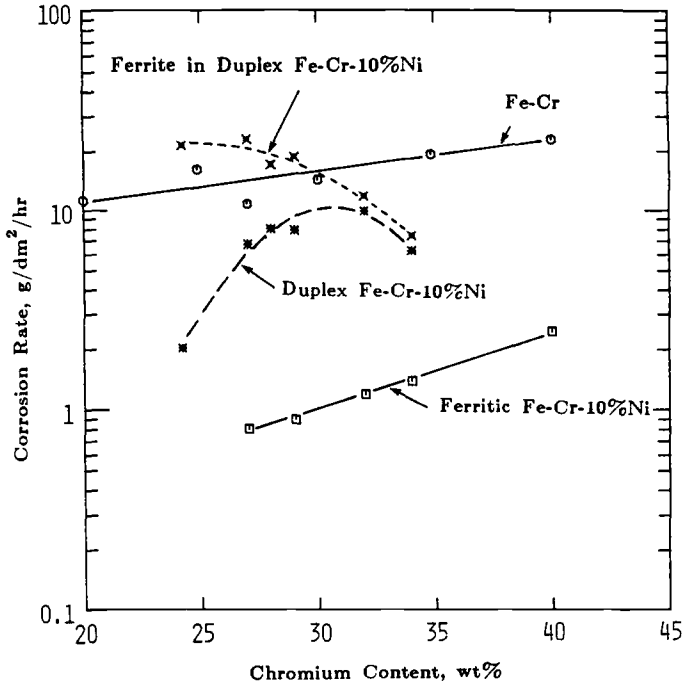


FIG. 7—Comparison between the corrosion rate of Fe-Cr and Ferritic Fe-Cr-10%Ni alloys and ferrite in duplex Fe-Cr-10%Ni alloys in boiling 1.0 N sulfuric acid.

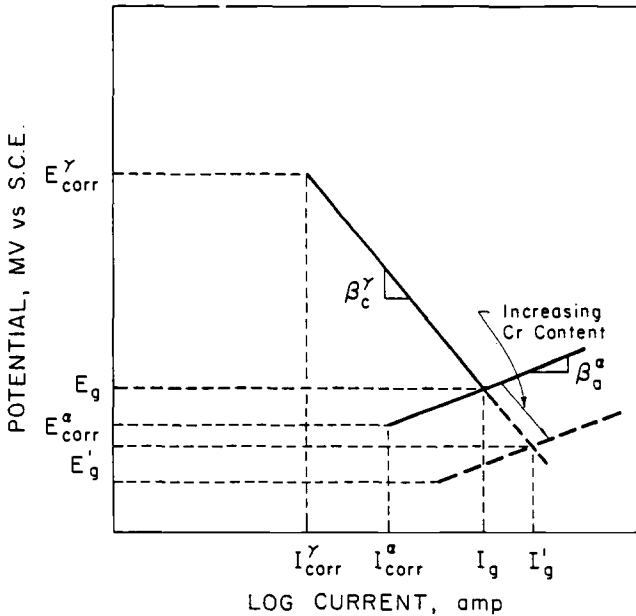


FIG. 8—Schematic polarization diagram for galvanic corrosion of duplex Fe-Cr-10%Ni alloys in boiling 1.0 N sulfuric acid.

If both the anodic and the cathodic reactions are under activation-polarization control, the intersection of these two polarization curves (Fig. 8) gives the galvanic corrosion potential E_g , and the galvanic corrosion current density i_a^α . Stern [2] and Mansfeld [3] have provided a mathematical analysis for the effect of anode and cathode surface areas on galvanic corrosion. For this treatment, they assumed two dissimilar metals of constant composition in the form of macroscopic parallel plates with various ratios of the surface areas of the cathode and the anode.

$$E_g = (\beta_a^\alpha E_{\text{corr}}^\gamma + \beta_c^\gamma E_{\text{corr}}^\alpha) / (\beta_a^\alpha + \beta_c^\gamma) + \beta_a^\alpha \beta_c^\gamma / (\beta_a^\alpha + \beta_c^\gamma) \left(\log \frac{1-f}{f} + \log \frac{i_{\text{corr}}^\gamma}{i_{\text{corr}}^\alpha} \right) \quad (2)$$

$$\log i_a^\alpha = M \log \frac{1-f}{f} + N \quad (3)$$

where

$$M = \beta_c^\gamma / (\beta_a^\alpha + \beta_c^\gamma) \quad (4)$$

$$N = M \log i_{\text{corr}}^\gamma + (1 - M) \log i_{\text{corr}}^\alpha + (E_{\text{corr}}^\gamma - E_{\text{corr}}^\alpha) / (\beta_a^\alpha + \beta_c^\gamma) \quad (5)$$

In the following discussion this mathematical treatment is applied to the microstructures of the Fe-Cr-10%Ni alloys in which the ferrite and austenite component are about $20 \mu\text{m}$ in diameter, (Figs. 5 and 6) and in which both the area ratios and the compositions of these phases vary with the alloy composition. The constant M can be calculated by Eq 4 from the Tafel slopes of the anodic and cathodic reactions. It has been found [1] that β_c^γ is about 120 mV/decade for a wide range of materials, including stainless steels of various compositions. The constant β_a^α for the anodic metal dissolution reaction has been found [1] to be 40 mV/decade for a wide range of stainless steels. Thus, it may be assumed that these values remain constant for various compositions of ferrite and austenite in the microstructures of the alloys of this investigation. When these values are substituted in Eq 4 above, M is found to be 0.75. The constant N , given by Eq 5, varies with the composition of ferrite and austenite, which also determines the free corrosion potentials, E_{corr}^α and E_{corr}^γ , and the free corrosion current densities, i_{corr}^α and i_{corr}^γ , of the ferrite and the corresponding austenite phases. Thus, the first term in Eq 3 is the effect of the surface-area ratio on the galvanic corrosion current density, and the second term N reflects the effect of changing composition of the two phases. Because none of these values for the corrosion potentials and corrosion current densities in Eq 5 is available, it is not possible to calculate N or the galvanic corrosion current density i_a^α for comparison with the corrosion rates determined from weight-loss data. However, values of N have been derived by the procedures shown in Fig. 9 for Eq 3. Values of $\log i_a^\alpha$ obtained by weight-losses have been plotted against $\log(1-f)/f$ derived from data in Table 3.

In the plot of $\log i_a^\alpha$ versus $\log(1-f)/f$ (Fig. 9), a set of parallel lines with a slope of 0.75 is drawn through each of the weight-loss data, and the constant N is given for each of them by the intercept at 1.0 on the log scale. If the surface area ratio were the only factor determining the galvanic current density, these values would fall on the straight lines. As the austenite/ferrite surface-area ratio is decreased with increasing bulk chromium content, there is an increase in the galvanic effect caused by the increasing difference in the composition between the ferrite and the corresponding austenite (Table 2). The free corrosion potential is decreased by increasing chromium concentration and also by decreasing the concentration of nickel. If it is assumed that a 1% increase in chromium is equal to a 1% decrease in nickel, we can add algebraically the differences between the composition of ferrite and austenite. As shown in Fig. 10, the value

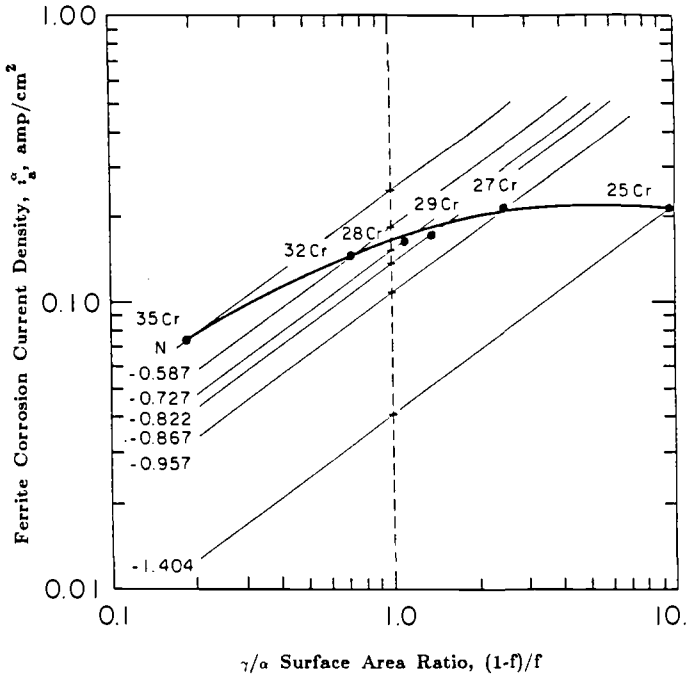


FIG. 9—Effect of austenite/ferrite surface-area ratio and of ferrite composition on ferrite corrosion current density. The diagonals show the effect of surface-area ratio only.

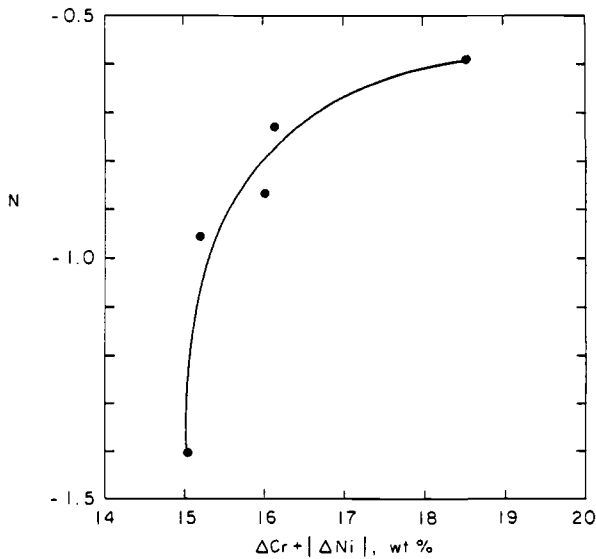


FIG. 10—Effect of the absolute sum of composition difference in chromium and nickel on the constant N in Eq 3.

of the constant N increases as the composition difference, $\Delta\text{Cr} + |\Delta\text{Ni}|$, increases. However, in the duplex structures studied, the galvanic corrosion current density increases as the austenite/ferrite surface-area ratio increases (Fig. 9). Thus, the effect of the surface-area ratio is greater than that of the variations in composition in determining the total corrosion current density on the ferrite phases.

The total galvanic corrosion current i_g , is given by the product of the anodic (ferrite) surface-area fraction f and the galvanic corrosion current density i_a^α . Thus

$$i_g = f i_a^\alpha \quad (6)$$

and using Eq 3 for i_a^α

$$\log i_g = \log f + M \log(1 - f)/f + N \quad (7)$$

As the surface-area fraction of the austenite increases, the galvanic effect increases, but the area (ferrite) available for preferential corrosion decreases. The competition between these two effects results in a maximum of the galvanic corrosion current i_g at a ferrite surface-area fraction of $1 - M$ [3].

The impact of changes in alloy composition on the ferrite corrosion current density can also be seen from Fig. 9. For example, when the Fe-27%Cr-10%Ni alloy is chosen as a reference point, the theoretical line, with a slope of 0.75, for pure surface-area ratio effect gives a value of -0.957 for the constant N . Equations 3 and 7 then become

$$\log i_a^\alpha = 0.75 \log(1 - f)/f - 0.957 \quad (8)$$

$$\log i_g = \log f + 0.75 \log(1 - f)/f - 0.957 \quad (9)$$

Equations 8 and 9 are for the ideal case of coupling two alloys having the compositions of ferrite and austenite in the duplex Fe-27%Cr-10%Ni alloy in the form of parallel plates of the same shape. The difference between this theoretical line and the measured ferrite corrosion current density gives the effect of changes in alloy composition on galvanic corrosion current density. For example, for a galvanic couple with the compositions of those in the duplex Fe-27%Cr-10%Ni alloy, Eq 7 gives a galvanic corrosion current density of 0.312 amp/cm^2 at an austenite/ferrite surface-area ratio of 0.186, which is equal to that of the Fe-35%Cr-10%Ni alloy. However, because the composition difference between austenite and ferrite in the duplex Fe-35%Cr-10%Ni alloy is larger than that in the Fe-27%Cr-10%Ni alloy, the measured galvanic corrosion current density gives a higher value of 0.73 amp/cm^2 . To verify this and to separate the composition and surface-area effects, galvanic corrosion measurements are proposed on two single phase alloys with a range of surface area ratios, one completely ferritic, Fe-32.9%Cr-6.9%Ni, and the other completely austenitic, Fe-23.7%Cr-12.8%Ni. These two compositions were found in the ferrite and the austenite phases of the duplex Fe-27%Cr-10%Ni alloy in this investigation.

The effect of alloy composition on the galvanic corrosion current is shown in Fig. 11. The dotted line represents the ideal case of constant alloy composition for the Fe-27%Cr-10%Ni with a maximum at a ferrite surface-area fraction of 0.25. For alloys with chromium contents higher than 27%, the differences of chromium and nickel contents between the ferrite and the austenite increase, and therefore the galvanic effects should be stronger as revealed by the higher galvanic corrosion currents, i_g .

The corrosion potentials in boiling 1.0 N sulfuric acid for alloys with various heat treatments are shown in Fig. 12. For pure metals, the corrosion potentials [1] are $E_{\text{Cr}} = -700 \text{ mV}$, $E_{\text{Fe}} = -490 \text{ mV}$, and $E_{\text{Ni}} = -150 \text{ mV}$. Heat treatment at 1066°C results in a corrosion potential of

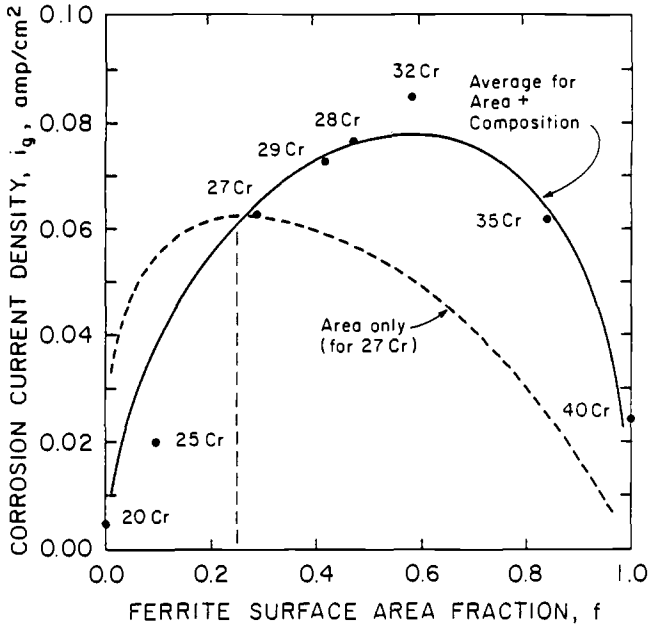


FIG. 11—Comparison of pure surface area effect with measured data on total of surface-area plus composition effect.

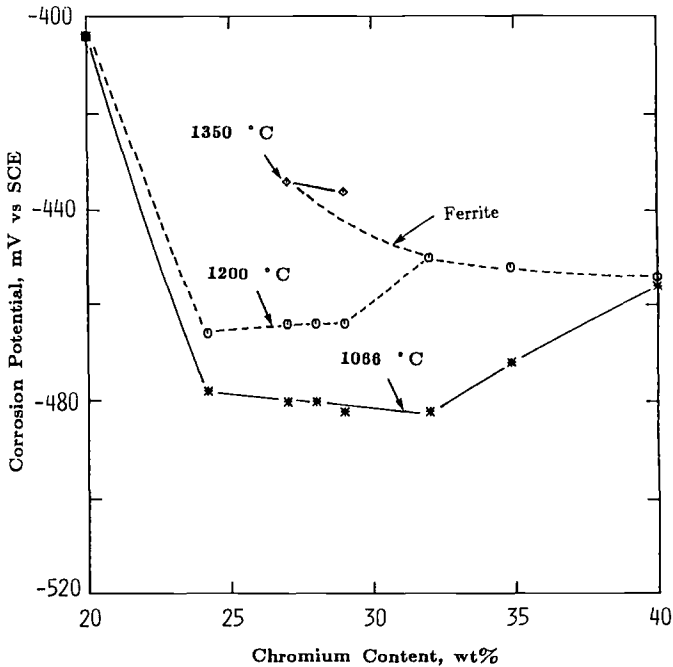


FIG. 12—Effect of chromium, content and annealing temperatures on corrosion potentials of Fe-Cr-10%Ni alloys in boiling 1.0 N sulfuric acid.

−404 mV (versus SCE) on austenitic Fe-20%Cr-10%Ni. For alloys with chromium contents between 25 and 35%, which have an austenite/ferrite duplex structure, the “mixed” potential of the ferrite and austenite (Fig. 8) is almost constant at about −480 mV. Thus, this potential is mostly determined by the potential of the ferrite phase and is not affected by the area of the ferrite. Only when the ferrite area exceeds 50% is there a change in corrosion potential toward that of the 40% chromium alloy with 10% nickel. For the pure ferritic Fe-40%Cr-10%Ni alloy, the corrosion potential is −456 mV. It might have been expected that this potential would also be near −480 mV. The move in the noble direction for the ferritic alloy with 40% chromium is a result of its higher nickel content. Without any nickel the corrosion potential of a Fe-40%Cr alloy was found to be −611 mV in boiling 1.0 *N* sulfuric acid. Addition of 10% nickel increases the corrosion potential by 155 mV. As shown in Table 3, the nickel content of the ferrite in the duplex structures is about 7%. The corrosion potential for this nickel content can be estimated by interpolation as −503 mV. This is even more active than the “galvanic” or “mixed” corrosion potentials of the duplex structures, whose nickel contents are in the range of 6 to 7% (Table 2).

The high corrosion rates resulting from preferential attack of ferrite in duplex structures have also been observed in several other reducing acids. As shown in Table 4, the corrosion rate of the Fe-32%Cr-10%Ni alloy with a pure ferritic structure is always lower than that with duplex structure. For example, the corrosion rate of the duplex alloy formed by heating at 1066°C is 3.4 g/dm²/h in boiling 1.2 *N* HCl. When the microstructure is converted to pure ferrite by heat treating at 1200°C the corrosion rate decreases to 0.83 g/dm²/h.

Thus, the galvanic effect in duplex structures may contribute to preferential attack in castings, in ferrite-bearing weld metal, for example, Type 308L and in the new duplex stainless steels, during exposure to reducing acids in pickling baths and during exposure in plant service. Such preferential attack of ferrite in cast stainless steels and in welded austenitic stainless steel tubing has been reported by Gurry et al. [10] and Bialosky [11].

Conclusions

1. On Fe-Cr-10%Ni alloy material that has a duplex, austenite-ferrite structure, there is preferential attack on the ferrite phase in reducing acids. The corrosion rate of ferrite increases with increasing chromium and with decreasing nickel content.
2. Attack on ferrite in duplex structures is increased by galvanic action between the anodic ferrite and the cathodic austenite.
3. The magnitude of the galvanic effect is a function of the ratio of the surface area of ferrite to austenite. Increasing the chromium content from 20 to 40% in alloys with 10% nickel (heated at 1066°C) converts the structure from pure austenite at 20% chromium to duplex structures with increasing amounts of ferrite in the range of 25 to 35% chromium, to pure ferrite at 40% chromium.

TABLE 4—Corrosion of duplex and pure ferritic Fe-32%Cr-10%Ni alloy in boiling reducing acids.

Solution	Pure α , g/dm ² /h	$\alpha + \gamma$ Duplex ^a , g/dm ² /h
1.0 <i>N</i> H ₂ SO ₄	1.20	8.80
5.8 <i>N</i> HCl	7.10	10.60
1.2 <i>N</i> HCl	0.83	3.37
12.0 <i>N</i> HCOOH	0.06	0.38

^aThe specimen corrodes in the active state, and the weight-loss of the duplex structure is from ferrite dissolution.

4. In the duplex alloys, not only the ratio of ferrite to austenite surface area changes with increasing chromium content, but also the composition of the ferrite and austenite phases. Previously developed mathematical treatments for macroscale galvanic corrosion have been used to separate the pure surface area ratio effect from the combined effect of relative areas and changes in compositions of phases. Converting duplex structures to 100% ferrite by high temperature heat treatments reduces corrosion rates to relatively low values.

5. The effect of the surface area ratio (galvanic effect) is greater than that of the variation in the compositions of the ferrite phases.

6. The above results may be applicable to studies of duplex structures in stainless steel castings, Type 308L weld metal and to the newer duplex stainless steels.

Acknowledgment

This material is based on work supported by National Science Foundation under Grant DMR-8011981.

References

- [1] Yau, Y.-H., Ph.D dissertation, Chemical Engineering Department, University of Delaware, Newark, DE, 1986.
- [2] Stern, M., *Corrosion*, Vol. 14, 1958, p. 329t.
- [3] Mansfeld, F., *Corrosion*, Vol. 27, 1971, p. 436.
- [4] Fontana, M. G. and Greene, N. D., *Corrosion Engineering*, 2nd ed., McGraw-Hill, New York, 1978, pp. 330-335.
- [5] Uhlig, H. H., *Corrosion and Corrosion Control*, John Wiley & Sons, Inc., New York, 1963, pp. 92-95.
- [6] American Society for Metals Handbook, *Metallography. Structures and Phase Diagrams*, 8th ed., Vol. 8, 1973, p. 425.
- [7] American Society for Metals Handbook, *Metallography. Structures and Phase Diagrams*, 8th ed., Vol. 8, 1973, p. 37.
- [8] Streicher, M. A., *Corrosion*, Vol. 29, 1973, p. 337.
- [9] Economy, G., Speiser, R., Beck, F. H., and Fontana, M. B., *Journal of the Electrochemical Society*, Vol. 108, 1961, p. 337.
- [10] Gurry, R. W., Jacob, E. M., and Allen, S. H., *Industrial Engineering Chemical Products Research and Development*, Vol. 10, 1971, p. 112.
- [11] Bialosky, J. M., *Corrosion*, Vol. 12, 1956, p. 59t.

Galvanic Corrosion Resistance of Welded Dissimilar Nickel-Base Alloys

REFERENCE: Corbett, R. A., Morrison, W. S., and Snyder, R. J., "Galvanic Corrosion Resistance of Welded Dissimilar Nickel-Base Alloys," *Galvanic Corrosion, ASTM STP 978*, H. P. Hack, Ed., American Society for Testing and Materials, Philadelphia, 1988, pp. 235-245.

ABSTRACT: A program for evaluating the corrosion resistance of various dissimilar welded nickel-base alloy combinations is outlined. Alloy combinations included Alloy ALLCORR, Alloy C-276, Alloy 72, and Alloy 690. The gas tungsten arc weld (GTAW) process involved both high and minimum heat input conditions. Specimens were evaluated in the as-welded condition, as well as after having been aged at various conditions of time and temperature. These were judged to be most representative of process upset conditions, which might be expected. Corrosion testing evaluated resistance to an oxidizing acid and a severe service environment in which the alloy combinations might be used. Mechanical properties are also discussed.

KEY WORDS: galvanic corrosion, welding, nickel-base alloys, radioactive waste

A facility, at the Department of Energy's Savannah River Plant, is under construction to immobilize high-level radioactive waste by combining it with a special glass frit and vitrifying it into a borosilicate glass. The molten glass will be cast into stainless steel canisters for permanent storage.

The high-level radioactive waste has a pH of 12+ and is stored in carbon steel tanks. Processing the waste with formic acid is required for combining it with the frit before vitrification. This acidic environment contains halides, nitrites, nitrates, copper, mercury, and many other elements and compounds. While Type 304L stainless steel has demonstrated suitability for some chemical and utility services, extensive testing [1,2] indicated this and other stainless steels had unsatisfactory resistance to pitting and stress corrosion cracking in the waste treatment process. Testing also indicated that mercuric and cupric ions reacted synergistically with halides to increase pitting and crevice corrosion [3]. This same testing indicated that special nickel-base alloys containing significant amounts of chromium and molybdenum were required to resist general, as well as localized corrosion. A variety of alloys was required to meet the specific requirements of several chemical compositions, temperatures, and pH values. The high-level radioactivity has made hands-on maintenance and replacement of equipment extremely difficult. Because crevice corrosion is a major concern, flanged and gasketed connections must be minimized. Several different alloys, exposed in adjoining process locations, have to be welded together rather than flanged. Each individual base alloy had been extensively corrosion tested and selected for the specific process exposure. Fusion welding of two base alloys produces zones of variable compositions. Little is known about their corrosion resistance or mechanical properties.

For this project alloys and alloy combinations have to resist a variety of process exposures, including the following:

- High-temperature corrosive environments from 400 to 900°C.

¹President and vice-president respectively, Corrosion Testing Laboratories, Inc., Newark, DE 19711.

²Maintenance engineer, E. I. du Pont de Nemours & Co., Inc., Wilmington, DE 19898.

- Rapid cooling with condensation of melter off-gas from 400°C down to 90°C.
- Extremely corrosive and complex condensate at about 90°C, which can cause chloride stress corrosion cracking in Type 304L stainless steel and severely pit Alloy 20.

Wrought alloys used in this study were ALLCORR™, Hastelloy™ Alloy C-276, and Inconel™ Alloy 690. Filler metals used to join these alloys and combinations included ALLCORR, Hastelloy Alloy C-276, Inconel Alloy 72, and Inconel Alloy 690 weld wires. Wrought alloy and filler metal compositions are found in Table 1.

Welding Processes

Extensive welding experience was already available for the individual alloys both from lengthy laboratory testing, as well as from fabrication of pilot plant and some full-scale process equipment. Equipment design for the project was far enough advanced so that a range of thicknesses for vessels and pipe could be estimated. With this information, joint detail, plate thickness, filler metal diameter, and the gas tungsten arc weld (GTAW) process, combination of alloys were selected.

Because the plant process equipment in question was expected to have a wall thickness range between 6.4 and 12.7 mm, the weld test specimens were made from a 9.5-mm-thick plate. Each weld specimen was made from two pieces of plate approximately 76.2 by 152.4 mm double beveled to approximately $37\frac{1}{2} \pm 2\frac{1}{2}^\circ$ with a 1.6-mm land. This weld sample configuration was chosen so as to provide a reasonably large weld area and at the same time approximate the type of weld used in vessel fabrication. Filler metals were either 1.6- or 2.4-mm-diameter bare wire. For the most part, the 1.6-mm wire was used for root passes while the 2.4-mm wire was used to fill out the remainder of the weld. Figure 1 shows the weld specimen joint detail, and Fig. 2 shows the layout of the typical test plate. Each test plate was fabricated by welding two 76.2- by 152.4-mm plates together to form a finished 152.4- by 152.4-mm plate. The GTAW process was used for all welding. All plates and weld wires were solvent cleaned using Dupont Freon® 113 before starting the welds. Depending on whether the coupons were high or low heat input, the current range was 100 to 130 amps at 10 to 14 V. Welding grade argon, at 1.1 m³/h was used with a gas lens torch having a 19.1-mm cup. Argon was also used as the backing gas. About 3.2-mm electrode “stick-out” from the gas cup was found to be important in making the quality welds required for this study. Quality was also maintained by mechanically removing about 3.2 mm of the oxidized end of the used filler wire before restarting the welding process.

For each combination of alloys, sample plates were prepared using both high and low levels of heat input during welding. For the low heat-input plates, six narrow stringer beads per side

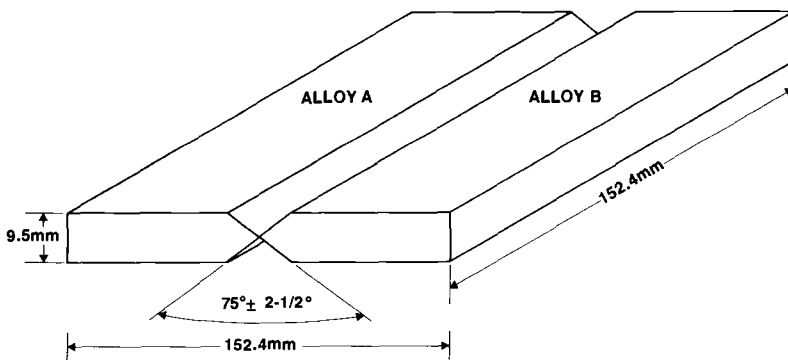


FIG. 1—Typical weld test plate.

TABLE 1—Analysis of alloys used in welded dissimilar nickel-base alloy corrosion studies.

Alloy	Producer	C	Cr	Ni	Mo	Fe	W	Ti	Al	Co
ALLCORR plate	Teledyne Allvac	0.03	30.93	balance	9.97	0.11?	1.97	0.24	0.23	...
ALLCORR filler	Teledyne Allvac	0.033	30.94	balance	10.13	0.13	2.01	0.26	0.26	0.01
C-276 plate	Cabot Corp.	0.002	15.70	balance	5.71	4.16	0.68	...
C-276 filler ^a	Cabot Corp.	0.004	15.76	balance	15.64	5.85	3.91	1.52
690 plate ^b	Huntington alloys	0.013	29.10	balance	0.09	7.35
690 filler ^c	Huntington alloys	0.043	29.45	balance	...	10.02	...	0.46	0.89	...
72 filler	Huntington alloys	0.03	44.22	balance	...	0.20

^aEniCrMo-4.^bSilicon 0.12%, manganese 0.22%.^cSilicon 0.07%, manganese 0.03%.

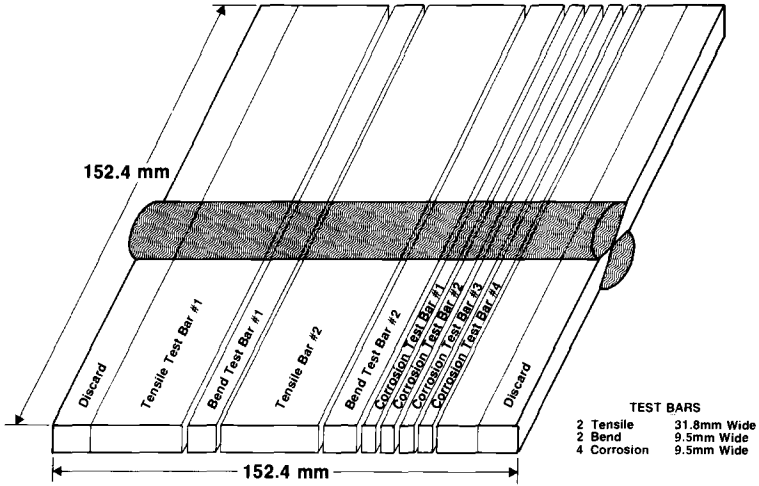


FIG. 2—Typical layout of weld test plate showing various test bars.

were used at the low end of the current range. Each pass was permitted to cool before starting the next. The plate temperatures never exceeded 120°C. To help insure that the temperature stayed below 120°C, the plate was held firmly in a special water cooled aluminum fixture. This fixture also permitted back purging of the weld with argon.

For the high heat-input plates, three wide weaving passes per side were used at the high end of the current range. The plates were held at about 260°C during the entire welding process. By using weaving passes and the higher current setting, the 260°C plate temperature was easily maintained. While the same aluminum fixture was used to hold the plates in place, no cooling water was used during the high heat welding process.

The temperature of the specimen plates was checked frequently during welding using either thermocouples or temperature indicating crayons. A stainless steel power brush was used to remove weld oxidation as required, but generally the welds were bright and needed no clean-up between welding passes. Root passes were dye penetrant inspected.

In general, the plates were fitted up with a minimum of gap. One side was first welded out completely; then the specimen was turned over, and the exposed root pass ground out. The weld was then completed. Alloy plate and filler metal combinations are shown in Table 2.

TABLE 2—Alloy and filler metal combinations.

Plate "A" Alloy	Plate "B" Alloy	Weld Filler Metal "C"
C-276	690	C-276
C-276	690	690
C-276	690	72
C-276	ALLCORR	72
690	ALLCORR	690
690	ALLCORR	ALLCORR
690	690	72
690	ALLCORR	72
ALLCORR	C-276	C-276
ALLCORR	C-276	ALLCORR
ALLCORR	ALLCORR	72

Depending on the alloy combinations and the expected process exposure, different post welding heat treatments were given some specimens. All alloy combinations were prepared and tested in the as-welded condition. Since a possible process upset in the plant could, in an extreme case, expose alloys and welds to temperatures as high as 870°C, sets of each welded alloy combination were aged at this temperature for 24 h. For most of the alloys involved in this test program, suppliers and fabricators alike agreed that exposure at this temperature was likely to have significant adverse effects on both corrosion resistance and mechanical properties. They also agreed that there would be the same and perhaps more severe adverse effect on the welded dissimilar combinations. As the test program progressed, the expected adverse effects were confirmed. Review of these preliminary results prompted a re-evaluation of the projected upset conditions. As the result of this re-evaluation, other lower temperatures and shorter times were included in the test program.

Weld Specimen Preparation

Each weld specimen plate was mechanically cut into eight individual specimen bars with the weld in the center of each bar (Fig. 2). For tension tests two bars approximately 32 mm wide were cut. Adjacent to each of the tensile bars two 9.5-mm-wide specimens for bend testing were also taken. Four bars for corrosion tests were cut approximately 9.5-mm-wide. Sufficient material from each side of the weld specimen plate was discarded to remove unwanted weld end effects.

Corrosion Testing

Each corrosion test bar was cut to produce three individual coupons. One from each end of the test bar, away from the weld, represents the base alloy. The third coupon came from the middle of the corrosion test bar to include the entire weld fusion zone, as well as some of the base alloy on each side of the weld (Fig. 3). Coupons were wet finished with 120 grit paper.

Coupon Acceptance Testing

One of the requirements for building this facility was the corrosion evaluation of alloys used in the radioactively hot process cells. Therefore, before accepting any metal shape for fabrication into process equipment, specimens representing each individual mill heat, heat treatment lot, size or thickness were required to pass an appropriate corrosion evaluation acceptance test to demonstrate its resistance to intergranular attack (IGA). Therefore, all wrought material for this test program was corrosion evaluated for IGA resistance. Suitable tests (that is, ASTM Practices for Detecting Susceptibility to Intergranular Attack in Austenitic Stainless Steels [A

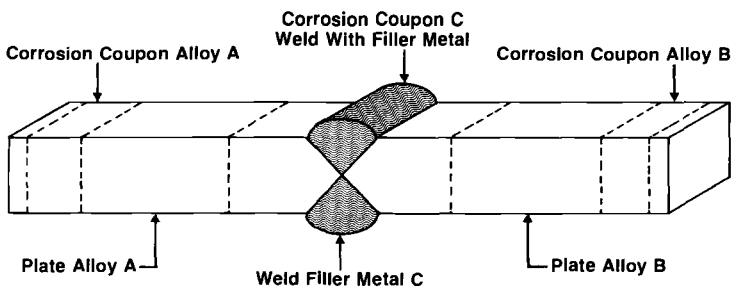


FIG. 3—Typical corrosion test bar.

262], ASTM Test Methods of Detecting Susceptibility to Intergranular Attack in Wrought, Nickel-Rich, Chromium-Bearing Alloys [G 28], and so forth) were performed as a quality assurance check to confirm proper chemical composition and correct heat-treatment.

Test Procedure

To determine the effect of welding, heat treatment, filler metal, and alloy composition combinations on corrosion resistance, two different test solutions were selected. To represent an acidic oxidizing condition, a boiling 50% sulfuric acid plus 42 g/L ferric sulfate solution was chosen to evaluate general corrosion resistance susceptibility to second phase attack and IGA caused by heat treatment. A second solution was chosen after extensive prior testing [1,2] had developed a composition and temperature (90°C), which was judged to represent the worst case for process stream corrosion (Table 3). These two solutions were used to corrosion evaluate each base alloy, as well as the weld zone and weld metal.

A serrated Du Pont Teflon® washer (of design recommended in ASTM Guide for Crevice Corrosion Testing of Iron-Base and Nickel-Base Stainless Alloys in Seawater and Other Chloride Containing Aqueous Environments [G 78]) was bolted in place to determine if crevice corrosion might be a problem. Coupons in the synthetic process solution test were generally exposed for 7 to 10 days depending on intermediate visual observations. In ferric sulfate-sulfuric acid tests coupons were exposed for 24 h. Coupons were immersed in apparatus similar to Fig. 1 in ASTM G 28 and held at test temperature. A condenser on each flask returned condensable vapors and maintained the correct test solution composition.

In addition to an initial visual inspection after exposure, all coupons were carefully inspected at magnification $\times 20$. To more clearly define any suspicious or locally attacked areas, higher magnifications were used. Specific corrosion information obtained included:

- general corrosion rates,
- galvanic corrosion,
- pitting,
- crevice corrosion, and
- end grain attack.

Corrosion Test Results

A major goal of this study was to determine if there was significant galvanic corrosion between two alloys of different compositions when joined by welding and exposed in a typical process stream. Other work [4] indicated that galvanic corrosion might be expected. In that work, coupons were mechanically coupled and used dissimilar alloy combinations, as well as different process exposures.

TABLE 3—Composition of synthetic melter off-gas condensate solution (pH 2.2, 90°C).

Ion	Weight, %
Cl ⁻ (as HgCl ₂ and NaCl)	0.25
F ⁻ (as NaF)	0.03
I ⁻ (as NaI)	0.003
SO ₄ ⁻ (as Na ₂ SO ₄)	0.08
NO ₃ (as Na ₂ NO ₃)	0.10
Hg ⁺⁺ (as HgCl ₂)	0.10
Water	balance

Ferric Sulfate-Sulfuric Acid Test—The boiling ferric sulfate sulfuric acid test is an oxidizing solution and was used to screen for harmful second phase precipitates in the nickel-base alloys. This solution was also used to evaluate chemical composition, heat treatment, and resistance to IGA.

Test results indicated no significant attack occurred on any alloy combination except those containing Alloy C-276. As a guide, if the corrosion rate of Alloy C-276 in this test is more than 12 mm/year [5] it usually indicates an increasing tendency toward intergranular attack or other related corrosion phenomenon. Any coupon containing Alloy C-276 that was aged for 24 h at 870°C had a very high corrosion rate in the acidified ferric sulfate test indicating severe intergranular corrosion. Corrosion rates on all as-welded and aged combinations of Alloy 690, Alloy ALLCORR, and Alloy 72 were acceptably low in this test.

Typical corrosion rates for alloy combinations exposed in this test are shown in Table 4.

Process Test Solution—The real test for alloys to be used in plant equipment involves exposure to the synthetic process solution. This solution represents the most aggressive environment expected, either in regular service or under upset conditions. While the solution used for this test does not appear aggressive, extensive testing [1,2] had determined that Type 304L stainless steel would generally corrode at 0.8 to 1.0 mm/year, stress corrosion crack in a matter of a few hours, and develop crevice corrosion as deep as 0.6 mm in 14 days. In these same tests Alloy 20 also suffered from severe crevice corrosion.

In this study, no significant general corrosion, galvanic corrosion, end grain attack, or pitting was seen on any of the test alloys. Weld heat input and post weld heat treatment appeared to have no significant effect on the corrosion rates of the galvanically coupled alloys in the synthetic process solution. Earlier testing programs determined the general acceptability of all the high alloy nickel-base materials in the synthetic process solution. They also indicated a potential problem with crevice corrosion of Alloy 690, particularly at 90°C. This was expected considering that Alloy 690 contains no molybdenum and the low-pH, high chloride nature of the testing solution. While Alloy 72 filler metal also contains no molybdenum, its high chromium content (44%) provided increased resistance to crevice corrosion. When Alloy 72 filler metal was used with Alloy 690 base metal, crevice corrosion was generally concentrated on the Alloy 690 component. This made Alloy 72 a possible candidate for joining plate alloy combinations.

TABLE 4—Corrosion of welded dissimilar nickel-base alloy combinations in boiling acidified ferric sulfate solution.^a

Alloy Combination ^b			Corrosion Rate, mm/year					
			As Welded			Aged 24 h at 8700°C		
A	C	B	A	C	B	A	C	B
C-276	C-276	690	4.32	3.30	0.15	48.26	38.10	0.17
C-276	690	690	4.57	1.73	0.17	45.72	19.05	0.15
C-276	72	690	4.57	1.68	0.17	40.64	27.94	0.19
C-276	72	ALLCORR	4.57	1.82	0.25	68.58	66.04	0.20
690	690	ALLCORR	0.19	0.20	0.23	0.14	0.23	0.23
690	ALLCORR	ALLCORR	0.16	0.17	0.22	0.14	0.18	0.24
690	72	690	0.14	0.14	...	0.14	0.15	...
690	72	ALLCORR	0.14	0.15	0.22	0.12	0.15	0.18
ALLCORR	C-276	C-276	0.25	3.81	4.57	0.20	48.26	45.72
ALLCORR	ALLCORR	C-276	0.23	1.91	4.32	0.17	66.04	96.52
ALLCORR	72	ALLCORR	0.23	0.17	...	0.21	0.20	...

^a50% sulfuric acid plus 42 g/L ferric sulfate.

^bSee Fig. 3 for corrosion test coupon layout.

This current work confirmed the earlier work in this respect and also revealed that weld zones containing an Alloy 690 component were particularly sensitive. Where there are no crevices, Alloy 690 proved to be an acceptable material for construction of equipment in this particular process. However, crevice corrosion rates for alloy combinations involving Alloy 690 were unacceptably high, and might result in penetration of a 9.5 mm thick weld in as little as five months.

Alloys with high chromium and molybdenum contents are known [2] to have improved general corrosion resistance as well as improved resistance to localized attack in the synthetic process solution. Therefore, where combinations include Alloy 690, welding with Alloy C-276 or Alloy ALLCORR filler metal appear to be the better choice. Alloy 72 filler metal, with its high chromium content, is judged also to be acceptable for joining Alloy C-276 to Alloy 690. For joining Alloy ALLCORR to Alloy C-276, either Alloy ALLCORR or Alloy C-276 filler metal can be recommended.

From an engineering standpoint, galvanic corrosion did not visually appear to be a significant problem, but elimination of crevices from any source in any form is necessary and will require special design, fabrication, and construction considerations.

Typical results obtained by corrosion testing alloy combinations in the synthetic process solution are tabulated in Table 5.

Mechanical Testing

Mechanical Coupons

Tension test bars were prepared from all welded alloy combination and conditions, and tested in accordance with requirements of the American Society for Mechanical Engineers (ASME) Boiler and Pressure Vessel Code, Section IX. Bend tests were either side or face, around a 38-mm mandrel. After some initial testing, side bends rather than face bends were judged to be more definitive. Since the side bends permitted the entire weld cross section to be evaluated they were used for the balance of the tests. Earlier work by others [6, 7] had indicated concern about

TABLE 5—Corrosion of welded dissimilar nickel-base alloy combinations in synthetic process solution (900°C, pH 2.2), see Table 3 for composition.

Alloy Combinations ^a			Corrosion Rate, mm/year					
			As Welded ^b			Aged 24 h at 870°C		
A	C	B	A	C	B	A	C	B
C-276	690	690	0.05	0.02 ^{0.05}	0.01	0.05	0.03 ^{0.03}	0.01
C-276	72	690	0.05	0.02	0.01	0.05	0.02 ^{0.1}	0.01
C-276	72	ALLCORR	0.05	0.02	0.01	0.06	0.02	0.01
690	690	ALLCORR	>0.01	0.01 ^{0.2}	<0.01	0.01	0.01 ^{0.2}	0.01
690	ALLCORR	ALLCORR	<0.01	0.01 ^{0.05}	<0.01	<0.01	0.01 ^{0.1}	<0.01
690	72	690	<0.01	<0.01 ^{0.2}	0.08 ^{0.5}	...
690	72	ALLCORR	<0.01	0.01 ^{0.1}	0.01	<0.01	<0.01 ^{0.1}	<0.01
ALLCORR	C-276	C-276	0.01	0.03	0.04	0.01	0.03	0.04
ALLCORR	ALLCORR	C-276	<0.01	0.02	0.04	<0.01	0.03	0.05
ALLCORR	72	ALLCORR	0.01	0.01	...	0.01	0.01	...

^aSee Fig. 3 for corrosion test coupon layout.

^bSuperscripts indicate depth of crevice corrosion in mm for one-week exposure. Example: 0.02^{0.1} represents a general corrosion rate of 0.02 mm per year with local crevice corrosion 0.1 mm deep occurring in 1 week.

inter-pass fusion in some alloys. While this was not found to be a problem in this study it was another reason for using side bends.

Mechanical Test Results

As-Welded—In the as-welded condition all specimens were sufficiently strong. Tensile strengths of the welded combination were always at least 95% of the strength of the unwelded lower strength alloy component. All elongations, at fracture, were in excess of 25% and most ranged between 35 and 50%. All face and side bends performed satisfactorily.

Post Weld Heat Treated—Many high-nickel alloys are sensitive to extended exposure at temperatures around 870°C. It is unfortunate that an extreme upset in this process could reach this temperature. While the aging treatment had little effect on the corrosion resistance of the alloy combinations (except for Alloy C-276), aging at 870°C for 24 h had a major effect on room temperature ductility (Tables 6 and 7).

The project engineers believed that a 24-h exposure at 870°C was an unrealistically long time for a high-temperature upset. One hour was judged to be more appropriate. To provide additional information about the effect of this shorter aging time, the same alloy combinations that failed in the 24-h exposure at 870°C (Table 6) were retested after aging for 1 h at 870°C. This time there were no failures, and all coupons exhibited acceptable ductility. See Table 8 for the corrosion rates in both the acidified ferric sulfate solution and the synthetic process solution on selected alloy combinations aged 1 h at 870°C.

Since all combinations were acceptably ductile after only 1 h at 870°C, other time-temperature combinations of alloys were scouted using bend test bars. The following alloy combinations were the most likely to be exposed to high-temperature process upsets; so they were exposed for 12 h at 815, 760, and 705°C.

- Alloy C-276 welded to ALLCORR with Alloy C-276 filler metal.
- Inconel 690 welded to ALLCORR with Inconel 72 filler.

The ductility of these alloy combinations was demonstrated to be satisfactory.

Conclusions

The current test work indicates there is little potential for galvanic corrosion in the nuclear waste vitrification process. At the same time, it confirms a crevice corrosion problem with Alloy 690, which was identified in earlier testing. From this work, it is concluded that

- Welds between the alloys tested will not galvanically corrode in synthetic condensate solution at 90°C.
- All alloys and welded alloy combinations in Table 1 are susceptible to crevice corrosion in melter off-gas condensate. Crevices should be minimized through appropriate engineering design and fabrication.
- Upset excursions to 870°C totalling more than 12 h should be avoided because of possible adverse effects on mechanical properties of the welded combinations in Table 2.

Acknowledgments

The information in this article was developed during the course of work under Contract DE-AC09-76SR0001 with the U.S. Department of Energy for the Savannah River Plant at Aiken, SC. The authors wish to thank G. L. Gaesser and R. F. Reynolds for helping prepare welded test specimens and arrange mechanical and other tests. The authors also wish to acknowledge the assistance of S. V. Fox and D. M. Tomic in conducting the corrosion tests.

TABLE 6—Typical mechanical properties of welded alloy combinations.

Alloy Combinations ^a			As Welded			Aged 24 h at 870°C		
A	C	B	Tensile, N/mm ²	Elong, %	Bend Test	Tensile, N/mm ²	Elong, %	Bend Test
C-276	C-276	690	685	29	OK	665	29	OK
C-276	690	690	673	33	OK	687	34	OK
C-276	72	690	679	31	OK	674	26	OK
C-276	72	ALLCORR	775	34	OK	755	4	F ^b
690	690	ALLCORR	637	34	OK	602	15	F
690	ALLCORR	ALLCORR	642	21	OK	569	13	F
690	72	690	635	40	OK	608	27	OK
690	72	ALLCORR	635	27	OK	643	19	F
ALLCORR	C-276	C-276	809	43	OK	707	9	F
ALLCORR	C-276	ALLCORR	782	39	OK	576	3	F
ALLCORR	72	ALLCORR	737	43	OK	700	2	F

^a See Fig. 2 for weld test plate layout.

^b Failed.

TABLE 7—Summary of mechanical tests.

Alloy (welded to)	Alloy (with)	Filler
ALLOY COMBINATIONS EXHIBITING POOR ROOM TEMPERATURE DUCTILITY AFTER AGING FOR 24 H AT 870°C ^a		
C-276	ALLCORR	72
690	ALLCORR	690
690	ALLCORR	ALLCORR
690	ALLCORR	72
ALLCORR	C-276	C-276
ALLCORR	C-276	ALLCORR
ALLCORR	ALLCORR	72
ALLOY COMBINATIONS EXHIBITING GOOD ROOM TEMPERATURE DUCTILITY AFTER AGING FOR 24 H AT 870°C		
C-276	690	72
C-276	690	C-276
C-276	690	690
690	690	72

^aTension test bars had 10% or less elongation at fracture or bend coupon failure.

TABLE 8—Corrosion rates, mm/year, on welded dissimilar alloy combinations aged for 1 h at 870°C.

Alloy Combinations ^a			Acidified Ferric Sulfate ^b			Synthetic Process Solution ^c		
A	C	B	A	C	B	A	C	B
C-276	72	ALLCORR	58.42	22.86	0.17
690	690	ALLCORR	0.13	0.17	0.18	0.01	0.06	0.01
690	ALLCORR	ALLCORR	0.15	0.21	0.14	0.01	0.02	<0.01
690	72	ALLCORR	0.12	0.18	0.25	<0.01	0.01	<0.01
ALLCORR	C-276	C-276	0.18	33.02	43.18	<0.01	0.02	0.03
ALLCORR	ALLCORR	C-276	0.22	8.38	22.86	<0.01	0.02	0.03
ALLCORR	72	ALLCORR	0.22	0.18	...	<0.01	0.01	...

^aSee Fig. 3 for corrosion test coupon layout.

^b50% sulfuric acid + 42-g/L ferric sulfate.

^cSee Table 3.

References

- [1] Bickford, D. F. and Corbett, R. A., "Material Selection for Defense Waste Processing Facility," *Corrosion of Nickel-Base Alloys*, R. M. Scarberry, Ed., American Society for Metals, 1985, pp. 59-67.
- [2] Corbett, R. A., Bickford, D. F., and Morrison, W. S., "Corrosion Evaluation of Alloys for Nuclear Waste Processing," *Materials Performance*, Vol. 26(2), 1987, pp. 40-47.
- [3] Bickford, D. F., Corbett, R. A., and Morrison, W. S., "Test Methods for Selection of Materials of Construction for High-Level Radioactive Waste Vitrification," *Advances in Ceramics*, Vol. 20, 1986.
- [4] Bickford, D. F. and Corbett, R. A., "DWPF Corrosion Testing Data Base," DPST-85-956, Savannah River Plant, Aiken, SC, 1985.
- [5] Streicher, M. A., "The Effect of Composition and Structure on Crevice, Intergranular and Stress Corrosion of Some Wrought Ni-Cr-Mo Alloys," *Corrosion*, Vol. 32, No. 3, 1976, pp. 79-93.
- [6] Jenkins, C. F. and James, T. A., "ALLCORR® Welding and Weldment Corrosion Resistance," ASM Congress, Metallography Welding, Toronto, Ontario, Canada, Oct. 1985.
- [7] Moyer, J. M. and Gerlock, R. J., "A New Corrosion Resistant Nickel-Base Alloy for Gas and Oil Industry Use," Paper 166, *Corrosion 83*, National Association of Corrosion Engineers, Houston, TX, 1983.

Industries

Galvanic Corrosion on Automobiles

REFERENCE: Baboian, R., Haynes, G., and Turcotte, R., "Galvanic Corrosion on Automobiles," *Galvanic Corrosion, ASTM STP 978*, H. P. Hack, Ed., American Society for Testing and Materials, Philadelphia, 1988, pp. 249-259.

ABSTRACT: Automobile manufacturers utilize a variety of metals to build a product that meets numerous functional and cosmetic demands. Since the auto environment is highly corrosive, they must consequently deal with galvanic corrosion problems. This paper describes some of the galvanic couples on automobiles, such as trim on painted auto-body steel, dissimilar metal fasteners, electroplated bumpers, galvanized steel, and dissimilar cooling system components. The resulting problems and mitigative measures for controlling galvanic corrosion are presented.

KEY WORDS: galvanic corrosion, automobile corrosion, paint blistering, automotive trim, dissimilar metal fasteners, electroplated bumpers, galvanized steel, automotive cooling system corrosion

Galvanic corrosion occurs when two or more dissimilar metals are in electrical and electrolyte contact. The more active metal corrodes at an accelerated rate while the more noble metal corrodes at a reduced rate. This phenomenon is usually detrimental but has also been used for beneficial effects in sacrificial cathodic protection systems, such as galvanizing.

Automobiles, though not immersed, are nonetheless subject to corrosive solutions. Externally, the combination of deicing salts and acid deposition mixed with natural precipitation results in a very corrosive electrolyte [1,2]. Subsequently a wet film deposits on cars and a poultice of mud and other road debris accumulates in recessed areas. The map in Fig. 1 shows that the most severe geographic areas for auto corrosion coincide with areas of high deicing salt usage, salt sea aerosols, and acid deposition. Internally, the automobile cooling system contains an inhibited glycol solution, which can become acidic as the organics break down.

Since auto manufacturers use various metals to produce a product that meets functional and cosmetic demands, the elements for galvanic attack are all present on external and internal components. The results can be perforation, premature loss of cosmetic attractiveness, fluid leaks, or loss of functionality.

Trim

A primary example of galvanic corrosion problems on automobiles involves the decorative metal trim. Brightly polished stainless steel is often used because it is cosmetically pleasing, dent resistant, abrasion resistant, and corrosion resistant. However, automotive body steel is anodic to stainless steel trim [3]. Because of this galvanic couple and an unfavorable area ratio (Fig. 2a), paint damage spots as far as 4 cm from the trim rust rather quickly [4,5].

Since elimination of the electrolyte is not realistic, because of inevitable holidays in paint systems, only two ways remain to resolve this problem. One is to electrically isolate the trim from the auto-body steel. However, efforts at this have been largely unsuccessful because of design constraints, deterioration of the insulators, which causes them to become conducting, or

¹Head, member of group technical staff, and member of technical staff, respectively, Texas Instruments Inc., Electrochemical and Corrosion Laboratory, Attleboro, MA 02703.

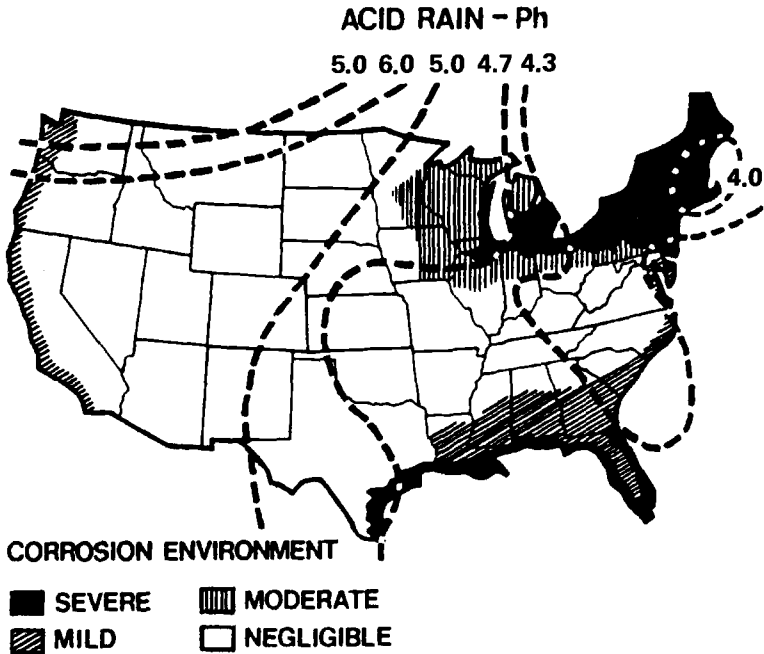


FIG. 1—Map of the United States showing high automobile corrosion rate areas and pH of acid precipitation.

the trim scratching through the paint at some point [2,3]. A more successful solution has involved the use of a metal more active than steel such as aluminum.

However, solid aluminum trim is not as abrasion resistant or corrosion resistant as stainless steel. It soon develops pits and “blush and bloom” [2]. Stainless steel clad with aluminum was therefore introduced to provide the best of both metals (Fig. 2b) [6]. The explanation for this phenomenon is shown in Fig. 3 [5]. Aluminum in this couple with steel and stainless steel becomes polarized above its pitting potential while the stainless steel and auto-body steel are polarized to more negative potentials where both steel and stainless steel are protected. The improvement in corrosion performance when stainless steel clad aluminum trim is chosen over solid stainless steel is very dramatic, as shown in Fig. 4.

General Paint Problem

The corrosion of steel in an aqueous environment consists of oxidation and reduction reactions occurring simultaneously. These reactions are normally dispersed evenly over the corroding area; however, under the influence of a galvanic couple, the reactions may significantly segregate, leading to problems.

As noted above, rust will form at holidays in painted auto-body steel coupled to metal trim if the steel is anodic. This will lift additional surrounding paint making the damage more extensive. If the auto-body steel is cathodic in the couple, rust formation is reduced, preventing such damage to the coating. However if the mixed potential of the couple is too negative, two other detrimental effects may occur [4]:

- Excessive hydrogen evolution at the steel cathode may blister the paint.

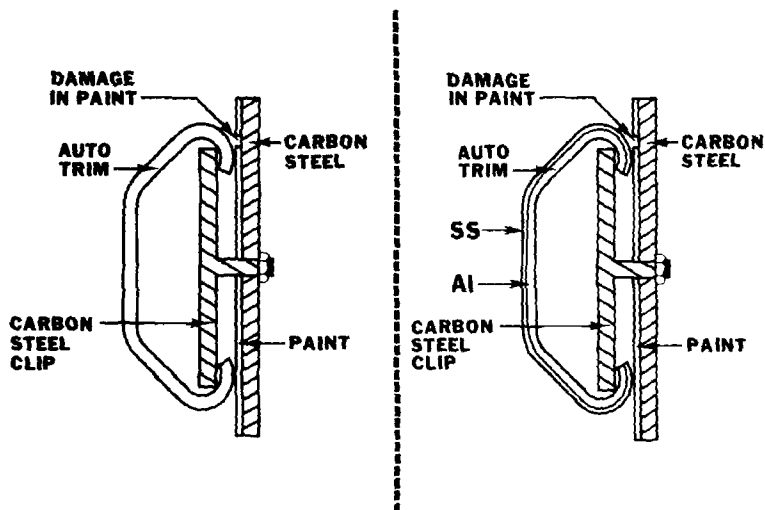


FIG. 2—Diagrammatic representation of auto trim auto-body assembly: (a) solid stainless steel and (b) stainless clad aluminum.

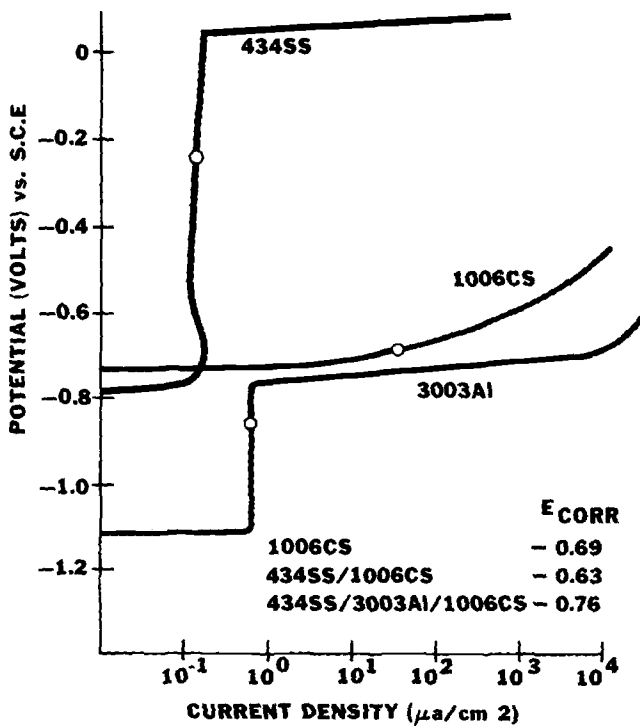


FIG. 3—Potentiodynamic polarization curves for metals in 5% NaCl solution (30°C).

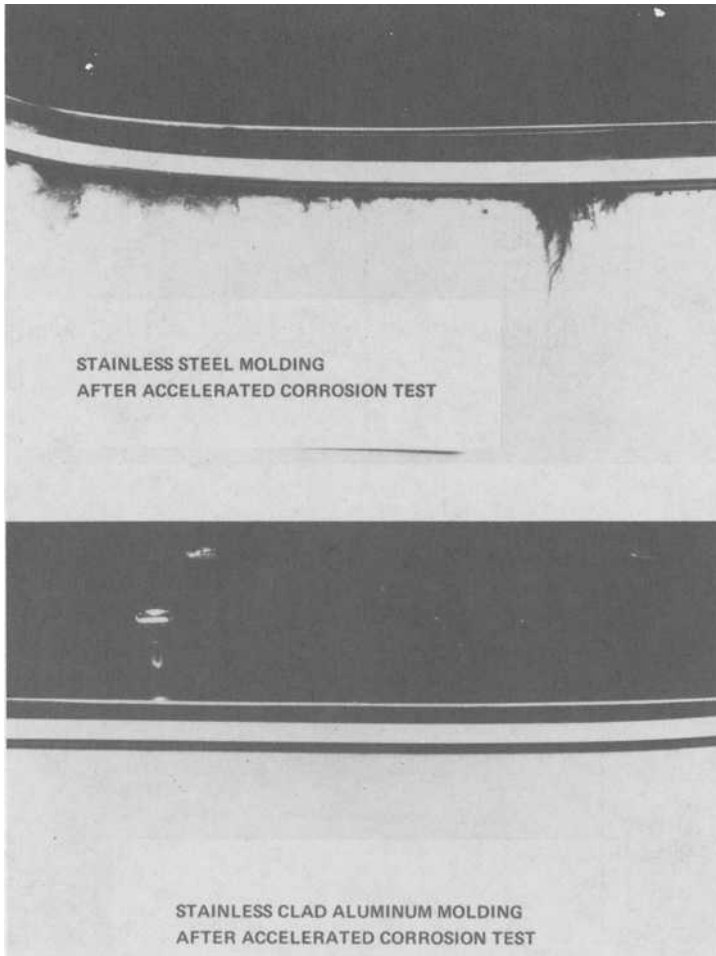


FIG. 4—Automobile manufacturer proving ground test track results showing corrosion of painted auto-body steel adjacent to stainless steel trim (right side of vehicle) and protection adjacent to stainless clad aluminum trim (left side of vehicle).

- Creation of a basic environment at the steel cathode may lead to “saponification,” especially of epoxy ester primers and paint failure.

Figures 5 and 6 demonstrate such typical paint failures adjacent to strongly anodic trim.

Tests have shown that, of the common automotive trim materials used, stainless steel clad aluminum is less likely to cause paint blistering problems than aluminum or anodized aluminum, which in turn are less likely to cause these problems than die cast zinc [4]. The reason is that the mixed potential of stainless steel clad aluminum and auto-body steel is less negative than the mixed potential of other trim materials, which also galvanically protect the auto-body steel.

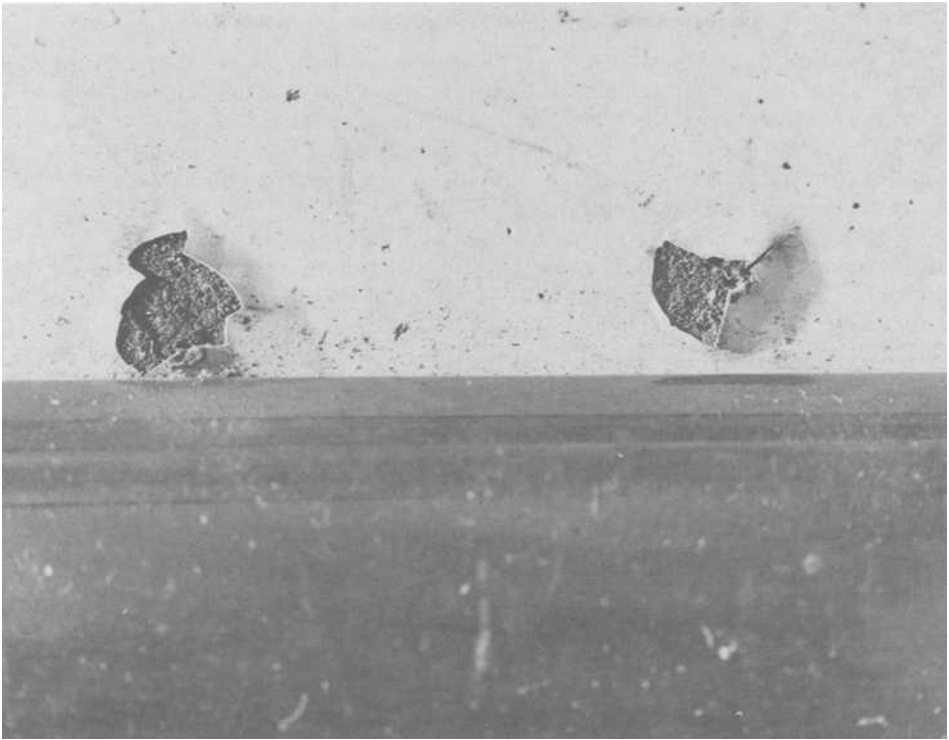


FIG. 5—*Photograph of blistering of painted auto-body steel adjacent to anodized aluminum trim after one year service in the Detroit, MI area.*

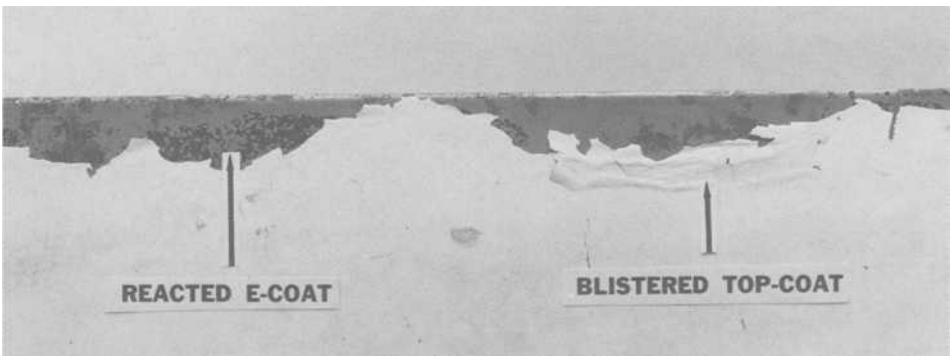


FIG. 6—*Photograph to show saponification of painted auto-body steel. Notice reaction of the primer (E-Coat) has caused blistering of the topcoat.*

Dissimilar Fasteners

Galvanic corrosion problems can also exist where dissimilar metal fasteners are used. One example occurs when high strength steel fasteners are used with aluminum parts. Corrosion control techniques commonly employed include the use of insulators or nonconductive connectors to eliminate the electrical path, or the use of paints and sealers to eliminate the electrolyte path [7]. The use of "waster sections" is also common; a piece of sacrificial metal is inserted under the fastener to sacrificially protect the assembly.

Transition metals, such as that shown in Fig. 7, have also been used [7,8]. The clad metal inserts not only provide sacrificial action but also eliminate the dissimilar metal crevice. The benefits obtained are evident in Fig. 8 and Table 1, which show that use of a clad metal insert between the steel and the aluminum reduced corrosion of the aluminum by a factor of five. The effect is not always so dramatic, as in the case of stainless steel fastened to aluminum. In the latter case, the stainless steel is readily polarized toward the aluminum potential. In either case, however, the aluminum weight loss with transition material was similar, indicating that the transition material insert eliminated the dissimilar metal crevice.

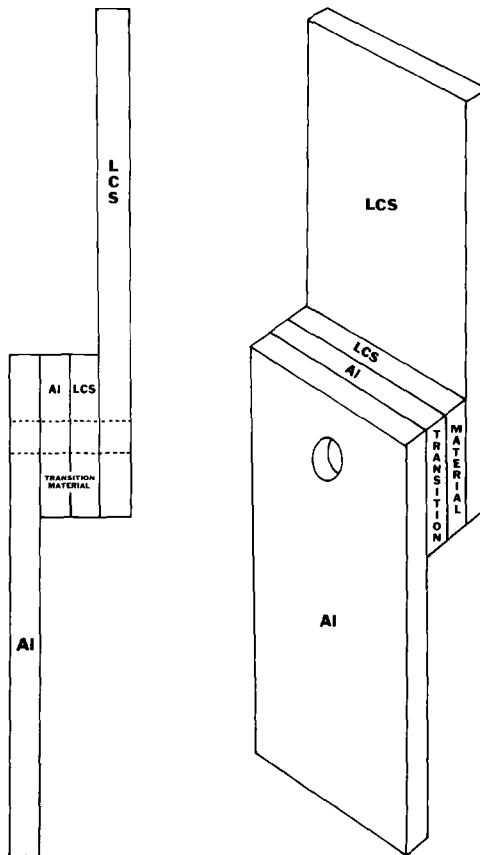


FIG. 7—Configuration of transition material inserts.

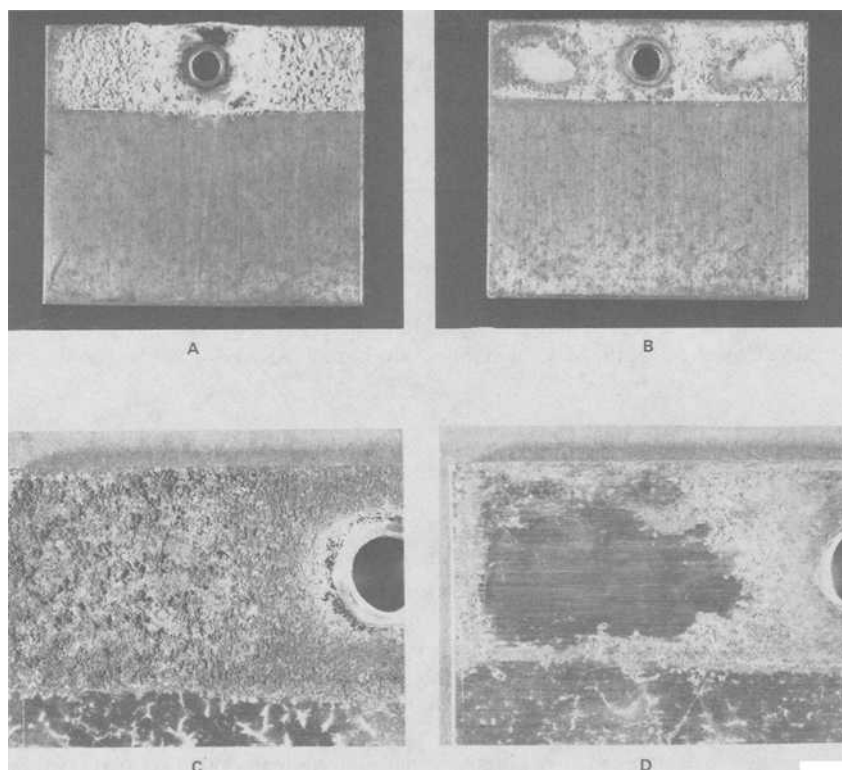


FIG. 8—Corrosion of aluminum in aluminum-steel galvanic couple after one-year exposure at Kure Beach (80-ft [24-m] lot): A and C without transition, B and D with aluminum/steel transition.

TABLE 1—Weight loss of aluminum from lap joint studies: one-year exposure, Kure Beach.

Couple	Transition	Bolt-Type	Weight Loss, gr
Steel to aluminum	none	insulated steel	0.61
Steel to aluminum	steel/Al	insulated steel	0.14
Steel to aluminum	none	steel	0.73
Steel to aluminum	steel/Al	steel	0.12
Steel to aluminum	none	aluminum	0.52
Steel to aluminum	steel/Al	aluminum	0.10
Stainless steel to aluminum	none	insulated steel	0.18
Stainless steel to aluminum	SS/Al	insulated steel	0.10
Stainless steel to aluminum	none	stainless steel	0.18
Stainless steel to aluminum	SS/Al	stainless steel	0.12

Electroplated Bumpers

Bumper materials are classified as noble metal coated systems when stainless steel, nickel, chrome, or a combination of these are applied to a base metal, such as steel or aluminum. Cracks, voids in the plating, and damage sites can result in severe galvanic corrosion because of the unfavorable area ratio. The result is blistering, peeling, and flaking of the outer decorative layer, especially in the case of chrome plated aluminum bumpers [9]. Figures 9 and 10 demonstrate this mechanism and its results.

Stainless steel clad aluminum is used very successfully for truck bumpers. The clad material provides a considerable weight savings even though the stainless steel component is thick enough to eliminate the problems of porosity or damage from stone impingement while in use. The edge of stainless steel/aluminum bumpers do not suffer excessive galvanic corrosion because equal areas of aluminum and of stainless steel are exposed in such locations.

Galvanizing

Automobile manufacturers are turning increasingly to galvanized steel as a replacement for conventional auto-body steel. In effect, they are using galvanic corrosion to their advantage since the zinc protects the steel substrate by sacrificial action. Studies have shown galvanizing to be very effective, with zinc protecting the steel while losing only about one-tenth the volume of metal of regular auto-body steel (Table 2) [10]. However, auto manufacturers must use specific galvanizing techniques and special primers, since it is difficult to paint zinc effectively because of the naturally occurring films that form on zinc. Paint peeling on two-side galvanized steel has been a problem in the past, and some companies have favored one and one-half side galvanized steel to avoid these problems. Also, because zinc corrosion products are more alkaline than those of steel, and the corresponding cathodic reactions can produce additional alkalinity, paint adhesion problems may develop, depending on the paint system [4]. The increased use of electrogalvanized steel and improvements in painting technology have resulted in increased use of painted two-side galvanized steel; however, long-term service performance has not been established.

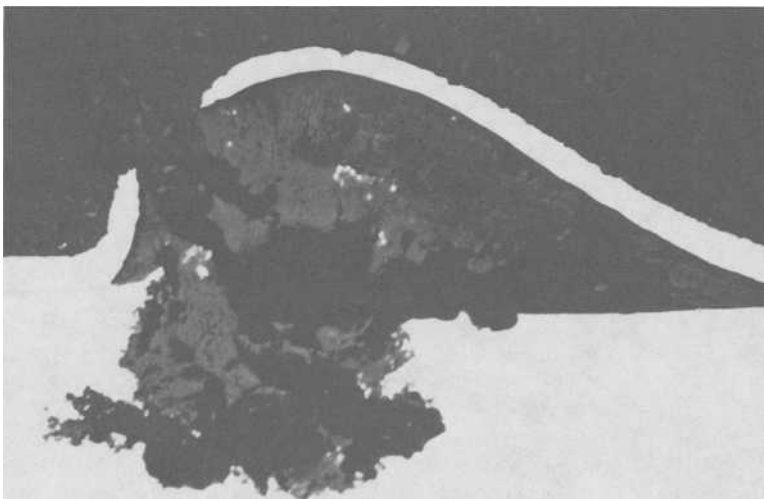


FIG. 9—Galvanic corrosion mechanism of chrome-plated aluminum at damage sites.

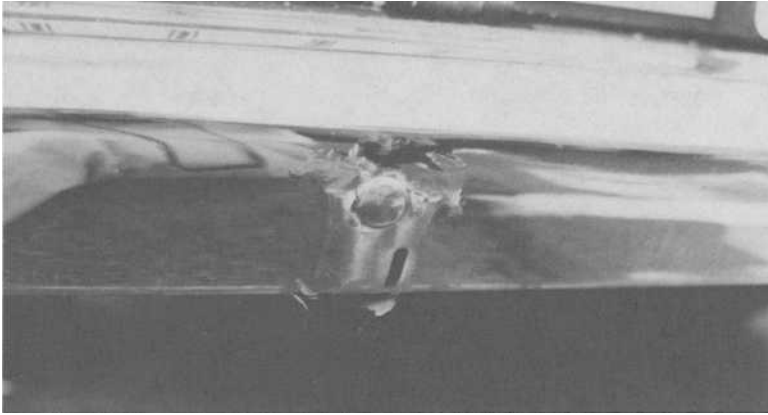


FIG. 10—Chrome-plated aluminum bumper after three years of service in Attleboro, MA.

Cooling Systems

A Department of Transportation study states that cooling system failure is the third most frequent cause of vehicle disablement [11]. A substantial proportion of these failures can be attributed to corrosion in the cooling system, causing leaks, inadequate heat transfer because of corrosion product deposits, and so forth [12]. This corrosion occurs largely because the public has not recognized the importance of coolant maintenance, and frequently ignores coolant change intervals. Tap water is also frequently used to compensate for system losses, leading to higher concentrations of contaminants such as chloride ion. The higher operating temperatures of today's more efficient engines have increased the rate of coolant inhibitor breakdown. High mileage, high speed air suction at pumps, exhaust gas leakage, rust deposits, and hot spots also accelerate the consumption of inhibitors [12].

The complex blend of anodic inhibitors in engine coolants is the first line of defense against cooling system corrosion. These form passive films on metal surfaces thereby changing the polarization characteristics and retarding further corrosion, as shown in Fig. 11 [13, 14]. They must protect an assembly that may consist of cast iron, copper, and aluminum parts all electrically interconnected such that numerous galvanic cells can exist with the coolant as electrolyte. Typical formulations consist of nitrites, nitrates, phosphates, borates, silicates, amines, benzoates, organic phosphates, and emulsifiable oils. Special formulations (for example, GM6043-M) have also been devised that reportedly provide better inhibition for aluminum, which is being used increasingly in newer cars [12].

A coolant condition sensor has recently been developed [12]. It has integrated circuitry that can (1) monitor the potential between a sensing and reference electrode, (2) interpret the measured potential, (3) distinguish a low coolant level condition, and (4) provide a signal to the

TABLE 2—Atmospheric corrosion rates during the winter of 1984 and 1985.

City	Bare Steel Average Corrosion Rate, mpy	Galvanized Steel Average Corrosion Rate, mpy
Boston	2.25	0.115
Dallas	0.114	0.0214
Detroit	1.78	0.0517
Montreal	2.55	0.260

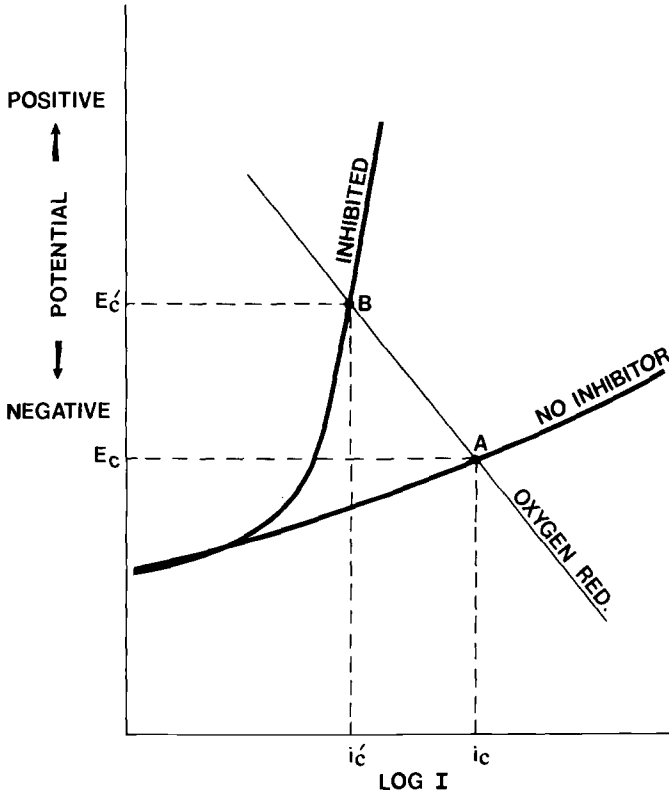


FIG. 11—Schematic polarization curves for steel in engine coolants containing passivating inhibitors.

vehicle computer when a corrosive or low level condition exists. It is resistant to underhood noise, environment, and temperature extremes, has low current draw and high input impedance, and is of a convenient size. This sensor should greatly help eliminate many cooling system problems related to owner neglect.

Summary

The automobile is a complex assemblage of many different materials chosen for functional, cosmetic, and economic reasons. As a result, galvanic corrosion has historically been a problem with road salts and acid deposition attacking external components and corrosive operating fluids. Automobile manufacturers have devised creative ways of dealing with galvanic corrosion. However, they must continue to refine their techniques to meet the challenges of an aggressive environment and more refined engines with tighter operating limits.

References

- [1] Baboian, R., "Chemistry of the Automotive Environment," *Designing for Automotive Corrosion Prevention Proceedings*, SAE Report 790908, SAE, 1978, p. 78.
- [2] Baboian, R., "Causes and Effects of Corrosion Relating to Exterior Trim on Automobiles," *Proceedings of the 2nd Automotive Corrosion Prevention Conference*, SAE Report 831835, 1983, p. 136.
- [3] Baboian, R., "Corrosion Behavior of Trim Materials on Automobiles," SAE Report 770110, 1977.

- [4] Baboian, R., "Effect of Galvanic Couples on Saponification of Auto-Body Steel," *Materials Performance*, Vol. 17, No. 11, Nov. 1978.
- [5] Baboian, R., "Clad Metals in Automotive Trim Applications," SAE Report 710276, 1971.
- [6] Baboian, R., "Designing Clad Metals for Corrosion Control," SAE Report 720514, 1982.
- [7] Haynes, G. and Baboian, R., "Reducing Galvanic Corrosion with Transition Metals," *Materials Performance*, Vol. 16, No. 6, June 1977.
- [8] Baboian, R. and Haynes, G., "Joining Dissimilar Metals with Transition Materials," SAE Report 760714, 1976.
- [9] Baboian, R. and Haynes, G., "Performance of Stainless Steel Clad Aluminum in Bumper Applications," SAE Report 840287, 1984.
- [10] Turcotte, R. and Baboian, R., "Comparative Corrosivity of the Automotive Environment," SAE Report 860108, 1986.
- [11] U.S. Department of Transportation, "HS 801 102 Vehicle Disablement Study," Technical Report, Washington, DC.
- [12] Haynes G., Gonsalves, E., and Baboian, R., "An Electrochemical Sensor for Monitoring Automotive Coolant Condition," *Materials Performance*, Vol. 24, No. 11, Nov. 1986.
- [13] Hirozawa, S. T., *Journal of the Electrochemical Society*. Vol. 130, 1983, p. 1718.
- [14] Walker, M. S. and France, W. D., *Materials Protection*. Vol. 8, No. 9, 1969, p. 47.

Galvanic Corrosion in Oil and Gas Production

REFERENCE: Efird, K. D., "Galvanic Corrosion in Oil and Gas Production," *Galvanic Corrosion, ASTM STP 978*, H. P. Hack, Ed., American Society for Testing and Materials, Philadelphia, 1988, pp. 260-282.

ABSTRACT: Published literature, service experience, and experimental data for galvanic corrosion in oil and gas production are reviewed and discussed. Data are presented in forms that can be used as aids for formal specifications, design criteria, and inspection requirements to help prevent galvanic corrosion failures: Emphasis is placed on downhole and wellhead applications, and oil and gas production equipment for carbon dioxide (sweet) and hydrogen sulfide (sour) environments. Particular attention is given to the effects of galvanic coupling on the noble metal and resulting failures. Galvanic corrosion in seawater environments is briefly reviewed as it pertains to seawater handling, offshore platforms, and subsea completions.

KEY WORDS: galvanic corrosion, carbon dioxide, hydrogen sulfide, crude oil, gas, seawater, hydrogen stress cracking, steels (carbon and alloy), stainless steels, nickel alloys

Galvanic corrosion failures in oil and gas production continue to occur, but because of research and greatly increased awareness and understanding of the galvanic corrosion phenomenon the majority of failures now fall into one of two classes: (1) failure of the noble metal in crude oil and gas systems and (2) failures in seawater environments.

There are a number of possible reasons for this situation:

- (1) the necessity for using a variety of metals and alloys in oil and gas equipment, particularly downhole, because of mechanical property requirements;
- (2) the wide variability of oil and gas produced fluids, and poorly defined understanding of the effects of these variables on galvanic corrosion;
- (3) relevant data are widely scattered throughout the literature and rarely address the actual environment of interest;
- (4) a continuing problem with communication of galvanic corrosion principles to designers, equipment manufacturers, and construction companies.

Scope, Organization, and Purpose

Galvanic corrosion is defined in ASTM Definitions of Terms Relating to Corrosion and Corrosion Testing (G 15) as "accelerated corrosion of a metal because of an electrical contact with a more noble metal or nonmetallic conductor in a corrosive electrolyte." This is the definition that will be used, that is, galvanic corrosion as a macrocorrosion phenomenon. The broader definition, which includes potential differences on the same metal because of welding, cold work, heat treatment, wear, and so forth, is not discussed in detail. The effect of iron sulfide corrosion product on galvanic corrosion is included because of the importance of corrosion prevention in sour environments, that is, oil field fluids that contain hydrogen sulfide.

¹Manager of corrosion engineering, Occidental International Exploration and Production Company, Bakersfield, CA 93309.

Carbon and alloy steels are the most widely used materials in the oil field by a very large margin. This makes the galvanic relationship of steels to other metals and alloys, and the environmental effects on steel electrochemical potentials and polarization, a primary concern.

Limitations and Cautions

Forms of corrosion other than galvanic corrosion (pitting, crevice corrosion, stress corrosion cracking, and so forth) are not considered in this review unless they are a direct manifestation of galvanic corrosion. These forms of corrosion can, however, have a significant effect on material selection and must be accounted for. The assumption is made that all other forms of corrosion are properly taken into consideration.

The phrase, "It's the little things that count," pertains very well to galvanic corrosion. A large proportion of galvanic corrosion failures involve small parts and details that were overlooked in the design or construction phase, or both, or instances where a supposedly unimportant material substitution was made. In these cases inexpensive and apparently insignificant parts have caused very expensive failures.

Compilations of data and experience from many diverse sources have been used in this review. References may refer to only a single data point, and data are, in many cases, drawn from references not necessarily directed toward galvanic corrosion. Potential data have been placed into corrosion potential charts to better define and explain the potential relationships of important metals and alloys in the environments of interest. Metals and alloys have been included that are generally used in oil and gas production where sufficient data could be found, and the seawater diagram has been updated. The inclusions or deletions were made to simplify the charts as much as possible. The data do not include the effects of velocity or the effect of crude oil and dissolved organic compounds.

Electrochemical Polarization

Electrochemical polarization of the anode and cathode in a galvanic couple has a major influence on the intensity and type of corrosion that will occur as the result of the galvanic potential difference. It determines the nature of the corrosion reactions that can occur and their kinetics. Discussion of the principles of polarization behavior of galvanically coupled metals has been given by Baboian [1], as summarized in Fig. 1. It is apparent from Fig. 1 that polarization characteristics of the active (A) and noble (B) metal as well as the polarization characteristics of the reduction reaction (generally H_2 reduction for oil and gas production) on each of these metals (R) is important in determining the overall effect of the galvanic couple on corrosion. The discussions of environmental effects on galvanic corrosion will refer to changes in the components of polarization behavior diagrammed in Fig. 1.

Polarization data for metals and alloys in seawater are readily available in the literature. Because crude oil compositions are highly variable, polarization data in crude oil systems are not generally available and when available are not easily compared. This variability limits the value of general research using a "standard" environment and is an area where additional research is needed. The need is not so much to generate additional data in specific environments but to determine the degree of cross correlation among primary environmental variables that can be safely used.

Effects of Oil and Gas Environments on Galvanic Corrosion

Galvanic corrosion in the oil and gas industry is concerned with a small number of specific environment types that are highly variable within each type. The primary corrosive constituents of oil and gas well production that define the environment types are carbon dioxide and hydro-

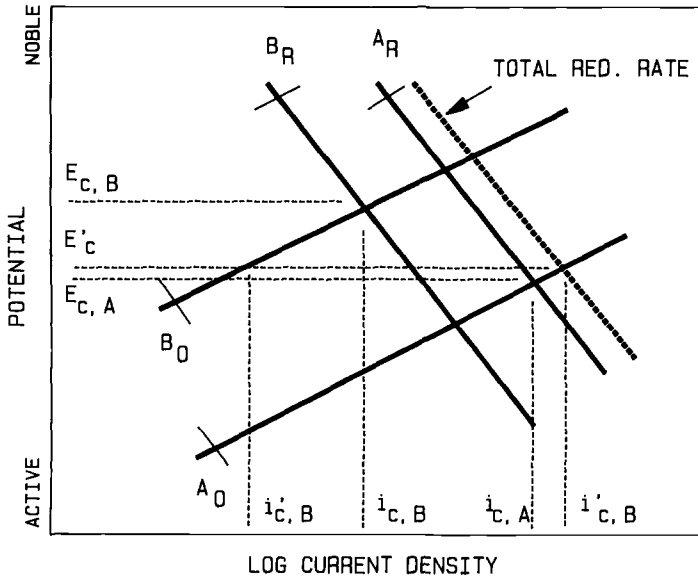


FIG. 1—Polarization behavior of galvanically coupled metals and alloys used to predict the effect of coupling on corrosion [1]. The anodic component is "A," and "B" is the noble component, while primes refer to the galvanic couple of the two. Subscripts O and R refer to the oxidation (corrosion) and reduction reactions, respectively. The subscript C refers to the corrosion potential E or current density i .

gen sulfide. They are produced along with condensed water and hydrocarbon condensate liquid phases in gas wells and crude oil and produced water liquid phases in oil wells.

The condensed water in gas wells generally contains a very low dissolved solids concentration with a correspondingly low conductivity, although some gas wells produce high salinity brines. The low conductivity inhibits macrocorrosion effects, such as galvanic corrosion, but not microcorrosion effects such as pitting.

The formation water produced along with the crude oil varies widely in salinity and composition as a percent of produced fluids, and may be produced as free water or water emulsified with the crude oil.

Macrocorrosion effects, such as galvanic corrosion, are influenced by surface wettability of the containing metal by the conductive water phase. The crude oil can have a major positive or negative effect on galvanic corrosion that is a function of the specific crude oil composition.

Seawater is used in oil and gas production in both the aerated and deaerated condition. Deaerated seawater is used primarily for secondary recovery and formation pressure maintenance through injection of the water into the oil bearing formation to replace the oil that is produced. Deaeration is accomplished by either inert gas stripping or vacuum stripping, with the subsequent addition of an oxygen scavenger, generally catalyzed bisulfite. Gas stripping lowers the seawater pH proportional to the stripping gas carbon dioxide concentration. Vacuum deaeration removes carbon dioxide from the seawater, resulting in a tendency toward calcium carbonate precipitation. Aerated seawater is used in oil and gas process systems as cooling water and for generation of fresh water.

Carbon Dioxide (Sweet) Environments

Oil and gas wells that contain carbon dioxide as the primary corrosive gas are termed "sweet" wells. The effect of carbon dioxide on galvanic corrosion and other forms of corrosion is gener-

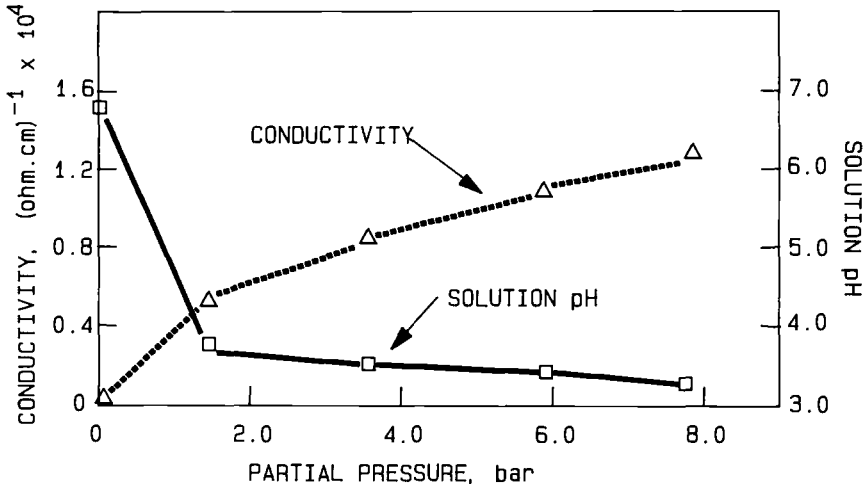


FIG. 2—The effect of carbon dioxide partial pressure on the pH and conductivity of pure water [3].

ally related to its partial pressure [2]. The carbon dioxide partial pressure is related to the pH and conductivity of the produced water (without dissolved salts) as shown in Fig. 2 [3]. An example of the range of carbon dioxide levels that may be encountered is given by the production data from several wells in Table 1 [4]. The carbon dioxide concentration in the water phase can vary significantly within an individual well at different depths because of the large changes in temperature and pressure. An example of this variation is given for a single well in Fig. 3 [5].

The corrosion potential chart for general carbon dioxide environments is given in Fig. 4. This chart was compiled from scattered data contained in Refs 6 through 11. The data are for carbon dioxide/water systems containing chloride at concentrations of 0.5 to 20 g/L at temperatures of 20 to 30°C. The carbon dioxide partial pressure ranged from 100 to 1000 kPa. This is obviously not an experimentally ideal situation for identifying detailed galvanic potential relationships in sweet oil and gas environments. It does, however give a good indication of the corrosion potential relationships of metals on a broad scale and is better than using charts for seawater as is often done for lack of better information.

The corrosion potential chart for carbon dioxide environments gives a general picture of the galvanic potential relationship of metals and alloys in sweet oil and gas production, but it gives no information on how severe the galvanic effects will be. This can only be determined by an examination of polarization effects. Carbon steel and low alloy steel are the primary materials of

TABLE 1—Well production data for sweet crude oil production [4]: analysis of water phase.

Crude	Carbon Dioxide Partial Pressure, psi	pH	Organic Acids, ppm
A	15	6.7	400
B	27	8.0	present
C	35	5.8	37
D	52	4.6	518
E	77	5.4	present

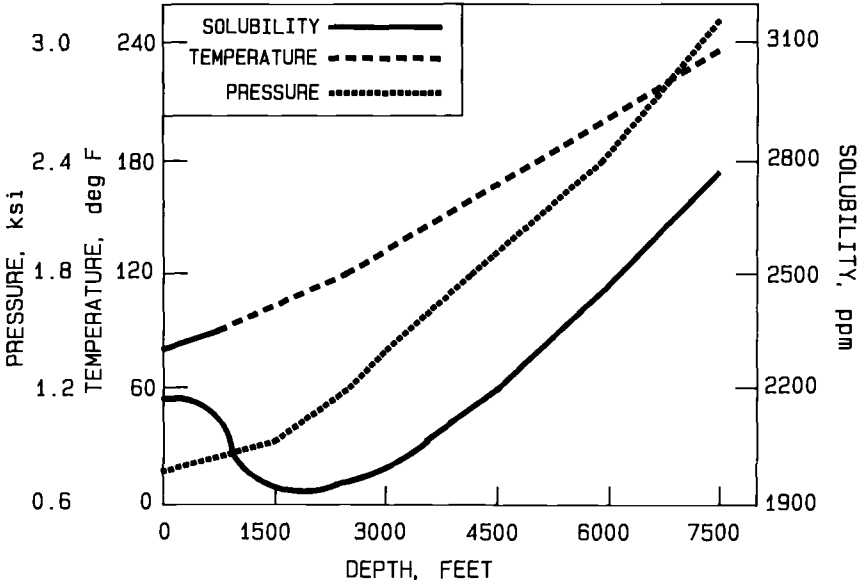


FIG. 3—Subsurface carbon dioxide solubility variation with depth in a well calculated from the pressure and temperature surveys of a corrosive well [5].

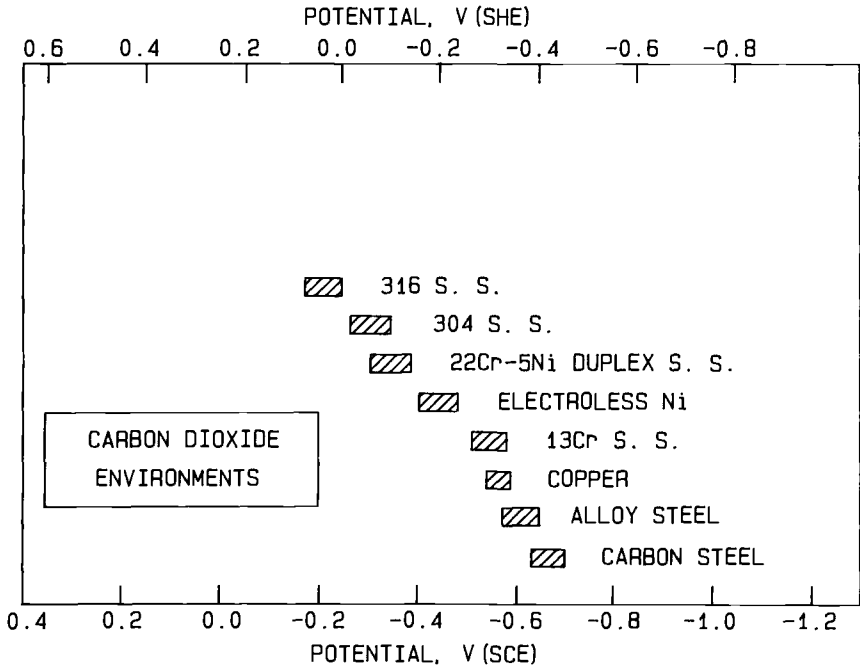


FIG. 4—Corrosion potential chart for metals and alloys in carbon dioxide environments giving the relationship of their free corrosion potentials. CO_2 partial pressure = 10 to 100 kPa, chloride = 0.5 to 20 g/L, and temperature = 20 to 30°C.

construction in oil and gas production, and as seen from Fig. 4 will generally be the anode in a galvanic couple.

The primary corrosion product for steels in sweet environments, in addition to iron oxides, is ferrous carbonate (FeCO_3). The equilibrium formation of ferrous carbonate on steel at 25°C in relation to the iron oxides is given by the potential-pH diagram for the $\text{Fe-CO}_2\text{-H}_2\text{O}$ system in Fig. 5 [8]. Ferrous carbonate is the thermodynamically stable phase in the pH range generally found in sweet oil and gas production. The importance of the corrosion product lies in its attenuating effect on the galvanic current through increased ohmic resistance (resistance polarization) and through a positive shift in the free corrosion potential (passivation).

The effect of increased CO_2 partial pressure on the polarization curve for carbon steel is shown in Fig. 6 [5]. The effect is not great in the range studied, with only a small increase in free corrosion potential. The occurrence of a passivating corrosion product on steel in carbon dioxide environments is a complex function of temperature, carbon dioxide partial pressure, and pH. While the precise interrelationships are not well defined, increases in any or all of these three variables promotes the formation of passivating corrosion products. The growth of this passivating corrosion product on iron is shown by the plot of free corrosion potential with time in Fig. 7 [8]. Approximately 20 h were required to form the passivating corrosion product under the test conditions. This is part of an extensive study conducted by Ikeda et al. [8] that details factors affecting corrosion product film formation on steels in carbon dioxide environments. The passivating carbonate corrosion products are often loosely adherent and so are subject to removal by turbulence.

The formation of the passivating corrosion product will decrease the negative effect of a galvanic couple with steel by increasing the total ohmic resistance and by lowering the galvanic potential difference. The time required for formation of the passivating corrosion product is significant with regard to the usefulness of test data. The galvanic current before formation will be much higher than after, and potential shifts on the steel from a galvanic couple could signifi-

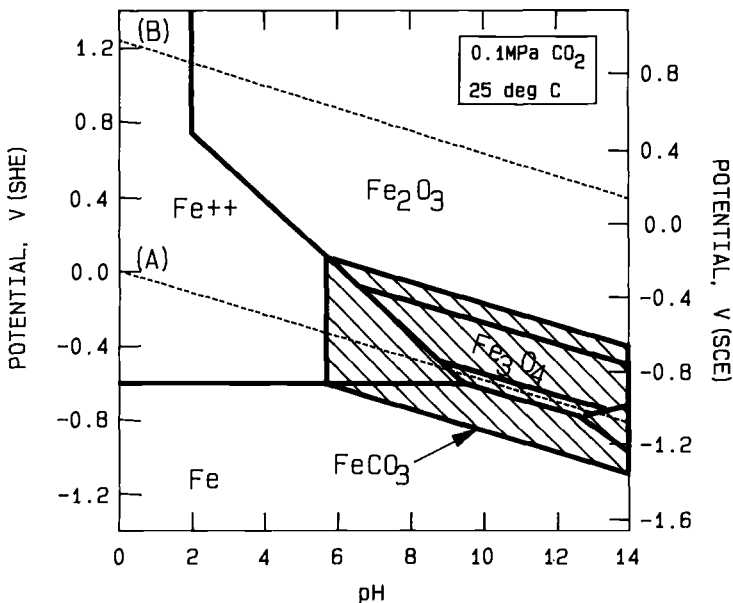


FIG. 5—Potential pH diagram for the $\text{Fe-CO}_2\text{-H}_2\text{O}$ system at 25°C . Ionic activity = 10^{-6} molar, and $\text{PCO}_2 = 0.1 \text{ MPa}$ [8].

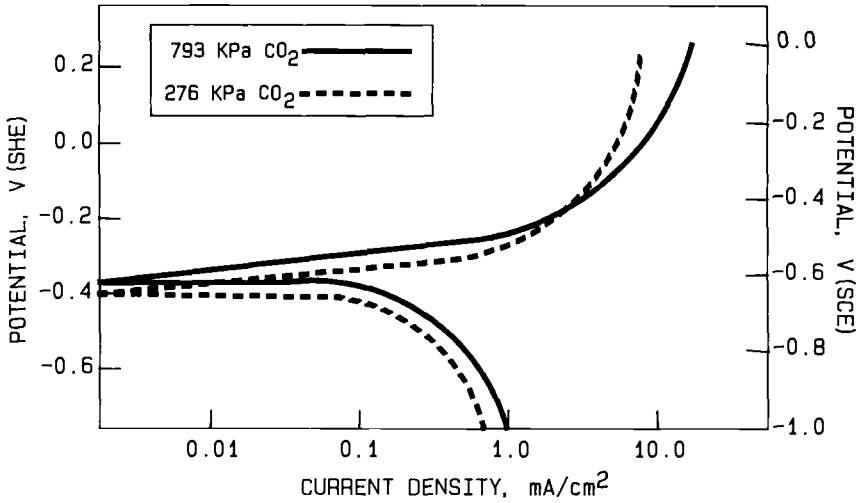


FIG. 6—The effect of CO_2 partial pressure on the polarization curve for carbon steel in a H_2O-CO_2 system at $23^\circ C$.

cantly alter the corrosion product. What is required is the ability to predict when the passivating corrosion product will be formed, when operating conditions could damage it, and how the galvanic couple alters its formation.

Hydrogen Sulfide (Sour) Environments

Oil and gas wells that contain hydrogen sulfide in the produced fluids are termed “sour” wells. Carbon dioxide may or may not be present at the same time. The effect of hydrogen sulfide (H_2S) on corrosion is universally related to the H_2S partial pressure in the literature. As with carbon dioxide concentrations for sweet wells, the concentration of hydrogen sulfide in sour wells can vary greatly from well to well as shown in Table 2 [12]. The effect of temperature

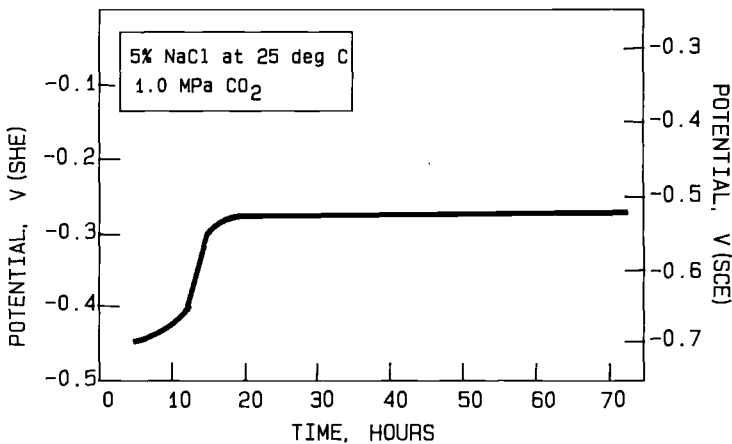


FIG. 7—Potential time curve for iron in CO_2-H_2O solution showing the growth of $FeCO_3$ passivating corrosion product [8].

TABLE 2—Hydrogen sulfide distribution in the produced phases for sour crude oil production [12].

Crude	H ₂ S Concentration in		
	Gas, %V	Oil, ppm	Brine, ppm
A	0.8	40	10
B	1.4	330	320
C	8.6	5200	1500
D	14.5	4000	1400

and pressure with depth in an individual well on the hydrogen sulfide concentration in the liquid phases is very similar to that for carbon dioxide.

The corrosion potential chart for metals and alloys in hydrogen sulfide environments is given in Fig. 8. This chart was also compiled from scattered data contained in a number of references [9, 10, 13-18]. The data are for the National Association of Corrosion Engineers (NACE) solution (5% NaCl + 0.5% CH₃COOH + H₂S) [19] at temperatures from 20 to 60°C, with 1-atm H₂S partial pressure. The greater uniformity of the test environment makes this chart more reliable than the chart for CO₂ environments. Of particular interest is the position of copper with respect to carbon steel and alloy steel [16]. Copper is normally noble to steel, but in H₂S environments this does not appear to be generally true.

The H₂S corrosion potential chart gives the galvanic potential relationships of metals and alloys in sour oil and gas environments but gives no information on the severity of attack.

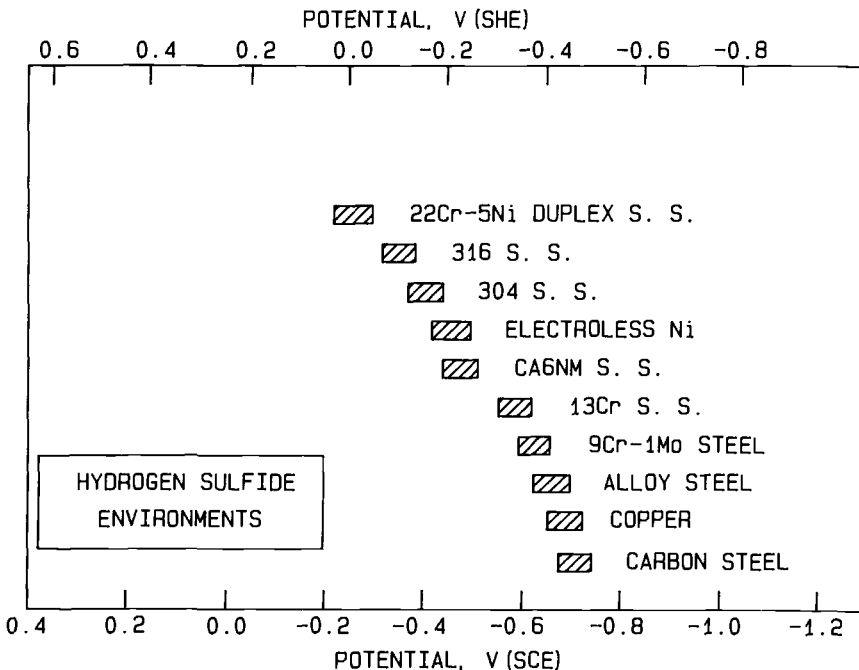


FIG. 8—Corrosion potential chart for metals and alloys in hydrogen sulfide environments giving the relationships of their free corrosion potentials. H₂S partial pressure = 1 atm, 5% NaCl + 0.5% CH₃COOH, and temperature = 20 to 60°C.

Carbon steel and alloy steels are the primary materials of construction in sour oil and gas production, and are generally the anode in any galvanic couple as seen in Fig. 8.

Anodic polarization of steel in aqueous H_2S solutions has been studied by Morris et al. [20]. The basic finding relative to galvanic corrosion was that the corrosion potential became more negative with increasing H_2S concentration, but the slope of the anodic polarization curve remained the same. This would effectively increase the anodic corrosion rate of the steel in a galvanic couple (Fig. 1).

The corrosion product on steel in sour oil and gas environments is iron sulfide. The equilibrium formation of iron sulfide (FeS) on steel at $25^\circ C$ is given by the potential-pH diagram for the Fe- H_2O - H_2S system in Fig. 9 [21]. Iron sulfide is the thermodynamically stable corrosion product in the pH range normally observed in oil and gas environments. The iron sulfide corrosion product not only provides an attenuating effect for galvanic corrosion through increased ohmic resistance and possible passivation, but the iron sulfides can be electrochemically active with respect to the hydrogen reduction reaction.

The task of evaluating galvanic corrosion problems involving steels in H_2S environments is compounded by the number of different iron sulfides that can form. A diagram summarizing the chemical interrelationships of the major iron sulfides is given in Fig. 10 [22]. Detailed studies of the corrosion and polarization effects on iron by the various iron sulfides have been conducted by Khazraji [24] and by Smith [25]. The significant shifts in the carbon steel corrosion potential caused by three iron sulfides are given in Table 3 [25]. The effect of these same three sulfides on the polarization curves for carbon steel is shown in Fig. 11 [25]. The iron sulfides alter both the slope and intercept of the hydrogen reduction curve as shown in Fig. 12 [25]. These changes in anodic polarization and hydrogen reduction have a major effect on the resulting corrosion current in a galvanic couple (Fig. 1), resulting in increased corrosion of the anode (steel) and increased hydrogen formation at the cathode over that without the iron sulfide.

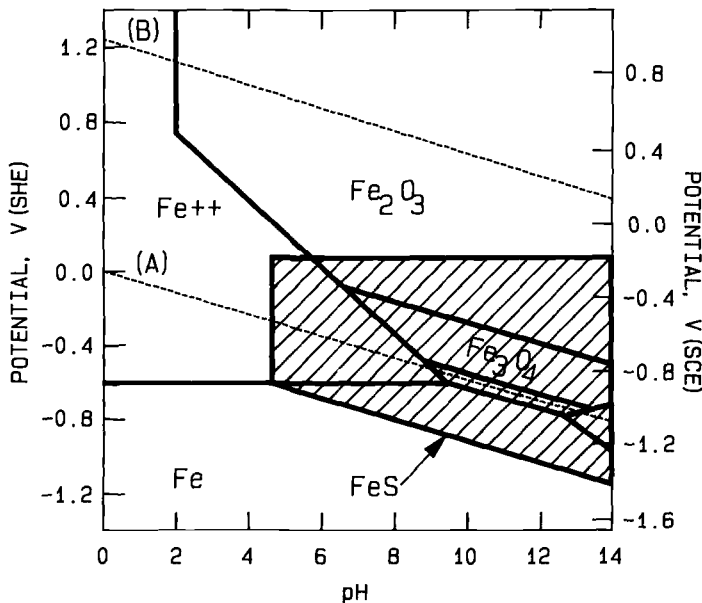


FIG. 9—Potential pH diagram for the Fe- H_2S - H_2O system at $25^\circ C$. Ionic activity = -6 molar, and $pH_2S = 0.1$ MPa [21].

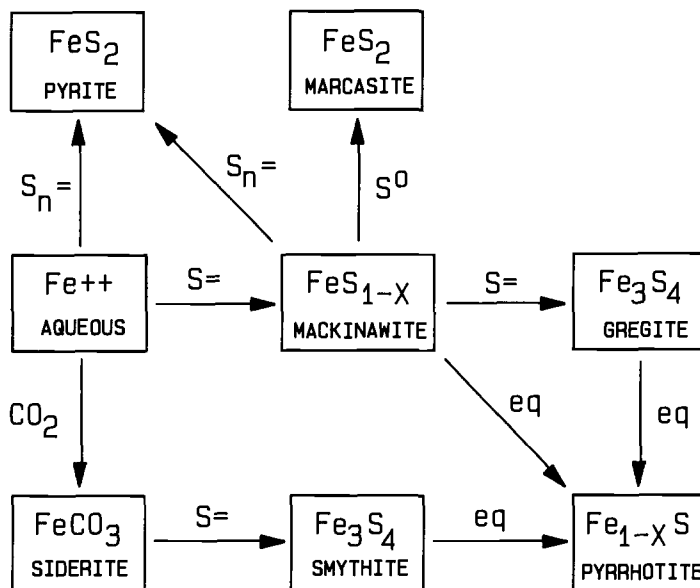


FIG. 10—Summary of the interrelationships of the major iron sulfides in aqueous solution. Reactions involving ferric ion are not included [22].

The significance of this with regard to galvanic corrosion is that, where steel is involved, the actual iron sulfide mineral that forms as the corrosion product can have a significant effect on to what degree and even if galvanic corrosion will occur. It can be rationalized that the galvanic corrosion occurring in sour environments is a significant function of the iron sulfide or sulfides present, but definitive data on this are not available.

Seawater Environments

The general occurrence and description of galvanic corrosion in seawater is well documented and will not be discussed in this review. A corrosion potential chart of metal and alloy corrosion potentials is given, however, in Fig. 13. The chart has been updated over those commonly in use using data from Lee [26] and a number of other sources [27-29]. Only metals and alloys presently used extensively in oil and gas production for seawater service are included to simplify its use.

TABLE 3—The effect of iron sulfides on the corrosion potential and polarization of carbon steel [25].

Steel	Corrosion Potential Shift	Effect on Polarization	
		Anode	Cathode
Makinawite (FeS _{1-x})	+40	depolarized	depolarized
Smythite (Fe ₃ S ₄)	+90	no effect	no effect
Pyrite (FeS ₂)	+120	depolarized	depolarized

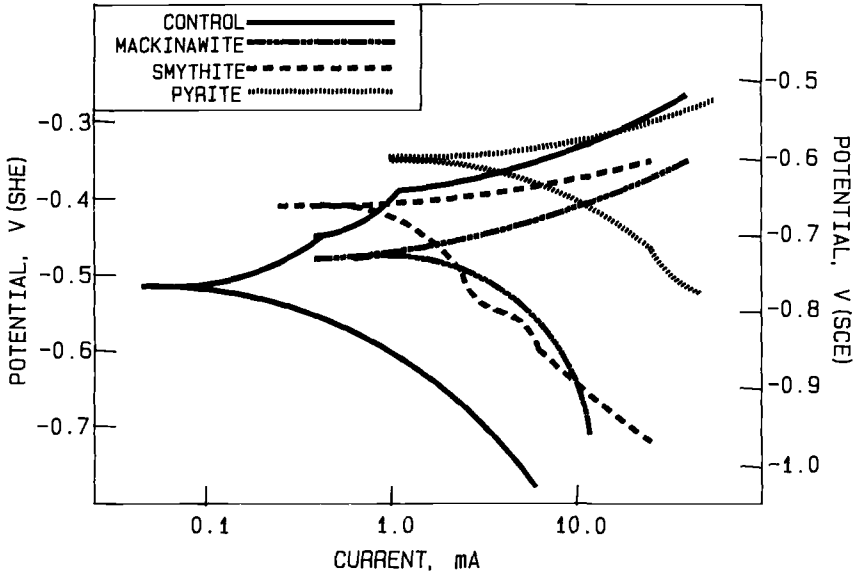


FIG. 11—The effect of various iron sulfides on the polarization curves for carbon steel at 25°C [25].

Other Environmental Parameters

The effect of the crude oil on galvanic corrosion, and other forms of corrosion, is to generally decrease the galvanic effect. There are a number of reasons for this. First, the crude oil can coat the metal surface, increasing the ohmic resistance. Second, some crude oils contain naturally occurring corrosion inhibitors that dissolve in the water phase and lower the overall corrosion reaction, reducing galvanic corrosion. Conversely, organic acids present in the crude oil (Table 1) dissolve in the water phase increasing the galvanic effect by lowering pH or acting as metal ion chelating agents. As evident from the detailed data given, the effects of crude oil composition variations are not well understood in relation to corrosion in general, much less galvanic corrosion.

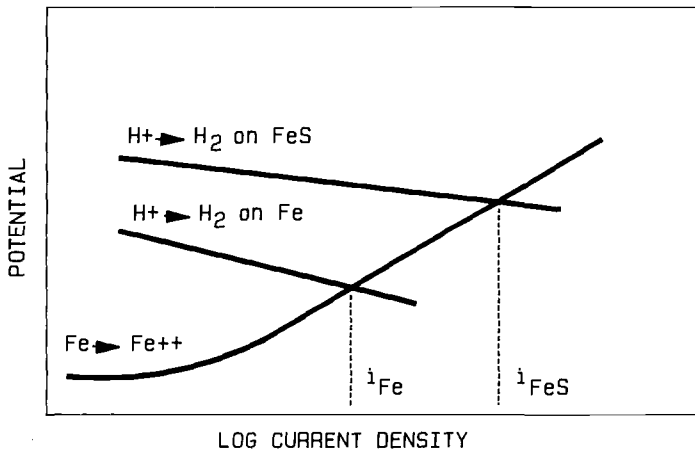


FIG. 12—The influence of FeS on the electrochemical of steel [25].

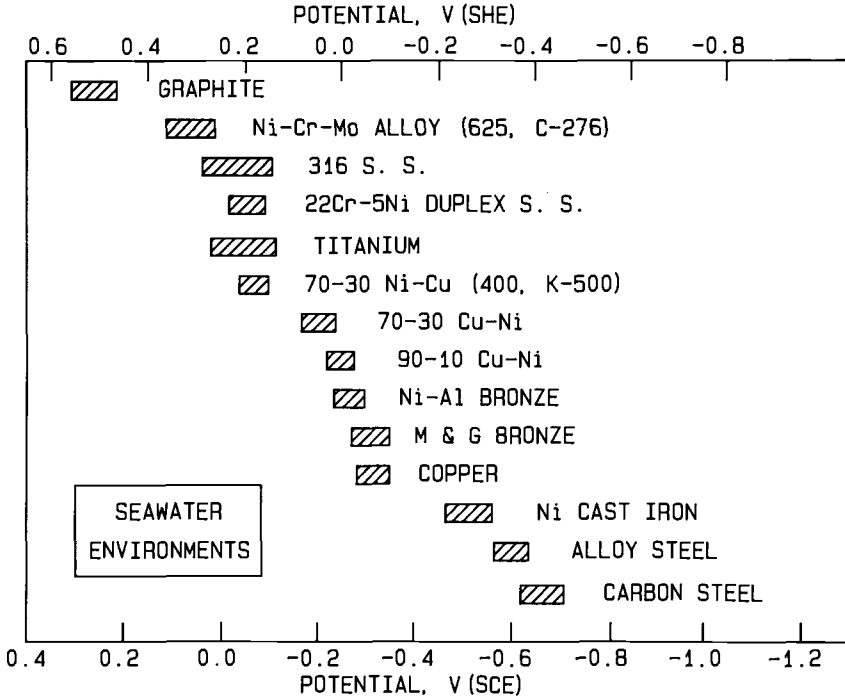


FIG. 13—Corrosion potential chart for metals and alloys in flowing seawater giving the relationships of their free corrosion potentials.

The chemical composition of produced water can have a significant effect on galvanic corrosion. The formation of mineral scales results in significant ohmic resistance lessening or eliminating galvanic corrosion that might otherwise occur. Mineral scales often form during production of a well when there are large decreases in temperature or pressure or both. The most commonly encountered scales are calcium carbonate, calcium sulfate, barium sulfate, and strontium sulfate. The single most important component of produced water is chloride ion, however, because of its pronounced lowering of solution resistivity and degradation of corrosion product protectiveness, which allows galvanic corrosion to occur more rapidly and over a wider range. Chloride ion concentrations in produced water can range anywhere from 10 to 100 000 ppm.

Galvanic Corrosion Effects on the Noble Metal

The galvanic corrosion effect on the noble metal component of a galvanic couple is a major cause of galvanic corrosion failures in oil and gas production. Detrimental galvanic corrosion effects on the noble component of a couple are very specific, since only certain metal/environment combinations are adversely affected. The most common effect encountered in oil and gas production is from the cathodic hydrogen reduction reaction and hydrogen charging of the noble metal, which is a prevalent phenomenon in a hydrogen sulfide environment.

Hydrogen charging of the noble metal (cathode) can have serious consequences, resulting in potential hydrogen embrittlement and hydrogen stress cracking of susceptible materials. Service failures by hydrogen stress cracking when coupled to carbon steel in sour gas wells have occurred in Monel® Alloy K-500, Inconel® Alloy 718 and X-750, and titanium [18,30-32,39]. An excellent review of stress cracking problems of all types in oil and gas production has been

given by Rhodes [18]. Laboratory experiments in hydrogen sulfide environments have produced hydrogen stress cracking for a wide range of stainless steels and nickel base alloys when galvanically coupled to carbon steel [17,18,31-35,38]. The problem of hydrogen cracking of the noble component in a galvanic couple can also occur in other environments. Hydrogen stress cracking of Monel® Alloy K-500 cathodically protected in seawater has been reported [37].

Laboratory data on galvanic corrosion effects on the noble metal or alloy generally address galvanic couples with steel under severe hydrogen sulfide conditions, for example, stress at 100% yield strength and 1 atm or more H₂S partial pressure. Metals and alloys that do not fail under these test conditions can generally be assumed safe to use under less severe conditions. Table 4 gives a compilation of test results for hydrogen stress cracking of noble alloys coupled to steel in NACE solution at the most severe condition where hydrogen stress cracking did not occur. Table 5 gives a compilation of test results at the least severe conditions where hydrogen stress cracking of the noble alloy did occur. For reference Table 6 gives the nominal compositions of the noble alloys included in the previous tables. These test results are conservative, and less expensive alternative materials that would provide good service might be overlooked. For moderately or slightly sour service, tests in the production environment are recommended. If this is not possible the tables and references can serve as a guide.

The standard most widely used for material selection in sour environments, NACE MR-01-75 [40], should be used with caution when dealing with these materials galvanically coupled to steel. The effect of galvanic coupling on hydrogen stress cracking is addressed for only a few materials, specifically titanium alloys. The cautions that are present are footnotes in the text, but are not apparent from the tables and could easily be overlooked. This is a major weakness in MR-01-75, and one that should be addressed. Maximum strength, hardness or heat treatment requirements, or both, for materials coupled to carbon steel should be included.

All of the failures of the noble metal discussed have been by hydrogen embrittlement and hydrogen stress cracking, but failures of some stainless steels and nickel base alloys can occur by stress corrosion cracking, particularly in chloride containing environments at elevated temperature. Galvanic couples can be used to protect the noble metal from stress corrosion cracking, but it will accelerate hydrogen embrittlement and hydrogen stress cracking if the noble metal is susceptible. It must be absolutely certain which form of corrosion, stress corrosion cracking or hydrogen stress cracking, is the operating failure mode before using the galvanic couple for prevention, or the results could be catastrophic.

Galvanic Corrosion in Downhole and Production Equipment

A producing oil or gas well contains a vast array of equipment below ground, and a complex arrangement of valves and controls at the wellhead. The condition and proper functioning of downhole equipment is of primary concern, since failures can result in severe safety hazards and very large expenses. Certain components are of particular importance. These include subsurface safety valves, gas lift mandrels and valves, a variety of downhole pumping systems, tubing string components, and wireline and well workover equipment. A schematic of a naturally flowing, dual completion well is given in Fig. 14. Figure 15 shows a schematic of a completion using an electric submersible pump.

Galvanic corrosion failures in downhole equipment, other than those of noble metal failures discussed previously, now primarily occur in relation to noble metal coatings. The noble metal coatings in most common use in oil and gas production are electroless nickel, hard chromium, and flame sprayed stainless steel or Monel® Alloy 400. The problem occurs if there is a defect in the coating. Since the coating is the cathode and the exposed steel substrate the anode, a very poor anode/cathode area ratio exists. An example of this type of failure is shown in Fig. 16 for an electroless nickel coating used to protect a steel subsurface safety valve. Porosity in the electroless nickel coating allowed the steel to corrode at the point of failure to the extent that the valve would not operate.

TABLE 4—The most severe test condition where no hydrogen stress cracking occurred for a noble alloy galvanically coupled to carbon steel in sour environments (NACE solution, 1-atm H₂S partial pressure).

Material	Condition ^a	Test Stress as % YS	Exposure		Reference
			Temperature, °C	Time, days	
9 Cr-1 Mo Steel	C-Ring Q&T, HRC 19, 86 ksi YS	100	22	28	35
SAF 2205 SS ^b	wire, 1580 MPa (229 ksi) YS	1100	93	7	17
Sanicro 28 SS ^c	wire, ?	1100	149	7	17
Pyromet 31 ^d	C-Ring, SA, HRC 33, 721 MPa (105 ksi) YS	100	22	28	35
	wire, ?	1100	93	7	17
Inconel Alloy 718 ^e	C-Ring, SA + Age HRC 31, 865 MPa (125 ksi) YS	100	22	28	35
	wire, 1480 MPa (215 ksi) YS	1100	149	7	17
Inconel Alloy 625 ^e	C-ring, MA, HRC 20, 486 MPa (71 ksi) YS	100	22	28	35
	wire, 1540 MPa (223 ksi) YS	1100	149	7	17
	C-ring, 59% CR 1289 MPa (187 ksi) YS	90	100	100	36
Hastelloy C-276 ^f	wire, 1400 MPa (203 ksi) YS	1100	140	7	17
	C-ring, 59% CR 1310 MPa (190 ksi) YS	100	100	100	36
MP35N ^g	C-ring, 59% CR, 184 ksi YS	90	5	42	38
	wire, 1480 MPa (215 ksi) YS	1100	204	7	17
	C-ring, 35% CR, 1103 MPa (160 ksi) YS	100	100	100	36
Incoloy Alloy 925 ^h	C-ring, CR HRC 36, 958 MPa (139 ksi) YS	100	25	42	41

^a Abbreviations used: CR = cold reduced, YS = 0.2% yield strength, SA = solution annealed, MA = mill annealed, Q&T = quenched and tempered.

^b Trademark, Sandvik Alloys, AB.

^c Trademark, Sandvik Alloys, AB.

^d Trademark, Carpenter Technology Corp.

^e Trademark, Huntington Alloys, Inc.

^f Trademark, Cabot Corp.

^g Trade name, Standard Pressed Steel.

TABLE 5—The least severe condition where hydrogen stress cracking occurred in a noble alloy galvanically coupled to carbon steel in sour environments (NACE solution, 1-atm H₂S partial pressure).

Material	Condition ^a	Test Stress as % YS	Experimental Temperature, °C	Time to Failure, Days	Reference
9 Cr-1 Mo Steel	C-ring N&T, HRC 22, 88 ksi Y.S.	100	22	12	35
SAF 2205 SS ^b	wire, 1580 MPa (229 ksi) YS	100	149	7	17
410 SS	C-ring, Q&DT (NACE) HRC 18, 82 ksi, YS	100	22	9	35
17-4 PH SS	C-ring, H-1150M, HRC 27, 114 ksi YS	100	22	9	35
Custom 450 ^c	C-ring, H-1150, HRC 31, 101 ksi Y.S.	100	22	22	35
316 S.S.	wire, 1410 MPa (205 ksi) Y.S.	100	93	7	17
Inconel Alloy X750 ^d	C-ring, A&A, HRC 31 104 ksi YS	100	22	1	35
Inconel Alloy 718 ^d	wire, 1480 MPa (215 ksi) Y.S.	100	177	7	17
Inconel Alloy 625 ^e	C-ring, 59% CR, 1289 MPa (187 ksi) YS	100	22	11	36
Hastelloy C-276 ^e	wire, 1540 MPa (223 ksi) YS	100	177	7	17
MP 35N ^f	wire, 1400 MPa (203 ksi) YS	100	177	7	17
	C-ring, 59% CR, 1345 MPa (195 ksi) YS	100	22	2	36

^a Abbreviations used: CR = cold reduced. YS = 0.2% yield strength. N&T = normalized and tempered. Q&DT = quench and double temperature. A&A = anneal and age.

^b Trademark, Sandvik Alloys, AB.

^c Trademark, Carpenter Technology Corp.

^d Trademark, Huntington Alloys, Inc.

^e Trademark, Cabot Corp.

^f Trade name, Standard Pressed Steel.

TABLE 6—Composition of alloys commonly used in oil and gas production that are noble to steel.

Alloy	Nominal Composition, %								Other
	C	Fe	Cr	Ni	Mo	Cu			
Alloy steel									
9 Cr-1 Mo	0.12	bal	9	...	1.0
Martensitic stainless steels									
AISI 410	0.1	bal	12
AISI 420	0.2	bal	13
CA6NM	...	bal	13	3.5	0.7
17-4PH ^e	...	bal	16	4	...	3.5
Custom 450 ^b	...	bal	15	6.5	0.8	1.5	...	0.7 Nb	...
Duplex stainless steels									
UNS 31803 ^c	...	bal	22	5.5	3.0	0.14 N	...
Ferrallium 255 ^d	...	bal	25	6	2.5	1.7	...	0.2 N	...
Uranus 50 ^e	...	bal	21	6	2.5	1.5
Austenitic Fe and Ni base alloys									
AISI 316	...	bal	17	12	2.5
Sanicro 28 ^f	...	bal	27	31	3.5	1.0
Incoloy 925 ^g	...	bal	21	42	3.0	2.0	...	2 Ti	...
Inconel 718 ^h	...	bal	18	52	3.0	5 Nb, 1 Ti, 0.5 Al	...
Pyromet 31 ^b	...	bal	23	55	2.0	1 Nb, 2 Ti, 2 Al	...
Inconel X-750 ^h	...	7	15	bal	2.5 Ti, 1 Nb, 0.7 Al	...
Monel K-500 ^h	65	...	29	...	3 Al, 0.5 Ti	...
Inconel 625 ^h	...	3	22	bal	9	3.5 Nb	...
Hastelloy C-276 ^h	...	6	16	bal	16	4 W, 2 Co	...
MP35N ⁱ	20	35	10	35 Co, 0.7 Ti	...

^a Trademark, Armco Steel Corp.^b Trademark, Carpenter Technology Corp.^c Known by several commercial names (AF 22, SAF 2205, VS 22).^d Trademark, Bonar—Langley Alloys, Ltd.^e Trademark, Soc. Creusot—Loire.^f Trademark, Sandvik Ab.^g Trademark, Huntington Alloys, Inc.^h Trademark, Cabot Corporation.ⁱ Trademark, Standard Pressed Steel Co.

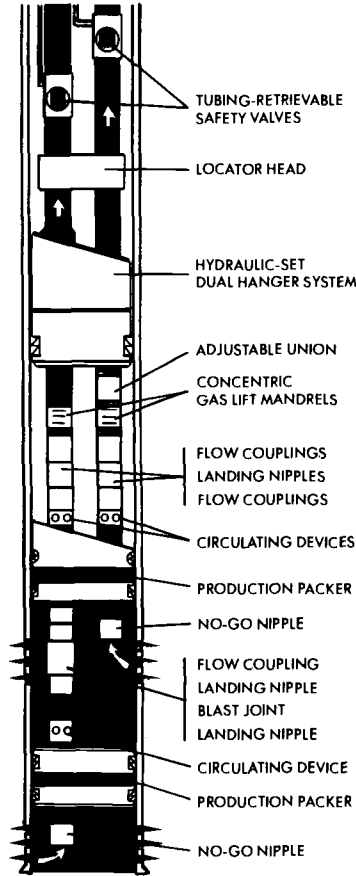


FIG. 14—Schematic of a typical well completion for a flowing well, producing from two zones (not to scale), showing the down hole equipment.

Galvanic Corrosion in Seawater

Galvanic corrosion in seawater continues to be a major source of failures in oil and gas production operations. Offshore seawater handling and injection systems are complex, consisting of pumps, valves, filtration equipment, deaeration equipment (gas stripping or vacuum stripping), and heat exchange equipment. Subsea completions take the complex sets of valves and controls in wellheads and place them on the ocean floor. General discussions of galvanic corrosion in platform seawater systems can be found in the literature [42,43]. Most seawater galvanic corrosion failures that occur at the present time are mistakes that should not have happened such as improper material substitutions. Following are several examples that demonstrate this point.

Pump Impeller Retaining Ring Failure

Vertical turbine pumps supply seawater to a large onshore seawater injection facility. The pump impeller casing, and bowls are Ni-Resist Type 1, with 316 stainless steel impeller retaining rings. Unfortunately, retaining rings of 410 stainless steel were inadvertently installed in the pump at the factory. The appearance of one of these 410 stainless steel impeller retaining rings

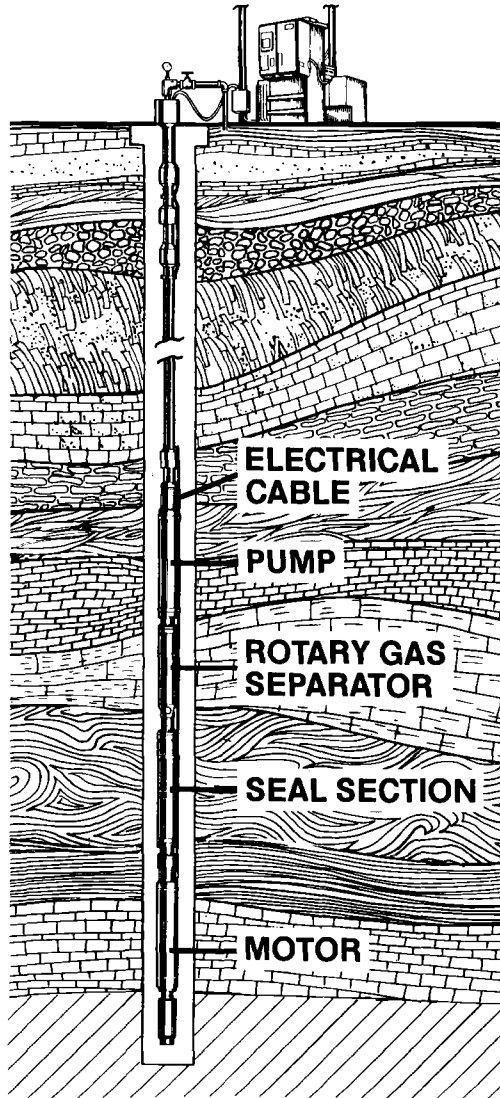


FIG. 15—Schematic of a typical well completion for a well produced by means of an electrical submersible pump (ESP).

after 1300-h operation is shown in Fig. 17. Failure was by extensive crevice corrosion. Ni-Resist will provide galvanic protection for 316 stainless steel sufficient to protect it from crevice corrosion, but not for 410 stainless steel.

Stainless Steel Bolt Failure

A filtration unit in a platform seawater injection system handling fully aerated seawater is constructed of 316 stainless steel. The attached piping upstream of each filter is heavy wall carbon steel to provide galvanic protection, preventing crevice corrosion of the 316 stainless steel. Inside each filter bolts are used to retain the nonmetallic filter elements. In several

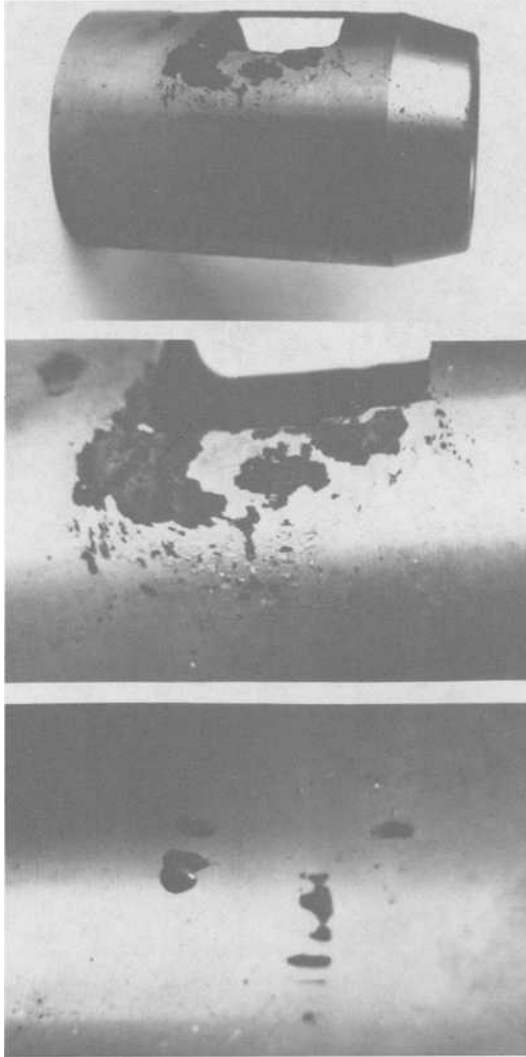


FIG. 16—*Failure of the electroless nickel coating on a subsurface safety valve originating from porosity in the coating. The unfavorable anode/cathode area ratio resulted in rapid attack of the steel substrate at the defects.*

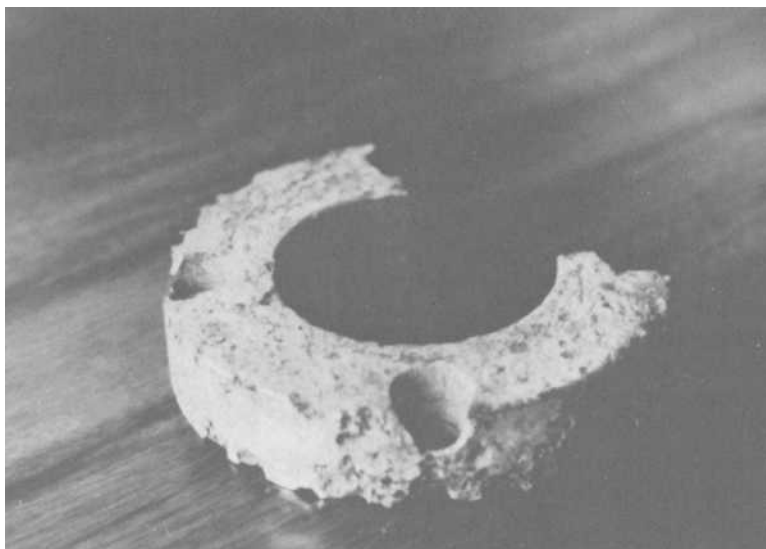


FIG. 17—Corrosion of a seawater pump impeller retaining ring, specified as 316 stainless steel, but actually 410 stainless steel. The Ni-resist impeller would have galvanically protected 316 stainless steel, but the 410 stainless steel failed by severe crevice corrosion.

instances 303 stainless steel bolts were substituted for 316 stainless steel bolts. The result is shown in Fig. 18. After six-months operation, crevice corrosion had virtually destroyed the 303 stainless steel. Carbon steel can galvanically protect 316 stainless steel from crevice corrosion, but not 303 stainless steel. The substitution of 303 stainless steel for 316 stainless steel is a very common problem that is particularly prevalent with small parts such as compression tube fittings and small valves.

Summary

Galvanic corrosion in oil and gas production occurs in three basic environmental types: sweet (carbon dioxide), sour (hydrogen sulfide), and seawater environments. Sweet and sour production is highly variable in composition from well to well and within individual wells.

Corrosion potential charts have been constructed from diverse references giving corrosion potential relationships of metals and alloys for the primary environmental areas. They allow a broad determination of the potential for galvanic corrosion for metals and alloys in common use in oil and gas production for each of the environmental areas.

Electrochemical polarization data define the type of corrosion and the corrosion kinetics resulting from a galvanic couple. Polarization of metals and alloys in seawater has been extensively studied and is fairly well defined. This is not the case for sweet and sour environments. The formation and protectiveness of the iron carbonate corrosion product in sweet environments is a function of time, temperature, and CO_2 partial pressure. These variables must be taken into account in order to apply experimental data. Galvanic corrosion in sour environments is complicated by the occurrence of several iron sulfides that have different polarization characteristics, and can alter polarization of the reduction reaction as well as the corrosion (oxidation) reaction. The effect of the galvanic couple in altering the anode steel corrosion product is not well defined.

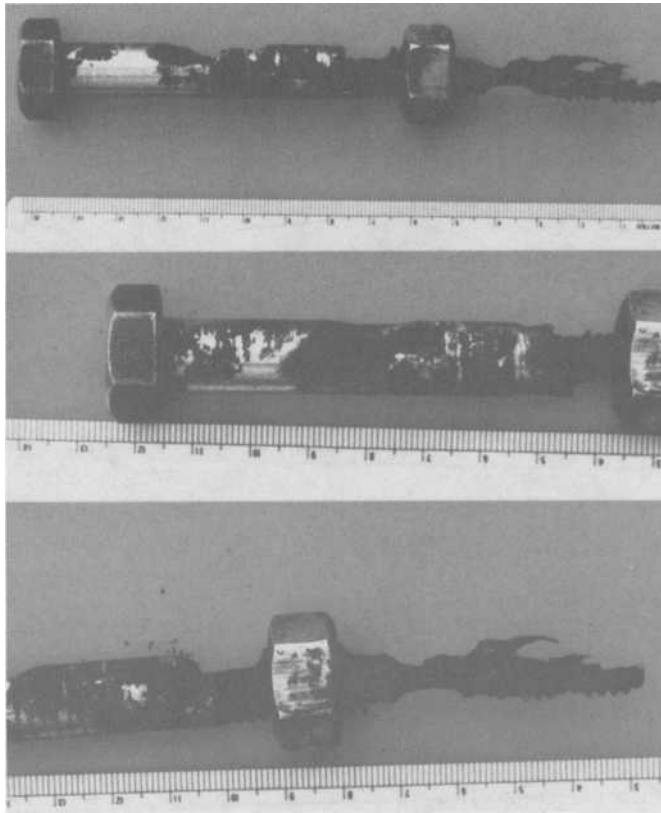


FIG. 18—Crevice corrosion on a 303 stainless steel bolt after six months service in a 316 stainless steel seawater filter. The bolt was specified as 316 stainless steel. Crevice corrosion protection for 316 stainless carbon steel was not sufficient to protect 303 stainless steel.

Galvanic corrosion failures in oil and gas production now occur primarily in two areas: the noble metal of the couple and in seawater systems. Failures of the noble metal in a galvanic couple are generally the result of hydrogen embrittlement and hydrogen stress cracking of susceptible alloys in a sufficiently severe environment in terms of pH, H_2S partial pressure, alloy metallurgical condition, and stress level. NACE MR-01-75 should be revised to include the effects of galvanic coupling on the noble metal, setting metallurgical property limits on the material when coupled to steel in sour environments. The galvanic corrosion failures in seawater are generally the result of improper substitutions or replacement of a material where the proper material was specified.

Additional research on galvanic corrosion in oil and gas production is needed in a number of areas. The effects of the composition of the crude oil and its importance needs study, the influence of the iron sulfides on galvanic corrosion of both the steel and noble metal require definition.

References

- [1] Baboian, R., *Localized Corrosion-Cause of Metal Failure*, STP 516, American Society for Testing and Materials, Philadelphia, 1982, pp. 145-163.
- [2] DeWaard, C. and Millams, D. E., *Corrosion*. Vol. 31, No. 5, May 1975, pp. 177-181.

- [3] Brown, A., Harrison, J. T., and Wilkins, R., *Carbon Dioxide Corrosion in Oil and Gas Production*, L. E. Newton et al., Eds., National Association of Corrosion Engineers, 1984, pp. 232-241.
- [4] Carlson, H. A., *Carbon Dioxide Corrosion in Oil and Gas Production*, L. E. Newton, et al., Eds., National Association of Corrosion Engineers, 1984, pp. 452-455.
- [5] Shock, D. A. and Sudbury, J. D., *Carbon Dioxide Corrosion in Oil and Gas Production*, L. E. Newton, et al., Eds., National Association of Corrosion Engineers, 1984, pp. 394-401.
- [6] Crolet, J. L., *Journal of Petroleum Technology*, Vol. 35, No. 8, Aug. 1983, pp. 1553-1558.
- [7] Snape, E. N. and Van Rooyen, D., ASMS 68-PET-3, Sept. 1968, p. 5.
- [8] Ikeda, A., Mukai, S., and Ueda, M., "Prevention of Carbon Dioxide Corrosion of Line Pipe and Oil Country Tubular Goods," *Corrosion/84*, Paper 289, National Association of Corrosion Engineers, April 1984.
- [9] Pathania, R. S., *8th International Congress on Metallic Corrosion*, Sept. 1981, pp. 1404-1411.
- [10] Crolet, J. L. and Bonis, M. R., *Materials Performance*, Vol. 25, No. 3, March 1986, pp. 41-49.
- [11] Ikeda, A., Miura, M., Mukai, S., Ueda, M., and Koso, K., "Corrosion Behavior of Duplex Stainless Steel for Wet Carbon Dioxide Environments," *Corrosion/86*, Paper 333, March 1986.
- [12] Bates, J. F., *Materials Protection*, Vol. 8, No. 1, Jan. 1969, pp. 33-40.
- [13] Herbsleb, G. and Popperling R. K., *Hydrogen Sulfide Corrosion in Oil and Gas Production*, R. N. Tuttle and R. D. Kane, Ed., National Association of Corrosion Engineers, 1981, pp. 339-346.
- [14] Wilhelm, S. M. and Kane, R. D., *Corrosion*, Vol. 40, No. 8, Aug. 1984, pp. 431-439.
- [15] Yoshino, Y. and Ikegaya, A., "A Study on the Performance of 12Cr-Ni-Mo Martensitic Stainless Steels in Chloride and Sulfide Environment," *Corrosion/84*, Paper 210, National Association of Corrosion Engineers, April 1984.
- [16] Sumotomo Metal Industries, Ltd., "Bimetallic Corrosion Test Results Between Copper and CRA Materials," April 1985, unpublished report.
- [17] Vaughn, G. A. and Chaung, H. E., *Materials Performance*, Vol. 21, No. 1, Jan. 1982, pp. 44-50.
- [18] Rhodes, P. R., "Stress Cracking Risks in Corrosive Oil and Gas Wells," *Corrosion/86*, Paper 322, National Association of Corrosion Engineers, March 1986.
- [19] TM-01-77, "Testing of Metals for Sulfide Stress Cracking at Ambient Temperatures," National Association of Corrosion Engineers, 1977.
- [20] Morris, D. R., et al., *Journal of the Electrochemical Society*, Vol. 127, No. 6, June, 1980, pp. 1228-1235.
- [21] Hovarth, G. and Novak, M., *Corrosion Science*, Vol. 4, 1964, pp. 159-178.
- [22] King, R. A. and Wakerley, D. S., *British Corrosion Journal*, Vol. 8, Jan. 1973, pp. 41-45.
- [23] Mara, D. D. and Williams, J. A., *British Corrosion Journal*, Vol. 7, March 1972, pp. 94-95.
- [24] Khazraji, A. T. H. A., "Potentiostatic Studies on the Corrosion of Iron by the Iron Sulfides," M.S. thesis, University of Manchester Institute of Science and Technology, 1975.
- [25] Smith, S. J., "Corrosion of Mild Steel by Mineral Sulfides," PhD dissertation, University of Manchester Institute of Science and Technology, 1979.
- [26] Lee, T. S. and Tuthill, A. H., *Materials Performance*, Vol. 23, No. 11, Nov. 1984, pp. 44-45.
- [27] Bernhardsson, S. and Melstrom, R., *Proceedings of the 5th International Congress on Marine Corrosion and Fouling*, Barcelona, Spain, May 1980.
- [28] Konoki, K., Shihohara, T., and Shirai, M., "Application of New Stainless Steels to Seawater Heat Exchanger Tubes," *Corrosion/81*, Paper 125, National Association of Corrosion Engineers, April 1981.
- [29] Asphahani, A. I., et al., "Highly Alloyed Stainless Materials for Seawater Applications," *Corrosion/80*, Paper 29, Corrosion/80, National Association of Corrosion Engineers, March 1980.
- [30] Tuttle, R. N. and Kochera, J. W., *Hydrogen Sulfide Corrosion in Oil and Gas Production*, R. N. Tuttle and R. D. Kane, Eds., National Association of Corrosion Engineers, 1981, p. 2.
- [31] Rhodes, P. R., "Stress Cracking Risks in Corrosive Oil and Gas Wells," *Corrosion/86*, Paper 322, National Association of Corrosion Engineers, March 1986.
- [32] Erlings, J. G., de Groot, H. W., and Van Roy, J. F., "Stress Corrosion Cracking and Hydrogen Embrittlement of High-Strength Non-Magnetic Alloys in Hot Concentrated Brines," Paper No. 162, Corrosion/86, National Association of Corrosion Engineers, March 1986.
- [33] Kolts, J., "Laboratory Evaluation of Corrosion Resistant Alloys for the Oil and Gas Industry," *Corrosion/86*, Paper 323, National Association of Corrosion Engineers, March 1986.
- [34] Kane, R. D., *Corrosion*, Vol. 34, No. 12, Dec. 1978, pp. 442-445.
- [35] Rice, P. W., *Materials Performance*, Vol. 17, No. 9, Sept. 1978, pp. 16-25.
- [36] Kane, R. D., Watkins, M., Jacobs, D. F., and Hancock, G. L., *Corrosion*, Vol. 33, No. 9, Sept. 1977, pp. 309-320.
- [37] Efird, K. D., *Materials Performance*, Vol. 24, No. 4, April 1985, pp. 37-40.
- [38] Asphahani, A. I., *Proceedings of the 7th International Congress on Metallic Corrosion*, Vol. 2, Rio de Janeiro, 1978, pp. 976-981.
- [39] Myers, J. B. et al., *Journal of Metals*, Vol. 36, No. 10, Oct. 1984, pp. 50-59.

- [40] NACE MR-01-75, "Sulfide Stress Cracking Resistant Metallic Material for Oil Field Equipment," National Association of Corrosion Engineers (1984 revision).
- [41] Huntington Alloys, Inc. Publication, 1OM 9-83-S-66, 1983.
- [42] Robson, D. N. C., *Corrosion and Marine Growth on Offshore Structures*, J. R. Lewis and A. D. Mercer, Ed., Society of the Chemical Industry, London, 1984, pp. 69-80.
- [43] Efird, K. D., *Marine Corrosion on Offshore Structures*, Society of Chemical Industry, London, pp. 53-61.

Avoiding Galvanic Corrosion Problems in the Telephone Cable Plant

REFERENCE: Schick, G., "Avoiding Galvanic Corrosion Problems in the Telephone Cable Plant," *Galvanic Corrosion. ASTM STP 978*, H. P. Hack, Ed., American Society for Testing and Materials, Philadelphia, 1988, pp. 283-290.

ABSTRACT: Telephone cable plant is exposed to practically all the corrosive environments that nature can provide. Designers of telephone plant components use various, sometimes galvanically incompatible, metals and alloys to satisfy strength, formability, conductivity, electrical safety, and cost requirements. Galvanic corrosion occurs when galvanically incompatible metallic couples are exposed to corrosive environments. Combinations of small cathode/anode surface area ratios, metallic and nonmetallic coatings, and cathodic protection are some of the means used to eliminate or reduce the harmful effects of galvanic corrosion. Examples of galvanic corrosion problems in the aerial, underground, and buried plant and solutions to these problems are described.

KEY WORDS: galvanic corrosion, telephone plants, corrosion protection

The various components of a telephone cable plant are exposed to practically all the corrosive environments that nature can provide. The aerial plant is most vulnerable at industrial centers, where sulfur dioxide (SO₂) and carbon dioxide (CO₂) are common atmospheric corrosive agents, and at sea coastal areas, where salt spray accelerates corrosion. The underground plant, where cables and associated hardware are placed in ducts and manholes, is often subject to high water levels. These waters are usually contaminated with soluble salt components of the native soils, and man-made contaminants, for example, deicing salts, fertilizers, and occasionally industrial effluents. The buried plant is subject to local soils of various corrosivity and to the above-mentioned man-made contaminants.

Galvanic Couples

If galvanic corrosion was the only consideration, we could eliminate galvanic couples by making all interconnected components of the same metal. That would not solve concentration cell (for example, differential aeration), stress corrosion cracking, stray current, and interference current problems. Furthermore, we also must consider strength, formability, conductivity, electrical safety, and cost. Thus, a plant free of galvanic couples is a utopian dream. A realistic telephone cable plant contains galvanic couples. However, the design considerations in most cases include the following basic principles to limit the effect of galvanic corrosion: (1) anode and cathode components are near each other in the galvanic series, and (2) the cathode/anode surface area ratio is as small as possible, especially if the galvanic cell is under cathodic control. Designers cannot always avoid the use of galvanically incompatible components, and predicted corrosion problems often are solved with metallic or nonmetallic coatings, polymer jacketing, or cathodic protection. In the following I shall describe several galvanic corrosion problems that occurred in the past 25 years and their solutions.

¹Member of technical staff, Bell Communications Research, 435 South St., Morristown, NJ 07960.

The Aerial Plant

The most common galvanic corrosion cell in the aerial plant exists between the zinc (anode) and steel (cathode) of the galvanized steel strand and support hardware in industrial and sea coastal environments. The high concentration of SO_2 in industrial areas, and salt spray at sea coasts, first partially corrode the zinc, then expose increasingly larger and larger surface areas of steel. This is particularly true in industrial areas where the acidic contaminants dissolve the amphoteric zinc. The resulting galvanic couple then corrodes away the remaining zinc at a high rate for two reasons: (1) industrially polluted moisture condensate and salt spray have good electrolytic conductivity, and (2) the zinc anode and exposed bare steel cathode are adjacent to each other (short electrolyte path). Class C galvanizing on steel strand and hardware (ASTM Specification for Zinc-Coated Steel Wire Strand [A 475]) and aluminum coated strand, especially in industrial atmospheres, can increase the life expectancy of the above aerial plant components.

Very few severe galvanic corrosion problems exist in the relatively benign rural and suburban atmospheres. I attribute this good "track record" to the following: (1) extensive use of plastic jacketed cables and plastic closures, (2) almost all support hardware is made of galvanized steel, (3) the corrosive environment is only a thin layer of contaminated moisture that represents relatively high electrolyte resistance, as compared to moisture layers containing dissolved SO_2 or dissolved sodium chloride (NaCl) or both, when it covers galvanically incompatible structures, and (4) the moisture evaporates in dry and windy weather.

An example of an unavoidable galvanic couple in the aerial plant is lead sheathed cable secured with galvanized steel lashing wire to galvanized steel strand. Although this combination represents a disadvantageous small anode (zinc), and large cathode (lead) coupling, galvanized steel lashed lead sheathed cable plant held up well in the past because of a combination of thin electrolyte layer, natural drying effects, and the use of heavy (Class C) galvanizing at the more corrosive areas (sea coasts and industrial areas).

Another example of galvanic corrosion in the aerial plant was presented by a ring-shaped contact element on cable shields. This item was made of mild steel and coated with 5.08×10^{-6} m (0.0002 in.) of tin. Such a thin coating of tin was found to be porous. Approximately 0.33 mm^2 of base metal is exposed per 1 m^2 of coated metal [1]. Under these conditions, a small quantity of condensate moisture is sufficient to create galvanic cells between small anode (steel) and large cathode (tin or tin oxide). The corrosion product mushroomed out on the tin surface, thereby increasing the contact resistance. The solution to this problem was to increase the thickness of tin to 2.54×10^{-5} m (0.001 in.). At this thickness the tin coating is not porous, thus, the offending galvanic cell is eliminated.

The Underground Plant

In the underground plant, cables and associated hardware would be free of corrosive environment if the ducts and manholes of the underground plant were dry. Unfortunately, contaminated water enters these structures at cracks, openings, and joints thereby providing the corrosive environment. With the proliferation of polyethylene jacketed cables, galvanic corrosion of the underground plant takes place almost exclusively in the manholes. In manholes of steel reinforced, pre-cast or cast-in-place concrete construction the rebars (reinforcing bars), passivated by the alkaline concrete, play the role of cathode in a galvanic couple with galvanized steel support hardware.

Galvanized Steel Support Hardware Corrosion

The potential of steel in concrete is about -0.2 V versus the Cu/CuSO_4 reference electrode, and that of galvanized steel is about -1.1 V [2] (Fig. 1). Obviously, when the rebars in con-

crete are coupled to the galvanized steel support hardware in a flooded manhole the galvanized steel is the corroding anode. Under certain conditions the rebars are part of the electric ground and are connected to the remainder of the plant. If the cables are all polyethylene jacketed, magnesium anodes placed on the manhole floor and connected to the support hardware provide a solution to this problem.

Under different conditions (for example, the plant contains lead sheathed cable in a nonstray current area), the rebars may not be part of the grounding system, and the galvanic coupling to the galvanized steel hardware can be eliminated. In steel reinforced concrete manholes, contacts usually are made to the rebars at four points, and inside the manholes 0.203-m (8-in.) tin-coated copper bonding ribbon pieces are attached to these contacts. Hence, they provide the option for bonding or isolating. Unfortunately, the mounting bolts of the support hardware more often than not make incidental direct contacts to the rebars, thereby eliminating the above option. The use of nylon bushings or nylon mounting bolts eliminates this problem (Fig. 2). Mr. Richard C. Eggebrecht of Illinois Bell Telephone Co. conducted a two-year field study in flooded manholes by mounting some of the galvanized steel support hardware with nylon bolts. Visual examinations indicated that the isolated galvanized steel hardware remained free of rust, while those connected to the rebars had most of the zinc coating and some of the underlying steel corroded away. This study showed the harmful effect of the rebar-support hardware galvanic couple and the beneficial effect of the electric isolation against incidental galvanic coupling (Figs. 1 and 2).²

Repeater Cases

Some carrier repeater cases contain electric circuits mounted on a galvanized cast iron base and protected from the environment by a 1.6×10^{-3} m (0.063 in.) thick cylindrical, mild steel cover, which, in turn, is coated with 3×10^{-5} m (0.0012 in.) of zinc. The covers, designated for manhole use, are coated with black paint. A Type 301 stainless steel V-band clamp fastens the cover to the base. The black paint can be damaged during installation, thus exposing small areas of galvanized steel. In flooded manholes the small anode (galvanized steel at damaged paint) large cathode (stainless steel V-band clamp) leads to fast perforation of the cover (Fig. 3). Laboratory experiments with various anode/cathode surface area ratios prove the validity of the above statement (Fig. 4). We provided two solutions for this problem. Since the black paint on the outside is not necessary, apply 3.8×10^{-4} to 4×10^{-4} m (0.015 to 0.018 in.) of flame sprayed zinc. For carrier cases already in service where the black paint cannot be eliminated, place magnesium anodes on the bottom of the manhole and connect their leads to the carrier cases.

The Buried Plant

Telephone and power utilities often bury their cables in joint trenches. For electrical safety these cable plants are bonded together at many locations. A galvanized steel mounting post ensures the perpendicular position of the terminal on the ground, but the post is subject to corrosion. In the past 15 to 20 years corrosion of concentric neutral wires has occurred in buried electric power installations [3-9]. Extruding carbon-black filled polyethylene over the neutral wires provided one of the solutions to this problem. Carbon-black filled polyethylene power cable jacketing represents a very large cathode against the small galvanized steel of the connected telephone mounting post anodes. The ensuing galvanic corrosion of the anode, while normally innocuous, can be particularly aggressive in porous and oxidizing soils [10]. Laboratory studies in 0.1 N NaCl solution predict 0.76- to 1165-mm/year (30- to 65-mpy) corrosion

²Eggebrecht, R. C., Illinois Bell Telephone Company, private communication.

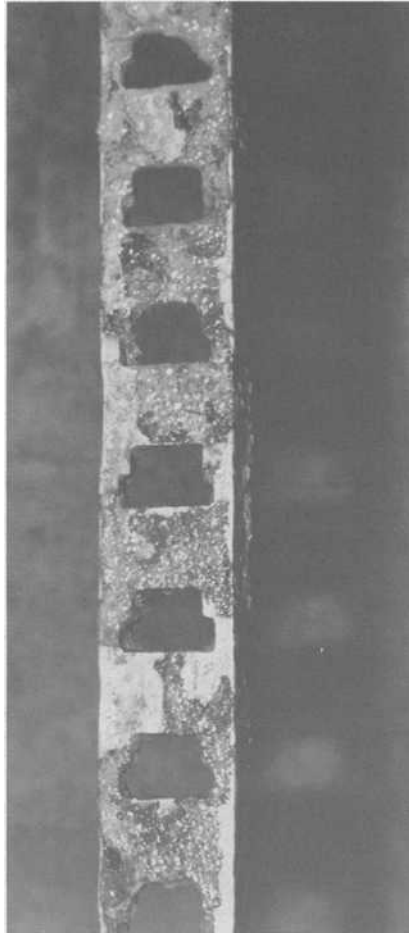


FIG. 1—Galvanized steel support hardware mounted with steel bolts.

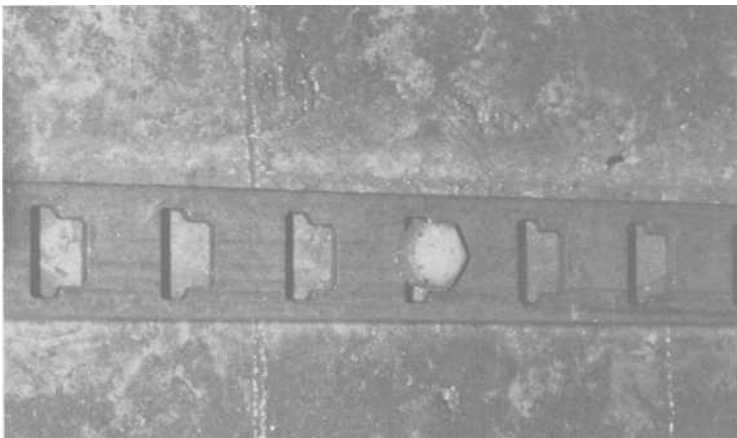


FIG. 2—Galvanized steel support hardware mounted with nylon bolts.

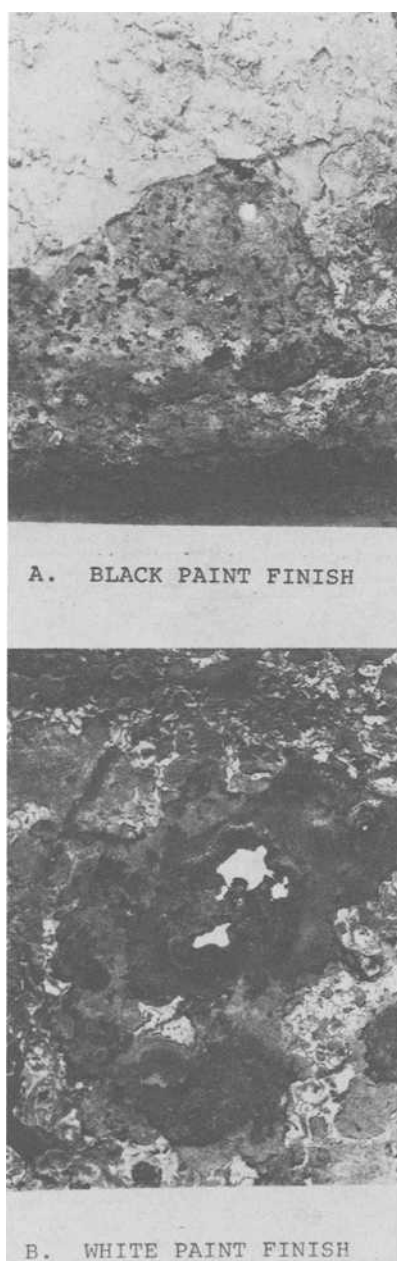


FIG. 3—Perforated *T-1* carrier case covers.

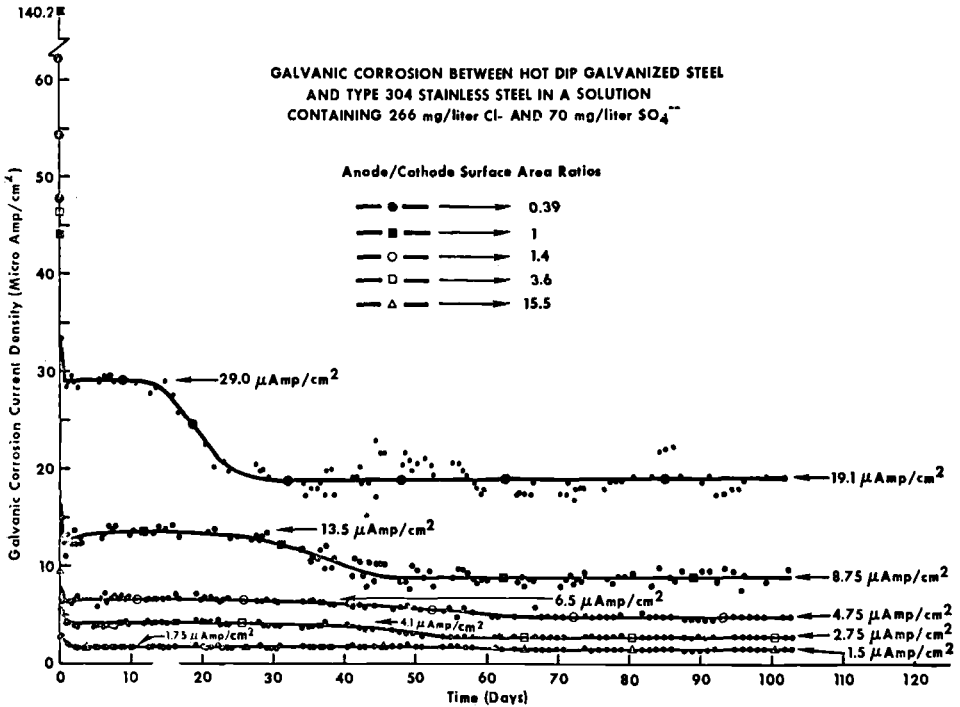


FIG. 4—Galvanic corrosion between hot dip galvanized steel and Type 304 stainless steel in a solution containing 266 mg/L Cl⁻ and 70 mg/L SO₄²⁻.

rates of galvanized steel when coupled to carbon-black filled polyethylene cable (35% carbon) at an anode/cathode ratio of 0.015, and 0.05 to 0.15 mm/year (2 to 6 mpy) when the same ratio was 1.0 (Fig. 5) [11]. Field experiments conducted for 1159 days in 11 200 Ω-cm resistivity soil showed that on the average galvanized steel posts connected to a carbon-black filled polyethylene jacketed power cable corroded at a 7.3 times higher rate than the same posts connected to bare concentric neutral type power cable (Table 1). The most likely reason for this large difference in corrosion rates is the stronger cathodic control and larger driving potential of the zinc-carbon galvanic cell as compared to a zinc-tin galvanic cell. Mounting an additional galvanized steel post on the pedestal terminal or connecting an additional post and placing it in the trench reduces the corrosion rate to an acceptable level.

TABLE 1—Corrosion of galvanized steel mounting posts. Environment: 11 200 Ω-cm soil. Length of test: 1159 days.

Number of Mounting Posts Connected to the Power Cable	Average Corrosion Rate	
	Posts Coupled to Carbon-Black Filled Polyethylene Jacketed Cable, mm/year (mpy)	Posts Connected to Cable with Bare Concentric Neutral Wires, mm/year (mpy)
1	0.25 (10.00)	0.041 (1.62)
2	0.19 (7.58)	0.024 (0.93)
3	0.17 (6.65)	0.021 (0.84)
4	0.16 (6.25)	0.023 (0.91)

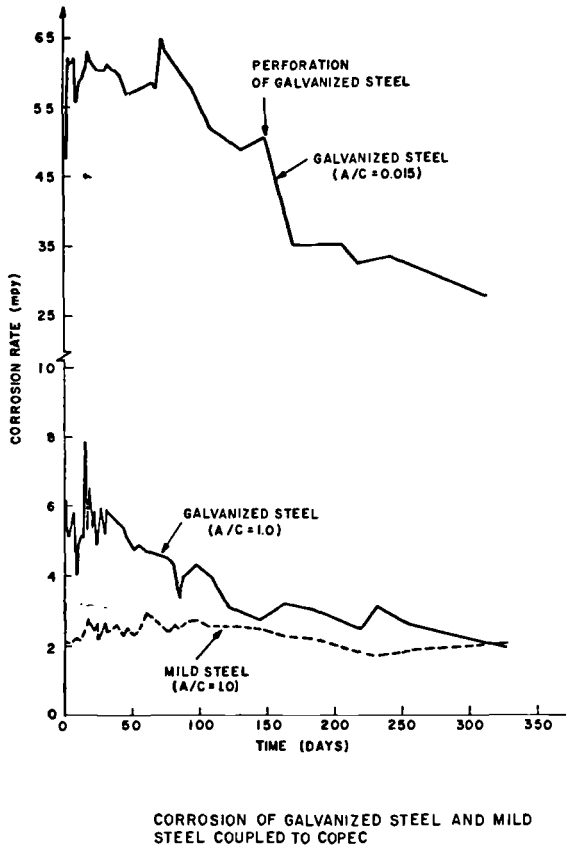


FIG. 5—Corrosion of galvanized steel and mild steel coupled to a conductive polyethylene jacketed power cable.

Summary

The above examples of galvanic corrosion in the telephone cable plant show that design needs and cost can override galvanic corrosion considerations. Consultations in the design stage of new equipment, visual examinations and laboratory testing of products, and in-plant corrosion tests help uncover the galvanic corrosion problem areas. Metallic and nonmetallic coatings, cathodic protection, and changes in installation techniques usually solve the above galvanic corrosion problems.

References

- [1] Uhlig, H. H., *The Corrosion Handbook*, John Wiley and Sons Inc., New York, 1963, p. 83.
- [2] Peabody, A. W., *Control of Pipeline Corrosion*, National Association of Corrosion Engineers, Houston, TX, 1967, p. 5.
- [3] Marwick, I. J. and McNamara, J. H., *Underground Engineering*, Vol. 2, No. 3, April/May 1971, pp. 17-24.
- [4] Zastrow, O. W., "Copper Corrosion in High Resistivity Soil," Rural Electrification Administration Staff Report, U.S. Department of Agriculture, Washington, DC, Oct. 1972.
- [5] Zastrow, O. W., "Soil Corrosion of Copper Concentric Neutral Wires on Underground Electric Cable," Rural Electrification Administration Status Report, U.S. Department of Agriculture, Washington, DC, Aug. 1973.

- [6] Zastrow, O. W., "Copper Corrosion in Medium and High Resistivity Soils," *Materials Performance*, Vol. 13, No. 8, 1974, pp. 31-36.
- [7] Schick, G. and Mitchell, D. A., "Galvanic Corrosion of Underground Power Distribution Cable Materials," *Galvanic and Pitting Corrosion—Field and Laboratory Studies, STP 576*, American Society for Testing and Materials, Philadelphia, 1976, pp. 69-80.
- [8] Zastrow, O. W., "Galvanic Behavior of Underground Cable Neutral Wires and Jacketing Material," *Materials Performance*, Vol. 16, 1977, pp. 18-21.
- [9] Zastrow, O. W., "Galvanic Behavior of Underground Cable Neutral Wires and Jacketing Materials, an Update," *Corrosion 179*, Paper 237, National Association of Corrosion Engineers, March 1979.
- [10] Schick, G., "The Effect of Oxygen, Salt Concentration, and pH on Galvanic Cells Between a Carbon-Black Filled Polyethylene Cathode and Various Metal Anodes," *Journal of Testing and Evaluation*, Vol. 8, No. 3, May 1980, pp. 143-54.
- [11] Schick, G., "Galvanic Corrosion of Metals Coupled to Carbon-Black Filled Polyethylene," *Proceedings of an International Symposium Honoring Professor H. H. Uhlig on his 75th Birthday CORROSION AND CORROSION PROTECTION*, R. P. Frankenthal and F. Mansfeld, Eds., The Electrochemical Society Proceedings, Vol. 8, 1981, pp. 259-265.

Galvanic Corrosion in Navy Ships

REFERENCE: Morton, A. G. S., "Galvanic Corrosion in Navy Ships," *Galvanic Corrosion, ASTM STP 978*, H. P. Hack, Ed., American Society for Testing and Materials, Philadelphia, 1988, pp. 291-300.

ABSTRACT: Galvanic corrosion concerns in Navy ships are discussed including the role that cathodic protection plays on the ship hull. The specific causes of a number of shipboard examples of galvanic corrosion are identified, with proposed solutions to each. Most problems occur in seawater connected tanks and in the piping systems, with relatively few on the external ship hull, machinery spaces, and topsides. Nearly all of the problems could have been eliminated through the application of good corrosion engineering practice at the design or construction stage, although occasionally a unique unpredictable problem emerges. The predictability of the problems re-emphasizes the need for greater corrosion awareness by all associated with the design, building, and maintenance of ships and their mechanical systems.

KEY WORDS: marine corrosion, galvanic corrosion, cathodic protection, metallic materials, corrosion engineering

Ships not only float on seawater, as traditionally thought, but also vast quantities of water are pumped into them and through essentially all ship areas. Further, the salt in the marine atmosphere accumulates on all surfaces, both external and internal. This leads to many more potential corrosion problem areas than the obvious one of the hull and its appendages. Although there are thousands of metal components aboard a ship, there are surprisingly few numbers of different alloys used in any significant quantity. So while on the one hand the corrosive environment is prevalent, galvanic corrosion occurs to a surprisingly small extent. The instances that occur however can have serious consequences, and constant attention is required at all stages of design, construction, and maintenance. Prevention of galvanic corrosion is important to shipbuilding however, because of the aggressive environment and long service lives expected of seagoing vessels.

Documentation

Many corrosion textbooks treat the subject of galvanic corrosion, therefore, its nature, prevalence, control techniques, and their theoretical basis are well understood and available. Government publications and reports on this topic also have been prepared, usually in connection with specific problems or research and development objectives. There are, however, two documents that are useful, readily obtainable, and cover the galvanic corrosion topic in a practical, corrosion engineering sense. The first is the Military Standardization Handbook entitled, *Corrosion and Corrosion Prevention of Metals* (Mil-Handbook-729, 29 Nov. 1983) [1], which covers the full scope of material deterioration in all environments. This includes the corrosion processes and types of attack, performance of specific metals, prevention, testing, and quality assurance. The second document is a Military Standard for Dissimilar Metals (Mil-Std-889B of 21 Nov. 1979) [2], which defines and classifies dissimilar metals and provides methods for

¹Supervising metallurgist, Marine Corrosion Branch, David Taylor Research Center, Bethesda, MD 21402.

protecting coupled dissimilar metals against corrosion. It is applicable to all military equipment and components. These two documents are referential, available, and technically sound sources for controlling galvanic corrosion in shipbuilding construction. Recent efforts by the author and his co-workers are addressing corrosion control for Navy ships more specifically [3]. Further, others have prepared corrosion control documentation for many specific classes of ships based upon Navy approved corrosion control systems [4].

Galvanic Effects

Galvanic corrosion is commonly referred to, and thought of, as a “form” of corrosion, whereas more properly, it should be thought of as an accelerating or decelerating mechanism for all other “forms” of corrosion. General corrosion is the most commonly used evidence of galvanic attack, and that convention is followed in some of the analyses in this paper. However, it is more accurate to think of general corrosion being stimulated (or retarded) by currents created by the presence of dissimilar metals, as stated in the definition contained in Mil-Handbook-729, which reads, “Galvanic corrosion—a type of corrosion associated with the current resulting from the coupling of dissimilar electrodes in an electrolyte.” Pitting and crevice attack are commonly thought of as being driven by the galvanic action of the large passive (more noble) area surrounding a small active site. The addition of even more passive (noble) surface area may further accelerate the local attack while the coupling to a more active metal may inhibit pitting/crevice attack. Thus localized attack may be stimulated or retarded by the coupling of these more or less noble metals (galvanic effects). Similar arguments apply to intergranular corrosion, erosion corrosion, cavitation, and corrosion fatigue. Hydrogen embrittlement of steels and other sensitive alloys may behave in reverse. In this case, the galvanic coupling to a less noble metal, for example, a zinc anode, can be highly detrimental because it stimulates the cathodic reaction that creates monoatomic hydrogen for potential absorption and transport in the cathode, thereby increasing the sensitivity to failure under load.

Galvanic Effects on Shipboard Systems

Hull

One of the effects of galvanic interactions is an important method of ship hull corrosion control, namely, cathodic protection. All underwater hulls of Navy ships are both painted and cathodically protected. While this cathodic protection is intended to protect the structural material (usually steel) from general corrosion, it also serves to prevent (or reduce) most other forms of corrosion, including galvanic corrosion caused by hull-propeller interactions with the exception of hydrogen embrittlement. Experience bears this out in the Navy because, as shown in Table 1, underwater corrosion of properly protected ships has not occurred in any form except an occasional instance of hydrogen assisted cracking of small, usually high strength attachments and fittings. One specific example of this is an anchor windless brake-band, made of nickel-copper alloy conforming to QQ-N-286 (K-Monel) at 160-ksi (1103-MPa) tensile strength. The environmentally assisted failure was determined to be hydrogen related, aggravated by cathodic protection whose presence was confirmed by calcareous deposits covering all of the adjacent brake-band. A related failure was discussed by Efird [5] of a Ni-Cu-Al alloy bolt that had been subjected to cathodic protection. Efird presents a specification for monel bolts for use in seawater, which is based on elimination of excessively hard areas at the bolt thread root. The guidelines in this specification, however, are applicable to all seawater use of K-Monel in stressed parts subject to cathodic protection.

Flow-induced corrosion of underwater appendages on the hull (struts, rudders, and so forth) is also not usually a problem on a well protected hull, in spite of ship speeds in excess of normal metal corrosion/erosion limits (for example, 10 ft/s [3 m/s] for 90:10 CuNi) and bare spots on

some leading edges (impacted and damaged paint). Obviously much of the lack of flow-induced corrosion is attributable to hydrodynamic design and low shear forces adjacent to leading edges of metal surfaces; but cathodic protection by a galvanic mechanism is a contributing factor.

Galvanic interactions can also occur between the steel of the hull and either the antifoulant paint or the weld beads. Certain paints may contain compounds (for example, carbon, cuprous ions) that cause the coating to be cathodic to the hull and corrosion at small bare spots (from impact or poor paint applications). With such a large cathode to anode ratio, even small differences in potential could be significant. The remedy for this is to have a good insulative primer and anti-corrosive paint system between the steel and the anti-foulant paint. Care should be taken in weld metal selection to insure that the as-deposited metal is cathodic to the base plate. Although this can normally be identified by comparison of the base plate and weld wire alloy content, confirmatory testing of weldments is prudent. The danger is that the large area of base metal will concentrate corrosion at the active weld metal, if the galvanic relationship is incorrect. This is the modern version of the often-repeated example of rivetting copper sheathing on wooden hulls with steel bolts. Although these examples are listed in Table 1, they are not common and do not occur on a cathodically protected hull.

Piping and Tanks

With steel hulled ships and copper alloy piping the opportunities for galvanic corrosion are legion. It would be expected that the most corrosion prone areas exist at sea-chest/hull connections. Reported problems at these locations are not within the author's experience, probably because of the presence of cathodic protection on the hull and anodes in the sea chests.

Sea connected voids, tanks, and so forth often contain operating machinery and associated mounting arrangements, and galvanic compatibility with the tank material is important. There was a recent instance where some aluminum components were found bolted to a steel frame and quietly corroded away in a seawater-flooded tank. While aluminum is unsuited to prolonged underwater service, it is even more inappropriate to attach it directly to steel, unless the intent is to protect the steel by galvanic action of aluminum.

Isolation of ship piping is not practical, so insulation of flanges and bolts would serve no purpose. Figure 1 shows an as-received 11-in. (280-mm) long section of steel pipe, which had been fabricated by the ship's crew to replace a leaking fitting. The thick bronze flange on the right (joined to the 90:10 copper-nickel pipe) is bolted to the steel pipe flange, and a rubber isolation gasket was installed. The steel pipe is covered with rubber insulation. The bolts, however, were not isolated, and electrical continuity was measured between the steel and copper pipe section. Extensive corrosion was the result and is shown in Fig. 2. The time that this couple was in service was between 5 and 9 months. Fairly uniform corrosion occurred over the surface with pipe wall thickness losses being typically 10 to 30 mils (0.3 to 0.8 mm) and maximum wall loss being 50 mils (1.3 mm). Generally the severe galvanic attack of the steel was limited to the weld areas and the pipe ends. The use of tape or other insulation on the bolt shanks and non-metallic washers under the bolt heads and nuts would have given this "temporary" fix quite a few years of useful service.

Pipe hangers and attachments can be a source of galvanic corrosion in sea-connected tanks. A problem occurred with a seawater compensated fuel tank, which had steel hangers and fasteners holding the copper-nickel piping. The piping was not painted and had caused corrosion on the hangers, nuts, bolts, and tank walls. Solutions to this include painting the copper nickel, isolating the hangers and fasteners, or changing them to copper nickel and Monel and providing cathodic protection in the steel tank (assuming that it does not create a spark or additive problem in the fuel), or all of these. Painting of noble metals (copper, nickel, and titanium base alloys), although recommended to reduce galvanic corrosion, is not usually performed in Navy ships because these metals do not themselves corrode. Consequently, paints and application procedures for these difficult-to-coat passive-film-forming metals are not commonly known or

TABLE 1—Specific cases of galvanic corrosion on shipboard systems.

Part	Materials	Cause	Solution
Hull			
underwater hull anchor windlass brake band	zinc anodes/steel hull k monel band/steel and zinc	H ₂ embrittlement after long use	cathodic protection essential for long life modify or substitute the band material
underwater hull	steel hull/antifoulant (AF) paint	noble constituents (C, Cu) in AF paint	good insulative paint under AF top-coats, cathodic protection
underwater hull	steel welds/steel baseplate	lean weld wire and anodic weld beads	sufficient alloying of wire to ensure weld is cathodic to base plate, cathodic protection
equipment mounts in sea-connected tanks	aluminum mount/steel tank	improper material selection	substitute material, cathodically protect, or isolate and protect
Piping			
pipe segment	steel pipe/copper-nickel pipe	improper material, flange bolts not isolated	use Cu-Ni, or fully isolate
pipe hangers	steel hanger/copper-nickel pipe	improper materials or design	paint Cu-Ni, isolate hangers or substitute material
piping in steel tanks	steel tank/copper-nickel pipe	poor detail design	isolation, paint Cu-Ni or cathodically protect the tank
hydraulic piping	steel piping/monel actuator	improper design/material selection	substitute materials or cathodically protect
heat exchanger tubing	copper-nickel tubing/carbon deposits	improper tube cleaning to remove drawing lubricants	adhere to specified procedures
Valves			
valve stems	nickel aluminum bronze stem-/monel or titanium balls	improper material	substitute material
valve plug	brass plug/bronze body	improper material selection or attention to details of specification	ensure suitability of "bronzes" specified
check valve flapper arm valve seat	copper nickel arm/monel flapper Monel seat (re-machined)/Monel seat (with oxide film)	improper alloy selection incomplete refurbishment	substitute materials clean all areas, coat bold surfaces
Atmospheric			
hydraulic valve actuators	aluminum subplate/steel frame	water entrapment in washers	complete isolation, avoid water retention
hydraulic valve actuators	aluminum valve/copper and steel components	condensation, water entrapment	paint faying surfaces

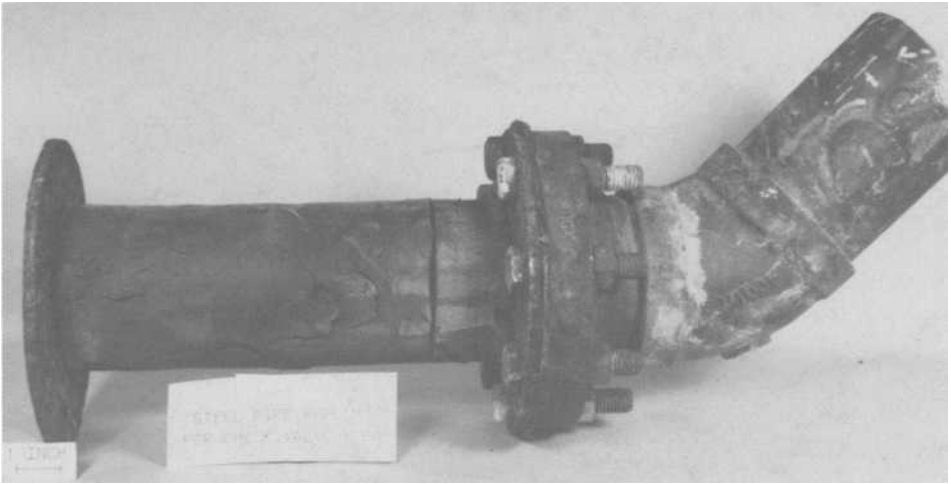


FIG. 1—Steel pipe replacement section attached to copper-nickel pipe.

in frequent usage. This aspect, and the value of coating these types of alloys when they see immersed service, is becoming more generally known and hopefully will be common practice in shipbuilding and ship maintenance in the next few years.

Hydraulic piping is sometimes routed through seawater tanks to operate hydraulic valves and other equipments. A coated 1020 carbon steel pipe with a wall thickness of 0.15 in. (3.8 mm), developed through pitting near the hydraulic valve after nine months of service. The damaged area is shown as Fig. 3. Analysis concluded that the adjacent Monel actuator rod had caused the



FIG. 2—Steel pipe replacement section attached to copper-nickel pipe after cleaning.

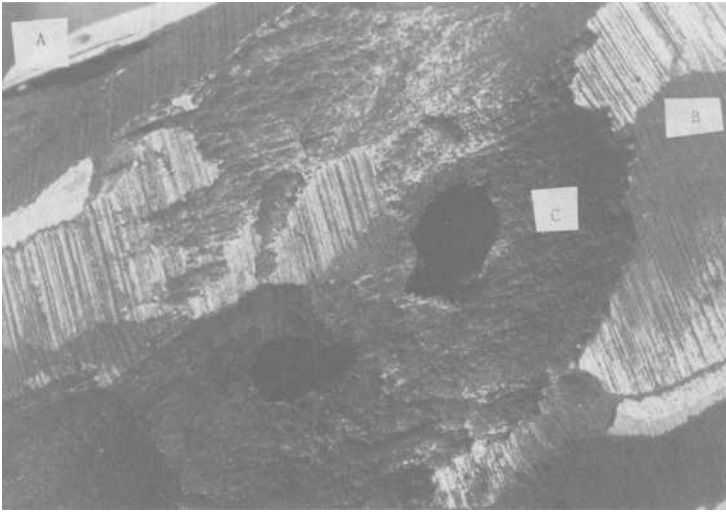


FIG. 3—Steel piping to Monel hydraulic actuator: (a) coating on outer diameter of the pipe, (b) grinding mark, and (c) corrosion and through wall pitting.

pitting at holidays in the coating of the pipe. All other parts of the actuator and its mounting were well-coated and in excellent condition. During system design, the galvanic effect of the bare actuator had apparently not been considered or thought significant, although careful preservation of all parts of the system had been accomplished, including painting of long piping runs in a ballast tank. The solution implemented was to change to copper-nickel piping.

The last example in this section on piping concerns a case of improper cleaning of copper nickel tubing during manufacturing of a heat exchanger. The problem surfaced with the appearance of voluminous corrosion products on the interior of the tubing and deep pitting after only a few months of seawater service. The most obvious possibilities (stray current, excessive velocity, and so forth) were examined and provided no explanations to account for observed facts. Unexposed material from the same manufacturing lot was requested and examined. Dark deposits were found and analyzed as carbon. The conclusion was that the tube drawing lubricant was not removed, and the carbon deposits galvanically stimulated the corrosion of the tubing in seawater service. For confirmation, a sample of the uncleaned tubing was exposed for 120 days in flowing natural seawater and exhibited similar attack.

Valves

Piping components such, as valves and pumps, need to be carefully selected to ensure their suitability for marine service in ships. Much equipment is manufactured, which will give many years of satisfactory service. There are, however, even within those equipments classified as "suitable for marine service" many instances of inappropriate materials with the resultant probability of galvanic corrosion.

Valve stems made of nickel aluminum bronze are sometimes used to operate valve balls made of either nickel-copper (Monel) or titanium. In either case the end of the stem corrodes at an accelerated rate because of its proximity to the more noble metal ball in the valve. Isolation is not practical and even though the ball may be coated with Teflon®, local action at the stem end will still occur, possibly aggravated by a crevice geometry. Valve parts are frequently identified as "bronze," but care must be taken that alloys actually used are accurately specified. One

recent example involved a valve found leaking in service, for which the drawing identified all materials as bronze. Chemical analysis showed that the corroded plug portion, shown in Fig. 4, was actually a brass with a composition of 62% copper—37% zinc, which was coupled to the bronze body of 85% copper—5% zinc—5% tin and was sacrificially corroding.

Parts with relative motion can corrode quite rapidly since the protective film that forms in copper base alloys will be continuously removed. An example of a check valve from a shipboard copper nickel piping system is shown in Fig. 5. The flapper disk is Monel and the flapper arm is copper-nickel. The combination of movement and galvanic corrosion caused the flapper arm to corrode completely away, releasing the flapper disk, which then jammed into the check valve exit slightly downstream. This in turn almost blocked the valve exit, causing extremely high flow around the wedged-in disk and subsequent erosion-corrosion, resulting in a massive leak in the check valve.

Galvanic corrosion can occur when the same material has different surface conditions. An example was found in a Monel gate valve. The seating surface of an old valve had been refinished and put back in service. Galvanic corrosion subsequently occurred in this region, since refinishing of these surfaces without removal of corrosion product films from the rest of the gate created a situation where the critical areas were made more anodic (fresh clean surface) than the rest of the gate (undisturbed corrosion films). Upon return to service, galvanic corrosion was concentrated on the critical seating surface.

Pumps

Pump seals, impellers, shafts, and so forth, in addition to galvanic compatibility must be designed to accommodate high flow rates and tight crevices. With the growing application of stainless steels and, more recently, titanium for long-life seawater pumps, galvanic corrosion within the pumps has been less of a problem. Materials selected for pumps for marine service tend to be galvanically compatible and corrosion is usually limited to flow-related and localized damage. Use of a pump with large quantities of noble metals can stimulate corrosion of adjacent piping, if suitable electrical isolation is not performed, however.

Heat Exchangers

Compatibility between water boxes, tube sheets, tubing, and shipboard piping is the galvanic corrosion concern for these components. With the extensive use of copper-nickel and bronze

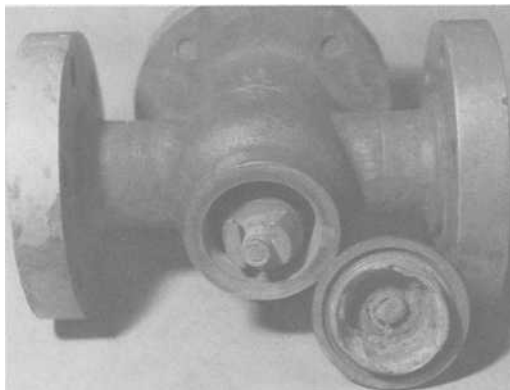


FIG. 4—Bronze valve body with brass plug.

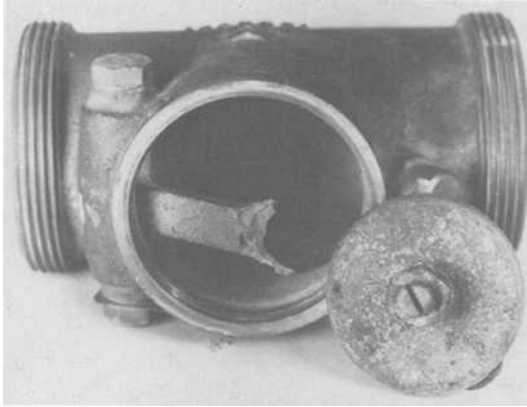


FIG. 5—Check valve with copper-nickel arm and a Monel flapper disk.

alloys for these components, galvanic corrosion has not been experienced to any significant degree. Flow related corrosion is the usual cause of shipboard failures. The future trend towards the use of stainless steel and titanium heat exchanger tubes can create galvanic corrosion problems on tube sheets, water boxes, and adjacent piping, unless proper electrical isolation or cathodic protection is utilized.

Marine Atmospheric Environments

Shipboard marine atmospheric environments will not cause as severe galvanic corrosion as immersion, since the time of wetness is limited, and even when wet, area ratios are limited by high resistivity of surface films. However, water entrapment can result in extensive galvanic attack at faying surfaces or other similar locations. This is prevalent on ship topsides with label plates and around fasteners and the items they join. Steel and aluminum are the most frequently seen dissimilar metals in this area and occasionally galvanic corrosion of aluminum results. Much of the topside corrosion is simply general corrosion of improperly coated steel or aluminum and is not galvanically stimulated.

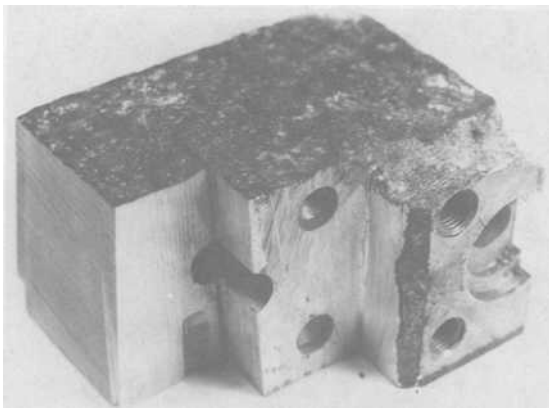


FIG. 6—Aluminum hydraulic valve subplate bolted to a steel frame.

One instance of engine room atmospheric galvanic corrosion is shown in Fig. 6 in which an aluminum alloy 2014 hydraulic control valve subplate has undergone corrosion up to $\frac{3}{4}$ in. (19 mm) deep in 10 years service. This subplate was bolted to a steel frame with "cotton duck" washers during assembly. These washers had absorbed moisture providing the necessary electrolyte for the galvanically accelerated corrosion of the aluminum. A similar situation, without a nonmetallic to entrap moisture, occurred on another aluminum hydraulic actuator, which had both steel and bronze components bolted to it. This unit was in an engine room where condensation had occurred to a sufficient degree to cause noticeable pitting on all dissimilar metal mating surfaces. While connection of aluminum and copper can never be recommended, coating the noble metal under and adjacent to the areas of contact is recommended for components in marine atmospheres when this connection is unavoidable. This problem has also been experienced in electrical equipment, where aluminum and copper alloys have been in contact. Special precautions are necessary for electronic equipment, and that subject has been dealt with elsewhere [6, 7].

Common Causes of Galvanic Corrosion

The problems cited earlier mainly involve the commonly used alloys in ship structural and piping applications. The list of metals normally considered suitable for ship applications is not very large. The overwhelming tonnage of metal used is steel, which when properly coated and cathodically protected gives many years of satisfactory service. Copper-base alloys are the next highest used alloy types with nickel and aluminum base alloys following. If galvanic problems occur with these alloys in systems other than specialized machinery or equipment, it is usually due to lack of attention to details or lack of application of good corrosion engineering practice. The lack of details includes careful attention to specifications and use of their latest revisions. These revisions may be alloy chemistry or heat treatment changes instituted to avoid a marine corrosion problem. Good corrosion engineering practices, dealt with extensively elsewhere [8, 9], include such things as alloy selection, isolation, coating noble metals to reduce surface area and application of cathodic protection. Many of the corrosion problems cited above resulted from ignoring one or more of the above practices.

Galvanic problems can also occur when machinery or equipment designed for use ashore is installed aboard ship. While again, galvanic corrosion will result from the two causes identified above (lack of attention to detail and violation of good corrosion engineering practices), in this instance, the equipment is being asked to perform a function for which it was not designed. This situation does occur, and sometimes problems can be reduced by careful installation and protection from the environment. An example of this was the use of fire sprinkler head, designed originally for freshwater, in a seawater fire system. Aluminum components in the valves, which would have performed adequately in freshwater service, failed in saltwater causing unexpected activation of the sprinkler.

A list of "do's" and "don'ts" may be a simplistic approach, but if applied at the correct time in the design/construction/installation/operation/maintenance cycle of shipbuilding would probably eliminate most of the galvanic corrosion problems.

DO

- Assume it will get wet.
- Use alloys whose marine performance is known.
- Consider cathodic protection.
- Completely isolate (for example, bushings on bolts).
- Coat noble metals.
- Provide drainage to remove standing water.

DO NOT

- Assume the environment is dry or constant.
- Think land-based designs work in water.
- Ignore specification details.
- Be casual regarding details.

Summary

A common cause of shipboard galvanic corrosion failures is improper design or selection of materials. In most cases, this should have been obvious and caught in the design stage; but in a few instances it is only apparent with hindsight. Another common factor is improper assumptions regarding the environment; usually that there will be no electrolyte when in fact, one does creep in. It is essential to increase the general awareness of maritime designers with education and emphasis on lessons learned.

References

- [1] *Corrosion and Corrosion Prevention—Metals*, Military Handbook 729, 21 Nov. 1983.
- [2] Dissimilar Metals, Mil-Std-889B, 21 Nov. 1979.
- [3] Morton, A. G. S., *Navy Corrosion Engineering Handbook*, David Taylor Research Center, Bethesda, MD, Nov. 1985.
- [4] Bleile, H. R. and Rodgers, S. D., *Shipboard Corrosion Engineering, 21st Annual Technical Symposium*, Association of Scientists and Engineers of the Naval Sea Systems Command, Department of the Navy, Washington, DC, 1984.
- [5] Efield, K. D., "Failure of Monel Ni-Cu-Al Alloy K-500 Bolts in Sea Water," *Materials Performance*, Vol. 24, No. 4, April 1985.
- [6] *Corrosion of Electrical Connectors*, MCIC Report 86-CI, Battelle Memorial Laboratory, Columbus, OH, 1986.
- [7] "Design Guidelines for Prevention and Control of Avionic Corrosion," Report NAVMAT P 4855-2, Department of the Navy, Washington, DC, June 1983.
- [8] Atkinson, J. T. N. and VanDroffelaar, H., *Corrosion and Its Control*, NACE, Houston, TX, 1982.
- [9] Pludek, V. R., *Design and Corrosion Control*, MacMillan Press, London, 1979.

Galvanic Corrosion in Power Plant Condensers

REFERENCE: Gehring, G. A., Jr., "Galvanic Corrosion in Power Plant Condensers," *Galvanic Corrosion, ASTM STP 978*, H. P. Hack, Ed., American Society for Testing and Materials, Philadelphia, 1988, pp. 301-309.

ABSTRACT: The use of dissimilar metal construction in power plant condensers is a common practice. It is not unusual to encounter condensers fabricated with stainless steel or titanium tubes, copper alloy tubesheets, and cast iron or carbon steel waterboxes. Furthermore, condensers initially furnished with copper alloy tubes and copper alloy tubesheets are frequently being retubed with stainless steel or titanium tubes. In several instances, the use of dissimilar alloys in power plant condensers has led to severe galvanic corrosion, particularly of the tubesheet.

The primary factors affecting galvanic corrosion in a condenser include the electrochemical characteristics (that is, potential and polarization) of the different alloys, the effective area relationships of the different alloys, and the specific characteristics of the cooling water (for example, conductivity, temperature, and so forth). A number of studies have been conducted to develop a better understanding of the relative influence and the interrelationship of these various factors. These studies, conducted under simulated condenser flow conditions, have shown that (1) the length of tube involved in a tubesheet/tube galvanic cell can extend beyond 6 m down the tube, depending on the tube alloy and water salinity; (2) the use of either titanium or stainless steel tubes with a copper alloy tubesheet can result in significant galvanic corrosion of the tubesheet; (3) galvanically coupling a Muntz metal tubesheet to either stainless steel or titanium can cause severe dezincification of the tubesheet; (4) the intensity of galvanic attack will tend to diminish as the salinity of the cooling water decreases; (5) the intensity of the galvanic attack will tend to diminish as the cooling water temperature decreases; (6) certain copper alloy tubesheets may be galvanically compatible with either stainless steel or titanium tubes if the cooling water salinity or temperature is sufficiently low; (7) as a tubesheet alloy coupled to either stainless steel or titanium tubes, aluminum bronze (Alloy D) is significantly less susceptible to galvanic attack than Muntz metal; (8) cathodic protection properly implemented can effectively mitigate galvanic attack of copper alloy tubesheets caused by more noble alloy tubes, and (9) the cathodic protection current required to mitigate galvanic corrosion will be greater in higher salinity, higher temperature cooling water.

KEY WORDS: steam condensers, galvanic corrosion, simulated testing, copper alloy tubesheets, stainless steel tubes, titanium tubes, cathodic protection

Until the late 1970s, copper alloy tubes were traditionally used in the steam surface condensers of coastal power plants. However, with increasing appreciation of the catastrophic consequences that condenser tube leaks could have on other components of their power generation systems, electric utilities began to retube with more corrosion resistant alloys such as the newer, more highly alloyed stainless steels or titanium. In several instances, after retubing with stainless steel or titanium, electric utilities experienced rapid and severe galvanic corrosion of their copper alloy tubesheets, usually either Muntz metal or aluminum bronze (Fig. 1). These incidents triggered several studies [1-4], conducted under simulated condenser flow conditions, which sought to develop a better understanding of the relative influence and interrelationship of

¹President, Ocean City Research Corporation, Tennessee Ave. and Beach Thorofare, Ocean City, NJ 08226.

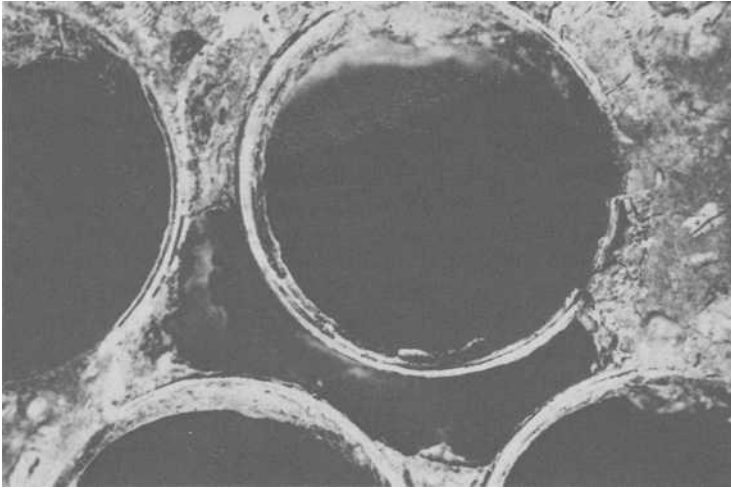


FIG. 1—Galvanic corrosion of Muntz metal tubesheet one year after retubing with AL-6X stainless steel tubes.

the important factors affecting galvanic corrosion in a condenser. This paper describes a simulated condenser setup used to investigate galvanic corrosion of condenser tubesheets and summarizes the more important results of studies using the apparatus.

Experimental Approach

Tubesheet and Tube Materials

Much of the experimental work focused on galvanic corrosion associated with the tubesheet/tube combinations is shown in Table 1.

The AL-6X alloy a 20% chromium, 24% nickel, 6% molybdenum, austenitic stainless steel developed by Allegheny Ludlum Steel Corporation primarily for use as a condenser tube alloy in high salinity (seawater) cooling water. Ti-50A is commercially pure titanium tubing supplied by TIMET Corporation. Muntz metal (60 Cu-40 Zn) and aluminum bronze (Alloy D, 91 Cu-7 Al-2 Fe) are widely used tubesheet alloys.

Test Apparatus

To simulate the physical configuration between tubesheet and tube, circular collars (approximately 3.6 cm outside diameter [OD]) were fabricated from the selected tubesheet alloys and fitted on the ends of the condenser tubes. The tubesheet alloy collars were insulated from the tubes by the use of polyolefin “shrink-fit” sleeves. An electrical lead wire was soldered to the

TABLE 1—*Tubesheet/tube combinations.*

Tubesheet	Tube
Aluminum bronze (Alloy D)	titanium (Ti-50A), AL-6X stainless steel
Muntz metal	titanium (Ti-50A), AL-6X stainless steel

collar to provide a means of completing the galvanic circuit to the tube as described below. After installation on the tube ends, the tubesheet collars were masked with epoxy so only the end faces were exposed to the seawater. The exposed tubesheet surface area for each tube was approximately 6 cm^2 . This represents the approximate tubesheet area per tube in most operating steam surface condensers. Figure 2 shows the arrangement.

To simulate waterbox conditions, the tube ends were terminated in 15.2-cm (6-in) diameter polyvinyl chloride (PVC) header pipes. The electrical lead wires, which had been soldered onto the tubesheet collars, were terminated outside the header pipe. This arrangement enabled the galvanic circuit to be completed outside of the header pipe, also permitting in-situ measurement of the galvanic current with a "zero-resistance" ammeter inserted between the tube and the tubesheet collar.

As part of the initial study, tests were conducted using a segmented condenser tube to determine the effective length of tube involved in a tubesheet/tube galvanic cell. Figure 3 shows the arrangement. Different lengths of tubing were coupled together with nylon connectors to form a single 12.2-m (40-ft) length of tube. The tube was made electrically continuous by shorting out the nylon tube connectors with external jumper leads. The distribution of galvanic current from the inlet end was determined by measuring the current flow across each of the nylon connectors with a zero resistance ammeter inserted in place of the jumper leads. The results of this initial work (to be discussed more in-depth later) suggested that the length of tube involved in a tubesheet/tube galvanic cell can extend significantly beyond 6 m for titanium or stainless steel tubing. As a result, subsequent studies were carried out using 12.2-m (40-ft) long tubes.

Figure 4 shows the general arrangement of a typical test unit. The test units consisted of parallel condenser tubes with tubesheet/tube joints simulated at the tube ends. Flow through each tube was regulated individually at a rate of $2.1 \pm 0.3 \text{ m/s}$ ($7 \pm 1 \text{ ft/s}$). Flow through the test units was either once-through or partially recirculated depending on the test. For those tests using recirculated water, the make-up rate was maintained sufficiently high to avoid stagnation or concentration effects.

For some tests, cathodic protection was applied at different levels at both inlet and outlet ends. Cathodic protection was achieved using a standard impressed current cathodic protection rectifier and platinized titanium anodes mounted in the wall of the PVC header pipes. Cathodic

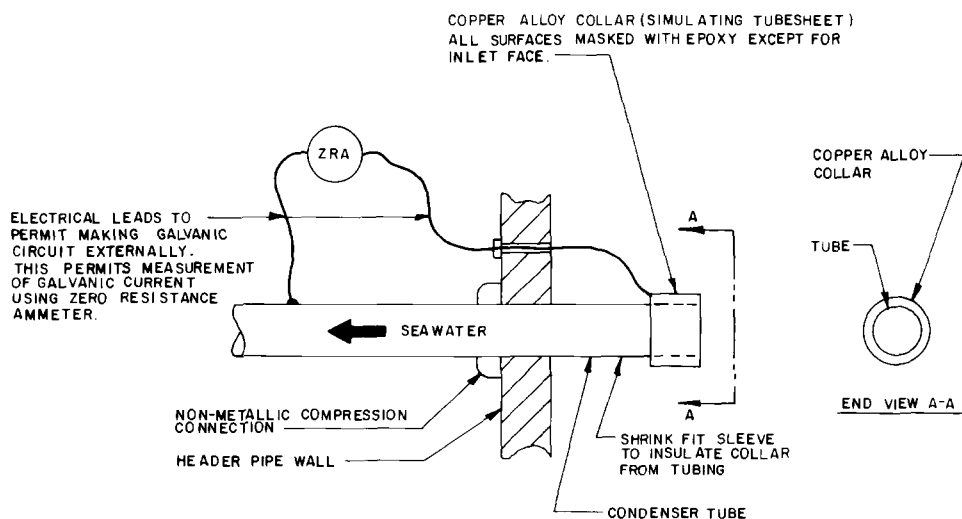


FIG. 2—Arrangement for simulating galvanic cell between tubesheet and condenser tube.

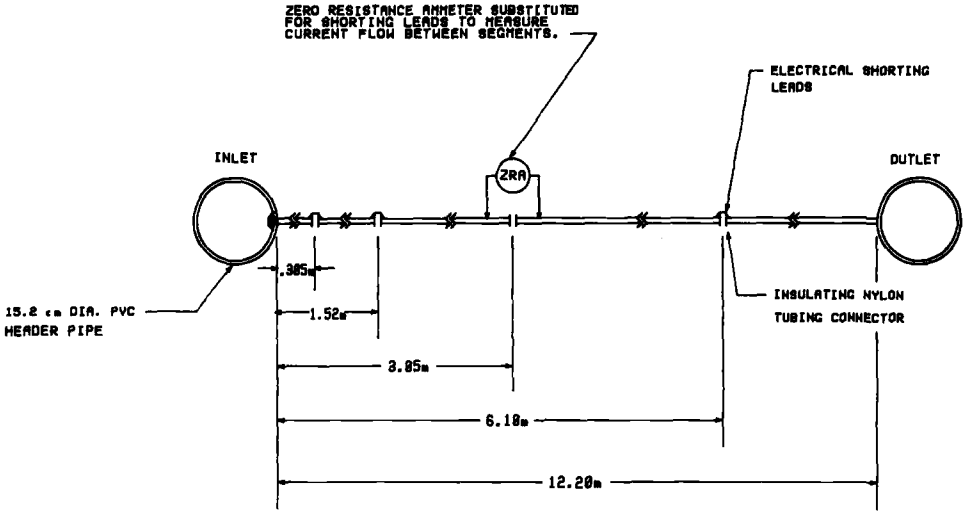
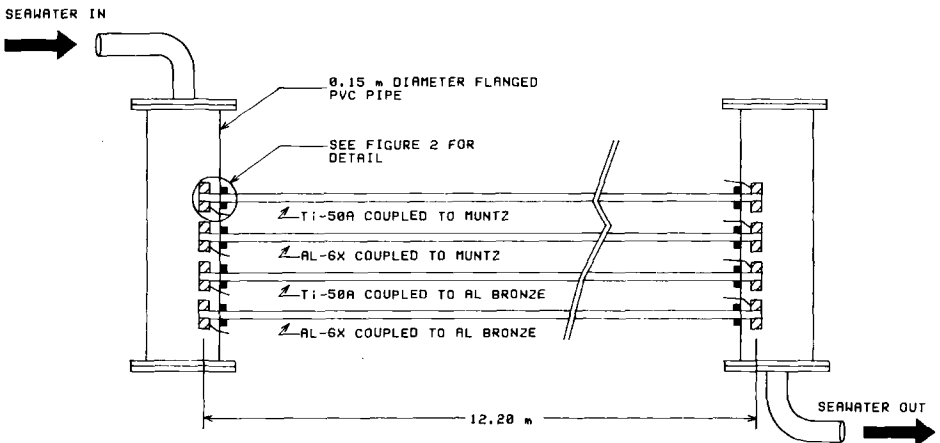


FIG. 3—Segmented tube setup for determining galvanic current distribution.

protection to the tubesheet/tube ends was maintained in a quasi-constant potential mode; that is, the cathodic protection current to the individual tubesheet/tube couples was periodically adjusted to maintain a predesignated potential as measured by a reference electrode mounted in the header pipe wall. An electrical control circuit was designed that permitted individual control and measurement of the current to each tube end.

Test Conditions

Tests were conducted to investigate the influence of cooling water salinity and cooling water temperatures on galvanic corrosion and the cathodic protection requirements for controlling



NOTE: ACCESS PORTS FOR COUNTER & REFERENCE ELECTRODES WERE LOCATED AROUND THE SURFACE OF THE HEADER PIPE.

FIG. 4—General arrangement of test unit.

galvanic corrosion. To investigate the effects of water salinity, full-strength seawater (salinity approximately 32 000 g/m³) was pumped through one test unit while brackish water (seawater diluted with freshwater to an average salinity of approximately 14 000 g/m³) was pumped through an identical test unit over a two-month period.

To investigate the effects of water temperature, duplicate tests were conducted over two two-month periods: a two-month period during the summer when the seawater temperature averaged 20°C and during the winter when the seawater temperature averaged 6°C.

Data Acquisition

All tubesheet alloy collars were weighed before assembly and exposure, using a balance accurate to ± 1 mg. After completion of the tests, the alloy collars were disassembled, descaled in 15% hydrochloric acid, rinsed, and reweighed to determine corrosion rates.

Pit depth measurements were also made on the tubesheet collars. The pit depth measurements were made using a depth micrometer or when greater sensitivity was required, by using an optical microscope with a calibrated focusing knob. Also, where appropriate, collars were cross-sectioned and examined under a metallurgical microscope for dealloying.

Throughout each test, the galvanic current flowing in each of the tubesheet/tube couples and the mixed potential of each were measured periodically using a zero-resistance ammeter and a saturated calomel reference electrode, respectively.

Throughout each test, seawater hydrology data were compiled daily including salinity, pH, dissolved oxygen, temperature, and turbidity.

Results and Discussion

Effective Tube Length Involved in Tubesheet/Tube Galvanic Cell

Figures 5 and 6 show the distribution of tubesheet/tube galvanic current along the condenser tube for selected couples in seawater and brackish water. In seawater, approximately 30 to 40% of the galvanic current flowed beyond 3 m from the inlet end. In brackish water, approximately 10 to 20% of the galvanic current flowed beyond 3 m. Thus, reducing the salinity of the water dramatically reduced current "throwing power" down the tube. These results agree with previous work by Gehring et al. [1] who demonstrated the effective length of tube involved in a tubesheet/tube galvanic cell could extend quite far depending on the tube alloy and cooling water salinity.

Effect of Cooling Water Salinity

Table 2 compares galvanic corrosion rates determined under seawater versus brackish water conditions. The corrosion rates were determined by weight loss measurements after two months of testing. The data demonstrate that the intensity of galvanic attack will tend to diminish as the salinity of the cooling water decreases. The electrical conductivity of the cooling water decreases with decreasing salinity. The decrease in electrical conductivity of the cooling water increases the resistance of the electrolyte path along the tube, reduces the effective length of the tube involved in the galvanic cell (changing the anode to cathode area ratio), and reduces the intensity of galvanic corrosion.

The data also show the severity of galvanic attack that might be encountered with certain alloy combinations. In seawater, Muntz metal coupled to titanium corroded at approximately 9 mm/year at the inlet end. Given the typical criteria of a 40-year service life, a corrosion rate of 9 mm/year would be unacceptably high for a 25-mm (nominal) thick tubesheet.

From a corrosion penetration standpoint, some of the data in Table 2 are deceiving. The corrosion rates in Table 2 were calculated by converting weight loss to a penetration rate assum-

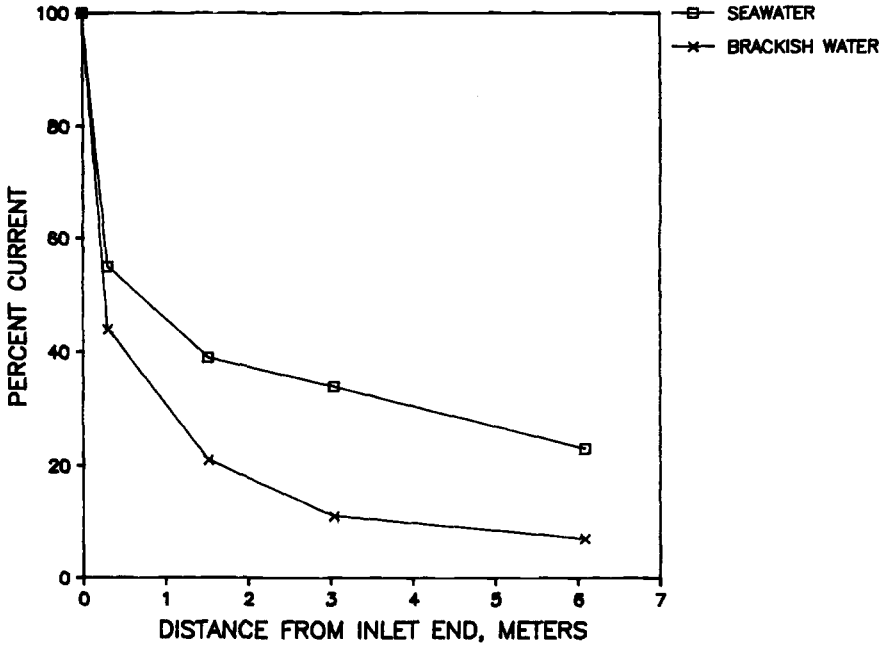


FIG. 5—Percent current distribution versus tube length for AL-6X (Muntz/AL-6X couple).

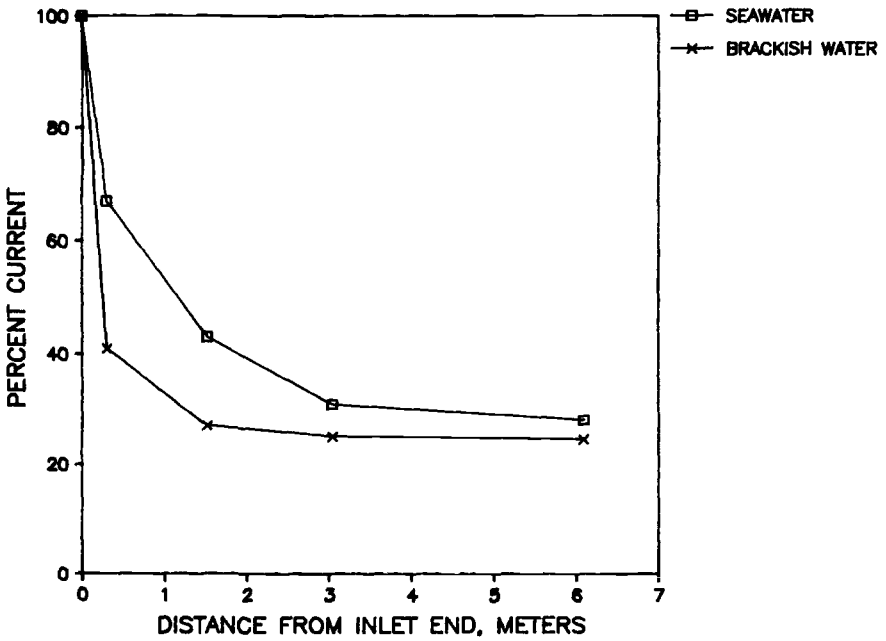


FIG. 6—Percent current distribution versus tube length for titanium (Muntz/Ti couple).

TABLE 2—*Tubesheet galvanic corrosion rates.*

Tubesheet/Tube Couple	Tube End	Galvanic Corrosion Rates, mm/year	
		Seawater	Brackish Water
Al bronze/AL-6X	inlet	0.633	0.117
Al bronze/AL-6X	outlet	0.634	0.150
Al bronze/Ti	inlet	1.86	0.201
Al bronze/Ti	outlet	3.03	0.373
Muntz/AL-6X	inlet	3.97	1.62
Muntz/AL-6X	outlet	3.79	0.979
Muntz/Ti	inlet	9.17	2.25
Muntz/Ti	outlet	6.32	0.825

ing uniform penetration over the surface. However, inspection of the collars showed that in several cases, corrosion penetration was far from uniform and that deep pitting had occurred. Also, the Muntz metal collars exhibited varying degrees of dezincification. Taking into account pitting and dezincification, the maximum penetration rates exhibited by Muntz metal and aluminum bronze were 26 and 7.4 mm/year, respectively. These rates were measured in seawater at the inlet end coupled to titanium tubes. Furthermore, the data indicate that Muntz metal coupled to titanium tubes will corrode at between 10 to 25 mm/year when pitting and dezincification are considered.

Effect of Cooling Water Temperature

Table 3 compares galvanic corrosion rates determined in seawater under warm water and cold water conditions. The rates were determined by weight loss measurements after two months testing. For every couple, the galvanic corrosion rate was significantly higher under warm water conditions.

Tubesheet Material Comparison

As a tubesheet alloy coupled to either titanium or AL-6X stainless steel tubes, aluminum bronze (alloy D) appears to be galvanically more compatible than Muntz metal. The data in Tables 2 and 3 show that the aluminum bronze alloy consistently exhibits a lower corrosion rate

 TABLE 3—*Tubesheet galvanic corrosion rates in warm versus cold seawater.*

Tubesheet/Tube Couple	Tube End	Galvanic Corrosion Rates, mm/year	
		Warm Seawater ^a	Cold Seawater ^b
Al bronze/AL-6X	inlet	0.633	0.048
Al bronze/AL-6X	outlet	0.634	0.087
Al bronze/Ti	inlet	1.86	0.059
Al bronze/Ti	outlet	3.03	0.049
Muntz/AL-6X	inlet	3.97	0.700
Muntz/AL-6X	outlet	3.79	0.356
Muntz/Ti	inlet	9.17	0.758
Muntz/Ti	outlet	6.32	0.363

^a Average water temperature of 22°C over a two-month period.

^b Average water temperature of 6°C over a two-month period.

than Muntz metal when coupled to the same tubing material and exposed to similar water conditions. In fact, the data in cold seawater and in brackish water suggest that aluminum bronze could be used with either titanium or AL-6X tubes without requiring supplementary corrosion control measures. The maximum corrosion rate observed under these conditions was 0.38 mm/year. Thus, aluminum bronze (Alloy D) may be galvanically compatible as a tubesheet material in a surface condenser tubed with either stainless steel or titanium depending on cooling water salinity and temperature.

Cathodic Protection Requirements

Protection potential requirements were determined by applying cathodic current and simultaneously measuring galvanic current flow in the tubesheet/tube cell. The cathodic current was increased in incremental steps until the measured galvanic current was reduced to zero. The potential of the tubesheet/tube cell at this point was then recorded. The protection potential was arbitrarily specified to be 50 mV more active than the potential at which galvanic current was reduced to zero. Using this criterion, the protection potentials versus a saturated calomel reference electrode ranged between -0.300 and 0.450 V. The current required to maintain a given protection potential decreased with decreasing water salinity and temperature, consistent with the observation that galvanic corrosion rates will also decrease with decreasing water salinity and temperature. The protective current requirements ranged between 0.28 and 3.8 mA per tube depending on water salinity, temperature, and tubesheet/tube combination.

Table 4 shows galvanic corrosion rates for aluminum bronze/titanium and Muntz metal/titanium couples that were cathodically polarized to -0.46 V (standard calomel electrode [SCE]). The corrosion rates in Table 4 represent the average for inlet and outlet ends. Comparison of these data with data in Table 3 shows that the galvanic corrosion rates were greatly reduced by cathodic polarization to -0.46 V. The only exception was the aluminum bronze/titanium couple in cold seawater, where the aluminum bronze exhibited a slightly higher corrosion rate under cathodic protection conditions. However, considering the relatively small magnitude (on the order of 0.02 mm/year), this difference may be indicative of the variation inherent in the experimental approach.

As noted earlier in this paper, the effective rate of Muntz metal corrosion penetration increased significantly when dezincification was considered. Cathodic protection at the level tested totally eliminated dezincification of the Muntz metal. Thus, considering dealloying damage, cathodic protection can effect a marked reduction in Muntz metal tubesheet penetration rates.

Summary and Conclusions

The simulated condenser flow tests demonstrated that the length of tube involved in a tubesheet/tube galvanic cell can extend beyond 6 m (20 ft) down the tube, depending on tube

TABLE 4—*Tubesheet corrosion rates when cathodically polarized to -0.46 V.^a*

Tubesheet/Tube	Corrosion Rate, mm/year	
	Warm Seawater	Cold Seawater
Aluminum bronze/titanium	0.120	0.071
Muntz/titanium	0.292	0.194

^a Average for inlet and outlet ends.

alloy and water salinity. The use of either titanium or stainless steel tubes with a copper alloy tubesheet can result in accelerated corrosion penetration of the tubesheet. The intensity of the galvanic attack will tend to diminish as cooling water salinity and temperature decreases. If cooling water salinity or temperature is sufficiently low, the copper alloy tubesheets may be galvanically compatible with stainless steel or titanium tubes. Finally, cathodic protection can effectively mitigate galvanic attack of copper alloy tubesheets. The cathodic protection current requirements will tend to increase with increases in cooling water temperature and salinity.

Acknowledgments

The author gratefully acknowledges the Electric Power Research Institute and the Public Service Electric and Gas Company of New Jersey for their financial support of the various studies that provided data for this paper.

References

- [1] Gehring, G. A., Kuester, C. K., and Maurer, J. R., "Effective Tube Length—A Consideration On The Galvanic Corrosion Of Marine Heat Exchanger Materials," *NACE Corrosion/80*, Paper 32, Chicago, IL, March 1980.
- [2] Gehring, G. A. and Maurer, J. R., "Galvanic Corrosion of Selected Tubesheet/Tube Couples Under Simulated Seawater Condenser Conditions," *NACE Corrosion/81*, Paper 202, Toronto, Ontario, Canada, April 1981.
- [3] Gehring, G. A. and Kyle, R. J., "Galvanic Corrosion in Steam Surface Condensers Tubed with Either Stainless Steel or Titanium," *NACE Corrosion/82*, Paper 60, Houston, TX, March 1982.
- [4] Gehring, G. A., Foster, R. L., and Syrett, B. C., "Effect of Sulfide on the Corrosion and Protection of Seawater-Cooled Condenser Alloys," *NACE Corrosion/83*, Paper 76, Anaheim, CA, April 1983.

Lawrence S. Redmerski,¹ John J. Eckenrod,¹ Kenneth E. Pinnow,¹
and Curtis W. Kovach²

Experience with Cathodic Protection of Power Plant Condensers Operating with High Performance Ferritic Stainless Steel Tubing

REFERENCE: Redmerski, L. S., Eckenrod, J. J., Pinnow, K. E., and Kovach, C. W., "Experience with Cathodic Protection of Power Plant Condensers Operating with High Performance Ferritic Stainless Steel Tubing," *Galvanic Corrosion, ASTM STP 978*, H. P. Hack, Ed., American Society for Testing and Materials, Philadelphia, 1988, pp. 310-322.

ABSTRACT: Galvanic corrosion is an important consideration in brackish or seawater cooled power plant condensers containing dissimilar metal components. Cathodic protection is often used to minimize galvanic corrosion, but under certain conditions of operation, many condenser components, including high performance ferritic stainless steel tubing, can become susceptible to hydrogen embrittlement. Results of laboratory experiments indicate that conditions can be defined for the operation of a cathodic protection system, which will minimize corrosion of dissimilar, less noble, tubesheet, and waterbox materials and avoid embrittlement of high performance ferritic stainless steel tubing. These conditions are similar to those now recommended for use with condensers operating with titanium tubing. Several power plant condensers using SEA-CURE® (Unified Numbering System [UNS] S44660) ferritic stainless steel tubing are now successfully operating with impressed current cathodic protection systems, and no difficulties with hydrogen damage to the tubing have been encountered.

KEY WORDS: cathodic protection, galvanic corrosion, impressed current, power plant condensers, high performance ferritic stainless steels, SEA-CURE® (UNS S44660) condenser tubing, hydrogen damage, crevice corrosion, dissimilar metal components

In recent years, high performance stainless steels have been developed that offer the corrosion engineer many new opportunities to resolve corrosion problems. Most of these stainless steels are highly alloyed with chromium and molybdenum to resist the chlorides in cooling water, and there is no doubt that they have superior resistance to localized and general corrosion when compared to stainless grades such as Types 304 (Unified Numbering System [UNS] S30400) and 316 (UNS S31600). This is well documented in several recent papers on high performance stainless steels, which also provide a good summary of the grades available and their typical properties [1-5]. SEA-CURE® (UNS S44660) ferritic stainless steel is one of the new high performance stainless steels and has proven to have excellent crevice corrosion resistance in the unwelded and welded conditions in waters containing high chloride concentrations [6-8].

One of the major applications for the high performance ferritic stainless steels has been in fresh, brackish, and seawater-cooled power plant condensers. In many instances, UNS S44660 tubes are used as replacements in condensers having dissimilar metal tube sheets and waterboxes, which introduces the possibility of galvanic action. Galvanic compatibility, or incompat-

¹Staff metallurgist, supervisor, and technical director, respectively, Crucible Materials Corporation, Crucible Research, P.O. Box 88, Pittsburgh, PA 15230.

²Consultant, Crucible Materials Corporation, Trent Tube Division, East Troy, WI.

ibility, depends upon the corrosion potential difference between the dissimilar metals, but more importantly on the corrosion current that flows between the metals, relative to their surface areas [9,10]. The polarization characteristics of the metals and the resistance of the metallic and electrolyte paths thus have a significant effect on the galvanic action. Some of the possible options to control or minimize galvanic action are to apply protective coatings, install a cathodic protection system, or a combination of both. In new condensers, stainless steel tubesheets compatible with UNS S44660 can be used. However, protection of the carbon steel (UNS G10110) or cast iron (UNS F10001) waterbox is still required.

Insulative coatings for tubes and tubesheets and zinc-rich coatings for the waterbox have been used with limited success [11]. However, cathodic protection has become the most widely used system of corrosion control in power plant condensers today, and impressed current systems rather than sacrificial anodes are most often used. While an impressed current system may adequately protect waterboxes and tubesheets from corrosion, attention must be given to other factors that can have a detrimental effect on the ductility of the components because of hydrogen generation. In this respect, there have been cases of ferritic stainless steel tube breakage caused by hydrogen introduced into the tubes by the cathodic protection system [12,13]. Titanium tubes (UNS R50250) have also been affected by hydrogen introduced by the cathodic protection system [14]. However, with the modern control now available, cathodic protection is being used successfully to provide corrosion protection without detrimental effects. This paper provides laboratory and field test data on galvanic relationships between UNS S44660 high performance ferritic stainless steel and various other materials used in condenser construction and summarizes current field experience indicating that cathodic protection can be used to mitigate galvanic corrosion without causing hydrogen damage to high performance ferritic stainless steel tubing.

Laboratory Investigations

Corrosion Potentials

For successful operation of a cathodic protection system, the operating potentials must be chosen such that they will reduce corrosion of the condenser components to an acceptable level without causing hydrogen damage. Thus, a knowledge of the single and mixed electrochemical potentials of the components is needed for design considerations. For this purpose, the single and mixed potentials of UNS S44660 and of several other alloys used in condenser construction were measured in the laboratory in aerated waters of different chloride contents at temperatures of 45 and 90°C (114 and 194°F). The various chloride contents were achieved by mixing distilled water with measured amounts of substitute sea salt (ASTM Specification for Substitute Ocean Water [D 1141]). The potential measurements were made using a potentiostat and a saturated calomel electrode (SCE) as a reference. To allow for polarization effects, the single metal and mixed couple potentials were determined after allowing the specimens to rest in the test solutions for 3 and 16 h, respectively. The chemical compositions of the alloys used in these measurements are given in Table 1.

The results of the potential measurements are given in Table 2 and show that the corrosion potential of UNS S44660 in water containing 18 000-ppm chloride is about -0.250 V (SCE) and similar to that of the alloy in natural seawater. As the chloride content of the water becomes lower, the electrode potential of UNS S44660 becomes somewhat less electronegative. The potentials of UNS S44660 in these test environments are similar to those measured for the other highly alloyed stainless steels given in Table 2 suggesting that there would be minimal current flow between these materials when coupled to each other. However, the potential of UNS S44660 is considerably more electropositive than the copper alloy tubesheet materials (-0.325 V), and the cast iron (-0.680 volts) or carbon steel (-0.750 V) waterbox materials. Thus, the

TABLE 1—Nominal compositions of the alloys used in the laboratory studies.

Alloy	UNS Number	Weight Percent									
		C	Ni	Cr	Mo	Cu	N	Ti	Fe	Other	
Type 410	S41000	0.12	...	12.0	Bal	...	
Type 304L	S30403	0.03	9.0	18.0	Bal	...	
Type 316L	S31603	0.03	12.0	17.0	2.5	Bal	...	
Type 317L	S31703	0.03	13.0	18.0	3.5	Bal	...	
Alloy 825	N08825	0.05	42.0	20.0	3.0	2.0	...	0.8	Bal	...	
Alloy 904L	N08904	0.02	25.0	20.0	4.0	1.0	Bal	...	
AL-6XN ^a	N08367	0.03	24.0	21.0	6.5	...	0.20	...	Bal	...	
254SMO ^b	S31254	0.02	18.0	20.0	6.0	0.75	0.20	...	Bal	...	
AL 29-4C ^a	S44735	0.02	...	28.0	4.0	...	0.20	0.4	Bal	...	
SEA-CURE ^c	S44660	0.02	2.0	27.0	3.5	...	0.20	0.4	Bal	...	
Carbon steel	G10110	0.10	Bal	...	
Cast iron	F10001	3.50	Bal	...	
90Cu-10Ni	C70600	...	10.0	90.0	Al-6.8	
AL-bronze	C61900	Bal	2.0	Zn-39.5	
Muntz	C28000	60.0	Pb-0.5	
Titanium	R50250	0.10	0.03	Bal	0.20	0-0.18	

^aTrademark of Allegheny Ludlum Steel Corporation.

^bTrademark of Avesta AB.

^cTrademark of Trent Tube Division, Crucible Materials Corporation.

TABLE 2—Corrosion potentials for various metals and alloys after three-hour exposure in aerated pH-7 waters.

Alloy	Corrosion Potential, Volts Versus SCE			
	45°C (114°F)	45°C (114°F)	45°C (114°F)	90°C (194°F)
	Substitute Seawater 18 000 ppm Cl	Water 500-ppm Cl	Water ~ 20 ppm Cl	Water 500 ppm Cl
Carbon steel	-0.750	...	-0.732	-0.749
Cast iron	-0.680	...	-0.735	...
90Cu-10Ni	-0.336	...	-0.092	...
Al-bronze	-0.330
Muntz metal	-0.315	-0.181	-0.098	...
Type 410	...	-0.174	...	-0.176
Type 304L	...	-0.133	-0.130	...
Type 316L	-0.278	-0.137	-0.070	-0.179
Type 317L	-0.235	-0.174	...	-0.197
Alloy 825	-0.250
Alloy 904L	-0.258	-0.135	...	-0.180
AL-6XN®	...	-0.157	-0.107	-0.201
254SMO	...	-0.166
AL 29-4C	...	-0.188	...	-0.214
SEA-CURE®	-0.250	-0.178	-0.095	-0.200
Titanium	-0.100
SEA-CURE®/ carbon steel ^a	-0.700
SEA-CURE® Muntz metal ^a	-0.290

^aCouples, 16-h test. 10 to 1 cathode to anode area ratio.

alloy is cathodic when coupled with copper alloys, cast iron, and carbon steel, and anodic currents on these tubesheet and waterbox materials would be expected. In the mixed couples between UNS S44660 and carbon steel or Muntz (UNS C28000) metal, the corrosion potentials of the mixed couples are close to the freely corroding potential of the anodic component of the couple. Thus, in theory and according to the results given in Table 2, an applied potential more electronegative than -0.750 V is needed to cathodically protect a carbon steel waterbox. This potential would also cathodically protect a Muntz metal tubesheet, which had a corrosion potential of -0.315 V in this investigation.

Corrosion Currents

Measurements of the current flow as well as of the mixed potentials developed between different materials can also provide information useful for the design or operation of an impressed current cathodic protection system. They serve to confirm predictions of galvanic corrosion based on differences in corrosion potential and reflect differences caused by polarization and differences in surface area. Measurements were therefore made in the laboratory of the current flow developed between UNS S44660 and several of the alloys listed in Table 1 in aerated water containing 500- and 18 000-ppm chloride using anode to cathode ratios of 10 to 1, 1 to 1, and 1 to 10. Also, measurements were made of the corrosion currents developed between UNS S44660 and various tubesheet materials in flowing substitute and natural seawater at 25 or 50°C (77 or 122°F).

The currents developed between UNS S44660 and Type 316, Type 317L (UNS S31703), and most of the other stainless steels listed in Table 2 were found to be extremely low at 45°C

(113°F) and difficult to measure accurately. Significant currents were measured for the couples made with Type 410 (UNS S41000) stainless steel, which because of its low alloy content is not normally used in highly corrosive environments. As expected, the corrosion currents measured for the couples made with carbon steel and cast iron were high and greater than those for any other couples measured.

The results of the current measurements made in flowing substitute and natural seawater are given in Table 3. In general, they show that the galvanic currents tend to increase as the difference in corrosion potential between UNS S44660 and a given alloy becomes greater. The currents are very high in the couples with steel. They are lower with Muntz metal and still lower with aluminum bronze (UNS C61900), but probably not low enough to eliminate the need for galvanic protection. The very low currents in the couple with Type 316 stainless steel indicates that galvanic protection may not be required when using a Type 316 tubesheet. However, factors other than galvanic compatibility, such as crevice corrosion resistance, must be considered in the selection of a tubesheet material. In this regard, there has been an instance where a Type 316 tubesheet has not performed well when used in combination with high performance ferritic stainless steel tubing [15].

Hydrogen Embrittlement

The use of cathodic protection can, depending upon the potential used, introduce hydrogen into the system, which may be detrimental to some components of that system [16,17]. The degree to which cathodic protection can be damaging is a function of the cathode potential and the environment, which control hydrogen concentration at the cathode surface, and the propensity of the metal (cathode) to absorb and be damaged by hydrogen. Susceptibility of a metal to hydrogen embrittlement can be evaluated by measuring the loss of bend ductility under a given set of hydrogen charging conditions. Laboratory hydrogen charging tests were conducted on annealed 0.071-mm (0.028-in.) thick strip of UNS S44660. Specimens approximately 15.2 cm (6 in.) long by 2.54 cm (1 in.) wide were potentiostatically charged in aerated 45°C (114°F) substitute seawater (pH 8) at various potentials, and the time required to produce failure as measured by loss in bend ductility was determined. The bend tests were made manually using a three-point bend test apparatus, and the radius of the mandrel was approximately 3.2 mm (0.125 in.). The results presented in Fig. 1 show that UNS S44660 stainless steel can be exposed at potentials more electropositive than about -0.800 V for at least 100 h without encountering

TABLE 3—Galvanic anode corrosion rates for various condenser tube-tubesheet metal couples. Corrosion rates are based on current measurements with 10:1 cathode:anode area ratio.

Couple		Inches Per Year			
		Substitute Seawater Velocity < 1 ft/s 25°C (77°F)			Natural Seawater Velocity 7 ft/s 50°C (122°F)
Cathode	Anode	1 Week	3 Weeks	5 Weeks	4 Weeks
SEA-CURE®	Carbon Steel	0.4088
SEA-CURE®	90-10 CuNi	0.0063
SEA-CURE®	Type 316	0.0002	0.0002	0.0002	...
SEA-CURE®	Muntz	0.0043	0.0039	0.0040	0.0160
Titanium	Muntz	0.0030	0.0018	0.0042	0.0160
SEA-CURE®	Al-Bronze	0.0040	0.0015	0.0007	< 0.0004
Titanium	Al-Bronze	...	0.0011	0.0018	< 0.0004

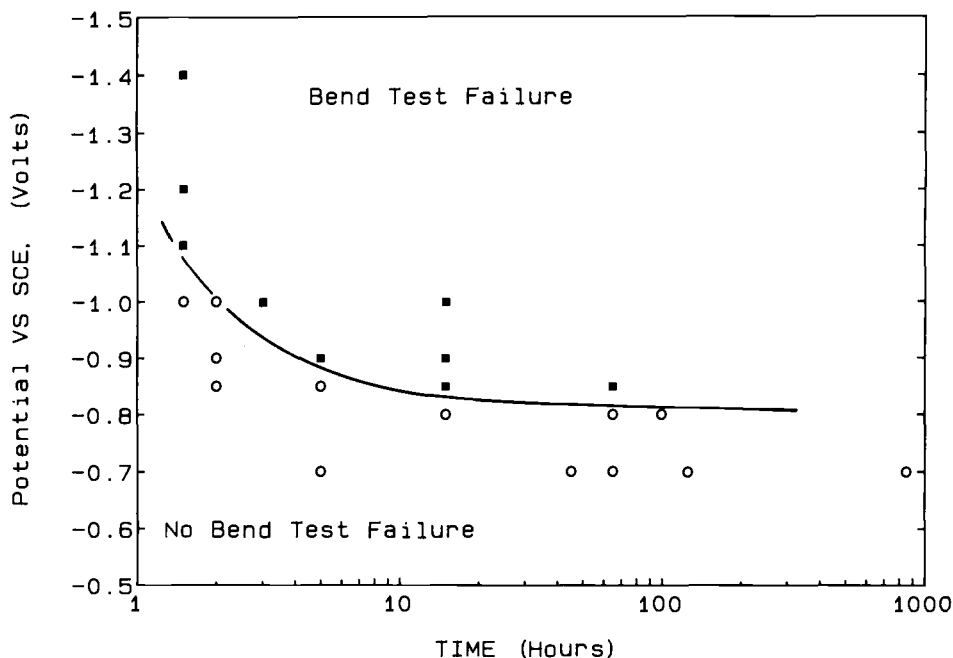


FIG. 1—Effect of cathodic charging potential and time on bend ductility of UNS S44660 in substitute seawater.

embrittlement, even though some hydrogen theoretically may be generated at this potential [18]. More electronegative potentials result in a rapid loss of bend ductility whereas, more electropositive potentials do not effect bend ductility. The limiting potential values to cause hydrogen damage found here for UNS S44660 are similar to those reported for other high performance ferritic stainless steels and titanium [14, 16, 17, 19, 20].

Tests to evaluate the susceptibility of UNS S44660 to hydrogen embrittlement were also conducted with pre-stressed U-bend specimens held at various electrochemical potentials in filtered, flowing natural seawater at Boca Raton, FL [21]. In these tests, performance was rated by determining the time necessary to produce spontaneous failure of the U-bends at various applied potentials. The results in Fig. 2 show that the potential needed to avoid spontaneous failure is about -0.900 V. This limiting value is more electronegative than the one obtained in the laboratory measurements, possibly as a result of differences in the nature of substitute and natural seawater or the severity of the procedures used to measure embrittlement or both.

UNS S44660 stainless steel condenser tubing is also used with cooling waters containing lower chloride content than seawater. Therefore, some additional hydrogen embrittlement tests were conducted on this steel at various potentials in waters with lower chloride content than seawater. The results in Fig. 3 indicate that potentials more electronegative than -0.800 V are required to produce embrittlement and that the time to produce embrittlement generally increases with a decrease in chloride concentration. Also, the potential at which UNS S44660 becomes susceptible to embrittlement appears to shift slightly to more electronegative values with a decrease in chloride concentration.

The loss of ductility of high performance ferritic stainless steels caused by hydrogen embrittlement is normally reversible [5, 17]. In contrast, the loss in ductility caused by hydrogen damage in titanium, which forms stable hydrides, is not easily recovered. Experiments were therefore conducted to determine whether various aging treatments would remove the hydrogen from UNS S44660 and fully restore bend ductility. For this purpose, strip specimens were

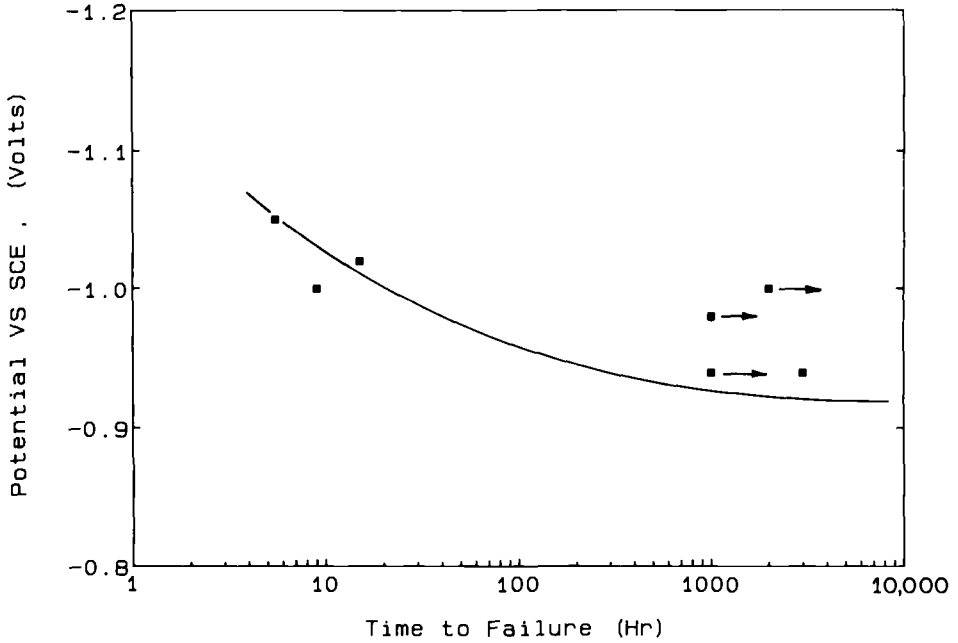


FIG. 2—Effect of cathodic changing potential and time on the spontaneous cracking of UNS S44660 U bends in flowing, filtered, and natural seawater.

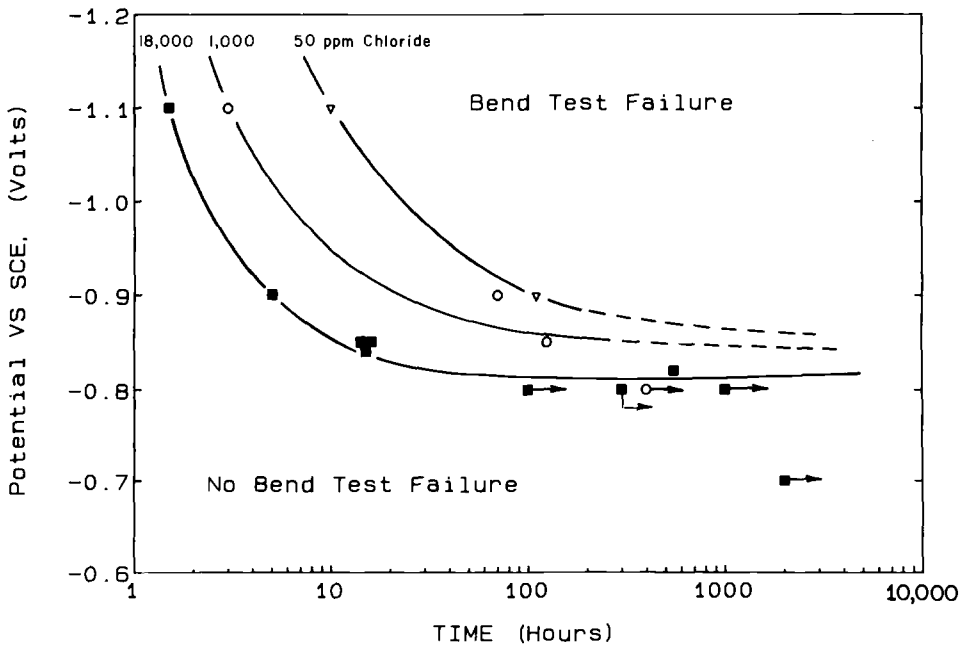


FIG. 3—Effect of cathode potential, time, and chloride concentration on bend ductility of UNS S44660.

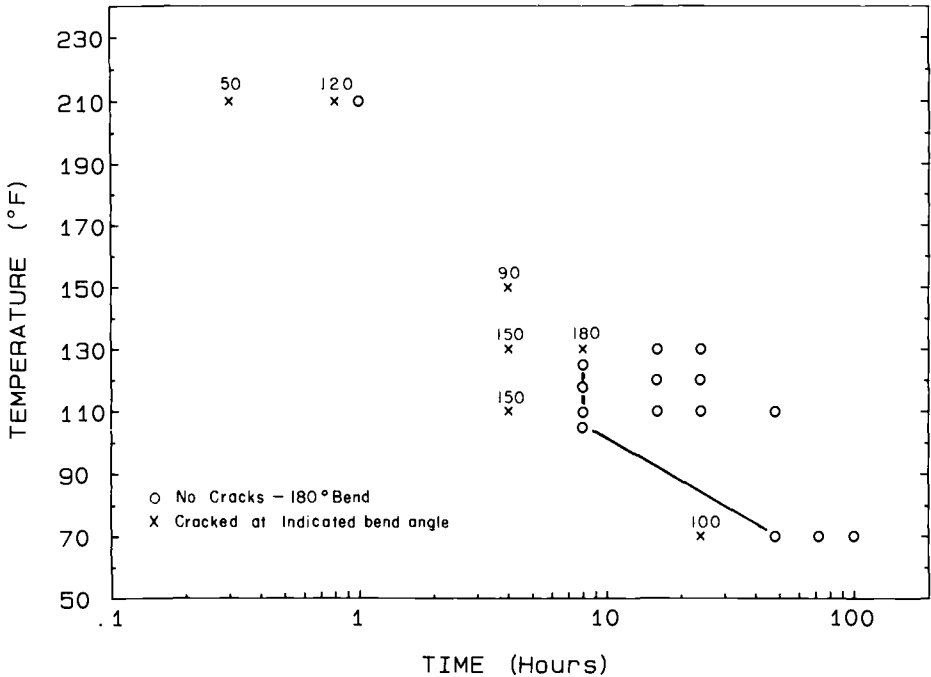


FIG. 5—Ductility recovery in water of hydrogen charged UNS S44660 stainless steel.

operating during periods when the circulating pumps were off. This evidently led to an excessive buildup of hydrogen at the outlet end.

Discussion

Field experience obtained in dealing with the few instances of tube failure caused by hydrogen embrittlement has shown that it is practical to use impressed current to protect both tubesheet and waterboxes without damaging UNS S44660 tubes. An important factor in this conclusion is the finding that there is a significant difference in potential between the waterbox and the tubesheet face. Detailed potential distribution measurements have been made using multiple reference electrodes on the tubesheet face in Units A and C listed in Table 4. As shown under "final conditions" in Table 4, the tubesheet potential tends to be about 200 mV less negative than that measured on the waterbox near the tubesheet junction. The potential across the tubesheet face was also found to be relatively uniform within a range of about 50 mV. Therefore, an impressed current cathodic protection system can be designed and operated to protect cast iron waterboxes at -0.850 V, for example, while still leaving the tubes at a safe potential of -0.650 V. This potential of -0.650 V is more than adequate to protect copper alloy tubesheets, such as Muntz, which exhibits a mixed potential with stainless steel of about -0.290 V, and which from our experience appears fully protected with the tubesheet face at -0.650 V.

Another important consideration is the need for automatic control with adjustable counter electrodes, and multiple reference electrodes located on the waterbox near the tubesheet junction and on the tubesheet face. Automatic control can provide potential control within a narrow range and can adjust for potential transients caused by such variables as water salinity. As shown by the laboratory data, the degree of control is particularly important in seawater where embrittlement appears to develop more rapidly than in waters with lower chloride content. With

TABLE 4—Summary of cathodic protection, embrittlement experience with UNS S44660 condenser installation.

Unit	Water Salinity	Initial Conditions				Final Conditions			
		Design	WB Potential, V	TS Potential, V	Tubes Failed	Design	WB Potential, V	TS Potential, V	Tubes Failed
A	high	manual CP system uncoated WB & TS	-1.70	...	0 ^a	automatic CP system coated WB & TS	-0.83	-0.57	0
B	high	Muntz TS, iron WB	-1.16	...	0	outlet extension elimination	-0.77	-0.55	0
		" "	-1.23	-1.53	2 ^b	reduce potentials ^c	...	-1.33	0
B	high	" " " "	-0.53	-0.94	0 ^a	automatic CP system	...	-1.03	0
		" " " "	-0.53	-0.94	0 ^a	coated WB & TS	...	-0.63	0
C	high	" " " "	-0.83	...	outlet extension elimination	...	-0.53	0	
D	high	CP system on with pumps off	automatic CP system	-0.83	-0.63	0
		" "	CP system off with pumps off	" "	-0.73
E	high	manual CP system uncoated WB & TS	-0.73	...	0	monitor potential & current	-0.64	...	0
		Muntz TS, iron WB	-0.63	...	0				
F	high	manual CP system coated WB & TS	control to -0.43/-0.73 V	...	0	no change	no change	no change	0
		brass TS, iron WB	potential	...	0				
G	moderate	manual CP system coated iron WB	0	no change	0
		uncoated stainless TS				
H	moderate	manual CP system coated iron WB	-1.04	...	0	no change	0
		uncoated stainless TS	-0.73				

NOTE: TS is tubsheet and WB is waterbox.
^aExtending outlet ends embrittled.
^bTransverse breaks immediately inside the inlet tubsheet.
^cTemporary measure used for a period of six months.
^dTransverse breaks immediately inside the outlet tubsheet.

multiple reference electrodes the system can be adjusted to assure that adequate waterbox protection is maintained at the tubesheet junction without exceeding the requirements of the tubesheet. The use of a tubesheet and waterbox coating has also been found to be helpful in achieving uniform potential control and in minimizing the power requirement of the cathodic protection system. The main precaution when using impressed current cathodic protection is to avoid conditions that produce potentials more electronegative than -0.800 V on the ferritic stainless steel tubing.

In installations where use of a galvanically compatible tubesheet material is being considered with high performance ferritic stainless steel tubing, attention must be given to the crevice corrosion resistance of the tubesheet material, since crevices can be formed at the tube/tubesheet joints, as for example, with improper tube expansion. UNS S44660 resists the initiation of crevice corrosion at all chloride concentrations up to and including that of seawater, and use of a tubesheet of compatible performance is desirable. Table 5 lists the crevice corrosion resistance of several stainless steels in various field and laboratory tests conducted in filtered, natural seawater and in acidified waters of different chloride content. For seawater service, a highly alloyed stainless steel, such as AL-6XN[®] (UNS N08367), is a candidate material, while lesser alloyed stainless steels, such as Types 316, 317 (UNS S31700), and 904L (UNS N08904), may be suitable for waters with lower chloride levels. Since cathodic protection will often be used in the system to provide protection of the waterbox, it can also provide added protection to a compatible tube-tubesheet system.

Conclusions

UNS S44660, similar to other high performance ferritic stainless steels and titanium, is susceptible to hydrogen embrittlement. In these experiments, UNS S44660 became susceptible to hydrogen embrittlement in substitute seawater at potentials more electronegative than about -0.800 V (SCE) and in natural seawater at potentials more electronegative than about -0.900 V. The time necessary to develop hydrogen embrittlement in UNS S44660 stainless decreases as the potential becomes more electronegative and as the chloride content of the water increases. The loss in ductility of UNS S44660 caused by hydrogen embrittlement can be recovered by aging the alloy for relatively short times at ambient or elevated temperature to allow for hydrogen out gassing. The recovery of ductility is more rapid in water than in air.

TABLE 5—Ranking of candidate stainless steel tubesheet materials for chloride crevice corrosion resistance.

Alloy	Ranking in ^a Natural Seawater ($S \times D$) ^b	Maximum Chloride ^c Without Crevice Attack, ppm
AL-6XN [®]	...	> 15 000 ^d
AL-6X [®]	2.5	15 000
Type 904L	3.7	5 000 ^d
Type 317LM	6.4	2 000
Alloy 2205	8 ^d	1 000
Type 317L	12	700 ^d
Type 316L	> 12 ^d	500

^a30 day tests at 30°C (86°F) in filtered seawater; three panels with 120 grit finish [22].

^b S = number of sides attacked, and D = maximum depth of attack, mm.

^cSix-month laboratory tests at 40°C (104°F).

^dEstimated.

The potentials discussed above are those measured on the actual metal surface. Because of polarization and other factors, these potentials will not be the same as those measured on the counter electrodes used in the cathodic protection system. Field data show that there can be a 0.100 to 0.200 V difference between the potentials measured near the tubes in a condenser and those measured on the control electrodes at the waterbox.

The conditions under which hydrogen embrittlement difficulties may be encountered in actual condenser service are considered to be a function not only of potential, but of environment and stress state. Although these conditions have not yet been precisely defined, field experience confirms that impressed current cathodic protection systems can be practically and successfully used with seawater cooled power plant condensers using UNS S44660 tubing and dissimilar tubesheet and waterbox materials. Eight installations are now operating with UNS S44660 tubing used in conjunction with cathodic protection, and no difficulties are being experienced with hydrogen damage.

Disclaimer

The material contained herein is intended for general information only and should not be used in relation to any specific application without independent study and determination of its applicability and suitability for the intended application. In some cases, a complete evaluation of performance is not possible without more extended tests over longer time periods. Anyone making use of this material or relying thereon assumes all risk and liability arising therefrom.

References

- [1] Davison, R. M., Deverall, H., and Redmond, J. D., "Ferritic and Duplex Stainless Steels," *Process Industries Corrosion*, 1986.
- [2] Streicher, M. A., "New Stainless Steels for the Process and Power Industries," *Metals Progress*, Oct. 1985, pp. 29-42.
- [3] Redmond, J. D. and Miska, K. H., "High-Performance Stainless Steels for High-Chloride Service—Parts I, II," *Chemical Engineering*, July 1983, p. 93, and Aug. 1983, p. 91.
- [4] Kovach, C. W. and Thackray, J. C., "The Development of SEA-CURE® Condenser Tubing," *Advanced Stainless Steels for Seawater Applications*, The Climax Molybdenum Company, pp. 81-92.
- [5] Streicher, M. A., "Development of Pitting Resistant Fe-Cr-Mo Alloys," *Corrosion*, Vol. 30, No. 3, p. 77, 1974.
- [6] Kovach, C. W., Redmerski, L. S., and Kurtz, H. D., "Crevice Corrosion Performance of a Ferritic Stainless Steel Designed for Saline Water Condenser and Heat Exchanger Applications," *NACE Corrosion/80*, Paper 95.
- [7] Kovach, C. W. and Redmerski, L. S., "Crevice Corrosion of Type 316 and Highly Alloyed Stainless Steels in Simulated Natural Environments Using the Multiple Crevice Assembly," *NACE Corrosion/81*, Paper 123.
- [8] Redmerski, L. S., Eckenrod, J. J., and Kovach, C. W., "Crevice Corrosion of Stainless Steel Welds in Chloride Environments," *Materials Performance*, Vol. 22, No. 6, 1983, p. 31.
- [9] Astley, D. J. and Rowland, J. C., "Modelling of Bimetallic Corrosion in Sea Water Systems," *British Corrosion Journal*, Vol. 20, No. 2, 1985.
- [10] Uhlig, H. H., *Corrosion and Corrosion Control*, John Wiley and Sons, Inc., Chapter 12, Sept. 1965.
- [11] Fulford, J. P. and Piazza, J. L., "Advances in Water Box Cathodic Protection," *NACE Corrosion/84*, Paper 51.
- [12] Kovach, C. W., "Experience with High Performance UNS S44660 Ferritic Stainless Steel Tubing in Power Plant Condenser," presented at the ASME Joint Power Conference, Toronto, Ontario, Canada, Sept. 1984.
- [13] Grubb, J. F. and Maurer, J. R., "Use of Cathodic Protection with Superferritic Stainless Steels in Seawater," *Corrosion/84*, Paper 28.
- [14] Hanson, C. F., *Titanium Condenser Tube Application in Practice*, *Materials in Power Plant*, Series 3, No. 3, Chameleon Press, London, 1975.
- [15] Kearns, J. R., Grubb, J. F., and Johnson, M. J., "Accelerated Corrosion in Dissimilar Metal Crevices," *NACE Corrosion/86*, Paper 228.

- [16] Grubb, J. F., "Hydrogen Embrittlement of Superferritic Stainless Steels," *1984 ASM International Conference on New Developments in Stainless Steel Technology*, No. 8410-28.
- [17] Redmerski, L. S., Eckenrod, J. J., Pinnow, K. E., and Kovach, C. W., "Cathodic Protection of Seawater-Cooled Power Plant Condensers Operating With High Performance Ferritic Stainless Steel Tubing," *NACE Corrosion/85*, Paper 208.
- [18] Pourbaix, M. J. N., *Atlas of Electrochemical Equilibria in Aqueous Solutions*, New York, Pergamon Press, 1966.
- [19] Mazzo, F., Torchio, S., and Ciaghe, L., "Some Aspects of the Corrosion Behavior of Some E.L.I. Superferritic Stainless Steels in Chloride Environment Under Cathodic Coupling," *NACE Corrosion/86*, Paper 117.
- [20] Tsai, C. H. and Lee, P., "A Study of Hydriding of Titanium Alloy in Seawater Under Cathodic Polarization," *NACE Corrosion/86*, Paper 259.
- [21] Krishnamurthy, R. M., "Characterization of the Embrittlement Tendency of a Cathodically Polarized Superferritic Stainless Steel in Seawater," Master of Science thesis, Florida Atlantic University, Boca Raton, FL, 1986.
- [22] Streicher, M. A., "Analysis of Crevice Corrosion Data from Two Sea Water Exposure Tests on Stainless Alloys," *Materials Performance*, May 1983, pp. 38-49.

Bimetallic Joints in Multistage Flash Desalination Plants

REFERENCE: Al Zaharani, S. G., Todd, B., and Oldfield, J. W., "Bimetallic Joints in Multistage Flash Desalination Plants," *Galvanic Corrosion. ASTM STP 978*, H. P. Hack, Ed., American Society for Testing and Materials, Philadelphia, 1988, pp. 323-335.

ABSTRACT: In order to achieve an optimum compromise of cost and performance, it is necessary to construct large multistage flash (MSF) desalination plants from a variety of materials, notably carbon steel, copper-base alloys, stainless steels, and titanium. This produces a number of situations where two or more materials are in contact, and special care is needed to ensure that serious galvanic corrosion is avoided. Examples of such bimetallic and multimetallic junctions in plants operated by the Saline Water Conversion Corporation of Saudi Arabia are titanium tube/aluminum bronze tubeplate and waterbox; carbon steel/stainless steel flash chamber linings; and copper alloy/carbon steel waterboxes and piping. Problems associated with some of these junctions in older plants and the techniques used to avoid problems in modern plants are described in the paper. It is concluded that by application of good corrosion engineering practice, serious galvanic corrosion at mixed-metal joints can be avoided.

KEY WORDS: desalination, multistage flash, galvanic corrosion, pitting, crevice corrosion, deaeration, bimetallic joints, cupronickel, stainless steels, Ni-resist, titanium, tubes tubeplates, pumps, flash chambers, waterboxes, anodes, acid cleaning

Rapid development in Middle Eastern countries has resulted in the growth of a large and important desalination industry to provide potable and process water. The most commonly used desalination process is multistage flash (MSF) distillation.

Saudi Arabia has the largest desalination plant capacity in the world. These plants are the responsibility of the Saline Water Conversion Corporation (SWCC).

The first large seawater plants built for the SWCC were Dubai and Al Wajh [1], which first operated in 1969. Current installed capacity in Saudi Arabia represents about 30% of the world total and is 2.5 million m³/day. Over this period the technology of building and operating MSF units has improved significantly. Notable advances both in materials selection and use of corrosion science have occurred so that plant reliability has improved and maintenance problems have decreased.

The purpose of this paper is to describe some of the galvanic corrosion problems experienced at bimetallic joints in the older plants and how, by the use of good corrosion engineering practice, these have been avoided or minimized in modern plants.

The MSF Process

Figure 1 is a schematic diagram of an MSF plant. These consist essentially of a large box-like steel structure, which is divided into a number of sections (flash chambers) by transverse walls. Situated at the top of these chambers are bundles of heat exchanger tubing.

¹SWCC Jubail, Saudi Arabia.

²Inco Middle East Projects Group, Wiggin St., Birmingham B16 OAJ, United Kingdom.

³Cortest Laboratories Ltd., Shepherd St., Sheffield S3 7BA, United Kingdom.

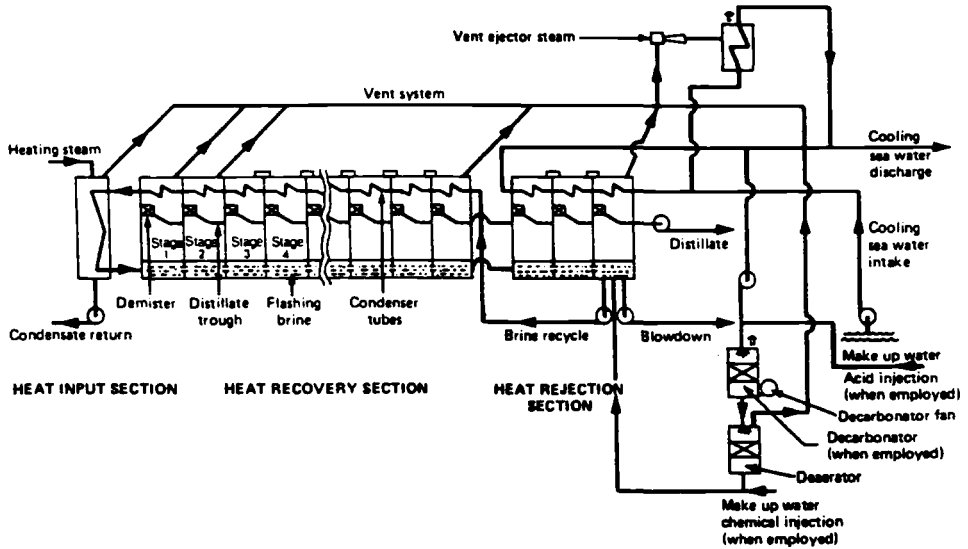


FIG. 1—Simplified multistage flash (MSF) flow diagram.

Seawater passes through the tubing and is preheated by steam condensing outside. This condensate is collected and is the product from the plant. The preheated seawater passes to a separate heat exchanger, the brine heater, where it is heated to the top process temperature by steam from an external source. The heated seawater or brine is passed to the first flash chamber, where the pressure is reduced so that it boils. It is then passed through successive flash chambers at progressively lower temperatures until it leaves the plant. In order to improve heat transfer and reduce corrosion, the seawater is often deaerated before entering the plant. Also in order to conserve chemicals, brine is usually recycled and mixed with incoming feed, only a small portion being blown down to maintain the concentration at an acceptable level.

These plants are large users of materials in the form of

- Heat exchanger tubing
- Flash chamber fabrications
- Waterboxes
- Piping
- Pumps
- Valves

In order to achieve an optimum compromise of cost and performance, it is necessary to construct the plants from a variety of materials. The most commonly used materials areas follows:

- Carbon steel—flash chambers and general structural usage.
- Copper-base alloys—heat exchanger tubing, tubeplates, piping, and waterbox linings.
- Stainless steels—flash chamber and pump internals.
- Titanium—heat exchanger tubing.

This produces a number of situations where two or more materials are in contact and special care is needed to ensure that serious galvanic corrosion is avoided. Examples of both failures and successes in dealing with this problem are given in the following section.

Corrosion at Carbon Steel/Alloy Junctions in Older Plants

Effect of Oxygen

In the early development stages of the industry, designers assumed that as the process involved deaerated brine solutions, the low oxygen levels in the brine would render it only mildly corrosive. They therefore chose carbon steel as the primary material of construction in the brine system, and alloy materials were confined to the tubing, tubeplates, pumps, and valves. This meant that there were many places where carbon steel and copper base alloys were connected and galvanic corrosion could occur.

Although reducing oxygen to a low level will certainly reduce corrosion in neutral brine solutions, it is necessary to achieve very low oxygen levels in the 0 to 10 part per billion (ppb) range—in order to reduce corrosion to an acceptable rate. It has been shown [1] that even at 10 to 50 ppb oxygen, corrosion rates exceeding 0.5 mm/year can be experienced at moderate flow rates, and temperature instrumentation capable of measuring these low levels on a continuous basis was not then available so that the oxygen level in the recirculating brine could not be accurately controlled.

Effect of pH

Two methods of scale control are used in MSF plants. One involves additives, such as polyphosphates, which inhibit the formation of hard scales. The other uses acid to decompose carbonates in the seawater so preventing alkaline scale formation.

In additive plants, the pH level is about 8.5 whereas in acid-dosed plants a pH of 7.5 to 7.8 is usual. However, in acid-dosed plants control of pH depends on accurate instrumentation, and the tendency for scales to form on the electrodes meant that the pH was often outside the design limits and sometimes in the acid region. Thus, even with good oxygen control, corrosion could occur with hydrogen evolution as the cathodic reaction.

Corrosion at Waterbox/Tube and Tubeplate Junction

In the Jeddah 1 plant the original waterboxes were made of carbon steel and were bolted direct to the 90/10 cupronickel tubeplate. The tubes were also of 90/10 cupronickel.

Figure 2 shows a waterbox that was scrapped after about 2-years service. The carbon steel has perforated.

Jeddah 1 is an acid-dosed plant, and there is evidence from failures elsewhere that sometimes it operated at low pH. Also, the deaerator in this plant was an internal unit built into the final low-temperature stages. Experience showed that this type of deaerator was less efficient than a completely separate unit so that the oxygen levels in the recirculating brine would normally be higher than the 0 to 10 ppb level.

The Jeddah 1 waterboxes were lined with 90/10 cupronickel sheet by the plant maintenance staff and thereafter performed satisfactorily.

Corrosion at Al Khobar [1] Inter-vessel Piping

This plant used 90/10 cupronickel clad steel waterboxes and avoided the problems experienced in Jeddah 1. However, the inter-vessel piping carrying the brine from vessel to vessel was made of carbon steel. These pipes connect the waterboxes at the ends of the vessels, which had suffered severe galvanic corrosion and perforations. Figure 3 shows temporary repairs used to keep the plant in operation.

In later SWCC plants, such as Jeddah 2 and 3, the waterboxes and interstage piping were all

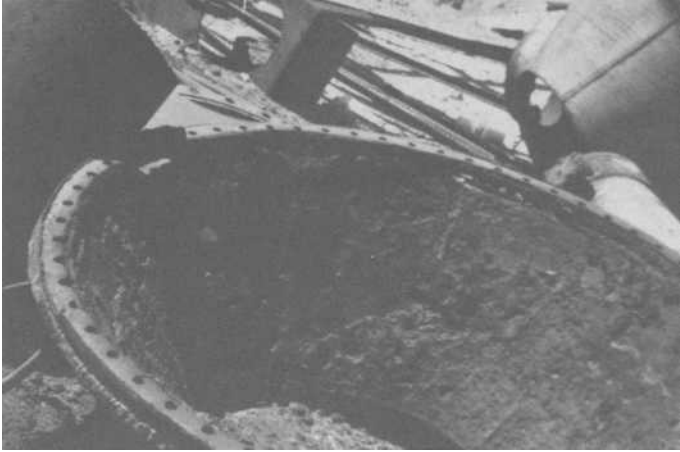


FIG. 2—Corroded steel waterbox.

made in 90/10 cupronickel clad steel. This means that the entire brine system is made from copper base alloys and the galvanic corrosion problem has been avoided. These systems have worked well in the modern SWCC plants.

Corrosion at Carbon Steel/Alloy Junctions in Newer Plants

General

As described above, the copper alloy/carbon steel junctions in the heat exchanger tubing and brine systems have been eliminated, usually by making the whole system of copper alloys or by using nonmetallic materials, such as glass fiber reinforced plastics (FRP) for the lower temperature piping. The 90/10 cupronickel piping/stainless steel vessel lining junction where the hot



FIG. 3—Perforations in steel pipe.

brine enters the vessel has proved not to be a problem in practice. This is probably because in hot deaerated brine the galvanic potentials of stainless steel and copper-base alloys are similar [2].

The only remaining bi-metallic junction causing concern in brine systems is the stainless steel/carbon steel junctions in the flash chambers.

Problems have been reported at this junction inside the flash chambers where only some of the stages are lined. This results in a large area of stainless steel, normally Type 316L, directly welded to a large area of carbon steel. Although the overall metal loss resulting from this is not usually serious when the oxygen level is low, the attack is more severe immediately at the junction and can result in a definite step developing at this point. Studies in operating desalination plants [3] gave the following results (Table 1).

These data indicate that the galvanic effect between Type 316L stainless steel and carbon steel in hot deaerated seawater is appreciable. These tests also showed somewhat greater metal loss close to the welded junction in the bi-metallic specimens.

Control Methods for Chamber Linings

As the evaporator vessels are essentially one-piece all-welded constructions, it is not possible to isolate the stainless steel or carbon steel.

The most cost effective method of controlling corrosion at this junction is to reduce the effective cathodic area by painting the stainless steel. This is usually confined to the flash chamber upstream from the junction.

Painting of stainless steel for controlling galvanic corrosion is well proven in other industries [4]. It is an inherently safe method since any holidays during the coating will not result in a significant increase in attack. If the carbon steel is painted, then attack is intensified at holidays because of the increased cathode/anode ratio, and pitting rates of 10 mm/year can be experienced. Painting of the carbon steel to control corrosion at the bimetallic junction is therefore not recommended. Where, for other reasons, the carbon steel is painted, the stainless steel should also be painted or anodes of carbon steel should be fitted to the stiffeners across the stage width, or both. These anodes also provide protection to the stainless steel against pitting during shut-downs.

Maintaining a paint coating on stainless steel in hot deaerated brine is difficult. It is recommended that the surface be roughened by grit blasting with copper slag followed by painting with epoxy-resin paints.

Zinc rich paints should be avoided on stainless steel as they can give cracking problems if at a later stage the stainless steel has to be welded.

This method of controlling corrosion at the stainless steel/carbon steel junction has proved effective in SWCC plants and is the normal method of control now applied.

TABLE 1—Galvanic corrosion of carbon steel/stainless steel couples in deaerated seawater.

Plant	Temperature, °C	Average Thickness of Carbon Steel, mm	
		Coupled to SS Type 316L	Plain
A	60	0.42	0.01 to 0.06
B	90	0.30	0.1 to 0.15
C	82	0.12 (pitting)	0.01 to 0.21
C	55	0.19	0.01 to 0.12

NOTE: Samples situated on floor of flash chamber, 15-months exposure.

Control Methods for Brine Gates

The gates controlling flow of brine from stage to stage are normally made from stainless steel because of its high resistance to turbulent brine. In the stainless-steel-lined stages this presents no problems, but in the carbon steel stages deep pitting sometimes occurs beneath the stainless steel gate. As adjacent carbon steel surfaces, although showing slight general corrosion, do not have these pits, it is assumed that these result from the galvanic effect from the stainless steel.

Because of the severe turbulence and vigorous flashing that occurs in this position, it is difficult to get a long life from paint in this area. It is usual to control this corrosion by electrically insulating the stainless steel by fitting plastic sleeves and washers to all fasteners connecting the stainless steel to the carbon steel structure. This has proved effective, but care is needed to ensure that insulation has been achieved. Omission of just one sleeve or washer will destroy the effectiveness of this method.

Tube/Tubeplate Joints in Clad Steel Tubeplates

Jubail 2 is fitted with 90/10 cupronickel clad steel tubeplates in the heat recovery and brine heater sections. With correctly rolled-in tubes no liquid should reach the 90/10 cupronickel to steel interface, and therefore no galvanic corrosion would be expected. However, after initial operation a random pattern of rust was noticed seeping from some tube/tubeplate joints. Although some of this was due to particles of rust in the circulating brine depositing on the tubeplate, some appeared to be actual seepage (bleeding) from the joint, which reappeared when cleaned off when the plant re-operated for a short period. The problem was particularly severe in a few tubes where protruding tube ends had been damaged during construction. When these tubes were removed, a shallow cavity was found to have been corroded in the steel adjacent to the steel/cupronickel interface.

The thickness of cladding in these plants is 9 mm ($\frac{1}{4}$ in.), and this is usually adequate to obtain a tight joint by normal roller expansion.

As the rust "bleeding" from undamaged tubes was minor it was decided to check the metal loss by removing a few tubes and, if slight, to re-expand all the affected tubes.

The tubes that were removed showed negligible metal loss at the steel/cupronickel interface.

It is interesting to note that this corrosion is not self-sealing as the rust forms only on the outface where some oxygen is available.

Seawater Pump Materials

MSF plants require large amounts of seawater both as plant feed and for cooling purposes. Vertical lift pumps are normally used, and for the pump internals, that is, impeller, shaft, sleeves, and so forth, the most widely used material is Type 316L stainless steel and its cast equivalent, CF3M. This selection is based on the following:

- (1) the excellent resistance of stainless steel to seawater under fast flowing conditions,
- (2) its good weldability so that any damage to the impeller can readily be repaired, and
- (3) wide availability and moderate cost.

Although the inlet bell, casing, diffusers, columns, and discharge head can also be made in the same material, care is needed during shutdowns. This pitting and crevice corrosion will occur.

Figure 4 shows pitting on the impeller of an all stainless steel seawater pump from Jubail 1. This pump was made entirely from Alloy 20 and was fitted several months before power was available to operate it. It therefore stood stationary in the seawater, and when inspected the immersed parts were found to have suffered pitting and crevice corrosion beneath sleeves and on flange faces. The maximum depth of pitting was about 6 mm.



FIG. 4—Pitting of Alloy 20 impeller.

The lower pump parts were renewed, and to avoid recurrence of the problem a ring of iron anodes was fitted in the suction bellmouth (Fig. 5). This has proved effective.

One method of avoiding this problem that is widely used in the Middle East is to use a material for the casing parts that provides cathodic protection to the stainless steel yet has sufficient corrosion resistance to give a long life. The materials that meet these requirements are the austenitic cast irons commonly known as Ni-resist irons. These have been shown [5] in laboratory tests to be capable of preventing crevice corrosion on Type 316L stainless steel in natural seawater. Relevant data are as shown in Table 2.

These laboratory results confirm SWCC's experience with seawater pumps in Medinah Yanbu, Al Khobar 2, and Al Jubail 2 where casing parts of Ni-resist Type D-2 with Type 316L internals have shown no pitting after up to 5-years operation.

Galvanic Considerations with Titanium Tubing

Natural Seawater

In seawaters that contain sulfides or large amounts of sand in suspension, or both, titanium tubing is sometimes used in the heat rejection section.

Because of the high cost of titanium, it is necessary to use other materials for tubeplates and waterboxes. As titanium has a high corrosion potential in seawater, about +0.1 V (standard calomel electrode [SCE]), it is cathodic to most commonly used alloys.

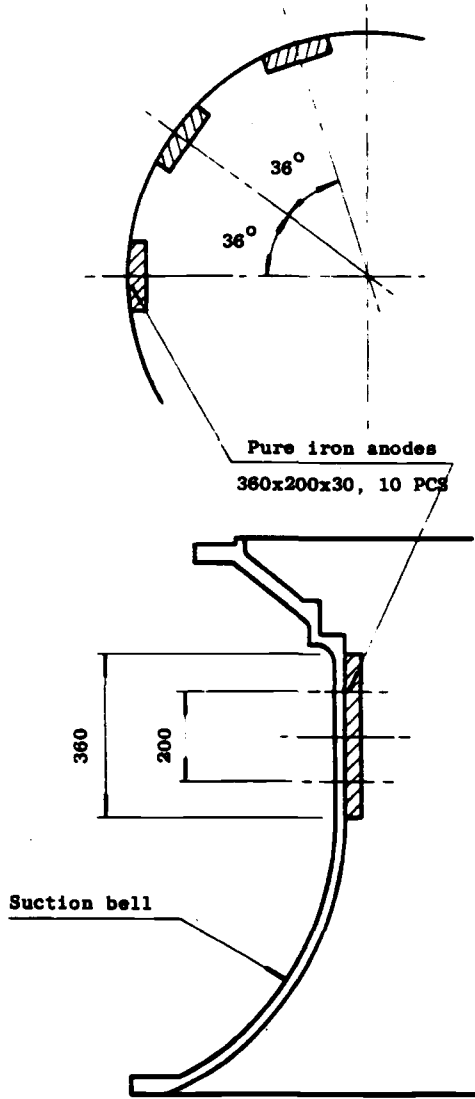


FIG. 5—Arrangement of pure iron anodes on suction bell.

TABLE 2—Comparison of carbon steel and Ni-resist anodes coupled to stainless steel in seawater at a velocity of 0.5 m/s.^a

Alloy	Anode Material	Crevice Attack	
		Number of Sites Initiated ^b	Maximum Attack Depth, mm
316	AISI 1010	5	0.02
316	Ni-resist Ttype II	0	0

^aTests for 30 days at 28°C with a 50:1 area ratio.

^bOut of possible 120 sites.

Early unpublished work by the British Navy showed that the copper base alloy, nickel-aluminum-bronze (Unified Numbering System [UNS] C63000) suffered only slight galvanic attack when coupled to titanium in seawater. Heat exchangers made using this material have performed well in service. However, this alloy is more difficult to machine than the normal tube-plate materials, and when large condensers with titanium tubes were first used, the more easily machined aluminum bronze UNS C61400 was used. This alloy proved to be much less compatible galvanically with titanium, but as early installations used either cast iron or fabricated steel waterboxes, or had cathodic protection fitted, this problem was not immediately revealed. However, in later installations with coated or nonferrous waterboxes, severe corrosion of the C61400 alloy was experienced, up to 7.6 mm/year being reported [6].

When the SWCC Jubail 1 plant was designed, it was decided to use titanium tubing for the heat rejection section, and the tubeplates and waterboxes were specified in C61400 aluminum bronze by the consultant. Before the plant was built, the possibility of problems with this materials construction was realized, and SWCC requested the contractor to fit an anode system to protect the tubes and tubeplates.

Although impressed current or various anode materials were all possible choices, it was decided that the safest option was iron anodes. This choice is confirmed by Japanese work [2], which shows that at potentials more negative than -0.75 V (SCE) titanium will absorb hydrogen and form hydrides in seawater at 25°C . Although this would not seriously reduce the corrosion resistance in seawater, the tubes would in time embrittle and fail under mechanical stress. As the corrosion potential of iron in natural seawater is about -0.6 V (SCE) the risk of hydrides is avoided with these anodes.

Figure 6 shows the anode system used in the Jubail 1 reject section waterboxes. These have proved effective, and no serious corrosion problems have been experienced on the aluminum bronze tubes and tubeplates. However, the necessity for the anodes is demonstrated by the slight corrosion damage on the tubeplate, which occurs during shutdowns when the system is drained.

At this time, seawater left in the tubes seeps out onto the tubeplate so that there is a film of liquid on the aluminum bronze, and this is retained by the slight protrusion on the tubes. As the

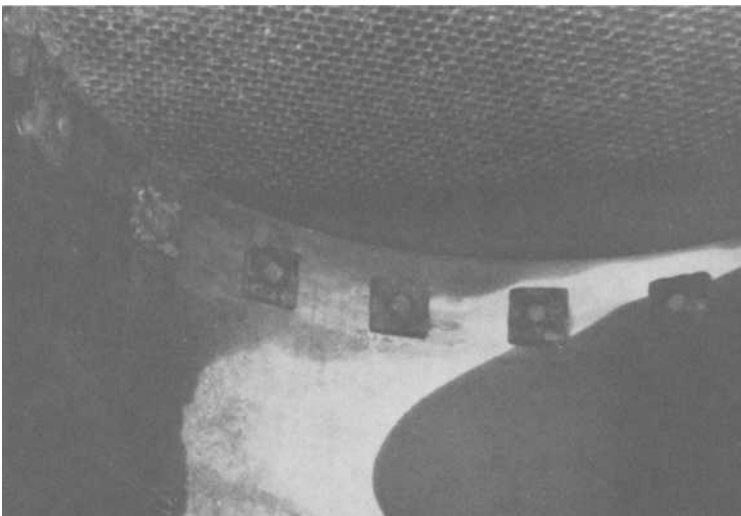


FIG. 6—Iron anodes in aluminum bronze (C61400) waterbox to prevent galvanic attack from titanium tubes.

anodes are not connected to the tubeplate via the seawater during shutdowns, there is no cathodic protection. After a few days a bright green film forms on the tubeplate, which is very easily wiped away to reveal an etched surface on the aluminum bronze (Fig. 7). Although the metal loss is slight, it is an indication of the serious attack that would occur during operation if no anodes were fitted. This corrosion has been controlled by careful flushing with freshwater.

Hot Deaerated Seawater

Jubail 1 was also built with titanium tubing in the heat recovery and brine heater sections. The same tubeplate and waterbox materials in the rejection section, aluminum bronze C61400, was again used. This presented a similar problem to the reject section, but in addition, information from elsewhere [7] indicated that the C61400 could suffer a type of intergranular stress corrosion cracking under desalination plant conditions, that is, hot deaerated seawater. Also cathodic protection criteria in hot deaerated seawater for titanium/aluminum bronze couples had not been established at that time.

Failures of titanium by crevice corrosion in hot deaerated seawater had been experienced [8] in a desalination plant in Japan after only 4-months operation. The corrosion effects at the crevice provided by the aluminum bronze tubeplate/titanium rolled in tube were not known. However, it was decided to again use cathodic protection, and iron anodes were selected.

SWCC, on the basis of data [2] showing that iron anodes could cause hydriding at elevated temperatures, used 9% nickel-iron alloy above 70°C. Table 3 provides these data. The data also show that the galvanic effect between copper alloy and titanium is prevented by the cathodic protection provided by the anodes.

The same paper [2] shows that the corrosion potential taken up by a copper alloy tubeplate/titanium tube crevice is in the range that avoids crevice corrosion or hydriding of the titanium. With anodes to prevent attack on the copper alloy, then, this connection to the tubeplate and waterboxes can be considered satisfactory.

No data on the intergranular stress corrosion cracking of aluminum bronze C61400 are available, but the Jubail 1 waterboxes have been carefully inspected for evidence of cracking. No cracks have been found suggesting that the cathodic protection system is effective in preventing this.

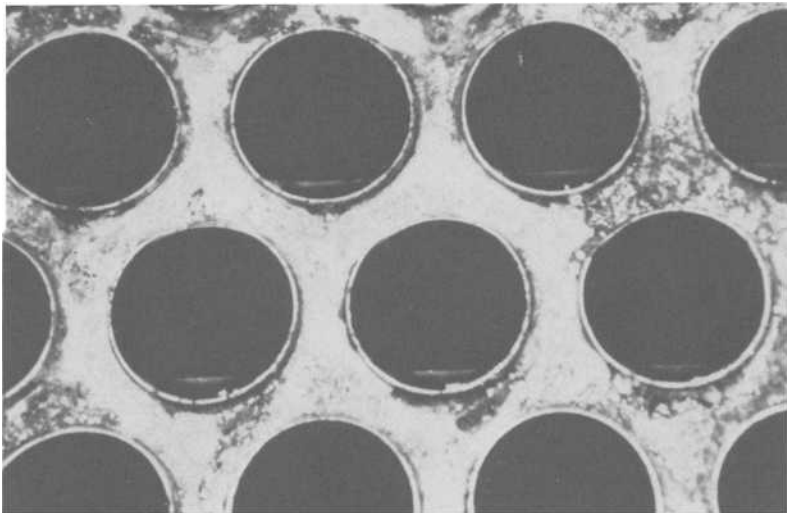


FIG. 7—Corrosion of aluminum bronze (C61400) tube plate.

TABLE 3—Effect of anode material on corrosion and hydriding of copper alloy.

Specimens	Corrosion Rate of Cu Alloy, mm/year		Hydrogen Absorption of Ti
	Al Bronze	Naval Brass	
Cu Alloy/Ti	0.03	0.05	0
Fe-9 Ni/Cu Alloy/Ti	0.005	0.005	0
Fe/Cu Alloy/Ti	0.005	0.005	19

NOTE: 30-days immersion in deaerated 6% NaCl solutions at pH 6 and 100°C.

Acid Cleaning

There is always a risk of scales forming on heat exchange surfaces in a distillation plant, and acid cleaning is sometimes required to remove them. Fortunately, with skilled operators and modern anti-scalants, the frequency of acid cleaning has diminished; nevertheless the plant must be capable of withstanding this treatment if it is used.

Sulfuric, hydrochloric, and sulfamic acids are used for descaling. Because of its higher cost, sulfamic acid is less favored for large plants, and although hydrochloric acid is favored by some operators because of personal safety considerations, sulfuric acid is probably the most widely used.

Data from Japanese work [9] indicated that sulfuric acid could be used in contact with titanium without causing hydriding provided an inhibitor was used. The same tests showed that hydrochloric acid did cause hydriding even with inhibitors present. Table 4 gives data from this paper [9]

As 300-ppm hydrogen would be sufficient to embrittle the titanium and as the hydrogen buildup would be cumulative with each acid cleaning there would be a risk of the tubes becoming brittle because of hydriding.

These results caused some concern as SWCC considered that MSF plant scales would be saturated with chlorides so that any addition of acid would result in acid chloride conditions on the metal surface. Also, as it would be impractical to remove the hundreds of anodes in the waterboxes, there might be a risk of hydriding results from the galvanic effect in acid environments. Tests were therefore carried out to test these effects (Table 5).

These results indicate that the risk of hydriding is slight if acid cleaning is carried out under the conditions shown. As extra safeguards, SWCC will restrict the temperature to 40°C, flush out with distilled water to reduce chloride levels before acid cleaning, and use as short a time as possible to perform the cleaning. If regular acid cleaning becomes necessary, then samples of tube will be removed for hydrogen analysis after some years of operation to ensure that damage to the tubes is avoided.

TABLE 4—Hydrogen absorption of titanium at 60°C.

Acid	Inhibitor	Time, hr	Hydrogen Content, ppm
4% sulfuric	none	6	89
"	"	60	483
"	inhibitor	6	3
"	"	60	3
4% hydrochloric	none	6	22
"	"	60	656
"	inhibitor	6	21
"	"	60	603

TABLE 5—Effect of galvanic couples and chloride on hydrogen absorption of titanium in 2% sulfamic acid.

Inhibitor	Chloride Concentration	Metal Couple	Hydrogen Content, ppm
0.2% S70S	250	Ti	1
		Ti + Al	
		Bronze	4
“ ”	1000	Ti + C Steel	3
		Ti	0
		Ti + Al	
“ ”	5000	Bronze	4
		Ti + C Steel	0
		Ti	1
None	5000	Ti + Al	1
		Bronze	1
		Ti ± C Steel	5
		Ti	1
		Ti ± C Steel	1

NOTE: Temperature $48 \pm 2^\circ\text{C}$. Time 48 h. Areas of Ti, C steel and Al bronze approximately equal.

Summary and Conclusions

The serious galvanic corrosion problems experienced in older MSF plants have now been overcome. In modern plants improved materials selection, good operation, and use of good corrosion engineering practice enables engineers to use a variety of materials so as to optimize cost and performance.

Acknowledgments

The authors wish to thank the governor of the Saline Water Conversion Corporation for permission to publish information on the MSF plants in Saudi Arabia. They also thank the management of Inco Europe Limited for the use of technical information from their researchers.

References

- [1] Oldfield, J. W. and Todd, B., "Corrosion Considerations in Selecting Metals for Flash Chambers," *Desalination*, Vol. 31, 1979, pp. 365-383.
- [2] Fukuzuka, T., Shimogori, K., Satoh, H., and Kamikubo, F., "Corrosion Problems and their Prevention of MSF Desalination Plant Constructed with Titanium Tube," *International Congress on Desalination and Water Re-use*, Nice, 1979, pp. 389-398.
- [3] Hodgkiss, T., Hanbury, W. T., and Mejazian, M. H., "Corrosion Tests of a Range of Materials in Three MSF Plants," *Proceedings of the First World Congress on Desalination and Water Re-use*, Vol. 1, May 1983, pp. 223-232.
- [4] Scales, G. L. and Todd, B., Nichtrostende Stähle für Chemikalien-Tankschiffe, Hansa Heft 16/71.
- [5] Lee, T. S. and Tuthill, A. H., "Use of Carbon Steel to Mitigate Crevice Corrosion of Stainless Steels in Seawater," *Materials Performance*, Vol. 22, No. 1, Jan. 1973.

- [6] Simon, P. D., "Tube Sheet Corrosion and Mitigation Techniques in a Seawater Cooled Titanium-Alumina Bronze Condenser," *Corrosion* 83, Paper 77.
- [7] Campbell, H. S., *Aluminium Bronze Alloys Corrosion Resistance Guide*, CDA Publication 80.
- [8] Kido, S. and Shinohara, T., "Corrosion under Heat Flux Encountered in Desalination Plant," *Desalination*, Vol. 22, 1977, p. 369.
- [9] Moroishi, T. and Kiyuki, H., "Hydrogen Absorption of Titanium in Seawater at High Temperature," *Titanium* 80, Vol. 4, May 1980.

Supplementary Article on Environments*

*Reprinted from *Journal of Testing and Evaluation*, JTEVA, Vol. 8, No. 2, March 1980, pp. 74-79.

Harvey P. Hack¹

Galvanic Corrosion of Piping and Fitting Alloys in Sulfide-Modified Seawater

REFERENCE: Hack, H. P., "Galvanic Corrosion of Piping and Fitting Alloys in Sulfide-Modified Seawater," *Galvanic Corrosion, ASTM STP 978*, Harvey P. Hack, Ed., American Society for Testing and Materials, Philadelphia, 1988, pp. 339-351.

ABSTRACT: Two wrought piping alloys, 70-30 and 90-10 copper-nickel, were each galvanically coupled to each of four fitting alloys in sulfide-modified seawater for 30 days. The fitting alloys used were bronze (Composition M), cast Monel[®], wrought nickel-aluminum bronze, and cast 70-30 copper-nickel. The piping material to fitting material area ratio was 3:1 and the seawater velocity was 2.4 m/s. Results indicated that the galvanic relationship between M-bronze or Monel and 70-30 copper-nickel is affected by sulfide additions, in a manner that increases the corrosion of the fitting material, whereas similar couples with 90-10 copper-nickel show little effect of sulfide.

KEY WORDS: galvanic corrosion, copper-nickel alloys, pipe fittings, sulfide-induced corrosion, seawater piping

The occurrence of accelerated corrosion of copper-nickel alloys exposed to flowing seawater containing sulfide pollutants has been of concern to both the Navy [1,2] and to industry [3-5]. Many studies of the corrosion of various copper based materials have been conducted [1,5-10], and some solutions to the problem have been investigated [11-20]. The corrosion mechanism has been postulated to involve an electropositive shift in the corrosion-product film potential in the copper-nickels, and such a potential shift has been documented [1]. It would therefore be expected that the galvanic relationships between the copper-nickels and other alloys in seawater could be altered in an environment containing sulfide pollution. In polluted environments this could lead to galvanic corrosion of materials that have usually been considered compatible in more normal environments. For example, both 90-10 and 70-30 copper-nickel piping have been coupled with bronze fittings in seawater systems without unacceptable galvanic corrosion of any of the materials involved. The purpose of this study was to determine if sulfide-containing seawater would cause galvanic corrosion in certain piping-fitting combinations that would not be observed in unpolluted seawater.

Material

The piping materials chosen for this study were 90-10 and 70-30 copper-nickel. The fitting materials selected were cast bronze (Composition M), cast Monel[®] (Composition E) wrought nickel-aluminum-bronze, and cast 70-30 copper-nickel. Compositions of all materials are listed in Table 1.

¹Metallurgist, Naval Ship Research and Development Center, Annapolis, MD 21402.

TABLE 1—Composition of test materials. % by weight.

	90-10 Copper-Nickel	70-30 Copper-Nickel	M-Bronze	Nickel-Aluminum Bronze	Cast 70-30 Copper-Nickel	Monel
Copper	88.09	68.52	87.52	80.41	Balance	29.7
Aluminum	9.23	...	0.19
Iron	1.50	0.49	0.15	3.94	0.61	2.88
Nickel	9.8	30.12	0.55	4.24	30.7	60.4
Manganese	0.46	0.74	...	1.46	1.03	1.32
Tin	5.86
Lead	<0.02	0.1	1.66	0.001	0.002	...
Zinc	0.09	...	Balance
Silicon	0.08	0.43	3.48 ^a
Phosphorus	<0.02	0.001	0.006
Niobium and tantalum	0.91	1.86
Sulfur	<0.02	0.004
Carbon	0.12
Others	0.04

^aThis analysis is suspect. Silicides not detected metallographically.

Apparatus and Experimental Procedures

Corrosion exposures were conducted in polarization cells located at the Francis L. LaQue Corrosion Laboratory at Wrightsville Beach, N.C. In each cell, one piping alloy specimen and one fitting alloy specimen were mounted with their surfaces parallel to the seawater flow. The piping material to fitting material area ratio was 3:1 and the seawater velocity was 2.4 m/s. One surface of each specimen was wetted while the other was kept dry with gasketing to allow for electrical contact. Wetted surfaces of the two specimens were mounted parallel and opposing with a 6-mm gap between them. Provisions were made for the use of a silver/silver-chloride reference cell for each test unit. The sulfide level in the seawater could be controlled by the addition of sodium sulfide with metering pumps. The seawater was not recirculated but was discharged after one pass through the test cell and the subsequent neutralization of the excess sulfide. Sulfide concentrations were measured by using the *p*-phenylenediamine colorimetric technique. The dissolved oxygen in the untreated water was 5 to 9 mg/litre. No detectable pH shift was observed during the sulfide injection.

The standard specimen dimensions for these cells are 72.5 by 30.5 by 6 mm. Reduced-size specimens were mounted with nonmetallic spacers to fill the specimen holders. Specimen surface finish was 32 rms.

Galvanic couples of each piping-fitting material combination were exposed to seawater flowing at 2.4 m/s and containing 0, 0.01, or 0.05 mg/litre sulfide for 30 days. Couple potential and galvanic current were monitored. At the conclusion of the exposures the specimens were cleaned and data were recorded on weight loss and pit depth, which were converted to corrosion rates and maximum depths of attack, respectively.

Corrosion Rate and Depth of Attack

The corrosion rate and maximum depth of attack data for the fitting alloys as a function of coupling and sulfide concentration are illustrated in Figs. 1 to 4. Two vertical lines appear on the bars representing uncoupled specimens because tests on them were run in duplicate.

Figure 1 presents data for the M-bronze. There was an overall increase in the corrosion of uncoupled M-bronze specimens as the sulfide concentration was increased, as expected. Also, predictably, there is little difference in the amount of corrosion between coupled and uncoupled bronze at 0 mg/l sulfide. As the sulfide level increases, there is still little difference in behavior between uncoupled bronze and material coupled to 90-10 copper nickel. However, a significant increase in both the corrosion rate and maximum depth of attack is evident in bronze coupled to 70-30 copper-nickel in sulfide-containing seawater. Thus, although M-bronze and 70-30 cop-

M-BRONZE

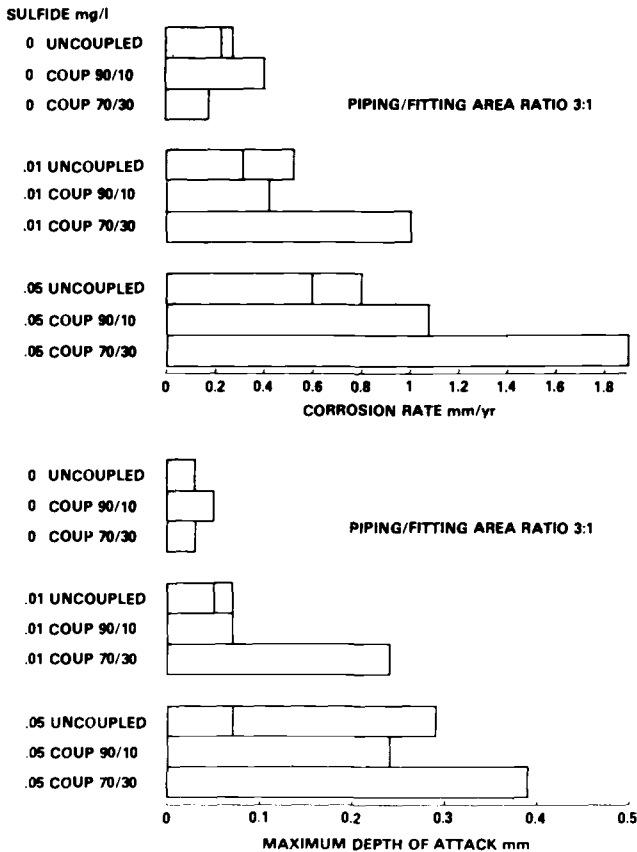


FIG. 1—Data for M-bronze.

per-nickel are galvanically compatible in unpolluted seawater, the addition of sulfide will cause galvanic attack to occur on the M-bronze. This does not take place in couples with 90-10 copper-nickel.

Figure 2 presents corrosion data for Monel. An increase in corrosion rate with increasing sulfide can be observed, although the depth of attack remains relatively unaffected. Galvanic coupling to either of the copper-nickels has little effect on the corrosion in unpolluted seawater. As sulfide is added, the corrosion of the Monel is decreased, that is, it is cathodically protected upon coupling to 90-10 copper-nickel. The amount of corrosion either remains the same or increases, depending on the sulfide level, when the Monel is coupled to 70-30 copper-nickel. This is another example of a material that is not affected by coupling to copper-nickels in unpolluted seawater but is affected by coupling to each alloy in polluted seawater.

Figures 3 and 4 present the corrosion data for nickel-aluminum-bronze and cast 70-30 copper-nickel specimens, respectively. For either material, corrosion increases with increasing sulfide and, with two exceptions, is unaffected by coupling at any sulfide level. The exceptions are the low amount of corrosion of cast 70-30 copper-nickel coupled to 90-10 copper-nickel, and the low depth of attack when it is coupled to 70-30 copper-nickel. Since these occurrences were not duplicated at either the higher or the lower sulfide level, they are not considered significant.

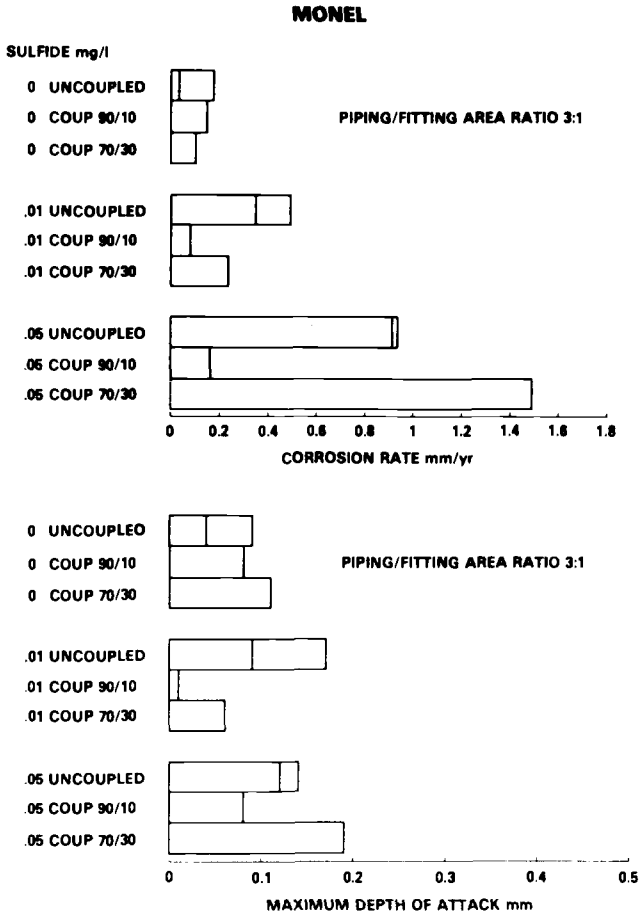


FIG. 2—Data for Monel.

NI-AL-BRONZE

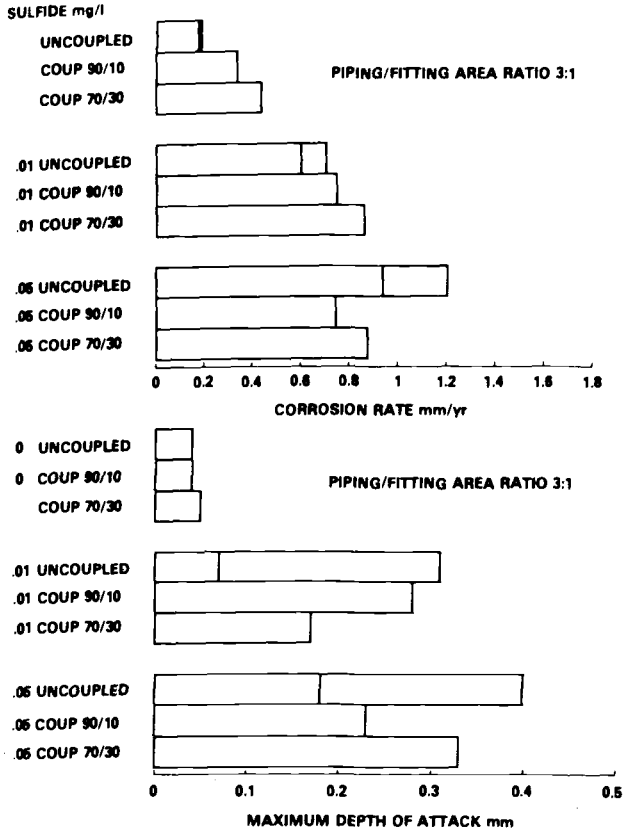


FIG. 3—Data for nickel-aluminum bronze.

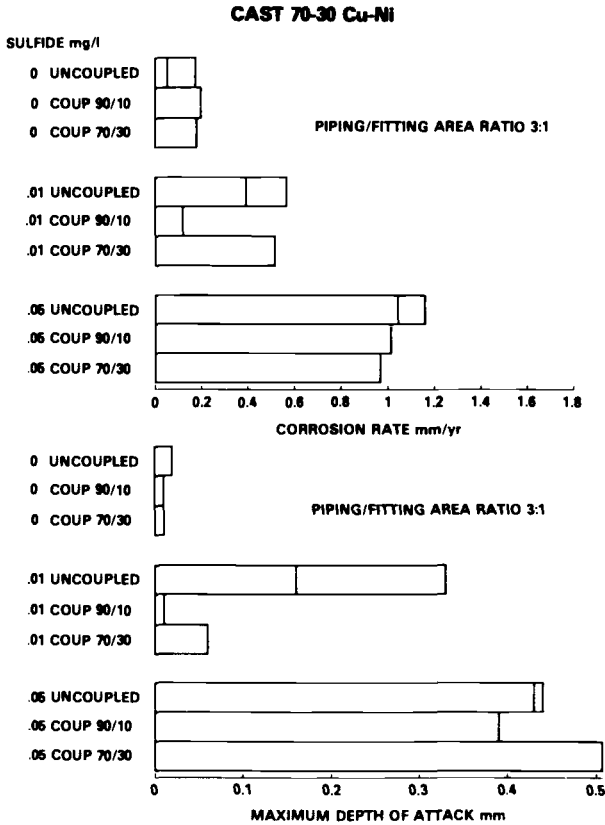


FIG. 4—Data for cast 70-30 copper-nickel.

Figures 5 and 6 illustrate the behavior of the wrought 90-10 and 70-30 copper-nickel piping specimens, respectively, in the couples with all the materials. Four uncoupled control specimens were tested at each sulfide level and therefore four lines are shown on these bars. Once again, a general increase in the corrosion of both copper-nickels was evident on uncoupled specimens as the sulfide concentration was increased. Because of the large scatter in the maximum depth of attack data from the uncoupled control specimens of both alloys, no additional conclusions could be drawn from these data. Several trends can be observed in the corrosion rate data, however. Coupling to M-bronze does not significantly affect the corrosion rate of 90-10 copper-nickel because coupled values are within the control specimen scatter. Even if scatter is considered, coupling to 70-30 copper-nickel decreases the corrosion rate if sulfide is present. Thus the 70-30 copper-nickel is receiving cathodic protection from the increased corrosion of the M-bronze in the sulfide-containing seawater. The increase in the corrosion rate of 90-10 copper-nickel coupled to Monel corresponds with the previously reported decrease in corrosion of the Monel in this couple in sulfide-containing seawater. No conclusion can be drawn about the corrosion of 70-30 copper-nickel when it is coupled to Monel, or about the behavior of either of the copper-nickels when coupled to nickel-aluminum bronze or to cast 70-30 copper-nickel.

Corrosion Potentials

Figures 7 to 14 present the average corrosion potentials of uncoupled alloys and couples as a function of sulfide concentration. The potentials illustrated are averaged only over the last 20

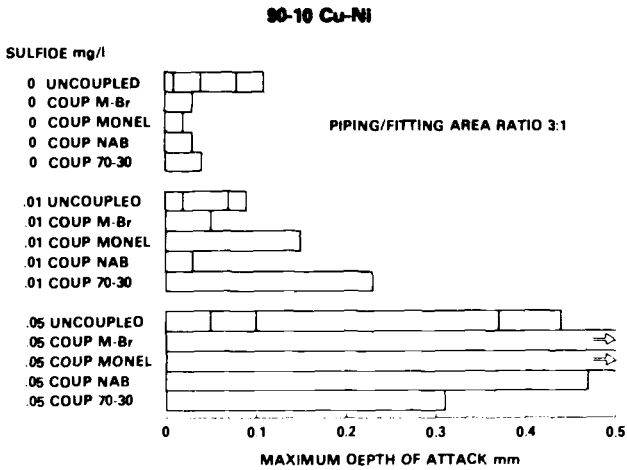
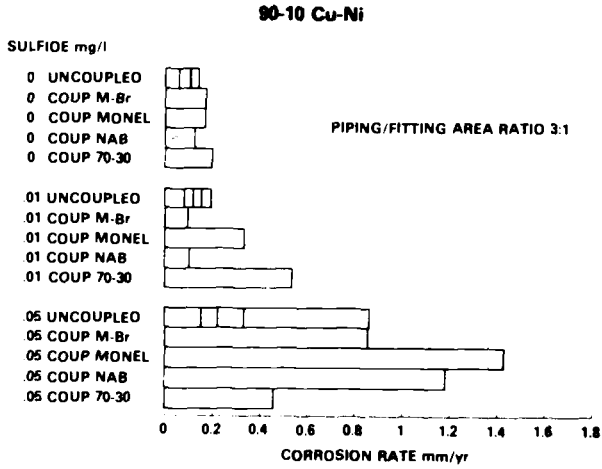


FIG. 5—Data for 90-10 copper-nickel.

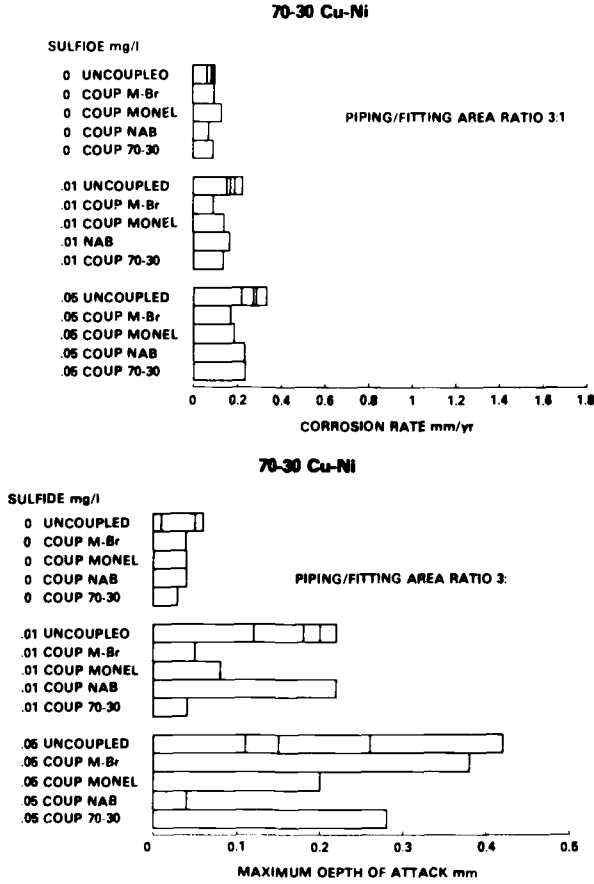


FIG. 6—Data for 70-30 copper-nickel.

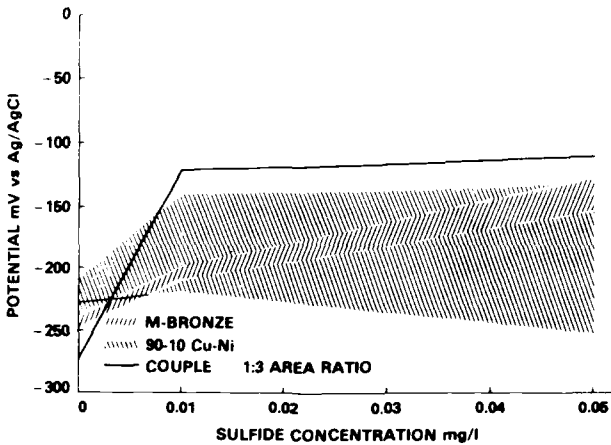


FIG. 7—Potentials of M-bronze and 90-10 copper-nickel.

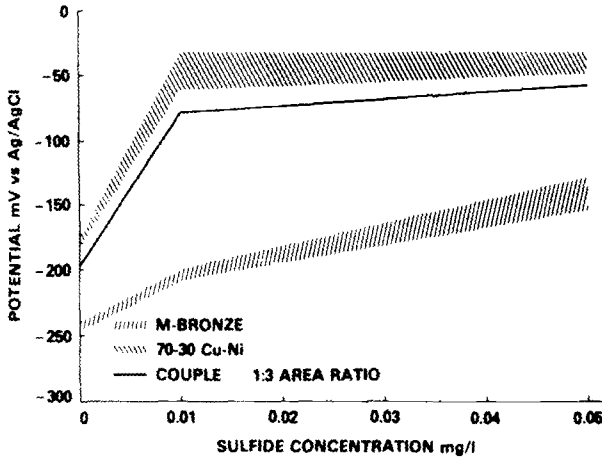


FIG. 8—Potentials of M-bronze and 70-30 copper-nickel.

days of testing. This information is presented as a band because there were four piping alloy control specimens for each material at each level. In addition, there were two fitting alloy control specimens for each material at each sulfide level and, therefore, this information is also presented as a band. The couple potential information was derived from individual coupled specimen pairs and is illustrated by a solid line on the figures.

Figures 7 and 8 present the data for M-bronze and 90-10 or 70-30 copper-nickel, respectively. In Fig. 7 all potentials are within the same range and significant galvanic interactions would not be expected. As mentioned earlier, none were observed. A small (50 mV) potential difference can be seen between 70-30 copper-nickel and M-bronze in Fig. 8 at 0 mg/litre sulfide. When sulfide is added this difference increases to 140 mV, which could be an explanation for the behavior of these couples.

Figure 9 indicates that Monel tends to be protected by 90-10 copper-nickel when sulfide is not present but has little galvanic interaction at higher sulfide levels. In Fig. 10 a reversal can be seen in the behavior of Monel and 70-30 copper-nickel. The Monel is protected when sulfide is

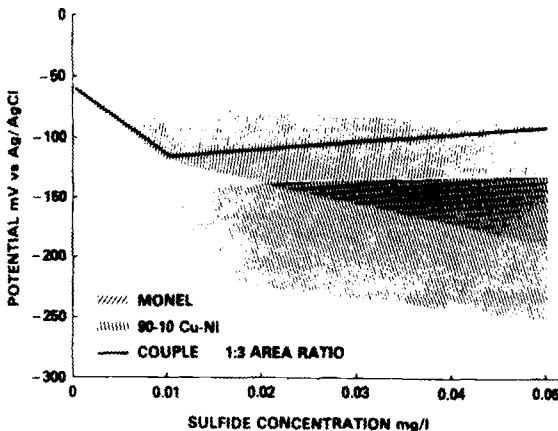


FIG. 9—Potentials of Monel and 90-10 copper-nickel.

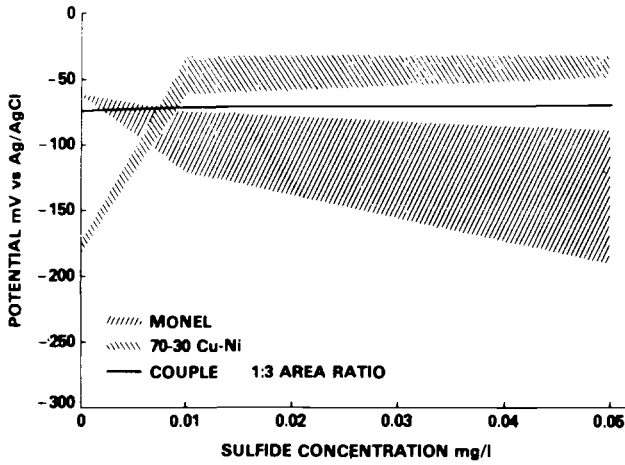


FIG. 10—Potentials of Monel and 79-30 copper-nickel.

not present and becomes subject to galvanically accelerated corrosion in the presence of sulfides. Both of these observations are verified by the corrosion data.

Nickel-aluminum-bronze tends to be equal in potential or to be slightly cathodic to 90-10 copper-nickel with the difference in potential increasing somewhat when sulfide is present. This can be seen in Fig. 11. Figure 12 indicates that the potential of nickel-aluminum bronze is similar to, or slightly anodic to, that of 70-30 copper-nickel throughout the range of sulfide concentrations. Thus a difference in corrosion behavior of nickel-aluminum bronze coupled to 90-10 or to 70-30 copper-nickel is expected. The reason this did not occur in these exposures may be due to the polarization characteristics of the nickel-aluminum bronze.

In Fig. 13 an increased potential difference can be observed in sulfide between cast 70-30 copper-nickel and 90-10 copper-nickel. Cathodic protection of the cast material and increased corrosion of the 90-10 copper-nickel should therefore be observed in sulfide-containing seawater.

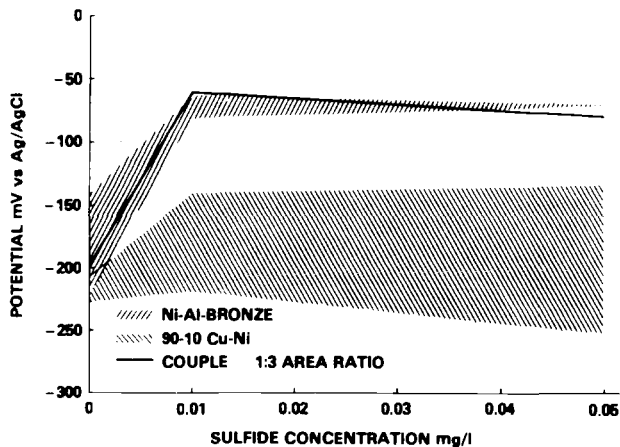


FIG. 11—Potentials of nickel-aluminum bronze and 90-10 copper-nickel.

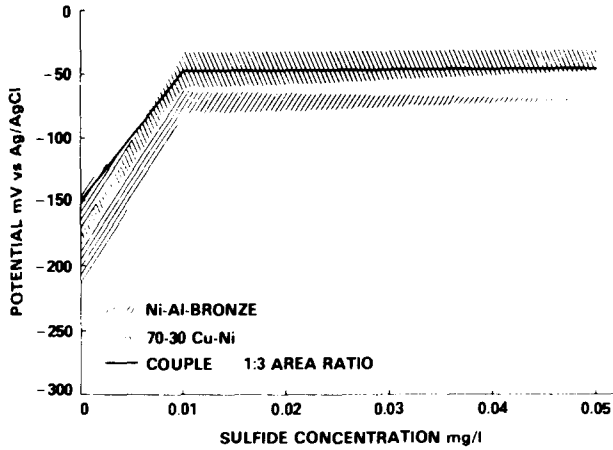


FIG. 12—Potentials of nickel-aluminum bronze and 70-30 copper-nickel.

ter. Although tendencies in this direction can be observed in the corrosion data in Figs. 4 and 5, these tendencies are small compared to the data scatter. Figure 14 illustrates that the potentials of cast and wrought 70-30 copper-nickel are similar throughout the range of sulfide concentrations. Therefore, no galvanic interaction was expected and none was observed.

It should be noted that the potentials of all alloys tested, except Monel, shifted in the electro-positive direction when sulfide was added. All of these materials derive their corrosion resistance from the buildup of a copper-oxide corrosion product film. The inclusion of sulfide ions into the film as it is being formed is thought to cause the cathodic shift by increasing film conductance through a semiconductor doping mechanism. The Monel derives its corrosion resistance from the formation of a complex nickel-oxide film that might not behave in the same manner as the copper oxide. In fact, the potential of the Monel shifted to being more electro-negative when sulfide was present.

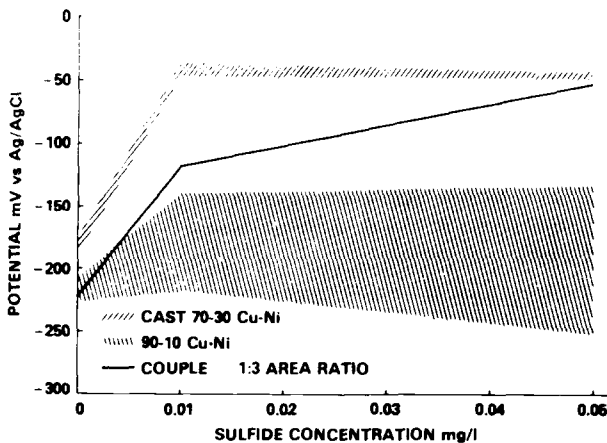


FIG. 13—Potentials of 70-30 copper-nickel and 90-10 copper-nickel.

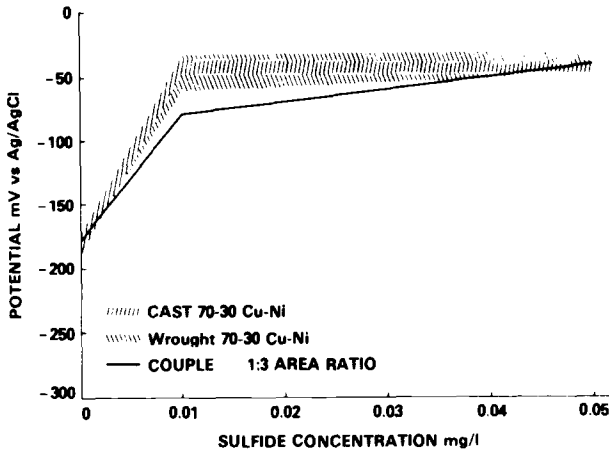


FIG. 14—Potentials of cast and wrought 70-30 copper-nickel.

Conclusions

There is a change in the galvanic relationship between normally compatible piping and fitting alloys in sulfide-containing seawater. This change causes an increase of corrosion of M-bronze or Monel when these materials are used with 70-30 copper-nickel in sulfide-containing seawater. The behavior of these alloys when they are coupled to 90-10 copper-nickel is relatively unaffected by the sulfides. All of these couples have been used and are usually considered compatible in environments without sulfide. Therefore, if a polluted environment is to be encountered, the galvanic interrelationships of all materials in the systems involved should be reappraised.

Acknowledgments

The author gratefully acknowledges the assistance of Mr. T. S. Lee of the Francis L. LaQue Corrosion Laboratory, Wrightsville Beach, N.C. in conducting the experiments reported here. Funding for this study was provided through the Naval Sea Systems Command, Code 03522, Dr. H. Vanderveldt, Materials Block Program (PE62761N SF54-500-591).

References

- [1] Gudas, J. P. and Hack, H. P., "Sulfide-Induced Corrosion of Copper-Nickel Alloys," Paper 93, presented at Corrosion/77, San Francisco, Calif., 14-18 March 1977.
- [2] Gudas, J. P., Danek, G. J., and Niederberger, R. B., "Accelerated Corrosion of Copper-Nickel Alloys in Polluted Water," Paper 76, presented at Corrosion/76, Houston, Tex., 22-26 March 1976.
- [3] Sato, S., "Engineering Experience—Japanese Utility Industry," paper presented at seminar on condensers, Columbus, Ohio, 2-4 June 1975.
- [4] Sato, S., "Corrosion and Its Prevention in Copper Alloy Condenser Tubes Under Modern Conditions," *Reviews on Coatings and Corrosion*, Freund Publishing House Ltd., Tel-Aviv, March 1976, pp. 1-23.
- [5] Newton, E. H. and Birkett, J. D., "Survey of Condenser Tube Life in Salt Water Service," Report 278, Contract No. 1401-0001-956, Report to the Office of Saline Water, Department of the Interior, Washington, D.C., Aug. 1967.
- [6] Bates, J. F. and Popplewell, J. M., "Corrosion of Condenser Tube Alloys in Sulfide Contaminated Brine," *Corrosion*, Vol. 31, No. 8, Aug. 1975, pp. 269-275.
- [7] LaQue, F. L., *Marine Corrosion: Causes and Prevention*, John Wiley and Sons, New York, 1975, pp. 122-123.

- [8] Kawai, K., "Study on 10% Copper-Nickel Condenser Tube Alloys," *Journal of the Japan Copper and Brass Research Association*, Vol. 11, No. 1, Jan. 1972, pp. 119-130.
- [9] Sato, S., "Some Factors Affecting the Performance of Copper Alloy Condenser Tubes in Recent Steam Power Plants," *Japan Journal of Thermal Power*, Vol. 21, No. 3, March 1970, pp. 295-305.
- [10] Gudas, J. P. and Hack, H. P., "Parametric Evaluation of Susceptibility of Cu-Ni Alloys to Sulfide-Induced Corrosion," Paper 22, presented at Corrosion/78, Houston, Tex., 6-10 March 1978.
- [11] Pearson, C., "Role of Iron in the Inhibition of Corrosion of Marine Heat Exchangers—A Review," *British Corrosion Journal*, Vol. 7, No. 3, March 1972, pp. 61-68.
- [12] "Ferrous Sulfate Treatment to Prevent Corrosion of Condenser and Heat Exchanger Tubes," Technical Bulletin TB/7, Yorkshire Imperial Metals Ltd., Leeds, England, April 1970.
- [13] Bostwick, T. W., "Reducing Corrosion of Power Plant Condenser Tubing with Ferrous Sulfate," *Corrosion*, Vol. 17, Aug. 1961, pp. 12-19.
- [14] Lockhart, A. M., "Reducing Condenser Tube Corrosion at Kincardine Generating Station with Ferrous Sulfate," *Proceedings of the Institution of Mechanical Engineers*, Vol. 179, Pt. 1, No. 16, 1964-1965, pp. 495-509.
- [15] Morgan, J. H., "Cathodic Protection, Iron Injection and Chlorination in Marine Heat Exchangers," Paper presented at the 3rd International Congress on Marine Corrosion and Fouling, National Bureau of Standards, Gaithersburg, Md., 2-6 Oct. 1972.
- [16] Sugawara, H. and Shimodaira, S., "On the Corrosion Protection of Aluminum Brass by Ferrous or Ferric Ion," *Journal of Japanese Institute of Metals*, Vol. 30, No. 9, Sept. 1966, pp. 869-873.
- [17] Hack, H. P. and Gudas, J. P., "Inhibition of Sulfide-Induced Corrosion of Copper-Nickel Alloys with Ferrous Sulfate," Paper 23, presented at Corrosion/79, National Association of Corrosion Engineers, Houston, Tex., 6-10 March 1979.
- [18] Isherwood, B. F., "The Experiments Made by Mr. Uthemann to Discover a Process for Preventing the Corrosion of Copper and Brass by Sea-Water Under the Conditions Found in the Surface-Condensers of Marine Steam-Engines," *Journal of the American Society of Naval Engineers*, Vol. 19, No. 3, Aug. 1907, pp. 601-624.
- [19] Hack, H. P. and Gudas, J. P., "Inhibition of Sulfide-Induced Corrosion with a Stimulated Iron Anode," Paper 234, presented at Corrosion/79, Atlanta, Ga., 12-16 March 1979.
- [20] North, R. F. and Pryor, M. J., "The Protection of Copper by Ferrous Sulfate Additions," *Corrosion Science*, Vol. 8, No. 3, March 1968, pp. 149-157.

Author Index

A-C

Adey, R. A., 96
 Astley, D. J., 53
 Baboian, R., 249
 Corbett, R. A., 235
 Crowe, C. R., 118

D-G

Doyle, D. P., 161
 Eckenrod, J. J., 310
 Efird, K. D., 260
 Escalante, E., 193
 Fu, J. W., 79
 Gehring, G. A., Jr., 301

H-K

Hack, H. P., editor, 1, 136, 339
 Haynes, G., 249
 Hinton, B. R. W., 35
 Jenkins, J. F., 174
 Kasper, R. G., 118
 Kolts, J., 203
 Kovach, C. W., 310

M-P

Morrison, W. S., 235
 Morton, A. G. S., 291
 Niku, S. M., 96
 Oldfield, J. W., 5, 323
 Pinnow, K. E., 310
 Pollock, W. J., 35

R-S

Redmerski, L. S., 310
 Schick, G., 283
 Scully, J. R., 136
 Snyder, R. J., 235
 Sridhar, N., 203
 Streicher, M. A., 220

T-Z

Todd, B., 323
 Turcotte, R., 249
 Turner, J. M., 178
 Wilhelm, S. M., 23
 Wright, T. E., 161
 Yau, Y.-H., 220
 Zaharani, al, S. G., 323

Subject Index

A

Acid cleaning, 323
 Acids, 203, 220
 Active-passive regions, 203
 Alloy 625, 136
 Aluminum (*See also* Galvanic couples)
 anodes, 186
 atmospheric corrosion, 161
 automobile trim, 249
 coatings, 35
 Ammeter, zero resistance, 203
 Anodes, sacrificial, 53, 178, 323
 Anodic reaction, 15, 53
 ASTM standards
 A 262: 239
 A 475: 284
 D 1141: 311
 D 1248: 184
 F 519: 36
 G 1: 162
 G 5: 120
 G 15: 178, 260
 G 28: 240
 G 51: 196
 G 57: 182, 196
 G 78: 240
 Automobile components, 249

B

BASIC programming language, 53
 Bimetallic joints, 323
 Boundary-element modeling, 79, 98
 Bumpers, electroplated, 249

C

Cadmium coatings, 35
 Carbon dioxide, 260
 Cathodic polarization, 53

Cathodic protection
 modeling by numerical analysis, 79, 96
 of navy ships, 291
 in power plant condensers, 301, 310
 in seawater systems, 53
 in soils, 178
 of telephone cable plant, 291
 Cathodic reaction, 16
 Cladding
 aluminum, 35
 cadmium, 35
 chromium, 163
 CLIMAT test, 161
 Coatings (*See* Cladding; Paint blistering)
 Computer modeling and prediction (*See also*
 Mathematical modeling and predic-
 tion)
 BASIC programming language, 53
 boundary-element modeling, 79
 COSMIC/NASTRAN program, 133
 finite-element modeling, 79, 136, 188
 general discussion, 96
 MARC program, 136
 in seawater systems, 53
 WECAN program, 136
 Condensers, power plant, 53, 301, 310
 Cooling systems, 53, 249, 323
 Copper alloys, 53, 136
 galvanic effect on aluminum, 162
 Muntz metal, 136, 301
 tubesheets, 301
 Corrosion, galvanic (*See also* Galvanic cou-
 ples; Hydrogen embrittlement; Steels)
 in acids, 203, 220
 atmospheric, 161, 298
 on automobiles, 249
 cathodic control methods, 53, 79, 96, 178
 causes, 299
 computer modeling and prediction, 53, 79,
 96, 133, 136, 188

Corrosion, galvanic (cont.)

- in condensers, power plant, 53, 301, 310
 - in cooling systems, 53, 249, 323
 - corrosion products, 23
 - in desalination plants, 323
 - designing for, 174
 - electrochemical theory (*See also* Galvanic couples; Ionic currents), 5, 16, 80, 178
 - in evaporators, 323
 - of fasteners, dissimilar metal, 249
 - of flash chambers, 323
 - in gas production, 260
 - in heat exchangers, 53, 79, 136, 297, 323
 - marine, 53, 96, 291
 - mathematical modeling and prediction, 5, 11, 118, 136
 - of offshore structures, 107
 - in oil and gas production, 260
 - in oxidizing solutions, 203
 - of pipes and piping systems, 53, 107, 178, 293
 - potential, 203
 - of pumps, 297, 323
 - in seawater, 53, 136, 260, 301, 310, 323
 - of ships, 53, 96, 291
 - in soils, 178, 193
 - of telephone cable plant, 283
 - testing
 - atmospheric corrosion of bare metals, 161
 - of cladded steel, 35
 - condensers, simulated, 301
 - wire-on-bolt, 161
 - tube-tubesheet, 53, 79, 136, 301, 323
 - tubing, 53, 136, 301, 310, 323
 - underground, 178, 283
 - of valves, 174, 296
 - of waterboxes, 323
- Corrosion prevention (*See* Cladding; Corrosion, galvanic; Paint blistering)
- Corrosion products, 23
- dielectric properties, table, 25
- COSMIC/NASTRAN computer program, 133
- Coupling (*See* Galvanic couples; Galvanic series)
- Crevice corrosion, 23, 310, 323
- Crude oil, 260
- Cupronickel, 323
- Current density mapping, 118, 136

D

- Deaeration, 323
- Desalination plants, 323
- Designing for corrosion control, 174

E

- Electric fields, 53, 118
- Electrode potential, 53
- Electroplated bumpers, 249
- Evaporators, 323

F

- Fasteners, dissimilar metal, 249
- Finite-element analysis, 79, 98, 118, 136
- Flash chambers, 323

G

- Galvanic corrosion (*See* Corrosion, galvanic)
- Galvanic couples (*See also* Galvanic series)
 - aluminum-steel, 35, 162, 249
 - cadmium-steel, 35
 - chromium-steel, 249
 - copper-nickel-Muntz metal, 136
 - iron-copper, 118
 - Monel-copper-nickel, 136
 - nickel-aluminum-bronze-Alloy 625, 136
 - in oxidizing solutions, 203
 - titanium-nickel-aluminum-bronze, 136
 - zinc-copper-nickel, 136
 - zinc-steel, 193, 249, 288
- Galvanic series, table, 17, 180
- Galvanized steel, 162, 249
- Gas production, 260
- Graphite
 - galvanic effect on aluminum, 162
 - in oxidizing solutions, 203

H

- Heat exchangers, 53, 79, 136, 297, 323
- Heyrovsky's reaction, 19
- Hydrogen embrittlement, 35, 193, 260, 310
- Hydrogen evolution, 5
- Hydrogen stress cracking, 35, 193, 260, 310
- Hydrogen sulfide, 260

I-L

- Impressed current protection, 53, 310
- Ionic currents, 118
- Joints, bimetallic (*See also* Galvanic couples), 323
- Lead, 162

M

- Magnesium anodes, 178
- MARC computer program, 136
- Marine propulsion, 53

- Marine systems, 53, 96, 291
- Mathematical modeling and prediction (*See also* Computer modeling and prediction)
- electrochemical theory, 5
 - nonlinear polarization, 118
 - Wagner numeric analysis, 11, 151
- Metal oxides, 23
- Metal sulfides, 23
- Metallic corrosion (*See* Corrosion, galvanic; Galvanic couples; Hydrogen embrittlement)
- Metals (*See under* specific metals; *See also* Galvanic couples)
- energy required to convert from ore, table, 179
 - galvanic series, tables, 17, 180
 - hydrogen evolution on, table, 20
 - on navy ships, 291
 - soil resistivity and temperature effects on, 193
 - standard potentials, table, 17
- Mixed potentials, 5
- Monel, 136, 162
- Muntz metal, 136, 301
- N**
- Nickel alloys
- ALLCORR, 235
 - Hastelloy, 203, 235
 - Inconel, 235
 - Monel, 136, 162
 - in oil and gas production, 260
 - in seawater systems, 53
 - welded dissimilar, 235, 310
- Ni-resist, 323
- Nonlinear polarization, 118
- Numerical analysis (*See* Computer modeling and prediction; Mathematical modeling and prediction)
- O**
- Offshore structures, 107
- Oil and gas production, 260
- One-dimensional flow, 53
- Oxidizing solutions, 203
- Oxygen reduction, 5
- P**
- Paint blistering, 249
- Pipes and piping systems, 339-351
- metal, 53, 107, 178, 293
 - plastic, 53
- Pitting, 23, 323
- Polarization curves
- iron-copper, illus., 126
 - oxidizing solutions, 203
- Polarization parameter, 11
- Potential distribution, 118, 136
- Primary current, 136
- Probes, vibrating, 118
- Protection, cathodic (*See* Cathodic protection)
- Pumps, 297, 323
- R**
- Radioactive waste, 235
- Rectifiers, 184
- S**
- Scanning vibrating electrodes, 118
- SEA-CURE (UNS S44660) condenser tubing, 310
- Seawater systems, 260,
- cathodic protection in, 53
 - condensers, 301, 310
 - desalination plants, 323
 - distribution of galvanic corrosion in, 53
 - oil and gas production, 260
 - tube-tubesheet galvanic corrosion, 136
- Secondary current, 136
- Semiconductor oxides, 23
- Semiconductor theory of corrosion, 23
- Ship hulls, corrosion in, 53, 96, 292
- Ships, naval, 291
- Simulated testing (*See also* Computer modeling and prediction), 301
- Simulation, computer (*See* Computer modeling and prediction)
- Soils, 178, 193
- Solution resistivity, 136
- Steam condensers, 53, 301, 310
- Steels
- austenitic stainless, 203, 220
 - chromium content, galvanic effects of, 220
 - chromium plated, 162
 - in desalination plants, 323
 - duplex Fe-Cr-10%Ni alloys, 203, 220
 - Ferrallium, 203
 - ferrite, 220
 - ferritic stainless tubing, 310
 - galvanized, 162, 249
 - high-strength 4340, 35
 - hydrogen evolution on, table, 20
 - low alloy, 35
 - mild, galvanic influence on aluminum, 162
 - in oil and gas production, 260

Steels (cont.)

- stainless tubing, 136, 301
- Type 301 stainless, 193
- Type 304 stainless, 162
- Type 316 stainless, 277
- Type 410 stainless, 276
- Stress cracking, 35, 193, 260, 310

T

- Tafel equations, 7, 203
- Tafel's reaction, 19
- Telephone cable plant, 283
- Tertiary current, 136
- Testing, simulated (*See also* Computer modeling and prediction), 301
- Three-dimensional electric fields, 118
- Titanium alloys, 53, 136, 203, 301, 323
- Trim, automotive, 249
- Tube-tubesheet galvanic corrosion, 53, 79, 136, 301, 323
- Tubing, 53, 136, 301, 310, 323

U-V

- Underground corrosion, 178, 283
- Valve engineering, 174, 296
- Volmer's reaction, 19

W

- Wagner number analysis, 11, 151
- Waterboxes, 323
- WECAN computer program, 136
- Welded dissimilar nickel alloys, 235
- Wire-on-bolt test, 161

Z

- Zero-resistance ammeter, 203
- Zinc anodes, 53, 136, 186

ISBN 0-8031-0981-4